Design and Development of Metal Oxides and Chalcogenides for Solar Fuel Synthesis from Carbon Dioxide

A Thesis submitted for the degree of

Doctor of Philosophy

As a part of

Ph.D. Programme (Chemical Science)

by

Mr. Risov Das

New Chemistry Unit

Jawaharlal Nehru Centre for Advanced Scientific Research

(A Deemed University)

Bangalore-560064 (INDIA)

July 2022

"It is right that we should stand by and act on our principles; but not right to hold them in obstinate blindness or retain them when proved to be erroneous."
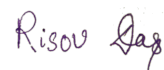
-Michael Faraday

Dedicated to Arunava Saha

Declaration

I hereby declare that the matter embodied in the thesis entitled *"Design and Development of Metal Oxidse and Chalcogenides for Solar Fuel Synthesis from Carbon Dioxide"* is the result of investigations carried out by me at the New Chemistry Unit, Jawaharlal Nehru Centre for Advanced Scientific Research, Bengaluru, India under the supervision of Prof. Sebastian C. Peter and that it has not been submitted elsewhere for the award of any degree or diploma. In keeping with the general practice in reporting scientific investigations, due acknowledgement has been made wherever the work described is based on findings of other investigators. Any omission that might have occurred by oversight or error of judgement is regretted.

Date: .28. 07. 2022

Bengaluru, India   Risov Das

Certificate

I hereby declare that the matter embodied in the thesis entitled "***Design and Development of Metal Oxides and Chalcogenides for Solar Fuel Synthesis from Carbon Dioxide***" has been carried out by Mr. Arjun Cherevotan at the New Chemistry Unit, Jawaharlal Nehru Centre for Advanced Scientific Research, Bengaluru, India under my supervision and that it has not been submitted elsewhere for the award of any degree or diploma.

Date: 28.07. 2022

Bengaluru, India   Prof. Sebastian C. Peter

Acknowledgement

"A grateful heart is a magnet of miracles"

❖ The successful accomplishment of my PhD thesis includes immense contribution from various people for their constant help, support and enthusiasm that motivated me to move ahead however, difficult the path be. The thesis would be incomplete without me expressing my gratitude towards them.

❖ First and foremost, with deepest gratitude and great humility I would like to extend my sincere thanks to my mentor, supervisor and guide, ***Prof. Sebastian C. Peter*** for his contribution in shaping the foundation of my research career. His persistent support, advice, criticism and wisdom not only inspired me to do better work each day but also helped me to grow as an independent individual. Apart from him being an excellent scientist I have known him as one the most extraordinary human being. Not only have I learnt science from him but also each of his words stimulated optimism and confidence in me. He taught me perseverance and most importantly how to remain calm and composed in every situation. Whenever a paper got rejected and most of us would be dejected, he is the one to always remain hopeful and positive. He has been like an umbrella for our SCP lab family. I am always indebted to him more than he knows. Today words are too less to express my gratefulness to him. Thank you, sir, for being so kind, gracious and for everything that helped me to improve myself each day.

❖ I would like to express my sincere thanks to **Prof. C. N. R. Rao, FRS, founder of New Chemistry Unit, Jawaharlal Nehru Centre for Advanced Scientific Research** for being the epitome of inspiration, generous support and encouragement throughout my JNC life.

❖ I also thank Prof. Subi J. George (chairman) for providing the infrastructure and necessary facilities to carry out my research work.

❖ I would like to thank all my course instructors Prof. Sebastian C. Peter, Prof. Chandrabhas Narayana, Prof. A. Sundaresan, Prof. Kanishka Biswas, Prof. Sarit S. Agasti, and Dr. Premkumar Senguttuvan for their excellent courses.

❖ I take this opportunity to thank my collaborators: Prof. Abhishek Kumar Singh (IISC Bangalore), Dr. Jhon Mondal (IICT Hyderabad) Dr. Vinod C. Prabhakaran (NCL Pune), Dr, Ritesh Kumar Singh (IISC), Arko Parui (IISC), Ratul Paul (IICT Hyderabad), Dr. Raju.

❖ My sincere thanks to all the technical staff of JNCASR: Mr. Sreenivas, Mrs. Usha, Mr. Anil, Ms. Selvi, Mr. Mahesh, Mr. Vasu, Mr. Deepak, Mr. Shivakumar, Mr. Rahul and Ms. Meenakshi for their help with the various characterization techniques.

❖ I would like to thank Melissa, Naveen, JNC administration and academic, complab, students residence, library, Dhanvantari and Security.

❖ I would like to thank CSIR for research fellowship. I would like to thank JNCASR, DST, DESY-Germany and RAK for various fundings.

Preface

The thesis is majorly divided into seven chapters.

Chapter 1 is about a brief overview of the climate change due to rising CO_2 concentration in the environment. The ever-increasing energy demand and over dependence on fossil fuel drive this process. The capture and conversion of CO_2 is a viable approach to tackle this challenge. Different routes used for the conversion of CO_2 to useful products and fuels will be discussed in this chapter. A particular focus will be given to Photocatalytic CO_2 reduction (PCR) and its advantages over other conversion methods will be explained. In photocatalysis, the major role is played by the surface of light active semiconductor. Hence the strategies explored in the literature to fine tune the surface and electronic properties of the semiconductors will be thoroughly described. The effect of morphology variation, heterojunction formation, vacancy generation, charge separation and strain engineering in tuning the activity and durability will be described in this chapter.

Chapter 2. The first working chapter of the thesis describes the suitable solvent selection during photocatalytic CO_2 reduction. Water is the commonly used reaction medium for PCR. However, for CO_2 reduction reaction the low solubility of CO_2 in water is a major drawback. Organic solvents such as acetonitrile, EAA, TEOA, TEA etc. have been used either for the better dissolution of CO_2 or as a sacrificial electron donor. Being susceptible to degradation under photo-illumination, the organic additives can give rise to carbonaceous products which can also be obtained from CO_2RR. This leads to inaccurate estimation of the results and inaccurate conclusion of the catalytic activity. In this chapter, we have systematically investigated the role of solvents and its effect towards the activity of catalyst during photocatalytic CO_2 reduction reaction. To study this, two model catalysts have been chosen- Pt-TiO_2@g-C_3N_4, a well explored photocatalyst and BCN/$CsPbBr_3$, a new photocatalyst which is sensitive to moisture. The catalytic tests have been performed under visible light and full arc which contains high energy UV light as well as visible light. The experimental results suggest that all the organic solvents deteriorated under full arc light giving rise to CO, CH_4, C_2H_4 and H_2. However, the catalysts are stable under visible light except ethyl acetate. On the basis of these observations, a guideline for the usability of organic solvents were given in this chapter.

In **Chapter 3**, we designed a metal oxide semiconductor heterojunction consisting of $BiVO_4$ and WO_3 as a photocatalyst for the efficient conversion of carbon dioxide (CO_2)

selectively to methane under visible light in the absence of a sacrificial agent. Good charge transport properties of WO_3 and good optical absorption properties of $BiVO_4$ has been coupled through the formation of heterostructure. Furthermore, analysis of the lattice parameters from XRD pattern suggests that the internal strain of $BiVO_4$ catalyst has been relaxed upon introduction of WO_3. Here Z-scheme system of electron transfer was proposed. The reason behind more than 99.5% methane selectivity and very high activity by strain relaxed heterojunction photocatalyst were found out by the help of DFT and DRIFTS. This chapter provides fundamental insights for constructing high-performance heterojunction photocatalysts for the selective conversion of CO_2 to desired chemicals and fuels.

Chapter 4 deals with another composite catalyst derived from TiO_2 and Bi_2MoO_6. Despite of the huge potential, TiO_2 suffers from fast photogenerated charge recombination and inappropriate bandgap for visible light driven charge generation which hinders its performance. In this chapter, TiO_2 was activated for visible light driven CO_2 reduction in the presence of Bi_2MoO_6 as an electron donor. The suitable band positions of the two semiconductors helps transfer the photogenerated electrons from the conduction band of Bi_2MoO_6 to the conduction band of TiO_2 even under visible light illumination. Furthermore, the introduction of oxygen vacancies in TiO_2 results in enhanced CO_2 adsorption and conversion. Finally, the mechanistic investigation for the formation of methanol on oxygen deficient TiO_2 have been understood from DRIFTS analysis. In previous chapters, only C1 products have been obtained from the photoreduction of CO_2.

Chapter 5 describes the importance of charge polarized centers in photocatalyst which facilitate the formation of C2 product. Obtaining multicarbon products via carbon dioxide (CO_2) photoreduction is a major catalytic challenge. Complex design of multicomponent interfaces that are exploited to achieve this chemical transformation, often leads to untraceable deleterious changes in the interfacial chemical environment affecting CO_2 conversion efficiency and product selectivity. Alternatively, robust metal centres having asymmetric charge distribution can effectuate C-C coupling reaction through the stabilization of suitable intermediates, for desired product selectivity. However, generating inherent charge distribution in a single component catalyst is a difficult material design challenge. To that end, herein, we present a novel photocatalyst, $Bi_{19}S_{27}Cl_3$, which selectively converts CO_2 to a C_2 product, ethanol, in high yield under visible light irradiation. The intrinsic electric field induced by the charge polarized bismuth centres renders better separation efficiency of photogenerated

electron-hole pair. Furthermore, the charge polarized centres yield better adsorption of CO*
intermediate and accelerate the rate determining C-C coupling step through the formation of
OCCOH intermediate. Formation of these intermediates was experimentally mapped by *in-situ*
FTIR spectroscopy and further confirmed by theoretical calculation.

In **Chapter 6**, we will go through another novel photocatalyst based on red phosphorus and
Bi_2MoO_6 for the reduction of CO_2 to ethanol. Direct photocatalytic conversion of CO_2 to
ethanol remains a scientific challenge because of the sluggish kinetics of C–C coupling and
complex multielectron transfer processes. To achieve a green transformation of CO_2 to C2
products using naturally abundant sunlight and water requires the smart design of an efficient
catalyst by selecting the right combination of atoms either in elemental or in compound form.
In this chapter, we have designed a composite photocatalyst composed of earth abundant red
phosphorus (RP) in nanosheet morphology decorated with Bi_2MoO_6 nano-particles. The
composite synthesised by a facile ultrasonication method produces 51.8 $\mu mol\ g^{-1}\ h^{-1}$ of ethanol
from CO_2. The ability of RP for the conversion of CO_2 to C1 has been altered by the
introduction of Bi_2MoO_6. *In-situ* Diffuse Reflectance Infrared Fourier Transform Spectroscopy
(DRIFTS) and Kinetic Isotopic Effect (KIE) analysis shed light on the mechanistic pathway,
which propose that the presence of Bi–Mo dual sites play a crucial role in the C–C coupling
toward the formation of ethanol. Spectroscopic evidence and isotope labelling experiments
suggest that the intermediate OCH_3* is the key active species for ethanol formation *via* self-
coupling followed by proton transfer.

Chapter 7 is about an organic-inorganic hybrid catalyst derived from a carbazole based porous
organic polymer (POP) and $In_{2.77}S_4$. By using a co-operative endeavour of catalytically active
In centres and light harvesting POPs, the composite catalyst showed 98.9% C_2H_4 formation
selectivity with 65.75 $\mu mol\ g^{-1}\ h^{-1}$ rate. Two different oxidation states of $In_{2.77}S_4$ spinel was
exploited for C-C coupling process and this phenomenon was investigated by X-ray
Photoelectron Spectroscopy (XPS), X-ray Absorption Spectroscopy (XAS) and Density
Functional Theory (DFT) calculations. The role of POP was unwrapped based on several
photophysical and photoelectrochemical studies. The electron transfer was mapped by several
correlated approaches and established the Z-scheme mechanism. Most importantly the
mechanistic insight of C_2H_4 formation was enlightened based on DRIFTS and DFT calculation
from multiple possible pathways.

List of Abbreviations

AQY	Apparent Quantum Yield
BET	Brunauer, Emmett & Teller equation
BPR	Back Pressure Regulator
CO_2RR	Carbon dioxide Reduction Reaction
COF	Covalent Organic Framework
CV	Cyclic Voltammetry
DFT	Density Functional Theory
DRS	Diffused Reflectance Spectroscopy
DRIFTS	Diffused Reflectance Infra-Red Fourier Transform Spectroscopy
EXAFS	Extended X-Ray Absorption Fine Structure
EPR	Electro Paramagnetic Resonance
EIS	Electrochemical Impedance Spectroscopy
GC	Gas Chromatography
HER	Hydrogen Evolution Reaction
HPLC	High Performance Liquid Chromatography
ICP	Inductive Couple Plasma
LSV	Linear Swipe Voltammetry
MeOH	Methanol
MOF	Metal Organic Framework
MS	Mass Spectroscopy
NMR	Nuclear Magnetic Resonance
O_v	Oxygen Vacancy
PCR	Photocatalytic CO_2 Reduction
POP	Porous Organic Polymer
PL	Photoluminescence
RDS	Rate Determining Step
RP	Red Phosphorus
SEM	Scanning Electron Microscopy
TEM	Transmission Electron Microscopy
TAS	Transient Absorption Spectroscopy
TPD	Temperature Programmed Desorption
TRPL	Time Resolved Photoluminescence
TEOA	Triethanol Amine
UV	Ultra Violet
XAS	X-ray Absorption Spectroscopy
XPS	X-ray Photoelectron Spectroscopy
XRD	X-ray Diffraction

TABLE OF CONTENTS

Chapter 6. Green Transformation of CO_2 to Ethanol Using Water and Sunlight by Cooperative Endeavour of Naturally Abundant Red Phosphorus and Bi_2MoO_6 ……..182

Chapter 1

Introduction

Risov Das, Subhajit Chakroborty, Mohammad Riaz, Sebastian C. Peter

To be submitted as a review

Summary

Solar fuel production from photocatalytic CO_2 reduction (PCR) process is the ultimate strategy to produce sustainable energy in green route without triggering global warming. The PCR process resembles natural photosynthesis, which controls the ecological systems of the earth. Currently, most of the work in this area has been focused on boosting productivity rather than controlling the distribution of products. The structural designing of the semiconductor photocatalyst, CO_2 photoreduction process on catalyst surface, product (gas and liquid) analysis, and understanding the CO_2 photoreduction mechanism are the key landscapes of PCR process to generate C1 and C2 based hydrocarbon fuels or even beyond. The selectivity of C1 and C2 products can be upgraded by suitable photocatalyst design, like introduction of co-catalyst, defects, surface vacancies and the impacts of the surface polarization state, etc. Monitoring product selectivity allows the establishment of a suitable strategy to produce a more reduced state of CO_2, such as methane (CH_4) or higher C2 hydrocarbons. This chapter concentrates on reports that demonstrate the production of single and multi-carbon products during CO_2 photoreduction using H_2O or H_2 as proton or hydrogen source. Finally, it highlights unresolved difficulties in achieving high efficiency and selectivity of this process. This chapter also deals with the importance of theoretical studies to explain observed experimental outcomes and predict suitable catalyst for desired product generation.

Risov Das, Subhajit Chakroborty, Mohammad Riaz, Sebastian C. Peter*

To be submitted as a review

1.1. Energy and environment

The global economic growth is now based on fossil fuel. However, extensive anthropogenic CO_2 emission is an unavoidable outcome of this process. Looking at current environmental crisis due to the increment of CO_2, the world is eying for a better sustainable alternative and carbon negative footprint. Among several approaches, the catalytic conversion of CO_2 to valuable carbon-based fuel feedstocks offers a promising route to the long-term storage of renewable energy that closes the carbon cycle.[1] Thermo-catalytic and electrocatalytic methods of CO_2 reduction have developed some state-of-art-catalysts and standard operating procedures for commercialization of this technology. However, due to higher cost of operation and secondary dependency on fossil fuels, these technologies have not fullfilled the need of current aggressive world. On the other, hand, photocatalytic route of CO_2 reduction is completely green and the availability of solar energy is enormous. Every hour, the amount of solar energy reaching earth contains more energy than is needed by humans to run our society in an entire year.[2] Fujishima and co-workers have introduced CO_2 reduction by photo-electrochemical route using semiconductor powder sample in 1979.[3] Since then, research in this area was not reported significantly. After 2010 rapid increment research in this area was seen in specifically catalyst designing strategies (**Figure 1.1a** and **1.1b**). However, this potential field has yet to find state-of-art-catalysts and standard operating procedures.

Realtime application: It is worth mentioning the fact that higher carbon CO_2 reduced products are more appealing compared to C1 products in terms of usability and economic values (**Figure 1.2**). Therefore, systematic development of CO_2 to C2 and C2+ product synthesis approach has been started in electrochemical CO_2 reduction route. On the other hand, very limited reports are available for multi-carbon product formation via photocatalytic route.
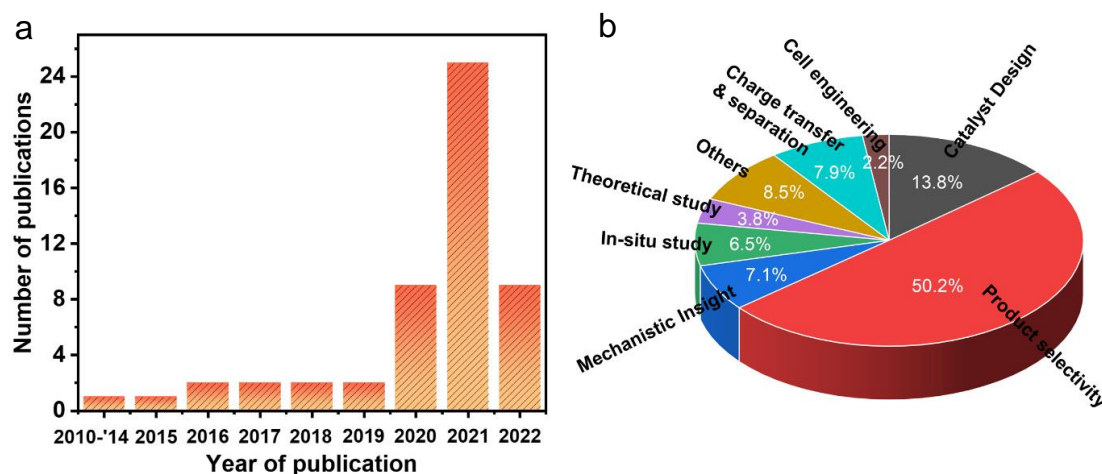
Figure 1.1. (a) List of publications on photocatalytic CO_2 reduction and **(b)** Pie-chart showing the main focus of those articles and their relative percentages.

However, recently some ground-breaking ideas and concepts have changed this era, and several multi-carbon products has been obtained by unique ideas. Importantly, these ideas are not catalyst specific, they can be extended for several more classes of catalysts with some smart modifications. Hence, extension of these idea is very essential to extend the horizon of this field. Moreover, the low efficiency of this method is mainly due to its unknown and complex mechanistic insight in terms of intermediates forms during CO_2 reduction and charge transfer pathways. In recent years tremendous effort has also been made to unwrap these phenomena by using several *in-situ* spectroscopic and microscopic techniques. Theoretical calculations have also predicted the feasibility of these methods; however, some doubts are still unclear. Interestingly, using machine learning techniques, researchers have predicted probable outcomes of CO_2 reduced products.[4] However, the experimental validations of these predictions were not done yet. Therefore, all these issues should be investigated chronologically for the advancement of this journey. Unfortunately, the proposed intermediates found in CO_2 reduction reaction (CRR) by electrocatalytic routes are not same for photocatalytic route due to choice of the catalyst and *in-situ* surface modification under applied potential or light irradiation. For example, carbide mechanism of hydrocarbon formation is well known in electrocatalysis.[5] However, recent studies showed that the M-C* (metal carbide) intermediate takes the lattice oxygen and goes back to M-CO* intermediate and hinders the hydrocarbon formation on $BiVO_4$ surface (**Figure 1.3**).
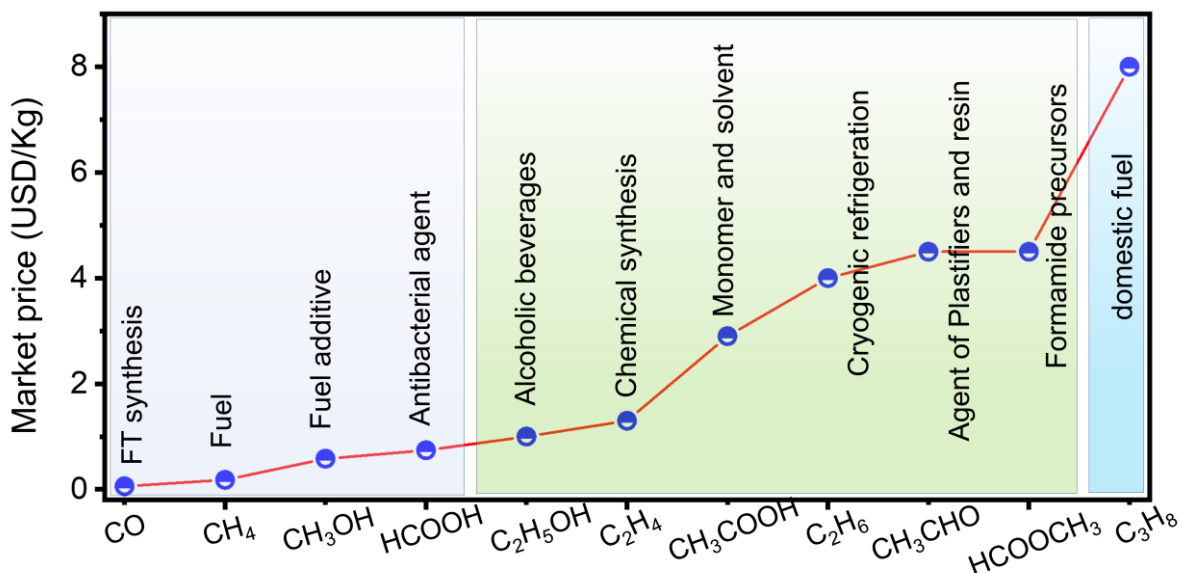
Figure 1.2. Main reported products from CO_2 reduction, some of their industrial use, and indicative market prices. First segment is C1 product, second denotes C2 product and 3rd is for C3 product. As the number of carbons increases the price also increases. FT: Fischer-Tropsch.
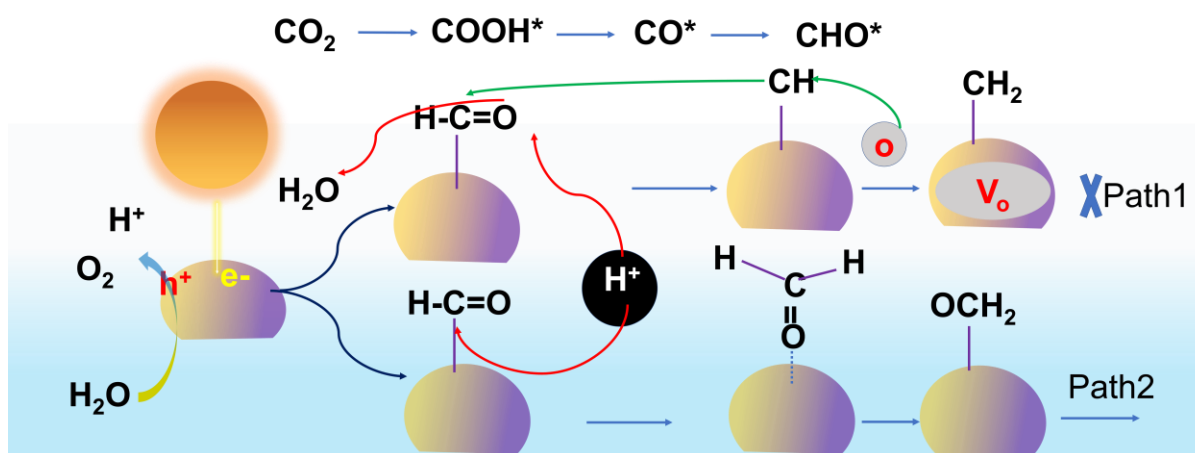
Figure 1.3. CO_2 reduction procedure via path 1 (carbide mechanism) and path 2 (formate mechanism). V_0 is represented oxygen vacancy generated upon abstraction of lattice oxygen from metal oxide catalyst. Green arrows imply the back reaction (CH* to CHO*), stopping the propagation of CO_2RR.

Here, worth mentioning the fact that metals, bimetallic, alloys, intermetallic, single atoms are major candidates in electro catalysis. On the other hand, oxide semiconductors and MOFs are majorly dominating in photocatalysis. Therefore, CO_2 photoreduction via metal oxide semiconductors are predominately happens through formate pathway instead of carbide path. Importantly, C2 and C2+ products are formed via separate catalyst designing strategies. Therefore, the product formation mechanisms are expected to follow different pathways in comparison with C1 products and already reported electrochemical route. In this thesis, I aimed to address these important untouched aspects of photocatalytic CO_2 reduction.

In the first part of this chapter, presents the common pitfalls of PCR and hydrogen evolution reaction (HER). The chance of overestimation of products or misjudgements of analysis are addressed here. This part also deals with the way out of these problems. We next look towards a few specific C1 products (CH_4, CH_3OH, CO) generating catalysts and involved mechanistic insight. The kinetic and thermodynamic limitations were also exploited here. Thereafter, the catalyst design strategies for C2 product synthesis with high selectivity are presented in detail. Next, the mechanistic aspects of multi-carbon product formation in light of in-situ spectroscopic, microscopic and chromatographic analysis. Here Gibbs energy of intermediates and transition states are very important. The importance and scope of studying intermediate species in excited-state compared to ground-state are manifested. Notably, during electrocatalysis, this particular aspect can be skipped without any controversy because there is no existence of excited-state. In this context, importance of charge polarised metal centres was investigated for multi-carbon product formation. We then focus on organic-inorganic hybrid

heterostructure catalyst, where charge polarization was introduced in the inorganic counterpart and further modulated by incorporating porous organic polymer support for improving CRR efficiency. Finally, based on our work, we propose an overview of materials design by considering all possible experimental and theoretical perspectives as a material scientist for CO_2 to useful chemical synthesis expert. We have also offered pertinent paths to achieve multi-carbon products from CO_2 photoreduction. Finally, new strategies required to implement this technology for real-time application as an alternative option to fossil fuel-based energy production are elaborated.

1.2. Major challenges

The exponential growth of publication in the field of CO_2 reduction indicates the importance and urgency of the work. Even after a surge of scientific research in several aspects of CO_2 photoreduction, the efficiency remained not promising. The efficiency of CO_2 photoreduction process were expressed in terms of apparent quantum yield (AQY), but most of the catalysts exhibited this as less than 1%. Only a few selected works have reported AQY near to 10%. However, a recent work said 85% AQY for methanol formation[6] provides a lot of hope on the potential capabilities of the field.

The central focus is to increase AQY% for C1 and C2 products for better economic benefits. This can be done not only by catalyst design, but other parameters like reactor engineering and reaction medium are also crucial. However, for C2+ products, the process had to undergo C-C coupling and multiple protons coupled electron transfer (PCET) process. Therefore, the challenges of C2+ product synthesis can be classified into two categories. Firstly, low-efficiency PCR and secondly, energetically unfavourable C-C coupling along with sluggish multistep step reaction kinetics. Depleted AQY% is due to limited visible light harvesting ability of catalyst originating from the inherent absorption band. The shallow life time of photogenerated charges also limits the availability of electrons for the reduction of CO_2. Use of photo sensitizer, hetero-structuring, creation of vacancies, doping and substitution can modulate the light absorption ability of a catalyst and charge loss due to recombination (**Figure 1.4**). These techniques can also suppress the phenomenon of charge recombination. Additionally, use of a co-catalyst can increase the charge separation lifetime by creating a Schottky barrier between semiconductor photocatalyst and metallic cocatalyst without changing the thermodynamics of CO_2 reduction. Strong light absorption ability of Au, Ag and Cu due to surface plasmon resonance (SPR) was also used to activate wide bandgap semiconductor for enhancing overall excited electrons viability for reduction.[7] Availability of

CO_2 on catalyst surface is another important factor for low CO_2 reduction efficiency. Solubility of CO_2 in reaction medium, adsorption on catalyst surface and activation of CO_2 by the catalyst are the key steps. The solubility of CO_2 was increased by increasing the pH of the medium. It can be also be achieved by using CH_3CN, ethyl acetate, DMF as reaction mediums. Unfortunately, the pitfalls involved in using organic additives during solar illumination were overlooked by many reported works. On the other hand, these pitfalls were pinpointed by other different articles reported in the literature. Therefore, the observed result can be believed only after scientific verification otherwise, there will be the chance of exaggerated results. This healthy scientific progression helped in advancing the field. Here, worth mentioning the fact that some carbonaceous product may also come from some other source instead of CO_2. This thesis incorporates these discussions to provide a guideline that all CO_2-reduced products proposed from various strategies are not entirely believable. Another unexplored part of this field is techno-economic analysis (TEA) of PCR. Since this field is in its infancy, PCR's TEA is not yet explored. Therefore, the industrial acceptability or commercial viability of this process is unknown to the community. However, as depicted in **Figure 1.2**, the market price of C2 products is more and therefore, the effort of this thesis was synthesising C2 molecules along with other C1 molecules.
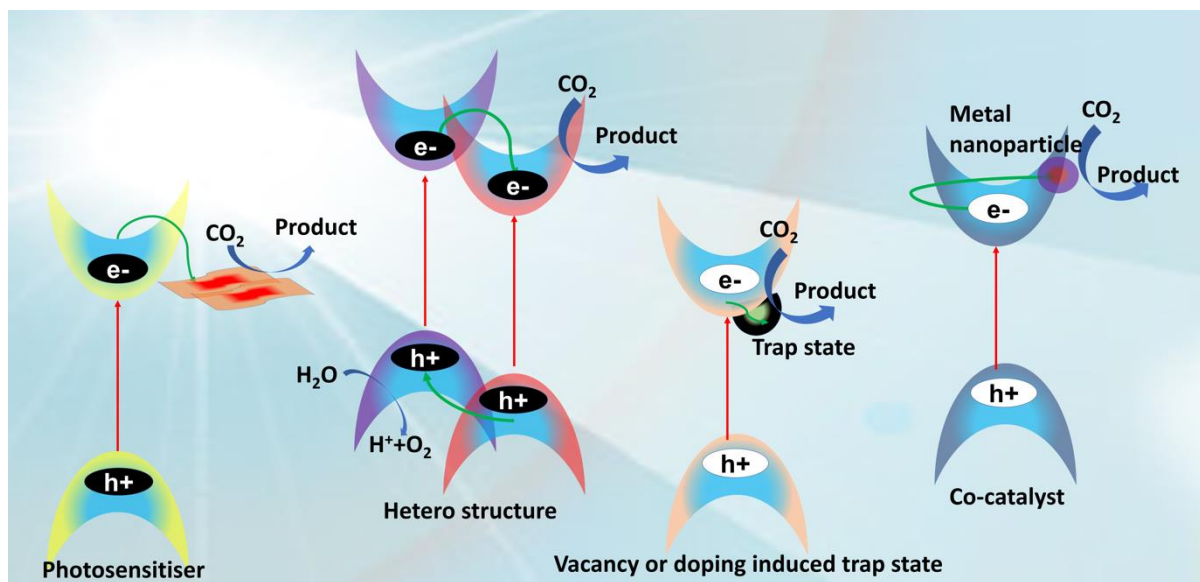
Figure 1.4. Different catalyst design strategies for suppressing photoexcited charge recombination. Here some of the strategies like introducing photosensitizer or making heterostructure can induce more photon absorption. Therefore, the overall electron excitation increases. Four major class of catalyst designing namely, photosensitizer, type-II heterostructure, anion and cation deficiency, and co-catalyst are shown schematically.

1.3. Fundamentals of photo-assisted CO$_2$ reduction

Photocatalytic CO$_2$ reduction: The reduction of CO$_2$ is a thermodynamically uphill process due to strong C=O bonds (750 kJ mol^{-1}). The semiconductor materials mainly govern PCR process. Photocatalysis means activating the semiconductor materials using sunlight or artificial light. Now the whole photocatalytic process can be conceptually simplified as: Absorption of Photon with suitable energy ($\geq$ band gap between the valance band (VB) and conduction band (CB)) leading to excitations of electrons from VB to CB. Excited charges can undergo recombination or separation and transportation of excitons (i.e., photo-generated electron-hole pairs). Separated charges can be utilized for chemical reaction of surface adsorbed species with charge carriers (**Figure 1.5a**).[8-9]

Again, the surface reaction process can be classified as:

(a) Reduction of CO$_2$: the photoexcited electrons can be captured by surface active species or the auxiliary catalyst and the adsorbed CO$_2$ at the surface is reduced,

(b) Oxidation of H$_2$O: The complementary reaction of CO$_2$ reduction is the oxidation of H$_2$O carried by photogenerated holes at the VB of the semiconductor,

However, most excited electrons recombine with photogenerated holes via radiative or no-radiative decay process. The main bottleneck of the process is that the charge recombination process (10^{-9} s) is much faster than surface reaction process (10^{-3}-10^{-8} s).[10] On top of that, all the photo-excited and long-lived electrons cannot reduce thermodynamically inert CO$_2$. The reduction reaction is endergonic and requires simultaneous supply of electrons and protons with compatible energy.[11] The PCR proceeds via proton-coupled electron transfer pathway and the product selectivity and fate of reaction are majorly controlled by the CB position of semiconductor catalyst because the redox potential of CO$_2$-reduced products should be less
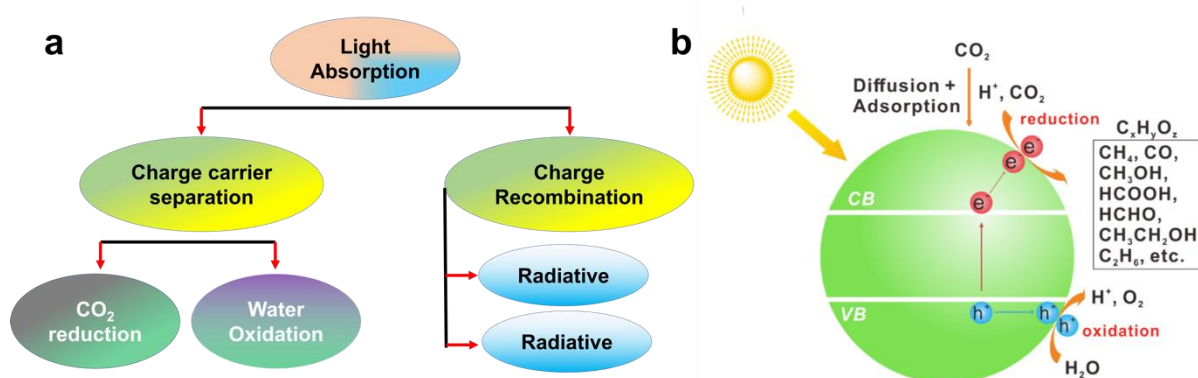
Figure 1.5. (a) Flow chart for photocatalysis after light irradiation on catalyst surface. (**b**) General process of photocatalytic CO$_2$ reduction (reproduced with permission from ref. 7).

negative than the CB of catalyst (**Figure 1.5b**).[7] Although the specific mechanism determines the final carbon-containing products, the rate of photo-generated charge to the adsorbed species in a reaction also contributes to the CO_2 reduction process.[12] Looking at the lower efficiency and selectivity of this process, the strategy of metal insertion on semiconductor catalyst surface was introduced. Plasmonic metals generate and inject hot electrons into the CBM of semiconductor. Meanwhile, co-catalyst traps the energetic electrons and eventually makes them participate in reduction reaction. Therefore, adapting such technique can produce more light energy with a lesser recombination rate.

Photo-induced plasmonic and co-catalyst

Co-catalyst: A metal nanoparticle with suitable band match work function with host semiconductor can act as co-catalyst. The two most important key functions of a suitable co-catalysts are to provide super electron capturing ability and sufficient active sites to adsorb CO_2 for reduction. It is because the photocatalytic CO_2 reduction conducted on the surface of co-catalysts mostly involves two characteristics of CO_2 adsorption and desorption. The protons and CO_2 adsorb on the active sites of co-catalysts, which eventually react in assistance with the trapped electrons to produce CO_2-reduced products. Besides this, co-catalysts lower the surface overpotential to favour photocatalytic process. Moreover, it increases the photo-stability of semiconductor by driving the catalysis process on co-catalyst instead of host semiconductor, thereby lowering the contact time between adsorbate and semiconductor. Especially, photo instability was seen in sulphide-based semiconductors because they easily oxidise by accumulating holes. Tremendous photo-stability was observed in case of CdS upon the reasonable use of CoP co-catalyst.[13] The factors which influence catalysis efficiency and selectivity are given below. i) Constituent element, ii) Inherent architecture, iii) particle size, iv) crystal phase, v) crystal facet, vi) loading amount, vii) inherent inaction between host semiconductor and co-catalyst.

Plasmonic: Localized surface plasmon resonance (LSPR) allows nanoparticles (NPs) to harvest the light energy by concentrating it near the NP surface and then converting the light energy into excited charge carriers as well as heat. This generated charge carriers drive the chemical reaction on the catalyst surface and allow novel selective reaction pathways. Photocatalysis by plasmonic materials can be explained by two major steps:

Generation of Charge carriers: In LSPR, a light wave is trapped within nanoparticles (NPs) whose size is smaller than the trapped light wavelength. Only noble metal-based NPs show this phenomenon because of the high energy gap for s→d transition. This interaction of

the light and free electrons in the NPs conduction band causes collective oscillation of the surface electrons with incident light. The LSPR process allows harvesting light photons and generates excited charge carriers and heat. These energetic charge carriers can be used to drive chemical reactions.

Charge carrier Mediated activation on Plasmonic nano catalyst: In plasmonic catalysis, high energetic charge carriers provide the energy required to activate chemical bonds (activation energy). On photoexcitation of plasmonic NPs, the reactant molecules adsorbed on NP surfaces get excited to a higher potential energy level, using plasmon energy (**Figure 1.6**; (1)). The reactant molecule in the excited state (due to extra energy from plasmon) reorganizes by changing the bond angle and bond length and undergoes reaction (**Figure 1.6**;(2)). If the reactant does not react in this excited state (due to a short lifetime, 10^{-15} s), it can react in an excited vibrational state (relatively longer lifetime, 10^{-12} s). This long, lifetime vibrational hot state is sufficient for the reactant to undergo a reaction (**Figure 1.6**, (3)).[14]

For semiconductor-plasmonic heterojunction, the semiconductors get activated by hot electron transfer from plasmons and heat transfer. The photoexcited hot electron can generate high temperature. Therefore light-induced photo-thermo-catalytic route was also explored, but since the used metals are noble, they cost more. Therefore, simultaneous supply of temperature and electricity with light energy for catalysis was also studied, and they are termed Photo-electro and Photo-thermo catalytic routes.
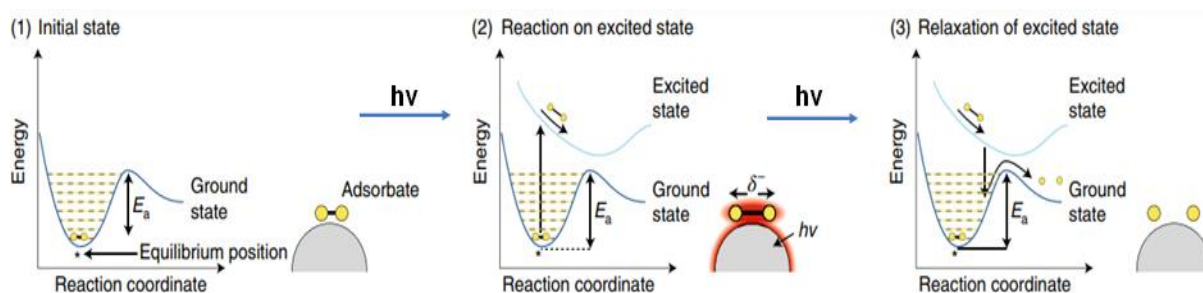
Figure 1.6. Mechanism of plasmon-facilitated bond activation and indication of charge-carrier-mediated reactions. Schematic of the desorption encouraged by electronic transitions mechanism for a dissociation reaction on a excited plasmonic metal. (1) At first adsorbates sit on its ground-state in equilibrium condition, demanding activation energy "Ea" to dissociate. (2) Deposits plasmon energy into the adsorbate upon photoexcitation and elevates the adsorbate to an excited potential energy level. The adsorbate then travels along the excited potential energy surface, achieving kinetic energy for reacting in the excited state. (3) If the reaction does not happen in the excited state, the adsorbate comes back to the ground-state in a vibrationally excited state successfully lowering the barrier for dissociation (Reproduced with permission from ref. 14).

Photo-electrocatalytic CO₂ reduction: Because of the limitation in photo induced catalytic reduction due to rapid recombination of excitons, an external electrical bias has been operated, which generates a new catalytic regime named photo-electrocatalytic CO_2 reduction (**Figure 1.7a**).[15] This process refers to the process in which the electrode is made up of semiconductor materials, under the photo-illumination that generates electron and hole and that migrated towards the catalysis surface with the assistance of the external bias.[16-18] The action of external electric field is helpful to promote the directional transfer of the photogenerated electrons and holes thus enhancing the separation efficiency to greatly improve the redox efficiency.[19] Meanwhile, when the band position of the photocatalyst is not enough to reduce the CO_2, the redox potential can be adjusted by applying electrical bias. Compared to the photocatalytic process, photo-electrocatalysis can be realized the reduction of CO_2 at the photo cathode under lower overpotential. According to the different semiconductor materials of photoelectrode the CO_2 reduction system can be divided into following categories

(a) n-type photoanode and dark cathode,

(b) p-type photocathode and dark anode,

(c) p-type photocathode and n-type photoanode,[20-22] the semiconductor photoelectrode has dual function of light harvesting and performing catalysis.

Photo-thermo-catalytic CO₂ reduction (PTCCR): Apart from the afore-mentioned photocatalytic CO_2 reduction, Photo-thermostatic CO_2 reduction (**Figure 1.7b,** and **1.7c**)[23-24] has attained immense attention due to having low energy cost and catalyst deactivation than single thermo-catalytic (TC) system, maximum uses of solar light and lower recombination than the single photocatalytic system.[25-26] Meanwhile, light energy associated with the thermal
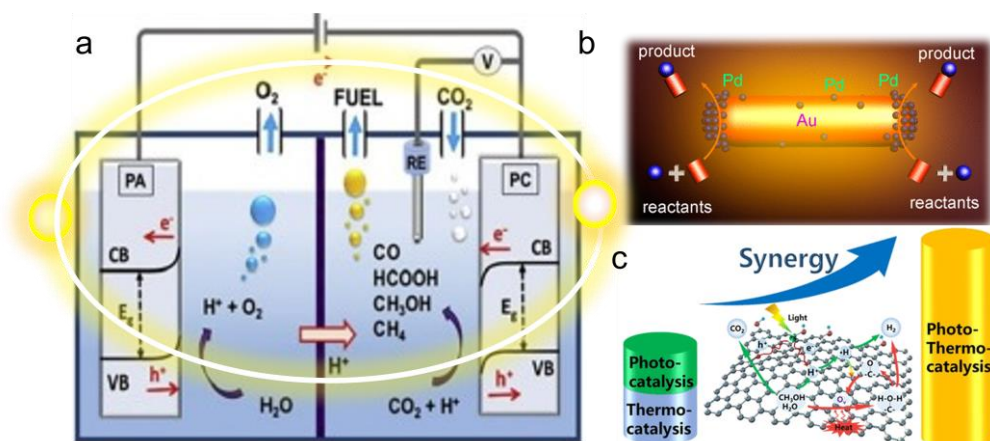
Figure 1.7. Different method of light driven CO_2 reduction instead of direct photocatalysis. (**a**) Photo-electrochemical process (reproduced with permission from ref. 15). Thermo-catalysis by (**b**) hot-electron and, (**c**) thermal energy (reproduced with permission from ref. 23, and 24).
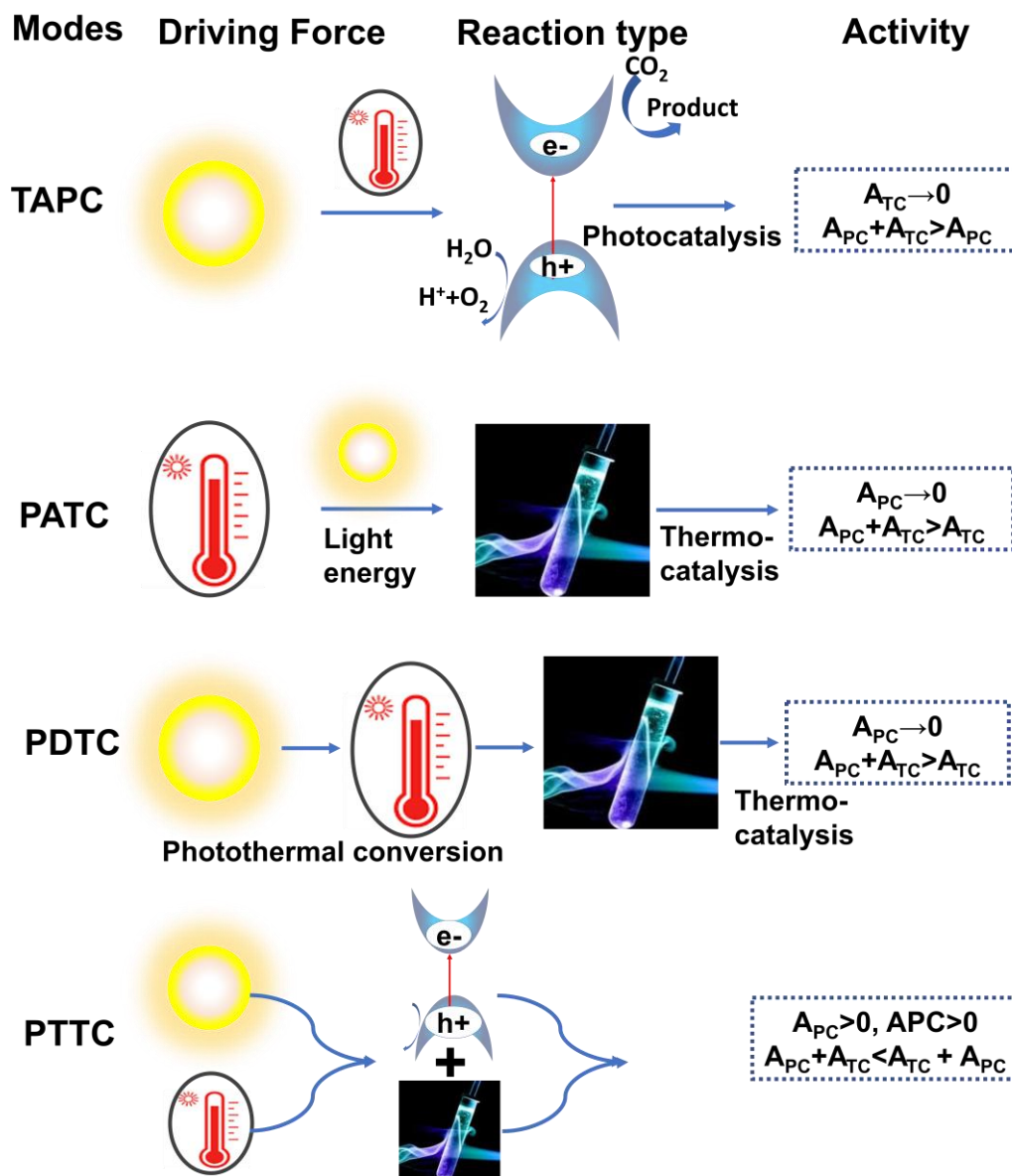
Figure. 1.8. Schematics of different photothermal synergistic modes.

energy may trigger the change in the electronic structure, which leads to another reaction path, thus tuning the products' selectivity.[27-28] Based on the progressing research and after minute observation of the mechanism, photothermal catalysis can be classified into four categories (**Figure 1.8**).

A.   *Thermal assisted PC (TAPC):* In this process, light is the main driving force for the reaction, whereas heat helps the process. Heat can accelerate the process in multiple ways by decreasing the activation energy barrier and increasing the population of the materials over the surface. Generally speaking, the catalysts in this mode barely have TC activity, or the reaction temperature is not high enough to reach the light-off temperature of TC. In this way, the activity of TAPC is higher than that of sole PC.[29-30]

B. *Photo assisted TC (PATC):* In this process, light is the main driving force for the reaction, whereas light assistant promotes the thermo-catalytic pathway. The light could assist in enhancing the TC activities in some ways, including the enhancement of the local temperature at the catalyst surface by electron relaxation and non-radiative recombination, decreasing the apparent activation barrier for TC, promoting the rate-determining step of TC by photo-excited catalytic active site, and so on.[31]

C. *Photo driven TC (PDTC):* PDTC can be defined as that photo-induced heat is the main driving force to the reaction, where light indirectly drives TC rather than directly drives PC through increasing the temperature above the light-off threshold of TC by photo-thermal effect of catalyst. Here, in that case, two prerequisites of the catalyst should satisfy primarily, the catalyst should absorb entire solar spectrum; secondly, the catalyst should possess excellent activity of TC.[32]

D. *Photo-thermal cocatalyst (PTCC):* We define the PTCC as that both light and heat are the driving forces to the reaction, where light directly drives PC and heat drives TC, achieving better synergistic performance than the sum of PC and TC. In this case, catalysts need to have both activities of PC and TC. In this way, it exhibits photo- and thermal-catalytic activities and better activity than the sum of both single activities.[33]

All these processes not only increase the efficiency of photocatalysis but also modulate product selectivity. However, there are several other methods of tuning the CO_2RR selectivity.

1.4. Product selectivity

Light-induced CO_2 has an inherent issue of selectivity due to competitive HER process. On top of that, CO, HCOOH and CH_4 often form together with different selectivity because of
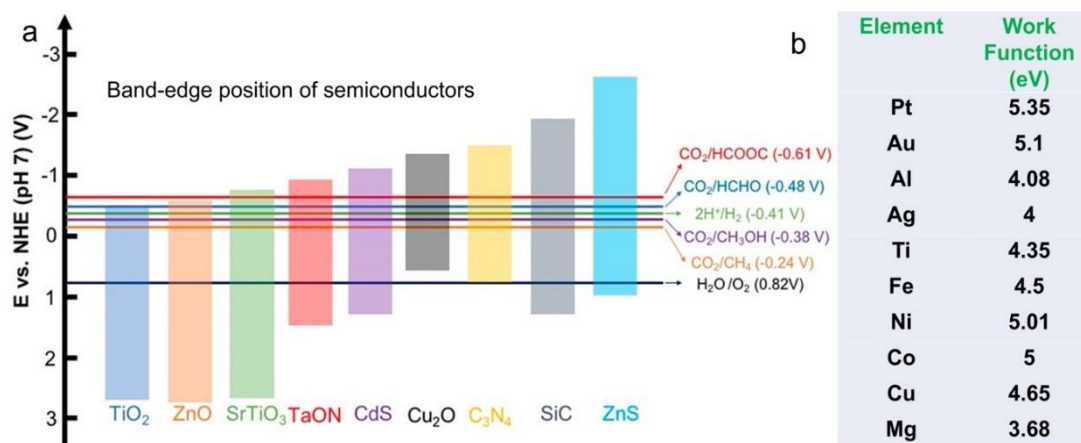
Figure 1.9. (a) Band gap energies of various semiconductor photocatalysts along with conduction band (CB), valence band (VB) potentials (reproduced with permission from ref. 34). **(b)** Work function values of different transition metals used as co-catalyst.

common reaction pathways (majorly formate mechanism). However, recent field advancement has identified strategies for getting particular CO_2-reduced products and suppressing HER process. Based on the reduction potential of CO_2 and band-edge of semiconductor catalyst (**Figure 1.9a**)[34] along with work function of metal co-catalyst selective product can be formed (**Figure 1.9b**). Selective CH_4 production was observed upon Pt incorporation in CO evolving catalyst.[35] Introduction of sulphur vacancies in ultra-thin $CuIn_5S_8$ has shown 100% CH_4 selectivity, whereas the pristine catalyst has produced CO in addition to
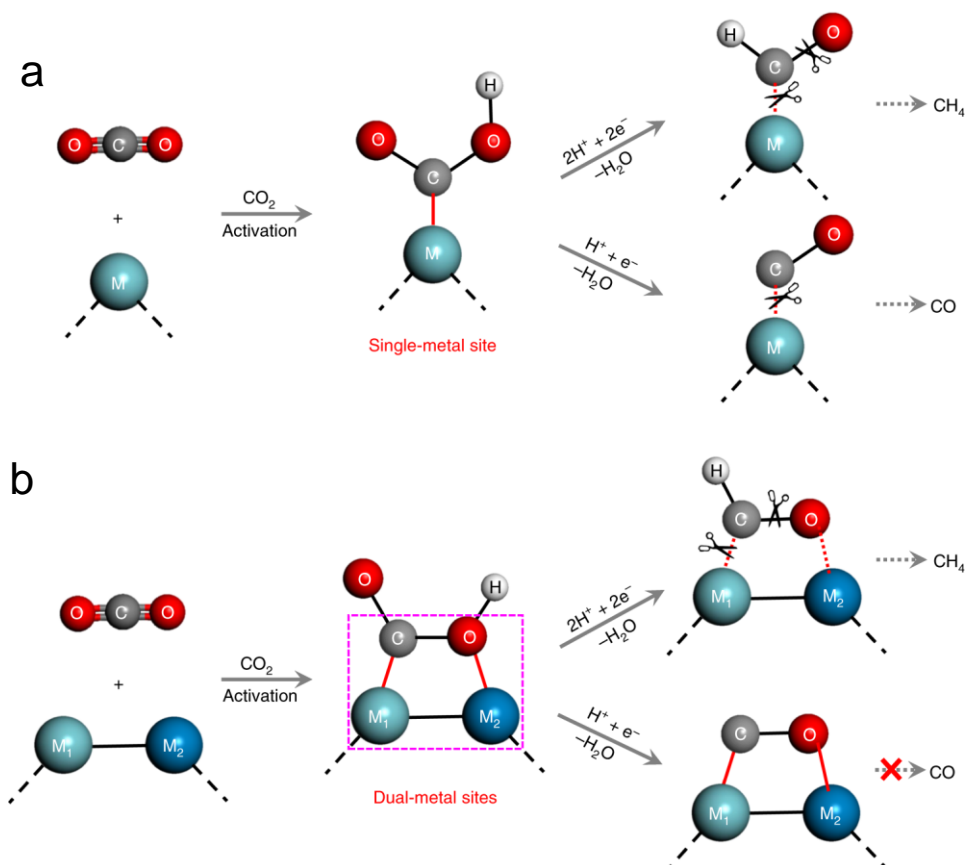
Figure 1.10. CO_2 photoreduction into fuels such as CH_4 and CO through the use of single-metal-site (**a**) and dual-metal-site (**b**) catalytic systems (M represents the metal site, 'H⁺ + e⁻' refers to the proton coupled electron transfer process and 'H_2O' means the desorption of H_2O molecules after the intermediates react with the proton–electron pair). The single metal site tends to weakly bond with the sole C or O atom of adsorbed CO_2 and produces a series of reactive intermediates, facilitating the formation of free CO molecules as well as hydrocarbon species such as CH_4 after protonation. Contrastingly, we suggest that the dual-metal sites tend to simultaneously bond with both the C and O atoms in CO_2 molecules, and hence give rise to a highly stable configuration of M–C–O–M intermediate. In this regard, it tends to need much more energy to simultaneously break the M–C and M–O bonds to form CO molecules, whereas further protonation of the C atom in the M–C–O–M intermediate is potentially easier, where the successive protonation results in the breakage of the C–O and C–M bonds to form exclusive hydrocarbon species like CH_4 (reproduced with permission form ref. 36).
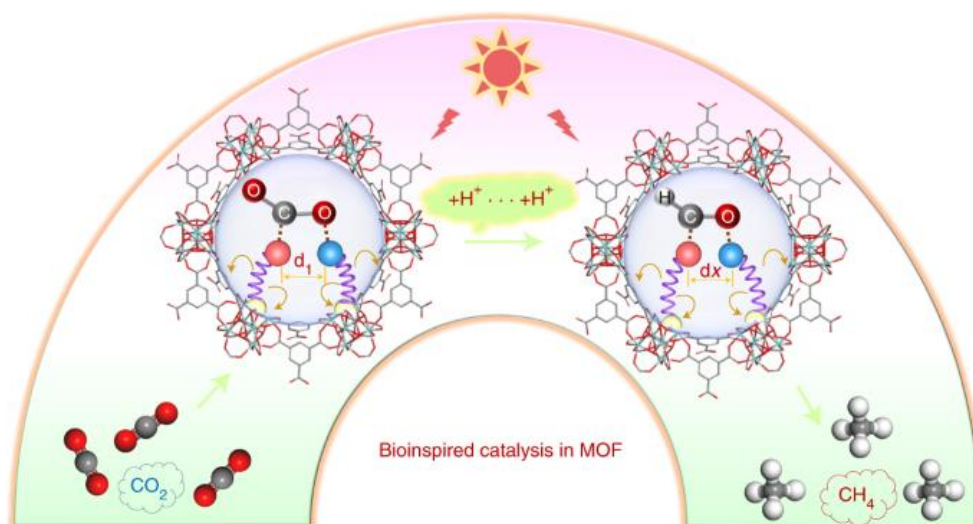
Figure 1.11. The flexible dual metal (Cu-Ni) site pair for self-adaptive CO_2-to-CH_4 photoreduction. This schematic diagram of bioinspired CO_2 photoreduction in MOF-808-CuNi. Carbon, oxygen, hydrogen, nitrogen, copper and nickel atoms are colored in grey, red, white, blue, orange and light-grey, respectively (reproduced with permission from ref. 37).

CH_4. The charge-enriched Cu-In dual sites have been shown to create highly stable Cu-C-O-In intermediate, which lowered CO* protonation steps for the formation of CHO*. Therefore, only methane was found despite following formate pathway (**Figure 1.10**).[36] Again, self-adjustable Cu-Ni active sites on EDTA grafted MOF-808 have shown optimum Cu-In distance for 97.5% methane evolution. Although this process followed formate mechanism but both "C" and "O" interacted with Cu and Ni sites, respectively (**Figure 1.11**). Interestingly, OCH$_3$* has not converted to CH_4 upon protonation on C. Another intermediate CH$_3$* was created, which eventually converted to CH_4.[37] Importantly, the reports on selective methanol formation are less than other C1 products. The specific strategy of methanol production is also not reported so far because the OCH$_3$* intermediate is common for methanol and methane formation. Contextually, "C" protonation results in methane and "O" protonation results in methanol formation. Therefore, controlling specific "O" protonation for obtaining methanol is difficult. On the other hand, the reduction potential of CO_2-reduced products is so close that choosing a suitable co-catalyst for selective methanol synthesis based on metals' work function is impossible. However, methanol synthesis from CO_2 reduction was obtained using metal-free, core−shell photocatalysts comprising graphitic carbon nitride (g-C_3N_4) covalently linked to melamine−resorcinol−formaldehyde (MRF) microsphere polymers.[38] Nevertheless, plenty of literature is available on selective C1 product formation from CO_2 photoreduction because the rate-determining steps (RDS) are already exploited. COOH* formation has been considered as the RDS for formate and CO synthesis. CHO* or CH$_2$O* formation was identified as RDS

for CH_4 and CH_3OH production. However, the identifying RDS, C-C coupling process and optimal binding energy between intermediate and catalyst surface were under the black box until last few years. Therefore, instead of a sequential increment of selectivity and activity towards CO_2 reduction, unlike the electrochemical route, some discreet reports are observed.[34]

In this context a harmonic development of C_2H_4 selectivity can be observed in electrocatalysis. A fluorine-modified copper catalytic system has been developed but unfortunately with very low yield of ethylene was obtained (**Figure 1.12a**).[39] Immediately after that 4H-Cu@Au (FCC) core-shell hetero-phase were designed for electrocatalytic system for CO_2 to C_2H_4 conversion and slight increment (Faradaic efficiency: 50%) was seen (**Figure 1.12b**).[40] Further improvement of selectivity (FE: 72%) was spotted upon investigating the influence of a library of molecules, derived by electro-dimerization of arylpyridiniums[41] adsorbed on copper (**Figure 1.12c,** and **1.12d**).[42] Moreover, the selectivity was improved recently up to 87% by polyamine-incorporated Cu electrode in KOH medium (**Figure 1.12e**).[43] Only Cu was investigated by introducing grain boundaries, facets, dopants and controlling morphologies and oxidation states to stabilise desired intermediates for ethylene production.[42]
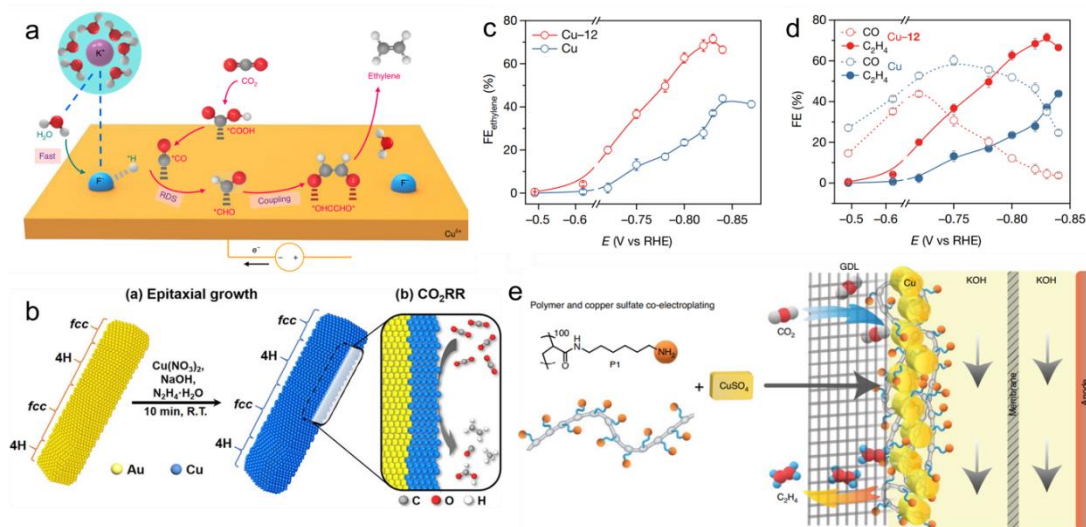
Figure 1.12. (a) A proposed reaction mechanism for the CO_2RR to C_2H_4 on F-incorporated Cu surface. Purple, potassium; blue, fluorine; red, oxygen; grey, carbon; white, hydrogen (reproduced with permission from ref. 39). **(b)** Epitaxial Growth of hetero-phase 4H/fcc Au@Cu Core–Shell NR under Room Temperature (R.T.), and electrochemical CO_2RR on 4H/fcc Au@Cu $NRCO_2RR$ performance in liquid-electrolyte flow cells (reproduced with permission from ref. 40). **(c)** FE of ethylene on Cu and Cu–12 using CO_2-saturated 1 M $KHCO_3$ as the supporting electrolyte. **(d)** FEs of CO and ethylene on Cu and Cu–12 at the applied potential range of −0.47 V to −0.84 V. The error bars for FE uncertainty represent one standard deviation based on three independent samples (reproduced with permission from ref. 42). **(e)** Preparation of the Cu–polymer catalyst. Schematic illustration of polymer and Cu co-electroplating on the GDL (reproduced with permission from ref. 43).

Unfortunately, such step wise development on increasing efficiency and selectivity for C_2H_4 or multi-carbon product formation is not started yet in the field of PCR. Although only few scattered reports are available in literature but a common similarity can be seen among them. Like electrochemical method here also Cu can be seen as C2 products generating element. Along with this, Bi based catalysts are also fond as excellent C2 product forming candidate. Interestingly, unlike Fischer−Tropsch (FT) synthesis, Ru, Ni, Co, or Fe are not found as appealing candidate in exhibiting C-C coupling reaction although CO was regarded as unavoidable intermediate of C-C coupling process in CO_2 reduction reaction also. That may be because hydrocarbon or liquid fuel synthesis by the FT process does not happen via PCET method, where the potential required for electron transfer is an essential governing factor along with catalyst-adsorbent binding energy. However, handful of reports is seen to produce C2 products by Ti and In-based photocatalysts. Here worth mentioning the fact that Ti-based catalyst is none other than TiO_2. The approach of introducing dopant, co-catalyst and heterostructure with TiO_2 succeeded in achieving C2 products up to certain extent. Multi-wall carbon nanotube-supported TiO_2 catalyses CO_2 to ethanol production with 69.7% selectivity.[44] Later, upon Rh doping in TiO_2 the selectivity has altered from ethanol to acetaldehyde, which means the process has modified from 12 electron transfer process to 10 electron transfer process. Moreover, the selectivity has also increased up to 69.7%.[45] The acetaldehyde selectivity was further improved up to 100% upon replacing Rh co-catalyst with Ni and introducing O vacancies in TiO_2.[46] Pure Ni/TiO_2 has exhibited the formation of methanol and acetaldehyde. However, introducing oxygen vacancies in Ni/TiO_2 (black TiO_2) provided acetaldehyde as a single product. Therefore, not only dual metal active sites but also the optimum adsorption energy of each active site with CO_2 or intermediates is crucial for achieving single C2 product. In this case, only change of metal co-catalyst cannot provide selective CH_3CHO because the reduction potential of CH_3OH (E^0 = -0.36 V) and CH_3CHO (E^0 = -0.38 V) are very similar (**Figure 1.13a,** and **1.13b**). Interestingly, complete reduction of C_2H_yO into C_2H_4 or C_2H_6 was seen upon changing metal co-catalyst because these hydrocarbons formed at relatively lower potentials ($E^0(C_2H_4)$ = - 0.24 V, $E^0(C_2H_4)$ = -0.28 V). Upon Pd incorporation in TiO_2, the CO_2 reduction has continued up to C_2H_6 but the selectivity was only 6.4%.[47] The selectivity was further improved to 7% upon addition of PdAu bimetallic NP in TiO_2. Although the selectivity of C_2H_6 has not improved significantly, but 7% C_2H_4 has also been detected.[48] Therefore, 14% hydrocarbon selectivity was observed. Switching the bimetallic co-catalyst from PdAu to PtCu has exhibited 14.3% C_2H_6 and 7.1 % C_2H_4.[49] Further

improvement (27% C_2H_6) was seen upon addition of only Au nano particle on TiO_2. Here C-C coupling process as function of light intensity and excitation wavelength was demonstrated. C_2H_6 formation onset light intensity and wavelength (l) were shown to be 330 mW/cm^2 and 490 nm (**Figure 1.14**).[50] Similar progression was seen in the case of Bi-based catalysts. However, the progression is arbitrary and scattered. This means that improvement of one Bi-based catalyst based on the drawbacks or limitations of previous studies was not attempted. Instead knowing the fact that Bi-based compounds will be catalytically active, several Bi-based compounds were designed, and obviously, some successful multi carbon product was obtained. Here a history of this research was discussed to highlight the common features of C2 producing Bi based catalysts. An interesting fact about all these catalysts is that methanol has been generated as a side product of the PCR process. However, in some cases, methane was also detected. The recent experiments with BiOCl and Pt, N co-doped BiOCl, have exhibited 48% and 41% ethanol selectivity.[51-52] However, the advancement and follow-up studies were done mainly with tree ternary Bi-based metal oxides (TBBMO), namely $BiVO_4$, Bi_2WO_6, and Bi_2MoO_6.[53-55] The ethanol selectivity has increased upon introducing a second material in these active catalysts. For example, introducing graphene oxide layers or MoS_2 into Bi_2WO_6 has improved the ethanol selectivity up to 57%.[56] On the other hand, Bi loading on Bi_2MoO_6 generated exhibited only 42.5% ethanol selectivity.[57] Hence, it is observed that dual component catalysts have improved the selectivity compared to single catalysts. However, the reasons for such increment are not common for all the catalysts. Moreover, it's better to say that the reason behind such increment was not clear. It is a well-accepted fact that Bi is the active site. However, the role of 2nd metal, such as Mo, W or V in TBBMO was not understood clearly.
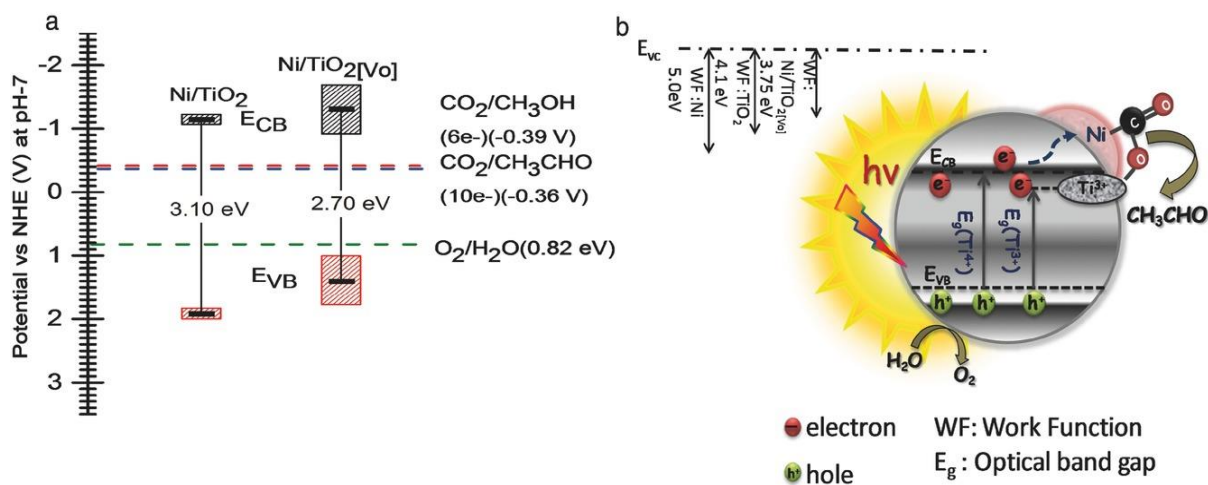
Figure 1.13. (a) Change of band-edge positions upon introduction of oxygen vacancy. **(b)** Schematic illustration of PCR mechanism of Ni/oxygen deficient black TiO_2 (reproduced with permission from ref. 46).
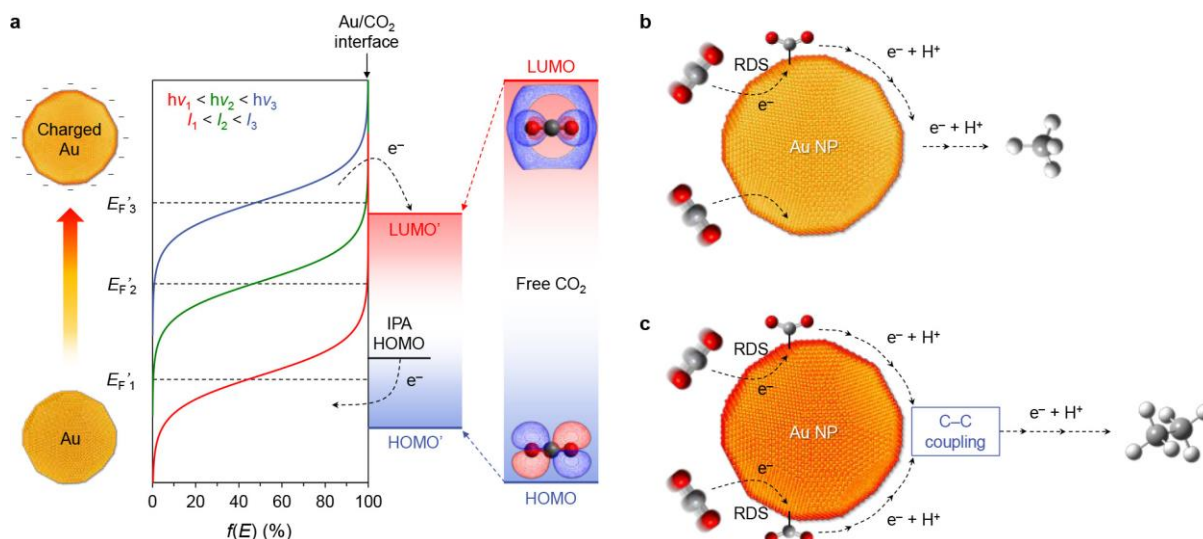
Figure 1.14. Mechanism for plasmon-assisted CO_2 reduction to C_1 and C_2 hydrocarbons. **(a)** Hot-electron-transfer process at the interface of Au and CO_2; adsorption of free CO_2 molecule onto an Au surface promotes hybridization of its electronic states with those of Au, narrowing its frontier orbitals and creating a reduced HOMO′–LUMO′ gap. CW illumination in the presence of the electron donor cathodically charges an Au NP, resulting in a Fermi–Dirac distribution with a raised (quasi) Fermi level, $E_F′$, at steady state. The $E_F′$ depends on the photon energy and light intensity. A higher $E_F′$ favors a higher rate at which hot electrons are transferred to adsorbed CO_2 molecules. **(b)** the plasmonic excitation of Au NPs causes a hot electron to be transferred to adsorbed CO_2 to form a radical ion intermediate, $CO_2^{•-}$ (or its hydrogenated form). After this rate-determining step (RDS for C_1 generation), the formed $CO_2^{•-}$ (or its hydrogenated form) proceeds through a cascade of hot-electron- and proton-transfer steps to result in CH_4 generation. **(c)** When the hot-electron-transfer rate is large (e.g., at high light intensity under interband excitation), more than one electron transfer can take place within the surface residence time of adsorbed CO_2, resulting in the simultaneous activation of two CO_2 adsorbates (RDS for C_2 generation). The formed $CO_2^{•-}$ intermediate pair can undergo C–C coupling. Subsequent transfer of a series of hot electrons and protons results in the formation of C_2H_6 (reproduced with permission from ref. 50).

Some spectroscopic and isotope levelling study can unwrap the fact. Therefore, this approach should be implemented for future investigation of intermediates via *in-situ* spectroscopic (mainly *in-situ* Raman and EXAFS) analysis and DFT calculations. Hence, the bottleneck of these systems is poor understanding of the governing factors like reaction process and role of individual components in the catalyst. Unlike Ti and Bi, Sn and In also exhibit similar behaviour (oxidation state and electronegativity; Ti: 1.54, In: 1.78, Sn: 1.96, Bi: 2.02). On top of that, In, Sn, and Bi share diagonal relationship. Therefore, the C-C coupling process was also observed in case of Sn and In-based catalysts. However, with pure In_2S_3, CO and H_2 evolution were observed. Interestingly, the C-C coupling process has initiated upon C-insertion
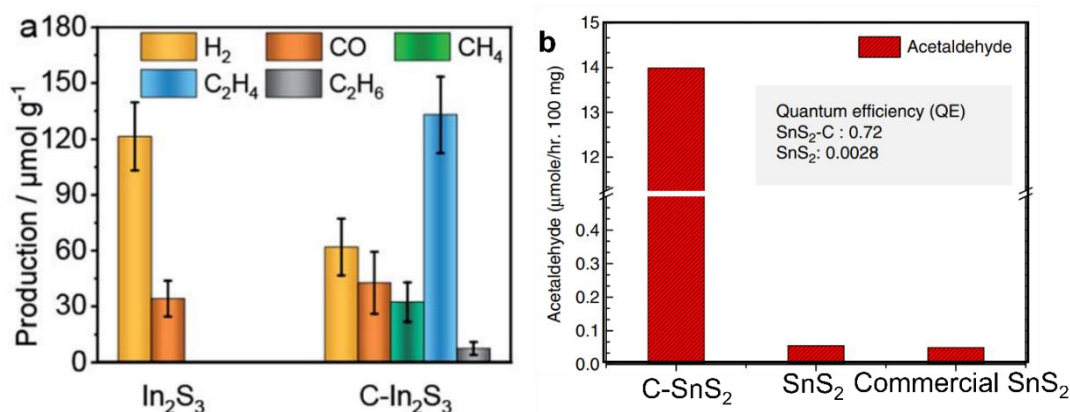
Figure 1.15. (a) Performance comparison of C-In$_2$S$_3$ and In$_2$S$_3$ under UV-visible light at 150 °C for 5 h (reproduced with permission from ref. 58**). (b)** Comparative solar fuel formation rate and quantum efficiency of C-SnS$_2$, SnS$_2$, and commercial SnS$_2$ under a visible light source (300 W halogen lamp) (reproduced with permission from ref. 59).

in the In$_2$S$_3$ lattice. Therefore, C$_2$H$_4$ and C$_2$H$_6$ both were detected, and 50% C$_2$H$_4$ selectivity was seen (**Figure 1.15a**).[58] Similarly, CH$_3$CHO production has improved 140 times upon C-insertion in SnS$_2$ lattice (**Figure 1.15b**).[59] However, the similar approach of C-doping in SnO$_2$ did not perform C-C coupling reaction. Only HER was suppressed, but product remained CO and CH$_4$.[60] Contextually, SnO$_2$ or doped SnO$_2$-based catalysts mainly performed CO$_2$ to C1 product formation.[61-62] However, C incorporated SnO$_2$ catalyst was not explored yet. Significantly, metal-free photocatalysts are increasing in recent years for low-cost higher gas adsorption and flexible synthetic approach toward desirable morphologies. This class of materials includes polymers, covalent organic frameworks, and porous organic polymers. Although most of them are C1-producing catalysts, a recent study found acetaldehyde formation by polymeric carbon nitride (PCN) catalyst, where selectivity was shown to improve from 49.5% to 98.3% upon modifying PCN. Gibbs free energy calculation depicted that the formation of CHO* intermediate on HCN-A surface is exothermic (**Figure 1.16a**). In contrast, the formation of CO* is endothermic, leading to favourable OC-CHO* formation (**Figure 1.16b**). Due to high energy barrier of acetaldehyde to ethanol formation, further oxidation has not happened (**Figure 1.16c**). Unfortunately, the reason behind favourable CHO* stabilization followed by C-C coupling on PCN catalyst surface (**Figure 1.16d**) and C1 selectivity for other similar metal-free catalyst was not rectified.[63] The multistep reaction process and complex reaction kinetics are bottlenecks of this process. However, the thermodynamics of CO$_2$ to C2 formation reaction has been explored up to a reliable extent. Hence, catalyst design strategies for overcoming kinetic barriers and optimizing the parameters influencing C1 intermediates for participating coupling process toward C2 product formation remain of utmost concern.
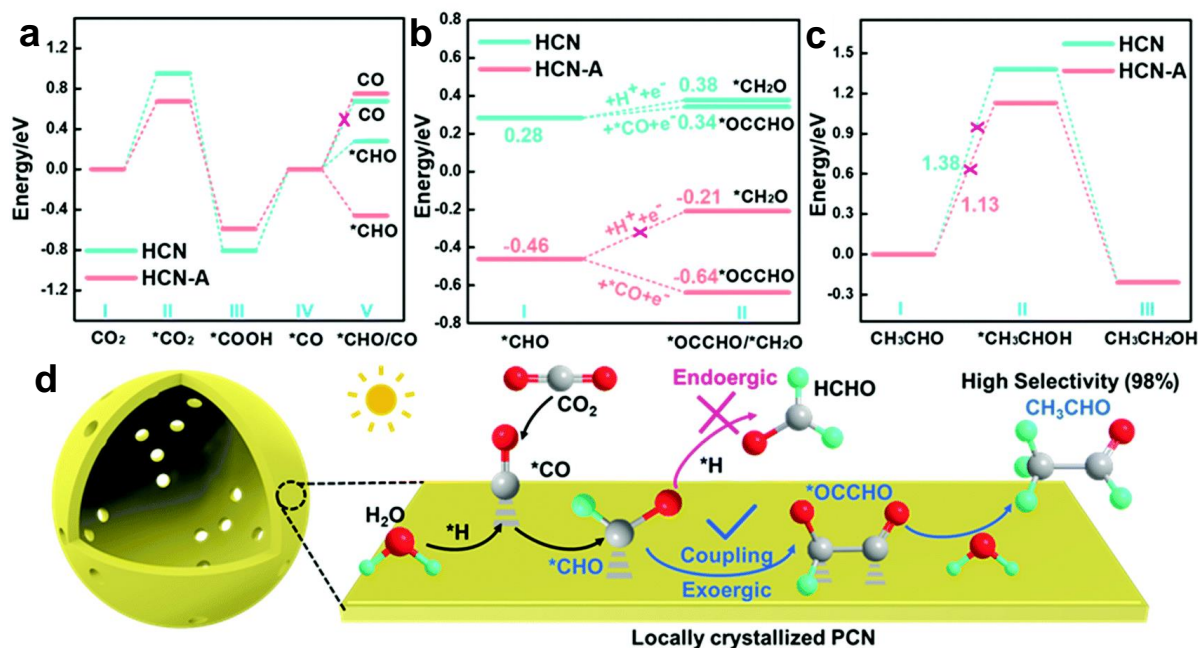
Figure 1.16. Calculated free energy diagram for the reduction of CO_2 to CH_3CHO on the HCN and HCN-A catalysts showing **(a)** stabilization of CHO* species and **(b)** surface bond OCCHO*. **(c)** High energy barrier of acetaldehyde to ethanol formation. **(d)** The proposed reaction mechanism for the photocatalytic CO_2 reduction conversion to CH_3CHO. The grey, red, and green color spheres denote carbon, oxygen, and hydrogen atoms, respectively (reproduced with permission from ref. 63).

1.5. Mechanistic Insight

Proper understanding of reaction mechanisms can open up the black box of selective product formation from CRR. Therefore, a tremendous effort has been put together from experimental and theoretical point of view. As a result, several studies have repeatedly confirmed almost all the C1 products and their reaction process. However, that luxury was not enjoyed for C2 products because the number of reports is less to the community. Like all other heterogenous catalysis for CO_2 reduction the photocatalytic methods also involve multiple intermediate complex rection steps where surface adsorbed species showed different reactivity based on the catalyst surface. Fortunately, the initial phases of CO_2 to C2 product formations are similar to C1 product formation. Needless to say, the same C1 intermediates are coupled together to generate C2 product. Yet the coupling can happen within two different C1 intermediates, CO* and CHO*. Majorly the C2 product formation mechanisms can be classified into 4 segments.

   A. Chemisorption of CO_2 on catalyst surface via electron transfer from the HOMO level of catalyst to LUMO of CO_2. Upon chemisorption, the LUMO energy of CO_2 reduces

due to bent structure of CO_2. Therefore, it becomes possible to break stronger C=O (Bond energy:750 KJ/mol) bond of CO_2.[64]

B. PCET on chemisorb CO_2 to form COOH* which is the first C1 intermediate.

C. Coupling of two C1 intermediates to form C2 intermediate. This is the most crucial step for obtaining higher carbonaceous $C_xH_yO_z$. This segment infers whether C2 products will form or not.

D. Desorption of C2 intermediates from the catalyst surface based on the thermodynamics and kinetics of proton and electron transfer to the C2 intermediate. This step decides the selectivity of C2 products.

Binding of CO_2 on catalyst surface: CO_2 can bind on catalyst surface by three different ways. I) C adsorbed species by accepting the electrons from catalyst surface(O-C*-O) (**Figure 1.17a**). II) O adsorbing species by donating the electron to catalyst surface (O*-C-O*) (**Figure 1.17b**) and III) mix C and O adsorbed species (**Figure 1.17c**). It was reported that O-C*-O has proceeded through the formation of COO· radical and favours CO formation along with several other products, including C2.[65] On the other hand, the O*-C-O* species was supposed to produce formate anion (HCOO⁻) upon C protonation which can provide only HCOOH.[64] Contextually, another thorough examination shows "C" and "O" site of CO_2 adsorption is favourable on Cu and Ag surface, respectively (**Figure 1.17d**).[66] Interestingly, Cu is known for producing C2 and several other products from CRR and Ag as CO and HCOOH producing elements. Therefore, based on these adsorption criteria, product selectivity can be predicted.
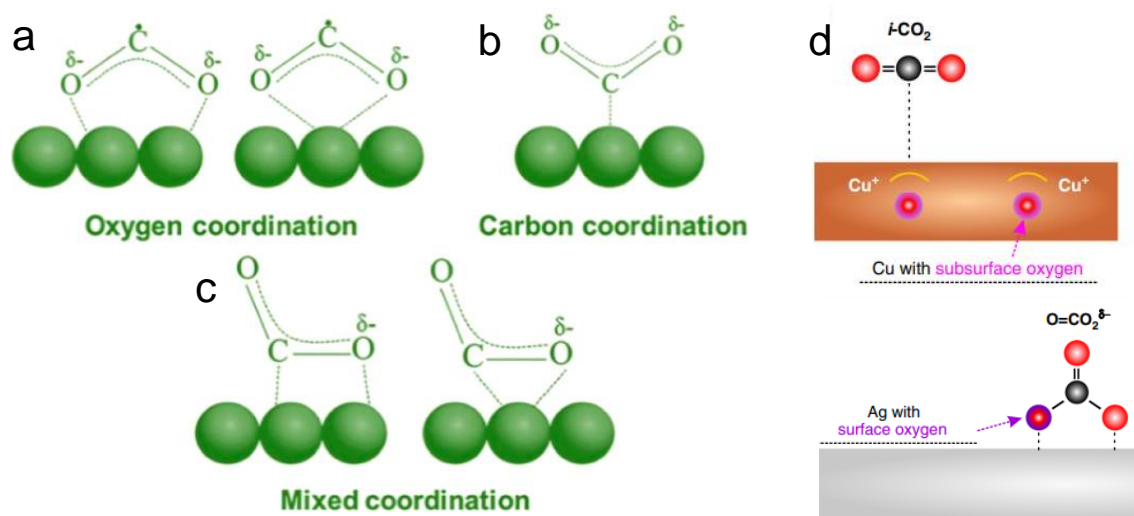
Figure 1.17. Possible structure of chemisorbed CO_2 on the surface of electrocatalysts **(a-c)** (reproduced with permission from ref. 65). **(d)** Overview of CO_2 surface adsorptions on Cu and Ag surfaces (reproduced with permission from ref. 66).

Responsible C1 intermediates: It has been well explored that the C1 intermediates (C1*) or C1 products can undergo further reaction procedures for generating multi-carbon products.[67] However, it is important to know about the fact that whether C1 intermediates (C1*), C1 product molecules or both C1* and C1 are participating in C-C coupling reactions. For example, CO (product) insertion in CO*, CH_2* and CH_3CHO* gives acetate, glyoxal and n-propanol. Therefore, reacting species are crucial for tuning selectivity (**Figure 1.18**).[68] Based on the previous reports, a few crucial intermediates and their coupling behaviour are presented here. In this context, CO*-CO*, CO*-COH*, CO*-CHO*, CO*-CH_x*, COOH*-COOH* CH_3*-CH_3* (methyl radical pathway), COH*-COH* (glyoxal pathway) coupling are reported as the first key step for promotion of a C1 intermediate to C2 intermediate.[42, 65, 69]

Selective C2 product from C2 intermediates: The difficulties of C2 product formation were discussed earlier. Among several multi-carbon products, one particular C2 product formation is even more difficult. Once the C2 intermediates are formed, there are possibilities for hydrocarbon formations by complete reduction. However, based on the interaction between catalyst surface and intermediates on, particular oxygenated species can desorb from the system (**Figure 1.19**). For example, CH_2-CHO* species can undergo "C" protonation and form C_2H_4. On the other hand, upon "O" protonation, it will convert to acetaldehyde (**Figure 1.19a**). Similarly, CH_3-CH_2O* species can form ethane and ethanol upon "C" or "O" protonation (**Figure 1.19b**). Here, the stability of surface and oxygen bond will decide whether surface-O bond will get cleave to promote oxygenated C2 products or O-C bond cleave will lead to the production of hydrocarbons.
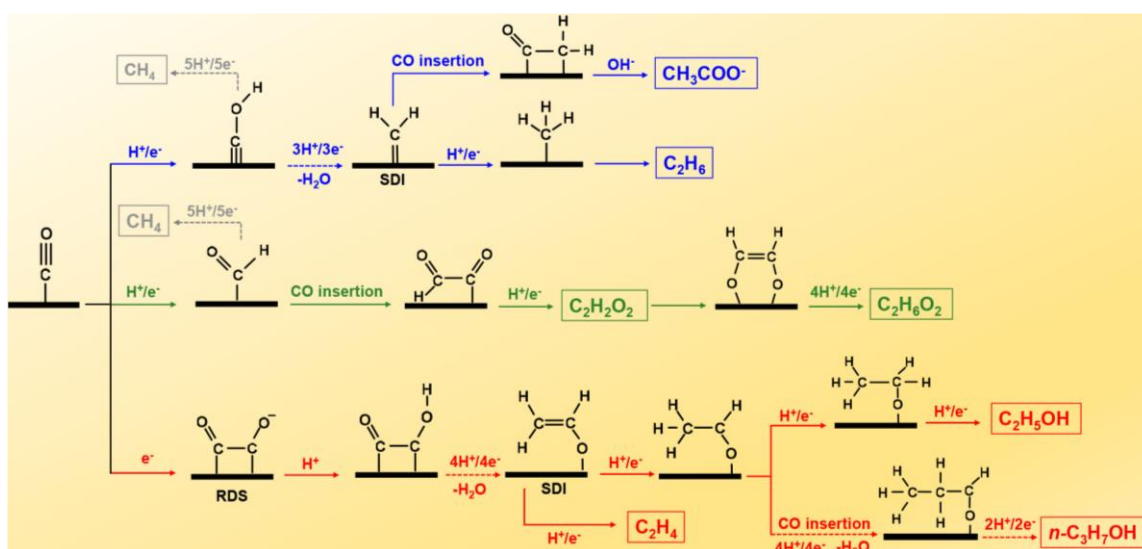
Figure 1.18. Most possible C_2 and C_3 pathways starting from *CO on Cu surfaces. Green, blue, and red routes are for trace, minor, and major C_2 products. Gray routes are for C_1 product. Dashed arrows indicate the multiple consecutive electron/proton transfer steps.
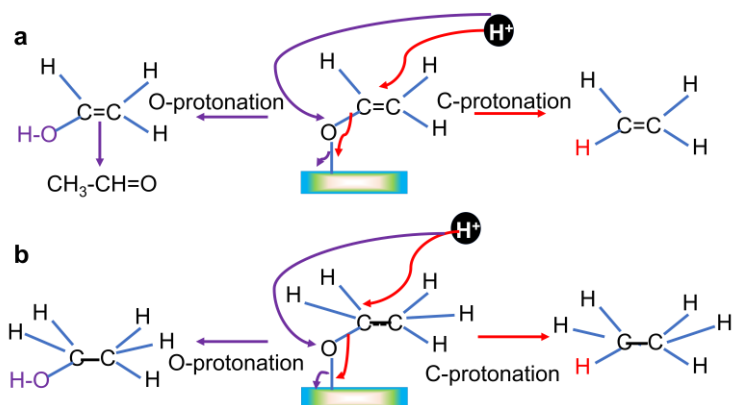
Figure 1.19. (a) Obtaining acetaldehyde and ethylene from sample intermediate upon "O" and "C" protonation. **(b)** Similarly, from same intermediate ethanol and ethane can be formed.

Interestingly, COCOH* (**Figure 1.20**) is also common intermediate for acetic acid. After the formation of CO-CO* intermediate, the reaction propagates towards CO-COH* (**Figure 20a**) intermediate, which upon water desorption generates C_2O^* and finally forms acetic acid through ethenone formation (**Figure 1.20b**).[70-71]
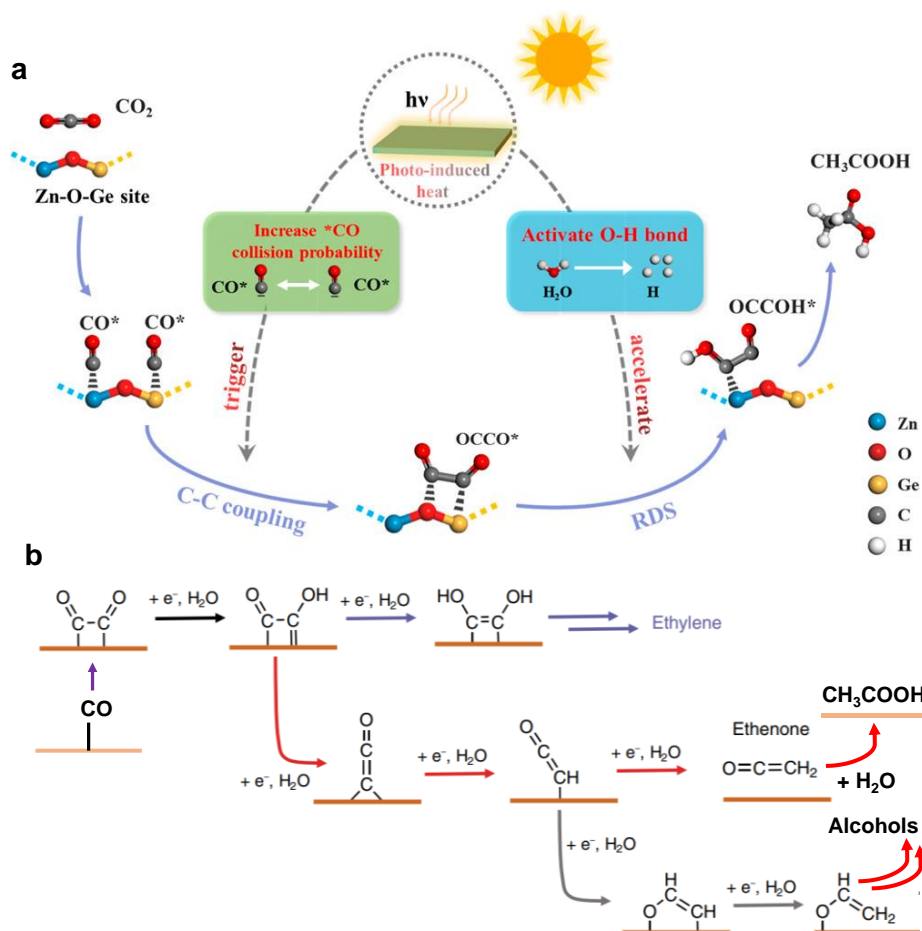
Figure 1.20. (a) Acetic acid formation mechanism on asymmetric Zn_2GeO_4 surface by photocatalytic route (reproduced with permission from ref. 70). **(b)** Acetic acid formation by two-dimensional Cu sheet via electrochemical route (reproduced with permission from ref. 71).

In this context, it is important to note the fact that photo-reduced products like ethanol or acetaldehyde can further undergo photo-oxidation by photogenerated holes in the valence band and produce acetic acid. Therefore, the photo-oxidation potential of products and the valence band position of catalyst is also very crucial for getting selective C2 product. Hence it is clear that a small variation in reaction condition can change the selectivity despite implementation of the same catalyst. In this context, the thermodynamic stability and Gibbs free energy of transition state determine the dominance of one particular pathway over others. Therefore, the catalyst surface engineering can alter the reaction pathway, which leads to the alteration of product. Hence, while engineering the catalyst surface, the identification of generated intermediates is crucial. Since these species are born during reaction; it is necessary to identify them in operando conditions by adopting *in-situ* spectroscopic techniques.

1.6. Techniques for probing CRR

Ultrafast response capacity and sensitivity of some spectroscopic techniques can efficiently map short-lived reaction intermediates during the progression of reaction. Surface modification and reconstruction is a common phenomenon during catalysis. Therefore, it will definitely impact reactivity and selectivity. Hence in-situ monitoring of catalyst surface is also important by *in-situ* XPS, XAS and XRD (**Figure 1.21a**).[72] In-situ scanning fluorescence X-ray microscopy (SFXM) and environmental transmission electron microscopy (TEM) was exploited to examine active facet of Cu_2O. This study indicated (110) plane of Cu_2O is responsible for methanol formation, whereas (100) plane is inert (**Figure 1.21b**).[6]
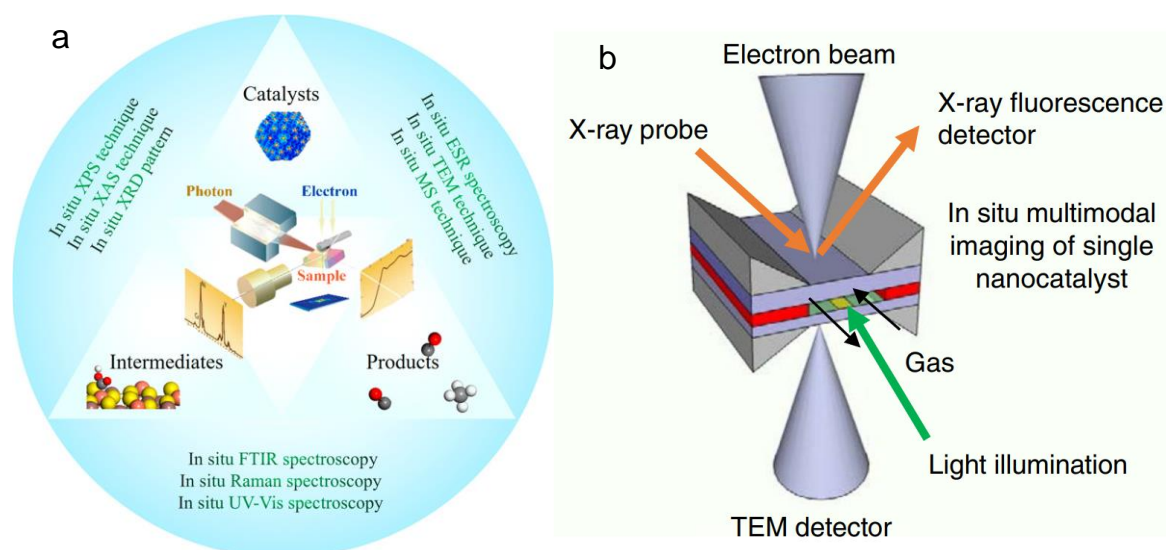
Figure 1.21. (a) In-situ techniques for understanding catalyst surface, intermediates and products (reproduced with permission from ref. 72). **(b)** Schematic of *In-situ* environmental TEM used for understanding active face of Cu_2O for CO_2 to methanol formation (reproduced with permission from ref. 6).

In-situ Diffuse reflectance Infra-red Fourier Transform Spectroscopy (DRIFTS) has been widely used to unwrap the intermediates. The important C1 intermediate species was observed from DRIFTS, and its transformation was well connected with the final products. For example, the formation OCH_3* eventually led to the formation of methanol or methane. Moreover, the evolution of IR stretching band corresponding to C-H hints at methane formation. On the other hand, such increment of C-H$_{str.}$bands was not observed in case of methanol formation.[73] Similarly, the absence of CHO* and OCH_3* bands clearly rule out the possibilities of methane, methanol or formaldehyde formation. However, COOH* and CO* are the first two intermediate species which generates $HCOO^-$ and CO upon desorption. This common procedure is well established and accepted by the scientific community. However, the real challenges start in detecting the C2 intermediates because the stretching or bending modes for C1 or C2 species are similar.

For example, deconvolution of OCH_3* (responsible for methane and methanol) and CH_3-OCH_2* (translates to ethane and ethanol) stretching bands is difficult because the C-O starting frequencies were probed here and for both the case it will arise in between 1050 cm^{-1} to 1100 cm^{-1}. Similar problem was encountered for C-H stretching bands when the reaction proceeds through carbide mechanism and CH_x*-CH_x* coupling happens. Recently few representative exclusive species were detected, which can provide direct evidence for the occurrence of C-C coupling reaction. The asymmetric stretching vibrations of C–C–O at 1038 cm^{-1} and for CHO-CO* at 917 cm^{-1} evolved with irradiation time on H-CN catalyst surface. The origin of this species was from CO* and CHO* coupling, where the appearance of CO* and CHO* were confirmed from the same DRIFT study.[63] Another finding was COO-COO* intermediate at 1307 cm^{-1} towards the formation of acetic acid.[74] Similar oxalate peak was reported earlier during oxalate decarboxylase reaction monitoring.[75] Here, the bottleneck of this study is the concentration of intermediate species and sensitivity of the techniques. Therefore, often misjudgement of intermediate was found in literature. Hence, other spectroscopic support is always beneficial. Nevertheless, it is worth mentioning the fact that in-situ DRIFTS was majorly explored for intermediate specs detection during PCR. Another exciting technique is *in-situ* Raman spectroscopy. Although this technique was often used during electrochemical CO_2 reduction, very few reports were found in the field of photocatalysis because the light irradiation during CO_2 reduction interferes with the Raman scattering. Except few plasmonic photo catalysts (surface plasmon resonance), the intensity of inelastic light scattering becomes less. C2, C3 intermediates).
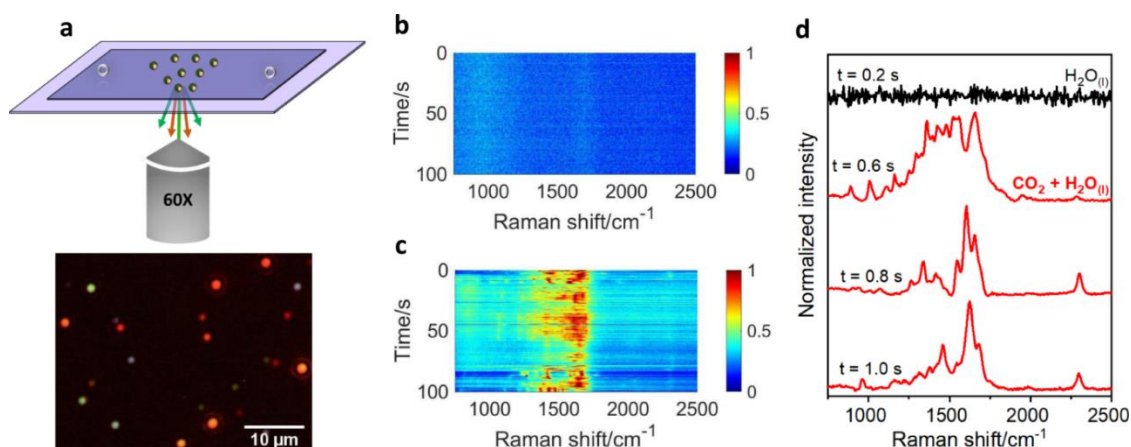
Figure 1.22. (a) Top panel shows a schematic of the single-NP-level SERS spectroscopy set-up used for probing CO_2 photochemistry on a Ag NP in water, i.e., $H_2O_{(1)}$. The Ag NP was immobilized inside a microfluidic cell placed in an inverted optical microscope and subject to continuous-wave focused laser excitation. Raman scattering was continuously collected using a ×60 objective. The bottom panel shows a representative dark-field scattering image of the substrate coated with spatially resolvable Ag NP emitters. Representative spectrograms showing time series of in situ SERS spectra acquired from an individual Ag NP scatterer in **(b)** CO_2-untreated $H_2O_{(1)}$, and **(c)** CO_2-saturated $H_2O_{(1)}$. The SERS intensity is coded by the color, as indicated by the legend. **(d)** Spectral slice, corresponding to t = 0.2 s, from the plot in **Figure 1.22b** shows the lack of any vibrational modes. Spectral slices, corresponding to t = 0.6, 0.8, and 1.0 s from the plot in **Figure 1.22c** show the spectral dynamics taking place in the presence of CO_2-saturated $H_2O_{(1)}$ under LSPR excitation (reproduced with permission from ref. 76).

The luxury of Surface Enhanced Raman Spectroscopy (SERS) can be availed for plasmonic photocatalyst. Silver NPs responded during the SERS experiment (**Figure 1.22a**).[76] Spectral evolution was found upon treating the micro fluidic *in-situ* reaction cell with CO_2 (**Figure 1.22b-d**). Very interestingly, C2 (acetic acid, acetone) and C2+ (butanol) products were obtained. The torsion, symmetric stretching, asymmetric stretching, and bending mode of an array of surface species, including C1, were detected. The best part of this study was predetermination of peak position of these species from DFT calculation and validation of those peaks from experimental findings, which rules out the possibility of misjudgement. The other importance of this technique is the region of interest. In DRIFTS, the focus generally remains on the region more than 1000 cm^{-1}. However, in case of SERS the information can be extracted from 300 cm^{-1}. Therefore, to get the benefit of such technique, a pseudo-in-situ Raman method can be tried to gather information where the Raman spectra can be captured immediately after light irradiation instead of complete operando operation. The knowledge of intermates and behaviour of catalyst surface under light illumination can be used for catalyst engineering. Hence, catalyst design is the major tool for selectivity and efficiency of the process.

1.7. Catalyst design for C1 and C2 products

Visible light-harvesting semiconductor materials are the potential candidate as a photocatalyst. Among different classes of catalysts metal oxide and chalcogenide-based semiconductor, and metal organic framework has been exploited most. Other classes of catalysts are covalent organic framework (COF), Porous organic polymer (POP), halide perovskite and single atom catalyst. Better catalytic efficiency was obtained with modified pristine catalyst. Introduction of doping, defects, vacancies can tune electronic properties as well as gas adsorption capabilities. Hetero-structuring, strain modulation, and organic-inorganic hybrid structure formation can also help in achieving targeted product with good turnover number (TON). A brief discussion of these strategies is given below.

Surface engineering: An advantage for semiconductor materials is that their electronic and catalytic properties can be tunable by using various types of chemical modifications, such as doping, defects, strain engineering and alloying etc.[77] In case of bulk materials, the dopants are mostly trapped inside the structure. However, in the case of the nanomaterial, dopants are mostly on the surface, so there is an eminent possibility of influencing the photocatalytic reaction. Doping a material with suitable metallic and non-metallic elements leads to the enhancement of the photocatalytic activity to either increase the light absorption or tune the electron density.[78-80] For metal doping, the doped metal will introduce a trap state within the band gap that enhances the visible light response (VLR). However, nonmetal doping creates a band near the valance band that reduces the band gap and can enhance the VLR. The demand for higher electron availability for C_2 products formation may sometimes require constructing hetero-junction with different materials. It was recently demonstrated that In doped TiO_2/g-C_3N_4 produces considerable amount of C_2H_4 under UV-Vis light. However, under visible light C_2H_4 has not formed. The lack of adequate electron availability hinders C_2H_4 formation process because TiO_2 cannot harvest visible light.[81] Doping can be introduced in g-C_3N_4 to generate a versatile photocatalyst. Recently, it has been demonstrated that Zn doped g-C_3N_4 is used for photocatalytic methane conversion where CO_2 is used as the soft oxidant.[81] It is found that the Zn-N bonds could serve as electron channels, accelerating the charge separation inside g-C_3N_4 and enabling rapid electron transfer from g-C_3N_4 to surface photo-deposited Ru cocatalyst. This unique behaviour changes the photocatalytic pathway and promotes the formation of CH_3CHO and CH_3CH_2OH demonstrated by in-situ Infra-red spectroscopy. Defects are sometimes responsible for the mid-gap or trap states, which can localize the respective electrons an holes, decreasing the recombination probability and overcoming the multiple

proton coupled electron transfer barrier.[82] For example, Pt sensitized graphene-wrapped defect induced blue TiO_2 in presence become visible light active compared to pure TiO_2 (**Figure 1.23a**).[83] It has been observed the defective blue TiO_2 consist of Ti^{3+} which generates a mid-gap state that can localize the electrons transferred to absorbed CO_2 (**Figure 1.23b**), mapped by Transient Absorption Spectroscopy (TAS). The graphene acts as the hole acceptor, and further, it stabilizes the $CH_3^{.}$ radical and promotes $CH_3^{.}$, $CH_3^{.}$ coupling, which leads to the formation of ethane ($14 e^- + 14 H^+$) (**Figure 1.23c**).

As catalysis is a surface phenomenon, surface defects play an important role. For example, the presence of oxygen vacancy (Vo) helps not only absorption of CO_2 but also the presence of V_o responsible for mid-band gap states, sometimes leading to the formation of dual active metal sites responsible for C-C coupling, leading to the multielectron CO_2-reduced products.[46, 84] Catalyst containing alkali metal dopants is often attributed to diminution of the work function of the catalyst. Na^+-promoted Co NPs coated by thin carbon layer (Na-Co@C) were used as photo-thermo-catalyst in the light-assisted CO_2 hydrogenation. The temperature-induced methane selectivity was altered to C2 hydrocarbons and ethanol by addition of Na+ along with the assistance of light. Na^+ helped in stabilizing CO* intermediate for C-C coupling reaction.[85] In photocatalysis, the defects are sometimes detrimental and usually avoided, but sometimes they play an active role in charge separation and mediating rate limited catalytic state. It will be necessary to go beyond current doping strategies and learn to control sub-bandgap states using defect–defect and defect–polaron interactions.

Metal Free catalyst: Since metal-free catalysts are in-expensive and non-toxic in nature, it has a massive demand for photocatalysis. However, only a few reports are found in this category.
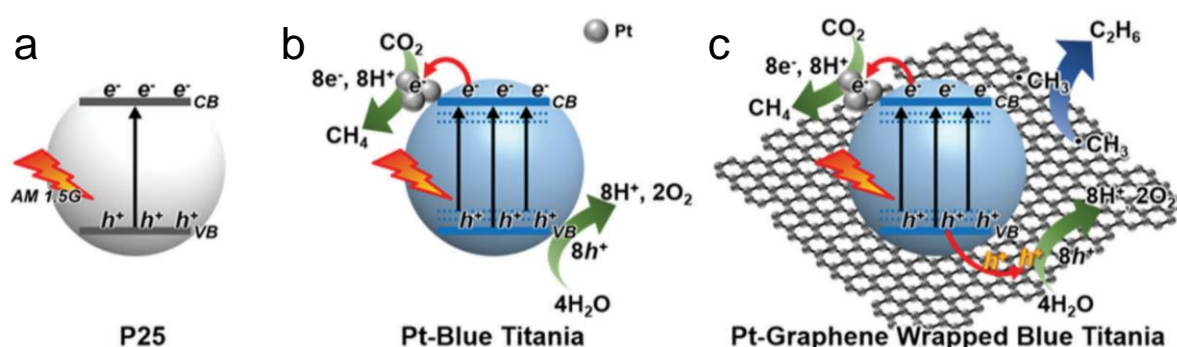
Figure 1.23. Schematic illustration showing photocatalytic CO_2 reduction activity over **(a)** P25 NPS, with sequential transformation of hydrocarbon product selectivity, over **(b)** Pt-sensitized reduced blue titania (RBT), and **(c)** Pt-sensitized graphene-wrapped RBT (reproduced with permission from ref. 83).

Rational design of redox-active conjugated microporous polymer (CMP) was employed comprising electron donating tris (4-ethynylphenyl) amine (TPA) and electron-accepting phenanthraquinone (PQ). This metal-free TAPA-PQ unit showed intra molecular electron transfer derives visible-light induce CO_2 to methane formation with extra ordinary yield (2.15 mmol h^{-1} g^{-1}).[86] Unfortunately, not much information regarding generalized concept of this class of catalysis was not known, and this class of catalysts are not stable for long-term operations. Hence, designing an inorganic-organic hybrid catalyst can offer stability, efficiency and selectivity.

Organic-inorganic hybrid catalyst: Organic counterpart in this short class of materials help as a photosensitizer by pushing the electrons in ground-state or excited-state conditions, thereby increasing local electron density near the active sites. It also wraps the catalyst and provides extra stability from environmental corrosion. Halide perovskites are champion material for light harvesting but suffer from moisture sensitivity. Hence, by designing Core@Shell $CsPbBr_3$@Zeolitic Imidazolate framework (ZIF-67), $CsPbBr_3$ can be stabilized and employed for CO_2 photoreduction in gas-phase reactor. This nano-composite not only showed extra stability but also absorbed more visible light with less charge recombination tendency. As a result of which, the activity has increased from 11 μmol $g^{-1}h^{-1}$ to 29 μmol $g^{-1}h^{-1}$ just by switching the catalyst from pure $CsPbBr_3$ to $CsPbBr_3$@ZIF-67 nano-composite.[87] It is evident that complex catalyst design has offered better CO_2 reduction efficiency. Therefore muti-component catalysts were investigated for PCR.

Multi-component catalyst: Instead of using only inorganic semiconductors and one organic support, an array of semiconductor-molecular catalysts p-n junction was developed for photo-electrocatalytic CO_2 to $HCOO^-$ production. Photo-anode was prepared by coating NiO on GaN coated Si electrode. After that Ru and Zr based molecular assembly was attached to it (**Figure 1.24**).[88] The electron transfer mechanism in such systems is complicated and needs to be understood for designing such assembly.

1.8. Electron transfer mechanism

The journey of photo-generated electrons from light absorbing material to CO_2 is one of the keys to determining the fact of the process because its availability, loss, and position determine the efficiency of the process and selectivity of the yield. For single component system, it is straightforward. However, for multi-component systems it happens through Z-scheme or type-II mechanism. In Z-scheme process, photo-generated holes of one semiconductor are annihilated by the excited electrons of another semiconductor.
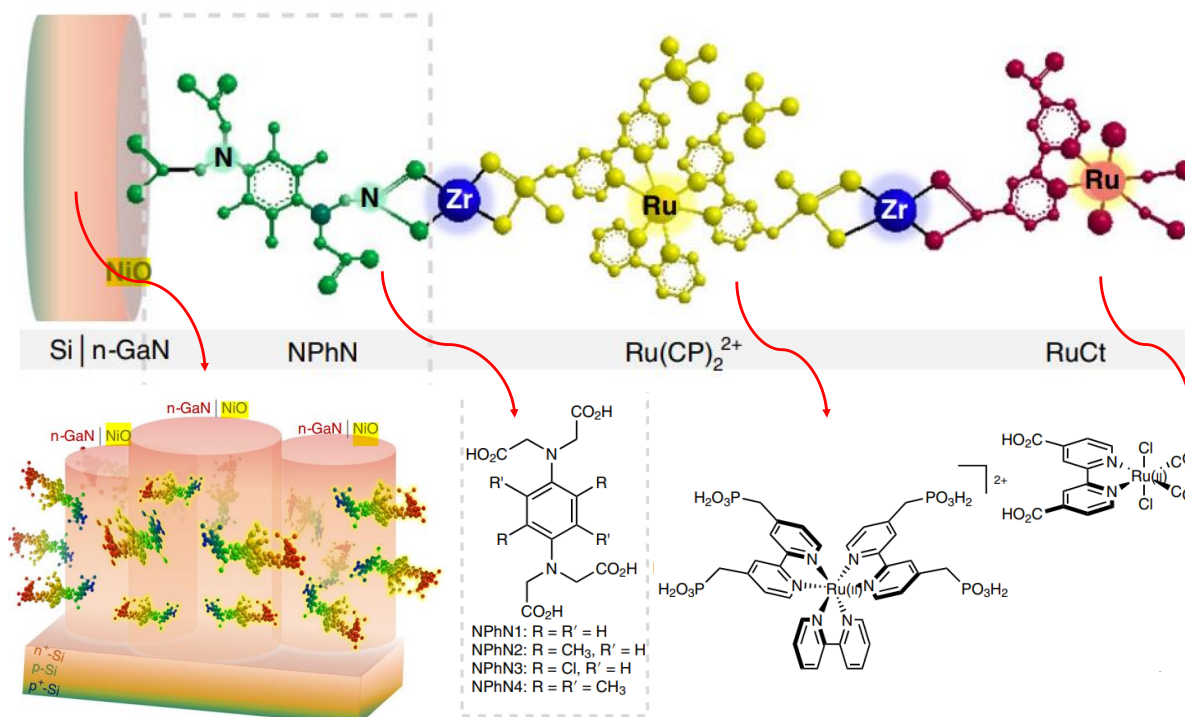
Figure 1.24. Layer-by-layer molecular p–n-junction assembly formed by Zr(iv)-phosphonate bridging. The NPhN, Ru(CP)$_2$$^{2+}$, RuCt and zirconium bridges are shown in green, yellow, red and blue, respectively, in the integrated photocathode structure. n-GaN nanowires on the silicon substrate with the surface-immobilized molecular assemblies are also shown here (reproduced with permission from ref. 87).

Therefore, another set of excited electrons and holes stabilizes in two different semiconductors' conduction band (CB) and valence band (VB), respectively (**Figure 1.25b**). On the other hand, during type-II process, electrons move from one semiconductor's CB to another CB, and holes migrate opposite to electrons' movement in VB. Here electron migration happens from higher energy CB to lower energy CB, and hole migration is opposite of electron migration (**Figure 1.25a**).[89] Another interesting process is relay electron transfer. This happens when there are more than two compartments in the catalytic assembly. The system depicted in **Figure 1.24** follows similar electron transfer pathway. Excited electrons of Si travel to NPhN electron acceptor via GaN. Then this electron annihilated photo generated hole of Ru(CP)$_2$$^{2+}$ (**Figure 1.26a**). Therefore, the excited electrons of Ru(CP)$_2$$^{2+}$ stabilise in its LUMO level. This electron travels to RuCt via Zr bridge and finally reduces CO$_2$ to formate (**Figure 1.26b**).[88] Please note that simultaneous two-photon excitation occurs in this catalytic process. Transient absorption spectroscopy (TAS) and time-resolved photoluminescence spectroscopy (TRPL) can help understand such complex reaction pathways.
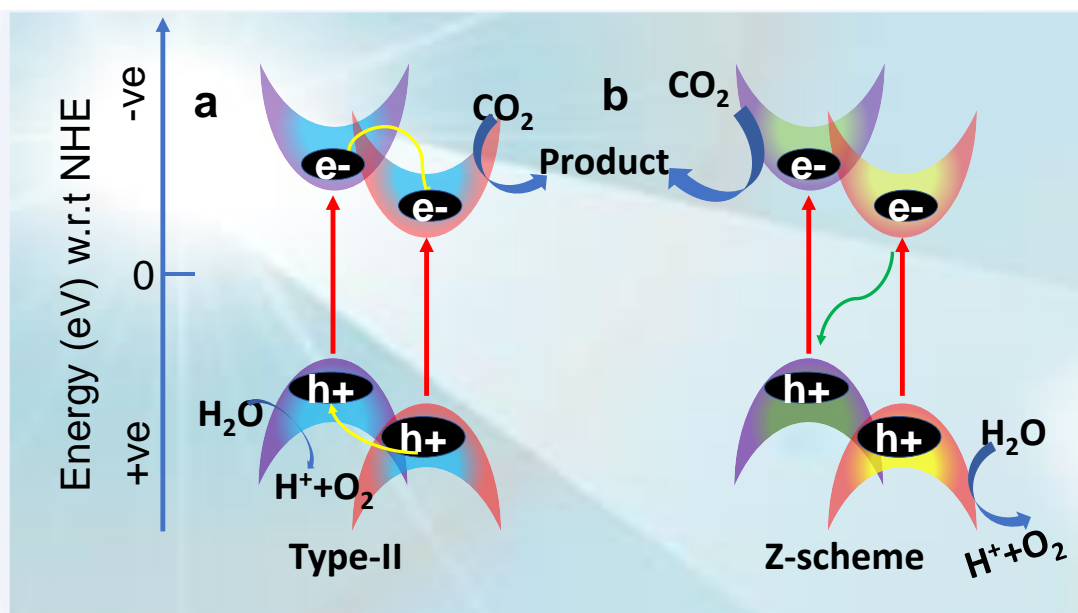
Figure 1.25. Schematic representation of type-II (**a**), and Z-scheme (**b**) process of electron transfer for CO_2 reduction.
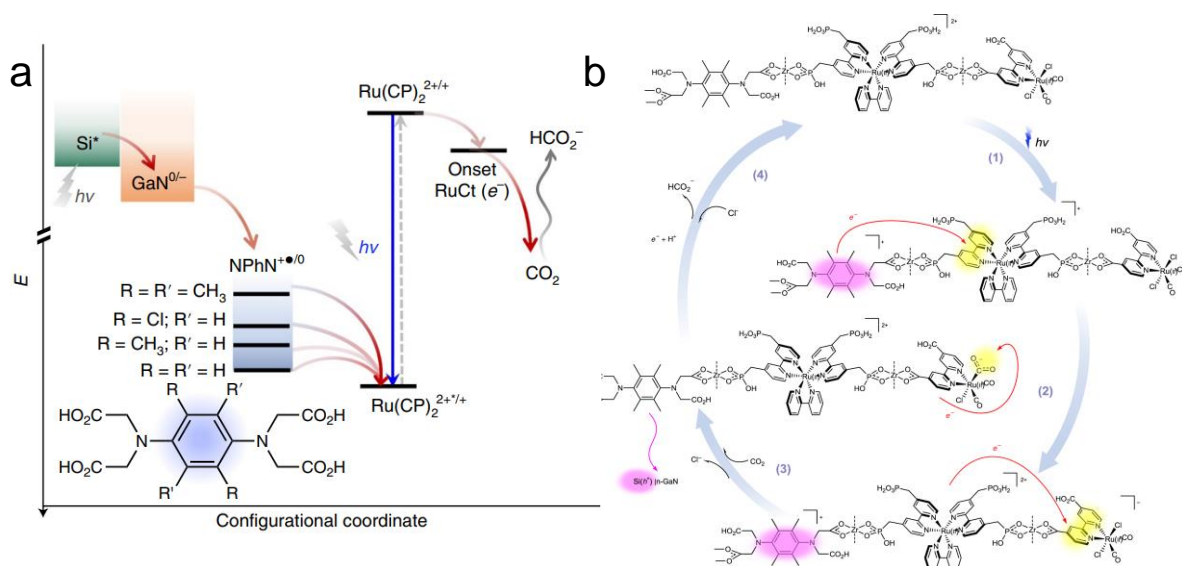
Figure 1.26. (a) Redox-potential diagram illustrating the relative energy levels (E), with red arrows showing the direction of photoinduced electron transfer. (**b**) Photoinduced electron transfer steps towards CO_2 reduction. Locations of photogenerated electron and hole centres are highlighted in yellow and pink, respectively. The red arrows illustrate the intra-assembly electron transfer. The pink arrow shows the interfacial hole transfer. Steps (1)–(4) represent light excitation, formation of the redox-separated state, reduction of CO_2 and regeneration of the initial state, respectively (reproduced with permission from ref. 87).

1.9. Computational chemistry catalysts design

The development of accurate computational algorithms with the augmentation of powerful computational resources played an important role in accelerating the progress in the field of catalyst design.[90-91] Computational catalyst design is a critical and emerging field as it

reduces time and cost due to its predictive nature and inspires new directions for experimental efforts. In the literature, Density functional theory (DFT) calculation with microkinetic modelling is one of the extensively addressed methods for designing efficient catalysts. This method enables direct investigation of mechanistic pathways, reaction kinetics, and identification of active sites on the atomistic scale. Achieving good activity with selectivity is the crux of catalyst design and understanding the reaction kinetics is central to modulating it. In the literature, there are several examples where the kinetics of various catalytic reactions have been modelled successfully based on DFT calculations and microkinetic modelling.[92-95] Hussain et al.[96] showed that calculated rates for electrocatalytic CO_2 reduction over Cu, Pt, Au, Ag, Ni, Rh, Ir, and Fe electrode, obtained using a combination of density functional and microkinetic, are in close agreement with the experimental data on the formation of the various products over a range of applied potential. These are essential benchmarks showing the applicability of the theoretical methods. Therefore, the help of Gibbs's free energy calculation for CO_2 reduction can also be exploited for photocatalysis.

However, those catalysts don't follow a similar mechanistic procedure resulting in different efficiency and selectivity. The efficiency of a photocatalytic conversion generally depends on the light absorption range, charge carrier separation, adsorption capacity for the reactant molecules, and finally desorption rate of the product. Therefore, the choice of catalysts is also different. For example, vacancy-induced product tunability is much common in case of photocatalysis in comparison with electrocatalysis and such observations were carefully studied from DFT. The stabilization of CHO* intermediate on sulphur deficient $CuIn_5S_8$ (*Vs*-CIS) surface compared to pure $CuIn_5S_8$ (CIS) was mapped from Gibbs free energy calculation. As a consequence of better CHO* stabilization, gaseous CO desorption was not observed in case of *Vs*-CIS, resulting 100% methane selectivity.[36] In this thesis, computational chemistry has been efficiently used to design and explain efficient photocatalysts for selective C1, and multi-carbon products.

The photocatalytic CO_2 conversion into high-energy-density C_2 products is challenging, while several reported electrocatalysts showed the reduction of CO_2 to C_2 products. This is more likely due to the low efficiency of multielectron transfer from semiconductor catalysts, excited under illumination, compared to the electrochemical counterpart that provides adequate electron density to reduce CO_2 under bias voltage.[97-98] Few reports in the literature showed the photocatalytic conversion of CO_2 to C_2 products.[99-102] These reports suggested the presence of asymmetric charge density on neighbouring atoms of the photocatalysts as the main factor for

C-C coupling. Using DFT computation, Sheng et al.[103] showed that the presence of a mixed-valence state of Cu, i.e. Cu(I) and Cu(II), in copper oxide photocatalysts favours C-C coupling.

CO* adsorption energy is significantly higher on CuO/Cu2O surface than pure Cu_2O. On the other hand, the change of Gibbs free energy (ΔG) for the formation CO*-CO* coupling is far smaller in case of CuO/Cu_2O compared to pure Cu_2O (111) surface (**Figures 1.27a,** and **1.27b**). Hence feasibility of the C-C coupling process on charge polarise surface can be understood from the analysis of rate-determining steps from DFT calculation. In case of symmetric charge distribution around the adjacent atoms, it brings out the same charge density on the C-atom of the neighbouring intermediates like CO*, CHO* or COOH* formed during the reduction process. This similar charge distribution induces strong dipole−dipole repulsion causing a high kinetic barrier for C−C coupling that hinders the C_2 product formation. So, charge polarization is an essential descriptor for C-C coupling.

Beginning from the Sabatier principle, the descriptor-based investigation has been critical in understanding the designing principles of various catalysts. For electrochemical C-C coupling, several descriptors are discussed in the literature like charge polarization, the position of the d-band centre, structure and composition of the catalysts, applied potential, etc. In this regard, computational chemistry has been an excellent tool for high throughput screening to optimize these descriptors (**Figure 1.28**). The adsorption energies of reaction intermediates are another important descriptor for product selectivity, and volcano plots based on scaling-relations[104] and (Brønsted−Evans−Polanyi) BEP relations[105] of these descriptors have been vastly used to model catalysts with good activity and selectivity.[106-109]
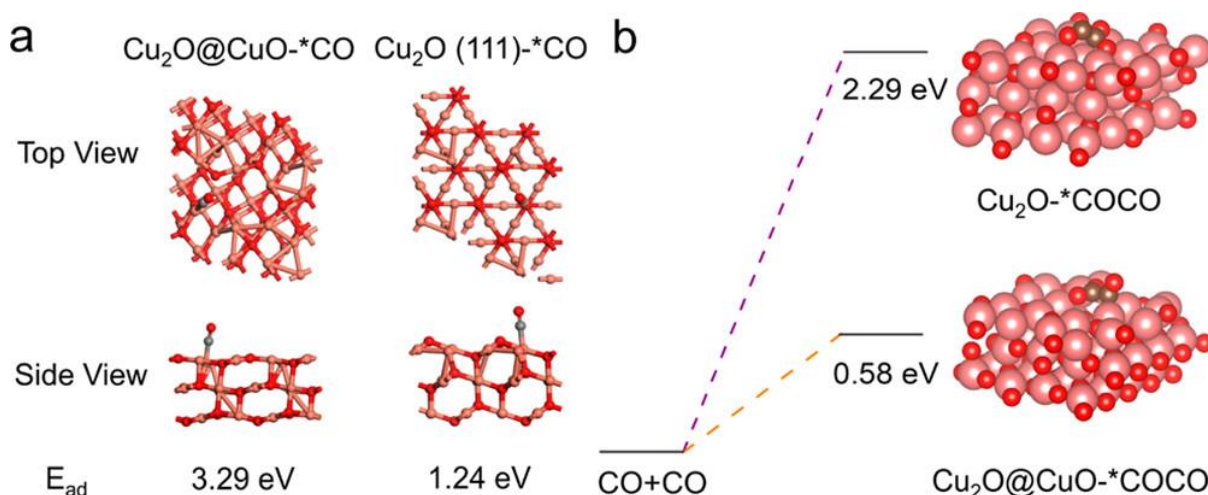
Figure 1.27. (**a**) The ball-and-stick structural models of the theoretical calculations of the adsorption energy of *CO on pristine Cu_2O and $Cu_2O@CuO$. (**b**) First-principles calculations of the C−C coupling step for Cu_2O and $Cu_2O@CuO$. Color code: Cu, pink; O, red; C, gray (reproduced with permission from ref. 101).
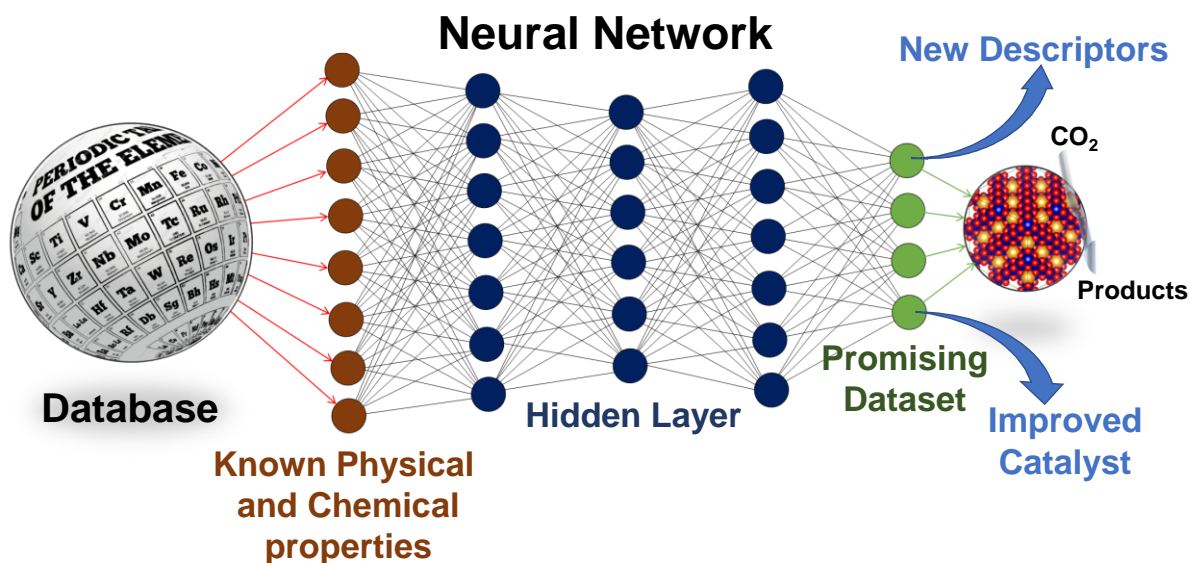
Figure 1.28. Schematic representation of theoretical analysis from known database to unknown CO_2 photo-reduction process.

The descriptor-based approach is not well discussed for photocatalysis as its mechanistic pathway and the dynamics of photo excitons are not very well understood. Time-dependent DFT (TD-DFT)[110] and non-adiabatic excited-state molecular dynamics (NAMD) are often used to study the excited state properties and to model the light-induced dynamics of the photo-excitons.[111] Using these non-trivial quantum mechanical methods in combination with conventional DFT, one can dig up various descriptors for selective C-C coupling to get multi-carbon products. TD-DFT has been successfully applied to the photochemistry of organic molecules.[112-114] Still, the problem with such DFT-based methods is attributed to the lack of double and higher excitations and the accuracy of the strongly correlated system.[111] Some auxiliary theories tackle these problems with standard DFT, such as the Hubbard U parameter used for the strongly correlated system.[115]

An alternative to TD-DFT is Green's functions[116] with the Bethe-Salpeter[117] equation that can give comparably accurate results.[118] It is important to note here that, due to the approximate nature of these computational approaches, one cannot rely entirely on these methods to understand the complex mechanism of PCR. Instead, studies should be performed both at the computational and experimental levels to gain a deeper understanding of the reaction mechanism. The synergy between these complementary approaches, i.e., the computational data combined with the evidence of the mechanism obtained from experimental spectroscopic studies, can be used to draw a global picture of the possible mechanisms of these reactions.

1.10. Scope of the thesis

CO_2 photo reduction is a green and potential field for simultaneously addressing energy and environmental issues. A potentially overlooked area is the overestimation of products from solvent photolysis, unwashed carbonaceous molecules, and oxidation of organic catalysts by photo-generated holes. These pitfalls have been identified, and possible way-out ways are described in this thesis. UV- light assisted photolysis of acetonitrile, tritanol amine, triethyl amine and ethyl acetate was investigated, and the photolysis phenomenon was cross verified by quantifying the oxygen evolution which is regarded as the oxidation counterpart of CO_2 reduction. The discrepancy in mass balance further suggested that all carbonaceous products have not been generated from CO_2 reduction.[119] There have been several scopes of studying catalyst engineering, catalyst characterization, product detection, and mechanism understanding. After this discussion, it is needless to mention that several new problems are still associated with the field of photocatalytic CO_2 reduction. Specifically, a significant modification can be introduced in metal oxide and sulphide-based semiconductor materials. Hetero-structure was reported for photocatalysis. However, strain manipulation upon heterostructure formation was not explored before. On top of that, the inherent problem of carbide mechanism of CO_2 reduction on oxide based semiconductor photocatalysts' surface was demonstrated here for the first time.[120] Next, the attempt was introducing oxygen vacancy in TiO_2 by high-temperature heating. Although this approach is not new but making TiO_2 catalytically active in visible light with the support of secondary semiconductor was introduced first time here in this work and adequate amount of methanol was synthesised by adapting this strategy.[121] Only C1 products were availed by these approaches. However, we have seen the importance of C2 products from above discussions. Therefore, the concept of charge polarization was utilized in single component and multi-component composite catalysts. Only few C-C coupling processes were investigated earlier, but the intermediates are analysed based on DRIFTS and DFT. The concept of primary kinetic isotopic effect in studying CO_2RR mechanism is introduced here. The probability of OCH_3-OCH_3* coupling reaction was rationally established based kinetic isotopic study.[122] Charge polarization coupled with hetero-structure formation can improve selectivity and efficiency synergistically. This phenomenon was not unwrapped earlier specially when the hetero-structure forms with porous organic polymer and inorganic semiconductor. Record high amount of ethylene was synthesised and the all the possible reaction pathway was explored by the help of DFT and DRIFTS. All these concepts are discussed in six chapters of this thesis.

1.11.   References

1.   van Vuuren, D. P.; Stehfest, E.; Gernaat, D. E. H. J.; van den Berg, M.; Bijl, D. L.; de Boer, H. S.; Daioglou, V.; Doelman, J. C.; Edelenbosch, O. Y.; Harmsen, M.; Hof, A. F.; van Sluisveld, M. A. E., Alternative Pathways to the 1.5 °C Target Reduce the Need for Negative Emission Tchnologies. *Nat. Clim. Change* **2018,** *8*, 391-397.

2.   Lewis Nathan, S.; Nocera Daniel, G., Powering the planet: Chemical Challenges in Solar Energy Utilization. *Proc. Natl. Acad. Sci.* **2006,** *103*, 15729-15735.

3.   Inoue, T.; Fujishima, A.; Konishi, S.; Honda, K., Photoelectrocatalytic Reduction of Carbon Dioxide in Aqueous Suspensions of Semiconductor Powders. *Nature* **1979,** *277*, 637-638.

4.   Chen, A.; Zhang, X.; Chen, L.; Yao, S.; Zhou, Z., A Machine Learning Model on Simple Features for CO_2 Reduction Electrocatalysts. *J. Phys. Chem. C* **2020,** *124*, 22471-22478.

5.   Sun, Z.; Ma, T.; Tao, H.; Fan, Q.; Han, B., Fundamentals and Challenges of Electrochemical CO_2 Reduction Using Two-Dimensional Materials. *Chem* **2017,** *3*, 560-587.

6.   Wu, Y. A.; McNulty, I.; Liu, C.; Lau, K. C.; Liu, Q.; Paulikas, A. P.; Sun, C.-J.; Cai, Z.; Guest, J. R.; Ren, Y.; Stamenkovic, V.; Curtiss, L. A.; Liu, Y.; Rajh, T., Facet-dependent Active Sites of a Single Cu_2O Particle Photocatalyst for CO_2 Reduction to Methanol. *Nat. Energy* **2019,** *4*, 957-968.

7.   Shin, H. H.; Suh, Y. D.; Lim, D.-K., Recent Progress in Plasmonic Hybrid Photocatalysis for CO_2 Photoreduction and C–C Coupling Reactions. *Catalysts* **2021,** *11*.

8.   Chen, X.; Shen, S.; Guo, L.; Mao, S. S., Semiconductor-based Photocatalytic Hydrogen Generation. *Chem. Rev.* **2010,** *110*, 6503-6570.

9.   Chen, H.; Nanayakkara, C. E.; Grassian, V. H., Titanium Dioxide Photocatalysis in Atmospheric Chemistry. *Chem.l Rev.* **2012,** *112*, 5919-5948.

10.   Xie, S.; Zhang, Q.; Liu, G.; Wang, Y., Photocatalytic and Photoelectrocatalytic Reduction of CO_2 Using Heterogeneous Catalysts with Controlled Nanostructures. *Chem. Commun.* **2016,** *52*, 35-59.

11.   Mao, J.; Li, K.; Peng, T., Recent Advances in the Photocatalytic CO_2 Reduction over Semiconductors. *Catal. Sci. Technol.* **2013,** *3*, 2481-2498.

12.   Yuan, L.; Xu, Y.-J., Photocatalytic Conversion of CO_2 into Value-added and Renewable Fuels. *Appl. Surf. Sci.* **2015,** *342*, 154-167.

13. Gai, Q.; Zheng, X.; Liu, W.; Dong, Q.; Wang, Y.; Gao, R.; Ren, S., 2D-2D Heterostructured CdS–CoP Photocatalysts for Efficient H_2 Evolution under Visible Light Irradiation. *Int. J. Hydrogen Energy* **2019,** *44*, 27412-27420.

14. Rao, V. G.; Aslam, U.; Linic, S., Chemical Requirement for Extracting Energetic Charge Carriers from Plasmonic Metal Nanoparticles to Perform Electron-Transfer Reactions. *J. Am. Chem. Soc.* **2019,** *141*, 643-647.

15. Kalamaras, E.; Maroto-Valer, M. M.; Shao, M.; Xuan, J.; Wang, H., Solar Carbon Fuel via Photoelectrochemistry. *Catal. Today* **2018,** *317*, 56-75.

16. Castro, S.; Albo, J.; Irabien, A., Photoelectrochemical Reactors for CO_2 Utilization. *ACS Sustain. Chem. Eng.* **2018,** *6*, 15877-15894.

17. Chang, X.; Wang, T.; Yang, P.; Zhang, G.; Gong, J., The Development of Cocatalysts for Photoelectrochemical CO_2 Reduction. *Adv. Mater.* **2019,** *31*, 1804710.

18. Zhang, N.; Long, R.; Gao, C.; Xiong, Y., Recent Progress on Advanced Design for Photoelectrochemical Reduction of CO_2 to Fuels. *Sci. China Mater.* **2018,** *61*, 771-805.

19. Wang, P.; Wang, S.; Wang, H.; Wu, Z.; Wang, L., Recent Progress on Photo-Electrocatalytic Reduction of Carbon Dioxide. *Part. Part. Syst. Charact* **2018,** *35*, 1700371.

20. Centi, G.; Perathoner, S., Catalysis: Role and Challenges for a Sustainable Energy. *Top. Catal.* **2009,** *52*, 948-961.

21. Halmann, M., Photoelectrochemical Reduction of Aqueous Carbon Dioxide on p-Type Gallium Phosphide in Liquid Junction Solar Cells. *Nature* **1978,** *275*, 115-116.

22. LaTempa, T. J.; Rani, S.; Bao, N.; Grimes, C. A., Generation of Fuel from CO_2 Saturated Liquids Using a p-Si Nanowire ‖ n-TiO_2 Nanotube Array Photoelectrochemical Cell. *Nanoscale* **2012,** *4*, 2245-2250.

23. Wang, F.; Li, C.; Chen, H.; Jiang, R.; Sun, L.-D.; Li, Q.; Wang, J.; Yu, J. C.; Yan, C.-H., Plasmonic Harvesting of Light Energy for Suzuki Coupling Reactions. *J. Am. Chem. Soc.* **2013,** *135*, 5588-5601.

24. Wang, D.; Chen, R.; Zhu, X.; Ye, D.; Yang, Y.; Yu, Y.; Li, J.; Liu, Y.; Zhao, H.; Liao, Q., Synergetic Photo-Thermo Catalytic Hydrogen Production by Carbon Materials. *J. Phys. Chem. Lett.* **2022,** *13*, 1602-1608.

25. Liu, H.; Meng, X.; Dao, T. D.; Liu, L.; Li, P.; Zhao, G.; Nagao, T.; Yang, L.; Ye, J., Light Assisted CO_2 Reduction with Methane over SiO_2 Encapsulated Ni Nanocatalysts for Boosted activity and Stability. *J. Mater. Chem. A* **2017,** *5*, 10567-10573.

26. Han, B.; Wei, W.; Chang, L.; Cheng, P.; Hu, Y. H., Efficient Visible Light Photocatalytic CO_2 Reforming of CH_4. *ACS Catal.* **2016,** *6*, 494-497.

27. Zhang, X.; Li, X.; Zhang, D.; Su, N. Q.; Yang, W.; Everitt, H. O.; Liu, J., Product Selectivity in Plasmonic Photocatalysis for Carbon Dioxide Hydrogenation. *Nat. Commun.* **2017,** *8*, 14542.

28. Robatjazi, H.; Zhao, H.; Swearer, D. F.; Hogan, N. J.; Zhou, L.; Alabastri, A.; McClain, M. J.; Nordlander, P.; Halas, N. J., Plasmon-Induced Selective Carbon Dioxide Conversion on Earth-Abundant Aluminum-Cuprous Oxide Antenna-Reactor Nanoparticles. *Nat. Commun.* **2017,** *8*, 27.

29. Nurlaela, E.; Shinagawa, T.; Qureshi, M.; Dhawale, D. S.; Takanabe, K., Temperature Dependence of Electrocatalytic and Photocatalytic Oxygen Evolution Reaction Rates Using NiFe Oxide. *ACS Catal.* **2016,** *6*, 1713-1722.

30. Nikitenko, S. I.; Chave, T.; Cau, C.; Brau, H.-P.; Flaud, V., Photothermal Hydrogen Production Using Noble-Metal-Free Ti@TiO_2 Core–Shell Nanoparticles under Visible–NIR Light Irradiation. *ACS Catal.* **2015,** *5*, 4790-4795.

31. Christopher, P.; Xin, H.; Linic, S., Visible-Light-Enhanced Catalytic Oxidation Reactions on Plasmonic Silver Nanostructures. *Nat. Chem.* **2011,** *3*, 467-472.

32. Mao, M.; Li, Y.; Hou, J.; Zeng, M.; Zhao, X., Extremely Efficient Full Solar Spectrum Light Driven Thermocatalytic Activity for the Oxidation of VOCs on OMS-2 Nanorod Catalyst. *Appl. Catal. B: Environ.* **2015,** *174-175*, 496-503.

33. Wang, L.; Wang, Y.; Cheng, Y.; Liu, Z.; Guo, Q.; Ha, M. N.; Zhao, Z., Hydrogen-Treated Mesoporous WO_3 as a Reducing Agent of CO_2 to Fuels (CH_4 and CH_3OH) with Enhanced Photothermal Catalytic Performance. *J. Mater. Chem. A* **2016,** *4*, 5314-5322.

34. Albero, J.; Peng, Y.; García, H., Photocatalytic CO_2 Reduction to C2+ Products. *ACS Catal.* **2020,** *10*, 5734-5749.

35. Verma, P.; Singh, A.; Rahimi, F. A.; Sarkar, P.; Nath, S.; Pati, S. K.; Maji, T. K., Charge-Transfer Regulated Visible Light Driven Photocatalytic H_2 Production and CO_2 Reduction in Tetrathiafulvalene Based Coordination Polymer gel. *Nat. Commun.* **2021,** *12*, 7313.

36. Li, X.; Sun, Y.; Xu, J.; Shao, Y.; Wu, J.; Xu, X.; Pan, Y.; Ju, H.; Zhu, J.; Xie, Y., Selective Visible-Light-Driven Photocatalytic CO_2 Reduction to CH_4 Mediated by Atomically Thin $CuIn_5S_8$ Layers. *Nat. Energy* **2019,** *4*, 690-699.

37. Li, J.; Huang, H.; Xue, W.; Sun, K.; Song, X.; Wu, C.; Nie, L.; Li, Y.; Liu, C.; Pan, Y.; Jiang, H.-L.; Mei, D.; Zhong, C., Self-Adaptive Dual-Metal-Site Pairs in Metal-Organic Frameworks for Selective CO_2 Photoreduction to CH_4. *Nat. Catal.* **2021,** *4*, 719-729.

38. Ding, J.; Tang, Q.; Fu, Y.; Zhang, Y.; Hu, J.; Li, T.; Zhong, Q.; Fan, M.; Kung, H. H., Core–Shell Covalently Linked Graphitic Carbon Nitride–Melamine–Resorcinol–Formaldehyde Microsphere Polymers for Efficient Photocatalytic CO_2 Reduction to Methanol. *J. Am. Chem. Soc.* **2022,** *144*, 9576-9585.

39. Ma, W.; Xie, S.; Liu, T.; Fan, Q.; Ye, J.; Sun, F.; Jiang, Z.; Zhang, Q.; Cheng, J.; Wang, Y., Electrocatalytic Reduction of CO_2 to Ethylene and Ethanol through Hydrogen-Assisted C–C Coupling over Fluorine-Modified Copper. *Nat. Catal.* **2020,** *3*, 478-487.

40. Chen, Y.; Fan, Z.; Wang, J.; Ling, C.; Niu, W.; Huang, Z.; Liu, G.; Chen, B.; Lai, Z.; Liu, X.; Li, B.; Zong, Y.; Gu, L.; Wang, J.; Wang, X.; Zhang, H., Ethylene Selectivity in Electrocatalytic CO_2 Reduction on Cu Nanomaterials: A Crystal Phase-Dependent Study. *J. Am. Chem. Soc.* **2020,** *142*, 12760-12766.

41. Han, Z.; Kortlever, R.; Chen, H.-Y.; Peters, J. C.; Agapie, T., CO_2 Reduction Selective for C≥2 Products on Polycrystalline Copper with N-Substituted Pyridinium Additives. *ACS Cent. Sci.* **2017,** *3*, 853-859.

42. Li, F.; Thevenon, A.; Rosas-Hernández, A.; Wang, Z.; Li, Y.; Gabardo, C. M.; Ozden, A.; Dinh, C. T.; Li, J.; Wang, Y.; Edwards, J. P.; Xu, Y.; McCallum, C.; Tao, L.; Liang, Z.-Q.; Luo, M.; Wang, X.; Li, H.; O'Brien, C. P.; Tan, C.-S.; Nam, D.-H.; Quintero-Bermudez, R.; Zhuang, T.-T.; Li, Y. C.; Han, Z.; Britt, R. D.; Sinton, D.; Agapie, T.; Peters, J. C.; Sargent, E. H., Molecular Tuning of CO_2-to-Ethylene Conversion. *Nature* **2020,** *577*, 509-513.

43. Chen, X.; Chen, J.; Alghoraibi, N. M.; Henckel, D. A.; Zhang, R.; Nwabara, U. O.; Madsen, K. E.; Kenis, P. J. A.; Zimmerman, S. C.; Gewirth, A. A., Electrochemical CO_2-to-Ethylene Conversion on Polyamine-Incorporated Cu Electrodes. *Nat. Catal.* **2021,** *4*, 20-27.

44. Xia, X.-H.; Jia, Z.-J.; Yu, Y.; Liang, Y.; Wang, Z.; Ma, L.-L., Preparation of Multi-Walled Carbon Nanotube Supported TiO_2 and its Photocatalytic Activity in the Reduction of CO_2 with H_2O. *Carbon* **2007,** *45*, 717-721.

45. Lee, C.-W.; Antoniou Kourounioti, R.; Wu, J. C. S.; Murchie, E.; Maroto-Valer, M.; Jensen, O. E.; Huang, C.-W.; Ruban, A., Photocatalytic Conversion of CO_2 to

Hydrocarbons by Light-Harvesting Complex Assisted Rh-Doped TiO_2 Photocatalyst. *J. CO$_2$ Util.* **2014,** *5*, 33-40.

46. Billo, T.; Fu, F.-Y.; Raghunath, P.; Shown, I.; Chen, W.-F.; Lien, H.-T.; Shen, T.-H.; Lee, J.-F.; Chan, T.-S.; Huang, K.-Y.; Wu, C.-I.; Lin, M. C.; Hwang, J.-S.; Lee, C.-H.; Chen, L.-C.; Chen, K.-H., Ni-Nanocluster Modified Black TiO_2 with Dual Active Sites for Selective Photocatalytic CO_2 Reduction. *Small* **2018,** *14*, 1702928.

47. Kim, W.; Seok, T.; Choi, W., Nafion layer-enhanced photosynthetic conversion of CO_2 into hydrocarbons on TiO_2 nanoparticles. *Energy Environ. Sci.* **2012,** *5*, 6066-6070.

48. Chen, Q.; Chen, X.; Fang, M.; Chen, J.; Li, Y.; Xie, Z.; Kuang, Q.; Zheng, L., Photo-Induced Au–Pd Alloying at TiO_2 {101} Facets Enables Robust CO_2 Photocatalytic Reduction into Hydrocarbon Fuels. *J. Mater. Chem. A* **2019,** *7*, 1334-1340.

49. Zhang, X.; Han, F.; Shi, B.; Farsinezhad, S.; Dechaine, G. P.; Shankar, K., Photocatalytic Conversion of Diluted CO_2 into Light Hydrocarbons Using Periodically Modulated Multiwalled Nanotube Arrays. *Angew. Chem. Int. Ed.* **2012,** *51*, 12732-12735.

50. Yu, S.; Wilson, A. J.; Heo, J.; Jain, P. K., Plasmonic Control of Multi-Electron Transfer and C–C Coupling in Visible-Light-Driven CO_2 Reduction on Au Nanoparticles. *Nano Lett.* **2018,** *18*, 2189-2194.

51. Sánchez-Rodríguez, D.; Jasso-Salcedo, A. B.; Hedin, N.; Church, T. L.; Aizpuru, A.; Escobar-Barrios, V. A., Semiconducting Nanocrystalline Bismuth Oxychloride (BiOCl) for Photocatalytic Reduction of CO_2. *Catalysts* **2020,** *10*, 1315-1321.

52. Maimaitizi, H.; Abulizi, A.; Kadeer, K.; Talifu, D.; Tursun, Y., In Situ Synthesis of Pt and N co-Doped Hollow Hierarchical BiOCl Microsphere as an Efficient Photocatalyst for Organic Pollutant Degradation and Photocatalytic CO_2 Reduction. *Appl. Surf. Sci.* **2020,** *502*, 144083.

53. Dai, W.; Xu, H.; Yu, J.; Hu, X.; Luo, X.; Tu, X.; Yang, L., Photocatalytic Reduction of CO_2 into Methanol and Ethanol over Conducting Polymers Modified Bi_2WO_6 Microspheres under Visible Light. *Appl. Surf. Sci.* **2015,** *356*, 173-180.

54. Liu, Y.; Huang, B.; Dai, Y.; Zhang, X.; Qin, X.; Jiang, M.; Whangbo, M.-H., Selective Ethanol Formation From Photocatalytic Reduction of Carbon Dioxide in Water with $BiVO_4$ Photocatalyst. *Catal. Commun.* **2009,** *11*, 210-213.

55. Liu, X.; Gu, S.; Zhao, Y.; Zhou, G.; Li, W., $BiVO_4$, Bi_2WO_6 and Bi_2MoO_6 Photocatalysis: A Brief Review. *J. Mater. Sci. Tech.* **2020,** *56*, 45-68.

56. Dai, W.; Yu, J.; Deng, Y.; Hu, X.; Wang, T.; Luo, X., Facile Synthesis of MoS_2/Bi_2WO_6 Nanocomposites for Enhanced CO_2 Photoreduction Activity under Visible Light Irradiation. *Appl. Surf. Sci.* **2017,** *403*, 230-239.

57. Zhao, D.; Xuan, Y.; Zhang, K.; Liu, X., Highly Selective Production of Ethanol Over Hierarchical $Bi@Bi_2MoO_6$ Composite via Bicarbonate-Assisted Photocatalytic CO_2 Reduction. *ChemSusChem* **2021,** *14*, 3293-3302.

58. Wang, L.; Zhao, B.; Wang, C.; Sun, M.; Yu, Y.; Zhang, B., Thermally Assisted Photocatalytic Conversion of CO_2–H_2O to C_2H_4 over Carbon Doped In_2S_3 Nanosheets. *J. Mater. Chem. A* **2020,** *8*, 10175-10179.

59. Shown, I.; Samireddi, S.; Chang, Y.-C.; Putikam, R.; Chang, P.-H.; Sabbah, A.; Fu, F.-Y.; Chen, W.-F.; Wu, C.-I.; Yu, T.-Y.; Chung, P.-W.; Lin, M. C.; Chen, L.-C.; Chen, K.-H., Carbon-Doped SnS_2 Nanostructure as a High-Efficiency Solar Fuel Catalyst under Visible Light. *Nat. Commun.* **2018,** *9*, 169.

60. Pan, Y.-X.; You, Y.; Xin, S.; Li, Y.; Fu, G.; Cui, Z.; Men, Y.-L.; Cao, F.-F.; Yu, S.-H.; Goodenough, J. B., Photocatalytic CO_2 Reduction by Carbon-Coated Indium-Oxide Nanobelts. *J. Am. Chem. Soc.* **2017,** *139*, 4123-4129.

61. Chowdhury, A. H.; Das, A.; Riyajuddin, S.; Ghosh, K.; Islam, S. M., Reduction of Carbon Dioxide with Mesoporous SnO_2 Nanoparticles as Active Photocatalysts under Visible Light in Water. *Catal. Sci. Technol.* **2019,** *9*, 6566-6569.

62. Yang, H.; Li, Y.; Zhang, D.; Li, Z.; Wang, J.; Yang, D.; Hao, X.; Guan, G., Defect-Engineering of Tin Oxide via (Cu, N) Co-Doping for Electrocatalytic and Photocatalytic CO_2 Reduction into Formate. *Chem. Eng. Sci.* **2020,** *227*, 115947.

63. Liu, Q.; Cheng, H.; Chen, T.; Lo, T. W. B.; Xiang, Z.; Wang, F., Regulating the *OCCHO Intermediate Pathway Towards Highly Selective Photocatalytic CO_2 Reduction to CH_3CHO over Locally Crystallized Carbon Nitride. *Energy Environ. Sci.* **2022,** *15*, 225-233.

64. Chang, X.; Wang, T.; Gong, J., CO_2 Photo-reduction: Insights into CO_2 Activation and Reaction on Surfaces of Photocatalysts. *Energy Environ. Sci.* **2016,** *9*, 2177-2196.

65. Xiao, C.; Zhang, J., Architectural Design for Enhanced C2 Product Selectivity in Electrochemical CO_2 Reduction Using Cu-Based Catalysts: A Review. *ACS Nano* **2021,** *15*, 7975-8000.

66. Ye, Y.; Yang, H.; Qian, J.; Su, H.; Lee, K.-J.; Cheng, T.; Xiao, H.; Yano, J.; Goddard, W. A.; Crumlin, E. J., Dramatic Differences in Carbon Dioxide Adsorption and Initial Steps of Reduction between Silver and Copper. *Nat. Commun.* **2019,** *10*, 1875.

67. Xie, S.; Ma, W.; Wu, X.; Zhang, H.; Zhang, Q.; Wang, Y.; Wang, Y., Photocatalytic and Electrocatalytic Transformations of C1 Molecules Involving C–C Coupling. *Energy Environ. Sci.* **2021,** *14*, 37-89.

68. Zheng, Y.; Vasileff, A.; Zhou, X.; Jiao, Y.; Jaroniec, M.; Qiao, S.-Z., Understanding the Roadmap for Electrochemical Reduction of CO_2 to Multi-Carbon Oxygenates and Hydrocarbons on Copper-Based Catalysts. *J. Am. Chem. Soc.* **2019,** *141*, 7646-7659.

69. Sun, S.; Watanabe, M.; Wu, J.; An, Q.; Ishihara, T., Ultrathin $WO_3 \cdot 0.33H_2O$ Nanotubes for CO_2 Photoreduction to Acetate with High Selectivity. *J. Am. Chem. Soc.* **2018,** *140*, 6474-6482.

70. Zhu, J.; Shao, W.; Li, X.; Jiao, X.; Zhu, J.; Sun, Y.; Xie, Y., Asymmetric Triple-Atom Sites Confined in Ternary Oxide Enabling Selective CO_2 Photothermal Reduction to Acetate. *J. Am. Chem. Soci.* **2021,** *143*, 18233-18241.

71. Luc, W.; Fu, X.; Shi, J.; Lv, J.-J.; Jouny, M.; Ko, B. H.; Xu, Y.; Tu, Q.; Hu, X.; Wu, J.; Yue, Q.; Liu, Y.; Jiao, F.; Kang, Y., Two-dimensional Copper Nanosheets for Electrochemical Reduction of Carbon Monoxide to Acetate. *Nat. Catal.* **2019,** *2*, 423-430.

72. Li, X.; Wang, S.; Li, L.; Sun, Y.; Xie, Y., Progress and Perspective for In Situ Studies of CO_2 Reduction. *J. Am. Chem. Soc.* **2020,** *142*, 9567-9581.

73. Wang, X.; Zhang, H.; Li, W., In situ IR Studies on the Mechanism of Methanol Synthesis from CO/H_2 and CO_2/H_2 over $Cu-ZnO-Al_2O_3$ Catalyst. *Korean J. Chem. Eng.* **2010,** *27*, 1093-1098.

74. Liu, Y.; Chen, S.; Quan, X.; Yu, H., Efficient Electrochemical Reduction of Carbon Dioxide to Acetate on Nitrogen-Doped Nanodiamond. *J. Am. Chem. Soc.* **2015,** *137*, 11631-11636.

75. Muthusamy, M.; Burrell, M. R.; Thorneley, R. N. F.; Bornemann, S., Real-Time Monitoring of the Oxalate Decarboxylase Reaction and Probing Hydron Exchange in the Product, Formate, Using Fourier Transform Infrared Spectroscopy. *Biochemistry* **2006,** *45*, 10667-10673.

76. Devasia, D.; Wilson, A. J.; Heo, J.; Mohan, V.; Jain, P. K., A Rich Catalog of C–C Bonded species formed in CO_2 reduction on a plasmonic photocatalyst. *Nat. Commun.* **2021,** *12*, 2612.

77. Luo, J.; Zhang, S.; Sun, M.; Yang, L.; Luo, S.; Crittenden, J. C., A Critical Review on Energy Conversion and Environmental Remediation of Photocatalysts with Remodeling Crystal Lattice, Surface, and Interface. *ACS Nano* **2019,** *13*, 9811-9840.

78. Xiang, Q.; Yu, J.; Jaroniec, M., Nitrogen and Sulfur co-Doped TiO_2 Nanosheets with Exposed {001} Facets: Synthesis, Characterization and Visible-Light Photocatalytic Activity. *Phys. Chem. Chem. Phys.* **2011,** *13*, 4853-4861.

79. Zong, X.; Sun, C.; Chen, Z.; Mukherji, A.; Wu, H.; Zou, J.; Smith, S. C.; Lu, G. Q.; Wang, L., Nitrogen Doping in Ion-Exchangeable Layered Tantalate towards Visible-Light Induced Water Oxidation. *Chem. Commun.* **2011,** , 6293-6295.

80. Ida, S.; Okamoto, Y.; Koga, S.; Hagiwara, H.; Ishihara, T., Black-Colored Nitrogen-Doped Calcium Niobium Oxide Nanosheets and their Photocatalytic Properties under Visible Light Irradiation. *RSC Adv.* **2013,** *3*, 11521-11524.

81. Park, J.; Liu, H.; Piao, G.; Kang, U.; Jeong, H. W.; Janáky, C.; Park, H., Synergistic Conversion of CO_2 into C1 and C2 Gases Using Hybrid In-Doped TiO_2 and g-C_3N_4 Photocatalysts. *Chem. Eng. J.* **2022,** *437*, 135388.

82. Bai, S.; Zhang, N.; Gao, C.; Xiong, Y., Defect Engineering in Photocatalytic Materials. *Nano Energy* **2018,** *53*, 296-336.

83. Sorcar, S.; Thompson, J.; Hwang, Y.; Park, Y. H.; Majima, T.; Grimes, C. A.; Durrant, J. R.; In, S.-I., High-Rate Solar-Light Photoconversion of CO_2 to Fuel: Controllable Transformation from C1 to C2 Products. *Energy Environ. Sci.* **2018,** *11* (11), 3183-3193.

84. Sun, S.; Watanabe, M.; Wu, J.; An, Q.; Ishihara, T., Ultrathin $WO_3 \cdot 0.33H_2O$ Nanotubes for CO_2 Photoreduction to Acetate with High Selectivity. *J. Am. Chem. Soc.* **2018,** *140*, 6474-6482.

85. Liu, L.; Puga, A. V.; Cored, J.; Concepción, P.; Pérez-Dieste, V.; García, H.; Corma, A., Sunlight-Assisted Hydrogenation of CO_2 into Ethanol and C2+ Hydrocarbons by Sodium-Promoted Co@C Nanocomposites. *Appl. Catal. B: Environ.* **2018,** *235*, 186-196.

86. Barman, S.; Singh, A.; Rahimi, F. A.; Maji, T. K., Metal-Free Catalysis: A Redox-Active Donor–Acceptor Conjugated Microporous Polymer for Selective Visible-Light-Driven CO_2 Reduction to CH_4. *J. Am. Chem. Soc.* **2021,** *143*, 16284-16292.

87. Kong, Z.-C.; Liao, J.-F.; Dong, Y.-J.; Xu, Y.-F.; Chen, H.-Y.; Kuang, D.-B.; Su, C.-Y., Core@Shell $CsPbBr_3$@Zeolitic Imidazolate Framework Nanocomposite for Efficient Photocatalytic CO_2 Reduction. *ACS Energy Lett.* **2018,** *3*, 2656-2662.

88. Shan, B.; Vanka, S.; Li, T.-T.; Troian-Gautier, L.; Brennaman, M. K.; Mi, Z.; Meyer, T. J., Binary Molecular-Semiconductor p–n Junctions for Photoelectrocatalytic CO_2 Reduction. *Nat. Energy* **2019,** *4*, 290-299.

89. Park, J.; Liu, H.; Piao, G.; Kang, U.; Jeong, H. W.; Janáky, C.; Park, H., Synergistic Conversion of CO_2 into C1 and C2 Gases Using Hybrid In-Doped TiO_2 and g-C_3N_4 Photocatalysts. *Chem. Eng. J.* **2022,** *437*, 135388.

90. Tian, Z.; Priest, C.; Chen, L., Recent Progress in the Theoretical Investigation of Electrocatalytic Reduction of CO_2. *Adv. Theory Sim.* **2018,** *1*, 1800004.

91. Vogiatzis, K. D.; Polynski, M. V.; Kirkland, J. K.; Townsend, J.; Hashemi, A.; Liu, C.; Pidko, E. A., Computational Approach to Molecular Catalysis by 3d Transition Metals: Challenges and Opportunities. *Chem. Rev.* **2019,** *119*, 2453-2523.

92. Prašnikar, A.; Jurković, D. L.; Likozar, B., Reaction Path Analysis of CO_2 Reduction to Methanol through Multisite Microkinetic Modelling over Cu/ZnO/Al_2O_3 Catalysts. *Appl. Catal. B: Environ.* **2021,** *292*, 120190.

93. Zijlstra, B.; Zhang, X.; Liu, J.-X.; Filot, I. A. W.; Zhou, Z.; Sun, S.; Hensen, E. J. M., First-Principles Microkinetics Simulations of Electrochemical Reduction of CO_2 over Cu Catalysts. *Electrochimica Acta* **2020,** *335*, 135665.

94. Posada-Borbón, A.; Grönbeck, H., A First-Principles-Based Microkinetic Study of CO_2 Reduction to CH_3OH over In_2O_3(110). *ACS Catal.* **2021,** *11*, 9996-10006.

95. Motagamwala, A. H.; Dumesic, J. A., Microkinetic Modeling: A Tool for Rational Catalyst Design. *Chem.l Rev.* **2021,** *121*, 1049-1076.

96. Hussain, J.; Jónsson, H.; Skúlason, E., Calculations of Product Selectivity in Electrochemical CO_2 Reduction. *ACS Catal.* **2018,** *8*, 5240-5249.

97. Ozin, G. A., Throwing New Light on the Reduction of CO_2. *Adv. Mater.* **2015,** *27*, 1957-1963.

98. Wu, J.; Huang, Y.; Ye, W.; Li, Y., CO_2 Reduction: From the Electrochemical to Photochemical Approach. *Adv. Sci.* **2017,** *4*, 1700194.

99. Zhu, S.; Li, X.; Jiao, X.; Shao, W.; Li, L.; Zu, X.; Hu, J.; Zhu, J.; Yan, W.; Wang, C.; Sun, Y.; Xie, Y., Selective CO_2 Photoreduction into C2 Product Enabled by Charge-Polarized Metal Pair Sites. *Nano Lett.* **2021,** *21*, 2324-2331.

100. Yu, F.; Jing, X.; Wang, Y.; Sun, M.; Duan, C., Hierarchically Porous Metal–Organic Framework/MoS_2 Interface for Selective Photocatalytic Conversion of CO_2 with H_2O into CH_3COOH. *Angew. Chem. Int. Ed.* **2021,** *60*, 24849-24853.

101. Liu, Q.; Cheng, H.; Chen, T.; Lo, T. W. B.; Xiang, Z.; Wang, F., Regulating the *OCCHO Intermediate Pathway towards Highly Selective Photocatalytic CO_2 Reduction to CH_3CHO over Locally Crystallized Carbon Nitride. *Energy Environ. Sci.* **2022,** *15*, 225-233.

102. Wang, T.; Chen, L.; Chen, C.; Huang, M.; Huang, Y.; Liu, S.; Li, B., Engineering Catalytic Interfaces in $Cu^{\delta+}/CeO_2$-TiO_2 Photocatalysts for Synergistically Boosting CO_2 Reduction to Ethylene. *ACS Nano* **2022,** *16*, 2306-2318.

103. Wang, W.; Deng, C.; Xie, S.; Li, Y.; Zhang, W.; Sheng, H.; Chen, C.; Zhao, J., Photocatalytic C–C Coupling from Carbon Dioxide Reduction on Copper Oxide with Mixed-Valence Copper(I)/Copper(II). *J. Am. Chem. Soc.* **2021,** *143*, 2984-2993.

104. Abild-Pedersen, F.; Greeley, J.; Studt, F.; Rossmeisl, J.; Munter, T. R.; Moses, P. G.; Skúlason, E.; Bligaard, T.; Nørskov, J. K., Scaling Properties of Adsorption Energies for Hydrogen-Containing Molecules on Transition-Metal Surfaces. *Phys. Rev. Lett.* **2007,** *99*, 016105.

105. Evans, M. G.; Polanyi, M., Further Considerations on the Thermodynamics of Chemical Equilibria and Reaction Rates. *Trans. Faraday Soc.* **1936,** *32*, 1333-1360.

106. Zhao, Z.-J.; Liu, S.; Zha, S.; Cheng, D.; Studt, F.; Henkelman, G.; Gong, J., Theory-Guided Design of Catalytic Materials Using Scaling Relationships and Reactivity Descriptors. *Nat. Rev. Mater.* **2019,** *4*, 792-804.

107. Craig, M. J.; Coulter, G.; Dolan, E.; Soriano-López, J.; Mates-Torres, E.; Schmitt, W.; García-Melchor, M., Universal Scaling Relations for the Rational Design of Molecular Water Oxidation Catalysts with Near-Zero Overpotential. *Nat. Commun.* **2019,** *10*, 4993.

108. Pérez-Ramírez, J.; López, N., Strategies to Break Linear Scaling Relationships. *Nat. Catal.* **2019,** *2*, 971-976.

109. Wang, T.; Sha, J.; Sabbe, M.; Sautet, P.; Pera-Titus, M.; Michel, C., Identification of Active Catalysts for the Acceptorless Dehydrogenation of Alcohols to Carbonyls. *Nat. Commun.* **2021,** *12*, 5100.

110. Marques, M. A.; Gross, E. K. J. A. r. o. p. c., Time-Dependent Density Functional Theory. **2004,** *55*, 427-455.

111. Nelson, T. R.; White, A. J.; Bjorgaard, J. A.; Sifain, A. E.; Zhang, Y.; Nebgen, B.; Fernandez-Alberti, S.; Mozyrsky, D.; Roitberg, A. E.; Tretiak, S., Non-adiabatic Excited-State Molecular Dynamics: Theory and Applications for Modeling Photophysics in Extended Molecular Materials. *Chem. Rev.* **2020,** *120*, 2215-2287.

112. Rigotti, T.; Casado-Sánchez, A.; Cabrera, S.; Pérez-Ruiz, R.; Liras, M.; de la Peña O'Shea, V. A.; Alemán, J., A Bifunctional Photoaminocatalyst for the Alkylation of Aldehydes: Design, Analysis, and Mechanistic Studies. *ACS Catal.* **2018,** *8*, 5928-5940.

113. Su, Y.-F.; Luo, W.-Z.; Lin, W.-Q.; Su, Y.-B.; Li, Z.-J.; Yuan, Y.-J.; Li, J.-F.; Chen, G.-H.; Li, Z.; Yu, Z.-T.; Zou, Z., A Water-Soluble Highly Oxidizing Cobalt Molecular Catalyst Designed for Bioinspired Water Oxidation. *Angew. Chem. Int.l Ed.* **2022,** *61*, 202201430.

114. Ullah, Z.; Kim, K.; Venkanna, A.; Kim, H. s.; Kim, M. I.; Kim, M.-h., Plausible Pnicogen Bonding of epi-Cinchonidine as a Chiral Scaffold in Catalysis. **2021,** *9*.

115. Dudarev, S. L.; Botton, G. A.; Savrasov, S. Y.; Humphreys, C. J.; Sutton, A. P., Electron-energy-loss spectra and the structural stability of nickel oxide: An LSDA+U study. *Phys. Rev. B* **1998,** *57*, 1505-1509.

116. Hedin, L., New Method for Calculating the One-Particle Green's Function with Application to the Electron-Gas Problem. *Phys. Rev. B* **1965,** *139*, A796-A823.

117. Salpeter, E. E.; Bethe, H. A., A Relativistic Equation for Bound-State Problems. *Phys. Rev.* **1951,** *84*, 1232-1242.

118. Leng, X.; Jin, F.; Wei, M.; Ma, Y., GW method and Bethe–Salpeter equation for calculating electronic excitations. *Wires Comput. Mol. Sci.* **2016,** *6*, 532-550.

119. Das, R.; Chakraborty, S.; Peter, S. C., Systematic Assessment of Solvent Selection in Photocatalytic CO_2 Reduction. *ACS Energy Lett.* **2021**, 3270-3274.

120. Das, R.; Sarkar, S.; Kumar, R.; D. Ramarao, S.; Cherevotan, A.; Jasil, M.; Vinod, C. P.; Singh, A. K.; Peter, S. C., Noble-Metal-Free Heterojunction Photocatalyst for Selective CO_2 Reduction to Methane upon Induced Strain Relaxation. *ACS Catal.* **2022,** *12*, 687-697.

121. Das, R.; Das, K.; Churipard, S. R.; Chirambatte Peter, S., Activating Oxygen deficient TiO_2 in visible region by Bi_2MoO_6 for CO_2 photoreduction to Methanol. *Chem. Commun.* **2022,** *58*, 6638-6641.

122. Das, R.; Das, K.; Ray, B.; Prabhakaran, V.; Chirambatte Peter, S., Green Transformation of CO_2 to Ethanol using Water and Sunlight by Cooperative Endeavour of Naturally Abundant Red Phosphorus and Bi_2MoO_6. *Energy Environ. Sci.* **2022,** *5*, 1967-1976.

Chapter 2

Systematic Assessment of Solvent Selection in Photocatalytic CO$_2$ Reduction
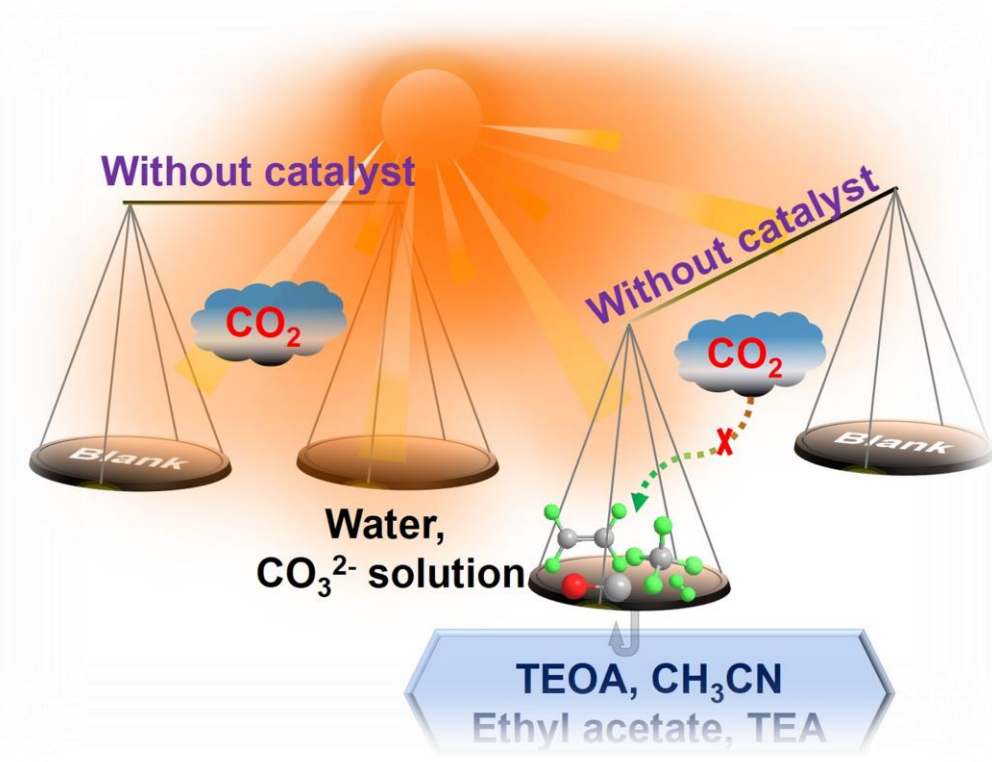
Risov Das, Subhajit Chakraborty, Sebastian C. Peter*. *ACS Energy Lett.* **2021**, *6*, 3270–3274.

Summary

The massive use of fossil fuels has led to a global energy crisis and severe greenhouse effects. Therefore, it is of immediate urgency to develop substitute energy resources and reduce the emission of CO_2. Photocatalytic CO_2 reduction is an up-and-coming method to scale up renewable energy generation and endorse carbon neutrality under mild conditions. However, the efficiency and selectivity of this process are far from satisfactory. Furthermore, using organic additives as a reaction mixture or sacrificial agents can affect the total yield, thus causing false-positive results. Hence, it is of great significance to identify and eliminate photolyze carbonaceous products from the yield. Carbon contaminants in the experiment. Mainly, tri-ethanol amine (TEOA), tri-ethyl amine (TEA), ethyl acetate (EAA), and acetonitrile (ACN) are used during CO_2 photoreduction. The stability of these additives was checked under UV and visible light irradiation in presence and absence of light. Two different case study (CS1, and CS2) were done with two different catalysts, namely $Pt/TiO_2@g-C_3N_4$ (CS1) and $CsPbBr_3/BCN$ (CS2) to understand solvent photolysis behavior. Oxygen quantification was done to prove that all the carbonaceous yields are not generated from CO_2 reduction because O_2 generation is the oxidation counterpart of CO_2 reduction as per the redox reaction. Finally, a guideline was introduced for using different solvents in different light irradiation conditions.

The work based on this chapter was published in ACS Energy Lett.

Systematic Assessment of Solvent Selection in Photocatalytic CO₂ Reduction

Risov Das, Subhajit Chakraborty, Sebastian C. Peter*.

2.1   Introduction

Large-scale combustion of fossil fuels leads to a mammoth deposit of 30 Giga tonnes CO_2 annually on the earth's surface and atmosphere.[1-2] The utilization of abundant solar energy for efficiently converting this anthropogenic CO_2 into the form of fuels and chemicals is a green solution.[3-4] To achieve this, several strategies have been employed. Mainly four factors influence the results of photoinduced reduction of CO_2: (1) Photocatalyst, (2) Reaction medium, (3) Intensity of light source and (4) Design of photocatalytic cell. Among them, the conversion of CO_2 to a particular product in high yield heavily depends on the photo-catalyst and the reaction medium it operates. Apart from the physical conditions like temperature and pressure, the chemical media drives the products selectivity and conversion efficiency.[5] Although extensive exploration of several photocatalysts was reported during the past four decades, only very few conclusive studies were done on the proper selection of reaction medium or solvent.[6] The choice of the solvent is extremely crucial in the photocatalysis pathway.[7]

Since the surge of this research, water has been used as the medium for the conversion of CO_2.[8] However, it suffers heavily due to the sluggish efficiency of the overall process because of the low solubility of CO_2 in water.[9] The efficient alternative to water should be less expensive, have higher solubility of CO_2 and should not degrade under light. In addition, among several processes involved in photocatalytic reactions, mass transfer of reactants and products is one of most important parameters which can be modulated by the wise selection of solvents. Acetonitrile, ethyl acetate, aqueous carbonate solutions and aqueous NaOH solution have been explored as solvents along with several hole scavengers like triethanol amine (TEOA), triethyl amine (TEA) etc.[10-13] These organic solvents are not only used for increasing solubility of CO_2 but also used for performing photo-catalysis with water sensitive samples like halide perovskite. However, the solvents can be photoactive and may lead to the decomposition of the same under selected conditions (wavelength of the light source, multiple combinations of the solvents, temperature, pressure etc.) to one of the CO_2-reduced products, which can mislead the efficiency of the catalysts and overall process. In this context, it is worth mentioning the fact that detecting these pitfalls is of utmost importance because such things may mislead the entire photocatalytic CO_2 reduction community. Unfortunately, this part is overlooked when selecting the solvent as a parameter for improving efficiency.

Here we have performed a detailed analysis of solvent photolysis under a wide range of light irradiation and introduced a flowchart for solvent selection in different regions of the spectrum. For performing this analysis, two composite catalysts were designed. Most importantly, validation of these claims was understood from redox equilibria, where O_2 quantification has implicitly indicated that all the products are not coming from CO_2 reduction. Here, the photo-degrading of BCN moiety in the presence of UV light was also highlighted.

2.2   Experimental details

Synthesis

Chemicals: The following chemicals were used: Titanium dioxide [TiO_2, Alfa Aesar], melamine [Merck], chloroplatinic acid [H_2PtCl_6, Sigma Aldrich], lead bromide [$PbBr_2$, Sigma Aldrich], caesium bromide [CsBr, Sigma Aldrich], boric acid [SDFCL], urea [SDFL], activated charcoal, DMF [Merck], toluene [Merck], hexane [Merck] were purchased from Sigma-Aldrich and used without further purification. All the chemicals used were commercially available and more than 98% pure. They were used without further purification.

Synthesis of g-C₃N₄: The porcelain crucible containing some melamine was placed in a muffle furnace, and the temperature was raised from room temperature to 600 °C for four h, and then cooled down naturally. The ceramic crucible was removed, and its content was grounded into powder to obtain the yellow g-C₃N₄ photocatalyst.

Synthesis of TiO₂@g-C₃N₄ composite: Commercially available P25-TiO_2 and pre-synthesised g-C₃N₄ were placed into a beaker. The mass ratio of g-C₃N₄/TiO_2 was maintained at 1:1. The raw materials were then added into deionized water, stirred evenly for 30 minutes, and ultrasonic mixed for 30 minutes until the powder had completely dispersed. The suspension was transferred into a ceramic crucible and heated at 80 °C for 5 h. Then, the ceramic crucible was calcined at 400 °C for 2 h in a muffle furnace. After being cooled to indoor temperature, the ceramic crucible was removed, and its content grounded into powder to obtain the composite photocatalyst.

Synthesis of Pt-TiO₂@g-C₃N₄ composite: For incorporation of Pt, a 50 ml 0.5 M aqueous solution of H_2PtCl_6 was prepared. The solution was stirred with a 0.5 g TiO_2@g-C₃N₄ composite for about 30 min under UV light irradiation (Newport, 450 W Xe lamp) to get 1 wt % Pt incorporation. The resulting solids were centrifuged and dried under vacuum oven at 80 °C.

Preparation of CsPbBr₃ NC: The synthesis method of the $CsPbBr_3$ was adopted from the literature with some modifications.[14] Briefly, CsBr (0.4 mmol 146.804 mg) and $PbBr_2$ (0.4 mmol, 85.124 mg) were dissolved in 10 ml of DMF, and the resulting solution was ultrasonicated until the solution became clear. The resulting solution (1.2 ml) was added to 10 ml of toluene. The yellow colour $CsPbBr_3$ nanocrystals were precipitated out from the solution. The product was centrifuged and washed with hexane several times and redispersed in hexane for further use.

Preparation of Borocarbonitrides (BCN): Synthesis was carried out by urea method.[15] In a typical synthesis, 60 mg of boric acid, 2.4 g of urea and 275 mg of activated charcoal were mixed step by step, ensuring full solubility of boric acid and urea in 20 mL DI water. Then the proportionate mixture was ultrasonicated (Elmasonic P 30H model, 37 kHz, 100% power) for 20 minutes to obtain a homogeneous dispersion which was heated at 80 °C. When a slurry was obtained as a result of evaporation of the solvent, it was transferred into a quartz boat and heated in a tubular furnace at 900 °C for 10 h under N_2 atmosphere (heating rate = 4°C/min). Subsequently, the obtained black sample was treated with NH_3 at 900 °C for 4 h (heating rate = 4 °C/min). Five different compositions of BCN nanosheets were obtained by varying the initial amount of B, N and C precursor, viz. boric acid, urea, and activated charcoal, respectively.

Preparation of BCN@CsPbBr₃ composite: In order to synthesis the composite, 10 mg of BCN was dispersed in 10 ml of toluene by ultrasonication for 30 mins. Then 1.2 ml of CsBr-$PbBr_2$-DMF solution was added dropwise into the toluene solution with continuous sonication. During the reaction the colour of the solution becomes black to yellowish black. Then the resulting suspension was further ultrasonicated for 10 mins and then kept in undisturbed condition for 30 mins. The product was centrifuged and washed with hexane several times and collected in an air-tight container for future use.

Characterization

X-Ray diffraction: The structural phase of TiO_2, g-C_3N_4, Pt-TiO_2@g-C_3N_4 samples were confirmed by X-ray diffraction (XRD, Rigaku Advance X-ray diffractometer equipped with Cu kα lamp source for irradiation 1.5 Å). All the samples are ground properly before starting the experiment. Data collections are done for 20 minutes for each sample. The phase purity was checked by comparing with reported data set obtained from Pearson crystal data base (PCD).

Microscopy: To understand the morphology of material transmission, electron microscopy (TEM) was taken using a JEOL 200 instrument. Sample preparation was done by drop casting small amount of sonicated powder in ethanol on a carbon coated copper grid. FESEM and Quantitative microanalysis on all the samples were performed with an FEI NOVA NANO SEM 600 instrument equipped with an EDAX® instrument. Data were acquired with an accelerating voltage of 15 kV. Small amount of sample was drop casted on Si wafer after making the dispersion in ethanol.

Photoluminescence (PL): PL spectra of all the solid samples were recorded at room temperature on a steady state Luminescence spectrometer Perkin-Elmer (LS 55) at different excitation wavelength.

The ultraviolet-visible diffuse reflectance spectrum (UV-vis DRS): UV-vis spectra was obtained in the range of 250 to 800 nm by using a Perkin-Elmer Lambda 900 UV/Vis/Near- IR spectrophotometer in reflectance mode for TiO_2, $g-C_3N_4$, $Pt-TiO_2@g-C_3N_4$ samples with an integrating sphere attachment. $BaSO_4$ was used as a 100% reflectance standard. The absorption was calculated data using the Kubelka−Munk equation, $\alpha/S = (1 - R)^2/2R$, where R is the reflectance and α and S are the absorption and scattering coefficients, respectively. Band gap was derived using Tauc plot.

Photoelectrochemical measurements: The transient photocurrent measurements under dark and light were done in a three-electrode system using a CHI 760 potentiostat under the illumination of a solar simulator (Newport) with an ultraviolet (UV) cut-off filter (CGA-400 and KG-2 filter Newport).

Pt-TiO₂@g-C₃N₄ composite catalyst: Ag/AgCl was reference electrode, and platinum as the counter electrode was used. All samples were spin coated on fluorine-doped tin oxide (FTO), which were used as working electrode. 0.5 M Na_2SO_3 was taken as electrolyte. The slurry was prepared by adding 10 mg of the sample, 200 μL of Nafion (5%), and 1 mL of isopropyl alcohol (IPA) to fabricated photoelectrodes. The obtained paste was spin-coated on FTO with 1 cm^2 area and annealed at 100 °C for 1 h to get a homogenous film. For every photo-electrocatalytic experiment separate set of electrodes were prepared. Here 3 experiments were done, namely, photocurrent measurement, electrochemical impedance spectroscopy (EIS) and Mott-Schottky (MS) study. MS plots were recorded at a scan rate of 10 mV/s in Na_2SO_3 neutral solution in the light at a frequency of 50 kHz. Photocurrent measurements were done by using constant negative potential and EIS was also done in constant potential and frequency.

BCN/CsPbBr₃ composite: Non aquas $Ag/AgNO_3$ reference electrode was used instead of $Ag/AgCl$. Platinum was used as the counter electrode. As a working electrode $CsPbBr_3$ and $BCN/CsPbBr_3$ composite were spin coated on FTO. The ethyl acetate with 0.1 M tetrabutylammonium hexafluorophosphate ($TBAPF_6$) was filled in the cell as electrolyte. The electrode was prepared by the above-mentioned method but for slurry preparation instead of IPA toluene was used.

Photocatalytic measurements: A quartz photoreactor was used for CO_2 hydrogenation experiment under the illumination of 450 W UV enhance xenon lamp (Newport). The full arc of this lamp provides wide range of spectral illumination. It contains UV-A, B, C, Visible light and IR light (l = 200-2400 nm). UV-cut-off CGA-400 filter along with KG-2 filter (Newport) was used to get visible light spectrum. For $Pt\_TiO_2\_g\text{-}C_3N_4$ model catalyst, 5 mg of the sample was well dispersed in 20 ml 0.5 M $CsCO_3$ solution. Before illumination, the reaction setup was purged with N_2 to remove the air and then purged with high purity CO_2 for 45 minutes. For $BCN/CsPbBr_3$ catalyst reactions, both vapour and liquid phase reactions were done.

Vapour phase: Five mg catalyst was coated on the wall of photoreactor. CO_2 was bubbled through the water for 1 hour so that the reaction medium will experience the presence of CO_2 and water vapour. In this process, catalyst surface is directly exposed to gas and vapour. That's why this process of reaction is called vapour phase reaction.

Liquid phase: Five mg catalyst were dispersed in a solvent mixture of 10 ml acetonitrile and 40 µl water. Like earlier CO_2 was purged for 45 minutes. Here the interface has created between catalyst surface and solvent mixture. Therefore, this is called liquid phase reaction.

During irradiation, 3 mL of the gaseous product from the setup was sampled, and ensuing study was done by GC (gas chromatography) (Agilent GC-7890 B) with TCD and FID detector and He carrier gas. For the detection of H_2 Ar was used as carrier gas. Blank tests were conducted in the absence of CO_2 and light to confirm that these two factors are key for photocatalytic CO_2 reduction reaction. Used photocatalyst was amassed after each test and washed with water, and its performance was rechecked by a similar procedure.

The results are represented as µ mol/h. Here the amount of catalyst was not taken into the calculation. However, to maintain a parity a constant (100) was multiplied with the obtained values. On the other hand, for $CsPbBr_3$ catalyst, catalyst amount (5 mg) was considered, and results were presented in µ mol/g/h unit. Here this constant (100) was not multiplied.

2.3 Results and discussions

To understand the role of solvent in depth, we have done a systematic investigation of its effect on the product selectivity and activity of the catalyst during photocatalytic CO_2 reduction (PCR) studies. Here, we synthesised a model catalyst $Pt-TiO_2@g-C_3N_4$ and a new catalyst $BCN/CsPbBr_3$ to study their activity towards CR in the presence of various solvents and hole scavengers under artificial UV-Vis light, visible light and sunlight. TiO_2, $Pt-TiO_2$, $g-C_3N_4$ and $Pt-TiO_2@g-C_3N_4$ composite are reported for efficient light harvesting capacity and CO_2 adsorption ability with optimum CR potential was prepared by facile synthetic strategies. The phase purity of materials was characterized by X-ray diffraction (**Figure 2.1a & 2.2b**). No extra peaks related to impurity were detected in the composite and pristine titania. The XRD peaks are properly matching with anatase TiO_2 (space group $Fm\bar{3}m$). Amount of Pt in the composite was very less. Therefore, its intensity was buried under other high intense peaks. However, zoomed version of **Figure 2.1a** depicted the presence of Pt (**Figure 2.1b**). The transmission electron microscopy (**Figure 2.2a,** and **2.2b**) cleared the interface between $g-C_3N_4$ and TiO_2. It also depicted the presence of Pt nanoparticles (**Figure 2.2b**). As shown in **Figure 2.3a,** diffuse reflectance spectra (DRS) coupled with Mott-Schottky measurements **(Figure 2.3b,** and **2.3c**) unravelled the bandgap and flat band potential of catalysts, which indicate the suitable VBM and CBM position of catalyst for PCR.
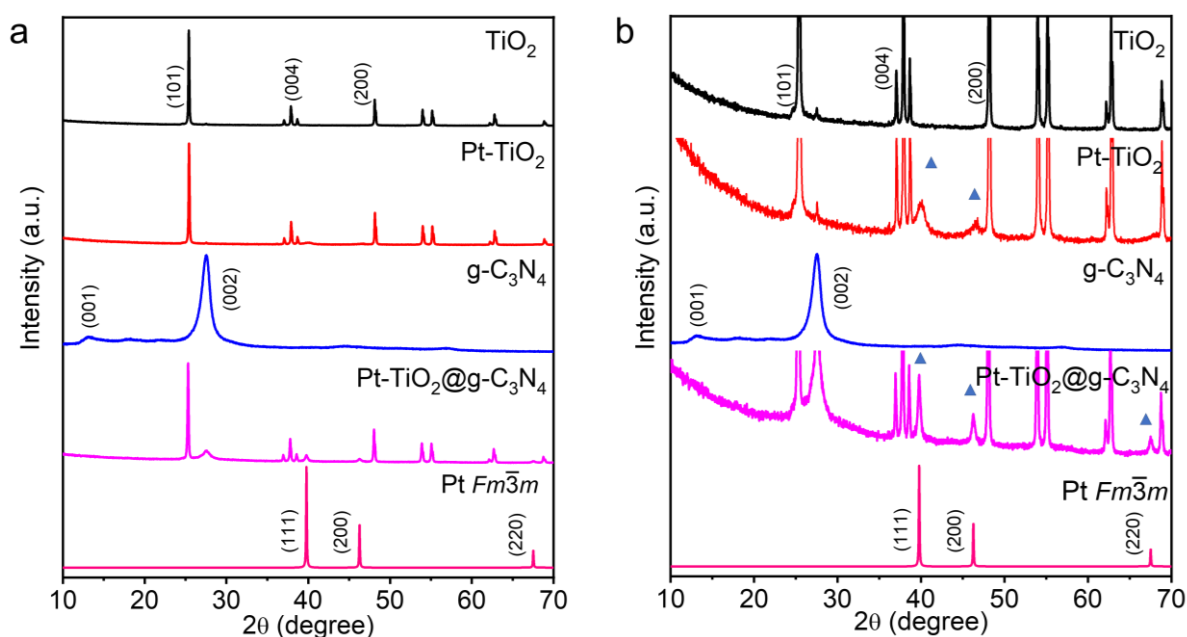
Figure 2.1. Powder XRD analysis. (**a**) Pure phase of TiO_2, $Pt-TiO_2$, $Pt-TiO_2@g-C_3N_4$ was confirmed from XRD. (**b**) The zoomed version of XRD**.** Presence of Pt peaks are shown by triangles.

Two different absorption edge was distinctly found in the spectra of Pt-TiO$_2$/g-C$_3$N$_4$ sample which came from intrinsic individual edges of each component. This confirms that the composite photocatalyst has UV as well as visible light harvesting capabilities. The bare TiO$_2$ can only harvest UV part of the solar spectrum, but upon the composite formation (Pt-TiO$_2$@g-C$_3$N$_4$), the light harvesting ability has been expanded to both UV and Visible region. Static photo-luminescence (PL) spectroscopy in **Figure 2.3d** shows lower emission intensity in case of Pt-TiO$_2$ and weakest intensity was found in case of Pt-TiO$_2$/g-C$_3$N$_4$ composite which implies least photogenerated charge separation in case of the composite. Similar observation was found from electrochemical impedance spectroscopy (**Figure 2.4a**) measurements and transient photocurrent measurements (**Figure 2.4b**). Composite material (Pt-TiO$_2$/g-C$_3$N$_4$) has least charge transfer resistance and highest photocurrent density.
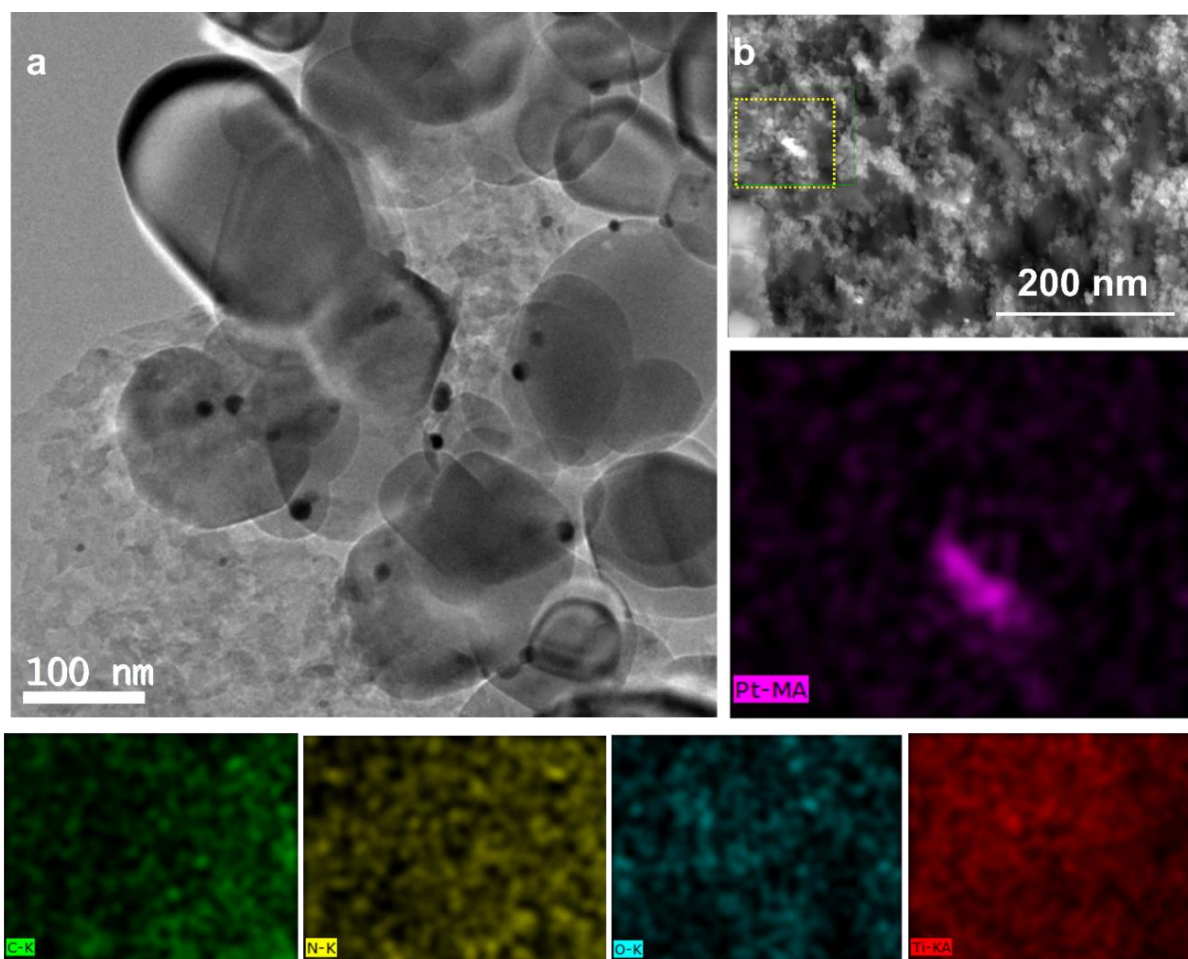
Figure 2.2. (a) TEM image of Pt-TiO$_2$@g-C$_3$N$_4$ shows the presence of TiO$_2$ nano particles on agglomerated g-C$_3$N$_4$ bed. Very small and darkest Pt nanoparticles are distributed over TiO$_2$. **(b)** SEM image of Pt-TiO$_2$@g-C$_3$N$_4$. Presence of Pt nanoparticle were shown inside the yellow box. The same was confirmed from colour mapping. Colour mapping of the composite indicates the presence of Pt, C, N, O and Ti in the composite.

Least resistivity of composite can provide fastest charge transfer pathway, which facilitates easy electron transfer from the catalyst to CO_2. Furthermore, a photocatalyst with more photo-current density can supply enough electron for the catalytic process. Therefore, these experiments clearly hinted that the composite photocatalyst has better charge separation, higher photocurrent generation and lesser charge transfer resistance, respectively. Therefore, Pt-TiO_2@g-C_3N_4 composite can be regarded as the best catalyst compared to the individual components and selected for studying the solvent effect in PCR. Catalytic activity was checked under full arc in the presence of 5 mg catalyst for 10 h in acetonitrile, 0.5 M $CsCO_3$, and ethyl acetate solution under UV-visible light and visible light.
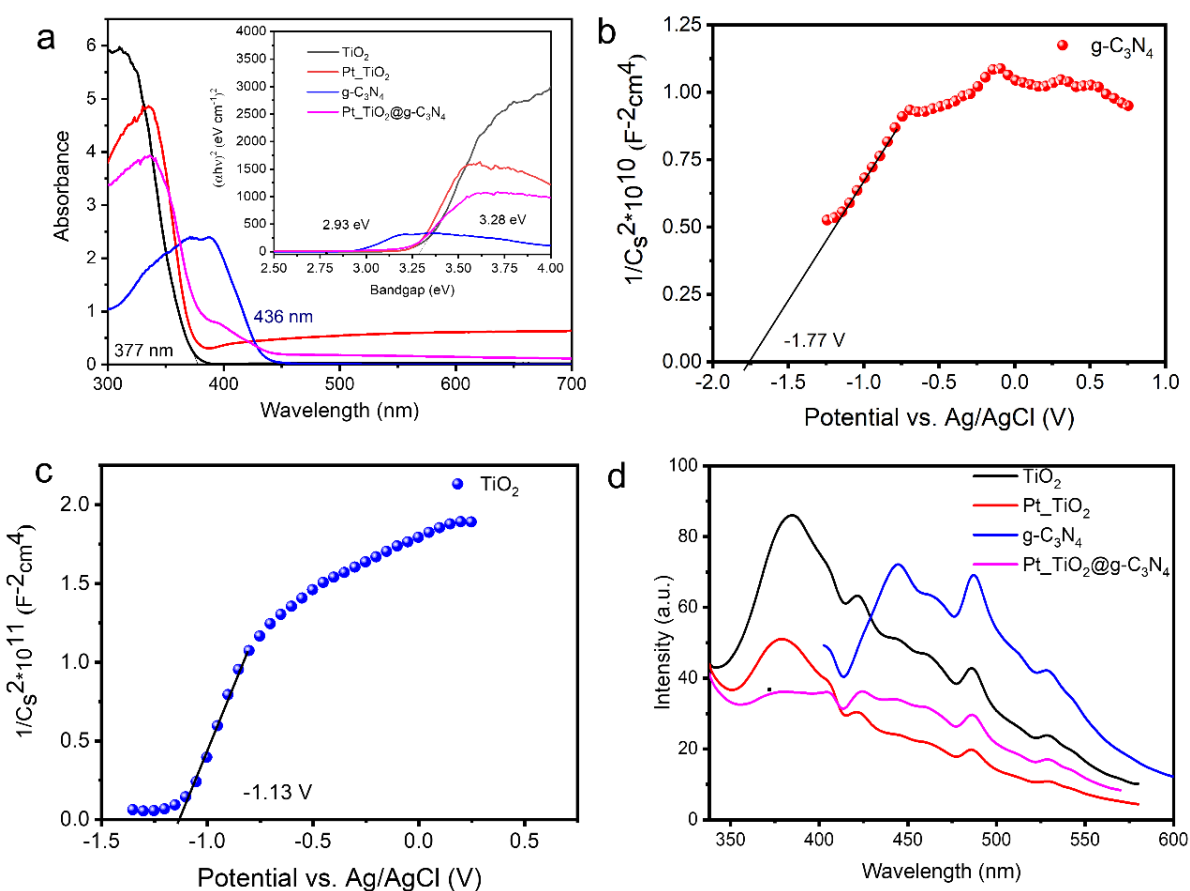
Figure 3. (a) Diffuse reflectance spectra (DRS) show clear absorption band at 436 nm and 377 nm, respectively for g-C_3N_4 and TiO_2 corresponding to the band gap of 2.93 eV and 3.28 eV (inset). Mott-schotky (MS) measurements were performed to determine CBM position of photocatalyst. N-type semiconducting feature of **(b)** g-C_3N_4 and **(c)** Pt-TiO_2 was understood from the positive slopes in MS plots. The flat band potential (equivalent to CBM) for g-C_3N_4 and Pt-TiO_2 are 1.08 V and -0.44 V versus NHE, respectively. **(d)** Photo-luminescence (PL) measurement was performed to understand recombination and separation characteristics of photo-generated charges (electrons and holes). The peaks at 384 nm and 445 nm correspond to the emission of pristine TiO_2 and g-C_3N_4, respectively, in line with the reported literature.

The effect of sacrificial hole scavengers was also checked by using triethanolamine (TEOA) and triethylamine (TEA).[16]

$$(TEOA + h^+ \rightarrow TEOA^+) \qquad \text{Eq. 2.1}$$

$$(TEA + h^+ \rightarrow TEA^+) \qquad \text{Eq. 2.2}$$
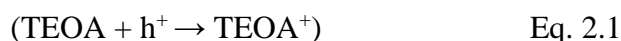
Before the catalysis test, the photocatalytic cell was purged with N_2 to ensure the cell is completely in an inert atmosphere. Then the cell was filled with CO_2 after 45 minutes of purging. **Figure 2.5a & Table 2.1** show the product distribution resulting from PCR and HER under UV-Visible light. As depicted in **Figure 2.5a,** CO, CH_4 and C_2H_4 are expected to originate from CR and H_2 from water splitting process. However, the significant production rate of these compounds in the presence of AC, TEOA, TEA and EAA was quite surprising. Therefore, activity was checked under visible light by following the same reaction condition. Interestingly, a sharp decrease in activity was observed (**Figure 2.5b & Table 2.2**). Under visible light $CsCO_3$ solvent showed relatively higher CR activity compared to other solvents except EAA. To investigate such an interesting fluctuation of activity we have exploited all the solvents under full arc and visible light, separately. **Figure 2.5c & Table 2.3** clearly shows the photolysis of all the organic solvents into CO, CH_4, C_2H_4 and H_2. On the other hand, under visible light AC remained completely silent and other solvents TEOA and TEA have only produced less amount of H_2. Surprisingly EAA still has photolyzed and generated CO, CH_4, C_2H_4 and H_2 (**Figure 2.5d & Table 2.4**). In these circumstances, we can clearly infer the use of AC, TEA, TEOA and EAA under full arc is completely misleading. According to most of the previous reports, the PCR in AC, TEOA, TEA or EAA favoured CO and CH_4 as the major gaseous products.[17-19]
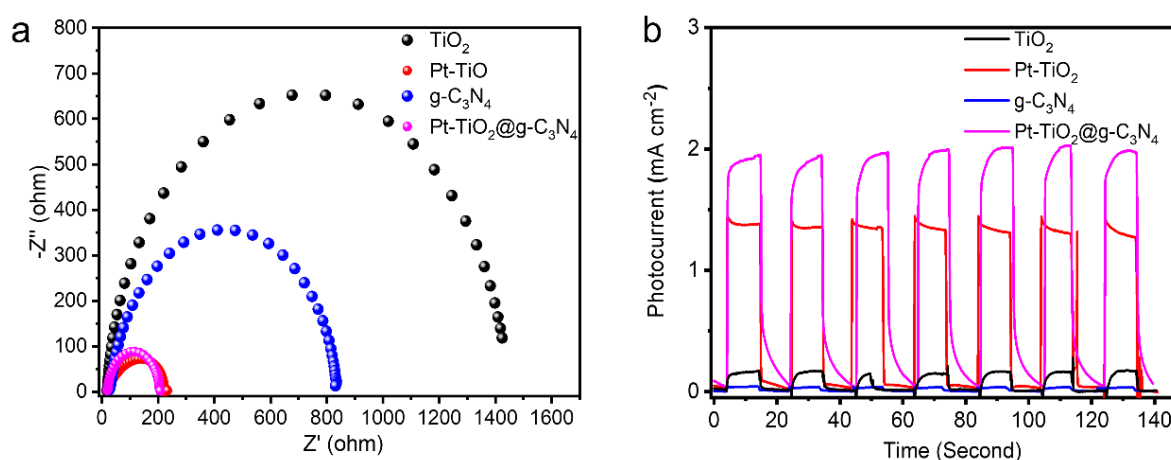
Figure 4. The charge transfer dynamics was studied by **(a)** Electrochemical impedance (EI) measurements and **(b)** Light on-off photocurrent measurements.

TEOA and TEA have generated some amount of H_2 in visible light irradiation which can lead to the underestimation of selectivity towards PCR. However, some reports also claim the absence of H_2 in spite of using TEOA or TEA as sacrificial hole scavenger. GC analysis using He as carrier gas (while doing GC analysis of CO, CH_4 by TCD or FID detector, He is used as carrier gas) cannot sense small amount of H_2 production because the thermal conductivity of H_2 and He are very close. This problem can be avoided by using Ar as carrier gas. Very small amounts of TEOA and TEA were used as sacrificial agents in conventional PCR studies. Therefore, H_2 production upon solvent photolysis under visible light is also very less for these studies.[20-22] EAA is generally used as a solvent in PCR by halide perovskite catalysts. It offers better stability of halide perovskites and good solubility of CO_2. The mixture of AC and water has also been reported as a reaction medium for testing halide perovskite.
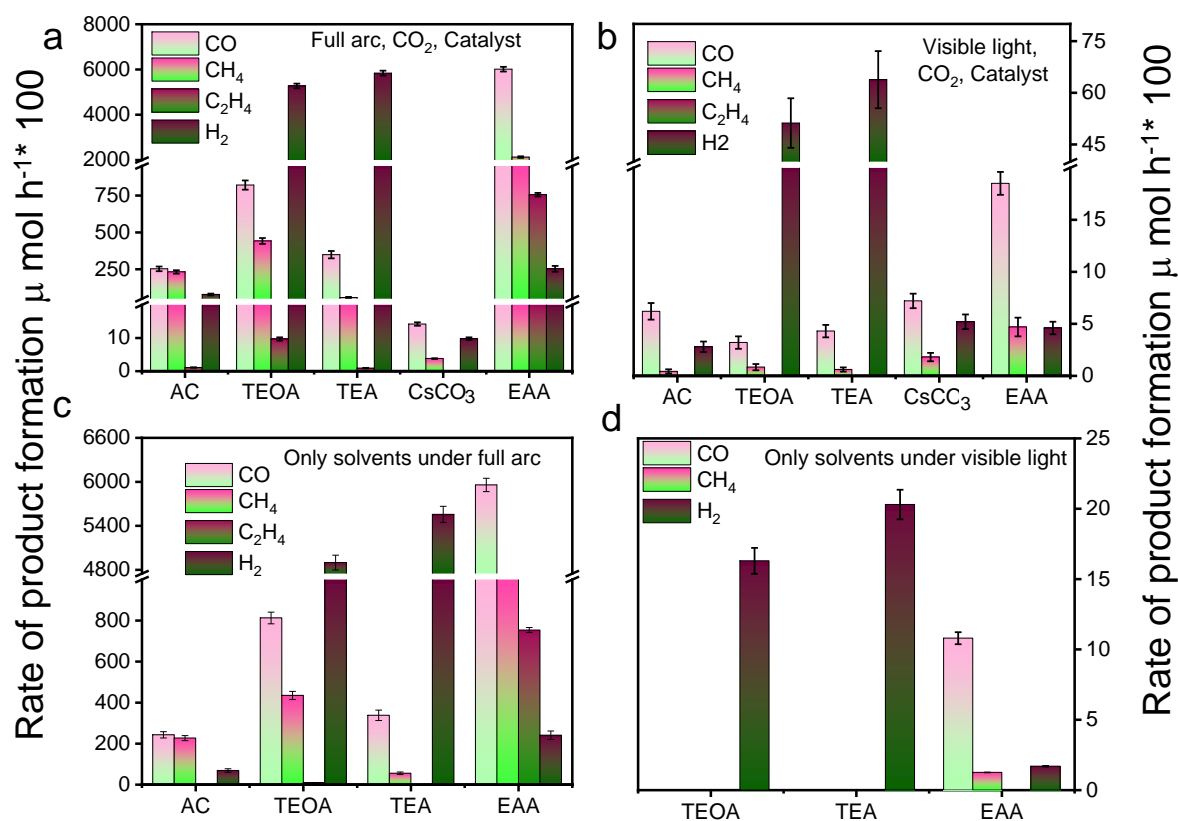
Figure 2.5. Rate of product formed during 450 W Xe (arc) lamp illumination in different conditions. Catalytic study done with Pt-TiO₂@g-C₃N₄ composite in the presence of CO_2 under UV-Visible light (full arc) **(a)**, and visible light **(b).** Solvent photolysis was observed in absence of catalyst and CO_2 under full arc **(c)**, and visible light **(d)**. AC - Acetonitrile, TEOA - Triethanolamine, TEA - Triethylamine, EAA - Ethyl acetate and $CsCO_3$ - 0.5 M caesium carbonate. Mixture of 10 ml organic solvents and 10 ml water were used in all condition. 20 ml 0.5 M $CsCO_3$ solution was used.

An extremely low amount of water was used to protect perovskites. For example, Man et. al used 30 ml AC and 100 µl water as the reaction medium. This procedure may lack adequate proton supply due to insufficient water in the medium. The role of reaction medium for such kind of further verified by designing a new photocatalyst composed of boroncarbonnitride (BCN) and $CsPbBr_3$ (1:3 weight ratio). Purity of the material was confirmed from XRD analysis (**Figure 2.6a**). Excellent light harvesting capacity, suitable band gap and band positions were confirmed from solid state UV-DRS study (**Figure 2.6b**). Betterment of the photocatalyst's quality of composite material ($BCN/CsPbBr_3$) compared to pristine individual elements was confirmed from photo-current, and PL measurements (**Figure 2.6c and 2.6d**). Week emission intensity of composite materials indicated lesser recombination tendency of composite catalyst. In the $CsPbBr_3/BCN$ composite, excited electrons in the $CsPbBr_3$ will rapidly transfer to the BCN since the Fermi level of BCN is more positive than the conduction band edge of $CsPbBr_3$ and due to the conductive nature of BCN. Therefore, separation of charges took place, and recombination process hampered drastically. Moreover, higher photocurrent was generated by composite catalyst upon light on-off experiment. The reason was investigated from analysis of charge transfer resistance from electrochemical impedance spectra (EIS) (**Figure 2.7a**) which shows less charge transfer resistance in composite. The radius of semiarch obtained in the EIS plot corresponds to the resistance of interfacial charge transfer. Potential dependent light responsive behaviour was also observed in case of the $BCN/CsPbBr_3$ composite materials (**Figure 2.7b, and 2.8a).** LSV was performed in presence of light and dark. Positive photocurrent was observed at positive potential whereas negative photocurrent was found in negative potential. Positive photocurrent generated due to the photogenerated hole which has the oxidation ability can perform water oxidation and the negative photocurrent hinted the reducing ability of the composite catalyst (**Figure 2.7b**).

Table 2.1. Results of photocatalytic CR and HER in presence of catalyst, CO_2 under *UV-visible* light (full arc). The results were multiplied with a factor of 100, corresponding to **Figure 2.5a. ND: Not detected.**

Solvents	CO	CH₄	C₂H₄	H₂
AC	253	232	1.1	79
TEOA	821	442	9.7	5271
TEA	349	58.3	0.91	5842
CsCO3	14.2	3.8	ND	9.8
EAA	6014	2129	756	253.2

Table 2.2. Results of PCR and HER in presence of catalyst, CO_2 under *visible* light. UV cut-off CGA-400 and KG-2 filter was used. The results were multiplied with a factor of 100 corresponding to **Figure 2.5b.**

Solvents	CO	CH$_4$	C$_2$H$_4$	H$_2$
AC	6.2	0.43		2.8
TEOA	3.2	0.84		171.2
TEA	4.3	0.61		213.8
CsCO3	7.2	1.81		5.2
EAA	122	14.7	4.8	4.6
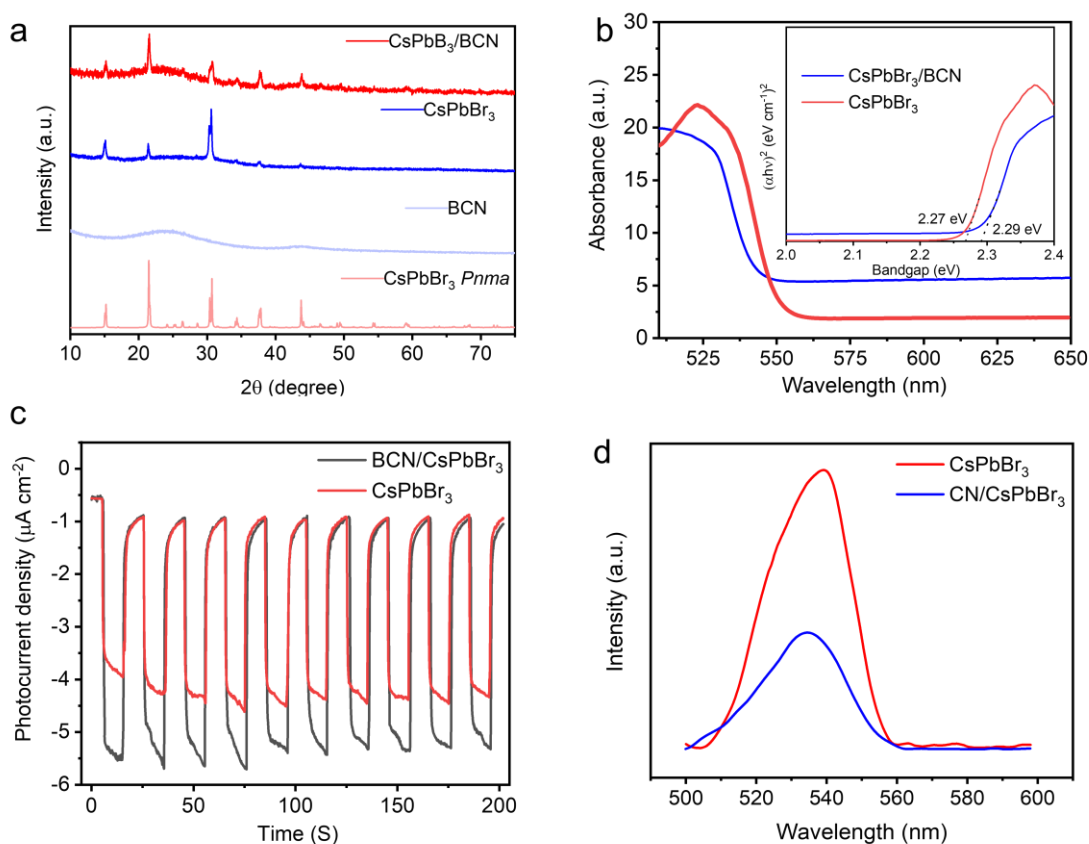
Figure 2.6. (a) Powder XRD patterns of Pristine CsPbBr$_3$, BCN and CsPbBr$_3$/BCN composite. Absence of any other extra peak implies the purity of pristine and composite CsPbBr$_3$. **(b)** DRS spectra of CsPbBr$_3$/BCN composite and pristine CsPbBr$_3$. Absorption edge and band gap (inset) clearly shows the visible light harvesting ability of this catalyst. **(c)** Light on-of photocurrent measurements at -0.7 V with respect to Ag/AgNO$_3$ reference electrode. Excellent photo response was obtained for both the material. However, the composite has generated more photocurrent compared to the pristine CsPbBr$_3$. **(d)** Steady state photoluminescence (PL) spectroscopy. Quenching of PL intensity was observed upon incorporation of CsPbBr$_3$ into BCN. The introduction of BCN provided an additional energy-transfer pathway in addition to the intrinsic radiative channel for excited-state electron transfer.

Table 2.3. Results of photocatalytic CR and HER in absence of catalyst, CO_2 under *UV-visible light* (full arc). The results were multiplied by a factor of 100, corresponding to **Figure 2.5c.**

Solvents	CO	CH₄	C₂H₄	H₂
AC	243	227	0.6	69
TEOA	813	435	9.4	4900
TEA	338	55.6	0.62	5557
EAA	5958	2114	754	241

Table 2.4. Results of photocatalytic CR and HER in absence of catalyst, CO_2 under *visible* light. UV cut-off CGA-400 and KG-2 filter was used. The results were multiplied with a factor of 100 corresponding to **Figure 2.5d.**

Solvents	CO	CH4	C₂H₄	H₂
TEOA				163
TEA				203
EAA	108	12.6	4.3	2.1
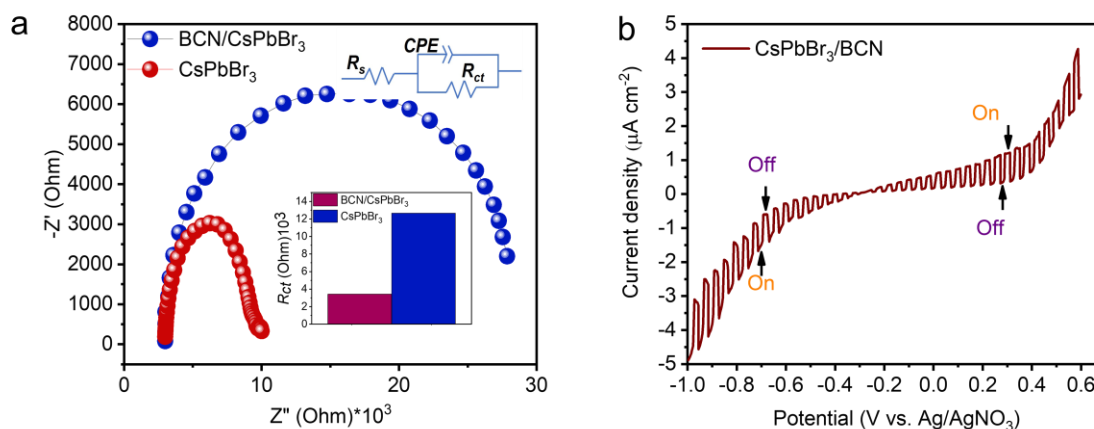
Figure 2.7. (**a**) the Nyquist plots indicated that the charge-transfer resistance obviously decreased for the CsPbBr₃/BCN composite, as evidenced by the smaller semicircle arc (**inset**). The pronounced decrease of the charge-transfer resistance by incorporating BCN clearly validates the better charge transport ability of the BCN/CsPbBr₃ composite. (**b**) Photocurrent density measurements in different potentials for BCN/CsPbBr₃ composite.

Hence this material can perform proton coupled CO_2 reduction where proton comes from the water oxidation. PCR activity of BCN/CsPbBr₃ composite was checked in the catalyst-liquid interface (5 mg catalyst was dispersed in the mixture of 10 ml AC and 40 µl water) and catalyst gas interface (5 mg catalyst was coated inside the photocatalytic cell and CO_2 was bubbled through water for 1 h) condition.[23] Test were not done in EAA because it photolyzes under UV-visible and only visible light irradiation.
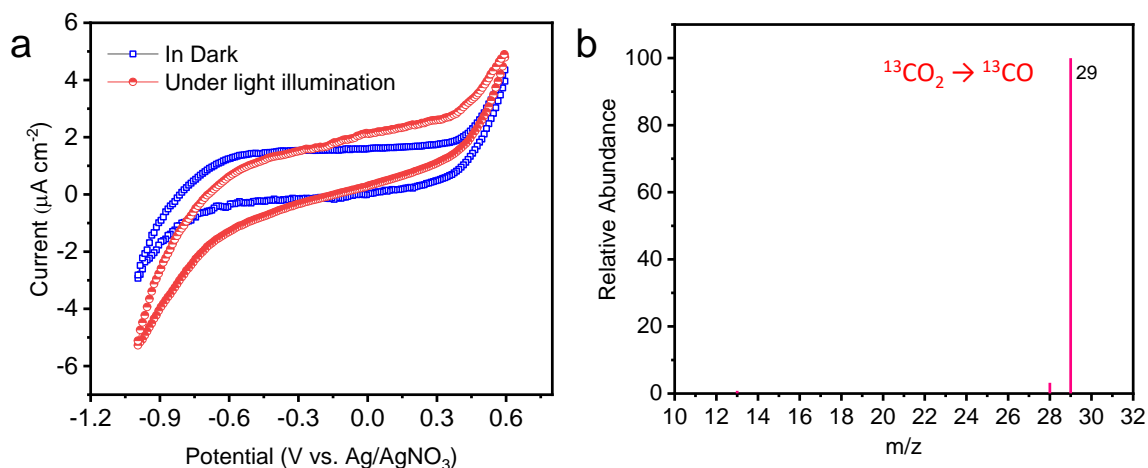
Figure 2.8. (a) CV was done in presence and absence of light with CsPbBr₃/BCN catalyst. Like previous experiment here also enhanced positive and negative current was observed in presence of light. **(b)** GC-MS chromatogram of carbon monoxide. Photocatalytic CO_2 reduction by CPB/BCN catalyst was checked in vapour phase condition where $^{13}CO_2$ was bubbled through water.
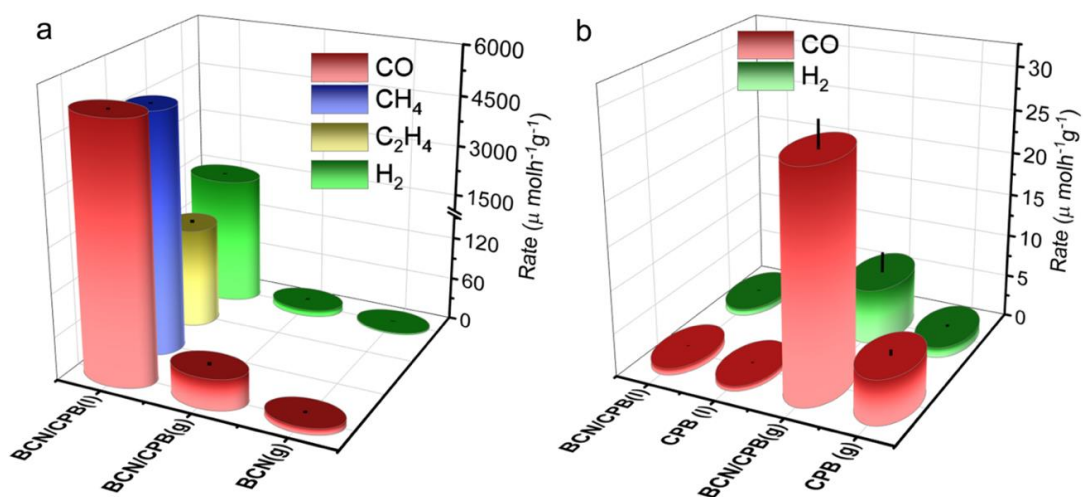
Figure 2.9. Rate of products formation with BCN/CsPbBr₃ composite catalyst in different reaction conditions. Photocatalytic study was done under **(a)** UV-Visible light (l<400 nm) and **(b)** visible light (l= 400-800 nm). CPB - CsPbBr₃, BCN - Boron carbon nitride. "g" and "l" refers the reaction condition. Catalysis was done in catalyst-gas interface condition (g) and catalyst-liquid interface condition (l). The rate has been shown in logarithmic scale.

Table 2.5. Results of PCR and HER with CsPbBr₃/BCN photocatalyst. The catalyst was tested in vapour phase and liquid phase. Catalytic tests were done under *UV-visible light* in presence of CO_2, corresponding to **Figure 2.9a.**

Catalyst	CO	CH₄	C₂H₄	H₂
CPB (g)	9.1			1.85
BCN/CPB (g)	43.3			4.4
BCN/CPB (l)	5240	4820	140	1420

63

Table 2.6. Results of photocatalytic CR and HER with CsPbBr$_3$/BCN photocatalyst. The catalyst was tested in vapour phase and liquid phase. Catalytic tests were done under *visible light* in presence of CO$_2$. UV cut-off CGA-400 and KG-2 filter was used, corresponding to **Figure 2.9b.**

Catalyst	CO	CH$_4$	H$_2$
CPB (g)	5.2	ND	1.2
BCN/CPB (g)	31.4	ND	7.1
CPB (l)	0.6	ND	0.9
BCN/CPB(l)	0.8	ND	0.8

Table 2.7. Representative examples of reaction mediums (as discussed in this study) reported for photocatalytic CO$_2$ reduction.

Material	Medium	Light source	Efficiency	Ref.
CsPbBr$_3$ NCs	ethyl acetate/water (0.3 vol%)	300 W Xe lamp (AM 1.5G)	CO: 4.4 µmol/g/h	24
CsPb(Br$_{0.5}$Cl$_{0.5}$)$_3$ NCs	ethyl acetate	300 W Xe lamp (AM 1.5G)	CO: 97.2 µmol/g/h	25
CsPbBr$_3$@TiO-CN	ethyl acetate/water (0.5 vol%)	300 W Xe lamp ($\geq$400nm)	CO: 12.9 µmol/g/h	26
CsPbBr$_3$ NCs/UiO-66(NH$_2$)	ethyl acetate/water (0.3 vol%)	300 W Xe lamp ($\geq$420nm)	CO: 8.2 µmol/g/h	27
Fe-CsPbBr$_3$ NCs	ethyl acetate/water (0.3 vol%)	450 W Xe lamp (AM 1.5G)	6.1 µmol/g/h for CH$_4$ formation	19
Cs$_2$AgBiBr$_6$ NCs	ethyl acetate	150 mW/cm^2 (AM 1.5G)	CO: 2.35 µmol/g/h	28
CsPbBr$_3$ NCs/GO	ethyl acetate	150 mW/cm^2 (AM 1.5G)	CO: 5 µmol/g/h	11
CsPbBr$_3$ NCs/MXene	ethyl acetate	300 W Xe lamp ($\geq$420nm)	CO: 26.3 µmol/g/h	29

MAPbI$_3$@PCN-221 (Fe$_x$)	ethyl acetate/water (0.3 vol%)	300 W Xe lamp ($\geq$400nm)	CO: 13.75 µmol/g/h	[30]
CsPbBr$_3$ Nc/g-C3N$_4$	acetonitrile/water (0.3 vol%)	300 W Xe lamp ($\geq$420nm)	CO: 148.9 µmol/g/h	[14]
Cs$_3$Bi$_2$I$_9$ NCs	water vapor/CO$_2$ gas	80.3 mW/cm^2 (AM 1.5G)	CO: 7.76 µmol/g/h	[31]
CsPbBr$_3$ Ncs/BZNW/MRGO	water vapor/CO$_2$ gas	150 W Xe lamp (AM 1.5G)	CH$_4$: 6.3 µmol/g/h	[32]
CsPbBr$_3$ NCs/Pd-NS	water vapor/CO$_2$ gas	150 W Xe lamp (AM 1.5G)	CO: 6.3 µmol/g/h	[33]
α-Fe$_2$O$_3$-RGO-CsPbBr$_3$	water vapor/CO$_2$ gas	150 W Xe lamp (AM 1.5G)	10.3 µmol/g/h for CH$_4$ formation	[23]
CsPbBr$_3$-Re (600)	Toluene/isopropanol (1 vol%)	150 W Xe lamp (AM 1.5G)	CO: 33.9 4 µmol/g/h	[34]
MAPbBr$_3$/GO	0.1 M TBAPF$_6$	100 mW/cm^2 (AM 1.5G)	CO: 1.05 µmol/(cm^2 h)	[35]
AgPd/TiO$_2$	Triethylamine (TEA) aqueous solution	300 W Xe lamp (wavelength was not mentioned but TiO$_2$ needs UV light)	H$_2$ 144 µmol/g/h CH$_4$ 79 µmol/g/h	[36]
rGO/TiO$_2$	Triethanolamine (TEOA) aqueous solution	8 W UV-A lamp, full arc	CH$_3$OH: 2330 µmol/g/h	[37]
MWCNT/TiO$_2$	TEOA aqueous solution	8 W UV-A lamp, full arc	H$_2$: 2360 µmol/g/h CH$_3$OH: 3246 µmol/g/h	[38]
CMP-P7	TEA aqueous solution	300 W lamp, ($\geq$295 nm)	H$_2$: 5800 µmol/g/h	[39]
CMP-3D	TEA aqueous solution	300 W lamp, ($\geq$295 nm)	H$_2$: 6076 µmol/g/h	[40]

All the tests were done under visible light as well as UV-visible lights for further validation of above claims. **Figure 2.9** depicts the overall product formation rates in different reaction conditions. Pristine $CsPbBr_3$ (CPB) and $BCN/CsPbBr_3$ composite (BCN/CPB) exhibited CO and H_2 production under full arc in vapour phase condition. Whereas, in liquid phase condition it produces a very high amount of CO, CH_4, C_2H_4 and H_2 (**Figure 2.9a & Table 2.5**), which may be originated from acetonitrile photolysis as we discussed earlier. As depicted in **Figure 2.9b & Table 2.6**, both CPB and BCN/CPB produced CO and H_2 under visible light in vapour phase condition. Although, the activity has decreased due to a lesser supply of photons under visible light compared to UV-visible light.
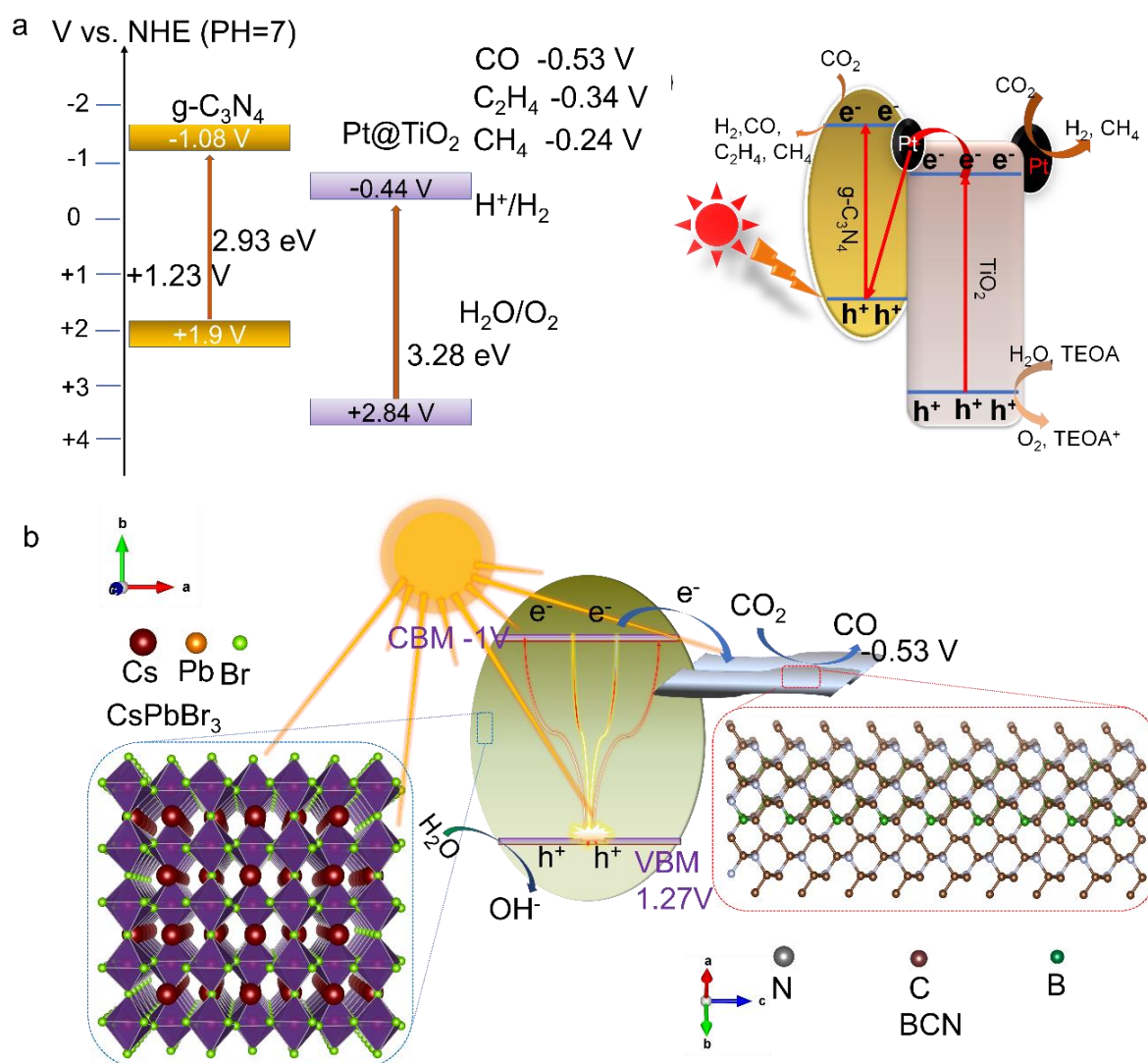
Figure 2.10. Band diagram and electron transfer process. **(a)** Overall band diagram was drawn with the help of MS study and Tauc plot (inset of **Figure 2.3a**). **(b)** Schematic illustration of overall photocatalytic process over $BCN/CsPbBr_3$ composite. In these schemes the electron transfer process was mainly depicted along with band alignment of used semiconductor with respect to CO_2 to product formation redox potential.

66

Interestingly, very little activity (which can be considered zero activity) was found in liquid phase condition (10 ml AC and 40 µl water). The catalyst surface may suffer from adequate water adsorption (or proton adsorption) due to an insufficient supply of water in the medium. The produced CO was solely originating from the reduction of CO_2 by CPB/BCN composite under visible light in vapour phase condition was firmly proved by using $^{13}CO_2$. Highest signal of ^{13}CO (m/z=29) was confirmed from GCMS (**Figure 2.8b**). The photocatalytic process and electron transfer pathway Pt-g-C_3N_4@TiO_2 in $CsCO_3$ solution and BCN/$CsPbBr_3$ composite catalyst in vapour phase are schematically shown in **Figures 2.10a,** and **2.10b.**

Figure 2.10a depicted the reduction potential of CO, CH_4, C_2H_4 and H_2 with respect to the conduction band minima (CBM) of g-C_3N_4 and TiO_2. Schematic representation of electron transfer in composite catalyst. CO, and CH_4 formation occurs on g-C_3N_4 CBM position. CH_4 formation can happen on TiO_2 CBM position as well. Due to inappropriate potential of TiO_2, it alone does not have the capabilities of CO production. Therefore, through Z-scheme process CH_4 formation took place on g-C_3N_4 counterpart. Pt act as a co-catalyst, which facilitates interfacial electron transfer between g-C_3N_4 and TiO_2. It also helps in transferring excited electrons from catalyst to CO_2 and water. In case of BCN wrapped perovskite catalyst (**Figure 2.10b**), photo excited electrons pass from the CBM of $CsPbBr_3$ to the conducting BCN. Then the adsorbed CO_2 get reduce to CO by these electrons. $CsPbBr_3$ has excellent hight harvesting capacity and BCN has conducting and gas adsorbing ability. Combination of these two components make the photocatalyst more effective. CBM and VBM position was understood from previous reports[26] and UV-DRS study.

Mass balance study: Oxygen evolution is the oxidation counterpart of PCR. Therefore, O_2 quantification can implicitly address whether the product originates from photocatalytic redox process or solvent photolysis. As seen from **Figure 2.11a**, the observed O_2 evolution rate is similar to the theoretically calculated O_2 evolution rate when the catalyst was tested in solvents like $CsCO_3$ (full arc and visible region) and ACN (visible region). A small discrepancy was observed when the catalysis was done in TEOA, TEA, and EAA. As observed in **Figure 2.5d**, TEOA, TEA, and EAA can undergo photolysis. Because some amount of products were formed from the photolysis, experimentally observed O_2 is less compared to theoretically calculated O_2 amount. Excess H_2 originated from the visible light driven photolysis of TEOA and TEA, whereas in case of EAA, excess CO, H_2, and CH_4 contribute to a higher theoretical value of O_2. Excessive solvent photolysis (**Figure 2.5a**, and **2.5c**) was observed in the case of organic solvents (ACN, EAA) and hole scavengers (TEA, TEOA) under full arc (200−2400

nm). Therefore, a drastic discrepancy between detected carbonaceous product and evolved O_2 was observed. The same was done for BCN/CPB catalyst. In gas medium and under visible light BCN/CPB or CPB both catalysts showed mass balance between reduced products (CO and H_2) and oxidized product (O_2) (**Figure 2.11b**). However, some amount of CO was obtained from photodegradation of BCN under full arc for BCN/CPB and only BCN in the absence of CO_2 (**Figure 2.11c**),[41] which may be the reason for a slightly lower O_2 evolution rate compared to the expected value for BCN/CPB(g) (**Figure 2.11b**).
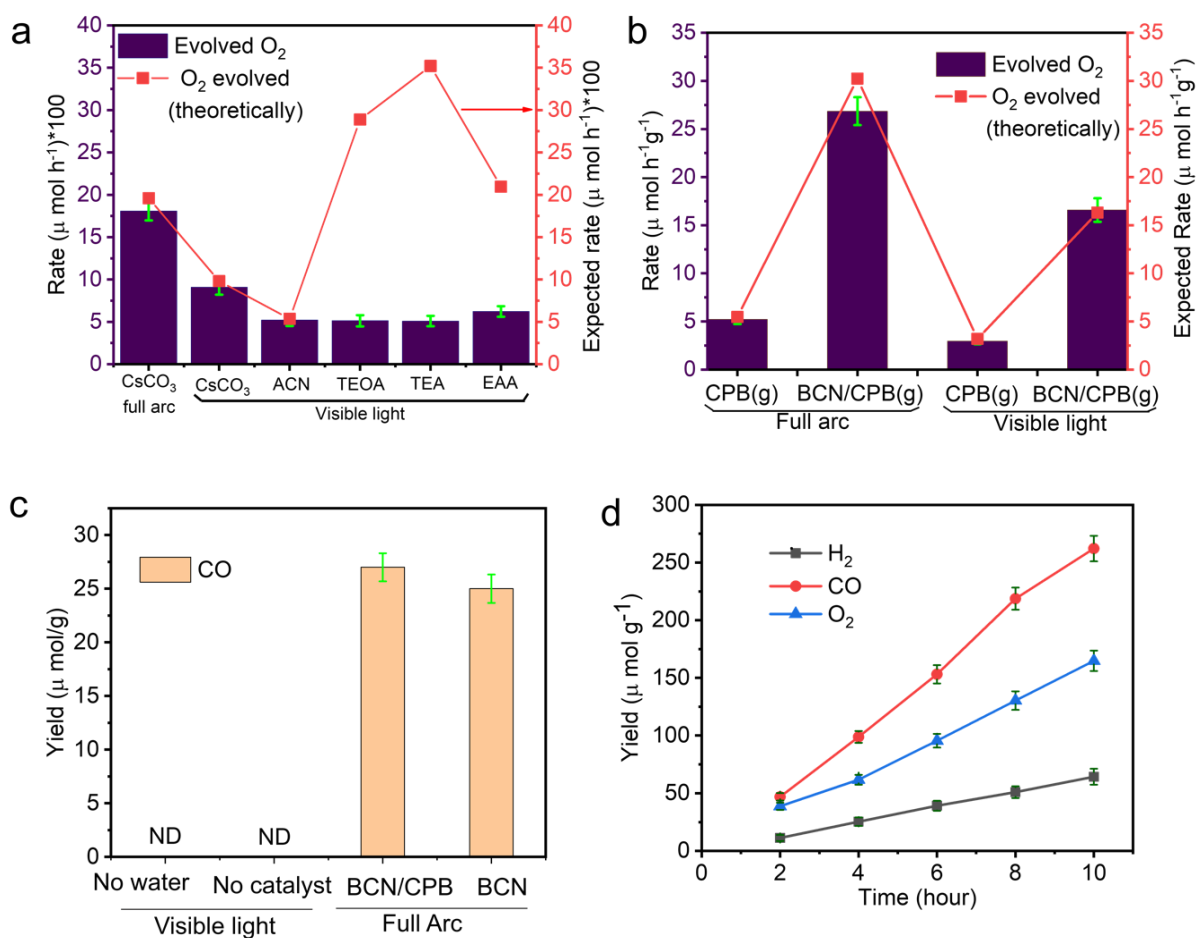
Figure 2.11. (a) Oxygen quantification after photocatalytic CO_2 reduction reaction with Pt-TiO_2@g-C_3N_4 catalyst. Photogenerated holes reduce water and produce O_2. **(b)** Rate of O_2 evolution with respect to theoretically calculated O_2 evolution rate for CPB and BCN/CPB composite catalyst in gas phase condition. **(c)** Control experiments with BCN and BCN/CPB catalyst in absence of CO_2 and water with 5 mg catalyst. Experiments were also done in absence of water vapor and presence of CO_2 in visible light. Another control study was done in absence of catalyst but presence of CO_2 and water vapor. ND: Not detected. **(d)** Total O_2 evolution with respect to time with BCN/CPB catalyst in gaseous medium under visible light.
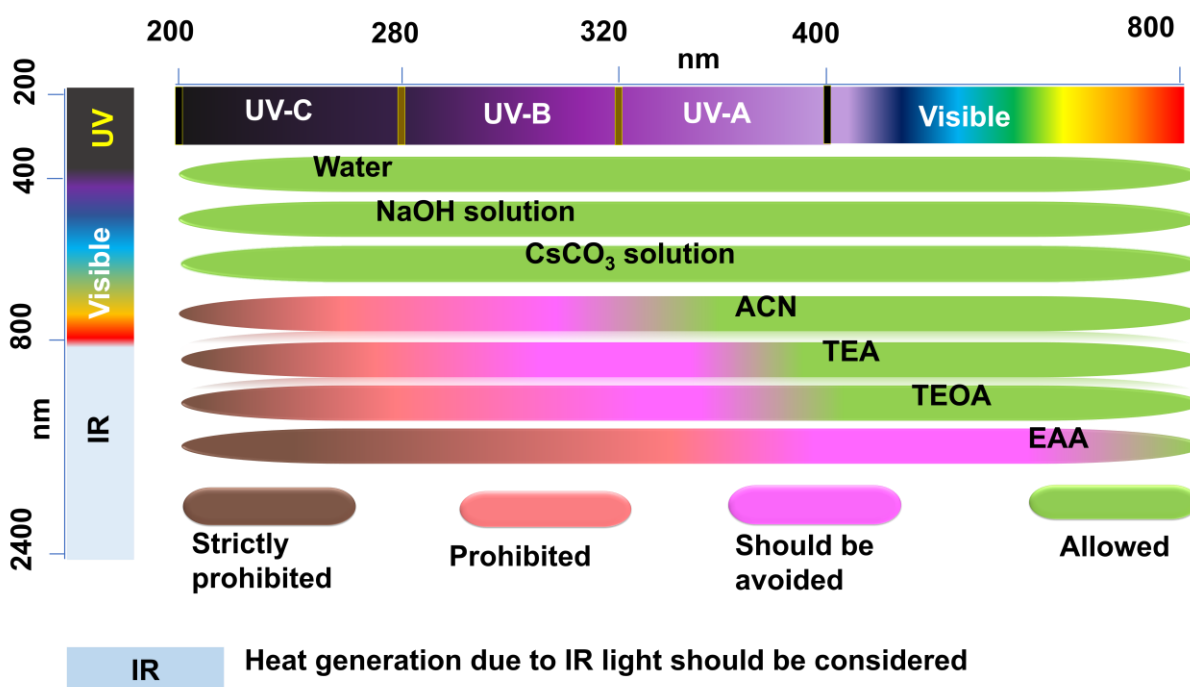
Figure 2.12. Guideline flowchart. Usability of different solvents and sacrificial agents under different energy light irradiation.

In the liquid phase reaction, O_2 was not detected for CPB and BCN/CPB catalysts under the full arc or visible region, clearly manifesting the fact that the generated carbonaceous products in the ACN/water mixture under full arc have not originated from CO_2 reduction. Furthermore, no gas production was observed under visible light in the absence of water vapor or the absence of catalyst (**Figure 2.11c**), which proves that CO_2 to CO production is just not a stoichiometric reaction where the O of CO_2 was left behind in the solid material. The observed CO is coming from the photocatalytic process where water oxidation to O_2 is happening by photogenerated holes. The rate of O_2 generation is proportional and stoichiometric to the rate of CO and H_2 production (**Figure 2.11d**), meaning observed CO and H_2 come from CO_2 reduction and water splitting by BCN/CPB catalyst in gaseous medium. From these observations, it can be clearly inferred that use of ACN, TEA, TEOA, and EAA under full arc leads to misleading results.

2.4. Conclusion

In conclusion, we rationalize the effect of solvent in the photocatalytic CO_2RR and HER. These reactions are often depending on the reaction conditions, particularly the solvent employed. To validate the role of solvent we have done a systematic PCR using several
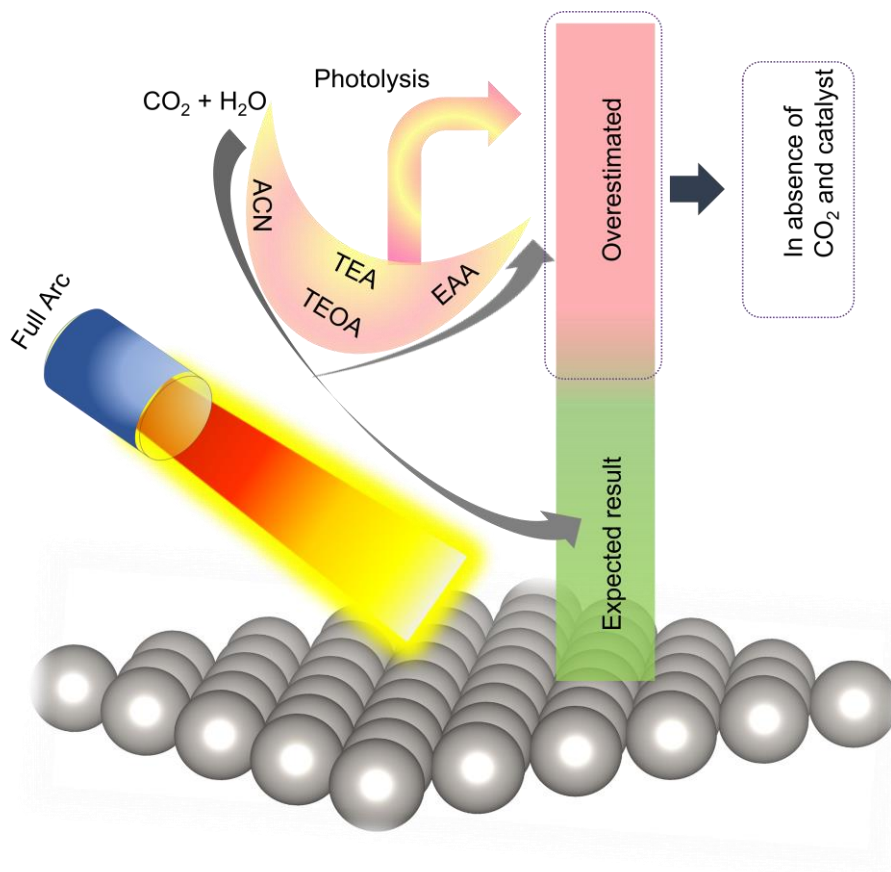
Figure 2.13. Schematic illustration of overestimation of products upon using organic reaction medium in full-arc.

Combinations of solvents under different sources of light using a known photocatalyst Pt-TiO$_2$/g-C$_3$N$_4$ and new composite BCN/CSPbBr$_3$. Our control studies confirmed that the photolysis of CH$_3$CN, Ethyl acetate, TEA and TEOA under UV-visible light, even without any catalysts, can produce CO, CH$_4$, C$_2$H$_4$ and H$_2$. These observations, unfortunately, were overlooked in the literature while selecting the solvent and might have ended up in the overestimation of the efficiency and product selectivity. These findings indicate that the widely used organic reaction medium is extremely sensitive to auto degradation under UV light. Arbitrary selection of organic solvents or sacrificial hole scavengers may lead to the overestimation.[42] Therefore a guideline flowchart for choosing appropriate solvent is provided in **Figure 2.12**. From these, it is clearly seen that EAA is not a suitable solvent for photocatalytic study even under visible light illumination (**Figure 2.13**). Another important one is that catalyst-vapour interface mode of reaction condition is the recommended procedure for water-sensitive samples. Therefore, we encourage scientists to choose proper solvents and hole-scavenger to get unbiased results.

2.5.   References

1. Ozin, G. A., Throwing New Light on the Reduction of CO_2. *Adv. Mater.* **2015,** *27*, 1957-1963.

2. Roy, S.; Cherevotan, A.; Peter, S. C., Thermochemical CO_2 Hydrogenation to Single Carbon Products: Scientific and Technological Challenges. *ACS Energy Lett.* **2018,** *3*, 1938-1966.

3. He, J.; Janáky, C., Recent Advances in Solar-Driven Carbon Dioxide Conversion: Expectations versus Reality. *ACS Energy Lett.* **2020,** *5*, 1996-2014.

4. Wagner, A.; Sahm, C. D.; Reisner, E., Towards Molecular Understanding of Local Chemical Environment Effects in Electro- and Photocatalytic CO_2 Reduction. *Nat. Catal.* **2020,** *3*, 775-786.

5. De Arquer, F. P. G.; Dinh, C.-T.; Ozden, A.; Wicks, J.; McCallum, C.; Kirmani, A. R.; Nam, D.-H.; Gabardo, C.; Seifitokaldani, A.; Wang, X. J. S., CO_2 Electrolysis to Multicarbon Products at Activities Greater Than 1 A cm^{-2}. *Science* **2020,** *367*, 661-666.

6. Liu, B.-J.; Torimoto, T.; Matsumoto, H.; Yoneyama, H., Effect of Solvents on Photocatalytic Reduction of Carbon Dioxide Using TiO_2 Nanocrystal Photocatalyst Embedded in SiO_2 Matrices. *J. Photochem. Photobio. A* **1997,** *108*, 187-192.

7. Chen, Y.-X.; Xu, Y.-F.; Wang, X.-D.; Chen, H.-Y.; Kuang, D.-B., Solvent Selection and Pt Decoration towards Enhanced Photocatalytic CO_2 Reduction over $CsPbBr_3$ Perovskite Single Crystals. *Sustain. Energy Fuels* **2020,** *4*, 2249-2255.

8. Li, X.; Sun, Y.; Xu, J.; Shao, Y.; Wu, J.; Xu, X.; Pan, Y.; Ju, H.; Zhu, J.; Xie, Y., Selective Visible-Light-Driven Photocatalytic CO_2 Reduction to CH_4 Mediated by Atomically Thin $CuIn_5S_8$ Layers. *Nat. Energy* **2019,** *4*, 690-699.

9. Shourong, Z.; Qingguo, H.; Jun, Z.; Bingkun, W., A Study on Dye Photoremoval in TiO_2 Suspension Solution. *J. Photochem. Photobio. A* **1997,** *108*, 235-238.

10. Wang, Y.; Huang, N.-Y.; Shen, J.-Q.; Liao, P.-Q.; Chen, X.-M.; Zhang, J.-P., Hydroxide Ligands Cooperate with Catalytic Centers in Metal–Organic Frameworks for Efficient Photocatalytic CO_2 Reduction. *J. Am. Chem. Soc.* **2018,** *140*, 38-41.

11. Xu, Y.-F.; Yang, M.-Z.; Chen, B.-X.; Wang, X.-D.; Chen, H.-Y.; Kuang, D.-B.; Su, C.-Y., A $CsPbBr_3$ Perovskite Quantum Dot/Graphene Oxide Composite for Photocatalytic CO_2 Reduction. *J. Am. Chem. Soc.* **2017,** *139*, 5660-5663.

12. Jeyalakshmi, V.; Mahalakshmy, R.; Krishnamurthy, K. R.; Viswanathan, B., Photocatalytic Reduction of Carbon Dioxide in Alkaline Medium on La Modified Sodium

Tantalate with Different co-Catalysts under UV–Visible Radiation. *Catal. Today* **2016,** *266*, 160-167.

13. Dimitrijevic, N. M.; Vijayan, B. K.; Poluektov, O. G.; Rajh, T.; Gray, K. A.; He, H.; Zapol, P., Role of Water and Carbonates in Photocatalytic Transformation of CO_2 to CH_4 on Titania. *J. Am. Chem. Soc.* **2011,** *133*, 3964-3971.

14. Ou, M.; Tu, W.; Yin, S.; Xing, W.; Wu, S.; Wang, H.; Wan, S.; Zhong, Q.; Xu, R., Amino-Assisted Anchoring of $CsPbBr_3$ Perovskite Quantum Dots on Porous g-C_3N_4 for Enhanced Photocatalytic CO_2 Reduction. *Angew.Chem. Int. Ed.* **2018,** *57*, 13570-13574.

15. Chhetri, M.; Maitra, S.; Chakraborty, H.; Waghmare, U. V.; Rao, C. N. R., Superior Performance of Borocarbonitrides, $B_xC_yN_z$, as Stable, Low-Cost Metal-Free Electrocatalysts for the Hydrogen Evolution Reaction. *Energy Environ. Sci.* **2016,** *9*, 95-101.

16. Cheng, Z.; Shifa, T. A.; Wang, F.; Gao, Y.; He, P.; Zhang, K.; Jiang, C.; Liu, Q.; He, J., High-Yield Production of Monolayer $FePS_3$ Quantum Sheets via Chemical Exfoliation for Efficient Photocatalytic Hydrogen Evolution. *Adv. Mater.* **2018,** *30*, 1707433.

17. Matsuoka, S.; Yamamoto, K.; Ogata, T.; Kusaba, M.; Nakashima, N.; Fujita, E.; Yanagida, S., Efficient and selective electron mediation of cobalt complexes with cyclam and related macrocycles in the p-terphenyl-catalyzed photoreduction of carbon dioxide. *J, Am. Chem. Soc.* **1993,** *115*, 601-609.

18. Rao, H.; Schmidt, L. C.; Bonin, J.; Robert, M., Visible-Light-Driven Methane Formation From CO_2 with a Molecular Iron Catalyst. *Nature* **2017,** *548*, 74-77.

19. Shyamal, S.; Dutta, S. K.; Pradhan, N., Doping Iron in $CsPbBr_3$ Perovskite Nanocrystals for Efficient and Product Selective CO_2 Reduction. *J. Phys. Chem. Lett.* **2019,** *10*, 7965-7969.

20. Lee, S. E.; Nasirian, A.; Kim, Y. E.; Fard, P. T.; Kim, Y.; Jeong, B.; Kim, S.-J.; Baeg, J.-O.; Kim, J., Visible-Light Photocatalytic Conversion of Carbon Dioxide by Ni(II) Complexes with N_4S_2 Coordination: Highly Efficient and Selective Production of Formate. *J. Am. Chem. Soc.* **2020,** *142*, 19142-19149.

21. Stanley, P. M.; Haimerl, J.; Thomas, C.; Urstoeger, A.; Schuster, M.; Shustova, N. B.; Casini, A.; Rieger, B.; Warnan, J.; Fischer, R. A., Host–Guest Interactions in a Metal–Organic Framework Isoreticular Series for Molecular Photocatalytic CO_2 Reduction. *Angew. Chem. Int. Ed.* **2021,** *60*, 17854-860.

22. Bonin, J.; Robert, M.; Routier, M., Selective and Efficient Photocatalytic CO_2 Reduction to CO Using Visible Light and an Iron-Based Homogeneous Catalyst. *J. Am. Chem. Soc.* **2014,** *136*, 16768-16771.

23. Jiang, Y.; Liao, J.-F.; Chen, H.-Y.; Zhang, H.-H.; Li, J.-Y.; Wang, X.-D.; Kuang, D.-B. J. C., All-Solid-State Z-Scheme α-Fe_2O_3/Amine-RGO/$CsPbBr_3$ Hybrids for Visible-Light-Driven Photocatalytic CO_2 Reduction. *Chem* **2020,** *6*, 766-780.

24. Hou, J.; Cao, S.; Wu, Y.; Gao, Z.; Liang, F.; Sun, Y.; Lin, Z.; Sun, L., Inorganic Colloidal Perovskite Quantum Dots for Robust Solar CO_2 Reduction. *Chem.Eur. J.* **2017,** *23*, 9481-9485.

25. Guo, S.-H.; Zhou, J.; Zhao, X.; Sun, C.-Y.; You, S.-Q.; Wang, X.-L.; Su, Z.-M., Enhanced CO_2 Photoreduction via Tuning Halides in Perovskites. *J. Catal.* **2019,** *369*, 201-208.

26. Guo, X.-X.; Tang, S.-F.; Mu, Y.-F.; Wu, L.-Y.; Dong, G.-X.; Zhang, M., Engineering a $CsPbBr_3$-Based Nanocomposite for Efficient Photocatalytic CO_2 Reduction: Improved Charge Separation Concomitant with Increased Activity Sites. *RSC Adv.* **2019,** *9*, 34342-34348.

27. Wan, S.; Ou, M.; Zhong, Q.; Wang, X., Perovskite-Type $CsPbBr_3$ Quantum Dots/UiO-66(NH_2) Nanojunction as Efficient Visible-Light-Driven Photocatalyst for CO_2 Reduction. *Chem. Eng. J.* **2019,** *358*, 1287-1295.

28. Zhou, L.; Xu, Y.-F.; Chen, B.-X.; Kuang, D.-B.; Su, C.-Y., Synthesis and Photocatalytic Application of Stable Lead-Free $Cs_2AgBiBr_6$ Perovskite Nanocrystals. *Small* **2018,** *14*, 1703762.

29. Pan, A.; Ma, X.; Huang, S.; Wu, Y.; Jia, M.; Shi, Y.; Liu, Y.; Wangyang, P.; He, L.; Liu, Y., $CsPbBr_3$ Perovskite Nanocrystal Grown on MXene Nanosheets for Enhanced Photoelectric Detection and Photocatalytic CO_2 Reduction. *J. Phys. Chem. Lett.* **2019,** *10*, 6590-6597.

30. Wu, L.-Y.; Mu, Y.-F.; Guo, X.-X.; Zhang, W.; Zhang, Z.-M.; Zhang, M.; Lu, T.-B., Encapsulating Perovskite Quantum Dots in Iron-Based Metal–Organic Frameworks (MOFs) for Efficient Photocatalytic CO_2 Reduction. *Angew. Chem. Int. Ed.* **2019,** *58*, 9491-9495.

31. Bhosale, S. S.; Kharade, A. K.; Jokar, E.; Fathi, A.; Chang, S.-m.; Diau, E. W.-G., Mechanism of Photocatalytic CO_2 Reduction by Bismuth-Based Perovskite Nanocrystals at the Gas–Solid Interface. *J. Am. Chem. Soc.* **2019,** *141*, 20434-20442.

32. Jiang, Y.; Liao, J.-F.; Xu, Y.-F.; Chen, H.-Y.; Wang, X.-D.; Kuang, D.-B., Hierarchical CsPbBr$_3$ Nanocrystal-Decorated ZnO Nanowire/Macroporous Graphene Hybrids for Enhancing Charge Separation and Photocatalytic CO$_2$ Reduction. *J. Mater. Chem. A* **2019,** *7*, 13762-13769.

33. Xu, Y.-F.; Yang, M.-Z.; Chen, H.-Y.; Liao, J.-F.; Wang, X.-D.; Kuang, D.-B., Enhanced Solar-Driven Gaseous CO$_2$ Conversion by CsPbBr$_3$ Nanocrystal/Pd Nanosheet Schottky-Junction Photocatalyst. *ACS Appl. Energy Mater.* **2018,** *1*, 5083-5089.

34. Kong, Z.-C.; Zhang, H.-H.; Liao, J.-F.; Dong, Y.-J.; Jiang, Y.; Chen, H.-Y.; Kuang, D.-B., Immobilizing Re(CO)$_3$Br(dcbpy) Complex on CsPbBr$_3$ Nanocrystal for Boosted Charge Separation and Photocatalytic CO$_2$ Reduction. *Sol. RRL* **2020,** *4*, 1900365.

35. Wang, Q.; Tao, L.; Jiang, X.; Wang, M.; Shen, Y., Graphene Oxide Wrapped CH$_3$NH$_3$PbBr$_3$ Perovskite Quantum Dots Hybrid for Photoelectrochemical CO$_2$ Reduction in Organic Solvents. *Appl. Surf. Sci.* **2019,** *465*, 607-613.

36. Tan, D.; Zhang, J.; Shi, J.; Li, S.; Zhang, B.; Tan, X.; Zhang, F.; Liu, L.; Shao, D.; Han, B., Photocatalytic CO$_2$ Transformation to CH$_4$ by Ag/Pd Bimetals Supported on N-Doped TiO$_2$ Nanosheet. *ACS Appl. Mater. Interfaces* **2018,** *10*, 24516-24522.

37. Olowoyo, J. O.; Kumar, M.; Singh, B.; Oninla, V. O.; Babalola, J. O.; Valdés, H.; Vorontsov, A. V.; Kumar, U., Self-assembled reduced graphene oxide-TiO$_2$ nanocomposites: Synthesis, DFTB+ calculations, and enhanced photocatalytic reduction of CO$_2$ to methanol. *Carbon* **2019,** *147*, 385-397.

38. Olowoyo, J. O.; Kumar, M.; Jain, S. L.; Babalola, J. O.; Vorontsov, A. V.; Kumar, U., Insights into Reinforced Photocatalytic Activity of the CNT–TiO$_2$ Nanocomposite for CO$_2$ Reduction and Water Splitting. *J. Phys. Chem. C* **2019,** *123*, 367-378.

39. Sprick, R. S.; Bonillo, B.; Clowes, R.; Guiglion, P.; Brownbill, N. J.; Slater, B. J.; Blanc, F.; Zwijnenburg, M. A.; Adams, D. J.; Cooper, A. I., Visible-Light-Driven Hydrogen Evolution Using Planarized Conjugated Polymer Photocatalysts. *Angew. Chem. Int. Ed.* **2016,** *55*, 1792-1796.

40. Sprick, R. S.; Bai, Y.; Guilbert, A. A. Y.; Zbiri, M.; Aitchison, C. M.; Wilbraham, L.; Yan, Y.; Woods, D. J.; Zwijnenburg, M. A.; Cooper, A. I., Photocatalytic Hydrogen Evolution from Water Using Fluorene and Dibenzothiophene Sulfone-Conjugated Microporous and Linear Polymers. *Chem. Mater.* **2019,** *31*, 305-313.

41. Williams, G.; Seger, B.; Kamat, P. V., TiO$_2$-Graphene Nanocomposites. UV-Assisted Photocatalytic Reduction of Graphene Oxide. *ACS Nano* **2008,** *2*, 1487-1491.

42. Christopher, P.; Jin, S.; Sivula, K.; Kamat, P. V., Why Seeing Is Not Always Believing: Common Pitfalls in Photocatalysis and Electrocatalysis. *ACS Energy Lett.* **2021,** *6*, 707-709.

Chapter 3

Noble Metal Free Heterojunction Photocatalyst for Selective CO$_2$ Reduction to Methane upon Induced Strain Relaxation
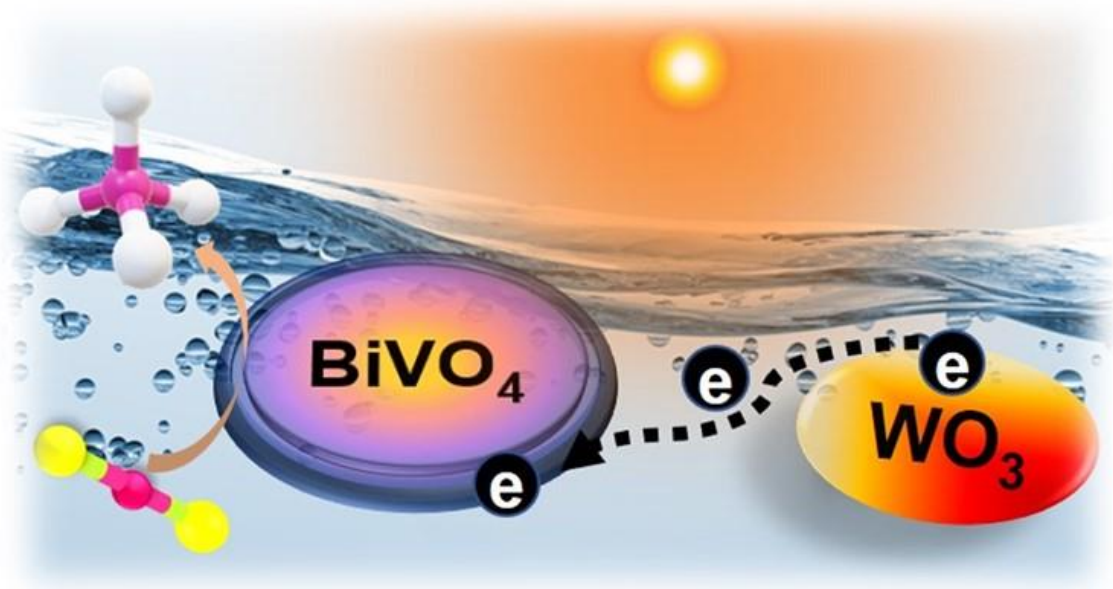
Risov Das, Shreya Sarkar, Ritesh Kumar, Seethiraju D. Ramarao, Arjun Cherevotan, Mohammed Jasil, Abhishek Kumar Singh, Chathakudath P. Vinod, Sebastian C. Peter*. *ACS Catal.* **2022**, *12*, 687-697.

Noble Metal Free Heterojunction Photocatalyst for Selective CO$_2$ Reduction to Methane upon Induced Strain Relaxation

Chapter 3

Summary

Sunlight-driven CO$_2$ hydrogenation has drawn tremendous attention. However, selective CH$_4$ formation via CO$_2$ photoreduction is very challenging. In this work, a metal oxide semiconductor heterojunction consisting of BiVO$_4$ and WO$_3$ developed as a photocatalyst for the efficient conversion of carbon dioxide (CO$_2$) selectively to methane (105 μmol g^{-1} h^{-1}) under visible light in the absence of a sacrificial agent. Wise selection of the reaction medium and the strategically tuned heterojunction upon strain relaxation suppresses the competitive hydrogen generation reaction. The detailed photophysical, photoelectrochemical, and X-ray absorption spectroscopy studies pointed to the Z-scheme mechanism of electron transfer, which favors superior electron and hole separation compared to the individual components of the composite catalyst and other well-known photocatalysts reported for CO$_2$ reduction. The observations are further corroborated by experimental diffuse reflectance infrared Fourier transform spectroscopy and theoretical density-functional theory calculations, which reveal that the heterojunction has a lower free-energy barrier for CO$_2$ conversion to CH$_4$ due to the larger stabilization of the *CH$_2$O intermediate on the strain-relaxed heterojunction surface, in comparison to the pristine BiVO$_4$ surface. The present work provides fundamental insights for constructing high-performance heterojunction photocatalysts for the selective conversion of CO$_2$ to desired chemicals and fuels.

Noble Metal Free Heterojunction Photocatalyst for Selective CO$_2$ Reduction to Methane upon Induced Strain Relaxation

Risov Das, Shreya Sarkar, Ritesh Kumar, Seethiraju D. Ramarao. Arjun Cherevotan, Mohammed Jasil, Abhishek Kumar Singh, Chathakudath P. Vinod, Sebastian C. Peter*.

3.1 Introduction

In previous chapter we have addressed the issue with organic additives and we found heterostructure can provide better results. Therefore, dual semiconductor heterostructure photocatalysts were chosen for catalysis. However, CO_2 activation is also a challenging previous step of CO_2 reduction. Photoactivation of CO_2 molecule is extremely difficult and complex[1] due to its high thermodynamic stability with C=O dissociation energy of ~750 kJ/mol.[2] Selective conversion of CO_2 to the desired product usually depends upon thermodynamic and kinetic barriers of the reaction pathways. Among the simple hydrocarbons, CH_4 production from CO_2 is highly kinetically unfavourable and extremely difficult as it involves complicated 8 e^- and 8 H^+ transfer. Methane is used in industrial chemical processes and as a principal component in liquefied natural gas, which is one of the cleanest burning fuels. Methane produces more heat and light energy compared to other fossil fuels with less CO_2 emission.

Semiconductor photocatalysts like $SnNb_2O_6$, Bi_2MoO_6, Zn_2GaO_4 and GaN, have been known for CO_2 photoreduction to CH_4, but most of their performances are limited by low conversion efficiency and product selectivity.[3-8] Thus, rational design of efficient and selective photocatalyst for CO_2 to CH_4 remains a huge challenge. Currently, TiO_2 and $BiVO_4$ are two of the most popular semiconducting materials exploited for photocatalytic water splitting and CO_2 reduction.[9-11] Although TiO_2 is one of the most explored (or utilized) photocatalysts, its large bandgap (3.2 eV) allows absorption of only the UV spectrum (8%), which is a significant drawback for viable CO_2 photoreduction technology. Thus, recent research has been focused on the development of visible light-active materials for maximizing solar energy utilization.[12-14] However, the traditional visible-light photocatalysts are either unstable in water under irradiation (e.g. CdS and CdSe)[15] or have low activity (e.g. WO_3 and Fe_2O_3).[16] Most of the photocatalyst suffers from lack of selectivity and activity due to competitive hydrogen evolution reaction (HER). HER can be avoided by proper selection of reaction medium and strategic tuning of catalyst. Therefore, inexpensive, stable, efficient visible-light photocatalysts are needed to be designed to meet the requirements of future environmental and energy technologies driven by solar energy.

In contrast to single component photocatalysts, composite heterojunction of two semiconductors has been recognized as an attractive method to develop highly efficient photoactive materials through synergistic enhancement in properties.[17-18] In addition, the

heterojunction in such materials can promote efficient electron-hole separation to minimize the energy-wasting recombination processes. Nature-inspired Z-scheme of electron transfer is one of the best strategies to separate e^- and h^+, yielding better photocatalytic activity and selectivity. Surprisingly, very few materials have been reported so far with Z-scheme e^- transfer routes for CO_2 photoreduction, the majority of which are assisted by sacrificial agents.[19-21] This indicates designing a scalable photocatalyst with proper band edge alignment for a direct Z-scheme mechanism is very challenging.

Herein, we report a new $WO_3/BiVO_4$ heterojunction photocatalyst exhibiting enhanced activity for CO_2 reduction in absence of any sacrificial agent. WO_3 is a water-stable matrix for harvesting visible light, which absorbs the blue part of the solar spectrum corresponding to the bandgap the energy of 2.7 eV.[22] This makes WO_3 a popular choice for visible-light photocatalyst, however, it's unfavourable band position limits the CO_2 reduction ability. $BiVO_4$ on the other hand has a bandgap of 2.4 eV, but its photoactivity is usually low because of inferior charge transport properties. In this work, we envisaged combining the merits of these two materials, i.e., WO_3 with good charge transport properties and $BiVO_4$ with good optical absorption properties, by forming a suitable heterojunction that can lead to a synergistic improvement of the photo-activity in the composite. Relaxation of strain upon composite formation was quantified, and the effect of it in increasing activity of CO_2 reduction (CR) and suppressing HER was discussed. We have also studied the role of pH in CR process. Our findings successfully established a mechanistic pathway for this enhanced conversion of CO_2 to methane with the support of DRIFTS and DFT calculation.

3.2 Experimental details

Chemicals: The following chemicals were used: Bismuth nitrate pentahydrate [$Bi(NO_3)_3.5H_2O$, Alfa Aesar], amonium metavanadate [NH_4VO_3, Merck], ethylene glycol [$(CH_2OH)_2$, Sigma Aldrich], tungstic acid [H_2WO_4, Alfa Aesar]. All the chemicals used were commercially available more than 98% pure, and used without further purification.

Catalyst synthesis procedure

Synthesis of BiVO₄/WO₃ heterostructures by solvothermal method: 0.2 mmol of pre-synthesized WO_3 and 0.2 mmol of $Bi(NO_3)_3$ were dissolved in 40 mL of ethylene glycol, a stochiometric amount of NH_4VO_3 with respect to $Bi(NO_3)_3$ was dissolved in 40 mL of hot water. Two solutions were stirred well to ensure the solutes completely dissolved giving a clear homogeneous solution. This solution was transferred into Teflon-lined autoclave and heated at

$100\ {}^{o}C$ for 12 h. After cooling down to room temperature, the resultant precipitate was collected and washed several times with ethanol and deionised water. Finally, the synthesized products were dried at $60\ {}^{o}C$ for 6 h to get $BiVO_4/WO_3$ powders, which resulted in **comp11**. For the other composites **comp12**, **comp14** and **comp15** we have used the same procedure with 0.4 mmol, 0.8 mmol and 1 mmol of WO_3, respectively.

Characterization

X-Ray diffraction: The structural phase of $BiVO_4$ and WO_3 samples were confirmed by X-ray diffraction (XRD, Rigaku Advance X-ray diffractometer equipped with Cu kα lamp source for irradiation 1.5 Å). Rietveld refinement was done on all these composites to further understand the phase purity and weight fraction of different phases. Open-source GSAS-II software was used for this refinement.

Microscopy: To understand the morphology, high-resolution transmission electron microscopy (HRTEM) was taken using a JEOL 200 instrument. Sample preparation was done by drop casting small amount of sonicated powder in ethanol on a carbon-coated copper grid.

Atomic force microscopy (AFM): A Bruker, Forevision (MMV 1045901 model) instruments microscope in tapping mode with 10 nm diameter containing antimony doped Silicon tip was used to carry out AFM studies. The sample was coated on a Si wafer to perform the study.

Photoluminescence (PL): PL spectra of all the solid samples were recorded at room temperature on a steady state Luminescence spectrometer Perkin-Elmer (LS 55) at different excitation wavelength.

The ultraviolet-visible diffuse reflectance spectrum (UV-vis DRS): UV-vis spectra was obtained in the range of 250 to 800 nm by using a Perkin-Elmer Lambda 900 UV/Vis/Near- IR spectrophotometer in reflectance mode for $BiVO_4$, WO_3 and composites. With an integrating sphere attachment. $BaSO_4$ was used as a 100% reflectance standard. The absorption was calculated data using the Kubelka−Munk equation, $\alpha/S = (1 - R)^2/2R$, where R is the reflectance and α and S are the absorption and scattering coefficients, respectively. Band gap was derived using Tauc plot.

X-ray absorption spectroscopy (XAS): XAS measurements of Bi L_{III} edge were done at the P64 beamline PETRA, DESY synchrotron source in Hamburg, Germany. The data was collected in fluorescence mode. The beamline optics mostly consists of a Rh/Pt coated

collimating meridional cylindrical mirror and Si (111) double crystal monochromator (DCM). The measurements were carried out on pellets which was made by mixing the sample with an inert cellulose matrix homogeneously to have an X-ray absorption edge jump close to one. All the data collection was performed at room temperature, and ambient pressure in presence of very low intensity focused light on sample. Standard analysis procedure was used to obtain the EXAFS signal from the measured absorption spectra. Background subtraction, normalization, and alignment of the EXAFS data were achieved by using the ATHENA software. EXAFS data of the catalyst materials was Fourier transformed in the range of $4-13.8$ Å^{-1}. Data were fitted in R-space between 1 and 4 Å for all the samples. The fitting parameters consist of bond length change between atoms (ΔR) and mean-square displacement of the bond length (σ^2). The coordination numbers (N) were taken from the respective crystal structures and varied until a low R-factor was achieved.

X-ray photoelectron spectroscopy (XPS): XPS measurements were carried out using Thermo K-alpha+ spectrometer using micro focused and mono chromated Al Kα radiation with energy 1486.6 eV. The pass energy for spectral acquisition was kept at 50 eV for individual core levels. The electron flood gun was utilized for providing charge compensation during data acquisition. Further, the individual core-level spectra were checked for charging using C1s at 284.6 eV as standard and corrected if needed. The peak fitting of the individual core-levels was done using XPS peak 41 software with a Shirley-type background. XPS spectra were measured to study the valence state, chemical composition and electronic interactions.

Photoelectrochemical measurements: The transient photocurrent measurements under dark and light were done in a three-electrode system using a CHI 760 potentiostat under the illumination of a solar simulator (Newport) with an ultraviolet (UV) ($\lambda > 380$ nm) cut-off filter. Ag/AgCl as reference electrode, and platinum as the counter electrode was used. All samples were spin-coated on fluorine-doped tin oxide (FTO), which were used as working electrode. 0.5 M Na₂SO₃ was taken as electrolyte. Photo-current has also measured in o.1 M NaOH solution. The slurry was prepared by adding 10 mg of the sample, 200 μL of Nafion (5%), and 1 mL of isopropyl alcohol to fabricated photoelectrodes. The obtained paste was spin-coated on FTO with 1 cm^2 area and annealed at 100 °C for 1 h to get a homogenous film. Mott-Schottky (MS) plots were recorded at a scan rate of 10 mV/s in Na₂SO₃ neutral solution in the light at a frequency of 50 kHz. The obtained values (w.r.t Ag/AgCl) was converted w.r.t NHE by adding 0.20 V.[23]

Photocatalytic measurements: Quartz photoreactor was used for CO_2 hydrogenation experiment under the illumination of 450 W xenon lamp (Newport) through UV cut-off filter (CGA 400 filter and KG2 filter). Using a power meter (Newport-843-R) the intensity of output light was measured. The measured intensity during catalytic reaction is 110 mW/cm^2. (Note: The distance between light source and reactor is 10 cm). About 5 mg of the sample was well dispersed in 30 mL of 0.1 M NaOH by ultrasonication. Before illumination, the reaction setup was purged with N_2 to remove the air and then purged with high purity CO_2 for 45 minutes. During irradiation, 3 mL of the gaseous product from the setup was sampled, and ensuing study was done by GC (gas chromatography) (Agilent GC-7890 B) with TCD and FID detector and He carrier gas. This can detect up to 0.25 ppm of methane and 16 ppm CO. To further verify the products gas chromatography Mass Spectrometry (SHIMAZU GC-2010 PLUS) was used. Products were quantified by using RT® Molecular sieve 5A column (45 m, 0.32 mm ID, 30 μm df) with a mass detector. The calibration was done by a standard gas mixture of H_2, CO, CH_4 of different concentrations at ppm level. It has a detection limit of 1 ppm for H_2, CO and CH_4. Another dedicated GC (Agilent 7890 B) with a TCD detector and Ar carrier gas used for the detection of H_2. It can sense up to 10 ppm of H_2. For liquid product analysis ^1H NMR (600 MHz, JEOL) and HPLC (Agilent 1220 Infinity II LC system) were employed. The following protocol was applied for the ^1H NMR analysis. Five hundred μL of the solvent (after filtration) and 30 μL of an internal standard solution were transferred into a centrifuge tube. The internal standard solution consisted of 50 mM phenol (99.5 %) and 10 mM dimethyl sulfoxide (99.9 %) made in D_2O solvent. The mixture is transferred into an NMR tube. Solvent suppression was used to decrease the intensity of the water peak. Blank tests were conducted in the absence of CO_2 and light to confirm that these two factors are key for photocatalytic CO_2 reduction reaction. Used photocatalyst was amassed after each test and washed with water, and its performance was rechecked by the similar procedure (**Scheme 3.1a**). Rate of the CH_4 evolution was calculated by considering maximum rate at 6th hour for **comp14** and **comp15**. Fourth hour was considered for maximum rate calculation for **comp11** and **comp12**. $^{13}CO_2$ was purged for 15 minutes and the reaction was continued for 2h. Then the products were checked by GC-MS to confirm the source of CH_4 is CO_2. All the photocatalytic reactions were done in an air conditioning room (22 °C). The local heat generated during light illumination was checked, and it was not more than 40 °C. Maintaining all the conditions similar to the reaction was done at 40 °C in absence of light. However, no product was detected. This proves that the local heating due to light illumination does not affect the catalytic performance.

In-situ photocatalytic fourier transform infrared spectroscopy (FT-IR): In-situ photochemical FT-IR spectroscopic studies were performed using a purged VERTEX FT-IR spectrometer equipped with the A530/P accessory and a mid-band Mercury Cadmium Telluride (MCT) detector. Spectra was recorded after 100 scans with a resolution of 4 cm^{-1}. A DRIFTS cell with a quartz window was used to perform catalytic experiment (**Scheme 3.1b**). Prior to catalytic testing, 5 mg of the sample was placed in the DRIFTS cell and treated in flowing N_2 for 30 min to remove impure gas mixtures. Then, CO_2 and water vapor were injected through rubber septa and light was illuminated through the quartz window for 90 minutes. Just before the light exposure on the DRIFTS cell the zero-minute data was collected and after that, data was collected every 15 minutes for 75 minutes.

pH dependent PCR study: pH dependent photocatalytic studies were done in 4 different pH of solvent. pH values 14, 13 and 10 were attained by using 1 M, 0.1 M, 0.1 Mm NaOH solution, respectively pH 6.8 was made by using disodium hydrogen phosphate and sodium hydrogen phosphate buffer. Reactions were done for 5 hours with **comp14** (best catalyst) under 450 W xenon lamp using CGA 400 (UV cutter) filter (Newport). The intensity of the outputting light was 104 mW/cm^2. Basic solution was used to increase the solubility of CO_2 in the reaction medium.

Dissolution of CO_2 in water follows three chemical reactions.

$$CO_2 + H_2O \leftrightarrow H_2CO_3 \ldots\ldots\ldots\ldots\ldots\ldots (3.1)$$

$$H_2CO_3 \leftrightarrow HCO_3^- + H^+ \ldots\ldots\ldots\ldots\ldots (3.2)$$

$$HCO_3^- \leftrightarrow CO_3^{2-} + H^+ \ldots\ldots\ldots\ldots\ldots\ldots (3.3)$$
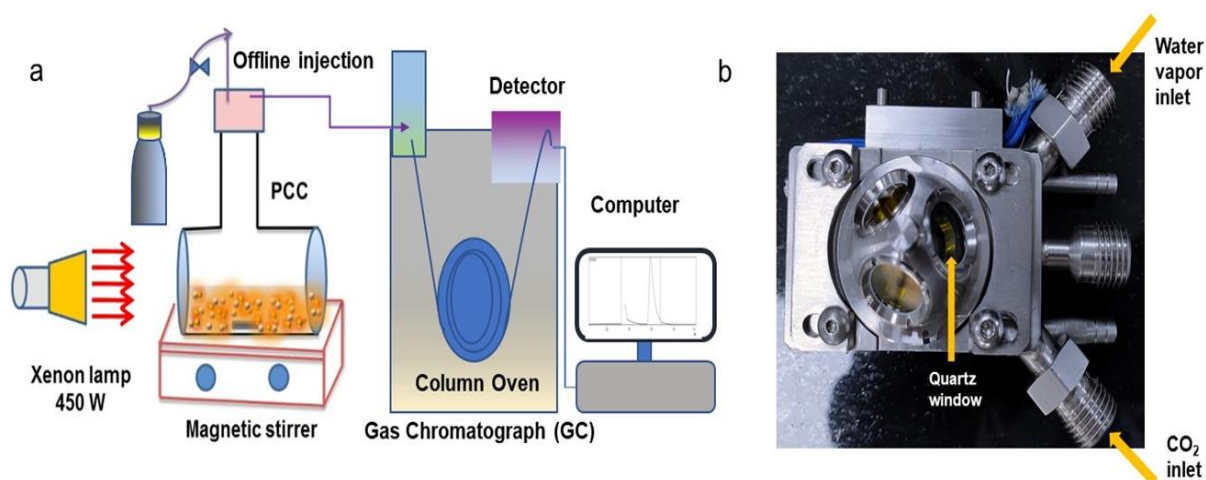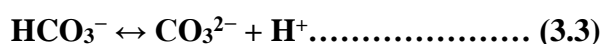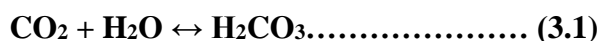
Scheme 3.1. (a) Schematic of the photocatalytic process. (**b**) Photograph of In-situ DRIFTS cell

Hydroxide consumes protons and promotes 3.1 and 3.2 reaction. Reaction 3.2 depletes H_2CO_3. As a result, reaction (3.3) is also forced to shift towards right. The net result is more CO_2 residing in solution (dissolved) as the solution becomes more basic in nature.

3.3 DFT calculation

Computational methodology: The Vienna ab-initio simulation (VASP) package (version 5.4.1) was used for carrying out the first-principles DFT calculations. Electron-ion interactions were described using the all-electron projector augmented wave pseudopotentials,[24] and the Perdew-Burke-Ernzerhof (PBE) under generalized gradient approximation (GGA) was used to approximate the electronic exchange and correlations.[25] The Brillouin zone was sampled using a 6x6x4 Monkhorst-Pack k-point grid for bulk $BiVO_4$ and a 3x5x1 Monkhorst-Pack k-point grid for $BiVO_4$ (110) surface calculations.

All structures were relaxed using a conjugate gradient scheme until the energies and each component of the forces converged to 10^{-6} eV and 0.01 eV $Å^{-1}$, respectively. The positions of atoms in the bottom two layers of the $BiVO_4$(110) surface structures were frozen, and the remaining top two layers were allowed to relax. A vacuum of 15 Å was kept in the *c*-direction to avoid interactions between the periodic images. For treating the localized nature of *d*-orbitals in $BiVO_4$, Dudarev's approach (DFT+U) was utilized.[26] The values of U (Hubbard parameter) and J (on-site Coulomb interaction) for V atoms were taken to be 6.0 and 1.0 eV, respectively. Dipole corrections were applied along the direction normal to the surface.

Free energy calculation details: To gain atomistic insights into the reaction mechanism of CO_2 reduction reaction at the $BiVO_4$ surface, density functional theory (DFT) calculations were performed. The U_{eff} value of 5 yielded a band gap of 2.63 eV, in close agreement with the experimental value (2.53 eV). The optimized lattice parameters of bulk $BiVO_4$ were found to be a = 5.36 Å, b = 12.01 Å, and c = 5.12 Å, and are also in good agreement with previous reports and the experiment. Therefore, this value of U-J was used in the rest of the study.[27-28] From the relaxed structure of $BiVO_4$, the (110) surface was cleaved and investigated for the CO_2RR process since it was found in abundance in the experiments. **comp14** was simulated by relaxing the strain in pristine $BiVO_4$ (110) structure to the same amount as observed in the experiments.

WO_3 was not explicitly included in this model structure, due to inaccurate description of WO_3 by the DFT+U method[29-30] and due to symmetry difference between $BiVO_4$ and WO_3

leading to a large system consisting of 192 atoms. It becomes computationally prohibitive to investigate catalytic studies on such a large system. Therefore, our study is limited to investigate the change in catalytic activity on $BiVO_4$ due to strain effect upon heterostructuring, neglecting the electronic effect.

To check which reaction pathway is favoured on the $BiVO_4$ (110) and **comp14** surface, reaction thermodynamics of both pathways were analysed using Computational Hydrogen Electrode (CHE) model.[31] For this purpose, the adsorption energies of the intermediates ($\Delta E_{ads}(int)$) involved in the CO₂RR process were first evaluated using the expressions:

$$\Delta E_{ads}(int) = E_{*int} - E_* - \sum E_{ref}$$

where E_{*int}, E_*, E_{ref} represents the energies of the adsorbed intermediate, pristine catalyst surface, and reference molecules, respectively. These intermediate adsorption energies were then converted into free energies ($\Delta G_{ads}(int)$) using the given expression:[31-33]

$$\Delta G_{ads}(int) = \Delta E_{ads}(int) + \Delta ZPE - T\Delta S + \Delta G_U$$

where ΔZPE is the difference in zero-point energies of the species, $T\Delta S$ is the difference in entropies due to contribution from only vibrational motion, and ΔG_U ($= -eU$; e is the number of electrons electrons involved in the PCET step, e.g., for the elementary reaction: *CO + H⁺ + e⁻ → *CHO, $\Delta G_U = -3U$) is the free energy corrections due to the applied electrode potentials. The zero-point energy (ZPE) is defined as ground state vibrational energy of the system, i.e.,

$$ZPE = \frac{1}{2} h \sum_K \nu_K$$

for each vibrational mode K. For entropic corrections, we included only vibrational contribution according to the expression:

$$S_v = R \sum_K \left(\frac{\frac{\Theta_{v,K}}{T}}{e^{\frac{\Theta_{v,K}}{T}} - 1} - \ln\left(1 - e^{-\frac{\Theta_{v,K}}{T}}\right) \right)$$

where, $\Theta_{v,K} = h\nu_K/k_B$. The vibrational frequencies (ν_K) of intermediates were calculated using density functional perturbation theory (DFPT), keeping the catalyst surface fixed. The value of temperature (T) is taken to be 300 K. The other conditions imposed for calculating Gibbs free energies, such as pressure and concentration, are the same as utilized in the work by Peterson *et al.*[32]

85

3.4   Calculation

Apparent quantum yield (AQY) calculation[34-35]: The wavelength dependent AQY of CO_2 photo-reduction by **comp14** were calculated using different monochromatic light source. Therefore, 6 (400±10 nm, 425±10 nm, 450±10 nm, 475±10 nm, 500±10 nm, 550±10 nm) different bandpass filters obtained from light source manufacturer (Newport) were used to obtain the monochromatic wavelengths and Newport-843-R power meter was used to measure the incident light intensity. After 6 hours of CO_2 reduction the AQY was estimated from the following equation:

$$AQY(\%) = \frac{Number\ of\ reacted\ electrons}{Number\ of\ incident\ photons} X\ 100\%$$

Number of reacted electrons were calculated from the yield of CO_2 reduced products (here, selectively methane was obtained). Because different number of electrons are required for the formation of different products, the total number of reacted electrons are

$$Number\ of\ reacted\ electrons = [\ 8n(CH_4)]\ X\ 2\ X\ N_A$$

$n(CH_4)$, is the yields of methane. N_A is Avogadro's number. Here 2 was multiplied because Z-scheme is the 2-step electron excitation process.[35-36]

Number of incident photons are calculated from the following equation:

$$Number\ of\ incident\ photons = \frac{PS\lambda t}{hc}$$

where, P is the power density of the incident monochromatic light (W/m^2), S (m^2) is the irradiation area, t (s) is the duration of the incident light exposure and λ (m) is the wavelength of the incident monochromatic light. h (Js) and c (m/s) correspond to planks constant and speed of light respectively.

Combining these two equations the AQY(%) for different monochromatic light was calculated. For example, the AQY(%)@400 nm is shown here-

$n(CH_4)$ =59 µmol/g, N_A = $6.023*10^{23}$ mol^{-1}, P= $51*10^{-3}$ W/cm^2, S= 4.52 cm^2, l= 400 nm, t=6h, h= $6.626*10^{-34}$ Joule second, c= $3*10^8$ m/s.

$$AQY(\%)@400\ nm = \frac{[(59\times16)\times10^{-6}]\times6.02\times10^{23}}{1} \times \frac{6.626\times10^{-34}\times3\times10^8}{51\times10^{-3}\times4.52\times400\times10^{-9}\times3600\times6} \times 100\%$$

$$= 5.67\%$$

Similarly, AQY were calculated for 425 nm, 450 nm, 475 nm, 500nm, 550nm.

Solar to methane (STM) efficiency calculation[35]: The solar to methane (STM) efficiency was evaluated using a 450W Xe lamp (Newport) with a UV cut-off filter (1100mWcm^{-2}) as the light source. The light spectrum was determined using a power meter (Newport-843-R). The irradiated area was set to 1.87 cm^2. Energy density of methane is 55.5 MJ/Kg or 1054 KJ/mol. Catalysis was done with 5mg **comp14** for estimating the STM.[2]

The solar-to-methane efficiency (STM) of the **comp14** sample was then calculated to be as high as 0.07% under 110 mw/cm^2 Xe light illumination.

$$STM(\%) = \frac{Energy\ of\ generated\ methane}{Solar\ energy\ irradiating\ the\ reactor} X\ 100\%$$

$$= \frac{(0.52 \times 1054000) \times 10^{-6}\ J}{1100\ W/m^2} \times \frac{1}{3600\ s \times 1.87 \times 10^{-4}\ m^{-2}} \times 100\%$$

$$= 0.074\%$$

3.5   Results and discussions

Synnergestic effect of BiVO₄ and WO₃ was not examined for CO₂ reduction under visible light. Therefore, to explore such catalytic systems for selective CO₂ reduction, we have developed the composites with different BiVO₄:WO₃ ratios- 1:1 (**comp11**), 1:2 (**comp12**), and 1:4 (**comp14**). Powder X-ray diffraction (PXRD) patterns of the composites were compared with the simulated patterns (**Figure 3.1a** and **3.1b**). The relative weight percentage distribution of BiVO₄ and WO₃ phases in the composites were determined through the Rietveld refinement of the XRD patterns.[37-38]

The XRD pattern clearly demonstrated that the phase is pure in case of composites and individual pristine materials because no unexpected peak was spotted. As shown in **Figure 3.2a-3.2f**, the observed PXRD data were well fitted with the multi phases of BiVO₄ (monoclinic, $C2/c$) and WO₃ (triclinic, $P\bar{1}$). The peaks observed at $2\theta = 23.1°$, $23.6°$ and $24.3°$ in bare WO₃ correspond to (002), (020) and (200) crystallographic planes for the triclinic phase of WO₃ ($P\bar{1}$).
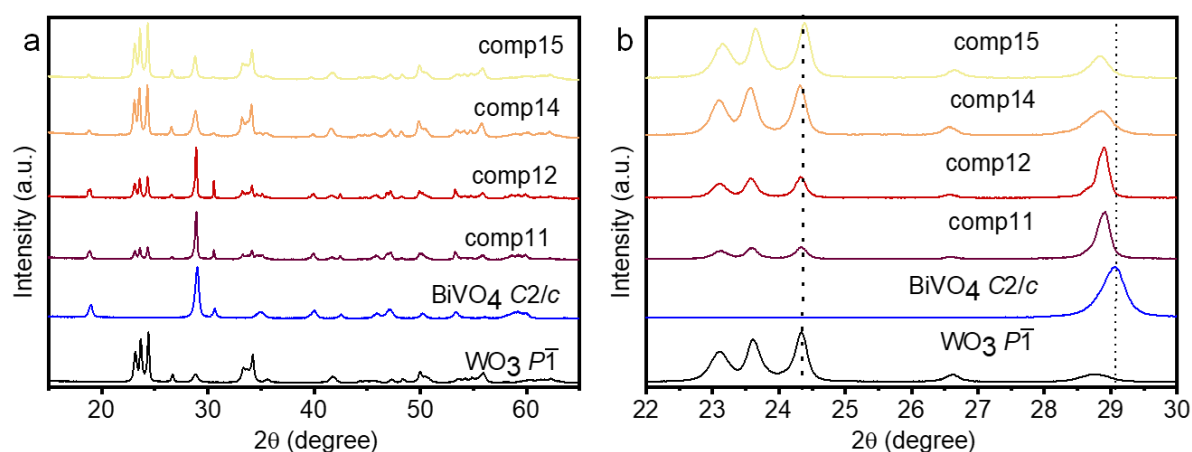
Figure 3.1. Characterization of synthesized catalyst. **(a)** Powder XRD patterns of $BiVO_4$/WO_3 composites compared with the pristine $BiVO_4$ and WO_3 PXRD patterns. **(b)** Shift in XRD upon composite formation w. r. t. $BiVO_4$ and WO_3.

On the other hand, the main peaks at 19° (110) and 29° (021) observed in the case of bare $BiVO_4$ represent a cheelite-monoclinic structure (*C*2/*c*). A left shift of $BiVO_4$ XRD peaks was observed upon composite formation. The shift can be attributed to the lattice parameter increment. The increment of the lattice parameters was further investigated by Extended X-ray Absorption Fine Structure (EXAFS) analyses (**Figure 3.3**). Upon composite formation, Bi-Bi radial distance has elongated due to strain relaxation inside $BiVO_4$ lattice. As a result of this, Bi-V, Bi-O1, and Bi-O2 radial distances were reorganized in $BiVO_4$ to relax the strain (**Figure 3.4b, Table 3.1**). The obtained lattice parameters and weight fraction values of these composites (**Figure 3.3a** and **Table 3.2)** clearly indicate that lattice parameters of $BiVO_4$ phase proportionally expanded upon the formation of the composite with WO_3. This can be attributed to the relaxation of internal strain upon heterostructure formation (**Figure 3.4a**).[39] Williamson-Hall (WH) method[40] was applied to calculate the strain in $BiVO_4$ and composites (**Figure 3.4a, Table 3.3**). A substantial relaxation of strain in $BiVO_4$ (~0.2 in pristine → ~0.08 in composites, **Table 3.3**) crystals upon composite formation can lead to a low-resistance fast electron transfer process,[41]enhancing the photoreduction activity. Transmission electron microscopy (TEM) was used to explore the morphology and microstructure of the pristine compounds and composites. **Figure 3.4c** shows the TEM image of $BiVO_4$/WO_3 heterostructures having two different morphologies due to the presence of both $BiVO_4$ and WO_3 phases. HRTEM images confirmed the formation of heterostructures, identifying the two crystalline phases with respective morphologies (**Figure 3.4d**). The left side of the green line corresponds to the $BiVO_4$ region and the right side correspond to WO_3.
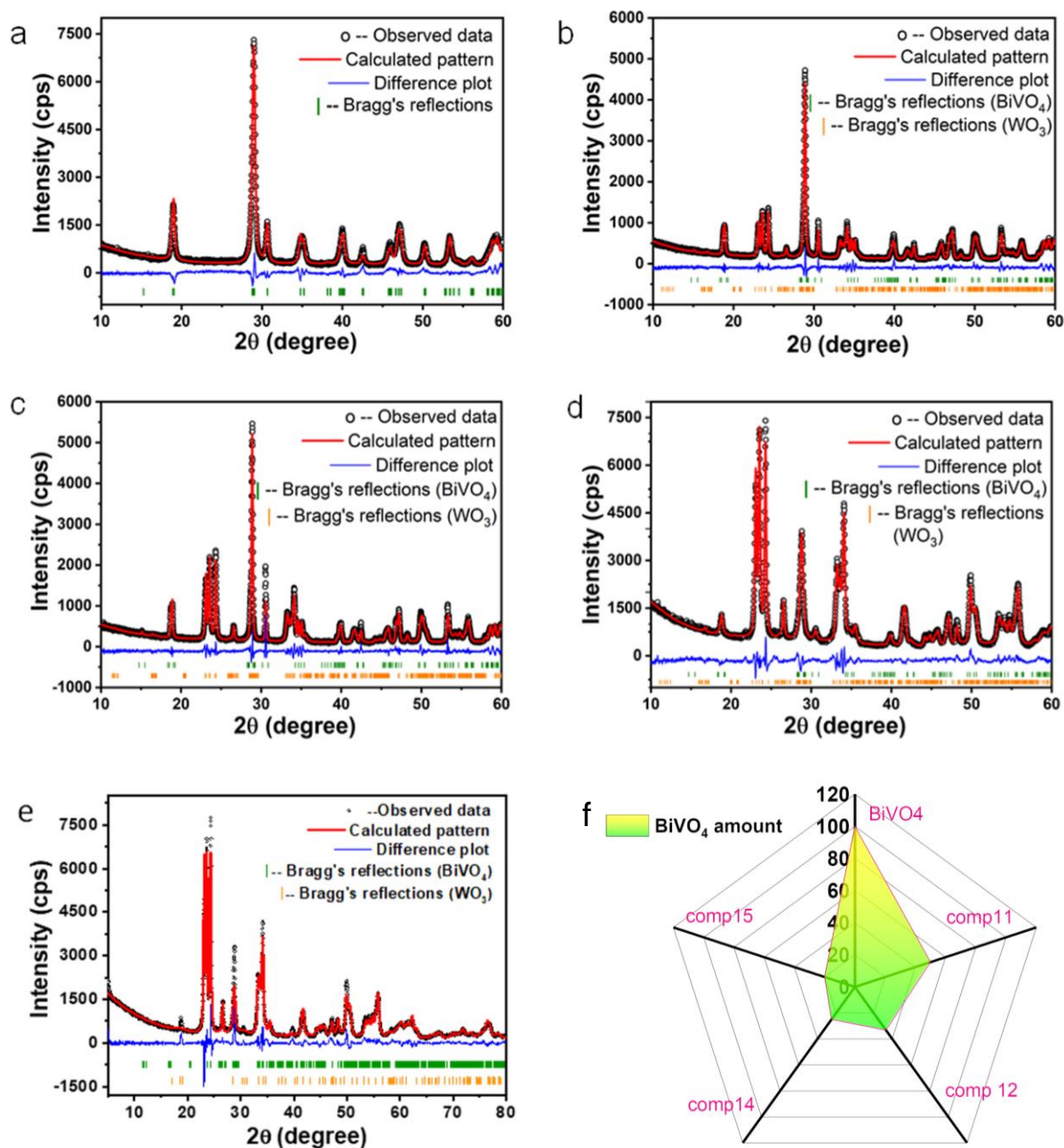
Figure 3.2. The synthesis of different composites were done by varying the reagent amount to get 1:1 to 1:5 weight ratio but the actual ratio may not follow the expection. Therefore, to know the exact ratio of $BiVO_4$ and WO_3 Rietveld refinement (RR) was performed. The RR plot of **(a)** $BiVO_4$, **(b) comp11**, **(c) comp1**2, **(d) comp14 and (e) comp15**. This shows that the data is well fitted with the $BiVO_4$ with monoclinic crystal structure and WO_3 with triclinic crystals structure. (**f**) the chart for expressing $BiVO_4$ amount in different composite and pristine metal oxide semiconductor photocatalyst. Please note that the microstrain were not calculated from RR. For microstrain calculation only single and unmarged peaks were selected manually. The 2θ position and full width and half maxima (FWHM) of 4 peaks were taken to calculate mixro-strain. RR was done to understand the actual ratio between $BiVO_4$ phase and WO_3 phase.
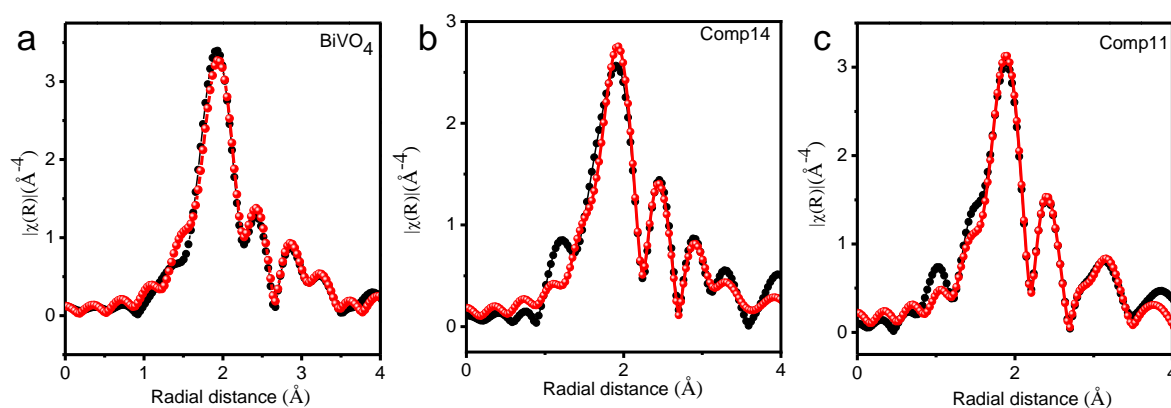
Figure 3.3. FT EXAFS at Bi L_{III}-edge **for (a)** $BiVO_4$, **(b) comp14** and **(c) comp11** in R-space.

Table 3.1. EXAFS fitting parameters for Bi L_{III} edge with distances (R) and Debye Waller factor (σ^2) for $BiVO_4$, **comp11** and **comp14**.

Samples		$BiVO_4$		Comp 11		Comp 14	
Paths	N	R (Å)	σ^2 (Å)^2	R (Å)	σ^2 (Å)^2	R (Å)	σ^2 (Å)^2
R_{Bi-O1}	4	2.242	0.010	2.260	0.009	2.274	0.010
R_{Bi-O2}	2	2.423	0.010	2.441	0.006	2.435	0.014
R_{Bi-O2}	2	2.528	0.015	2.516	0.022	2.503	0.007
R_{Bi-V1}	4	3.532	0.007	3.54	0.007	3.521	0.009
R_{Bi-V3}	2	3.671	0.009	3.695	0.008	3.682	0.009
R_{Bi-Bi}	2	3.613	0.021	3.632	0.013	3.645	0.022

The d spacing in $BiVO_4$ is 0.47 nm corresponding to (110) surface (**Figure 3.3d**), whereas the d-spacing value (0.37 nm) on the nanoparticles can be assigned to (020) planes of triclinic WO_3. Increased d spacing in heterostructure was observed because the $BiVO_4$ lattice has expanded upon strain relaxation. The FFT pattern has been taken from **Figure 3.4d** and presented in **Figure 3.4e**. The FFT pattern clearly shows the presence of two different compounds and the creation of heterojunction shared by the crystallographic (110) and (020) planes of $BiVO_4$ and of WO_3, respectively. The sheet-like morphology and formation of the composite were further supported by the atomic force microscopy (AFM) analysis in **Figure 3.4f** and **3.4g**. $BiVO_4$ sheets have exhibited a thickness of ∼4 nm which may be helpful in providing more active sites for PCR.

Table 3.2. Lattice parameters and weight fractions of composites.

Compound	Parameter	comp11	comp12	comp14	Pristine BiVO₄
BiVO₄	Crystal system	Monoclinic ($C2/c$)	Monoclinic ($C2/c$)	Monoclinic ($C2/c$)	Monoclinic ($C2/c$)
	a	7.287 Å	7.291 Å	7.297 Å	7.277
	b	11.695 Å	11.697 Å	11.690 Å	11.706
	c	5.174 Å	5.177 Å	5.164 Å	5.144
	β	135.427°	135.420°	135.365°	135.294°
WO₃	Crystal system	Triclinic (P)	Triclinic (P)	Triclinic (P)	Triclinic (P)
	a	7.313 Å	7.316 Å	7.315 Å	
	b	7.539 Å	7.542 Å	7.543 Å	
	c	7.693 Å	7.697 Å	7.694 Å	
	α	89.728°	89.734°	90.303°	
	β	89.487°	89.486°	89.479°	
	γ	89.935°	89.991°	90.018°	
(BiVO₄:WO₃)	Weight Fraction	0.586:0.414	0.464:0.536	0.182:0.818	

Table 3.3. Strain values calculated from WH plot for pristine BiVO₄ and other composites.

Sample	Slope of WH plot	Strain
BiVO₄	0.825	0.206
comp11	0.292	0.073
comp12	0.349	0.087
comp14	0.384	0.096
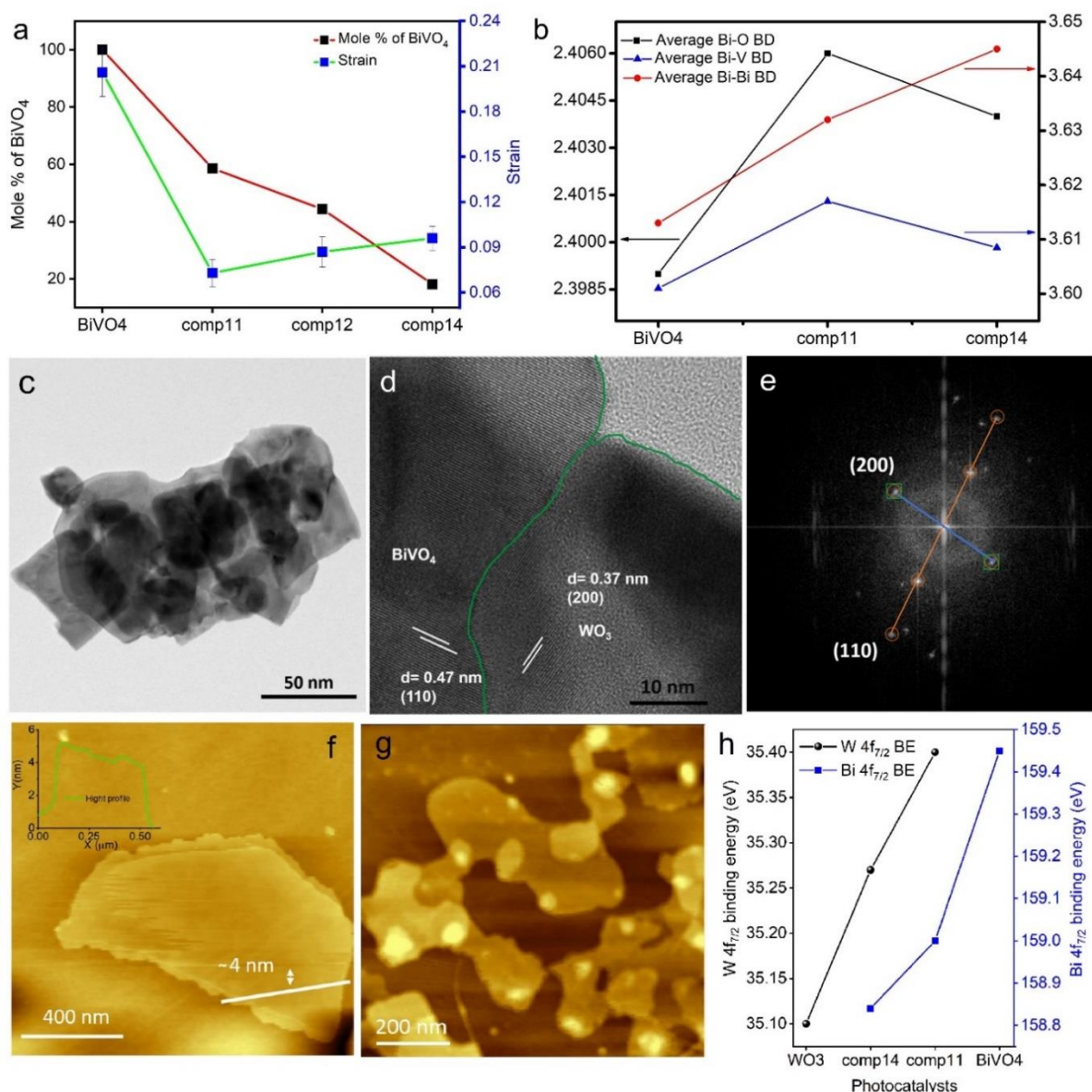
Figure 3.4. Structure and morphology analysis of catalysts. (**a**) Relative wt% of $BiVO_4$ and WO_3 phases in each composite obtained from the Rietveld refinement of PXRD and strain calculated by Williamson-Hall method. (**b**) trend of the bond distance in the composite with respect to $BiVO_4$ obtained from Bi L_{III} edge XAFS data (BD: Bond Distance). (**c**) TEM image of **comp14**. **d,** HRTEM image of **comp14**, and (**e**) First Fourier Transform (FFT) pattern taken from **Figure 4d**. AFM images of (**f**) 4 nm thick pristine $BiVO_4$ sheet and (**g**) **comp14** showing WO_3 nanoparticle on $BiVO_4$ sheet. (**h**) 'Bi' and 'W' $4f_{7/2}$ binding energy shift in $BiVO_4$, WO_3 and **comp14** observed in XPS.

  Figure 3.4g shows the formation of hetero-structure where WO_3 nanoparticles were decorated on $BiVO_4$ sheet. The XPS technique was adopted to understand the surface chemical bonds of the composites. The W 4f Peaks around 35.38 eV and 37.52 eV belong to W $4f_{7/2}$ and W $4F_{5/2}$, attributed to W^{6+}. Peaks around 159.31 eV ($4f_{7/2}$) and 164.66 eV ($4f_{5/2}$) indicate +3

oxidation state of Bi in pristine and composite $BiVO_4$.[42] Bi $4f_{7/2}$ peak has shifted towards lower energy upon composite formation, indicating a change of chemical environment of $BiVO_4$ after WO_3 incorporation. Similarly, the W $4f_{7/2}$ peak has shown a higher energy shift with an increasing $BiVO_4$ counterpart (**Figure 3.4h**, **3.5a-5h** and **3.6a-3.6d**). The shifts of binding energy establish the formation of heterojunction and infer composites are not just a simple physical mixture. ESR measurements showed negligible amount of oxygen vacancy.

All the catalysts were tested for the photoreduction of CO_2 with H_2O under visible light irradiation for a period of 10 hours under visible light illumination (**Figure 3.7a**). Methane (CH_4) was obtained as the product for all the catalysts until 10 hours of reaction with no traces of other common products like CO or H_2. The formation of CH_4 requires the complete reduction of CO_2 to C, and a subsequent reaction with available protons from the decomposition of water on the same catalyst surface. As seen in **Figure 3.7b,** and **3.7c** the methane production increases upon increasing WO_3 percentage in the composite **comp14** and then decreases with further addition of WO_3. The test for each sample was repeated multiple times (a fresh catalyst was used each time), and the errors were within reasonable experimental uncertainties.
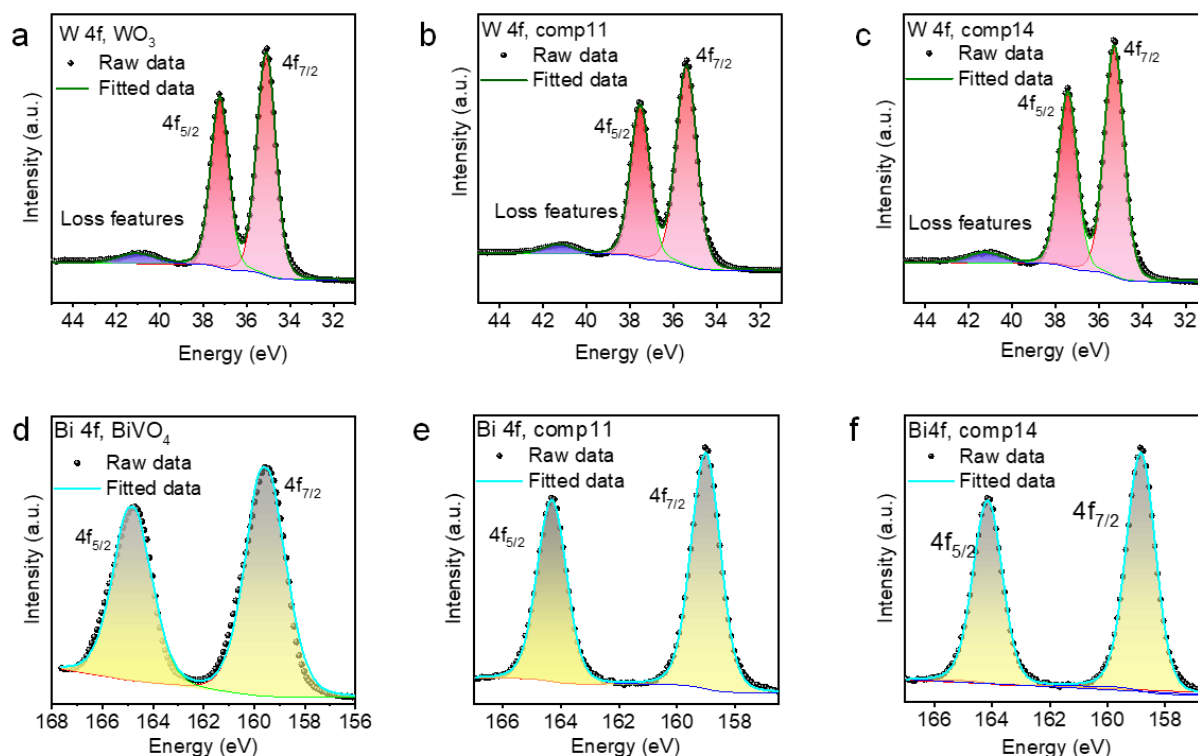
Figure 3.5. XPS spectra of $BiVO_4/WO_3$ composites and individual components. **(a, c)** W 4f XPS for WO_3, **comp11** and **comp14**, **(d-f)** Bi 4f XPS for $BiVO_4$, **comp11**, **comp14**.
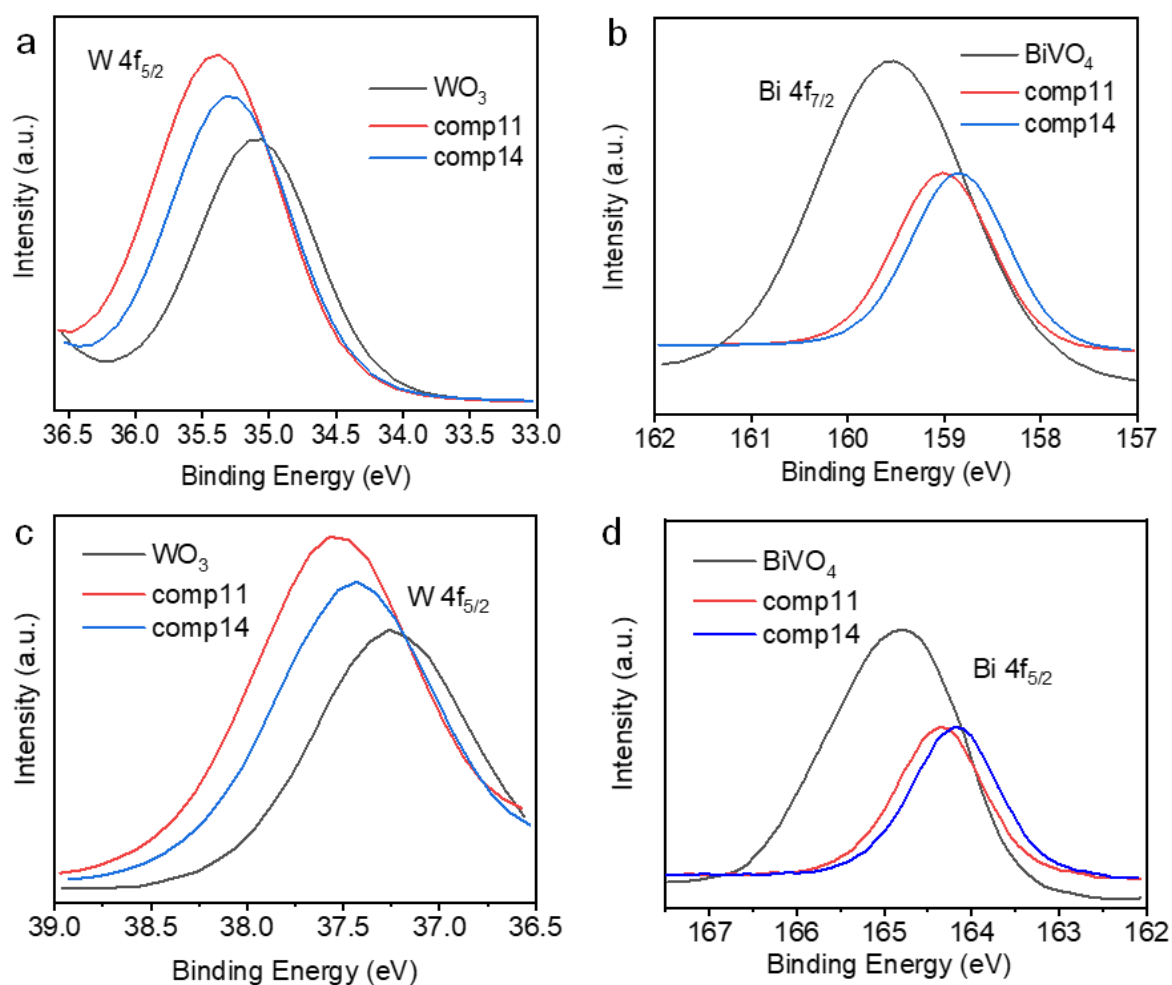
Figure 3.6. Shift of binding energy in **(a)** W $4f_{7/2}$, **(c)** W $4f_{5/2}$, **(b)** Bi $4f_{7/2}$, and **(d)** Bi $4f_{5/2}$ for individual components, **comp11** and **comp14** obtained from XPS analysis.

Bare WO_3 samples showed no activity toward CO_2 reduction reaction (CO_2RR) under similar conditions. However, very small amount of methane was observed with pristine $BiVO_4$ (**Figure 3.7d**). **Comp14** was found to be the best photocatalyst for the reduction of CO_2 to CH_4 with 629 µmol/g of CH_4 production compared to the negligible formation rates of 36 µmol/g/h, and 83 µmol/g/h in the case of **comp11** and **comp12**, respectively. All three catalysts showed more than 99% selectivity towards CH_4 till 10 hours after the reaction. Better methane formation efficiency was observed at higher pH (**Figure 3.7e**). Solubility of CO_2 increases at higher pH. More dissolved CO_2 concentration near the catalyst surface increases the CO_2 reduction efficiency. At higher pH, the surface of $BiVO_4$ becomes more negative (**Figure 3.8d**), and the electronic interaction between acidic CO_2 and $BiVO_4$ increases. Consequently, more CO_2 will adsorb on negative $BiVO_4$ surface. This may lead to better CO_2 reduction ability of **comp14** at higher pH. Photogenerated holes produce proton from water splitting.
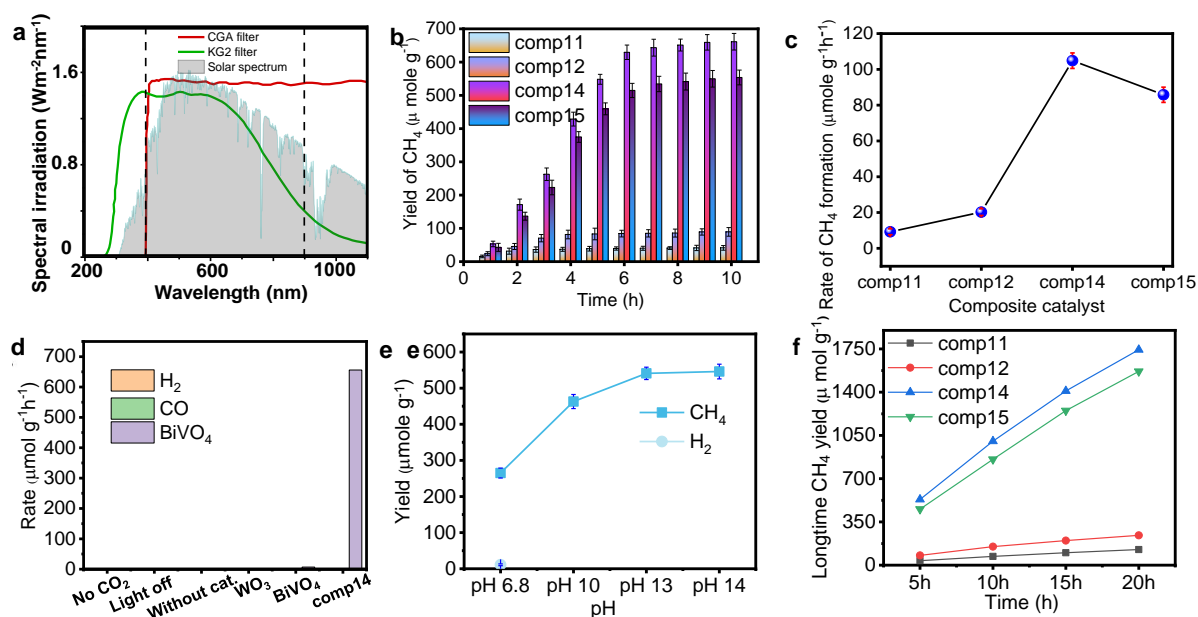
Figure 3.7. Photocatalytic activity. **(a)** the illumination spectrum of our light source with the used filter compared with solar spectrum. **(b)** Yield of methane in batch process reaction at 0.1 M NaOH with different composite catalysts. **(c)** Rate of methane formation with composite catalysts. **(d)** Control experiments in absence of CO_2, in dark without catalyst with pristine WO_3 and $BiVO_4$. **(e)** pH-dependent CO_2 reduction study with **comp14** for 5 hours. **(f)** Long time methane production ability in 20 hours reaction.

Surface adsorbed protons used for CO_2 reduction. At higher pH CO_2 will get less supply of surface adsorbed proton which hindered further CO_2RR. This negative effect of increasing pH restricted further increment of CH_4 yield upon increasing the pH from 13 to 14. From **Figure 3.7e** 11.3 µmol/g H_2 was observed at neutral pH. Here, we have seen pH of the solution plays a crucial role in the suppression of HER and the formation of selective CH_4. We also checked the long-term activity of composites where data collections were done after each 5h instead of every 1h. After 20 h of reaction, the composites remained active (**Figure 3.7f**). Further modification of the photoreactor and light intensity can make this catalyst useful for large-scale commercial applications. As a controlled study, the concentration of WO_3 was further increased in the composite (**comp15**), however, the photocatalytic activity declined slightly in this case (**Figure 3.7 b, c**). This can be interpreted that excessive WO_3 covering the active sites of $BiVO_4$, which hinders CO_2 adsorption on the catalyst interface. Composite catalysts did not give any hint of CO formation after 10 hrs of reaction (**Figure 3.8a, b**). A comparison with the well-known photocatalysts (**Table 3.4**) clearly confirms the superior activity of **comp14** towards CO_2 to methane formation.

Table 3.4. Comparison of the activity of $BiVO_4/WO_3$ composites for photocatalytic CO_2 reduction with the catalysts reported in literature.

Catalyst	Reduction medium)	Sacrificial agent	Light source	Product	Maximum Evolution rate (μmol g^{-1} h^{-1})
Comp14	30 ml 0.1M NaOH soln.	No	420W Xe Lamp	CH$_4$	CH$_4$: 104
Comp15					CH$_4$: 85
Comp12					CH$_4$: 20
Comp11					CH$_4$: 9
[43]Pt/TiO$_2$	Pure water		300 W Xe lamp	CH$_4$	CH$_4$: 6.8
[44]SnS$_2$/TiO$_2$	water			CH$_4$ CO	CH$_4$: 23 CO: 2.5
[2]V_S-CuIn$_5$S$_8$	Water Vapor			CH$_4$	CH$_4$: 8.7
[45]CdS/WO$_3$	0.14M NaHCO$_3$			CH$_4$	CH$_4$: 1.02
[46]Zinc Phthalo-cyanine/BiVO$_4$	100mg 5 ml water			CO CH$_4$	CO: 4 CH$_4$: 0.6
[47]Au/CdS/TiO$_2$	Pure water vapor		450 W Xe lamp	CH$_4$ H$_2$	CO: 4.5 CH$_4$: 41
[48]Rb$_3$Bi$_2$I$_9$ film	H$_2$O vapor		32 W UV lamp	CO CH$_4$	CO: 77.6 CH$_4$: 15
[49]N doped graphene/CdS	Water vapour		350 W Xe Lamp	CO CH$_4$	CO: 2.59 CH$_4$: 0.33
[50]WO$_3$/g-C$_3$N$_4$ (10 wt %)	water	TEOA	300 W Xe Lamp	CO CH$_4$	CO: 1.37 CH$_4$: 0.75
[51]3 mol% Mo-doped WO$_3$·0.33H$_2$O.	Water spray	NO	500 W Xe Lamp	CH$_4$	CH$_4$: 5.3
[52]Pt/C-In$_2$O$_3$	20 ml, 10 mol% TEOA	TEOA	300 W Xe Lamp	CO CH$_4$	CO: 630 CH$_4$: 139.5
[53]Zn$_2$GeO$_4$/RuO$_2$/Pt	water	NO		CH$_4$	CH$_4$: 6
[6]GaN/Cr$_2$O$_3$/Rh	water	NO		CH$_4$	CH$_4$: 3.5

Liquid product analysis by HPLC and ^{1}H NMR after CO₂RR revealed that no liquid product was obtained (**Figure 3.8b**). Photocatalysis with $^{13}CO_2$ by **comp14** in **Figure 3.8c** shows BiVO₄/WO₃ only produced $^{13}CH_4$ (m/z=17). This result confirmed that the evolved methane indeed originated from the photoreduction of CO₂ in presence of water and catalyst. The effect of NaOH concentration was studied by varying the pH of the reaction medium. Basic medium indces negative surface charge as depicted from zeta potential calculation (**Figure 3.8d**). Electrophilic CO₂ can bind more facile way on BiVO₄ surface because it has negative surface charge. The activity remains the same even after 3 runs on the same catalyst (**Figure 3.8e**).The catalyst (**comp14**) remains completely stable after light irradiation and base treatment as evident from the post-photocatalytic PXRD patterns (**Figure 3.8f**). To understand the origin of the enhanced CO₂ to CH₄ activity, optoelectronic properties of the composites were analyzed through Ultraviolet-Visible (UV-vis) Diffuse reflectance Spectroscopy (DRS), and Photoluminescence (PL) studies. From the DRS spectra (**Figure 3.9a**) it is clear that BiVO₄ and WO₃ have absorption band edge at around 500 nm and 425 nm, respectively, corresponding to their characteristic band gaps of 2.53 eV and 3.05 eV as calculated from the Tauc plot (**inset of Figure 3.9a**).[22, 54-55] The composites of BiVO₄ and WO₃ show two discrete optical absorption edges attributed to the collective intrinsic absorption edges of the constituents. The U_{eff} (= U-J) study yields a bandgap of 2.63 eV for bulk BiVO₄ (**Figure 3.9b**), which is again in excellent agreement with previous reports.[27-28] PL analysis was performed to study the interfacial charge transfer and separation efficiency of the photogenerated electrons and holes in BiVO₄/WO₃ composites. The PL spectra shown in **Figure 3.9c** display a broad PL emission peak focused at 530 nm and 490 nm for pristine BiVO₄ and WO₃, respectively, which is in agreement with the previous reports.[56-57] BiVO₄/WO₃ heterostructures show a completely diminished emission peak, which indicates that the heterostructure can effectively arrest the recombination of photogenerated carriers and enhance charge transfer efficiency.[52, 58] Furthermore, charge transfer and separation efficiency was evaluated by transient photocurrent measurements as shown in **Figure 3.9d.** The enhanced photocurrent in the case of **comp14,** compared to pristine BiVO₄ and WO₃, reveals the higher separation rate of photo-generated charges in the composite. As a consequence of which better CO₂ reduction performance was observed at higher pH. Nyquist plot of **comp14** was obtained from electrochemical impedance spectra (EIS) (**Figure 3.9e**). The diameter of the semi-circular arc in the Nyquist plot gives the measure of the charge transfer resistance (R_{ct}) at the electrode/electrolyte interface, wherein a

larger diameter manifests higher resistance and hence greater possibility of electron-hole pair recombination.[59]
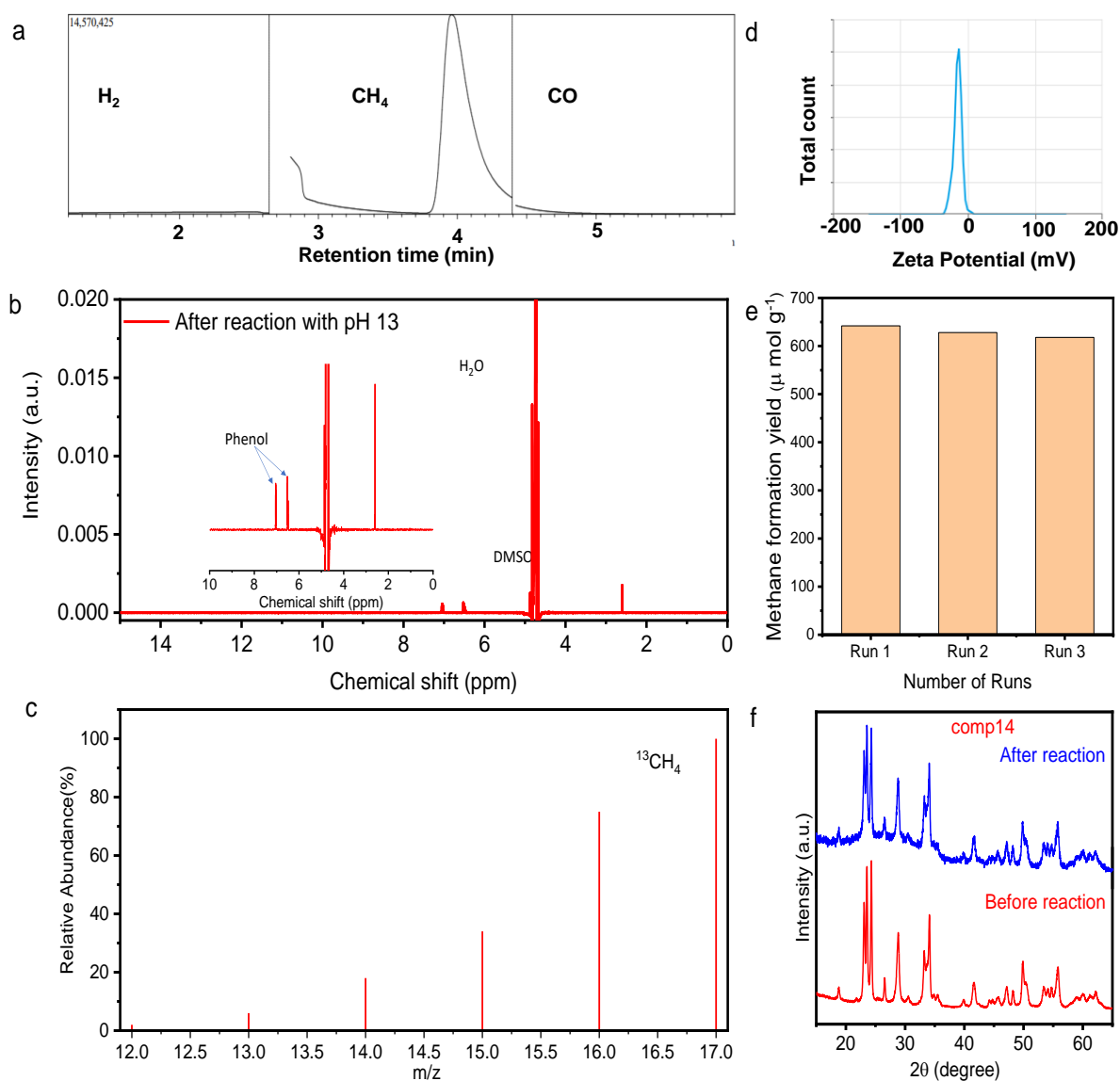
Figure 3.8. (a) Gas analysis by Gas chromatography. Screenshot of gas chromatogram of CO_2 photoreduction with **comp14** at 0.1 M NaOH solution. **(b)** Post reaction liquid analysis**.** NMR taken after 10h of reaction with **comp14** at pH 13. No liquid product was detected. **(c)** ^{13}C analysis. Product detection with GCMS after $^{13}CO_2$ photoreduction by **comp14**. Mass spectra (m/z=17) suggests that the formed methane came from photocatalytic CO_2 reduction. **(d)** Effect of pH on catalyst 14. Zeta potential measurements at basic and neutral medium by dispersing **comp14** in NaOH solution. Malvern (MPT-3) instrument was used for zeta potential measurements. At pH 7 the observed overpotential was zero. **(e)** Stability profile after consecutive 3 runs. After each cycle and photocatalytic cell was purged with fresh batch of CO_2. **(f)** Post reaction stability. PXRD patterns of **comp14** before and after photocatalytic CO_2 reduction.
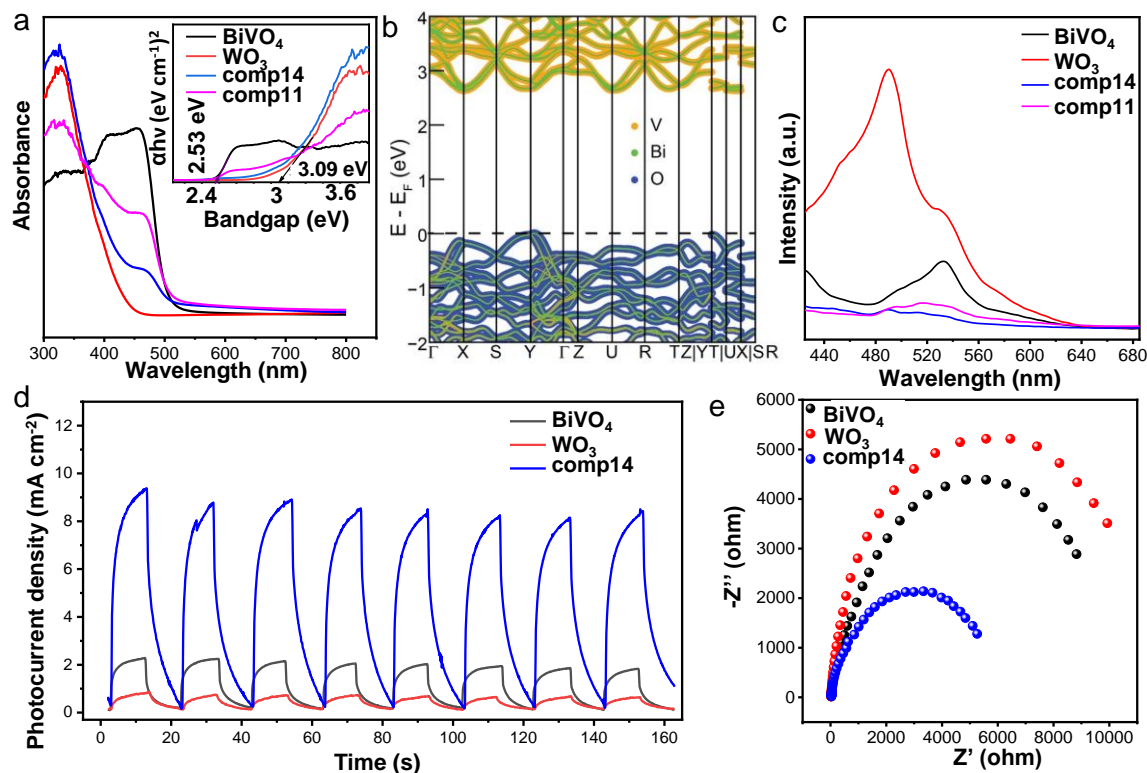
Figure 3.9. Photophysical and photoelectrochemical characterization. **(a)** UV-Vis diffuse reflectance spectra (displayed in absorbance) of BiVO$_4$, WO$_3$, **comp11** and **comp14** with Tauc plot at inset. **(b)** Electronic band structures of **comp14** (cyan lines) and bulk BiVO$_4$ (orange shade) calculated using the DFT+U method. The contributions to the electronic bands from Bi, V, and O atoms are shown by green, orange, and blue lines. **(c)** Photoluminescence (PL) spectra of BiVO$_4$, WO$_3$, **comp11** and **comp14** heterostructures. **(d)** Transient photocurrent density of BiVO$_4$, WO$_3$ and **comp14** measured at pH 13. **(e)** EIS Nyquist plot of BiVO$_4$, WO$_3$ and **comp14** film on FTO electrodes.

Under light irradiation, charge transfer resistance was found to follow the trend, **comp14** < **BiVO$_4$** < **WO$_3$**. The reason lies in the well-built interface of the BiVO$_4$/WO$_3$ composite, which was also reflected in the PL studies. The photocurrent was measured using different concentrations of NaOH solution, and better photocurrent was observed at higher pH (**Figure 3.10a**). This suggests a better reducing ability of photogenerated electrons at higher pH.

To understand the band edge position of BiVO$_4$ and WO$_3$ Mott-Schottky (MS) plots of all these materials were carried out in 0.5 M Na$_2$SO$_3$ electrolyte. The flat band potentials calculated from the MS plots of WO$_3$ (**Figure 3.10b**) and BiVO$_4$ (**Figure 3.10c**) are +0.29V and -0.31V with respect to NHE. The positive slope in MS plots indicates that both these materials are n-type semiconductors. Since it is known that for n-type semiconductors, the

Fermi energy lies near to the conduction band minima (CBM), the CBM and the flat band potential would be close. Thus, the flat band potentials give an approximate estimation of CBM levels.[60] Based on CBM and bandgap from **Figure 3.9a**, the valence band maxima (VBM) position of the composites can be determined. **Figure 3.11a** shows CBM and VBM positions of $BiVO_4$ and WO_3 with respect to CO_2 to CH_4 redox potential **(-0.24 eV)**. It can be clearly seen that the CBM position of $BiVO_4$ is more negative than the CO_2 to CH_4 reduction potential, whereas the CBM maxima of WO_3 lies further below. Photocatalytic reduction of CO_2 with water using the composites resulted in 100% methane selectively. In general, the transfer of electrons to CO_2 can happen either from the CBM of WO_3 (type II mechanism) or from the CBM of $BiVO_4$ (Z-scheme mechanism). The redox potential of CH_4 formation from CO_2 is -0.24 eV, and CBM position of WO_3 is +0.20 eV (**Figure 3.11a**). So, electron transfer from the CBM of WO_3 to CO_2 is not possible. Consequently, the only possible route of electron transfer can happen from the CBM of $BiVO_4$. Thus, the transfer of electrons from the CBM of $BiVO_4$ in this heterostructure can only be explained by the Z-scheme model (**Figure 3.11b**).[61]
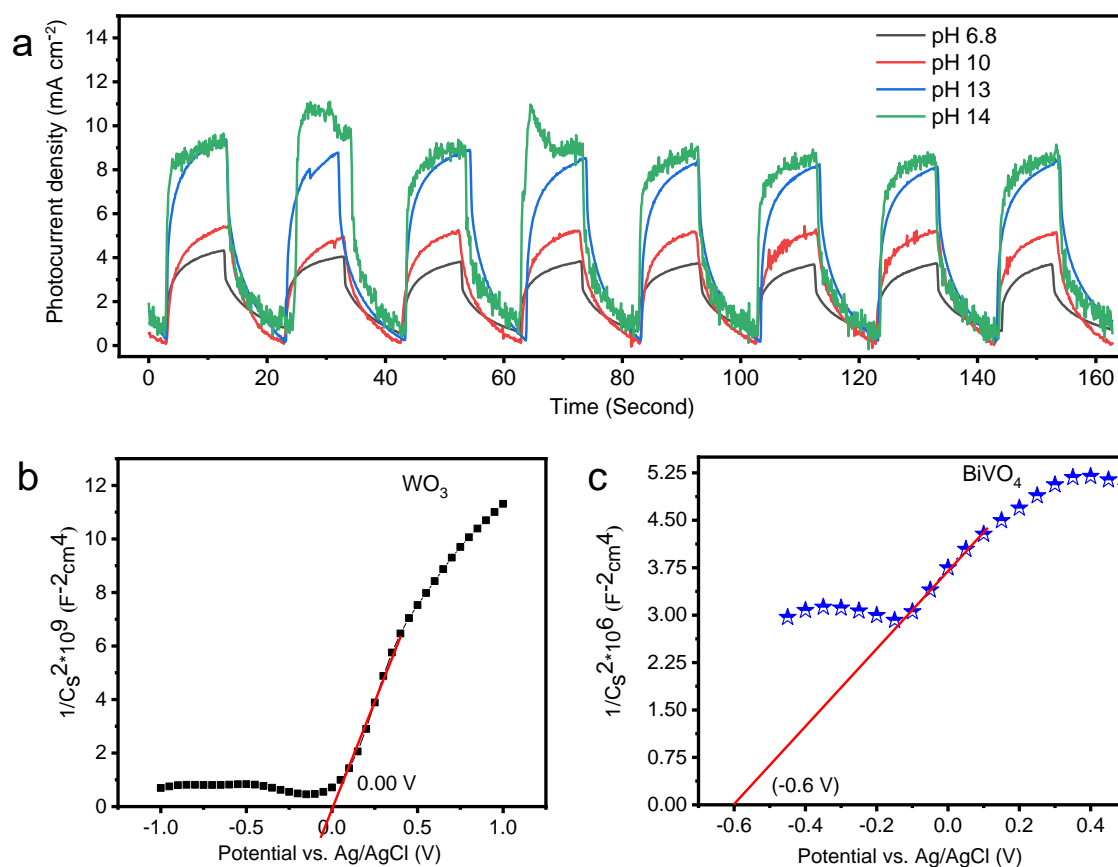
Figure 3.10. (a) Photocurrent measurements at different pH. Mott-Schottky plots of **(b)** WO_3, **(c)** $BiVO_4$ in 0.5M Na_2SO_3 electrolyte at an applied frequency of 50 kHz.
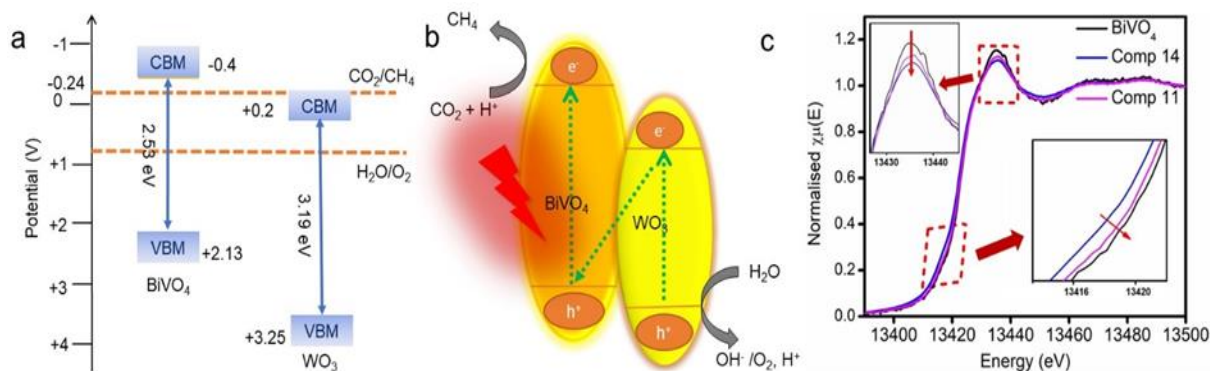
Figure 3.11. Electron transfer pathway. (**a**) The proposed Z-Scheme of $BiVO_4/WO_3$ hetero structure towards CO_2 to CH_4 production, (**b**) Conduction band minimums (CBM) and valance band maximas (VBM) of $BiVO_4$ and WO_3 with respect to CO_2 to CH_4 redox, (**c**) Bi-L_{III} edge XANES spectra of $BiVO_4$, **comp11** and **comp14**. Inset of **Figure 3.11c** shows the reduction of Bi oxidation state (left side) and the progressive drop of white line intensity (right side).

In general, Z-scheme is proposed in the presence of sacrificial electron transporter redox system like I^-/IO_3^-.[62] Bi L_{III} edge X-ray absorption near-edge structure (XANES) spectra reveal the charge transfer within the composites (**Figure 3.11c**). Electron transfer from WO_3 to $BiVO_4$ results in a reduction of Bi oxidation state (inset of **Figure 3.11c**) and the progressive drop of white line intensity (**inset** of **Figure 3.11c**) upon composite formation. As the percentage of WO_3 increases, the oxidation state of Bi in $BiVO_4$ is further reduced, showing a minimum white line intensity in **comp14**. This observation strongly supports the proposed mechanism of electron transfer and rationalizes the activity enhancement in **comp14,** compared to the other composites (**comp11** and **comp12**). To further confirm the Z-scheme mechanism, EPR analysis was done to detect the spin active $^.O_2^-$ and $^.OH^-$ species using 5,5-dimethyl-1-pyrroline N-oxide (DMPO) as the spin trapping agent. As shown in **Figure 12a,** only signals corresponding to DMPO-$^.OH$ adduct was detected for WO_3 since its conduction band (CB) is not negative enough to perform O_2 to $^.O_2^-$ reaction. On the other hand, only signals attributed to DMPO-$^.O_2^-$ adduct was found for pristine $BiVO_4$ since its valence band (VB) is not positive enough to oxidize OH^- to $^.OH$ (**Figure 12b**). Importantly, both DMPO-$^.OH$ and DMPO-$^.O_2^-$ ESR peaks were detected for **comp14**. These findings eliminate the possibility of type II heterojunction in these composite catalysts (**Figure 12c**). In such case, excited electrons in $BiVO_4$ should travel to the CB of WO_3 while the photo-induced holes of WO_3 should transfer on the VB of $BiVO_4$, therefore, neither signals attributing to DMPO-$^.O_2^-$ nor DMPO-$^.OH$ could be observed. Therefore, on the basis of above findings, the creation of Z-scheme charge transfer mechanism in $BiVO_4/WO_3$ composites can be confirmed. Additionally, higher accumulation of electrons

and holes in **comp14** can be observed from more intance ESR signals. Therefore, it can be inferred that via Z-scheme process, availability of photo-generated charges increased due to better charge separation.[63] The reaction intermediates in CO_2RR process were detected by in-situ DRIFTS experiments (**Figure 3.13**). The peak at 1652 cm^{-1} for **comp14** was observed, and this peak intensity increased gradually with increasing time (**Figure 3.14a**). This peak is ascribed to the *COOH group, which is commonly referred to as a crucial initial intermediate of CO_2 reduction reaction.[64-65] FTIR peaks at 1118 cm^{-1} and 1153 cm^{-1} in **Figure 3.14b** are attributed to the characteristic bands of *CHO and *OCH$_3$ group respectively.[66] *OCH$_3$ is regarded as the most important intermediate of CH$_4$ formation by CO_2 photoreduction.[67]
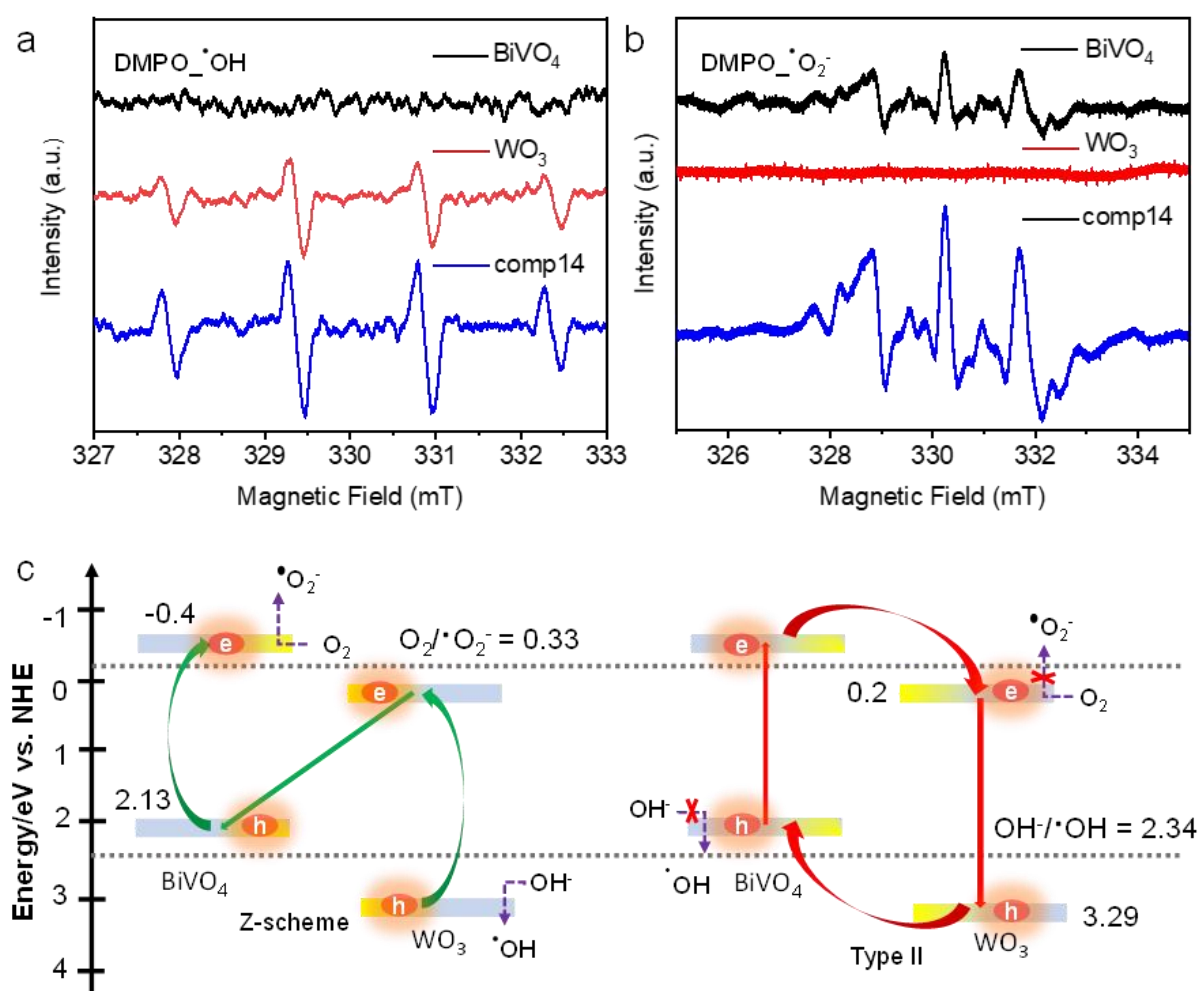
Figure 3.12. ESR study for understanding Z-scheme electron transfer in BiVO$_4$/WO$_3$ composite catalyst. ESR spectra of DMPO-$^{\cdot}$OH in water (**a**) and DMPO-$^{\cdot}$O$_2^-$ in methanol (**b**) in the presence of **BiVO$_4$**, **WO$_3$**, and **comp14**. (**c**) Energy band alignment and reaction mechanism of Z-scheme and type II (pH = 0).

1. 1088 cm⁻¹ (CHO)
2. 1155 cm⁻¹ (OCH₃)
3. 1298 cm⁻¹ (CO₃ Asy. Str.)
4. 1447 cm⁻¹ (HCO₃ Sy. Str.)
5. 1638 cm⁻¹ (COOH)
6. 1687 cm⁻¹ (HCO₃ Asy. Str.)

Absence of **CO** peak (2000-2100 cm⁻¹)
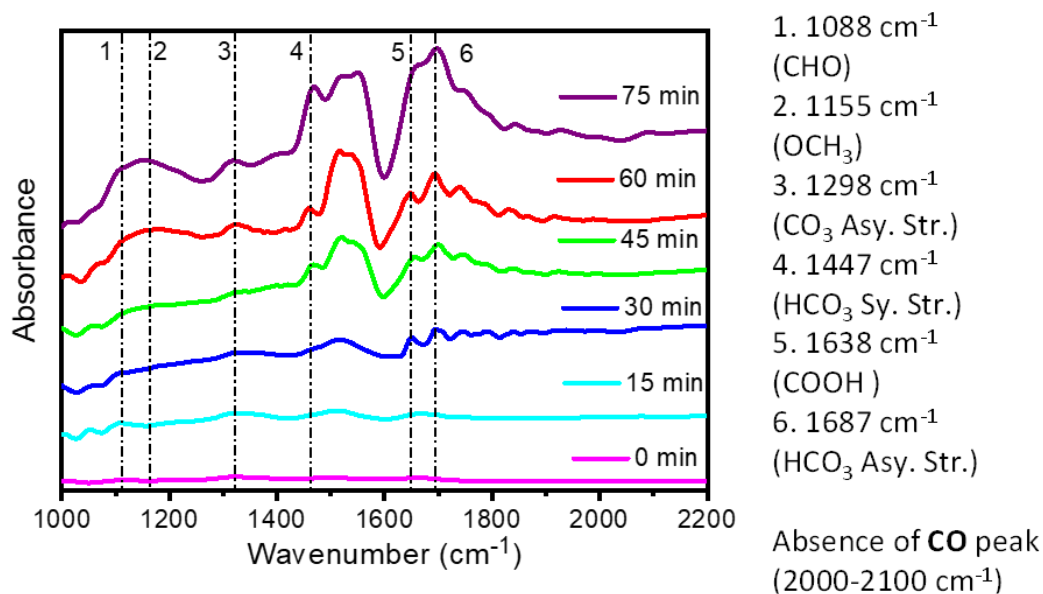
Figure 3.13. In-Situ FTIR spectra for **comp14** in presence of CO_2 and water vapour under light illumination.

No peak evolution upon extension of irradiation time was observed in 2000 cm⁻¹ to 2100 cm⁻¹ region, which suggests the absence of abundant stable *CO intermediate on catalyst surface.[68-69] A similar absorption band of carbonates asymmetric stretching is also observed at 1298 cm⁻¹.[70] To further unwrap the unrevealed reasons for improved activity in composites compared to pristine $BiVO_4$ and selective CH_4 production, we calculated Gibbs free energy on possible reaction pathways (**Figure 3.14c**).[71-72] The conversion of CO_2 to CH_4 usually follows two types of reaction pathways (Mechanism-I and Mechanism-II; **Table 3.5**),[31] where the first two elementary steps are common in both the mechanisms. To check which reaction pathway is favoured on the $BiVO_4$ (110) and **comp14** (110) surface reaction thermodynamics of both pathways were analyzed. The TEM analysis showed that $BiVO_4$ (110) is the most exposed plane (**Figure 3.4d**). Therefore, the DFT calculations were carried out on this facet of $BiVO_4$. Upon investigating the Mechanism-I[73] pathway, it was found that the *COH and *C intermediates change to *COOH and *CO intermediates, respectively, upon structural optimization by taking oxygen from the lattice. The instability of the intermediates involved in Mechanism-I (*C—O—H and *C) arises due to their carbon atoms being more electron deficient than those involved in Mechanism-II (e.g., *C(H)=O or *CHO) (**Figure 3.14d**). Therefore, Mechanism-I is not feasible on the materials under study. It is further validated from DRIFTS experiments where peaks for intermediates of Mechanism-I were not observed, but those of Mechanism-II such as *CHO and *OCH₃ were observed. Hence, for $BiVO_4/WO_3$ composite system CH_4 formation route via mechanism-II is more feasible than mechanism-I.

The stronger bonds on $BiVO_4$ surface with O in **comp14** lead to easier breaking of O-C bonds from *OCH_3 group. Therefore CH_4 desorption became very facile. Based on DRIFTS and DFT calculations, a plausible schematic mechanism scheme has been drawn and presented in **Figure 3.14e**. Next, the free energy diagram for photoreduction of CO_2 to CH_4 on pristine $BiVO_4$ (110) (blue lines) and **comp14** (110) (red lines) through the Mechanism-II pathway was plotted in **Figure 3.14c**. The conversion of *CHO to *CH_2O intermediate is the potential determining step (PDS) on both surfaces. However, the free energy barrier for PDS on strain relaxed **comp14** (1.84 eV) is lesser than that on pristine $BiVO_4$ (110) (2.32 eV), which renders CO_2RR more facile on **comp14** (110). This is in complete agreement with experiments, where CH_4 was observed in appreciable amounts only on **comp14** surface due to relaxation of strain upon composite formation. The decrease in free energy barrier of PDS can be ascribed to the
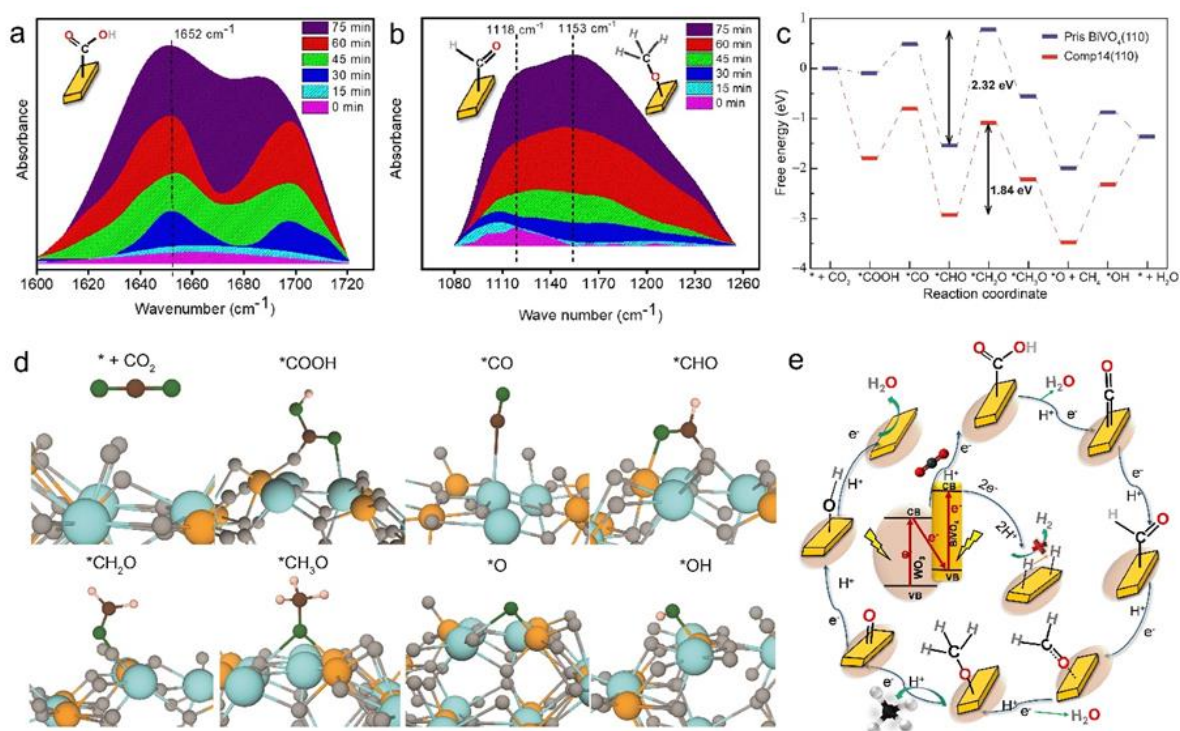
Figure 3.14. Methane formation mechanism. In-situ DRIFTS for adsorption mixture of H_2O vapour and CO_2 on **comp14**. (**a**) Amplifications of areas from 1080 cm^{-1} to 1260 cm^{-1} and (**b**) 1600 cm^{-1} to 1720 cm^{-1}, (**c**) free energy diagram for CO_2RR on pristine $BiVO_4$ (110) and **comp14** (110) and (**d**) Optimized structures of the intermediates on the **comp14** (110) surface involved in the CO_2RR. The cyan, orange, grey, brown, green, and pink spheres represent Bi, V, O (of $BiVO_4$), C, O (of intermediates), and H atoms. (**e**) Schematic illustration for selective methane formation.

Table 3.5. Eight elementary steps are involved in the CO_2RR process[31]

Mechanism-I	Mechanism-II
$CO_2 + H^+ + e^- \rightarrow {}^*COOH$	$CO_2 + H^+ + e^- \rightarrow {}^*COOH$
${}^*COOH + H^+ + e^- \rightarrow {}^*CO$	${}^*COOH + H^+ + e^- \rightarrow {}^*CO$
${}^*CO + H^+ + e^- \rightarrow {}^*COH$	${}^*CO + H^+ + e^- \rightarrow {}^*CHO$
${}^*COH + H^+ + e^- \rightarrow {}^*C + H_2O$	${}^*CHO + H^+ + e^- \rightarrow {}^*CH_2O$
${}^*C + H^+ + e^- \rightarrow {}^*CH$	${}^*CH_2O + H^+ + e^- \rightarrow {}^*CH_3O$
${}^*CH + H^+ + e^- \rightarrow {}^*CH_2$	${}^*CH_3O + H^+ + e^- \rightarrow {}^*O + CH_4$
${}^*CH_2 + H^+ + e^- \rightarrow {}^*CH_3$	${}^*O + H^+ + e^- \rightarrow {}^*OH$
${}^*CH_3 + H^+ + e^- \rightarrow {}^* + CH_4$	${}^*OH + H^+ + e^- \rightarrow {}^* + H_2O$

${}^*CH_2O$ intermediate being stabilized to $[\Delta G_{BiVO_4-comp14}({}^*CH_2O) = 1.87$ eV] on **comp14** than the ${}^*CHO$ intermediate $[\Delta G_{BiVO_4-comp14}({}^*CHO) = 1.39$ eV]. The density of states (DOS) calculations has been performed to explain the trends in relative stability of the two key intermediates in **Figure 3.15a,** and **b.** The filled states of ${}^*CH_2O$ intermediate are further away from the Fermi level on **comp14** (**Figure 3.15b**), and hence are more stabilized compared to ${}^*CHO$, whose filled states remain almost unchanged on the **comp14** surface (**Figure 3.15a**).

Furthermore, the IR peak corresponding to the ${}^*CO$ intermediate is not observed. In order to explain this observation, we calculated CO desorption free energies $(\Delta G({}^*+CO))$ for $BiVO_4$ and **comp14** (**Figure 3.15c,** and **d**). The formation of ${}^*CHO$ intermediate is more exothermic than CO desorption on both pristine $BiVO_4$ (by 1.83 eV) and **comp14** (by 2.11 eV) surfaces, favouring the formation of ${}^*CHO$ intermediate rather than desorption of the CO gas. The reaction free energy for the elementary step ${}^*CO + H^+ + e^- \rightarrow {}^*CHO$ is also highly exothermic (-2.13 eV) for **comp14**. Both the findings imply that the ${}^*CO$ intermediate will get quickly protonated to form the ${}^*CHO$ intermediate and hence finally produce CH_4 gas as the product. Therefore, the IR peaks for ${}^*CO$ intermediate and CO as product are not observed in the experiments. The $\Delta G({}^*H)$ values at pH=0 for pristine $BiVO_4$ and **comp14** are -2.56, and -4.02 eV, respectively. The $\Delta G({}^*H)$ value is more exothermic for **comp14**, hence it is more difficult for the adsorbed H to desorb from the surface, leading to reduced HER activity on **comp14** at pH=0.
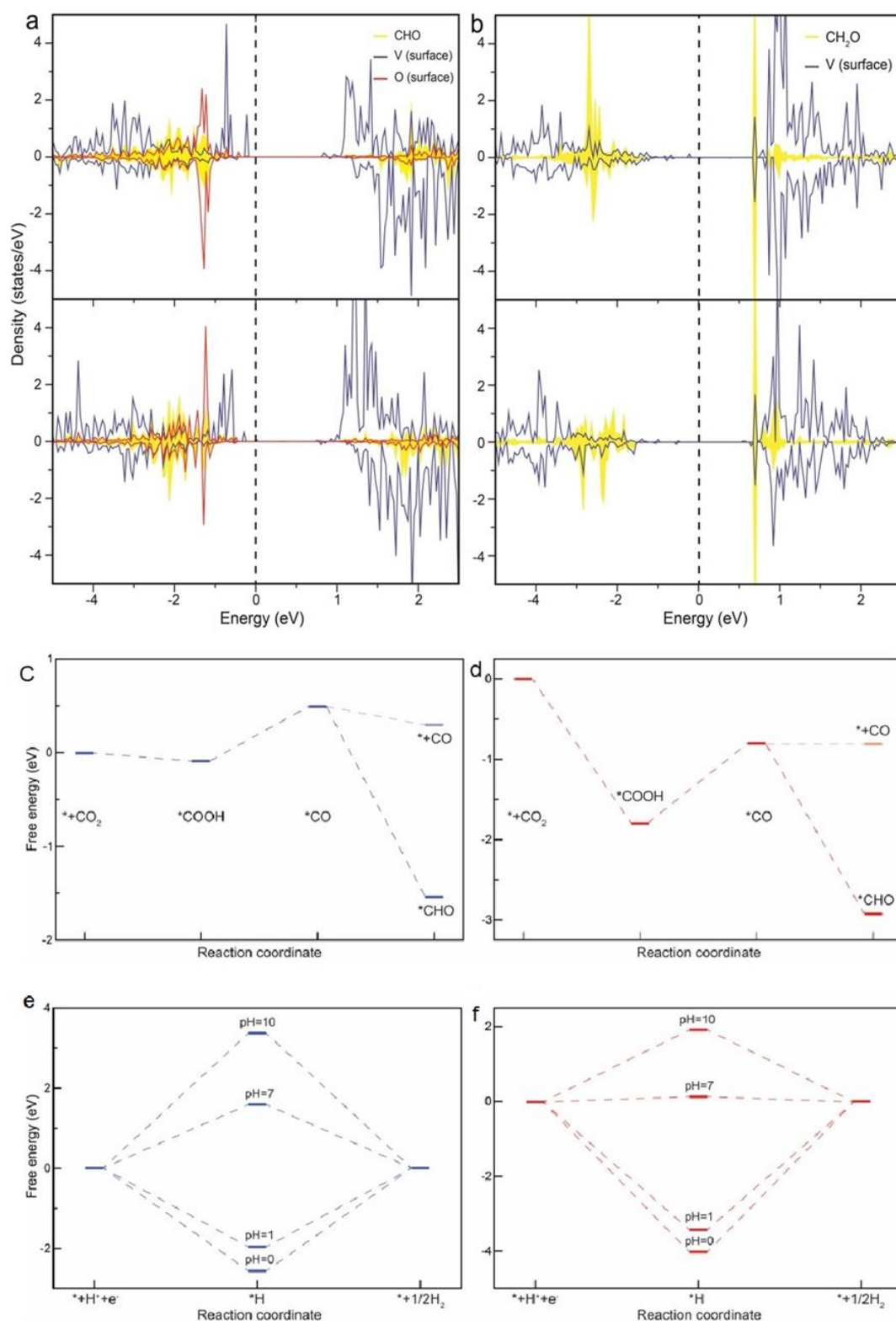
Figure 3.15. Density of states (DOS) showing states of the intermediate and adsorbent for **(a)** *CHO on pristine BiVO₄ (top) and **comp14** (bottom), and for **(b)** *CH₂O on pristine BiVO₄ (top) and **comp14** (bottom). Free energy diagrams showing competing CO desorption with CO₂RR for **(c)** pristine BiVO₄ (110), and for **(d) comp14** (110). Free energy diagrams showing HER for **(e)** pristine BiVO₄ (110), and for **(f) comp14** (110) at different pH values.

At neutral pH (7), the values of ΔG(*H) for pristine $BiVO_4$ and **comp14** become 1.58 and 0.12 eV, respectively. The HER activity is usually observed when ΔG(*H) ≈ 0[74]; therefore, the **comp14** at neutral pH should exhibit HER, which is in agreement with the experiments (**Figure 3.7e**, pH=6.8). On further increasing the pH, the ΔG(*H) values become endothermic and hence HER is again suppressed. All these advantages of composite photocatalyst drive CO_2 photoreduction to highly selective methane formation by suppressing competitive HER without applying any sacrificial hole scavenger. It is anticipated that this low cost and stable photocatalyst may be suitable for long-term and large-scale utilization.

3.6   Conclusion

In conclusion, we have developed a heterojunction photocatalyst, $BiVO_4/WO_3$, to achieve more than 99% selective conversion of CO_2 to the energy-dense fuel CH_4 under visible light. The interfaces between WO_3 nanoparticles and $BiVO_4$ nanosheets drive the expansion of lattice parameters and relaxation of strain in $BiVO_4$ upon composite formation, favoring fast photoinduced charge transport without the support of any sacrificial agent. The enhancement in charge transfer and electron−hole separation along with suitable reaction medium selection leads to a multifold increase in activity and selectivity. The suitable band alignment with respect to the CH_4 reduction potential and the existence of intersystem charge transfer unravels a Z-scheme mechanistic pathway for electron transfer in composites. Moreover, DRIFTS and Gibbs free-energy calculations confirmed the lowering of overall reaction barrier on the heterojunction surface and elucidated the CH_4 formation pathway. This work showcases new design strategies to generate potential photocatalysts for efficiently converting CO_2 to desired chemicals under visible light.

3.7   References

1. Corma, A.; Garcia, H., Photocatalytic Reduction of CO_2 for Fuel Production: Possibilities and Challenges. *J. Catal.* **2013,** *308*, 168-175.
2. Li, X.; Sun, Y.; Xu, J.; Shao, Y.; Wu, J.; Xu, X.; Pan, Y.; Ju, H.; Zhu, J.; Xie, Y., Selective Visible-Light-Driven Photocatalytic CO_2 Reduction to CH_4 Mediated by Atomically Thin $CuIn_5S_8$ Layers. *Nat. Energy* **2019,** *4*, 690-699.
3. Zhu, S.; Liang, S.; Bi, J.; Liu, M.; Zhou, L.; Wu, L.; Wang, X., Photocatalytic Reduction of CO_2 with H_2O to CH_4 over Ultrathin $SnNb_2O_6$ 2D Nanosheets under Visible Light irradiation. *Green Chem.* **2016,** *18*, 1355-1363.

4. Zhang, Y.; Li, L.; Han, Q.; Tang, L.; Chen, X.; Hu, J.; Li, Z.; Zhou, Y.; Liu, J.; Zou, Z., Bi_2MoO_6 Nanostrip Networks for Enhanced Visible-Light Photocatalytic Reduction of CO_2 to CH_4. *ChemPhysChem* **2017,** *18*, 3240-3244.

5. Liu, Q.; Wu, D.; Zhou, Y.; Su, H.; Wang, R.; Zhang, C.; Yan, S.; Xiao, M.; Zou, Z., Single-Crystalline, Ultrathin $ZnGa_2O_4$ Nanosheet Scaffolds To Promote Photocatalytic Activity in CO_2 Reduction into Methane. *ACS Appl. Mater. Interfaces* **2014,** *6*, 2356-2361.

6. AlOtaibi, B.; Fan, S.; Wang, D.; Ye, J.; Mi, Z., Wafer-Level Artificial Photosynthesis for CO_2 Reduction into CH_4 and CO Using GaN Nanowires. *ACS Catal.* **2015,** *5*, 5342-5348.

7. Jiang, Z.; Sun, H.; Wang, T.; Wang, B.; Wei, W.; Li, H.; Yuan, S.; An, T.; Zhao, H.; Yu, J.; Wong, P. K., Nature-Based Catalyst for Visible-Light-Driven Photocatalytic CO_2 Reduction. *Energy Environ. Sci.* **2018,** *11*, 2382-2389.

8. Sorcar, S.; Hwang, Y.; Grimes, C. A.; In, S.-I., Highly Enhanced and Stable Activity of Defect-Induced Titania Nanoparticles for Solar Light-Driven CO_2 Reduction into CH_4. *Mater. Today* **2017,** *20*, 507-515.

9. Zhu, M.; Sun, Z.; Fujitsuka, M.; Majima, T., Z-Scheme Photocatalytic Water Splitting on a 2D Heterostructure of Black Phosphorus/Bismuth Vanadate Using Visible Light. *Angew.Chem. Int. Ed.* **2018,** *57*, 2160-2164.

10. Iwase, A.; Yoshino, S.; Takayama, T.; Ng, Y. H.; Amal, R.; Kudo, A., Water Splitting and CO_2 Reduction under Visible Light Irradiation Using Z-Scheme Systems Consisting of Metal Sulfides, CoO_x-Loaded $BiVO_4$, and a Reduced Graphene Oxide Electron Mediator. *J. Am. Chem. Soc.* **2016,** *138*, 10260-10264.

11. Woo, S.-J.; Choi, S.; Kim, S.-Y.; Kim, P. S.; Jo, J. H.; Kim, C. H.; Son, H.-J.; Pac, C.; Kang, S. O., Highly Selective and Durable Photochemical CO_2 Reduction by Molecular Mn(I) Catalyst Fixed on a Particular Dye-Sensitized TiO_2 Platform. *ACS Catal.* **2019,** *9*, 2580-2593.

12. De, S.; Zhang, J.; Luque, R.; Yan, N., Ni-Based Bimetallic Heterogeneous Catalysts for Energy and Environmental Applications. *Energy Environ. Sci.* **2016,** *9*, 3314-3347.

13. Peng, C.; Reid, G.; Wang, H.; Hu, P., Perspective: Photocatalytic Reduction of CO_2 to Solar Fuels over Semiconductors. *J. Chem. Phys* **2017,** *147*, 030901.

14. Habisreutinger, S. N.; Schmidt-Mende, L.; Stolarczyk, J. K., Photocatalytic Reduction of CO_2 on TiO_2 and Other Semiconductors. *Angew.Chem. Int. Ed.* **2013,** *52*, 7372-7408.

15. Meissner, D.; Memming, R.; Kastening, B., Photoelectrochemistry of cadmium sulfide. 1. Reanalysis of Photocorrosion and Flat-Band Potential. *J. Phys. Chem.* **1988,** *92*, 3476-3483.

16. Dotan, H.; Sivula, K.; Grätzel, M.; Rothschild, A.; Warren, S. C., Probing the Photoelectrochemical Properties of Hematite (α-Fe_2O_3) Electrodes using Hydrogen Peroxide as a Hole Scavenger. *Energy Environ. Sci.* **2011,** *4*, 958-964.

17. Sommers, J. M.; Alderman, N. P.; Viasus, C. J.; Gambarotta, S., Revisiting the Behaviour of $BiVO_4$ as a Carbon Dioxide Reduction Photo-Catalyst. *Dalton Trans.* **2017,** *46*, 6404-6408.

18. Qin, H.; Li, L.; Guo, F.; Su, S.; Peng, J.; Cao, Y.; Peng, X., Solution-Processed Bulk Heterojunction Solar Cells Based on a Porphyrin Small Molecule with 7% Power Conversion Efficiency. *Energy Environ. Sci.* **2014,** *7*, 1397-1401.

19. Ma, K.; Yehezkeli, O.; Domaille, D. W.; Funke, H. H.; Cha, J. N., Enhanced Hydrogen Production from DNA-Assembled Z-Scheme TiO_2–CdS Photocatalyst Systems. *Angew.Chem. Int. Ed.* **2015,** *54*, 11490-11494.

20. Hu, L.; He, H.; Xia, D.; Huang, Y.; Xu, J.; Li, H.; He, C.; Yang, W.; Shu, D.; Wong, P. K., Highly Efficient Performance and Conversion Pathway of Photocatalytic CH_3SH Oxidation on Self-Stabilized Indirect Z-Scheme g-C_3N_4/I_3^--BiOI. *ACS Appl. Mater. Interfaces* **2018,** *10*, 18693-18708.

21. Hutton, G. A. M.; Martindale, B. C. M.; Reisner, E., Carbon Dots as Photosensitisers for Solar-Driven Catalysis. *Chem. Soc. Rev.* **2017,** *46*, 6111-6123.

22. Cao, J.; Zhou, C.; Lin, H.; Xu, B.; Chen, S., Surface Modification of m-$BiVO_4$ with Wide Band-Gap Semiconductor BiOCl to Largely Improve the Visible Light Induced Photocatalytic Activity. *Appl. Surf. Sci.* **2013,** *284*, 263-269.

23. Qin, J.-S.; Yuan, S.; Zhang, L.; Li, B.; Du, D.-Y.; Huang, N.; Guan, W.; Drake, H. F.; Pang, J.; Lan, Y.-Q.; Alsalme, A.; Zhou, H.-C., Creating Well-Defined Hexabenzocoronene in Zirconium Metal–Organic Framework by Postsynthetic Annulation. *J. Am. Chem. Soc.* **2019,** *141*, 2054-2060.

24. Kresse, G.; Joubert, D., From Ultrasoft Pseudopotentials to the Projector Augmented-Wave Method. *Phys. Rev. B* **1999,** *59*, 1758-1775.

25. Perdew, J. P.; Burke, K.; Ernzerhof, M., Generalized Gradient Approximation Made Simple. *Phys. Rev. Lett.* **1996,** *77*, 3865-3868.

26. Dudarev, S. L.; Botton, G. A.; Savrasov, S. Y.; Humphreys, C. J.; Sutton, A. P., Electron-Energy-Loss Spectra and the Structural Stability of Nickel Oxide: An LSDA+U Study. *Phys. Rev. B* **1998,** *57*, 1505-1509.

27. Lindberg, A. E.; Wang, W.; Zhang, S.; Galli, G.; Choi, K.-S., Can a $PbCrO_4$ Photoanode Perform as Well as Isoelectronic $BiVO_4$? *ACS Appl. Energy Mater.* **2020,** *3*, 8658-8666.

28. Toma, F. M.; Cooper, J. K.; Kunzelmann, V.; McDowell, M. T.; Yu, J.; Larson, D. M.; Borys, N. J.; Abelyan, C.; Beeman, J. W.; Yu, K. M.; Yang, J.; Chen, L.; Shaner, M. R.; Spurgeon, J.; Houle, F. A.; Persson, K. A.; Sharp, I. D., Mechanistic Insights into Chemical and Photochemical Transformations of Bismuth Vanadate Photoanodes. *Nat. Commun.* **2016,** *7*, 12012.

29. Bondarenko, N.; Eriksson, O.; Skorodumova, N. V., Polaron Mobility in Oxygen-Deficient and Lithium-Doped Tungsten Trioxide. *Phys. Rev. B* **2015,** *92*, 165119.

30. Wang, F.; Di Valentin, C.; Pacchioni, G., Electronic and Structural Properties of WO_3: A Systematic Hybrid DFT Study. *J. Phys. Chem. C* **2011,** *115*, 8345-8353.

31. Kortlever, R.; Shen, J.; Schouten, K. J. P.; Calle-Vallejo, F.; Koper, M. T. M., Catalysts and Reaction Pathways for the Electrochemical Reduction of Carbon Dioxide. *J. Phys. Chem. Lett.* **2015,** *6*, 4073-4082.

32. Peterson, A. A.; Abild-Pedersen, F.; Studt, F.; Rossmeisl, J.; Nørskov, J. K., How Copper Catalyzes the Electroreduction of Carbon Dioxide into Hydrocarbon Fuels. *Energy Environ. Sci.* **2010,** *3*, 1311-1315.

33. Nellaiappan, S.; Kumar, R.; Shivakumara, C.; Irusta, S.; Hachtel, J. A.; Idrobo, J.-C.; Singh, A. K.; Tiwary, C. S.; Sharma, S., Electroreduction of Carbon Dioxide into Selective Hydrocarbons at Low Overpotential Using Isomorphic Atomic Substitution in Copper Oxide. *ACS Sustain. Chem. Eng.* **2020,** *8*, 179-189.

34. Wang, Q.; Warnan, J.; Rodríguez-Jiménez, S.; Leung, J. J.; Kalathil, S.; Andrei, V.; Domen, K.; Reisner, E., Molecularly Engineered Photocatalyst Sheet for Scalable Solar Formate Production from Carbon Dioxide and Water. *Nat. Energy* **2020,** *5*, 703-710.

35. Zhao, D.; Wang, Y.; Dong, C.-L.; Huang, Y.-C.; Chen, J.; Xue, F.; Shen, S.; Guo, L., Boron-Doped Nitrogen-Deficient Carbon Nitride-Based Z-Scheme Heterostructures for Photocatalytic Overall Water Splitting. *Nat. Energy* **2021,** *6*, 388-397.

36. Wang, Q.; Hisatomi, T.; Jia, Q.; Tokudome, H.; Zhong, M.; Wang, C.; Pan, Z.; Takata, T.; Nakabayashi, M.; Shibata, N.; Li, Y.; Sharp, I. D.; Kudo, A.; Yamada, T.; Domen, K.,

Scalable Water Splitting on Particulate Photocatalyst Sheets with a Solar-to-Hydrogen Energy Conversion Efficiency Exceeding 1%. *Nat. Mater.* **2016,** *15*, 611-615.

37. Araújo, J. C.; Sader, M. S.; Moreira, E. L.; Moraes, V. C. A.; LeGeros, R. Z.; Soares, G. A., Maximum Substitution of Magnesium for Calcium Sites in Mg-β-TCP Structure Determined by X-ray Powder Diffraction with the Rietveld Refinement. *Mater. Chem. Phys* **2009,** *118*, 337-340.

38. Lee, E.-J.; Chen, Z.; Noh, H.-J.; Nam, S. C.; Kang, S.; Kim, D. H.; Amine, K.; Sun, Y.-K., Development of Microstrain in Aged Lithium Transition Metal Oxides. *Nano Lett.* **2014,** *14*, 4873-4880.

39. de la Mata, M.; Magén, C.; Caroff, P.; Arbiol, J., Atomic Scale Strain Relaxation in Axial Semiconductor III–V Nanowire Heterostructures. *Nano Lett.* **2014,** *14*, 6614-6620.

40. Kibasomba, P. M.; Dhlamini, S.; Maaza, M.; Liu, C.-P.; Rashad, M. M.; Rayan, D. A.; Mwakikunga, B. W., Strain and Grain Size of TiO₂ Nanoparticles from TEM, Raman Spectroscopy and XRD: The Revisiting of the Williamson-Hall plot Method. *Results Phys.* **2018,** *9*, 628-635.

41. Udayabhaskar, R.; Sahlevani, S. F.; Prabhakaran, T.; Pandiyarajan, T.; Karthikeyan, B.; Contreras, D.; Mangalaraja, R. V., Modulation of Optical and Photocatalytic Properties by Morphology and Microstrain in Hierarchical Ceria Nanostructures. *Sol. Energy Mater Sol.* **2019,** *195*, 106-113.

42. Lee, B. R.; Lee, M. G.; Park, H.; Lee, T. H.; Lee, S. A.; Bhat, S. S. M.; Kim, C.; Lee, S.; Jang, H. W., All-Solution-Processed WO₃/BiVO₄ Core–Shell Nanorod Arrays for Highly Stable Photoanodes. *ACS Appl. Mater. Interfaces* **2019,** *11*, 20004-20012.

43. Pan, J.; Wu, X.; Wang, L.; Liu, G.; Lu, G. Q.; Cheng, H.-M., Synthesis of Anatase TiO₂ Rods with Dominant Reactive {010} Facets for the Photoreduction of CO₂ to CH₄ and Use in Dye-Sensitized Solar Cells. *Chem. Commun.* **2011,** *47*, 8361-8363.

44. She, H.; Zhou, H.; Li, L.; Zhao, Z.; Jiang, M.; Huang, J.; Wang, L.; Wang, Q., Construction of a Two-Dimensional Composite Derived from TiO₂ and SnS₂ for Enhanced Photocatalytic Reduction of CO₂ into CH₄. *ACS Sustain. Chem. Eng.* **2019,** *7*, 650-659.

45. Jin, J.; Yu, J.; Guo, D.; Cui, C.; Ho, W., A Hierarchical Z-Scheme CdS–WO₃ Photocatalyst with Enhanced CO₂ Reduction Activity. *Small* **2015,** *11*, 5262-5271.

46. Bian, J.; Feng, J.; Zhang, Z.; Li, Z.; Zhang, Y.; Liu, Y.; Ali, S.; Qu, Y.; Bai, L.; Xie, J.; Tang, D.; Li, X.; Bai, F.; Tang, J.; Jing, L., Dimension-Matched Zinc Phthalocyanine/BiVO₄ Ultrathin Nanocomposites for CO₂ Reduction as Efficient Wide-

Visible-Light-Driven Photocatalysts via a Cascade Charge Transfer. *Angew. Chem. Int. Ed.* **2019,** *58*, 10873-10878.

47. Wei, Y.; Jiao, J.; Zhao, Z.; Liu, J.; Li, J.; Jiang, G.; Wang, Y.; Duan, A., Fabrication of Inverse Opal TiO_2-Supported Au@CdS Core–Shell Nanoparticles for Efficient Photocatalytic CO_2 Conversion. *Appl. Catal. B: Environ.* **2015,** *179*, 422-432.

48. Bhosale, S. S.; Kharade, A. K.; Jokar, E.; Fathi, A.; Chang, S.-m.; Diau, E. W.-G., Mechanism of Photocatalytic CO_2 Reduction by Bismuth-Based Perovskite Nanocrystals at the Gas–Solid Interface. *J. Am. Chem. Soc.* **2019,** *141*, 20434-20442.

49. Bie, C.; Zhu, B.; Xu, F.; Zhang, L.; Yu, J., In Situ Grown Monolayer N-Doped Graphene on CdS Hollow Spheres with Seamless Contact for Photocatalytic CO_2 Reduction. *Adv. Mater.* **2019,** *31*, 1902868.

50. Li, X.; Song, X.; Ma, C.; Cheng, Y.; Shen, D.; Zhang, S.; Liu, W.; Huo, P.; Wang, H., Direct Z-Scheme WO_3/Graphitic Carbon Nitride Nanocomposites for the Photoreduction of CO_2. *ACS Appl. Nano Mater.* **2020,** *3*, 1298-1306.

51. Wang, H.; Zhang, L.; Wang, K.; Sun, X.; Wang, W., Enhanced Photocatalytic CO_2 Reduction to Methane over $WO_3 \cdot 0.33H_2O$ via Mo Doping. *Appl. Catal. B: Environ.* **2019,** *243*, 771-779.

52. Pan, Y.-X.; You, Y.; Xin, S.; Li, Y.; Fu, G.; Cui, Z.; Men, Y.-L.; Cao, F.-F.; Yu, S.-H.; Goodenough, J. B., Photocatalytic CO_2 Reduction by Carbon-Coated Indium-Oxide Nanobelts. *J. Am. Chem. Soc.* **2017,** *139*, 4123-4129.

53. Liu, Q.; Zhou, Y.; Kou, J.; Chen, X.; Tian, Z.; Gao, J.; Yan, S.; Zou, Z., High-Yield Synthesis of Ultralong and Ultrathin Zn_2GeO_4 Nanoribbons toward Improved Photocatalytic Reduction of CO_2 into Renewable Hydrocarbon Fuel. *J. Am. Chem. Soc.* **2010,** *132*, 14385-14387.

54. Díaz-Reyes, J.; Castillo-Ojeda, R.; Galván-Arellano, M.; Zaca-Moran, O., Characterization of WO_3 Thin Films Grown on Silicon by HFMOD. *Adv. Cond. Matt. Phys.* **2013,** *2013*, 591787.

55. Sotelo-Vazquez, C.; Quesada-Cabrera, R.; Ling, M.; Scanlon, D. O.; Kafizas, A.; Thakur, P. K.; Lee, T.-L.; Taylor, A.; Watson, G. W.; Palgrave, R. G.; Durrant, J. R.; Blackman, C. S.; Parkin, I. P., Evidence and Effect of Photogenerated Charge Transfer for Enhanced Photocatalysis in WO_3/TiO_2 Heterojunction Films: A Computational and Experimental Study. *Adv. Funct. Mater.* **2017,** *27*, 1605413.

56. Ho-Kimura, S.; Moniz, S. J. A.; Handoko, A. D.; Tang, J., Enhanced Photoelectrochemical Water Splitting by Nanostructured $BiVO_4$–TiO_2 Composite Electrodes. *J. Mater. Chem. A* **2014,** *2* , 3948-3953.

57. Katsumata, H.; Tachi, Y.; Suzuki, T.; Kaneco, S., Z-Scheme Photocatalytic Hydrogen Production over WO_3/g-C_3N_4 Composite Photocatalysts. *RSC Adv.* **2014,** *4*, 21405-21409.

58. Tan, Y.-X.; Chai, Z.-M.; Wang, B.-H.; Tian, S.; Deng, X.-X.; Bai, Z.-J.; Chen, L.; Shen, S.; Guo, J.-K.; Cai, M.-Q.; Au, C.-T.; Yin, S.-F., Boosted Photocatalytic Oxidation of Toluene into Benzaldehyde on $CdIn_2S_4$-CdS: Synergetic Effect of Compact Heterojunction and S-Vacancy. *ACS Catal.* **2021,** *11*, 2492-2503.

59. Xu, Y.-F.; Yang, M.-Z.; Chen, B.-X.; Wang, X.-D.; Chen, H.-Y.; Kuang, D.-B.; Su, C.-Y., A $CsPbBr_3$ Perovskite Quantum Dot/Graphene Oxide Composite for Photocatalytic CO_2 Reduction. *J. Am. Chem. Soc.* **2017,** *139*, 5660-5663.

60. Pareek, A.; Paik, P.; Borse, P. H., Characterization of Nano-Titania Modified CdS /Polysulfide Electrolyte Interface by Utilizing Mott-Schottky and Electrochemical Impedance Spectroscopy. *Electroanalysis* **2014,** *26*, 2403-2407.

61. Bhosale, R.; Jain, S.; Vinod, C. P.; Kumar, S.; Ogale, S., Direct Z-Scheme g-C_3N_4/$FeWO_4$ Nanocomposite for Enhanced and Selective Photocatalytic CO_2 Reduction under Visible Light. *ACS Appl. Mater. Interfaces* **2019,** *11*, 6174-6183.

62. Sekizawa, K.; Maeda, K.; Domen, K.; Koike, K.; Ishitani, O., Artificial Z-Scheme Constructed with a Supramolecular Metal Complex and Semiconductor for the Photocatalytic Reduction of CO_2. *J. Am. Chem. Soc.* **2013,** *135*, 4596-4599.

63. Jiang, Y.; Liao, J.-F.; Chen, H.-Y.; Zhang, H.-H.; Li, J.-Y.; Wang, X.-D.; Kuang, D.-B., All-Solid-State Z-Scheme α-Fe_2O_3/Amine-RGO/$CsPbBr_3$ Hybrids for Visible-Light-Driven Photocatalytic CO_2 Reduction. *Chem* **2020,** *6*, 766-780.

64. Wang, T.; Meng, X.; Li, P.; Ouyang, S.; Chang, K.; Liu, G.; Mei, Z.; Ye, J., Photoreduction of CO_2 over the well-crystallized ordered mesoporous TiO_2 with the confined space effect. *Nano Energy* **2014,** *9*, 50-60.

65. Sibi, M. G.; Verma, D.; Setiyadi, H. C.; Khan, M. K.; Karanwal, N.; Kwak, S. K.; Chung, K. Y.; Park, J.-H.; Han, D.; Nam, K.-W.; Kim, J., Synthesis of Monocarboxylic Acids via Direct CO_2 Conversion over Ni–Zn Intermetallic Catalysts. *ACS Catal.* **2021**, 8382-8398.

66. Tan, T. H.; Xie, B.; Ng, Y. H.; Abdullah, S. F. B.; Tang, H. Y. M.; Bedford, N.; Taylor, R. A.; Aguey-Zinsou, K.-F.; Amal, R.; Scott, J., Unlocking the Potential of the Formate Pathway in the Photo-Assisted Sabatier Reaction. *Nat. Catal.* **2020,** *3*, 1034-1043.

67. Liu, Y.; Chen, S.; Quan, X.; Yu, H., Efficient Electrochemical Reduction of Carbon Dioxide to Acetate on Nitrogen-Doped Nanodiamond. *J. Am. Chem. Soc.* **2015,** *137*, 11631-11636.

68. Liu, L.; Li, Y., Understanding the Reaction Mechanism of Photocatalytic Reduction of CO_2 with H_2O on TiO_2-Based Photocatalysts: A Review. *Aerosol Air Qual. Res.* **2014,** *14*, 453-469.

69. Boccuzzi, F.; Chiorino, A., FTIR Study of Carbon Monoxide Oxidation and Scrambling at Room Temperature over Copper Supported on ZnO and TiO_2. 1. *J Phys Chem.* **1996,** *100*, 3617-3624.

70. Wu, J. C. S.; Huang, C.-W., In Situ DRIFTS Study of Photocatalytic CO_2 Reduction Under UV Irradiation. *Front. Chem. Eng. China* **2010,** *4*, 120-126.

71. Capdevila-Cortada, M.; Łodziana, Z.; López, N., Performance of DFT+U Approaches in the Study of Catalytic Materials. *ACS Catal.* **2016,** *6*, 8370-8379.

72. Frei, M. S.; Capdevila-Cortada, M.; García-Muelas, R.; Mondelli, C.; López, N.; Stewart, J. A.; Curulla Ferré, D.; Pérez-Ramírez, J., Mechanism and Microkinetics of Methanol Synthesis via CO_2 Hydrogenation on Indium Oxide. *J. Catal.* **2018,** *361*, 313-321.

73. Xie, C.; Niu, Z.; Kim, D.; Li, M.; Yang, P., Surface and Interface Control in Nanoparticle Catalysis. *Chem. Rev.* **2020,** *120*, 1184-1249.

74. Hinnemann, B.; Moses, P. G.; Bonde, J.; Jørgensen, K. P.; Nielsen, J. H.; Horch, S.; Chorkendorff, I.; Nørskov, J. K., Biomimetic Hydrogen Evolution: MoS_2 Nanoparticles as Catalyst for Hydrogen Evolution. *J. Am. Chem. Soc.* **2005,** *127*, 5308-5309.

Chapter 4

Activating Oxygen Deficient TiO$_2$ in The Visible Region by Bi$_2$MoO$_6$ for CO$_2$ Photoreduction to Methanol
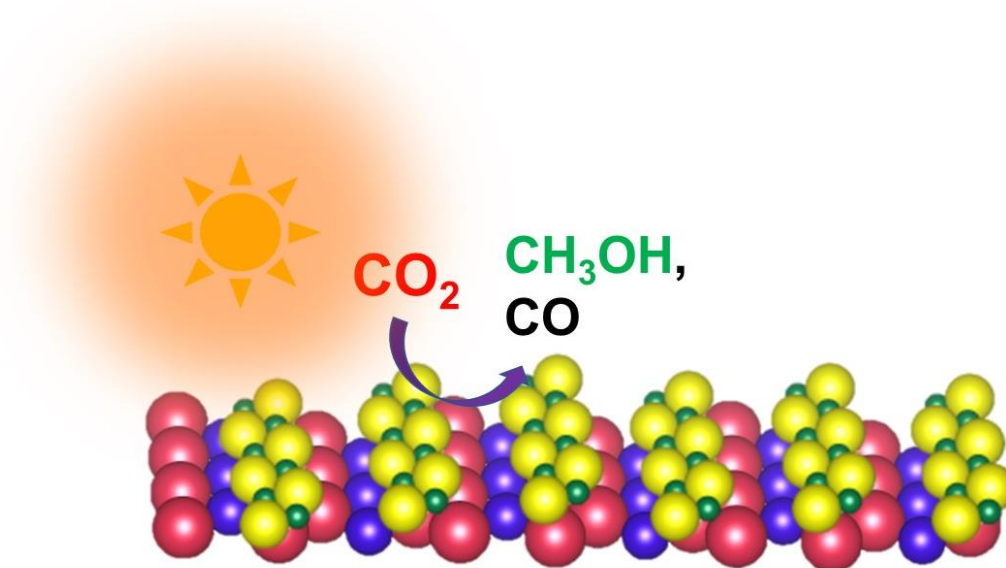
Risov Das, Kousik Das, Sathyapal R. Churipard, Sebastian C. Peter

Summary

Heterojuncituin photocatalysts has already been explored for bettter catalysis in earlier chapter. Therefore, similar approach were introduced for addressing the shortcomings of TiO_2. Fast photo-generated charge recombination and inappropriate bandgap for visible-light-driven charge generation hinder the performance of TiO_2. In this study, TiO_2 was activated for visible-light-driven CO_2 reduction in the presence of Bi_2MoO_6 as an electron donor. Furthermore, the introduction of oxygen vacancies resulted in enhanced CO_2 adsorption and conversion. The best catalyst gives 27.1 µmol g^{-1} h^{-1} methanol formation. DRIFTS were used to explain the methanol formation mechanism on oxygen deficient TiO_2. The oxygen vacancies were quantified by X-ray photoelectron spectroscopy (XPS) spectra and the enhanced CO_2 adsorption capacity was understood from CO_2 temperature programmed desorption (TPD) study.

Risov Das, Kousik Das, Sathyapal R. Churipard, Sebastian C Peter

4.1. Introduction

Metal oxide semiconductors have identified as potential CO_2 reduction candidate. Selective methane formation was carried out by hetero-structure photocatalyst. However, methane and methanol both forms via the same intermediate formation. Therefore, methanol synthesis was targeted because methanol has a more economical interest compared to methane.[1] In this context, transition metal oxide-based semiconductors are considered to be promising photocatalysts due to their suitable band edge position and excellent stability against photodegradation. For example, TiO_2,[2] WO_3,[3] Bi_2MoO_6,[4] $BiVO_4$[5] etc. have been extensively used for the photocatalytic hydrogen evolution reaction (HER) and photocatalytic CO_2 reduction reaction (PCR).[6]

Despite having promising photocatalytic activity, the practical application of TiO_2 is constrained by its poor visible light activity and its tendency to undergo extensive electron-hole recombination, reducing the extent of photo-generated electrons (e^-s) available for photoconversion. Similarly, Bi_2MoO_6, a promising visible light driven photocatalyst shows low quantum efficiency owing to its poor charge separation and slow carrier mobility.[7] Establishing a heterojunction between two semiconductors is an excellent strategy to significantly increase the photoconversion efficiency by not only modulating the light sensitivity towards the visible region but also promoting the charge carrier separation.[8-9] In addition, surface engineering leading to the generation of oxygen vacancies (O_v) can also increase the lifetime of photo-generated e^-s by creating trap states between the conduction and valence band.[10-11] Here, Bi_2MoO_6 is used as an e^- donor to activate TiO_2 under visible light. In addition, O_v was created deliberately to offer optimum CO_2 chemisorption opportunities at the TiO_2 surface. With the help of this dual strategy, we were able to achieve a dramatic increment of PCR performance by suppressing the drawbacks of the individual components. CH_3OH was obtained as the major product, which is regarded as a high energy dense fuel.[12]

4.2. Experimental section

Materials: Titania P25 [TiO_2, Alfa Aesar], sodium hydroxide [NaOH, Spectrochem], hydrochloric acid [HCl, Merck], sulfuric acid [H_2SO_4, Merck], ethylene glycol [$(CH_2OH)_2$, Sigma Aldrich], bismuth nitrate pentahydrate [$Bi(NO_3)_3 \cdot 5H_2O$, Alfa Aesar], sodium molybdate dihydrate [$Na_2MoO_4 \cdot 2H_2O$, Alfa Aesar]. All the chemicals used were commercially available certified reagents and without further purification.

Synthesis of catalysts[13]

Preparation of TiO₂ nanobelts: P25 (0.2 g) was immersed in 40 mL of a 10 M NaOH solution. The suspension was transferred to a 50 mL Teflon-lined autoclave and maintained at 180 °C for 48 h. After washing thoroughly with deionized water, the obtained products were dissolved in a 0.1 M HCl solution for 48 h to get $H_2Ti_3O_7$ nanobelts, then the above products were immersed in a 0.02 M H_2SO_4 solution and maintained at 180 °C for 10 h. After washing thoroughly with deionized water, the sample was annealed at 600 °C for 2h.

Preparation of 2D Bi₂MoO₆/TiO₂ heterostructure: Bi_2MoO_6 nanoparticles/TiO_2 nanobelt heterostructures (mole ratios from 1:1 to 4:1) were synthesized by a coprecipitation hydrothermal method. $Bi(NO_3)_3 \cdot 5H_2O$ (0.4-1.6 mmol), $Na_2MoO_4 \cdot 2H_2O$ (0.2-0.8 mmol), and TiO_2 nanobelts (0.2 mmol) were immersed in 15 mL of ethylene glycol, respectively, and then were mixed together. The resulting suspension was maintained at 160 °C for 24 h in a 50 mL Teflon-lined autoclave. Finally, the products were washed thoroughly with deionized water. For comparison, pure Bi_2MoO_6 nanoparticles were also synthesized in the same manner without adding TiO_2 nanobelts. We varied the ratio of Bi_2MoO_6:TiO_2 in the composition 1:1(**Bi1@Ti1**), 2:1 (**Bi2@Ti1**) and 3:1 (**Bi3@Ti1**)

Material characterization

X-Ray diffraction: The structural phase of Bi_2MoO_6 and TiO_2 samples were confirmed by X–ray diffraction (XRD, Rigaku Advance X-ray diffractometer equipped with Cu kα lamp source for irradiation 1.5 Å).

Microscopy: To understand the morphology of material, transmission electron microscopy (TEM), and scanning electron microscopy w done using JEOL 200 and oxford instruments. Sample preparation was done by drop casting small amount of sonicated powder in ethanol on a carbon coated copper grid and little more concentrated solution on silicon wafer.

Electron spin resonance (ESR) measurements: 10 mg sample was loaded in EPR tube (made of quartz) and the EPR signal was detected by Bruker instrument. Before the experiment, the instrument was standardized by a standard Mn sample.

CO₂ Temperature programmed desorption (TPD): The CO_2 TPD analysis was performed in Altamira AMI-300 Lite instrument using 10% CO_2 in Helium. In a typical procedure, around 150 mg of material was taken in the U-shaped TPD cell. The sample was pre-treated at 500 °C for 1h with a ramp rate of 10 °C/min with Helium prior to the CO_2 treatment. The material was

allowed to cool to 50 °C and it was saturated for 60 minutes with CO_2 by passing a mixture of gas containing 5 ml/min CO_2 and 45 ml/min helium. Further, the sample was flushed with Helium to remove any physisorbed CO_2. The TPD analysis was performed from 50 °C till 500 °C with a ramp rate of 10 °C/min and helium as carrier gas with a flow rate of 25 ml/min. The amount of CO_2 desorbed from the material was detected by the TCD detector. After every analysis, the TCD response is calibrated to calculate the amount of CO_2 chemisorbed on the sample.

Photocatalytic measurements: A quartz photoreactor was used for CO_2 hydrogenation experiment under the illumination of 450 W xenon lamp (Newport) through UV cut-off filter (CGA 400 filter and KG2 filter). The intensity of output light was measured using a power meter (Newport-843-R). The measured intensity during the catalytic reaction is 110 mW/cm². (Note: The distance between light source and reactor is 10 cm). About 5 mg of the sample was well dispersed in 20 mL of 0.1 M NaOH by ultrasonication. Before illumination, the reaction setup was purged with N_2 to remove the air and then with high purity CO_2 for 45 minutes. During irradiation, 5 mL of the gaseous product from the setup was sampled, and ensuing study was done by GC (gas chromatography) (Agilent GC-7890 B) with TCD and FID detector and He carrier gas. This can detect up to 0.25 ppm of methane and 16 ppm CO. To further verify the products gas chromatography Mass Spectrometry (SHIMAZU GC-2010 PLUS) was used. Products were quantified by using RT® Molecular sieve 5A column (45 m, 0.32 mm ID, 30 μm df) with a mass detector. The calibration was done by a standard gas mixture of H_2, CO, CH_4 of different concentrations in ppm-level. It has a detection limit of 1 ppm for H_2, CO and CH_4. Another dedicated GC (Agilent 7890 B) with a TCD detector and Ar carrier gas was used to detect H_2. It can sense up to 10 ppm of H_2. For liquid product analysis ¹H NMR (400 MHz, JEOL) and HPLC (Agilent 1220 Infinity II LC system) were employed. The following protocol was applied for the ¹H NMR analysis. Five hundred μL of the solvent (after filtration) and 10 μL of an internal standard solution were transferred into a centrifuge tube. The internal standard solution consisted of 50 mM phenol (99.5%) and 10 mM dimethyl sulfoxide (99.9%) made in D_2O solvent. The mixture is transferred into an NMR tube. Blank tests were conducted in the absence of CO_2 and light to confirm that these two factors are critical for the photocatalytic CO_2 reduction reaction. Used photocatalyst was amassed after each test and washed with water, and its performance was rechecked by similar procedure. Rate of the product formation was calculated by considering maximum rate at 6th hour for all the catalysts. ¹³CO_2 was purged for 20 minutes and the reaction was continued for 2h. Then the products were checked by GC-MS

to confirm the source of CO and CH_3OH is CO_2. All the photocatalytic reactions were done in an air conditioning room (22 °C). The local heat generated on the catalyst surface during light illumination was checked by an infrared temperature gun (GM320) and it was not more than 45°C. Maintaining all the conditions similar to the reaction was done at 45°C in the absence of light. However, no product was detected. This proves that the local heating due to light illumination does not affect the catalytic performance.

Role of basic medium in PCR study: Basic solution was used to increase the solubility of CO_2 in the reaction medium. Dissolution of CO_2 in water follows three chemical reactions.

$$CO_2 + H_2O \leftrightarrow H_2CO_3 \dots\dots\dots\dots\dots \textbf{(4.1)}$$

$$H_2CO_3 \leftrightarrow HCO_3^- + H^+ \dots\dots\dots\dots. \textbf{(4.2)}$$

$$HCO_3^- \leftrightarrow CO_3^{2-} + H^+ \dots\dots\dots\dots \textbf{(4.3)}$$
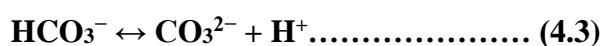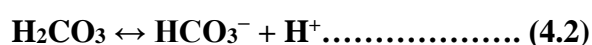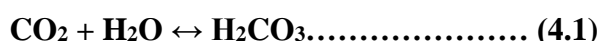
Hydroxide consumes protons and promotes 4.1 and 4.2 reactions. Reaction 4.3 depletes H_2CO_3. As a result, reaction (r1) is also forced to shift towards right. The net result is more CO_2 residing in solution (dissolved) as the solution becomes more basic in nature.

The ultraviolet-visible diffuse reflectance spectrum (UV-vis DRS): UV-vis spectra was obtained in the range of 250 to 800 nm by using a Perkin-Elmer Lambda 900 UV/Vis/Near- IR spectrophotometer in reflectance mode for $BiVO_4$, WO_3 and composites. With an integrating sphere attachment. $BaSO_4$ was used as a 100% reflectance standard. The absorption was calculated data using the Kubelka−Munk equation, $\alpha/S = (1 - R)^2/2R$, where R is the reflectance and α and S are the absorption and scattering coefficients, respectively.[14] Band gap was derived using Tauc plot.

Photoluminescence (PL): PL spectra of all the solid samples were recorded at room temperature on a steady state Luminescence spectrometer Perkin-Elmer (LS 55) at different excitation wavelength.

Electron paramagnetic resonance (ESR): Five mg of sample (P25 commercially available TiO_2 and Ov-TiO_2 nano belt were poured in a quartz ESR tube. Before starting the experiment, the machine was calibrated by slandered Mn^{2+} sample. The experiment was done by Brucker ESR instrument with S-band magnet. First the Q-band was identified at 330 mT and then data collection was done in the region of 300 to 360 mT. Here Mt refers: Mili Tesla.

Photoelectrochemical measurements: The transient photocurrent measurements under dark and light were done in a three-electrode system using a OrigaLys potentiostat under the

illumination of a solar simulator (Newport) with an ultraviolet (UV) ($\lambda > 400$ nm) cut-off filter (CGA-400). Hg/Hg_2Cl_2 (SCE) was reference electrode, and platinum as the counter electrode was used. The slurry was prepared by adding 10 mg of the sample, 200 µL of Nafion (5%), and 1 mL of isopropyl alcohol to fabricated photoelectrodes. The obtained paste was spin-coated on FTO with 1 cm² area to get a homogenous film. All samples were spin coated on fluorine-doped tin oxide (FTO) which were used as working electrode. 0.5 M Na_2SO_4 was taken as electrolyte for Nyquist plot and Mott-Schottky measurement. Mott-Schottky (MS) plots were recorded at a scan rate of 10 mV/s in Na_2SO_4 neutral solution in the light at a frequency of 75 kHz. The obtained values (w.r.t SCE) were converted w.r.t NHE by adding 0.20 V. Photocurrent was obtained by 10s light on and 10s off experiment with sample spin coated on FTO electrode in 0.1M NaOH solution.

In-situ photocatalytic Fourier transform infrared spectroscopy (FT-IR): In-situ photochemical FT-IR spectroscopic studies were performed using a purged VERTEX FT-IR spectrometer equipped with the A530/P accessory and a mid-band Mercury Cadmium Telluride (MCT) detector. Spectra was recorded after 100 scans with a resolution of 4 cm⁻¹. A DRIFTS cell with a quartz window was used to perform catalytic experiment. Prior to catalytic testing, 5 mg of the sample was placed in the DRIFTS cell and treated in flowing N_2 for 30 min to remove impure gas mixtures. Then, CO_2 and water vapor were injected through rubber septa and light was illuminated through the quartz window for 150 minutes. Just before the light exposure on the DRIFTS cell the zero-minute data was collected and after that, data was collected every 10 minutes for 150 minutes.

4.3. Apparent quantum yield (AQY) calculation[15-16]

The wavelength dependent AQY of CO_2 photo-reduction by comp14 were calculated using different monochromatic light source. Therefore, 6 (400±10 nm, 425±10 nm, 450±10 nm, 475±10 nm, 500±10 nm, 550±10 nm) different bandpass filters obtained from light source manufacturer (Newport) were used to obtain the monochromatic wavelengths and Newport-843-R power meter was used to measure the incident light intensity. After 6 hours of CO_2 reduction the AQY was estimated from the following equation:

$$AQY(\%) = \frac{Number\ of\ reacted\ electrons}{Number\ of\ incident\ photons} X\ 100\%$$

Number of reacted electrons were calculated from the yield of CO_2 reduced products (here selectively methane was obtained). Because different number of electrons are required for the formation of different products, the total number of reacted electrons are

$$Number\ of\ reacted\ electrons = [\,6n(CH_4) + 2n(H2) + 2n(CO)]X\ N_A$$

$n(CH_4)$, is the yield of methane. N_A is Avogadro's number.

Number of incident photons are calculated from the following equation:

$$Number\ of\ incident\ photons = \frac{PS\lambda t}{hc}$$

where, P is the power density of the incident monochromatic light (W/m^2), S (m^2) is the irradiation area, t (s) is the duration of the incident light exposure and λ (m) is the wavelength of the incident monochromatic light. h (Js) and c (m/s) correspond to planks constant and speed of light respectively.

Combining these two equations the AQY(%) for different monochromatic light was calculated. For example, the AQY(%)@400 nm is shown here-

$n(CH_3OH) = 18.4\ \mu mol/g$, $n(H_2) = 2.8\ \mu mol/g$, $n(CO) = 9.4\ \mu mol/g$, $N_A = 6.023*10^{23}\ mol^{-1}$, P= $44*10^{-3}$ W/cm^2, S= 4.52 cm^2, l= 400 nm, t=6h, h= $6.626*10^{-34}$ Joule second, c= $3*10^8$ m/s

AQY(%)@400 nm

$$= \frac{[(18.4\times6)+(2.8\times2)+(9.4\times2)\times10^{-6}]\times6.02\times10^{23}}{1} \times \frac{6.626\times10^{-34}\times3\times10^8}{44\times10^{-3}\times4.52\times400\times10^{-9}\times3600\times6} \times 100\%$$

$$= 0.89\%$$

Similarly, AQY% were calculated for 425 nm, 450 nm, 475 nm, 500nm, 550nm. For each AQY% calculation 5 mg new batch of photocatalysts were used to perform CO_2 reduction.

4.4. Results and discussions

TiO_2, Bi_2MoO_6 and their composites were synthesised by solvothermal processes. Pre-synthesized TiO_2 was added to an autoclave along with $Bi(NO_3)_3$ and Na_2MoO_4 to make a suitable interface between TiO_2 and Bi_2MoO_6 for facile e$^-$ transfer within the heterojunction. The formation of the heterojunction is depicted *via* TEM and SEM images in **Figure 4.1a**, and **4.1b**, which demonstrate the anchoring of Bi_2MoO_6 nano-seeds on TiO_2 nanoribbons. The HRTEM image in **Figure 4.1c** depicts the (101) plane of TiO_2 and (131) plane of Bi_2MoO_6, which are in intimate contact with each other to form the heterostructure in the composite catalyst. EDX colour mapping showed that seed like morphology mostly contains Bi, Mo, O (**Figure 4.1d-g**) and ribbon like morphology mainly constitutes of Ti and O (**Figure 4.1h-k**). The ratio of Bi_2MoO_6 and

TiO$_2$ was varied during the synthesis process to optimize the composite composition for best CO$_2$ photoreduction activity. The weight ratio of Bi$_2$MoO$_6$ and TiO$_2$ was varied

from 3:1, to 2:1 and 1:1 and termed as **Bi3@Ti1**, **Bi2@Ti1** and **Bi1@Ti1**. Henceforth this nomenclature will be used throughout the manuscript. The PXRD patterns of the TiO$_2$, Bi$_2$MoO$_6$, and Bi$_2$MoO$_6$/TiO$_2$ heterostructures are shown in **Figure 4.2a.** Six distinctive peaks observed for TiO$_2$ at 2θ = 25.28° (101), 37.80° (004), 48.05° (200), 53.89° (105), 55.06° (211) and 62.69° (204) corroborate with anatase TiO$_2$ (*I4$_1$/amd*).[17] In the case of Bi$_2$MoO$_6$, the diffraction peaks at 28.25°, 32.59°, 33.07°, 46.72°, 47.07°, 55.46°, 55.53° and 56.16° could be perfectly indexed to the (131), (002), (060), (202), (260), (331), (133) and (191) planes of orthorhombic Bi$_2$MoO$_6$ (*Pca2$_1$*).[18]
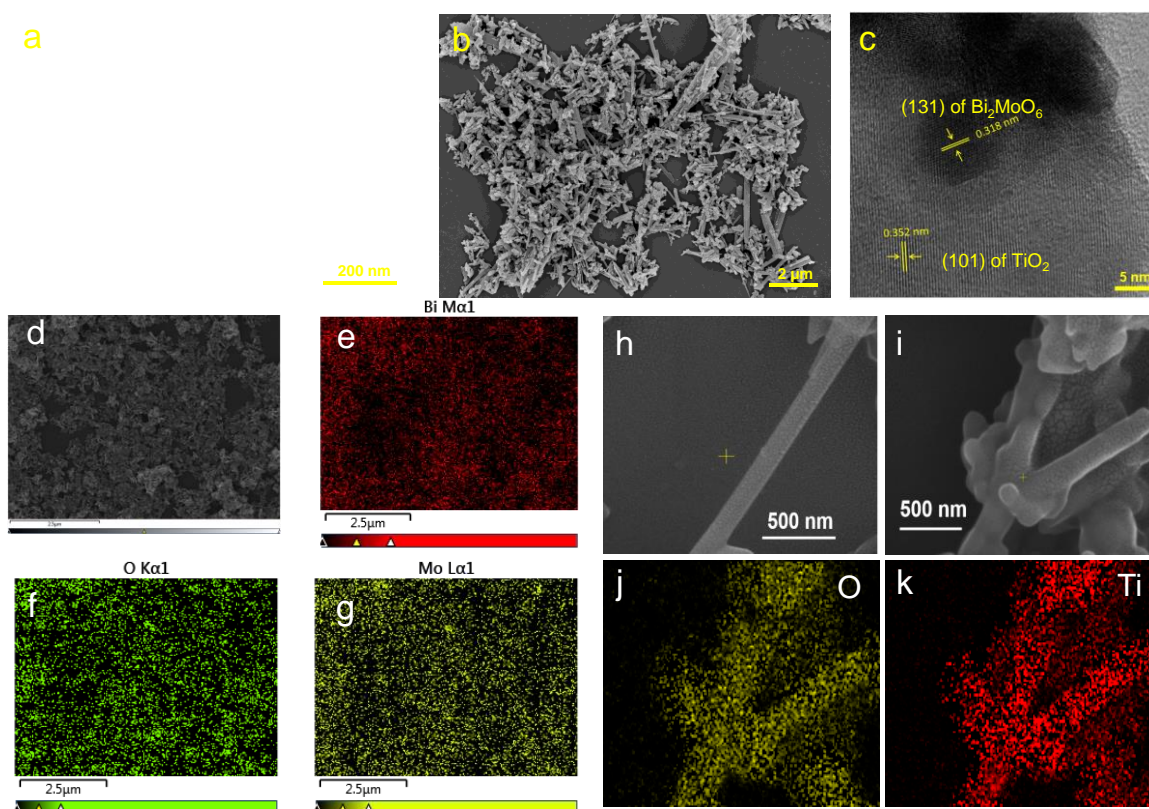
Figure 4.1. Characterization of PCR performing catalyst including pristine and composites. **(a)** TEM and **(b)** SEM image of TiO$_2$ nanoribbon and Bi$_2$MoO$_6$ nanoparticle composite. **(c)** HRTEM image of Bi2@Ti1 composite shows the presence of Bi$_2$MoO$_6$ (131) plane and TiO$_2$ (101) plane. Higher molecular weight of Bi$_2$MoO$_6$ makes darker image compared to the TiO$_2$. The different d-spacing and colour contrast further implies that Bi$_2$MoO$_6$ and TiO$_2$ are held together in composite. **(d)** SEM image of pristine Bi$_2$MoO$_6$. SEM–EDX elemental mapping images showing uniform distribution of **(e)** Bi, **(f)** O, and **(g)** Mo for pristine Bi$_2$MoO$_6$. **(h, i)** SEM image of pristine Bi$_2$MoO$_6$ taken in 2 different regions. SEM–EDX elemental mapping images showing uniform distribution of **(j)** O, and **(k)** Ti for pristine TiO$_2$. Colour mapping was taken on SEM image.

123

For the Bi_2MoO_6/TiO_2 heterostructures, all the peaks can be assigned to either TiO_2 or Bi_2MoO_6. Absence of extra peak proves the formation of a pure heterojunction. A very less intense (101) plane of TiO_2 is observed in the XRD patterns of the composite, which is due to the lower diffraction ability of TiO_2 compared to Bi_2MoO_6.
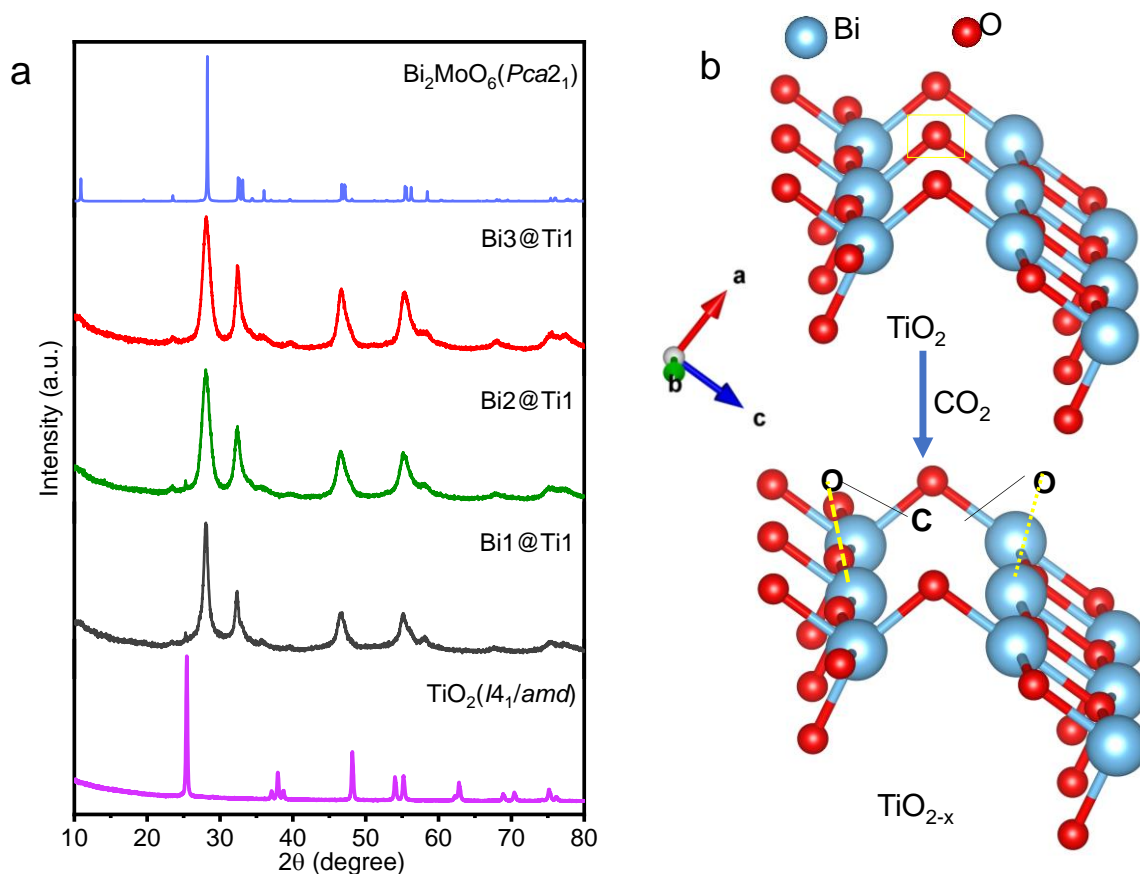
Figure 4.2. (a) PXRD all the composites and as synthesized pristine TiO_2 and simulated pattern of Bi_2MoO_6. **(b)** Schematic representation of CO_2 adsorption in 'O' deficient TiO_2.
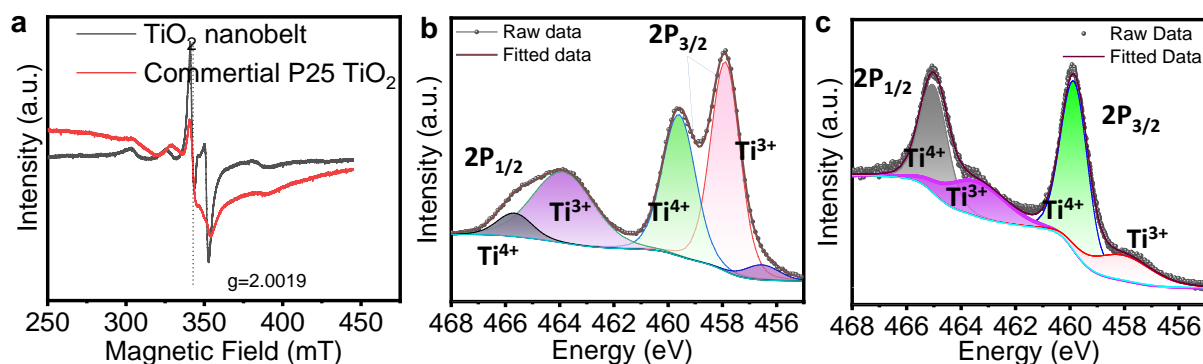
Figure 4.3. (a) ESR spectra of as synthesized TiO_2 nanoribbon and commercially available P25 TiO_2 for qualitative understanding of O_v. Ti 2p XPS spectra for understanding the presence of Ti^{3+} and Ti^{4+} in **(b)** TiO_2 nanoribbon and, **(c)** commercially available P25 TiO_2.

With an increase in the amount of TiO_2, the peak intensity also increases (**Figure 4.2a**). Instead of using commercially available TiO_2 (P25), here TiO_2 was treated with a base for increasing O_v in it (**Figure 4.2b**). The presence of more O_v in TiO_2 nanoribbon compared to P25 was understood from EPR spectroscopy (**Figure 4.3a**). Oxygen vacancies induces the formation of Ti^{3+} along with Ti^{4+} ($Ti^{4+}O_2 \rightarrow Ti^{3+}Ti^{4+}O_{(2-X)} + X/2O_2$). The presence of more Ti^{3+} compared to Ti^{4+} in TiO_2 nanoribbon was depicted from X-ray photoelectron spectroscopy (XPS) in **Figure 4.3b,** and **4.3c**. The deconvoluted spectra of P25 also indicated the presence of Ti^{3+} although in much lower quantity compared to the TiO_2 nanoribbons. The $3d^1$ e^- in Ti^{3+} generates an EPR signal.[19] Hence, the more intense EPR signal of the TiO_2 nanoribbons compared to P25 clearly indicates the presence of more Ti^{3+} or more O_v in TiO_2 nanoribbons. These O_v act as hole scavengers ($Ti^{3+} + h^+ \rightarrow Ti^{4+}$) and lower the CO_2 adsorption energy on TiO_2 surface, which in turn facilitates the CO_2 reduction process (**Figure 4.2b**).[20-21] CO_2 Temperature Programmed Desorption (TPD) in **Figure 4.4a** revealed that the TiO_2 with vacancies has better CO_2 uptake capacity (1.85 µmol g^{-1}) compared to pure TiO_2 (0.53 µmol g^{-1}) (**Table 4.1**). The CO_2 photoreduction performance of all the catalysts was tested under solar simulated 450W Xe light illumination in a sealed quartz tube. Methanol was obtained as the major product and CO as a minor product. The CO_2 reduction performance (rate of product formation) of all the catalysts is summarized in **Figure 4.4b** and **Table 4.2**. Among all the composite catalysts, **Bi2@Ti1** exhibited the best catalytic activity. It achieved methanol formation rate of 27.1 mmol g^{-1} h^{-1} (**Figure 4.4c**), which is better than most of the TiO_2 based catalyst reported for methanol (**Table 4.3**).

Table 4.1. Amount of CO_2 chemisorbed on the sample calculated from CO_2 TPD analysis.

Sample	CO₂ uptake (µmol/g)
TiO₂	0.53
TiO₂₋ₓ	1.85

Table 4.2. Summering photocatalytic activity of all the sample.

Sample	CO (µmol/h/g)	H₂ (µmol/h/g)	CH₃OH (µmol/h/g)
Bi	1.3	0.5	1.9
Bi3@Ti1	13.16	3	14.7
Bi2@Ti1	16.21	5.1	27.1
Bi1@Ti1	8	2.2	4.9
Ti (FA)	6.8	16	2.1
Ti (V)	0.7	1	0.2

Table 4.3. Comparing photocatalytic activity of our sample and best results reported with TiO_2 for methanol formation upon CO_2 photo reduction. NM: Not mentioned.

Catalyst	Reduction medium)	Sacrificial agent	Light source	Product	Maximum Evolution rate (µmol g^{-1}h^{-1})
Bi3@Ti1	20 ml 0.1M NaOH soln.	No	450W Xe Lamp	CO, CH$_3$OH	CH$_3$OH:14.7
Bi2@Ti1	20 ml 0.1M NaOH soln.	No	450W Xe Lamp	CO, CH$_3$OH	CH$_3$OH:27.1
Bi1@Ti1	20 ml 0.1M NaOH soln.	No	450W Xe Lamp	CO, CH$_3$OH	CH$_3$OH:4.9
[22]TiO$_2$@GaP	0.5M NaCl	No	NM	CH$_3$OH	CH$_3$OH: 0.75
[23]CeO$_2$@TiO$_2$	0.1M NaOH	No	500 W Xe lamp	CH$_3$OH	CH$_3$OH: 3.2
[24]CdSe/Pt/TiO$_2$	Water	No	NM (l>400 nm)	CH$_3$OH, CO, CH$_4$	CH$_3$OH: 3.3 ppm/g/h
[25]TiO$_2$/GO	KOH solution	No	250 W Hg lamp	CH$_3$OH, CH$_4$	CH$_3$OH: 2.2
[26]Amine functionalize TiO$_2$	NaHCO$_3$ solution	No	300 W Xe lamp	CH$_3$OH, HCOOH	CH$_3$OH: 2
[27]Fluorinated TiO$_2$	NaOH solution	No	18 W lamp	CH$_3$OH, CH$_4$	CH$_3$OH: 1.09
[28]WSe$_2$/Graphene /TiO$_2$	Na$_2$SO$_3$ aq. Solution	No	300 W Xe lamp	CH$_3$OH	CH$_3$OH:6.33
[29]Carbon@TiO$_2$	Water vapour	No	300 W Xe lamp	CH$_3$OH, CH$_4$	CH$_3$OH:9.1
[30]TiO$_2$/SBA-15	Water	No	100 W Hg lamp (l>250 nm). N.B: UV light	CH$_3$OH, CH$_4$	CH$_3$OH:27.7
[31]2.5%CuInS$_2$/TiO$_2$	Water	No	350 W Xe lamp	CH$_3$OH, CH$_4$	CH$_3$OH:0.86
[32]SCN-H-Ni-black TiO$_2$	Water vapour		NM	CH$_3$CHO, CH$_3$OH	CH$_3$OH:1.2
[33]Bi$_2$MoO$_6$/PVP	Water	No	300 W Xe lamp	CH$_3$OH	CH$_3$OH:6.2
[34]Ultra-thin Bi$_2$MoO$_6$	Water	No	300 W Xe lamp	CO	CO:3.62
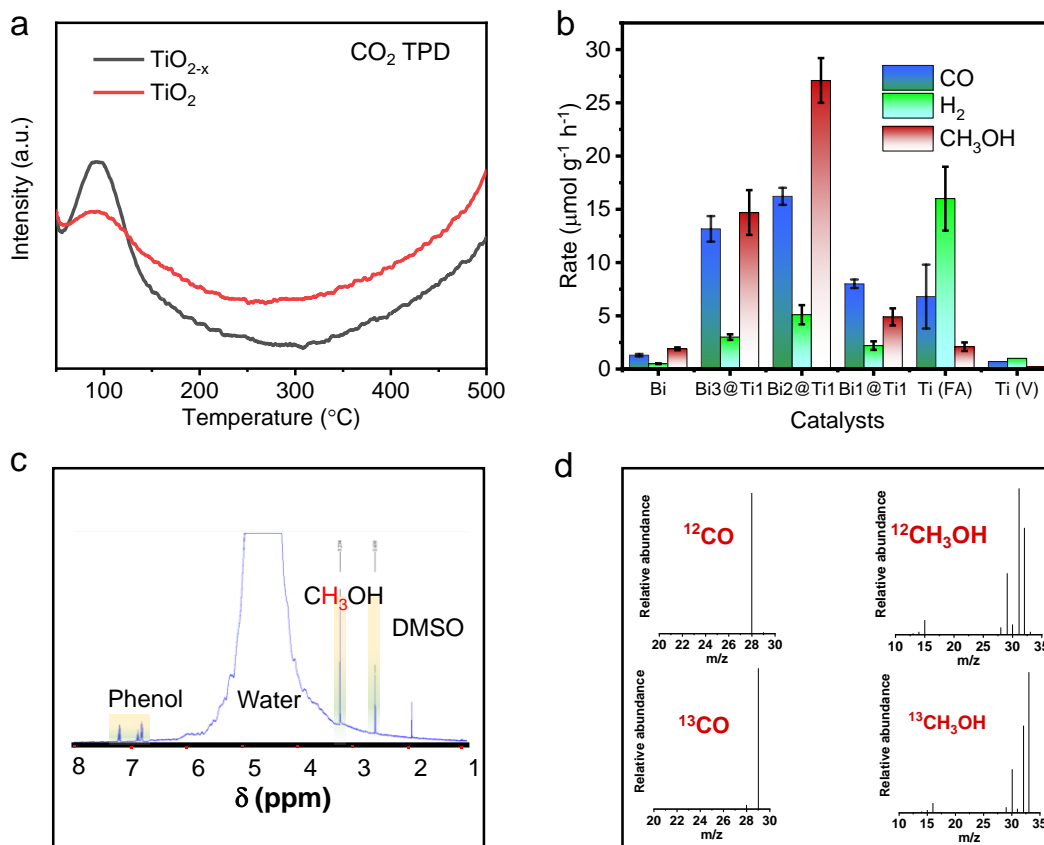
Figure 4.4. **(a)** CO_2 TPD profiles of TiO_2 and oxygen deficient TiO_2 (TiO_{2-X}). **(b)** comparison of the photocatalytic activity of all the catalysts after 6 h. (FA) means full arc contains UV-visible light and (V) means Visible light illumination. **(c)** NMR spectrum of liquid products generated after 6h reaction with **Bi2@Ti1** catalyst. **(d)** GC-MS data of CO and methanol obtained after the experiment with $^{12}CO_2$ by **Bi2@Ti1** catalyst. MS signal for ^{13}CO and $^{13}CH_3OH$ obtained after the catalysis with $^{13}CO_2$ by **Bi2@Ti1**.

Interestingly, pristine TiO_2 produced more CO compared to methanol under UV Visible light illumination. Upon switching the illuminated light to visible region, the activity reduced drastically as e⁻s and holes cannot be generated by visible light (>400 nm) illumination on TiO_2 due to its large band gap. On the other hand, pristine Bi_2MoO_6 also could not perform satisfactorily due to fast charge recombination. In the composite material, photo-generated e⁻s of Bi_2MoO_6 were transferred to the neighbouring TiO_2 nanoribbons and activates TiO_2 for photocatalysis under visible light. The optimum supply of e⁻s from Bi_2MoO_6 and the presence of O_v in TiO_2 for CO_2 adsorption and activation rendered **Bi2@Ti1** the best catalyst for methanol formation. The presence of more Bi_2MoO_6 facilitates more e⁻ for the kinetically demanding methanol formation process (6e⁻) in comparison to the production of CO (2e⁻).[35] Therefore, better methanol formation rate was observed for **Bi3@Ti1** compared to **Bi1@Ti1** and pristine TiO_2.

127

Furthermore, the role of each component of PCR was confirmed from a series of control experiments. Finally, the PCR was carried out with $^{13}CO_2$ and the obtained methanol and CO was examined by GCMS, which clearly shows the formation of ^{13}CO (**Figure 4.4d**) and $^{13}CH_3OH$ (**Figure 4.4d**) confirming that the generated products are solely coming from the PCR. Cyclability of the spent catalyst showed unaltered product formation rate for six consecutive cycles meaning that the catalyst is stable for repeated performance (**Figure 4.5a**).
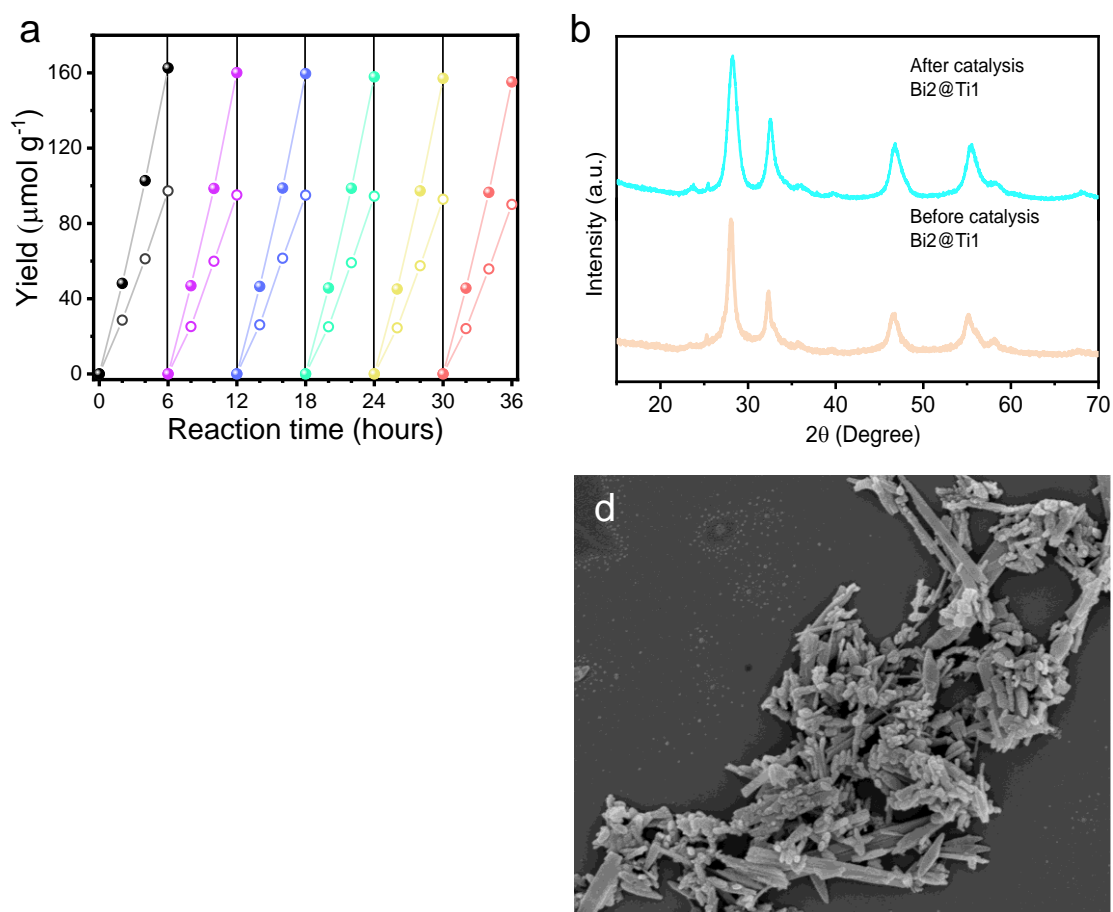
Figure 4.5. (a) Yield of methanol and CO after 6h of photocatalysis with **Bi2@Ti1** for 6 consecutive cycles with same spent catalyst and new batch of CO_2 and reaction solvent (20ml 0.1M NaOH solution). Data collection was done after each 2 hours for one single cycle. Here the solid balls represent methanol and empty balls represents CO evolution. Five different colors were used to indicate five different catalytic tests. **(b)** Post catalytic catalyst characterization by PXRD. **Bi2@Ti1** was employed for 6 catalytic cycles and then post catalytic XRD analysis was done. Post catalytic characterization of **Bi2@Ti1** catalyst was also performed via **(c)** TEM, and **(d)** SEM analysis. It showed TiO_2 and Bi_2MoO_6 are having ribbon and particle like morphology upon base and light treatment meaning no chemical or photo corrosion occurred after 6 cycles. After each catalytic 6th catalytic test, the **Bi2@Ti1** was washed and dried overnight for performing these characterizations. Here the TEM image was process by using Gatan digital micrograph software.
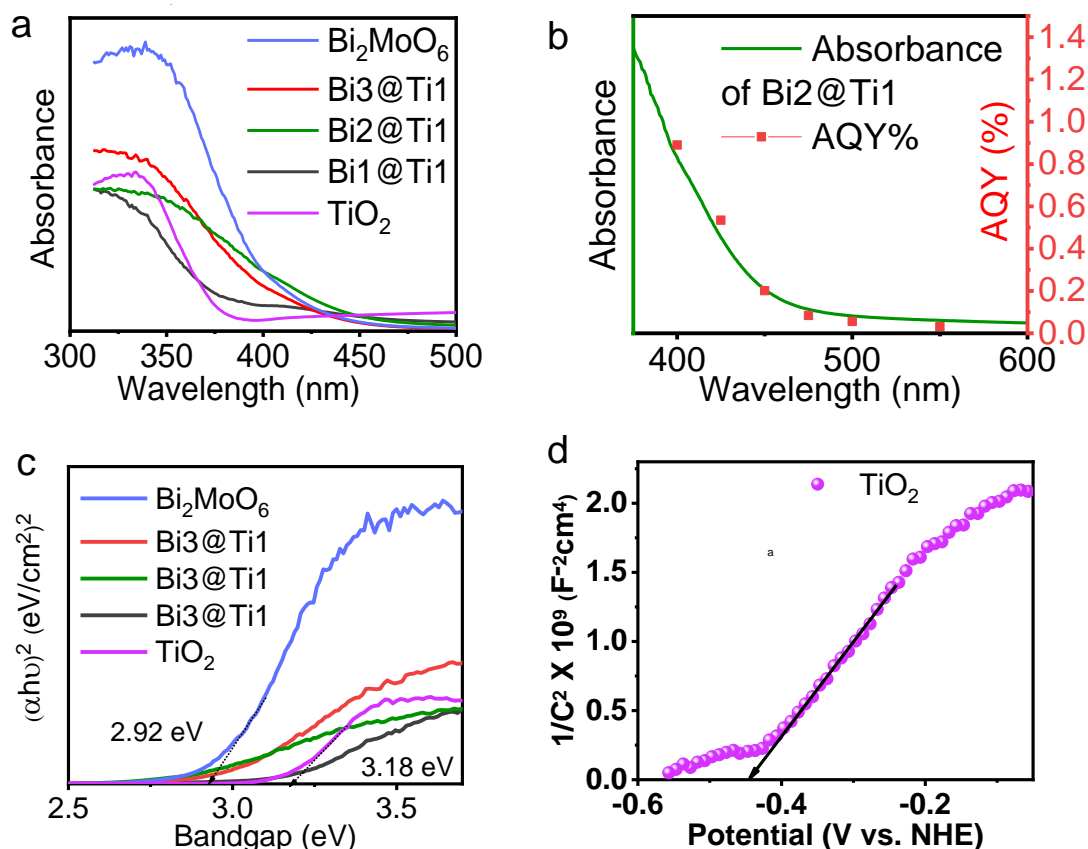
Figure 4.6. Band structure and Charge transfer process. **(a)** UV-DRS spectra of all the composites and pristine individuals. **(b)** Comparison of absorbance and AQY% to check the co-relation between absorbance and activity of **Bi2@Ti1** catalyst. **(c)** Tauc plot of Bi_2MoO_6, TiO_2 and their composites obtained from the absorbance (UV-DRS) measurements. $n = 2$ refers that these are direct band gap semiconductors. Here n means the power given in the y-axis: $(\alpha h\upsilon)^n$. **(d)** Mott-Schottky measurements for TiO_2.

PCR in absence of CO_2, light, catalyst and 0.1M NaOH solution showed neither gaseous nor any liquid product formation, indicating the crucial role played by these components. After six cycles, the catalysts were examined *via* XRD (**Figure 4.5b**), TEM (**Figure 4.5c**) and SEM (**Figure 4.5d**) analyses to understand structural and morphological integrity. Post catalysis samples displayed similar XRD patterns and morphology compared to the pristine catalyst. All the catalyst has produced some amount of H_2 because the reaction was done in water medium and photogenerated electron can be transfer to adsorbed water molecules instead of adsorbed CO_2 intermediates.

However, upon composite formation with Bi_2MoO_6, the HER was suppressed dramatically compared to pristine TiO_2. Therefore, it can be inferred that **Bi2@Ti1** not

only performed better towards CO_2 reduction but also suppressed e^- wasting competitive HER, which is considered as one of the biggest challenges in PCR. Improved activity of composites and the role of Bi_2MoO_6 as an e^- donor can be understood by analysing the band structure and charge transfer process. As depicted in **Figure 4.6a**, the absorbance spectra revealed that TiO_2 can only harvest UV part of the solar spectrum. On the other hand, Bi_2MoO_6 has an absorption edge in the visible region. Therefore, the Composite materials have UV as well as visible light absorption capability. The agreement between the absorption onset of **Bi2@Ti1** and overall apparent quantum yield (AQY%) was understood upon different wavelength chopped light illumination (**Figure 4.6b**). The CO_2 reduction process terminated at more than 475 nm light irradiation and the AQY% trends followed the **Bi2@Ti1** absorption pattern meaning the photocatalysis proceeded *via* excited e^-s of Bi_2MoO_6. Therefore, highest AQY of 0.89% was obtained by 400 ± 10 nm light irradiation where Bi_2MoO_6 shows maximum absorption. Further insight of e^- transfer was understood by band gap calculation through the Tauc plot (**Figure 4.6c**) and band alignment calculation by Mott-Schottky measurements. It showed that TiO_2 and Bi_2MoO_6 have bandgaps of 3.19 eV and 2.92 eV, respectively. The Mott-Schottky measurements suggests that both the semiconductors are n-type and hence their conduction band maxima (CBM) stay near to the Fermi level**.** Therefore, the CBM position was obtained by adding -0.1V with the flat band potential (V_{fb}) obtained from Mott-Schottky plots (**Figure 4.6d** and **4.7a**).
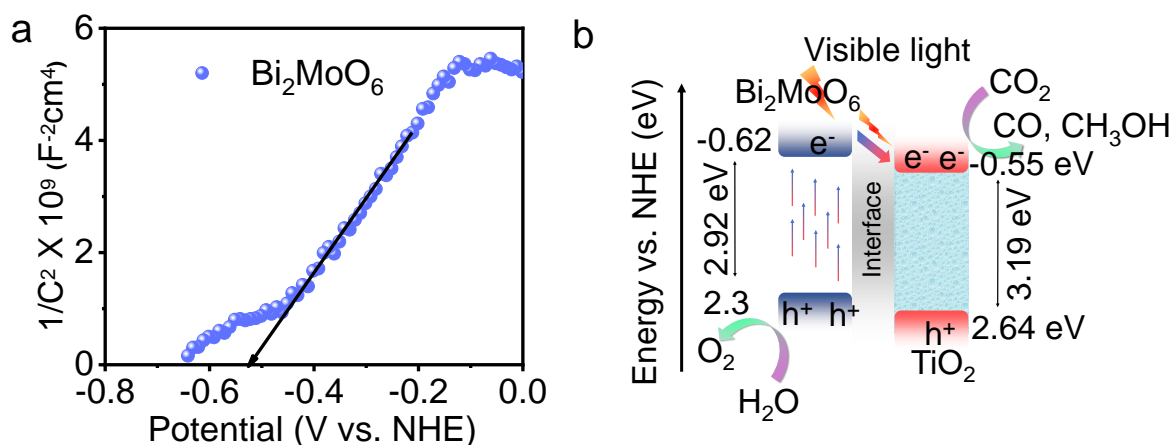
Figure 4.7. (**a**) Bi_2MoO_6 to understand flat-band potential (V_{fb}). The extrapolation of slope on X-axis (as shown by arrow) is regarded as V_{fb}. The negative sole of impedance inferring that these two are n-type semiconductor. (**b**) Electron transfer route in Bi_2MoO_6/TiO_2 composite catalysts via type-II mechanism.

As depicted in **Figure 4.7b**, the CBM position of Bi_2MoO_6 and TiO_2 are situated at -0.71 V and -0.58 V. Therefore, the excited e^-s of Bi_2MoO_6 can easily be transferred to TiO_2 upon visible light irradiation. **Figure 4.7b** clearly shows that TiO_2 has enough potential to produce methanol or CO from CO_2 by utilizing the excited e^-s of Bi_2MoO_6, because -0.36 V and -0.54 V is the CO_2 to methanol and CO formation potential, respectively. The photo-generated holes in the valence band of Bi_2MoO_6 participated in the water oxidation reaction. The evolved O_2 was quantified by GC, which showed that the amount of evolved O_2 is approximately matching with the stoichiometric amount (**Figure 4.8a**). Time-dependent photoluminescence study further elucidated the e^- transfer pathway. **Figure 4.8b**, and **Table 4.4** show that the pristine Bi_2MoO_6 has lower lifetime for the excited electrons ($\tau_{avg} = 2.2$ ns) compared to **Bi2@Ti1** ($\tau_{avg} = 2.7$ ns).
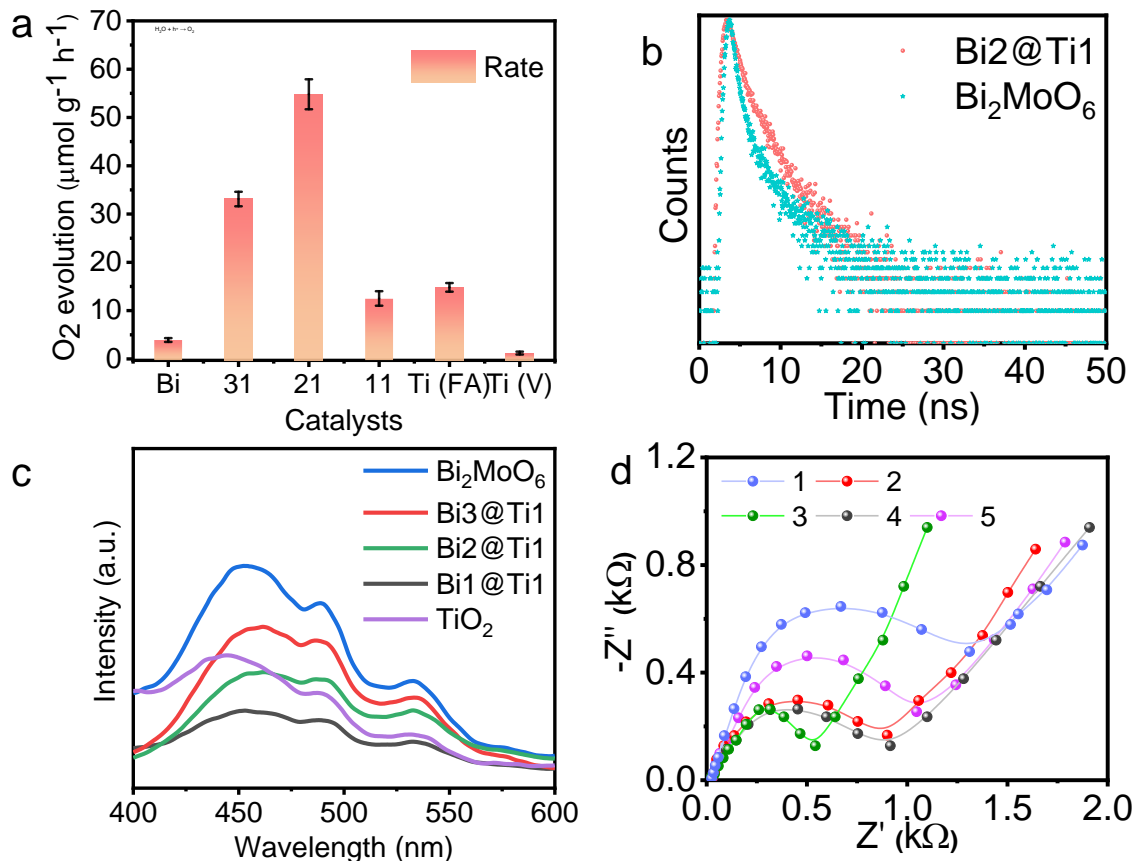
Figure 4.8. **(a)** Quantification of evolved O_2 generated from water oxidation by photo-generated holes. Based on the obtained products (CH_3OH, CO and, H_2). **(b)** Time dependent photoluminescence spectra of pure Bi_2MoO_6 and **Bi2@Ti1**. **(c)** Steady state photoluminescence (PL) of composites and pristine individuals obtained upon 330 nm light excitation. Photoelectrochemical study. **(d)** Electrochemical impedance spectra for understanding interfacial charge transfer resistance.

Table 4.4. Calculation of excited state lifetime by fitting time-resolved photo-luminescence data using the given equation. $A + B_1 \exp(-t/\tau_1) + B_2 \exp(-t/\tau_2)$. where, B_1 and, B_2 are the pre-exponential factor (amplitude) corresponding to decay lifetimes τ_1 and τ_2 respectively. Here t_{avg} is the average life time and χ is goodness of fit.[36]

Catalyst	τ_1 (ns)	B_1 (%)	τ_2 (ns)	B_2 (%)	τ_{avg} (ns)	χ^2
Bi_2MoO_6	0.6	53	4	47	2.2	1.19
Bi2@Ti1	1.55	64	4.72	36	2.7	1.05

On the other hand, as shown in **Figure 4.8c,** static photoluminescence (PL) study shows that the composites have weaker PL intensities compared to pristine Bi_2MoO_6. This manifests that the excited e⁻s of pristine Bi_2MoO_6 quickly recombine with photo-generated holes, whereas in the composites, the e⁻s go to neighbouring TiO_2 instead of recombination.[37] Photoelectrochemical measurements including interfacial charge transfer resistance and light induce current generation capacity were understood from electrochemical impedance spectroscopy (**Figure 4.8d**) and transient photocurrent measurements. **Bi2@Ti1** and pristine Bi_2MoO_6 has the least and the highest charge transfer resistance respectively. Interestingly, TiO_2 showed rapid photocurrent decay compared to the composites upon light off (**Figure 4.9a**).
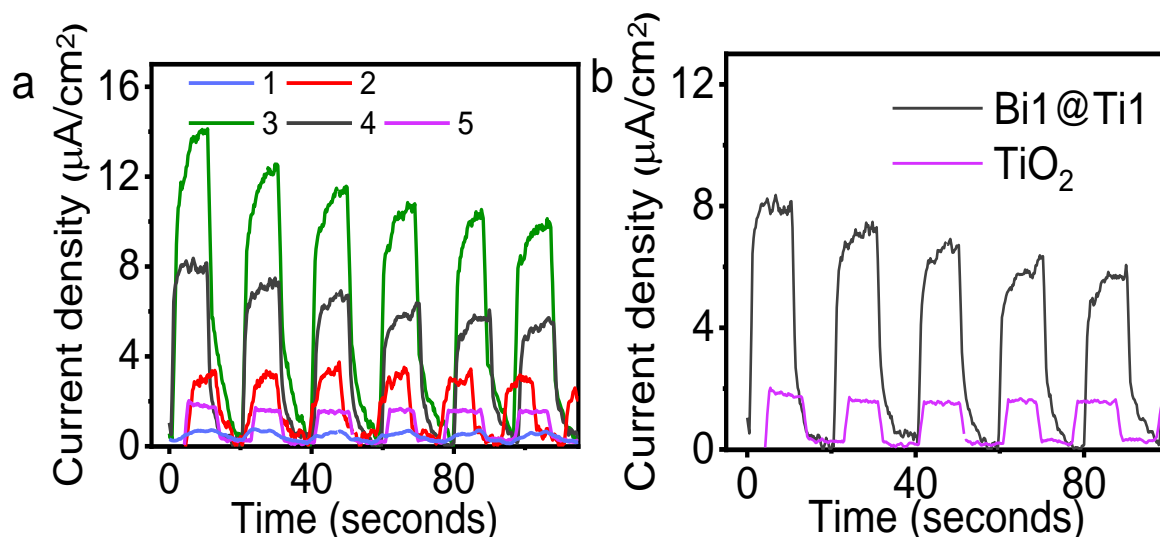
Figure 4.9. **(a)** Transient photocurrent measurements in presence of light and dark for understanding light driven current generation ability of different photocatalysts. Here, in **Figure (a)**, and **(b)** the number 1, 2, 3, 4 and, 5 represents Bi_2MoO_6, **Bi3@Ti1**, **Bi2@Ti1**, **Bi1@Ti1** and TiO_2, respectively. **(b)** Photocurrent of **Bi2@Ti1** and TiO_2 for one cycle shows that photocurrent diminishes faster in case of TiO_2 compared to **Bi2@Ti1** upon light off. Photocurrent of TiO_2 generated upon UV-visible light illumination (**Figure 4.9a**).
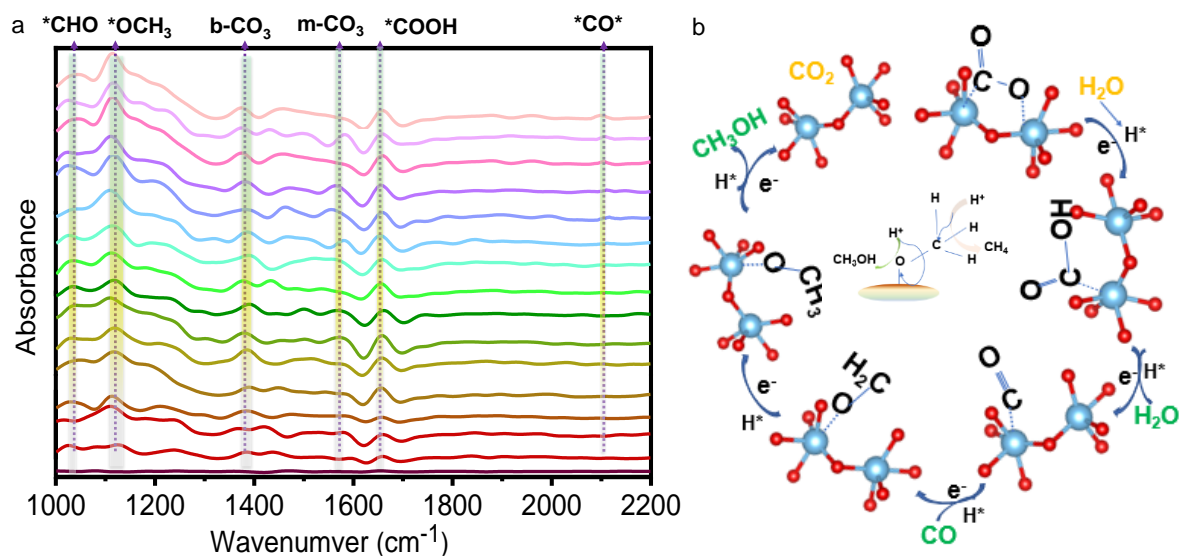
Figure 4.10. *In situ* study for understanding methanol formation mechanism. **(a)** Operando DRIFTS with CO_2 and water vapour under 450W Xe light illumination with **Bi2@Ti1** catalyst. **(b)** Plausible methanol formation mechanism on O_v-TiO₂ surface. It also shows without Bi₂MoO₆, CH_3OH formation became difficult. Inset represents a schematic representation of methanol and methane formation upon protonation in 'O' center and 'C' center of *OCH₃.

Moreover, **Bi2@Ti1** exhibited the highest photocurrent. Pristine TiO₂ has delivered no photocurrent under visible light illumination. The featured photocurrent for TiO₂ in **Figure 4.9b** is due to UV-visible light irradiation. Pristine Bi₂MoO₆ has much less photocurrent production ability and high charge transfer resistance. However, upon composite formation these drawbacks were overcome and PCR performance increased. The methanol formation pathway was understood by identifying intermediates formed during CO₂ hydrogenation *via* operando DRIFTS (**Figure 4.10a**). The peaks observed at 1372 cm⁻¹ and 1583 cm⁻¹ represent the bidentate and monodentate carbonates generated *via* adsorption of CO₂ in the O_v-TiO₂ surface.[38] Most importantly, the intensity of the band at 1655 cm⁻¹ corresponding to *COOH has increased with light irradiation time.[39] The *COOH intermediate is regarded as the first and most common intermediate for CO₂ hydrogenation.[39] A tiny peak evolution at 2095 cm⁻¹ corresponding to the *CO intermediate was also found. The most important intermediates of methanol formation are *OCH₃ and *CHO. A monotonous evolution of IR peaks at 1036 cm⁻¹ and 1114 cm⁻¹ implicitly indicates the presence of these two critical intermediates.[5] The *CO intermediate was rapidly converted to *CHO intermediate; therefore, the intensity of the *CO intermediate remained negligible.

On the other hand, the *OCH₃ intermediate showed a prominent peak. Therefore, it can be inferred that the *OCH₃ intermediate has chemisorbed on O_v-TiO₂ surface for

longer time and got protonated on the O site for methanol formation.[40] The absence of methane eliminates the probability of proton adsorption on C centre of the $*OCH_3$ intermediate (**Figure 4.10b**). Based on the knowledge of these intermediates, a mechanistic scheme for methanol formation *via* 6 protons coupled e⁻ transfer process is shown in **Figure 4.10b**. CO and H_2O were obtained as the by-products through this mechanism. Upon $*OCH_3$ protonation the catalyst bed can be regenerated without any chemical corrosion. Moreover, as mentioned previously, the formed heterojunction allows TiO_2 to utilize visible light energy more effectively *via* additional photo-generated e⁻ transfer from Bi_2MoO_6 for the reaction, whereby the yield of methanol formation is greatly enhanced.

4.5. Conclusion

In summary, introducing Bi_2MoO_6 into O_v-TiO_2 allows e⁻ transfer through the intimate interface. Thereby, the active sites of TiO_2 were used for CO_2 adsorption, and photo-generated charges of Bi_2MoO_6 were used for PCR. A series of photophysical and photoelectrochemical studies established the regions of the best activity in the **Bi2@Ti1** catalyst. Finally, the methanol formation mechanism was predicted based on the intermediate information from operando DRIFTS. Further modification of reaction conditions can lead to a better increment of performance and can be used for large-scale applications owing to the high durability of this composite.

4.6. References

1. Albero, J.; Peng, Y.; García, H., Photocatalytic CO_2 Reduction to C2+ Products. *ACS Catal.* **2020,** *10*, 5734-5749.

2. Das, R.; Chakraborty, S.; Peter, S. C., Systematic Assessment of Solvent Selection in Photocatalytic CO_2 Reduction. *ACS Energy Lett.* **2021,** *6*, 3270-3274.

3. Zhang, L. J.; Li, S.; Liu, B. K.; Wang, D. J.; Xie, T. F., Highly Efficient CdS/WO_3 Photocatalysts: Z-Scheme Photocatalytic Mechanism for Their Enhanced Photocatalytic H_2 Evolution under Visible Light. *ACS Catal.* **2014,** *4*, 3724-3729.

4. Das, R.; Das, K.; Ray, B.; Prabhakaran, V.; Peter, S. C., Green Transformation of CO_2 to Ethanol using Water and Sunlight by Cooperative Endeavour of Naturally Abundant Red Phosphorus and Bi_2MoO_6. *Energy Environ. Sci.* **2022,** *5*, 1967-1976.

5. Das, R.; Sarkar, S.; Kumar, R.; D. Ramarao, S.; Cherevotan, A.; Jasil, M.; Vinod, C. P.; Singh, A. K.; Peter, S. C., Noble-Metal-Free Heterojunction Photocatalyst for Selective

CO_2 Reduction to Methane upon Induced Strain Relaxation. *ACS Catal.* **2022,** *12*, 687-697.

6. Wei Zhou, J.-K. G., Sheng Shen,Jinbo Pan,Jie Tang,Lang Chen,Chak-Tong Au,Shuang-Feng Yin, Progress in Photoelectrocatalytic Reduction of Carbon Dioxide. *Acta Phys. -Chim. Sin.* **2020,** *36*, 1906048.

7. Yu, H.; Jiang, L.; Wang, H.; Huang, B.; Yuan, X.; Huang, J.; Zhang, J.; Zeng, G., Modulation of Bi_2MoO_6-Based Materials for Photocatalytic Water Splitting and Environmental Application: a Critical Review. *Small* **2019,** *15* (23), 1901008.

8. Hao, R.; Wang, G.; Tang, H.; Sun, L.; Xu, C.; Han, D., Template-Free Preparation of Macro/Mesoporous $g-C_3N_4/TiO_2$ Heterojunction Photocatalysts with Enhanced Visible Light Photocatalytic Activity. *Appl. Catal. B: Environ.* **2016,** *187*, 47-58.

9. Etgar, L.; Gao, P.; Xue, Z.; Peng, Q.; Chandiran, A. K.; Liu, B.; Nazeeruddin, M. K.; Grätzel, M., Mesoscopic $CH_3NH_3PbI_3/TiO_2$ Heterojunction Solar Cells. *J. Am. Chem. Soc.* **2012,** *134*, 17396-17399.

10. Zhang, Y.; Xu, Z.; Li, G.; Huang, X.; Hao, W.; Bi, Y., Direct Observation of Oxygen Vacancy Self-Healing on TiO_2 Photocatalysts for Solar Water Splitting. *Angew. Chem., Int. Ed.* **2019,** *58* (40), 14229-14233.

11. Fang, Y.; Liu, Z.; Han, J.; Jin, Z.; Han, Y.; Wang, F.; Niu, Y.; Wu, Y.; Xu, Y., High-Performance Electrocatalytic Conversion of N_2 to NH_3 Using Oxygen-Vacancy-Rich TiO_2 In Situ Grown on Ti_3C_2Tx MXene. *Adv. Energy Mater.* **2019,** *9*, 1803406.

12. Cherevotan, A.; Raj, J.; Dheer, L.; Roy, S.; Sarkar, S.; Das, R.; Vinod, C. P.; Xu, S.; Wells, P.; Waghmare, U. V.; Peter, S. C., Operando Generated Ordered Heterogeneous Catalyst for the Selective Conversion of CO_2 to Methanol. *ACS Energy Lett.* **2021,** *6*, 509-516.

13. Tian, J.; Hao, P.; Wei, N.; Cui, H.; Liu, H., 3D Bi_2MoO_6 Nanosheet/TiO_2 Nanobelt Heterostructure: Enhanced Photocatalytic Activities and Photoelectochemistry Performance. *ACS Catal.* **2015,** *5*, 4530-4536.

14. Shi, J.; Ye, J.; Zhou, Z.; Li, M.; Guo, L., Hydrothermal Synthesis of $Na_{0.5}La_{0.5}TiO_3$–$LaCrO_3$ Solid-Solution Single-Crystal Nanocubes for Visible-Light-Driven Photocatalytic H_2 Evolution. *Chem. Eur. J.* **2011,** *17*, 7858-7867.

15. Wang, Q.; Warnan, J.; Rodríguez-Jiménez, S.; Leung, J. J.; Kalathil, S.; Andrei, V.; Domen, K.; Reisner, E., Molecularly Engineered Photocatalyst Sheet for Scalable Solar Formate Production from Carbon Dioxide and Water. *Nat. Energy* **2020,** *5*, 703-710.

16. Zhao, D.; Wang, Y.; Dong, C.-L.; Huang, Y.-C.; Chen, J.; Xue, F.; Shen, S.; Guo, L., Boron-doped Nitrogen-Deficient Carbon Nitride-Based Z-Scheme Heterostructures for Photocatalytic Overall Water Splitting. *Nat. Energy* **2021,** *6*, 388-397.

17. Yang, H. G.; Sun, C. H.; Qiao, S. Z.; Zou, J.; Liu, G.; Smith, S. C.; Cheng, H. M.; Lu, G. Q., Anatase TiO_2 Single Crystals with a Large Percentage of Reactive Facets. *Nature* **2008,** *453*, 638-641.

18. Jia, Z.; Lyu, F.; Zhang, L. C.; Zeng, S.; Liang, S. X.; Li, Y. Y.; Lu, J., Pt Nanoparticles Decorated Heterostructured g-C_3N_4/Bi_2MoO_6 Microplates with Highly Enhanced Photocatalytic Activities under Visible Light. *Sci. Rep.* **2019,** *9*, 7636.

19. Pan, X.; Yang, M.-Q.; Fu, X.; Zhang, N.; Xu, Y.-J., Defective TiO_2 with Oxygen Vacancies: Synthesis, Properties and Photocatalytic Applications. *Nanoscale* **2013,** *5*, 3601-3614.

20. Pipornpong, W.; Wanbayor, R.; Ruangpornvisuti, V., Adsorption CO_2 on the Perfect and Oxygen Vacancy Defect Surfaces of Anatase TiO_2 and its Photocatalytic Mechanism of Conversion to CO. *Appl. Surf. Sci.* **2011,** *257*, 10322-10328.

21. Pan, J.-B.; Wang, B.-H.; Wang, J.-B.; Ding, H.-Z.; Zhou, W.; Liu, X.; Zhang, J.-R.; Shen, S.; Guo, J.-K.; Chen, L.; Au, C.-T.; Jiang, L.-L.; Yin, S.-F., Activity and Stability Boosting of an Oxygen-Vacancy-Rich $BiVO_4$ Photoanode by NiFe-MOFs Thin Layer for Water Oxidation. *Angew. Chem., Int. Ed.* **2021,** *60*, 1433-1440.

22. Zeng, G.; Qiu, J.; Li, Z.; Pavaskar, P.; Cronin, S. B., CO_2 Reduction to Methanol on TiO_2-Passivated GaP Photocatalysts. *ACS Catal.* **2014,** *4*, 3512-3516.

23. Abdullah, H.; Khan, M. R.; Pudukudy, M.; Yaakob, Z.; Ismail, N. A., CeO_2-TiO_2 as a Visible Light Active Catalyst for the Photoreduction of CO_2 to Methanol. *J. Rare Earths* **2015,** *33*, 1155-1161.

24. Wang, C.; Thompson, R. L.; Baltrus, J.; Matranga, C., Visible Light Photoreduction of CO_2 Using CdSe/Pt/TiO_2 Heterostructured Catalysts. *J. Phys Chem Lett.* **2010,** *1*, 48-53.

25. Liu, J.; Niu, Y.; He, X.; Qi, J.; Li, X., Photocatalytic Reduction of CO_2 Using TiO_2-Graphene Nanocomposites. *J. Nanomater.* **2016,** *2016*, 6012896.

26. Liu, S.; Xia, J.; Yu, J., Amine-Functionalized Titanate Nanosheet-Assembled Yolk@Shell Microspheres for Efficient Cocatalyst-Free Visible-Light Photocatalytic CO_2 Reduction. *ACS Appl. Mater. Interfaces* **2015,** *7*, 8166-8175.

27. He, Z.; Wen, L.; Wang, D.; Xue, Y.; Lu, Q.; Wu, C.; Chen, J.; Song, S., Photocatalytic Reduction of CO_2 in Aqueous Solution on Surface-Fluorinated Anatase TiO_2 Nanosheets with Exposed {001} Facets. *Energy & Fuels* **2014,** *28*, 3982-3993.

28. Biswas, M. R. U. D.; Ali, A.; Cho, K. Y.; Oh, W.-C., Novel Synthesis of WSe_2-Graphene-TiO_2 Ternary Nanocomposite via Ultrasonic Technics for High Photocatalytic Reduction of CO_2 into CH_3OH. *Ultrason. Sonochem.* **2018,** *42*, 738-746.

29. Wang, W.; Xu, D.; Cheng, B.; Yu, J.; Jiang, C., Hybrid Carbon@TiO_2 Hollow Spheres with Enhanced Photocatalytic CO_2 Reduction Activity. *J. Mater. Chem. A* **2017,** *5*, 5020-5029.

30. Hwang, J.-S.; Chang, J.-S.; Park, S.-E.; Ikeue, K.; Anpo, M., Photoreduction of Carbondioxide on Surface Functionalized Nanoporous Catalysts. *Top Catal.* **2005,** *35*, 311-319.

31. Xu, F.; Zhang, J.; Zhu, B.; Yu, J.; Xu, J., $CuInS_2$ Sensitized TiO_2 Hybrid Nanofibers for Improved Photocatalytic CO_2 Reduction. *Appl. Catal. B: Environ.* **2018,** *230*, 194-202.

32. Fu, F.-Y.; Shown, I.; Li, C.-S.; Raghunath, P.; Lin, T.-Y.; Billo, T.; Wu, H.-L.; Wu, C.-I.; Chung, P.-W.; Lin, M.-C.; Chen, L.-C.; Chen, K.-H., KSCN-Induced Interfacial Dipole in Black TiO_2 for Enhanced Photocatalytic CO_2 Reduction. *ACS Appl. Mater. Interfaces* **2019,** *11*, 25186-25194.

33. Dai, W.; Yu, J.; Xu, H.; Hu, X.; Luo, X.; Yang, L.; Tu, X., Synthesis of Hierarchical Flower-Like Bi_2MoO_6 Microspheres as Efficient Photocatalyst for Photoreduction of CO_2 into Solar Fuels under Visible Light. *CrystEngComm* **2016,** *18*, 3472-3480.

34. Di, J.; Zhao, X.; Lian, C.; Ji, M.; Xia, J.; Xiong, J.; Zhou, W.; Cao, X.; She, Y.; Liu, H.; Loh, K. P.; Pennycook, S. J.; Li, H.; Liu, Z., Atomically-Thin Bi_2MoO_6 Nanosheets with Vacancy Pairs for Improved Photocatalytic CO_2 Reduction. *Nano Energy* **2019,** *61*, 54-59.

35. Fang, Y.; Wang, X., Photocatalytic CO_2 Conversion by Polymeric Carbon Nitrides. *Chem. Commun.* **2018,** *54*, 5674-5687.

36. Xu, Y.-F.; Yang, M.-Z.; Chen, B.-X.; Wang, X.-D.; Chen, H.-Y.; Kuang, D.-B.; Su, C.-Y., A $CsPbBr_3$ Perovskite Quantum Dot/Graphene Oxide Composite for Photocatalytic CO_2 Reduction. *J. Am. Chem. Soc.* **2017,** *139*, 5660-5663.

37. Xie, Y. P.; Yang, Y.; Wang, G.; Liu, G., Oxygen Vacancies Promoted Interfacial Charge Carrier Transfer of CdS/ZnO Heterostructure for Photocatalytic Hydrogen Generation. *J. Colloid Interface Sci.* **2017,** *503*, 198-204.

38. Tan, T. H.; Xie, B.; Ng, Y. H.; Abdullah, S. F. B.; Tang, H. Y. M.; Bedford, N.; Taylor, R. A.; Aguey-Zinsou, K.-F.; Amal, R.; Scott, J., Unlocking the Potential of the Formate Pathway in the Photo-Assisted Sabatier Reaction. *Nat. Catal.* **2020,** *3*, 1034-1043.

39. Li, X.; Sun, Y.; Xu, J.; Shao, Y.; Wu, J.; Xu, X.; Pan, Y.; Ju, H.; Zhu, J.; Xie, Y., Selective Visible-Light-Driven Photocatalytic CO_2 Reduction to CH_4 Mediated by Atomically Thin $CuIn_5S_8$ Layers. *Nat. Energy* **2019,** *4*, 690-699.

40. Sun, Z.; Ma, T.; Tao, H.; Fan, Q.; Han, B., Fundamentals and Challenges of Electrochemical CO_2 Reduction Using Two-Dimensional Materials. *Chem* **2017,** *3*, 560-587.

Chapter 5

Intrinsic Charge Polarization Promotes Selective C-C Coupling Reaction During Photoreduction of CO₂ to Ethanol
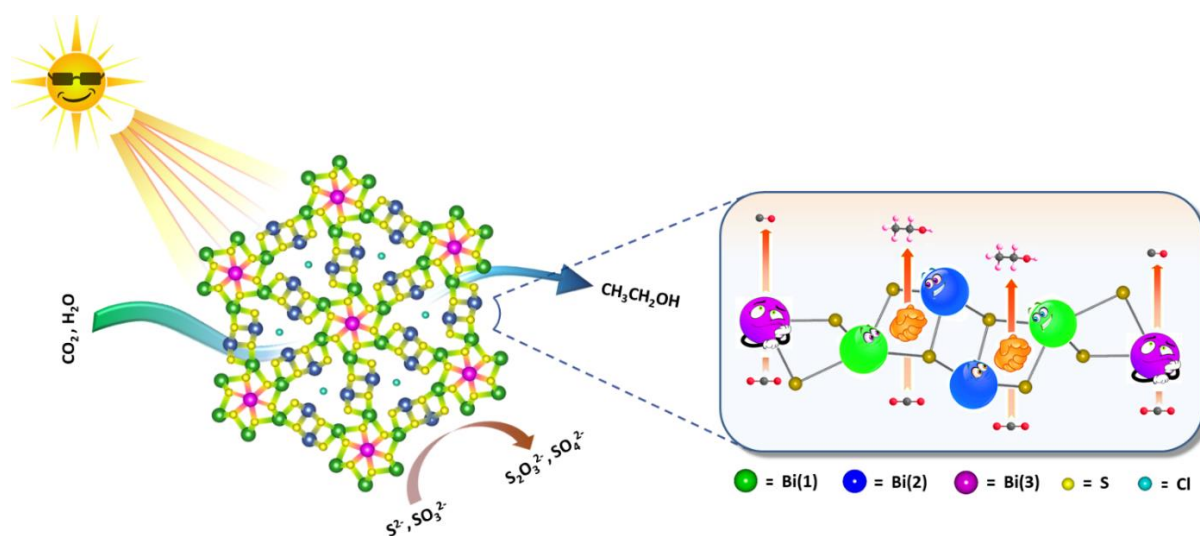
Risov Das, Kousik Das, Arko Parui, Abhishek Kumar Singh, Chathakudath P. Vinod, Sebastian C. Peter*. Manuscript under review in *ACS Nano*.

Summary

Obtaining multicarbon products via carbon dioxide (CO_2) photoreduction is a major catalytic challenge involving multielectron mediated C-C bond formation. Complex design of multicomponent interfaces that are exploited to achieve this chemical transformation, often leads to untraceable deleterious changes in the interfacial chemical environment affecting CO_2 conversion efficiency and product selectivity. Alternatively, robust metal centres having asymmetric charge distribution can effectuate C-C coupling reaction through the stabilization of suitable intermediates, for desired product selectivity. However, generating inherent charge distribution in a single component catalyst is a difficult material design challenge. To that end, herein, we present a novel photocatalyst, $Bi_{19}S_{27}Cl_3$, which selectively converts CO_2 to a C2 product, ethanol, in high yield under visible light irradiation. Structural analysis through X-ray diffraction (XRD), X-ray photoelectron spectroscopy (XPS) and X-ray absorption spectroscopy (XAS) reveal the presence of charge polarized bismuth centres in $Bi_{19}S_{27}Cl_3$, which is well complemented by DFT calculation. The intrinsic electric field induced by the charge polarized bismuth centres renders better separation efficiency of photogenerated electron-hole pair. Furthermore, the charge polarized centres yield better adsorption of CO* intermediate and accelerate the rate determining C-C coupling step through the formation of OCCOH intermediate. Formation of these intermediates was experimentally mapped by in situ FTIR spectroscopy and further confirmed by theoretical calculation.

The work based on this chapter is under consideration in ACS Nano

Intrinsic Charge Polarization Promotes Selective C-C Coupling Reaction During Photoreduction of CO_2 to Ethanol

Risov Das, Kousik Das, Arko Parui, Abhishek Kumar Singh, Chathakudath P. Vinod, Sebastian C. Peter*.

5.1. Introduction

The heterostructure catalysts discussed in the earlier chapters succhessfully produced C1 products in high yield. However, synthesising C2 products on single component photocatalyst are more economically profitable process. In this regard, the reported selectivity of C2 products is also not satisfactory. Henec, the use of abundant solar light and the sustainability of the process is, however, marred by the meager product tunability achieved so far, which is mostly limited to gaseous C_1 products such as CO, CH_4, CH_3OH etc.[5-8] Higher carbon liquid products are more desired because of their higher energy density and various industrial applications.[9-10] Among these, ethanol is extremely valuable because of its high enthalpy of combustion (-1366.8 kJ mol^{-1}) leading to its wide use as a clean fuel additive (E15 in 2007 in the U.S.A, also in China) and also for the synthesis of a range of specialty and commodity chemicals.[11] Ethanol production usually relies on the fermentation of agricultural feedstocks which is detrimental to the environment. Thus, using CO_2 as the feedstock for ethanol production by harvesting solar radiation can have significant advantages including the mitigation of greenhouse gas CO_2.[12-13] However, kinetically sluggish nature of the multi-electron transfer process and high activation barrier of C-C coupling reaction make the process catalytically very challenging. In electrocatalysis, this problem is usually addressed via the formation of intermetallic compounds, metal-oxide interfaces or metal alloys where two or more metal centers having distinct electronic structures perform the C-C coupling reaction.[14-17] Moreover, recent studies have demonstrated that through *in-situ* modulation of the active site oxidation states, it is also possible to obtain C_2 products with good selectivity.[18-20] However, multi-carbon products are rarely achieved in photocatalytic systems due to the inherent operational limitation because of the kinetic competition between the electron-hole recombination and catalysis both of which operate at the similar time scale.[21-22] Besides, proton coupled conversion of CO_2 to higher carbon products are endothermic process which also accounts for their low yield and selectivity compared to C_1 products. So far only limited success has been accomplished in photochemistry through the formation of heterojunction between different semiconductor materials.[23-25] By manipulating the charge distribution over the metal centers at the heterojunction interface, different intermediates are being stabilized to favor the C-C coupling reaction by minimizing the activation barrier.[26] However, conventional heterostructures usually suffer from low selectivity and limited efficiency. This is primarily due to the lack of microstructural and nanoscale control in their synthesis which limits the

interactions between different materials and eventually restricts electron mobility and charge separation.[27] Another shortcoming of the photocatalytic process is that the electrons are constantly supplied under a bias voltage in electrochemical process whereas only a limited amount of electrons can be excited under light irradiation. Therefore, the success of finding a worthy photocatalyst that can overcome these obstacles without sacrificing the catalytic efficiency and selectivity is a significantly challenging task. Owing to their excellent visible light harvesting property and ability to form different morphologies, bismuth based chalcogenides and chalcohalides have been extensively used for the photocatalytic conversion of CO_2.[28-31] Moreover, similar to other chalcohalide catalysts, the band structure can be tuned by halide modification whereas their catalytic activity can be easily enhanced through the creation of defect sites in terms of chalcogen vacancy.[32-33] Although a few of these catalysts have shown promising activity towards liquid products; thus far they have been mostly used with a co-catalyst for the synthesis of multi-carbon products.[34-35] In light of these observations, we first judiciously selected a bismuth chalcohalide photocatalyst namely, $Bi_{19}S_{27}Cl_3$ with suitably positioned charge polarized metal sites. Being a closely related member of Bi_2S_3 and $BiSCl$, $Bi_{19}S_{27}Cl_3$ exhibited strong structural resemblance and excellent visible light absorption property. Detailed structural analysis showed that bismuth sites present in $Bi_{19}S_{27}Cl_3$ are in fact in charge polarized state which is crucial for C-C coupling reaction. A combination of experimental studies and Density Functional Theory (DFT) calculations also reinstated our preliminary observation of asymmetric charge distribution between different bismuth sites. As a consequence, $Bi_{19}S_{27}Cl_3$ showed excellent photocatalytic conversion and selectivity towards ethanol from CO_2 donor under visible light. The major reaction intermediates including CO, COH and OCCOH (C-C coupling intermediate) were identified during photocatalytic CO_2 reduction by *in-situ* FTIR analysis. Theoretical studies further showed the importance of different charge polarized bismuth centres during the C-C bond formation and eventually ethanol formation. This study reiterates the importance of metal centers having distinct charge distribution for C-C coupling reaction during photocatalytic CO_2 reduction.

5.2. Experimental methods

Materials. Bismuth(III) Chloride ($BiCl_3$, ≥98%) and thiourea ((NH_2)$_2$CS, ≥99%) were purchased from Sigma-Aldrich. Bismuth(III) nitrate pentahydrate ($Bi(NO_3)_3 \cdot 5H_2O$, ≥98%) was purchased from Alfa Aesar. Sodium sulfide (Na_2S, ≥98%) and sodium sulfite (Na_2SO_3, ≥98%) were purchased from Merck. High purity $^{13}CO_2$ (99.0 atom %) was acquired from Sigma-

Aldrich. All the reagents were used as received and without further purification. Deionized water was used throughout the experiments.

Synthesis

$Bi_{19}S_{27}Cl_3$ nanorods: $Bi_{19}S_{27}Cl_3$ was synthesized following a previously reported method.[36] Typically, 788 mg of $BiCl_3$ (2.5 mmol), 175 mg of thiourea (2.3 mmol) and 35 ml of ethanol was taken in a 100 ml beaker. The mixture was mixed vigorously with continuous stirring for 1 hour. The light-yellow colored dispersion was then poured into a 50 ml autoclave. The autoclave containing the mixture was then heated to 180 °C for 3 days. After completion, the autoclave was cooled to room temperature. The black colored slurry thus obtained was then taken out and thoroughly washed with water to remove the unreacted compounds. The black solid was then dried at 80 °C overnight in a vacuum oven. Finally, $Bi_{19}S_{27}Cl_3$ nanorods were obtained as black powder in a yield of up to 390 mg (0.08 mmol).

Bi_2S_3 nanoribbons: Bi_2S_3 was synthesized using a previously reported procedure[34]. First 290 mg of thiourea (3.8 mmol) was dissolved in 35 ml water. Then 610 mg $Bi(NO_3)_3 \cdot 5H_2O$ (1.26 mmol) was added slowly into the mixture. During the addition, the transparent solution turned yellow. The mixture was stirred for another 4 hours. After that the solution was transferred to a 50 ml autoclave and heated at 160 °C for 12 hours. The autoclave was cooled to room temperature. The brown precipitate was thoroughly washed with water and dried at 80 °C for overnight in a vacuum oven. Bi_2S_3 nanoribbons were finally obtained as grey powder in a yield of up to 230 mg (0.45 mmol).

Characterization of materials

Microscopy: TEM and HRTEM (High resolution TEM) images were recorded using a JEOL transmission electron microscope at an accelerating voltage of 200 kV. Small amount of sample was first properly dispersed in water through sonication and the dispersion was then drop casted on a carbon coated copper grid and subsequently dried for TEM imaging. A FEI NOVA NANOSEM 600 scanning electron microscope equipped with an energy-dispersive X-ray spectroscopy (EDAX) instrument (Bruker 129 eV EDAX instrument) was used to conduct SEM analysis and elemental mapping. The sample was drop casted on a silicon wafer and the data was acquired on an accelerating voltage of 20 kV. The elemental analyses were performed using the P/B-ZAF standardless method (where, P/B = peak to background model, Z = atomic no. correction factor, A = absorption correction factor and F = fluorescence factor) for Bi, S, Cl at multiple areas on the sample coated Si wafer.

Powder X-ray diffraction (PXRD): PXRD patterns were collected using a Rigaku Advance X-ray diffractometer equipped with Cu $k\alpha$ lamp source ($\lambda = 1.5406$ Å).

Proton NMR: ^{1}H NMR was performed in JEOL NMR spectrometer operating at 600 MHz. For the analysis 500 µL of the reaction mixture was transferred into an NMR tube and 30 µL of internal standard solution containing 50 mM phenol (99.5 %) and 10 mM dimethyl sulfoxide (99.9 %) in D_2O was added. After the ^{1}H NMR experiment, excitation sculpting (solvent suppression) was performed so that the peaks corresponding to the CO_2 reduced products become prominent.

Chromatography: Gas analysis was done by Agilent GC-7890B gas chromatogram equipped with TCD and FID detectors using He as carrier gas. An Agilent 1220 Infinity II LC system was utilized for the quantification of liquid products using 0.5M H_2SO_4 as eluent.

X-ray photoelectron spectroscopy (XPS): XPS data were obtained using Omicron Nanotechnology spectrometer using an Al-Kα X-ray source. All the binding energies were referenced to the C 1s peak at 284.8 eV. Bi L_{III}-edge XAS measurements of the catalysts were carried out in fluorescence mode at PETRA III, P64 beamline of DESY, Germany. The XAS data processing were done using the ATHENA software and theoretical EXAFS models were constructed and fitted to the experimental data in ARTEMIS. Nitrogen adsorption-desorption isotherms were conducted using a BELSORP-MR6 Surface Area and Porosity Analyzer at 77 K after degassing the samples at 100°C for 12 h. The specific surface area and pore volume were determined using the Brunauer-Emmett-Teller method and the pore size distribution was calculated using the Barrett-Joyner-Halenda method.

UV-Visible spectroscopy: UV-visible DRS were recorded using a Perkin-Elmer Lambda 900 UV/Vis/Near-IR spectrophotometer in the range of 300 cm^{-1} to 1000 cm^{-1}. BaSO$_4$ was used as a 100% reflectance standard. The obtained UV-vis diffuse reflectance spectra were first transformed to absorption spectra according to the Kubelka-Munk function,

$$F(R) = \frac{(1-R)^2}{2R} \times 100\%$$

where, R was the relative reflectance of samples with infinite thickness compared to the reference. Next, the band gaps of samples were estimated based on the Tauc equation,

$$F(R)h\nu = A(h\nu - E_g)^{\frac{n}{2}}$$

where, h, ν, A, and E_g represents Planck constant, incident light frequency, proportionality constant and band gap, respectively, while n depends on the nature of transition in a semiconductor. Values of 1, 3, 4 and 6 for n correspond to allowed direct, forbidden direct, allowed indirect, and forbidden indirect transitions, respectively. The values of E_g were then determined from the plot of $(F(R)h\nu)^{2/n}$ versus $h\nu$ corresponding to the intercept of the extrapolated linear portion of the plot near the band edge with the $h\nu$ axis. Both $Bi_{19}S_{27}Cl_3$ and Bi_2S_3 being direct bandgap semiconductors, their values of E_g were thus determined from the plot of $(F(R)h\nu)^2$ against $h\nu$. The time-resolved transient PL decay spectra were measured at room temperature using a Horiba Delta Flex time correlated single-photon-counting (TCSPC) instrument. A 405 nm laser diode with a pulse repetition rate of 1 MHz was used as the light source. The instrument response function (IRF) was collected using a scatterer (Ludox AS40 colloidal silica, Sigma-Aldrich). The value of the goodness-of-fit parameter (χ^2) calculated from the bi-exponential decay kinetics method is much closer to unity (χ^2 value for $Bi_{19}S_{27}Cl_3$ fitting is 1.309 and the same for Bi_2S_3 fitting is 1.334), which indicates a good fit of the data. Thus, the emission signals were analyzed by the bi-exponential decay kinetics method rather than mono-exponential kinetics methods. The following equation was applied to carry out the bi-exponential kinetic analysis and to calculate the decay lifetimes τ_1 and τ_2-

$$Fit = B_1 exp(-t/\tau_1) + B_2 exp(-t/\tau_2)$$

where, B_1 and B_2 are the pre-exponential factor (amplitude) corresponding to decay lifetimes τ_1 and τ_2, respectively. The average lifetimes (τ_{avg}) were calculated using the following equation-

$$\tau_{avg} = \sum B_i \tau_i^2 / \sum B_i \tau_i$$

Photocatalytic CO₂ reduction measurement: Photocatalytic CO_2 reduction was performed in quartz cell with an approximate volume of 90 ml. A 420 W Xenon-arc lamp provided by Newport was used as light source. To obtain the visible light spectrum 20CGA-400 long pass filter (UV light cut-off) and FSR-KG2 short pass filter (IR light cut-off) were used in tandem. In the typical CO_2 photocatalytic reduction process, 10 mg of the $Bi_{19}S_{27}Cl_3$ was initially dispersed in 20 ml deionized water with continuous ultrasonication for 30 minutes. Sodium sulfite and sodium sulfide were used as sacrificial electron donor. An amount of 0.4 mg of sodium sulfide and 2.9 mg of sodium sulfite were added to the dispersion and the mixture was sonicated for another 30 minutes to obtain homogeneity. The dispersion was first purged with
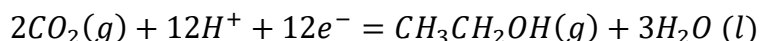
N_2 to remove the dissolved air and then pure CO_2 gas was purged for 1 hour to saturate the solution. The reaction cell was properly sealed and kept 10 cm away from the light source during illumination. After the catalysis the products were detected and quantified by GC, HPLC and NMR. In the beginning of a new catalytic cycle, the catalyst was washed by distilled water to remove surface-adsorbed reactants.

***In-situ* diffuse reflectance FT-IR spectroscopy (DRIFTS):** *In-situ* photochemical FT-IR spectroscopic studies were performed using a purged VERTEX FT-IR spectrometer equipped with the A530/P accessory and a mid-band Mercury Cadmium Telluride (MCT) detector. Spectra were recorded after 100 scans with a resolution of 4 cm^{-1}. A DRIFTS cell with a quartz window was used to perform catalytic experiment. Prior to catalytic testing, 20 mg of the sample was placed in the DRIFTS cell and treated in flowing N_2 for 30 min to remove air. Then CO_2 and water vapor mixture were injected into the cell through a rubber septa and light was illuminated through the quartz window. Just before the light exposure on the DRIFTS cell, the zero-minute data was collected and after that data were collected after 2 minutes interval.

Photo-electrochemistry: A CHI 760 potentiostat with three-electrode configuration under the illumination of a solar simulator (Newport) with an ultraviolet (UV) ($\lambda > 400$ nm) cut-off filter was used for photoelectrochemical experiments. A slurry containing 10 mg of the sample, 200 μL of Nafion (5%), and 1 mL of IPA was spin-coated on FTO with 1 cm^2 area to fabricate the working electrode. For all the experiments, a platinum rod was used as the counter electrode whereas an Ag/AgCl was used as reference electrode in 0.5M Na_2SO_4 aqueous solution.

5.3. Calculations

Calculation of selectivity of CH$_3$CH$_2$OH

$$CO_2(g) + 2H^+ + 2e^- = CO(g) + H_2O\ (l)$$

$$CO_2(g) + 6H^+ + 6e^- = CH_3OH(g) + H_2O\ (l)$$

$$CO_2(g) + 8H^+ + 8e^- = CH_4(g) + 2H_2O\ (l)$$

$$2CO_2(g) + 12H^+ + 12e^- = CH_3CH_2OH(g) + 3H_2O\ (l)$$
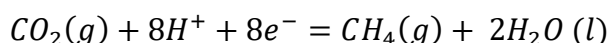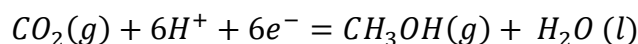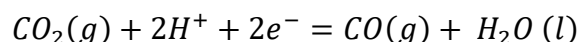
The selectivity of CO_2 reduced products have been calculated on an electron basis using the following equation (n represented the yield (μmol) of the products in the CO_2 photoreduction):

Selectivity of *CH₃CH₂OH (%) = [12n(CH₃CH₂OH)] / [12n(CH₃CH₂OH) + 8n(CH₄) + 6n(CH₃OH) + 2n(CO)] × 100%*

Apparent quantum yield (AQY) calculation: The wavelength dependent AQY of $Bi_{19}S_{27}Cl_3$ nanorods for photocatalytic CO_2 reduction reaction were calculated using different monochromatic light source. Four different light filters obtained from Newport were used to obtain the monochromatic wavelengths (square bandpass filter with a centre wavelength range of $\pm$ 10nm) and 919P-010-16 Thermopile Sensor was used to measure the incident light intensity. After 12 hours of CO_2 reduction the AQY was estimated from the following equation:

$$AQY(\%) = \frac{Number\ of\ reacted\ electrons}{Number\ of\ incident\ photons} X\ 100\%$$

Number of reacted electrons were calculated from the yield of CO_2 reduced products. Because different number of electrons are required for the formation of different products, the total number of reacted electrons are

$$Number\ of\ reacted\ electrons = [12n(CH_3CH_2OH) + 8n(CH_4) + 6n(CH_3OH) + 2n(CO)]\ X\ N_A$$

where, n(CH₃CH₂OH), n(CH₄), n(CH₃OH), n(CO) are the yields of ethanol, methane, methanol and carbon monoxide in moles, respectively. N_A is Avogadro's number.

Number of incident photons are calculated from the following equation:

$$Number\ of\ incident\ photons = \frac{PS\lambda t}{hc}$$

where, P is the power density of the incident monochromatic light (W/m²), S (m²) is the irradiation area, t (s) is the duration of the incident light exposure and λ (m) is the wavelength of the incident monochromatic light.

Combining these two equations the AQY(%) for different monochromatic light was calculated. For example, the AQY(%)@700 nm is shown here-

AQY(%)@700 nm

$$= \frac{[(22.7\times12+1.9\times8+4.1\times6+2.2\times2)\times10^{-6}]\times6.02\times10^{23}}{1} \times \frac{6.626\times10^{-34}\times3\times10^8}{48\times10^{-3}\times3.46\times700\times10^{-9}\times3600\times12} \times 100\%$$

$$= 0.76\%$$

5.4. Details of calculations used in density functional theory (DFT)

DFT calculations were done using VASP package and Quantum expresso both. Bader charge calculation and density of state analysis were done using VASP. However, Gibbs free energy (ΔG) of CO_2 to ethanol formation intermediates were calculated using Quantum

Espresso. The calculation of Gibbs free energy using VASP became expensive and time consuming considering multiple intermediate steps and large no of atoms in $Bi_{19}S_{27}Cl_3$ surface. The details of each calculation are given below.

DFT calculations were done with Vienna ab initio simulation (VASP) package.[37] The Electron-ion interactions were described using all-electron projector augmented wave pseudopotentials,[38] and Perdew-Bruke-Ernzehof (PBE) generalized gradient approximation (GGA)[39] was used to approximate the electronic exchange and correlations. The plane-wave kinetic energy cut off of 520 eV was used for all the calculations. The Brillion zone was sampled using a $5\times5\times5$ Monkhorst-Pack k-grid for bulk $Bi_{19}S_{27}Cl_3$ and Bi_2S_3 and $3\times3\times1$ Monkhorst-Pack k-grid. Bulk structures and surfaces were relaxed using a conjugate gradient scheme until the energies and each component of the forces converged to 10^{-6} eV and 0.001 eV $Å^{-1}$ and 10^{-5} eV and 0.01 eV $Å^{-1}$. All the calculations are spin polarized. A vacuum of 12 Å was added for surfaces to avoid interactions among periodic images. p-band centre was calculated by considering the first moment of p-states for Bi atoms.

The DFT computations for energy calculations were performed using the PWscf (Plane-Wave Self-Consistent Field) method implemented in Quantum Espresso Simulation Package.[40] The Perdew-Becke Ernzerhof (PBE)[41] exchange-correlation functional was used in combination with Vanderbilt ultra-soft pseudopotential[39] that represents the interaction between ionic cores and valence electrons. The Brillouin zone was set to $2 \times 2 \times 1$ Monkhorst-Pack k-point mesh and the kinetic energy cutoff of 455 eV is applied to truncate the plane-wave basis used to represent the Kohn-Sham orbitals. The convergence threshold of 0.03 eV/Å is accounted for forces on the atoms for ionic minimization. The slab model of $Bi_{19}S_{27}Cl_3$ consists of four atomic layers of Bi and S atoms and is separated by a vacuum gap of 14 Å on the z-axis.

$$\Delta G = \Delta E + \Delta ZPE - T\Delta S \qquad (5.1)$$

During optimization, the atoms in the bottom layer were fixed at their bulk position, and the remaining layers were allowed to relax. The correction to long-range dispersion interactions was included by employing the D3 correction method by Grimme et al.[42]

The computational hydrogen electrode model by Norskov et al.[43] was used to calculate the energy of proton-coupled with electron and the reaction-free energy change:

Where ΔE is the DFT calculated change in reaction energy, ΔZPE is the zero-point energy change, and $T\Delta S$ is the entropy change at 300 K. Here the total entropy change for the adsorbed intermediates is approximated with contribution from vibrational entropy only. The frequency calculation for the intermediates was done on a single Bi_2S_3 unit. The entropy and ZPE values for the gas-phase molecules are taken from the NIST Chemistry WebBook.[44]

5.5.   Results and discussions

Material design: $Bi_{19}S_{27}Cl_3$ has been synthesized from the reaction of $BiCl_3$ and thiourea using solvothermal method at 180 °C. Initial addition of thiourea into the ethanolic solution of $BiCl_3$ at room temperature leads to the formation of $[Bi(thiourea)]^{3+}$ complex due to strong chelation between Bi^{3+} and thiourea. At higher temperature, the $[Bi(thiourea)]^{3+}$ complex decomposes to form Bi_2S_3, which eventually reacts with remaining $BiCl_3$ to form $Bi_{19}S_{27}Cl_3$ (**Figure 5.1**).[45]
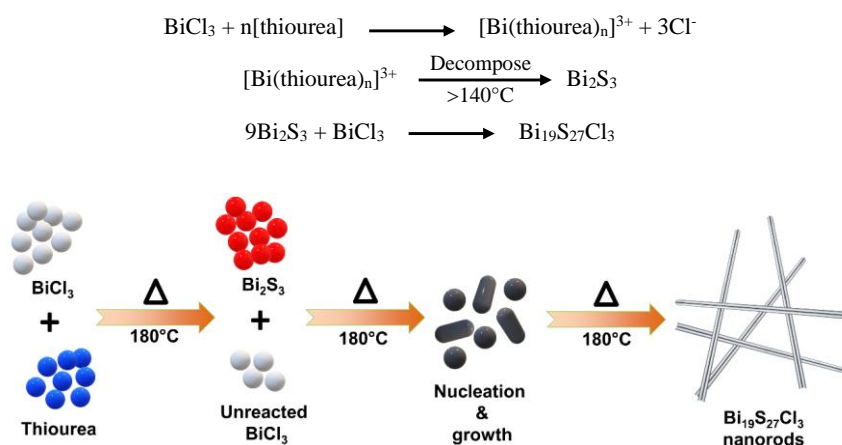
Figure 5.1. Formation of $Bi_{19}S_{27}Cl_3$ Schematic illustration of the synthesis of $Bi_{19}S_{27}Cl_3$ nanorods.
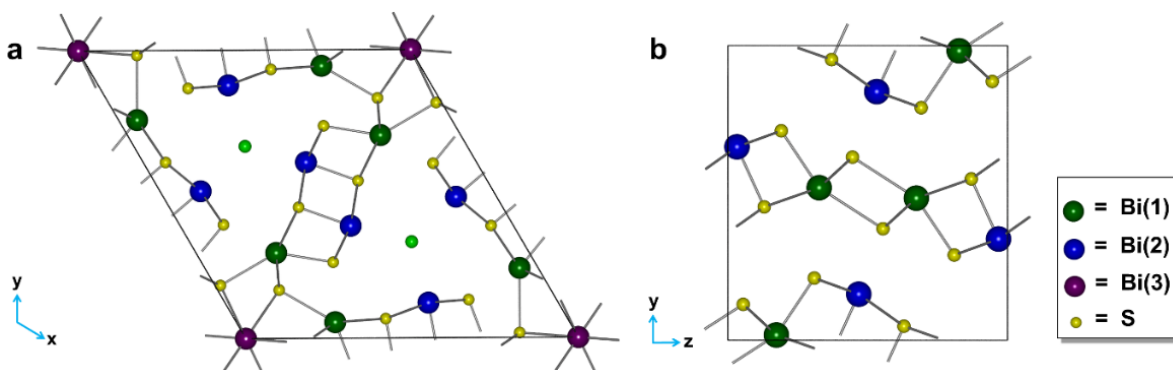
Figure 5.2. Unit Cell crystal structure of **(a)** $Bi_{19}S_{27}Cl_3$, and **(b)** Bi_2S_3.

Hence, the formation of $Bi_{19}S_{27}Cl_3$ can be proposed as the reaction between Bi_2S_3 and $BiCl_3$ with an effective ratio of 9:1. This is also evident from the structural similarity between Bi_2S_3

and $Bi_{19}S_{27}Cl_3$ (**Figure 5.2a,** and **5.2b**). The common Bi_2S_3 building block contains ladder–like structure where the individual ladders are connected together to form a continuous chain. Introduction of $BiCl_3$ unit into the Bi_2S_3 lattice transforms the individual ladder structure of Bi_2S_3 into highly symmetrical star-shaped structure where the central hexagonal star-shaped moiety is connected to six individual ladders. The Cl atoms can be found inside the channel created by the three interconnected star-shaped units. It should be pointed out that the distance between the chlorine and the nearest bismuth atom (Bi2) is 3.54 Å, which is much larger than the covalent bond distance of Bi-Cl in $BiCl_3$ (2.51 Å). This is very similar to other open framework structures like clathrate $(Ba_8Ga_{16}Ge_{30})$.[46] Incidentally, another bismuth chalcohalide namely, BiSCl also possesses a similar ladder-shaped structure, although with smaller length of the ladder. Several spectroscopic and microscopic techniques were employed to characterize the as synthesized materials (**Figure 5.3**). The crystal-phase purity and visible light absorption capabilities of the samples was examined by powder X-ray diffraction (XRD) and DRS analysis (**Figure 5.3a** and **5.3b**).
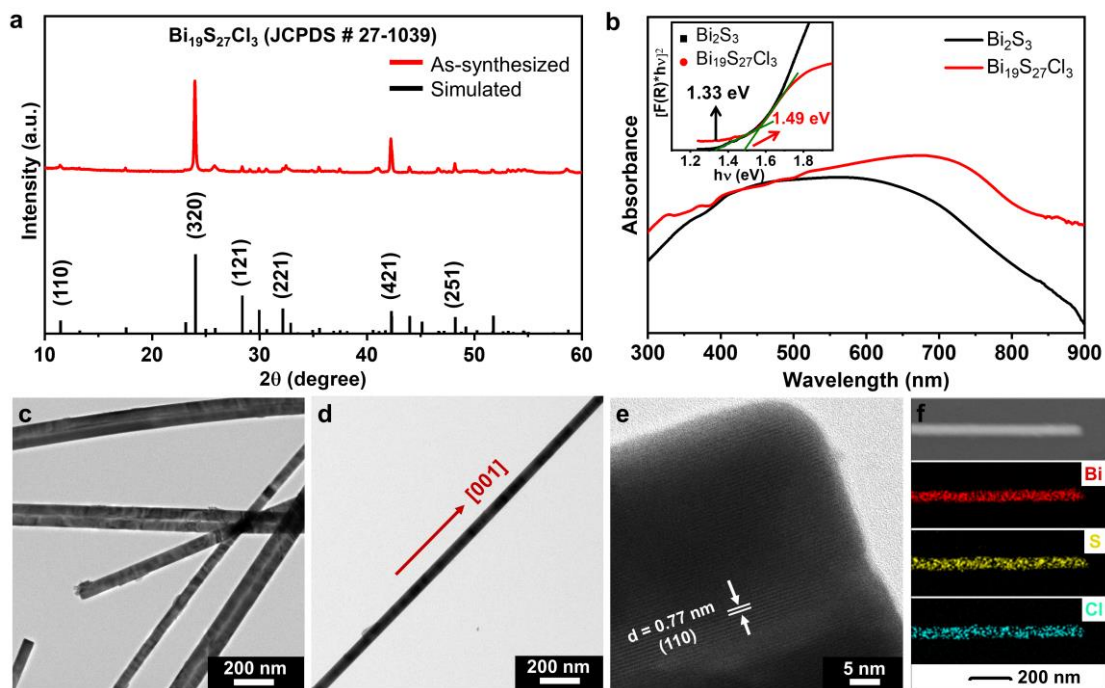
Figure 5.3. Characterization of $Bi_{19}S_{27}Cl_3$ nanorods. **(a)** Powder XRD pattern of as synthesized $Bi_{19}S_{27}Cl_3$. The simulated diffraction pattern was obtained from hexagonal $Bi_{19}S_{27}Cl_3$ structure with lattice parameters of $a = b = 15.403$ Å, $c = 4.015$ Å (PDF card no. 27-1039, space group $P6_3/m$). **(b)** UV-Vis diffuse reflectance spectra (DRS) and the corresponding bandgaps of $Bi_{19}S_{27}Cl_3$ and Bi_2S_3, calculated from Kubelka-Munk plot (inset). **(c-d)** TEM images of the as-synthesized $Bi_{19}S_{27}Cl_3$ showing rod-shaped morphology. The nanorods grow along the z-axis. **(e)** HRTEM image of the $Bi_{19}S_{27}Cl_3$ showing lattice plane (110) with d spacing value 0.77 nm. **(f)** FESEM image and the EDS mapping of Bi, S and Cl atoms of $Bi_{19}S_{27}Cl_3$.

The structure and morphology of $Bi_{19}S_{27}Cl_3$ were examined under field-emission scanning electron microscopy (FESEM) and transmission electron microscopy (TEM). As shown in **Figure 5.3c** and **Figure 5.3d**, the TEM images show typical rod-shaped structure of $Bi_{19}S_{27}Cl_3$ with an average diameter of 100 nm and several micrometers in length. Moreover, lattice fringes having d spacing of 0.77 nm can be identified in the HRTEM image of the individual nanorod which corresponds to the (110) plane of $Bi_{19}S_{27}Cl_3$ (**Figure 5.3e**). This suggests that the nanorods anisotropically grow along the [001] axis or z-axis which is parallel to (110) plane (**Figure 5.3d**). The similar rod-shaped morphology can be also detected under SEM (**Figure 5.3e**). In addition to that the Energy-dispersive X-ray spectroscopy (EDS) mappings show that Bi, S and Cl atoms uniformly coexist in the $Bi_{19}S_{27}Cl_3$ (**Figure 5.3f**). The gas adsorption properties of these nanocrystals were understand from BET measurements, which follows type-II isotherm (**Figure 5.4a**). Furthermore, the as synthesized Bi_2S_3 was also characterized by powder XRD and its nanoribbon morphology was confirmed from TEM analysis (**Figure 5.4b,** and **5.5a-e**). Before diving into the catalytic property of $Bi_{19}S_{27}Cl_3$, its light absorption property and the band structures were investigated by different spectroscopic techniques. To check the photo absorption efficiency, UV-Vis diffuse reflectance spectra (DRS) were collected and compared with the data of Bi_2S_3. Both $Bi_{19}S_{27}Cl_3$, as well as Bi_2S_3, showed excellent visible light absorption property (**Figure 5.3b**). Compared to Bi_2S_3, $Bi_{19}S_{27}Cl_3$ showed enhanced visible light absorption property suggesting better light harvesting efficiency. Moreover, the bandgaps of these materials were also calculated using Kubelka-Munk function from their corresponding DRS spectrum. As can be seen from **Figure 5.3b** (inset), the bandgap values of $Bi_{19}S_{27}Cl_3$ and Bi_2S_3 were 1.49 V and 1.33 V, respectively.
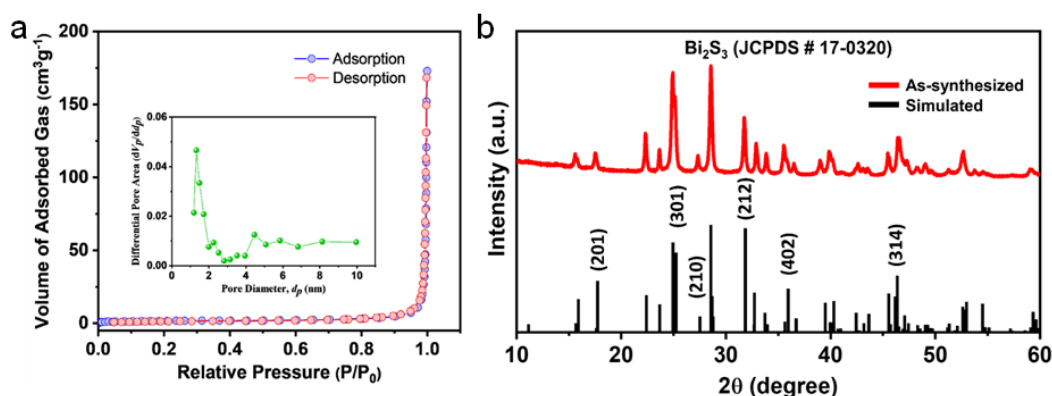
Figure 5.4. (a) Surface area analysis of $Bi_{19}S_{27}Cl_3$ BET surface area and pore size distribution of $Bi_{19}S_{27}Cl_3$. The surface area and pore volume were determined by the Brunauer−Emmett−Teller (BET) (type II isotherm) and Barrett−Joyner−Halenda (BJH) models, respectively. **(b)** XRD of Bi_2S_3 Powder XRD pattern of as synthesized Bi_2S_3 (*Pnma*).
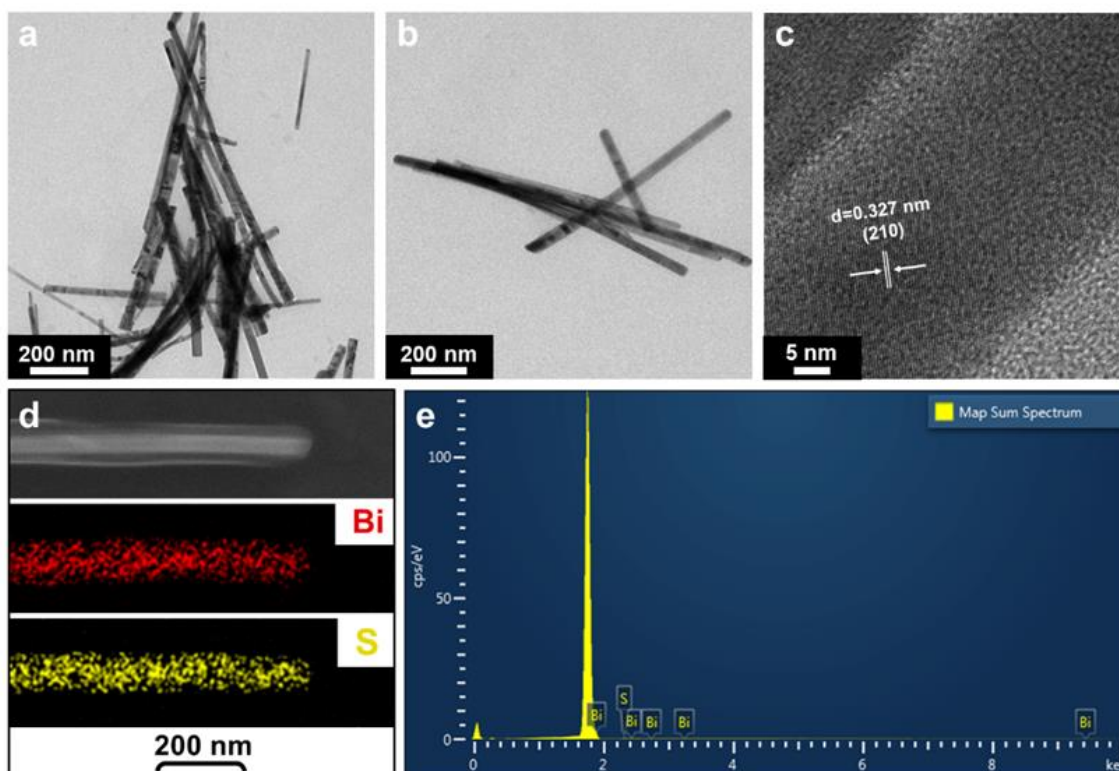
Figure 5.5. Microscopic images of Bi_2S_3 nanoribbons. **(a-b)** TEM images of the as-synthesized Bi_2S_3 showing ribbon-shaped morphology. The Bi_2S_3 nanoribbons have less depth compared to $Bi_{19}S_{27}Cl_3$ nanorods and that is why the nanoribbons seems transparent in the TEM image. **(c)** HRTEM image of the Bi_2S_3 showing lattice plane (210) with d spacing value 0.327 nm. **(d)** FESEM image and the EDS mapping of Bi and S atoms of Bi_2S_3. **(e)** Overall EDS spectrum of the Bi_2S_3 nanoribbons.

Mott-Schottky plot was further employed to find the exact band positions. From the electrochemical experiment, the flat band potential of $Bi_{19}S_{27}Cl_3$ was calculated to be -0.43 V versus normal hydrogen electrode (**Figure 5.6a**). A positive slope from the capacitance measurement in Mott-Schottky plot generally indicates n-type semiconductor and the conduction band potential (E_{cb}) of an n-type semiconductor usually considered as 0.1 V more negative than the flat band potential.[47] This translates to the E_{cb} of $Bi_{19}S_{27}Cl_3$ to be at -0.53 V and thus the valence band position (E_{vb}) to be at 0.96 V. Incidentally, the E_{cb} and E_{vb} values of Bi_2S_3 were very similar to $Bi_{19}S_{27}Cl_3$ (**Figure 5.6b**). Apparently, the E_{cb} value of $Bi_{19}S_{27}Cl_3$ is sufficient to reduce CO_2 into CH_3OH and CH_3CH_2OH and barely capable of producing CO (**Figure 5.6c**).

Photocatalytic CO_2 reduction to ethanol: Photocatalytic CO_2 reduction has been performed on $Bi_{19}S_{27}Cl_3$ and Bi_2S_3 catalysts in aqueous medium using a 420 W Xenon-arc lamp with UV cut-off filter (<400 nm) (**Figure 5.6d**). As seen in **Figure 5.7a**, Bi_2S_3 favoured the

conversion of CO_2 to C_1 products (CO, CH_4 and CH_3OH), which is consistent with the earlier reports.[29] However, $Bi_{19}S_{27}Cl_3$ catalyst favoured the production of C_2 product, CH_3CH_2OH, in high selectivity and high yield. After 21 hours of continuous light irradiation, 22 µmol g^{-1} of ethanol was obtained when $Bi_{19}S_{27}Cl_3$ was used as the catalyst along with CO, CH_4, CH_3OH and H_2 as the minor products (**Figure 5.7b**). H_2 was obtained as the by-product from the competitive HER during photocatalytic CO_2 reduction reaction **(Figure 5.7c)**. A further 4.9 times increment in the production of CH_3CH_2OH (109 µmol g^{-1}) was observed with the addition of Na_2S and Na_2SO_3 as sacrificial electron donors. The reason behind the simultaneous addition of Na_2S and Na_2SO_3 was to prevent the formation of sulphur particles from the oxidation of S^{2-}.
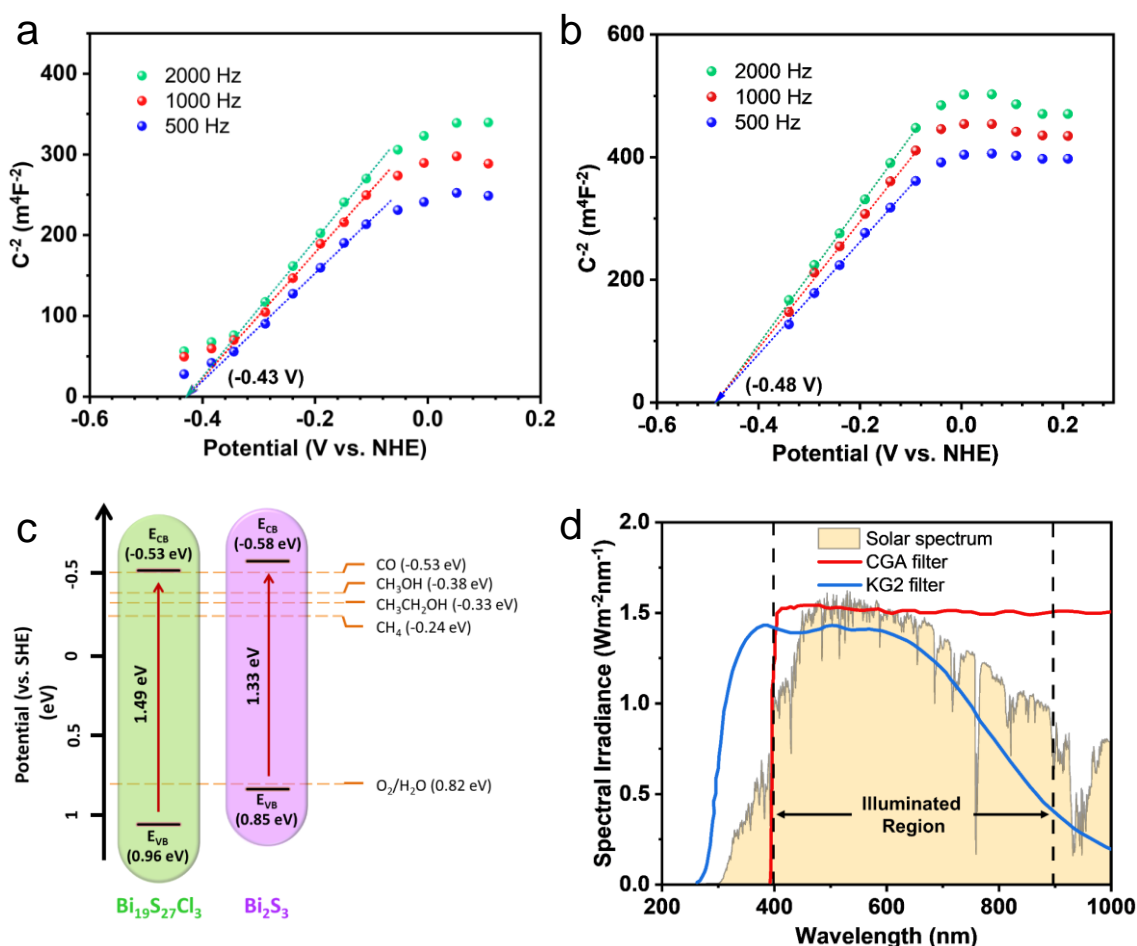
Figure 5.6. (a) Mott–Schottky plots of interfacial capacitance derived from EIS data for $Bi_{19}S_{27}Cl_3$ in 0.5 M Na_2SO_4. **(b)** Mott–Schottky plots of interfacial capacitance derived from EIS data for Bi_2S_3 in 0.5 M Na_2SO_4. **(c)** Electronic band structure. Schematics representation of the electronic band structures for $Bi_{19}S_{27}Cl_3$ nanorods and Bi_2S_3 nanoribbons. **(d)** Spectra of illuminated light**.** Illuminated region of our used light source comparing with sunlight. Two light filters namely 20CGA-400 longpass filter (UV cut-off) and FSR-KG2 shortpass filter (IR cut-off) were used in combination to obtain the visible light.

It is worth noting that the CH_3CH_2OH selectivity also increased from 66% to 85% upon the addition of sacrificial electron donor (**Figure 5.7d**). Because the reduction of CO_2 to CH_3CH_2OH is a dominant electron transfer process compared to CO_2 to C_1 products (CO, CH_4 and CH_3OH), the selectivity has been shifted towards CH_3CH_2OH upon the addition of sacrificial electron donors whose sole purpose is to consume the photogenerated holes and thus increase the number of photoexcited electrons by minimizing the recombination. When the same reaction was performed under full range of UV-Visible light, the yield of each product increased. However, the selectivity of CH_3CH_2OH was disturbed due to unwanted reactions happening in presence of UV light (**Figure 5.7b**).
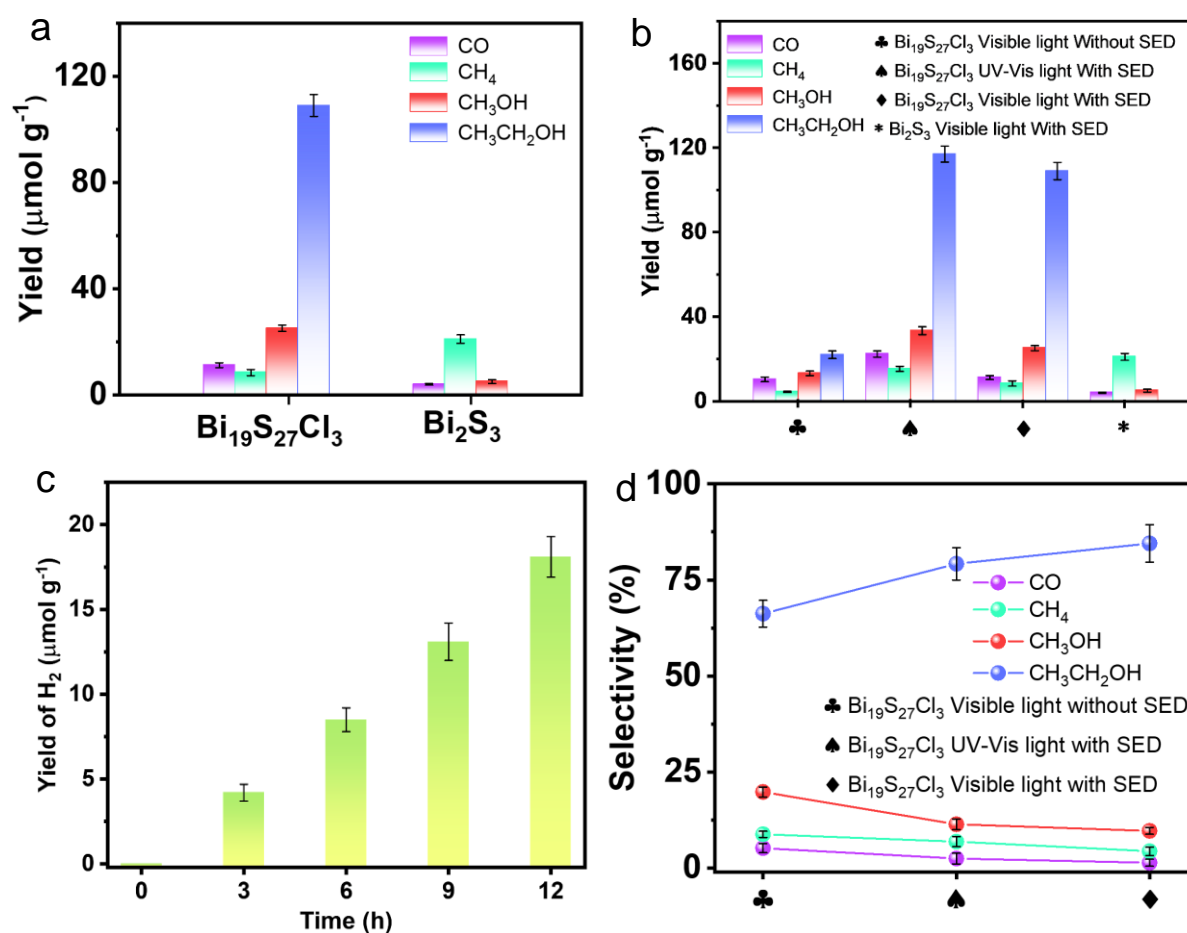
Figure 5.7. Photocatalytic CO_2 reduction and charge polarization. (**a**) Evolution of different products during photocatalytic CO_2 reduction with $Bi_{19}S_{27}Cl_3$ and Bi_2S_3 with sacrificial electron donor under visible light irradiation. (**b**) Evolution of different products during photocatalytic CO_2 reduction under different catalytic conditions. (SED = sacrificial electron donor). (**c**) The yield of H_2 during the photocatalytic CO_2 reduction over $Bi_{19}S_{27}Cl_3$ nanorods with sacrificial electron donor. (**d**) Selectivity of CO_2 reduced products for $Bi_{19}S_{27}Cl_3$ catalyst under different reaction conditions. The selectivity of the products was calculated based on the electrons required for their formation.
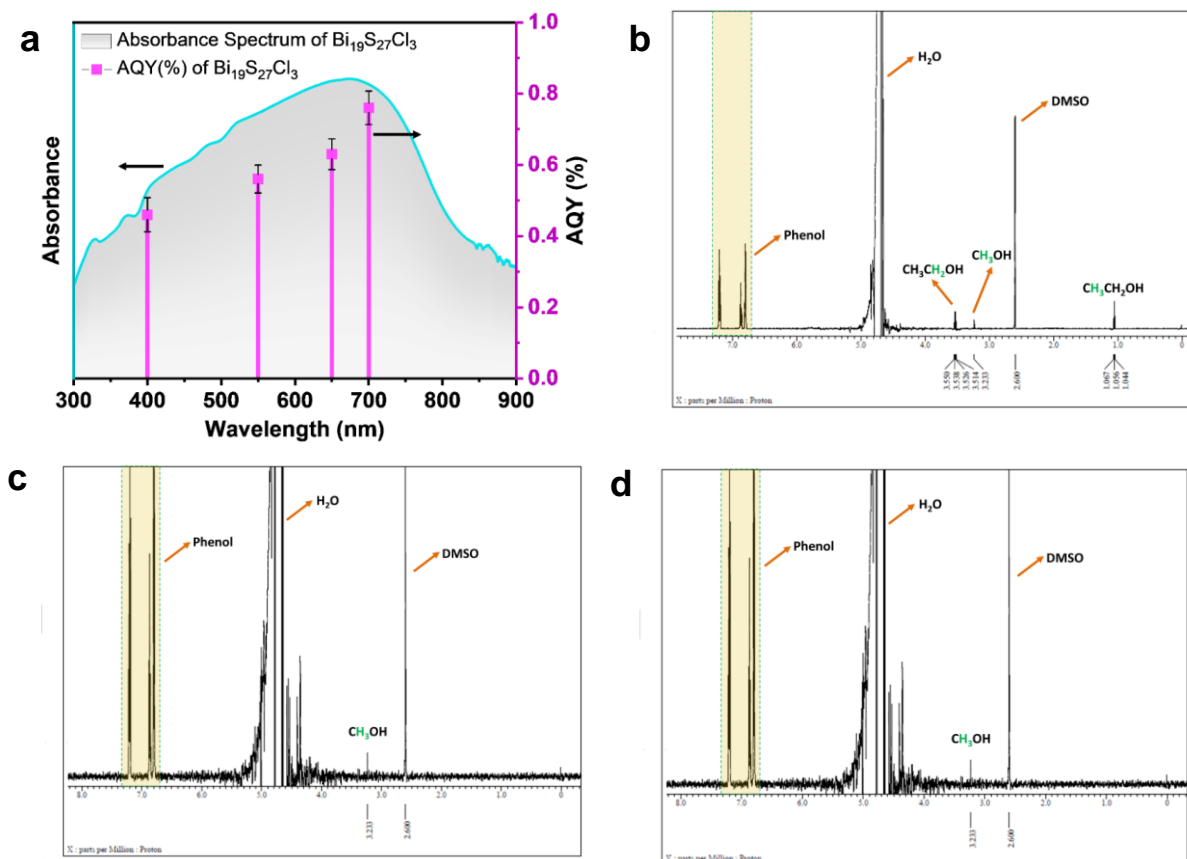
Figure 5.8. (a) Apparent quantum yield (AQY%) of $Bi_{19}S_{27}Cl_3$ under different monochromatic light. AQY% matches well with the absorption spectrum of $Bi_{19}S_{27}Cl_3$. AQY(%) were measured using 400 nm, 550 nm, 650 nm and 700 nm bandpass filter. **(b)** Liquid product analysis ^1H NMR of the liquid products obtained from the visible light CO_2 reduction with $Bi_{19}S_{27}Cl_3$. DMSO and phenol were used as internal standards. The broad peak ranging from 4.5 to 5.0 ppm value is due to water. DMSO peak was locked to 2.6 ppm as a reference and other peak positions were measured accordingly. The triplet peak from 1.067-1.044 ppm and quartet peak from 3.550-3.514 ppm are due to the CH_3- and -CH_2- protons of ethanol, respectively. The singlet peak at 3.233 ppm is due to the CH_3- protons of methanol. **(c)** ^1H NMR of the liquid products obtained from the visible light CO_2 reduction with Bi_2S_3. Only methanol was detected in ^1H NMR for Bi_2S_3. **(d)** ^1H NMR of the liquid products obtained under N_2 environment with $Bi_{19}S_{27}Cl_3$. No liquid product was detected.

The AQY (Apparent Quantum Yield) (%) of the $Bi_{19}S_{27}Cl_3$ catalyst for overall CO_2 reduction reaction was also calculated using different monochromatic light (**Figure 5.8a**). The AQY (%) at different wavelengths were consistent with the absorption spectra of $Bi_{19}S_{27}Cl_3$ which suggests the CO_2 reduction reaction is indeed driven by the light absorption of the catalyst. To determine the origin of all the reduced products, a series of control experiments were performed as per the guidelines provided in our recent viewpoint article.[48] The CO_2 reduced products were confirmed by GC as well as NMR experiments (**Figure 5.8b-5.8d**). As

shown in **Figure 5.9a,** and **5.9b** no gaseous or liquid product was detected in the absence of light and CO_2. When the reaction was conducted under $^{13}CO_2$ environment, only ^{13}C enriched products were detected in GC-MS and the corresponding mass peaks clearly shifted to higher value for ^{13}C incorporated products compared to the ^{12}C incorporated products (**Figure 5.10).**
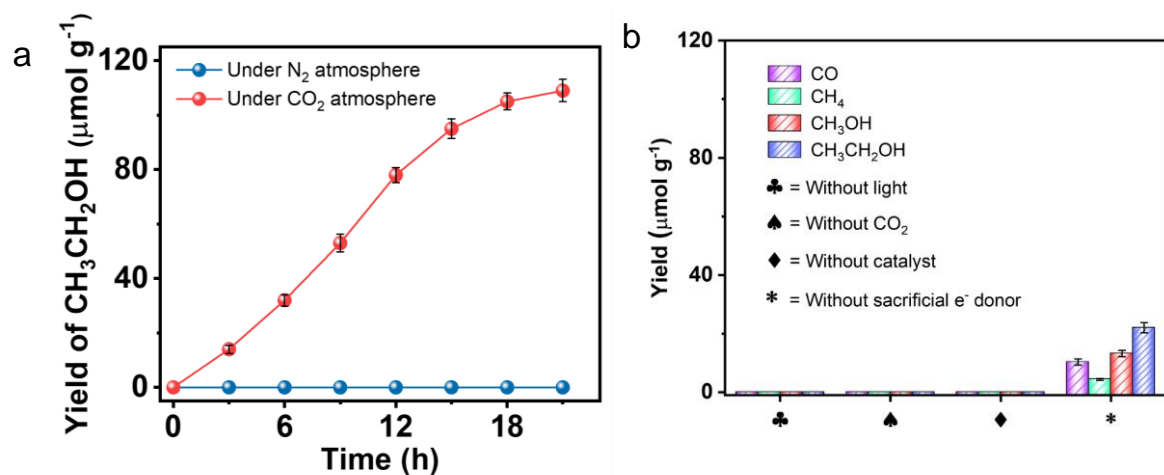
Figure 5.9. (a) Time dependant yield of CH_3CH_2OH during visible light CO_2 reduction with $Bi_{19}S_{27}Cl_3$ in presence of sacrificial electron donor. Error values were calculated from three separate catalytic reactions. **(b)** Yield of CO_2 reduced products for different control experiments. No products were detected in the absence of light or without CO_2 or without catalyst, keeping all the other parameters same. Only small amounts of products were detected without sacrificial e⁻ donor where water serves as the electron donor.
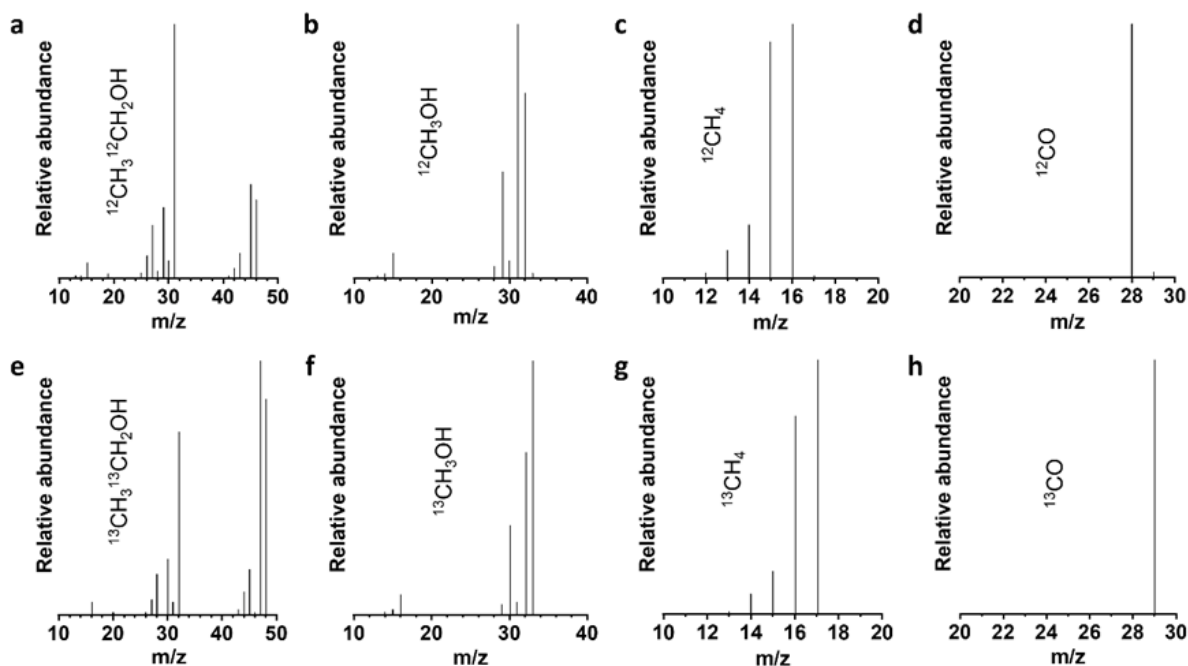
Figure 5.10. GC-MS study. Mass spectra of **(a)** $^{12}CH_3CH_2OH$, **(b)** $^{12}CH_3OH$, **(c)** ^{12}CO, and **(d)** $^{12}CH_4$ were obtained from reduction of $^{12}CO_2$. Mass spectra of **(e)** $^{13}CH_3CH_2OH$, **(f)** $^{13}CH_3OH$, **(g)** ^{13}CO, and **(h)** $^{13}CH_4$ were obtained from the reduction of ^{13}CO.
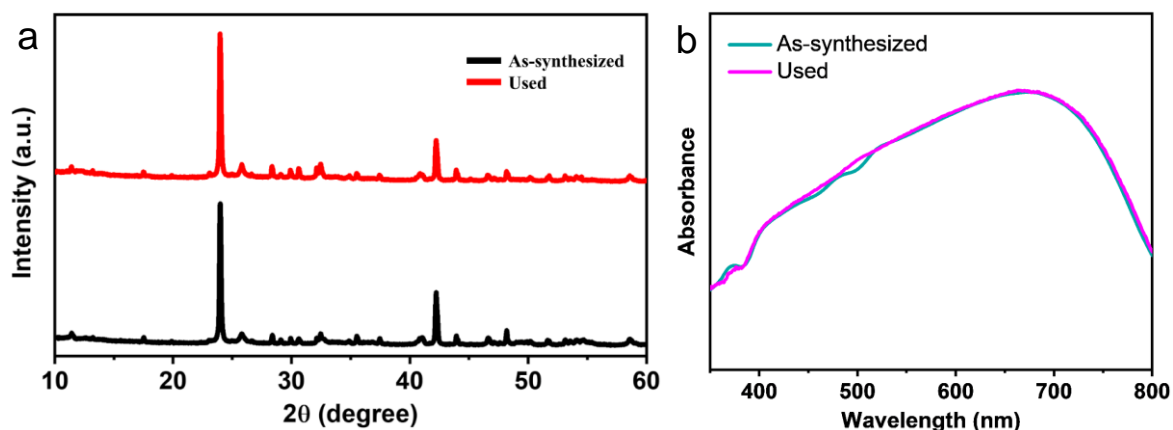
Figure 5.11. After catalysis study. **(a)** XRD after catalysis. XRD pattern of $Bi_{19}S_{27}Cl_3$ after the continuous 21 h test of CO_2 photoreduction under 420 W visible light. **(b)** UV-Vis DRS spectra of $Bi_{19}S_{27}Cl_3$ nanorods before and after CO_2 reduction reaction.

It did not show any degradation after 60 hours of reaction as evident from the powder XRD pattern This clearly demonstrates that the products were indeed derived from the CO_2 rather than other sources. Besides, $Bi_{19}S_{27}Cl_3$ also showed excellent durability during repeated photocatalytic tests. and UV-Vis diffuse reflectance spectra (**Figures 5.11a,** and **5.11b**). Further, SEM and TEM analysis confirmed that the rod-shaped morphology of $Bi_{19}S_{27}Cl_3$ also remained unaltered during the photocatalysis (**Figure 5.12**). It should be mentioned here that the reaction rate decreases considerably after 15 hours of continuous reaction (**Figure 5.9a**).
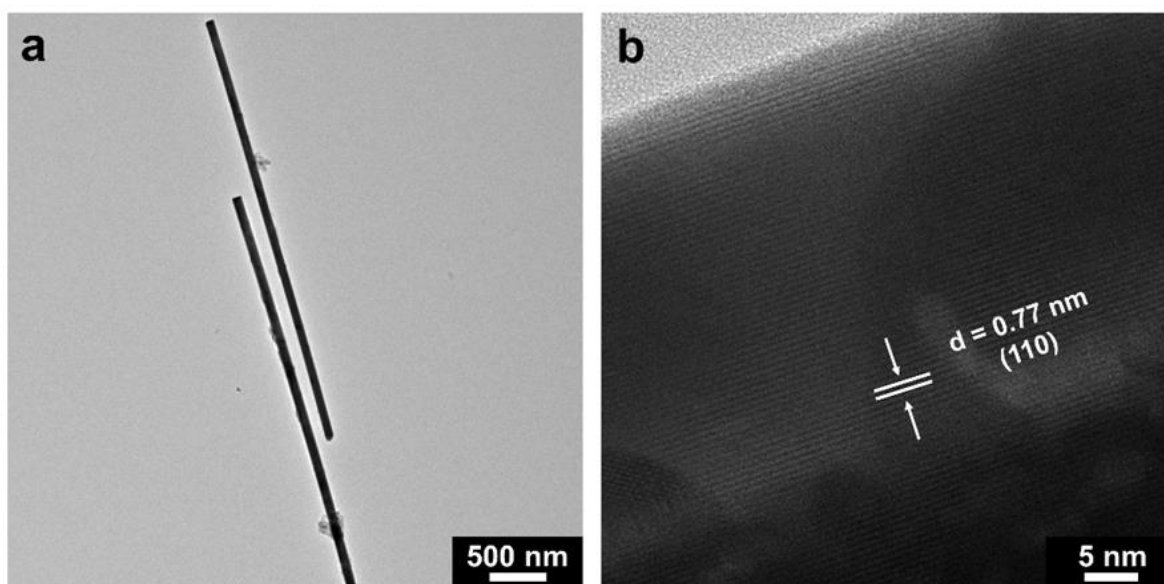
Figure 5.12. Microscopic image after catalysis. **(a)** TEM, and **(b)** HRTEM image of the $Bi_{19}S_{27}Cl_3$ nanorods after the photocatalytic CO_2 reduction reaction. The nanorods remains unaltered during the reaction. The (110) lattice plane can be seen in the used catalyst as well.
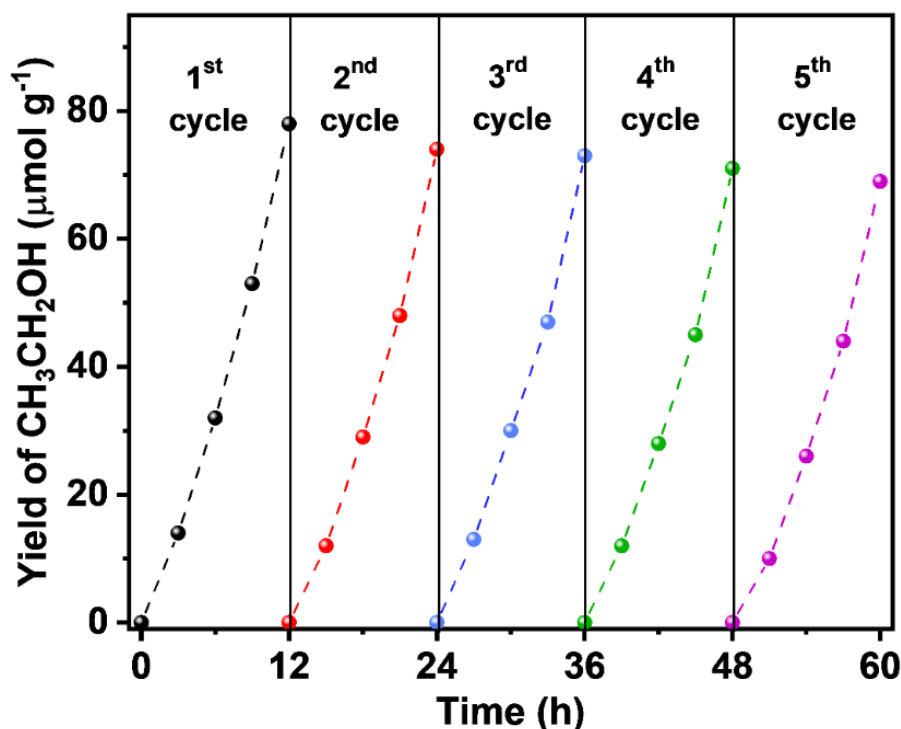
Figure 5.13. Reusability test of $Bi_{19}S_{27}Cl_3$ for 5 cycles. After the catalysis, the catalyst was separated from the reaction mixture and washed with distilled water to remove adsorbed reactants. It was then redispersed in water and purged with CO_2 for the next catalytic cycle.

This could be due to the depletion of dissolved CO_2 in the solution and also probable adsorption of carbon species on the surface of the catalyst during prolong reaction.[49] Hence, the catalytic cycle tests were performed for 12 hours which resolved the issue and the subsequent catalytic cycles even produced similar yield of all the products retaining the selectivity of CH_3CH_2OH (**Figure 5.13**).

Intrinsic Charge Polarization: In order to find out the underlying reason behind the excellent efficiency and selectivity towards C_2 product formation, we investigated the electronic properties of different bismuth centres present in $Bi_{19}S_{27}Cl_3$. To explain this, a deep understanding of connectivity and bond lengths of Bi centres with their neighbouring S atoms is necessary. There are three different types of bismuth centres present in $Bi_{19}S_{27}Cl_3$ (**Figure 5.14a**). The central Bi atom (from now on denoted as Bi3) has the highest average Bi-S bond length compared to others. The higher bond length for a particular metal centre with same neighbouring atoms indicates lower charge over the metal centre. This suggests a lower oxidation state of Bi3 compared to other two Bi centres. In fact, Groom *et al.* recently reported that the central disordered Bi atom (Bi3) exists in the +2 oxidation state forming $[Bi_2]^{4+}$ dimer based on the single crystal XRD data analysis.[50] Similarly, the average Bi-S bond distance values in $Bi_{19}S_{27}Cl_3$ have been compared with that of Bi_2S_3 and found that the average Bi-S

distance has decreased from Bi_2S_3 (2.86 Å) to $Bi_{19}S_{27}Cl_3$ (2.82 Å) (**Figure 5.14b,** and **5.14c**). This means the charge over the Bi atoms has been redistributed upon the introduction of $BiCl_3$ unit to the Bi_2S_3 structure.[51] Additionally, the Bi atoms present inside the ladder (from now on denoted as Bi2) as well as Bi atoms present on the edge of the star-shaped unit (from now on denoted as Bi1) have lower average Bi-S bond length and hence higher charge compared to Bi3. To compensate the lower charge of Bi3, other two Bi atoms get more positively charged. The chlorine atoms having higher electronegativity compared to Bi also help this charge polarization by withdrawing the electrons from Bi atoms. Upon this asymmetrical local charge distribution, an intrinsic electric field has been created in $Bi_{19}S_{27}Cl_3$. On the other hand, the bismuth centres in Bi_2S_3 have very similar structural environment facilitating uniform charge distribution.
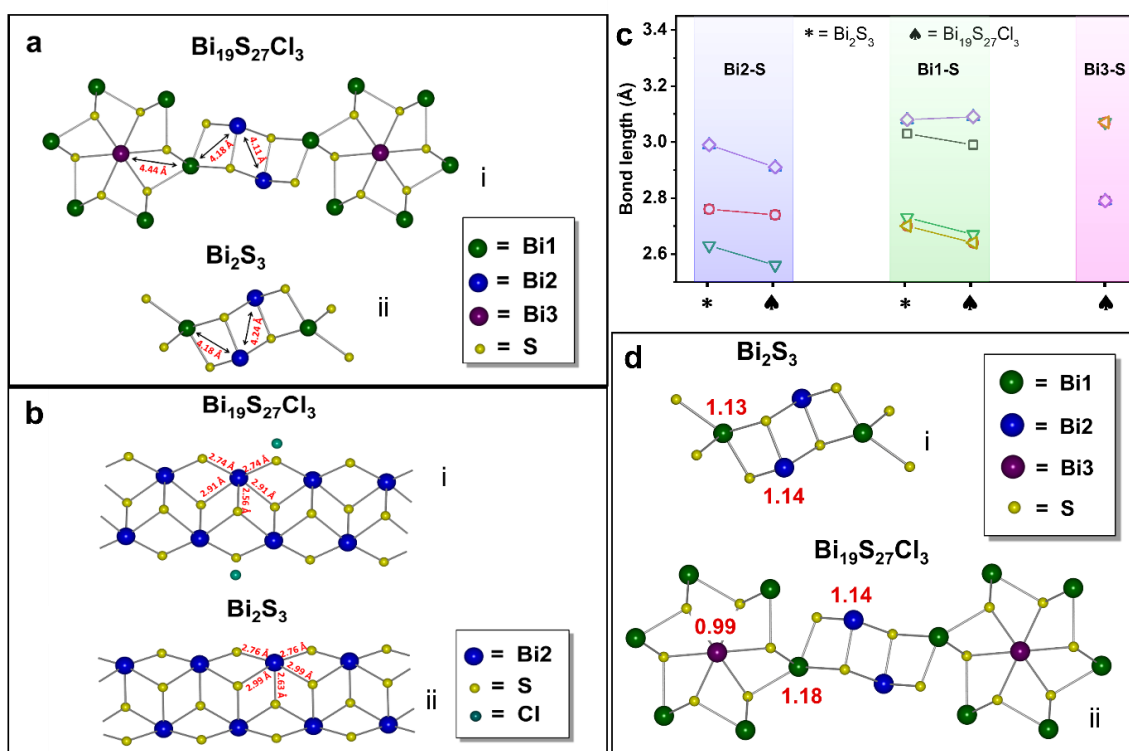
Figure 5.14. (a) Different bismuth centres present and their distance in **i)** $Bi_{19}S_{27}Cl_3$, and **ii)** Bi_2S_3. There are 2 types of bismuth centre present in Bi_2S_3 whereas 3 types of Bi centres present in $Bi_{19}S_{27}Cl_3$. The Bi1-Bi2 and Bi2-Bi2 bonds are less in $Bi_{19}S_{27}Cl_3$ compared to Bi_2S_3. Bi1-Bi3 bond distance (only present in $Bi_{19}S_{27}Cl_3$) is much higher compare to other two distances. **(b)** Connectivity and Bi-S bond lengths for Bi2 centre in **i)** $Bi_{19}S_{27}Cl_3$, and **ii)** Bi_2S_3. There are 5 Bi-S bonds for each Bi2 centre. In case of $Bi_{19}S_{27}Cl_3$, the Bi2 centres are also connected with chlorine atoms in addition to the 5 S atoms. Bi2-S bond lengths are higher in Bi_2S_3 compared to $Bi_{19}S_{27}Cl_3$. **(c)** Bi-S bond length for different bismuth centres in $Bi_{19}S_{27}Cl_3$ and Bi_2S_3. **(d)** Structure of different bismuth centres present in **i)** Bi_2S_3, and **ii)** $Bi_{19}S_{27}Cl_3$ and their corresponding Bader charge calculated from the DFT calculations.

Therefore, we anticipate that the suitably situated charge polarized Bi sites in $Bi_{19}S_{27}Cl_3$ are responsible for the high catalytic activity and selectivity towards C_2 product. It is important to mention here that the intrinsic charge polarization can furthermore promote the separation efficiency of photogenerated carriers which is beneficial for photocatalytic reactions.[52] To further validate the charge polarization, Bader charges of the different bismuth centres were calculated from density-functional-theory (DFT), which also estimate their electronic states (**Figure 5.14d**). Two different Bi-sites Bi1 and Bi2 in Bi_2S_3 have similar Bader charges of 1.13 and 1.14, respectively. Whereas three different Bi sites Bi1, Bi2 and Bi3 were identified on the surface of $Bi_{19}S_{27}Cl_3$, having Bader charges of 1.18, 1.14 and 0.99, respectively and this led to the formation of charge polarized Bi sites. All these experimental and theoretical findings further corroborate the charge polarized metal centers present in $Bi_{19}S_{27}Cl_3$. X-ray Photoelectron Spectroscopy (XPS) was utilized to elucidate the charge polarized Bi centres in $Bi_{19}S_{27}Cl_3$ nanorods (**Figures 5.15a, 5.15b, 5.16a, 5.16b**). The deconvoluted Bi 4f spectrum of $Bi_{19}S_{27}Cl_3$ revealed 3 different Bi centers having different charge densities (**Figure 5.16b**), which is in excellent agreement with the structural data. The three peaks observed at 165.5 eV, 164.1 eV and 162.6 eV can be assigned to the binding energy of Bi $4f_{5/2}$ whereas the peaks at 159.9 eV, 158.6 eV and 156.9 eV can be indexed to the binding energy of Bi $4f_{7/2}$. The additional peaks found at 162.1 eV and 160.4 eV can be allocated to the binding energy of S $2p_{1/2}$ and S $2p_{3/2}$, respectively. In comparison, the deconvoluted Bi 4f spectrum of Bi_2S_3 showed only two types of Bi centers with the binding energy peaks centered at 164.7 eV and 163.8 eV for Bi $4f_{5/2}$ and 159.6 eV and 158.5 eV for Bi $4f_{7/2}$ (**Figure 5.16a**). From the Bi 4f XPS spectra it can be inferred that two of the Bi centers present in $Bi_{19}S_{27}Cl_3$ (Bi1 and Bi2) are more positively charged compared to that for Bi_2S_3.
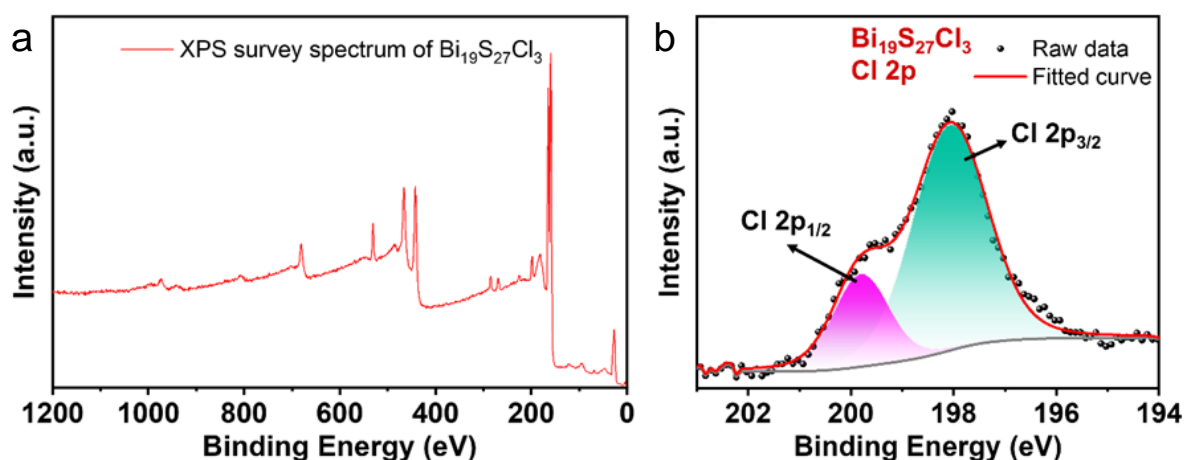
Figure 5.15. XPS analysis of $Bi_{19}S_{27}Cl_3$. (**a**) XPS survey spectrum of $Bi_{19}S_{27}Cl_3$. (**b**) Deconvoluted Cl 2p XPS spectrum of $Bi_{19}S_{27}Cl_3$.

This is because of the higher binding energy shift of the two Bi centers in $Bi_{19}S_{27}Cl_3$. Whereas the lower binding energy shift of the other Bi center in $Bi_{19}S_{27}Cl_3$ suggests less positive charge on Bi atom (Bi3). To gain further insight into the charge polarization induced by the differently charged bismuth centers, X-ray absorption spectra were measured at Bi-L_{III}-edge. In the X-ray Absorption Near Edge Structure (XANES), the absorption edge of $Bi_{19}S_{27}Cl_3$ was found to be at lower energy compared to Bi_2S_3 suggesting lower overall charge on the Bi center of $Bi_{19}S_{27}Cl_3$ (**Figure 5.16c**).[53] This could be due to the presence of Bi^{2+} centers along with the Bi^{3+} centers in $Bi_{19}S_{27}Cl_3$. In order to gain more intuitive evidence, the Fourier transform extended X-ray absorption fine structure (FT-EXAFS) were analysed. The FT-EXAFS for Bi_2S_3 showed a peak at 2.1 Å corresponding to the first shell of Bi-S bond. In case of $Bi_{19}S_{27}Cl_3$, the peak was found to be at 1.8 Å with broader feature compared to the Bi_2S_3. The coordination structure of Bi in the Bi_2S_3 and $Bi_{19}S_{27}Cl_3$ was further analysed by fitting the k^3-weighted FT-EXAFS curves (**Figure 5.16d**). The fitting parameters are listed in **Table 5.1** which sows 2 different Bi centres in Bi_2S_3 with very similar Bi-S distances. Whereas, the fitting parameter of $Bi_{19}S_{27}Cl_3$ showed 3 different Bi-S distances with similar distances of two Bi-S bond and another Bi-S bond with higher bond distance.
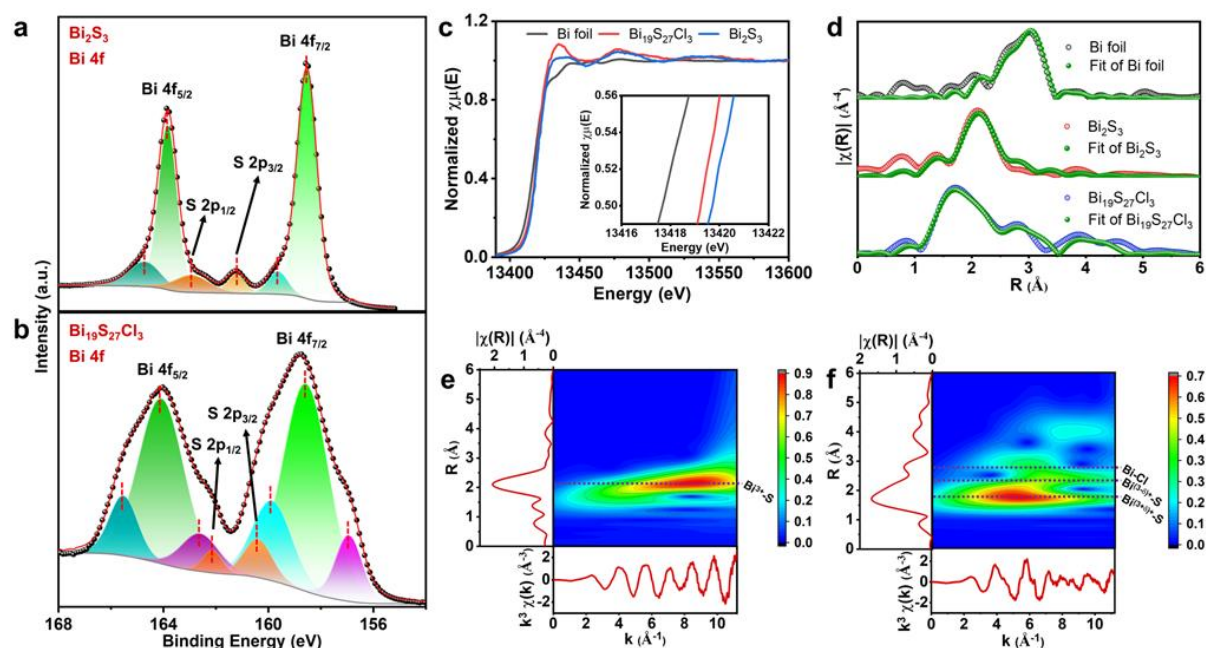
Figure 5.16. Investigation of charge polarization. Bi 4f XPS spectra of **(a)** Bi_2S_3 nanoribbons, and **(b)** $Bi_{19}S_{27}Cl_3$ nanorods. **(c)** Bi L_{III}-edge XANES spectra, and **(d)** the corresponding k^3-weighted $\chi(k)$ function of the FT-EXAFS spectra and the fitting curves for $Bi_{19}S_{27}Cl_3$ nanorod, Bi_2S_3 nanoribbon and Bi foil. Wavelet transforms for the k^3-weighted EXAFS signals of **(e)** $Bi_{19}S_{27}Cl_3$, and **(f)** Bi_2S_3.

Table 5.1. EXAFS fitting parameters at the Bi L_{III}-edge for $Bi_{19}S_{27}Cl_3$ nanorod, Bi_2S_3 nanoribbon and Bi foil.

Sample	Shell	R_{eff} (Å)	ΔR (Å)	ΔE_0 (eV)	R-factor
Bi foil	Bi-Bi	3.062	0.013	-0.309	0.0239
	Bi-Bi	3.503	-0.047		
Bi_2S_3 nanoribbon	Bi-S	2.628	-0.055	-4.618	0.0236
	Bi-S	2.709	-0.059		
$Bi_{19}S_{27}Cl_3$ nanorod	Bi-S	2.559	-0.125	-9.773	0.0212
	Bi-S	2.642	-0.134		
	Bi-S	3.072	-0.012		
	Bi-Cl	3.546	-0.066		

To further deconvolute the precise coordination environment around bismuth, wavelet transform analysis was performed using Morlet function. Bi_2S_3 displays a single intense feature at R ≈ 2.1 Å and k ≈ 8.6 Å^{-1} which represents the Bi-S shell (**Figure 5.16d**). For the $Bi_{19}S_{27}Cl_3$ sample, the most intense feature was observed at R ≈ 1.8 Å and k ≈ 5.1 Å^{-1} which corresponds to the $Bi^{(3+\delta)-}$-S shell. In addition to that, two additional features with less intensity were observed at R ≈ 2.3 Å and k ≈ 7.2 Å^{-1} as well as R ≈ 2.8 Å and k ≈ 5.9 Å^{-1} which correspond to the $Bi^{(3-\delta)-}$-S shell and Bi-Cl shell, respectively (**Figure 5.16e**, and **5.16f**). This further validates the charge polarized Bi centres present in $Bi_{19}S_{27}Cl_3$. Photocurrent and electrochemical impedance spectroscopy tests were employed for the testing of carrier separation and migration ability, which further confirmed the difference in the CO_2 reduction ability. A stronger photocurrent suggests higher electron–hole separation efficiency whereas, higher charge mobility in a photocatalyst generally results in a smaller arc radius in electrochemical impedance spectroscopy (EIS). $Bi_{19}S_{27}Cl_3$ has higher current density and lower arc diameter of electrochemical impedance spectra, suggesting that it possesses better catalytic performance compared to Bi_2S_3 (**Figure 5.17a**, and **5.17b**). To verify the above observations, time-resolved photoluminescence was performed. The spectra show an exponential decay which was fitted to a biexponential function (**Figure 5.18a**). The decay lifetime values τ_1 and τ_2 obtained from the fitted curve correspond to the non-radiative and radiative lifetime, respectively (**Table 5.2**). For comparison, the lifetime values were calculated for Bi_2S_3 as well.
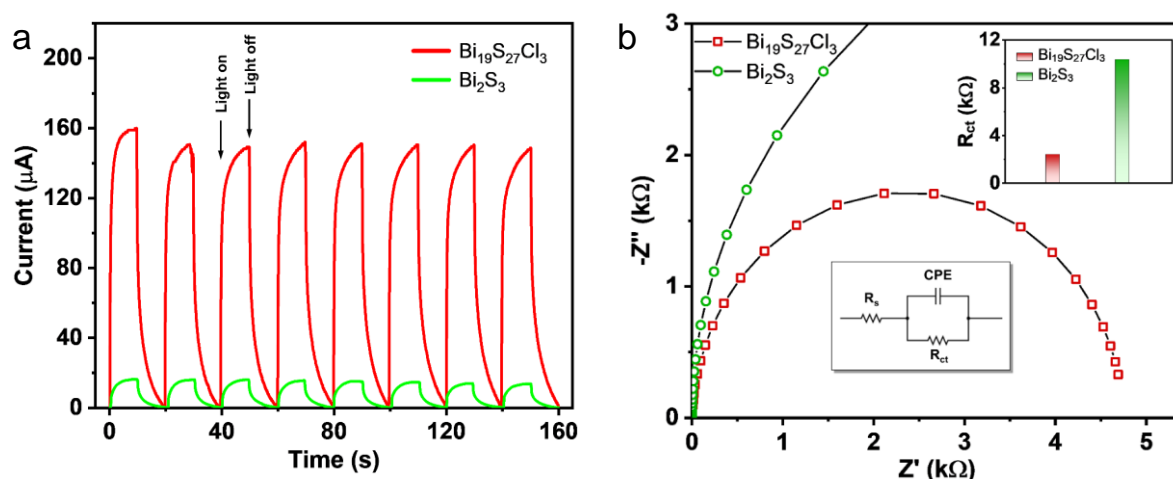
Figure 5.17. (a) Transient photocurrent response of $Bi_{19}S_{27}Cl_3$ and Bi_2S_3 at a bias voltage of 0.2 V vs. Ag/AgCl. The spectra were recorded under sequential illumination condition with an interval of 10 s on/off switch. The plot suggests that $Bi_{19}S_{27}Cl_3$ have better charge separation efficiency compared to Bi_2S_3. **(b)** Electrochemical impedance spectra of $Bi_{19}S_{27}Cl_3$ and Bi_2S_3 in 0.1 M K_2SO_4 solution. R_{ct} is calculated from the radius of the half circle.

Higher radiative lifetime in case of $Bi_{19}S_{27}Cl_3$ means better photogenerated electron-hole separation. The presence of intrinsic electric field induced by the charge polarized metal centres leads to better stabilization of electron-hole pair and thus increase the decay lifetime. In addition to that, the greater amplitude of τ_2 for $Bi_{19}S_{27}Cl_3$ also suggests better quantum efficiency of the catalyst.[54]Furthermore, because the reaction was performed in aqueous medium, the interaction between the catalytic surface and water molecules or in other words hydrophilicity of the catalysts were measured. Smaller water contact angle for $Bi_{19}S_{27}Cl_3$ implies better hydrophilicity of $Bi_{19}S_{27}Cl_3$ compared to Bi_2S_3 (**Figure 5.18b,** and **5.18c**). This could be due to the intrinsic charge polarization in $Bi_{19}S_{27}Cl_3$ which leads to better interaction with polar water molecules. Simultaneous availability of water dissolved CO_2 as well as protons on the surface of $Bi_{19}S_{27}Cl_3$ assist the proton coupled CO_2 reduction reaction.[55] All these studies strongly prove that the presence of charge polarized centres and hence superior catalytic activity of $Bi_{19}S_{27}Cl_3$.

Table 5.2. τ values obtained from the fitted bi-exponential curve.

	$Bi_{19}S_{27}Cl_3$				Bi_2S_3		
τ_1	1.134 ns	B_1	88.34%	τ_1	1.068 ns	B_1	93.12%
τ_2	6.425 ns	B_2	11.64%	τ_2	4.298 ns	B_2	6.88%
Average τ		3.39 ns		**Average τ**		1.81 ns	

Figure 5.18. (**a**) Time resolved photoluminescence spectra of $Bi_{19}S_{27}Cl_3$ and Bi_2S_3. The decay kinetics is fitted with bi-exponential function. The intensity was calculated by taking the logarithm value of counts. Water contact angles of (**b**) $Bi_{19}S_{27}Cl_3$, and (**c**) Bi_2S_3. γ_{VL}, γ_{SV} and γ_{SL} are the liquid−vapor, solid−vapor, and solid−liquid interfacial tensions, respectively. The equilibrium contact angle depends on these three different interfacial tensions. The water contact angle is much smaller in case of $Bi_{19}S_{27}Cl_3$ compared to Bi_2S_3. The smaller contact angle means higher surface energy of the surface and hence higher solid-liquid interfacial tension between water and $Bi_{19}S_{27}Cl_3$. This translates to better hydrophilicity of $Bi_{19}S_{27}Cl_3$ and the dissolved CO_2 and H^+ ions will be better available on the catalyst surface of $Bi_{19}S_{27}Cl_3$. (**d**) In-situ FTIR spectra for co-adsorption of a mixture of CO_2 and H_2O vapour on the $Bi_{19}S_{27}Cl_3$ catalyst for the detection of intermediate species (900 cm^{-1} – 2200 cm^{-1}).

CO₂ to ethanol mechanistic pathway: Now we investigate how these charge polarized bismuth centres in $Bi_{19}S_{27}Cl_3$ facilitate the C-C coupling reaction during photocatalytic CO_2 reduction. *In situ* Fourier-transform Infrared Spectroscopy (FTIR) was employed to detect the active intermediate species and the reduction pathway during photocatalytic CO_2 reduction. The measurement was done from 0 to 30 minutes and spectra were collected after an interval of 2 minutes. As can be seen from **Figures 5.18d**, and **Figure 5.19**, with increasing irradiation

time new bands have appeared and evolved monotonously in the *in-situ* FTIR spectra. The peaks observed at 1354 cm^{-1} and 1467 cm^{-1} can be attributed to the asymmetric vibration mode of CO_3* and symmetric stretching of HCO_3*, respectively.[56] These are the initial intermediates formed from the reaction of gaseous CO_2 and water vapor. Additionally, the newly appeared infrared peak at 1609 cm^{-1} can be attributed to the absorbed *COOH group, which is a crucial intermediate during CO_2 reduction reaction. Most importantly, the absorption bands observed at 986 cm^{-1} and 1112 cm^{-1} can be assigned to the characteristic peaks of *COH and *OCH_3 groups. Interestingly, single and double bonded *CO intermediate are also observed in the *in situ* FTIR spectra at 2049 cm^{-1} and 1703 cm^{-1}, respectively.[66] These are the active intermediates which take part in C-C coupling reaction during the photoreduction of CO_2 to ethanol. Moreover, the peak at 1234 cm^{-1} could possibly be due to the formation of OCCOH* intermediate which might have formed from the coupling of *CO and *COH intermediate.[67] Because the adjacent Bi centres in $Bi_{19}S_{27}Cl_3$ have asymmetric charge redistribution, they stabilize different intermediates (*CO and *COH) which facilitate the CH_3CH_2OH formation by reducing the activation energy barrier of CO* and COH* coupling for the formation of 1st C-C coupled intermediate (OC-COH*).
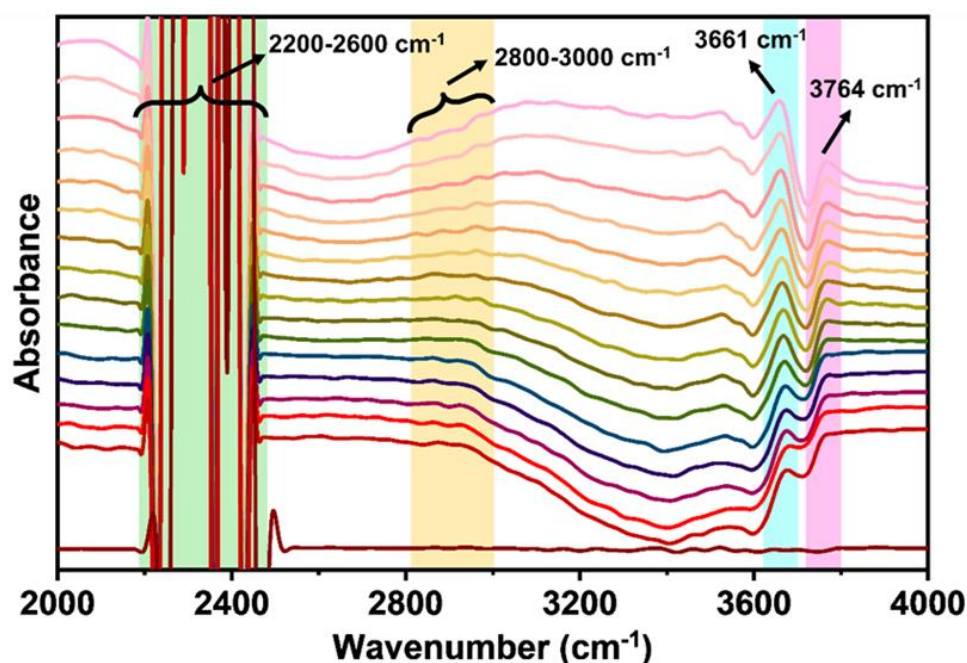
Figure 5.19. In-situ FTIR analysis. In-situ FTIR spectra for co-adsorption of a mixture of CO_2 and H_2O vapour on the $Bi_{19}S_{27}Cl_3$ catalyst in the range of 2000 cm^{-1} – 4000 cm^{-1}. The high intense peak ranging from 2200 cm^{-1} - 2600 cm^{-1} arises due to the gaseous CO_2 molecules whereas the IR peaks at 3661 cm^{-1} and 3764 cm^{-1} can be indexed to the hydroxyl group of *COOH intermediate. The small peaks in the range of 2800 cm^{-1} - 3000 cm^{-1} can be attributed to the C-H vibrations of different intermediates.

To substantiate this mechanistic proposition, theoretical calculations were performed for $Bi_{19}S_{27}Cl_3$ and Bi_2S_3. In order to unwrap the trend of intermediate species adsorption over different Bi sites (3 Bi sites of $B_{19}S_{27}Cl_3$ (Bi1, Bi2, Bi3) and 2 Bi sites of Bi_2S_3 (Bi1 and Bi2)), p-band centre of different Bi centres were calculated (**Figure 5.20a**). The band centre model proposed by Norskov *et. al* has been used extensively to understand the role of electrons in the bonding with the adsorbent.[68] According to this model, band centre of the adsorbent being close in energy with respect to the Fermi energy enhances the bond stability with adsorbate, having more electrons in the bonding state and less electron in the antibonding state. Therefore, having most suitable p-band centre, Bi1 of $Bi_{19}S_{27}Cl_3$ shows relatively stronger adsorbent and adsorbate interactions compared to other Bi Centres. However, this model does not explain the reason behind the better stability of adsorbent over Bi2 in comparison with other remaining sites, though having the least suitable p-band positions.
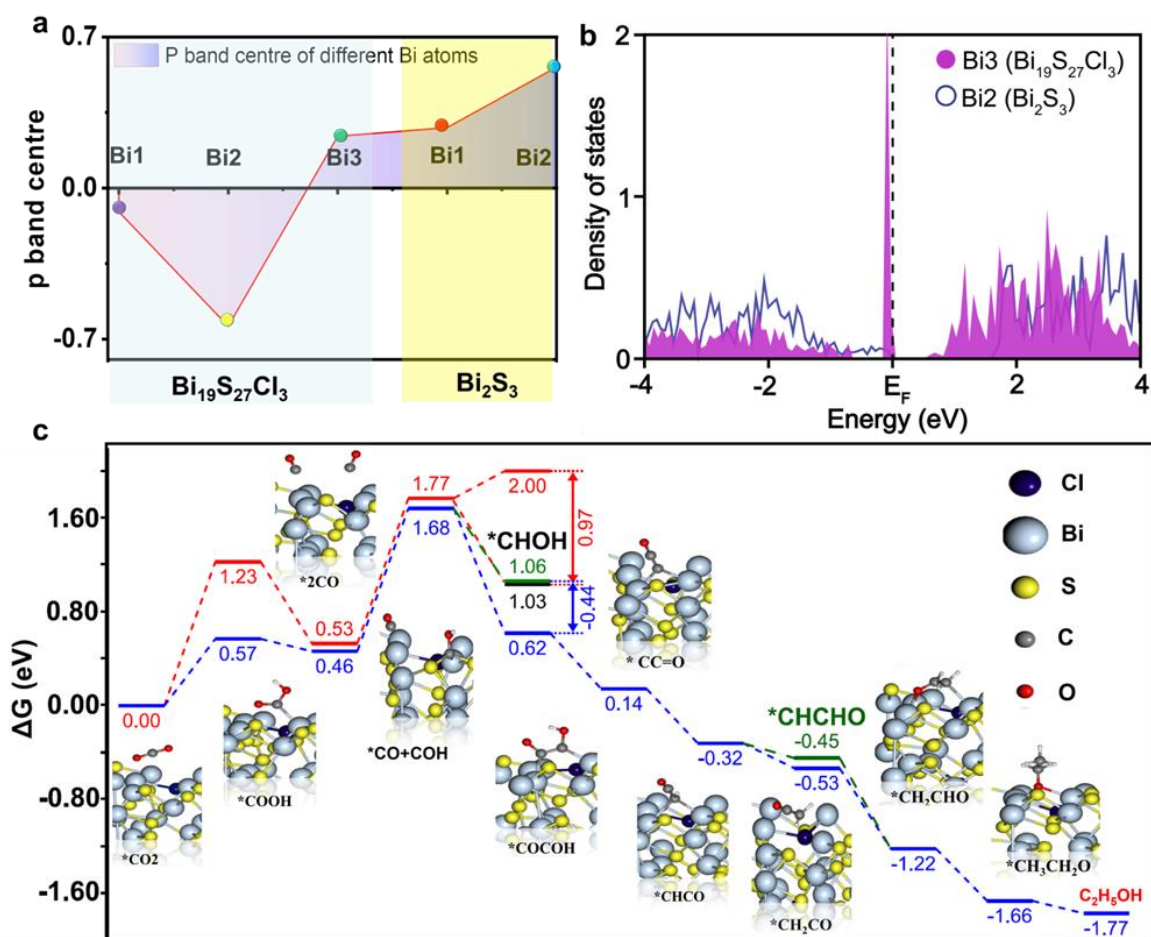
Figure 5.20. Theoretical calculation. **(a)** p band centres of different Bi atoms in $Bi_{19}S_{27}Cl_3$ and Bi_2S_3. **(b)** Partial density of p-states forms Bi3 (in $Bi_{19}S_{27}Cl_3$) and Bi2 (in Bi_2S_3). Plausible reaction pathway for the formation of CH_3CH_2OH from the photoreduction of CO_2. **(c)** Free energy diagrams of CO_2 photoreduction to C_2H_5OH for the $Bi_{19}S_{27}Cl_3$ Vs. C1 product formation on Bi_2S_3 surface.

However, this model does not explain the reason behind the better stability of adsorbent over Bi2 in comparison with other remaining sites, though having the least suitable p-band position. Hence, further extending this, the exact position of the p-band centres was also considered. If the p-band centre lies below Fermi level, then the band is more than half-filled and can donate electrons easily. Whereas, if the p-band centre lies above Fermi level, the band is less than half-filled and cannot donate electrons easily. Therefore, having p-band centre below the fermi level Bi1 and Bi2 in $Bi_{19}S_{27}Cl_3$ show better adsorption capability. However, Bi1 is still a better active site in comparison with Bi2. This is because the p-band centre of Bi1 is closer to the fermi level. Bi1 and Bi2 in Bi_2S_3 show weak adsorption as their p-band centre is far from the fermi level, as well as above fermi level. Bi3 (in $Bi_{19}S_{27}Cl_3$) behaves as a considerable active site though having unfavourable p-band centre comparable with Bi2 (in Bi_2S_3). This can be explained by the partial density of p-states of the corresponding Bi sites (**Figure 5.20b**). Bi3 in $Bi_{19}S_{27}Cl_3$ dominated with large number of filled p-states, which are localized near the fermi level and can easily donate electrons to adsorbent. However, the p-states of Bi2 (in Bi_2S_3) are totally dispersed (**Figure 5.20b**). Therefore, the intermediates of CO_2 reduction are better activated over charge polarise Bi centres of $Bi_{19}S_{27}Cl_3$ surface compared to Bi_2S_3 by transferring the electrons from p-band centre. Furthermore, to validate better C-C coupling reaction over $Bi_{19}S_{27}Cl_3$ surface, we performed Gibbs free energy calculations considering different possible reaction pathways (**Table 5.3**).

Being a common intermediate for both the catalysts, we first examined the formation of CO* on $Bi_{19}S_{27}Cl_3$ compared to Bi_2S_3 because of very high energy barrier of COOH* formation over Bi_2S_3 surface. The charge polarization significantly reduces the activation energy barrier for the CO_2 hydrogenation on $Bi_{19}S_{27}Cl_3$ due to better charge transfer from p-band. After the formation of CO* intermediate two CO* are adsorbed at two different sites i.e. Bi1-Bi2 and Bi1-Bi1 bridge sites. Here, worth mentioning the fact that, first hydrogenation of CO* intermediate is very crucial for the formation of COH* intermediate which was also tracked from in-situ FTIR. However, this short-lived intermediate immediately gets coupled with nearby CO* and form OCCOH* which is regarded as the most important step of C-C coupling reaction in CO_2 reduction. As depicted in **Figure 5.20c** the energy barrier of COH* formation is uphill on both $Bi_{19}S_{27}Cl_3$ and Bi_2S_3 surface by 1.22 eV and 1.24 eV respectively suggesting it is the rate-determining step. However, upon coupling with CO* in the next step, the OCCOH* (the presence of it was confirmed from in-situ FTIR also) obtained remarkable stability over $Bi_{19}S_{27}Cl_3$ surface leading to the favourable C-C coupling reaction over polarise

Bi centres (**Figure 5.21a,** and **5.21b**). Contextually, the involvement of differentially charged Bi centres in the course of C-C coupling process was also understood during calculation. Initially, CO* were placed on Bi1, Bi2 and Bi3 of $Bi_{19}S_{27}Cl_3$ then C-C bond of OCCOH* was placed along with via COOH* intermediate, and it can be seen in the energy profile that CO* formation is easy the bridging bonds of Bi1-Bi2 (**Figure 5.22a**).

Table 5.3. Contribution to the free energy from zero-point energy correction and entropy. (Only vibrational entropy is considered for adsorbed system).

Species	ZPE (eV)	TS (eV)	ZPE - TS
H_2	0.27	0.42	-0.15
CO_2	0.31	0.65	-0.34
CO	0.14	0.67	-0.53
H_2O	0.58	0.65	-0.07
CH_3CH_2OH	2.18	2.81	-0.53
*CO_2	0.30	0.09	0.21
*COOH	0.69	0.19	0.50
*CO	0.21	0.14	0.07
*COH	0.46	0.24	0.22
*CHO	0.34	0.10	0.24
*CH_2O	0.65	0.17	0.48
*OCCOH	0.66	0.29	0.37
*HOCCOH	0.90	0.31	0.59
*CCO	0.41	0.16	0.25
*CHCO	0.68	0.25	0.48
*CH_2CO	0.98	0.14	0.84
*CH_2CHO	1.28	0.21	1.07
*CH_3CH_2O	1.91	0.26	1.65
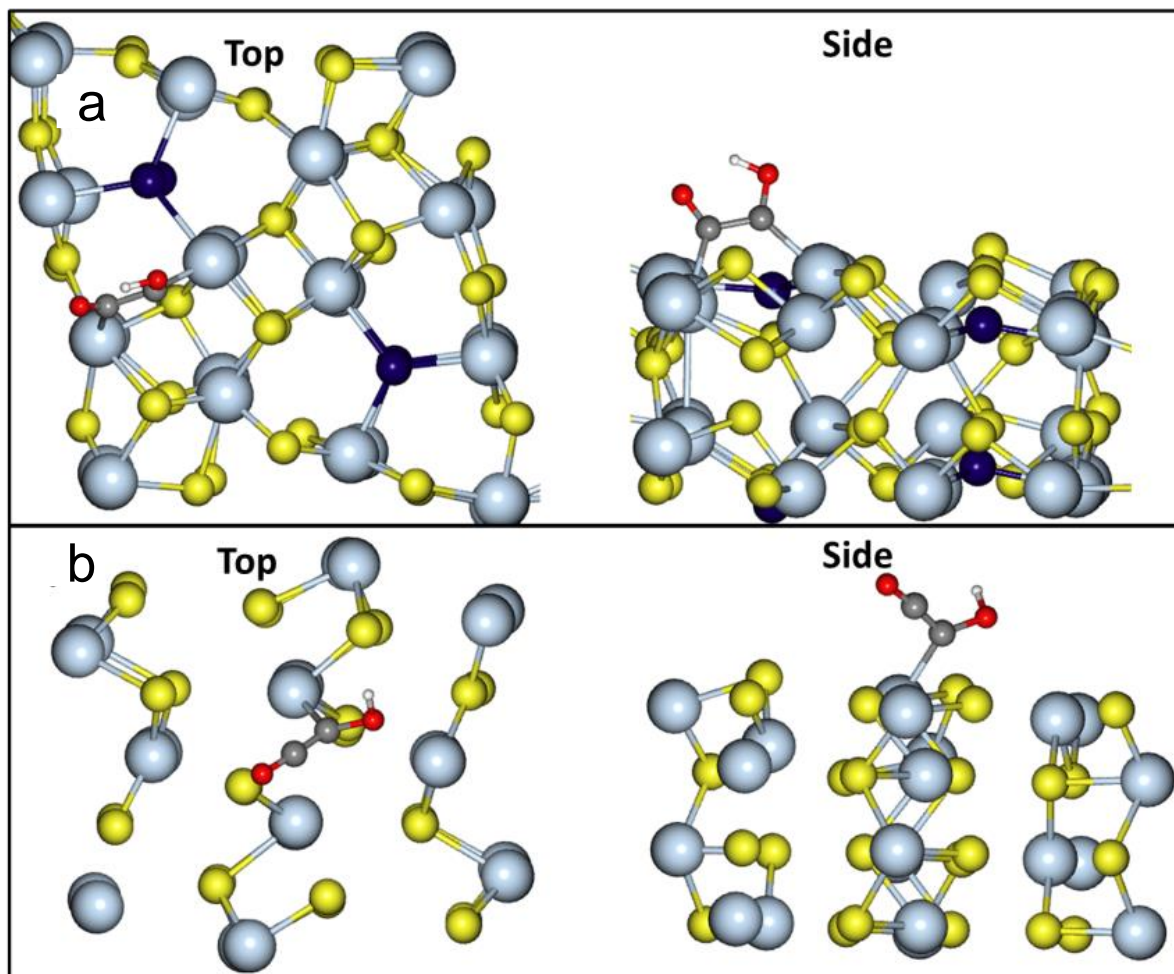
Figure 5.21. Top and Side view of **(a)** $Bi_{19}S_{27}Cl_3$, and **(b)** Bi_2S_3 with the coupled intermediate (OCCOH*).

However, the adsorbed CO* over Bi3 (in $Bi_{19}S_{27}Cl_3$) was unable to undergo any C-C coupling reaction because of the higher distance between Bi1 and Bi3 centres compared to that of Bi1 and Bi2 in $Bi_{19}S_{27}Cl_3$. The lower binding energy for CO* adsorption as well as the position of p-band centre for Bi3 (in $Bi_{19}S_{27}Cl_3$) also restricted further protonation of the intermediate. Hence, CO* desorption from Bi3 centre resulted in gaseous CO production by $Bi_{19}S_{27}Cl_3$ catalyst. On the other hand, the OCCOH* on Bi_2S_3 surface suffered further dis- stabilisation because of large Bi-Bi distance and CO*, COH* repulsion as in case of Bi_2S_3 the there are no polarise Bi centres. Therefore, no C2 product was obtained by B_2S_3 photocatalyst. Further investigation on COH* protonation for the formation of COH_2* over $Bi_{19}S_{27}Cl_3$ and Bi_2S_3 surface showed that the energy of COH_2* formation is similar for both. Interestingly, COH_2* is more stable compared to OCCOH* on Bi_2S_3 and less stable for $Bi_{19}S_{27}Cl_3$. Therefore, in the case of $Bi_{19}S_{27}Cl_3$ catalyst C2 products dominated over C1 products and Bi_2S_3 only produced C1 molecules. In the next step, OCCOH* got further protonation followed by water desorption

and C_2O^* intermediate was formed. Interestingly, the ΔG values of all other intermediates of CO_2 to ethanol formation are negative and monotonously downhill.

Therefore, the reaction became extremely favourable. Stepwise proton-coupled electron transfer on C_2O^* intermediate finally resulted in the formation of ethanol. Based on the above *in situ* FTIR analysis and theoretical calculation stepwise ethanol formation mechanism over $Bi_{19}S_{27}Cl_3$ photocatalyst was schematically presented in **Figure 5.22b.** An attempt of understanding CO_2 to ethanol formation mechanism via in-situ technique and theoretical study has been done for electrochemical route. However, this attempt is completely novel for photochemical route. Most importantly, the concept of charge polarization has been implicitly exploited for C-C coupling process in CO_2 reduction reaction. This approach could enable the $Bi_{19}S_{27}Cl_3$ catalyst to reach 85% ethanol selectivity along with high CO_2 reduction activity. This low-cost material can easily be scaled up and it is anticipated that this proposed concept applicable for other charge polarized molecules like spinal for multi carbon product formation.
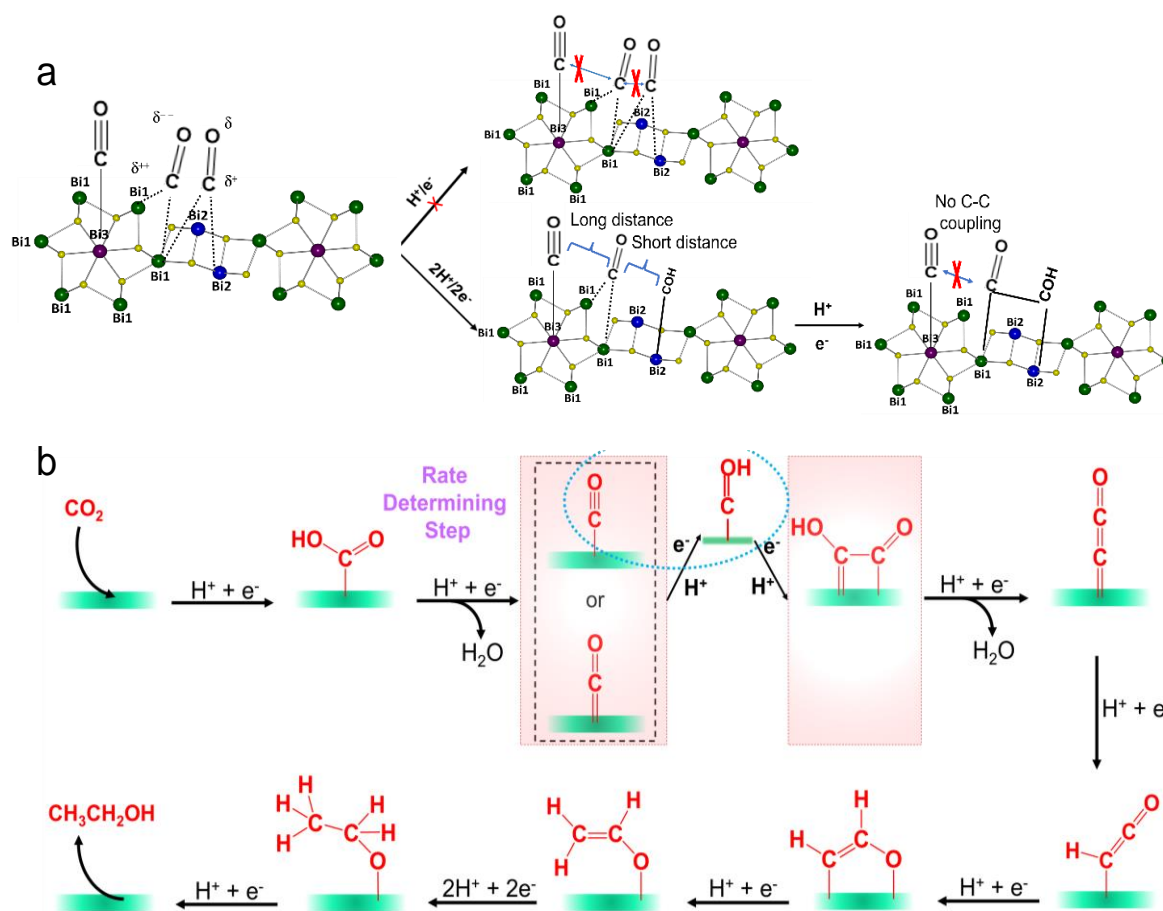
Figure 5.22. (a) C-C coupling. Plausible C-C coupling reactions between the CO intermediates adsorbed on different Bi centres. **(b)** Schematic representation of stepwise reaction pathway for the formation of CH_3CH_2OH from the photoreduction of CO_2 on $Bi_{19}S_{27}Cl_3$ photocatalyst.

5.6. Conclusions

In conclusion, to induce C-C coupling reaction during photochemical CO_2 reduction, we have chosen $Bi_{19}S_{27}Cl_3$ catalyst with intrinsic charge polarized Bi centres. The asymmetric charge distribution over different bismuth centres were confirmed from crystal structure, XPS analysis, XAS analysis and well corroborated by Bader charge distributions from the DFT calculation. A combination of experimental studies and theoretical calculations demonstrated that the charge polarized Bi centres are capable of performing C-C coupling reaction due to lower activation energy barrier. In comparison, Bi_2S_3 despite having similar light absorption property and band edge position could not perform C-C coupling reaction due to the lack of charge polarized centres. As a result, $Bi_{19}S_{27}Cl_3$ can selectively reduce CO_2 to CH_3CH_2OH with a yield of 109 µmol g^{-1} after 21 hours. Remarkably the selectivity towards CH_3CH_2OH formation can reach up to 85% by modifying the reaction conditions. In comparison to the of bismuth based photocatalysts reducing CO_2 to CH_3CH_2OH, $Bi_{19}S_{27}Cl_3$ showed highest ever ethanol selectivity (**Table 5.4**). For C-C coupling reaction, two suitably arranged metal centres are required. As evident from the earlier reports, this has been thus far achieved by multicomponent system (**Table 5.5,** and **5.6**). However, for the first-time we report single compartment catalyst for C-C coupling reaction. This work thus showcases the importance of charge polarized metal centres in photoinduced C-C coupling reactions, which can be generally adapted as a key material design strategy for tailoring higher carbon product pathways across various catalytic systems.

Table 5.4. Benchmarking of bismuth based photocatalysts reducing CO_2 to CH_3CH_2OH in CO_2 saturated aqueous solution.

S. No.	Catalyst	Product	Yield (µmol g^{-1} h^{-1})	Ethanol Selectivity	Stability test (hours)	References
1	$Bi_{19}S_{27}Cl_3$ nanorods	CH_3CH_2OH CH_3OH CH_4 CO	5.2 1.2 0.4 0.5	**85%**	**60**	This work
2	Red P/Bi_2MoO_6[13]	CH_3CH_2OH CH_3OH HCOOH CH_4	51.8 31.2 20.1 11.3	66%	30	Energy Environ. Sci. 15 (2022) 1967-1976
3	MoS_2/Bi_2WO_6 nanocomposites[57]	CH_3CH_2OH CH_3OH	9.15 9.18	66%	16	Appl. Surf. Sci. 403 (2017) 230–239

4	WS$_2$ quantum dots seeding in Bi$_2$S$_3$ nanotubes[58]	CH$_3$CH$_2$OH CH$_3$OH	6.95 9.55	59%	20	Chem. Eng. J. 389 (2020) 123430-123437
5	Bi$_2$MoO$_6$ quantum dots *in situ* grown on reduced graphene oxide layers[59]	CH$_3$CH$_2$OH CH$_3$OH	14.37 21.2	57%	20	ACS Appl. Mater. Interfaces 12 (2020) 25861−25874
6	Nanocrystalline BiOCl[60]	CH$_3$CH$_2$OH, CH$_3$OH CH$_4$	1.87×10^{-2} 1.57×10^{-2} 1.87×10^{-2}	48%	43	Catalysts 10 (2020) 998-1004
7	Conducting polymers modified Bi$_2$WO$_6$ microspheres[61]	CH$_3$CH$_2$OH CH$_3$OH	5.13 14.13	42%	20	Appl. Surf. Sci. 356 (2015) 173–180
8	Bi@Bi$_2$MoO$_6$[62]	CH$_3$CH$_2$OH CH$_3$OH CO	6 8 0.1	42.5%	24	ChemSusChem 14 (2021) 3293-3302
9	Pt and N co-doped hollow hierarchical BiOCl[63]	CH$_3$CH$_2$OH CH$_3$OH	14.15 41.08	41%	32	Appl. Surf. Sci. 502 (2020) 144083-144091
10	Single unit cell o-BiVO$_4$ layers[64]	CH$_3$OH	398.3	No C2 product 0%	96	J. Am. Chem. Soc. 139 (2017) 3438−3445
11	Bi$_2$S$_3$ nanoribbons[29]	CH$_3$OH	32	0%	30	Appl. Surf. Sci. 394 (2017) 364–370
12	Bi$_2$S$_3$/CdS photocatalyst[65]	CH$_3$OH	122.6	0%	5	J. Nat. Gas Chem. 20 (2011) 413–417

Table 5.5. Literature reports of CO$_2$ photoreduction to ethanol in aqueous solution.

S. No.	Catalyst	Product	Yield (µmolg^{-1}h^{-1})	Ethanol Selectivity	Reaction condition
1	Bi$_{19}$S$_{27}$Cl$_3$ nanorods	CH$_3$CH$_2$OH CH$_3$OH CH$_4$ CO	5.2 1.2 0.4 0.5	**85%**	Water
2	Red P/Bi$_2$MoO$_6$[69]	CH$_3$CH$_2$OH CH$_3$OH HCOOH CH$_4$	51.8 31.2 20.1 11.3	**66%**	Water
3	AgBr–NG–g-C$_3$N$_4$[70]	CH$_3$CH$_2$OH CH$_3$OH	51 21	**83%**	0.1M NaHCO$_3$ solution

4	Cu^{2+} doped TiO_2[71]	CH_3CH_2OH CH_3OH	47 24	**80%**	Vapor phase
5	Red Ag/AgCl[72]	CH_3CH_2OH CH_3OH	44.6 29.2	**75%**	0.1M NaHCO₃ solution
6	ZnO/g-C_3N_4[73]	CH_3CH_2OH CH_3OH CH_4 CO	2.5 19.0 5.4 38.7	**11%**	Water
7	$LaVO_4$[74]	CH_3CH_2OH CH_3CHO CH_3OH	12.7 negligible 1.20	**95%**	CO₂-saturated NaHCO₃ solution
8	STO/Cu@Ni/TiN[75]	CH_3CH_2OH CH_3OH HCOOH C_2H_4 CO	21.3	**79.3%**	Water
9	Bi_4TaO_8Cl/Bi[76]	CH_3CH_2OH CH_3OH	5.11 2.34	**92% (CH_3CH_2OH + CH_3OH)**	Water (Continuous flow)
10	Bi_2MoO_6/PVP[77]	CH_3CH_2OH CH_3OH	4.7 6.2	**60%**	Water

Table 5.6. Literature reports of CO₂ to liquid C2 products other than ethanol in aqueous solution.

S. No.	Catalyst	Product	Yield (μmolg^{-1}h^{-1})	Reaction condition
1	Carbon-doped SnS_2[78]	CH_3CHO	14	Vapor phase
2	O-vacancy-rich Zn_2GeO_4[79]	CH_3COOH HCOOH CO	12.7 12.4 13.2	Water
3	O-vacancy-rich $WO_3 \cdot 0.33H_2O$[56]	CH_3COOH HCOOH CO	9.4 15 1.12	Water
4	*d*-UiO-66/MoS_2[80]	CH_3COOH CH_3OH CH_4 CO	39.0 Trace Trace Trace	Vapor phase

5.7. References

1. Sen, R.; Goeppert, A.; Kar, S.; Prakash, G. S., Hydroxide based integrated CO₂ capture from air and conversion to methanol. *J. Am. Chem. Soc.* **2020,** *142* , 4544-4549.

2. Roy, S.; Cherevotan, A.; Peter, S. C., Thermochemical CO₂ Hydrogenation to Single Carbon Products: Scientific and Technological Challenges. *ACS Energy Lett.* **2018,** *3*, 1938-1966.

3. Zhou, Y.; Wang, Z.; Huang, L.; Zaman, S.; Lei, K.; Yue, T.; Li, Z. a.; You, B.; Xia, B. Y., Engineering 2D photocatalysts toward carbon dioxide reduction. *Adv. Energy Mater.* **2021,** *11*, 2003159.

4. Peter, S. C., Reduction of CO_2 to Chemicals and Fuels: A Solution to Global Warming and Energy Crisis. *ACS Energy Lett.* **2018,** *3*, 1557-1561.

5. Yu, H.; Haviv, E.; Neumann, R., Visible-Light Photochemical Reduction of CO_2 to CO Coupled to Hydrocarbon Dehydrogenation. *Angew. Chem.* **2020,** *132*, 6278-6282.

6. Cherevotan, A.; Raj, J.; Dheer, L.; Roy, S.; Sarkar, S.; Das, R.; Vinod, C. P.; Xu, S.; Wells, P.; Waghmare, U. V., Operando Generated Ordered Heterogeneous Catalyst for the Selective Conversion of CO_2 to Methanol. *ACS Energy Lett.* **2021,** *6*, 509-516.

7. Bagchi, D.; Raj, J.; Singh, A. K.; Cherevotan, A.; Roy, S.; Manoj, K. S.; Vinod, C. P.; Peter, S. C., Structure-Tailored Surface Oxide on Cu–Ga Intermetallics Enhances CO_2 Reduction Selectivity to Methanol at Ultralow Potential. *Adv. Mater.* **2022,** *34*, 2109426.

8. Zhang, T.; Li, W.; Huang, K.; Guo, H.; Li, Z.; Fang, Y.; Yadav, R. M.; Shanov, V.; Ajayan, P. M.; Wang, L.; Lian, C.; Wu, J., Regulation of Functional Groups on Graphene Quantum Dots Directs Selective CO_2 to CH_4 Conversion. *Nat. Commun.* **2021,** *12*, 5265.

9. Chen, C.; Kotyk, J. F. K.; Sheehan, S. W., Progress toward Commercial Application of Electrochemical Carbon Dioxide Reduction. *Chem* **2018,** *4*, 2571-2586.

10. Goud, D.; Gupta, R.; Maligal-Ganesh, R.; Peter, S. C., Review of Catalyst Design and Mechanistic Studies for the Production of Olefins from Anthropogenic CO_2. *ACS Catal.* **2020,** *10*, 14258-14282.

11. Dagle, R. A.; Winkelman, A. D.; Ramasamy, K. K.; Lebarbier Dagle, V.; Weber, R. S., Ethanol as a Renewable Building Block for Fuels and Chemicals. *Ind. Eng. Chem. Res.* **2020,** *59*, 4843-4853.

12. Liu, Y.; Zhang, Y.; Cheng, K.; Quan, X.; Fan, X.; Su, Y.; Chen, S.; Zhao, H.; Zhang, Y.; Yu, H., Selective Electrochemical Reduction of Carbon Dioxide to Ethanol on a Boron- and Nitrogen-Co-Doped Nanodiamond. *Angew. Chem.* **2017,** *129*, 15813-15817.

13. Das, R.; Das, K.; Ray, B.; Prabhakaran, V.; Peter, S. C., Green Transformation of CO_2 to Ethanol using Water and Sunlight by Cooperative Endeavour of Naturally Abundant Red Phosphorus and Bi_2MoO_6. *Energy Environ. Sci.* **2022**, 15, 1967-1976.

14. Torelli, D. A.; Francis, S. A.; Crompton, J. C.; Javier, A.; Thompson, J. R.; Brunschwig, B. S.; Soriaga, M. P.; Lewis, N. S., Nickel-Gallium Catalyzed Electrochemical Reduction

of CO_2 to Highly Reduced Products at Low Overpotentials. *ACS Catal.* **2016,** *6*, 2100-2104.

15. Hoang, T. T.; Verma, S.; Ma, S.; Fister, T. T.; Timoshenko, J.; Frenkel, A. I.; Kenis, P. J.; Gewirth, A. A., Nanoporous Copper-Silver Alloys by Additive-Controlled Electrodeposition for the Selective Electroreduction of CO_2 to Ethylene and Ethanol. *J. Am. Chem. Soc.* **2018,** *140*, 5791-5797.

16. Morales-Guio, C. G.; Cave, E. R.; Nitopi, S. A.; Feaster, J. T.; Wang, L.; Kuhl, K. P.; Jackson, A.; Johnson, N. C.; Abram, D. N.; Hatsukade, T., Improved CO_2 Reduction Activity towards C_{2+} Alcohols on a Tandem Gold on Copper Electrocatalyst. *Nat. Catal.* **2018,** *1*, 764-771.

17. Xiao, H.; Goddard, W. A.; Cheng, T.; Liu, Y., Cu Metal Embedded in Oxidized Matrix Catalyst to Promote CO_2 Activation and CO Dimerization for Electrochemical Reduction of CO_2. *Proc. Natl. Acad. Sci.* **2017,** *114*, 6685-6688.

18. Chou, T.-C.; Chang, C.-C.; Yu, H.-L.; Yu, W.-Y.; Dong, C.-L.; Velasco-Vélez, J.-J. s.; Chuang, C.-H.; Chen, L.-C.; Lee, J.-F.; Chen, J.-M., Controlling the Oxidation State of the Cu Electrode and Reaction Intermediates for Electrochemical CO_2 Reduction to Ethylene. *J. Am. Chem. Soc.* **2020,** *142*, 2857-2867.

19. Wang, W.; Deng, C.; Xie, S.; Li, Y.; Zhang, W.; Sheng, H.; Chen, C.; Zhao, J., Photocatalytic C-C Coupling from Carbon Dioxide Reduction on Copper Oxide with Mixed-Valence Copper(I)/Copper(II). *J. Am. Chem. Soc.* **2021,** *143*, 2984-2993.

20. Zhou, Y.; Che, F.; Liu, M.; Zou, C.; Liang, Z.; De Luna, P.; Yuan, H.; Li, J.; Wang, Z.; Xie, H., Dopant-Induced Electron Localization Drives CO_2 Reduction to C_2 Hydrocarbons. *Nat. Chem.* **2018,** *10*, 974-980.

21. Albero, J.; Peng, Y.; García, H., Photocatalytic CO_2 Reduction to C_{2+} Products. *ACS Catal.* **2020,** *10*, 5734-5749.

22. Corby, S.; Rao, R. R.; Steier, L.; Durrant, J. R., The Kinetics of Metal Oxide Photoanodes from Charge Generation to Catalysis. *Nat. Rev. Mater.* **2021**, *6*, 1136-1155.

23. Wang, K.; Lu, J.; Lu, Y.; Lau, C. H.; Zheng, Y.; Fan, X., Unravelling the C-C Coupling in CO_2 Photocatalytic Reduction with H_2O on Au/TiO$_{2-x}$: Combination of Plasmonic Excitation and Oxygen Vacancy. *Appl. Catal., B* **2021**, *292*, 120147.

24. Sorcar, S.; Thompson, J.; Hwang, Y.; Park, Y. H.; Majima, T.; Grimes, C. A.; Durrant, J. R.; In, S.-I., High-Rate Solar-Light Photoconversion of CO_2 to Fuel: Controllable Transformation from C_1 to C_2 Products. *Energy Environ. Sci.* **2018**, *11*, 3183-3193.

25. Das, R.; Sarkar, S.; Kumar, R.; D. Ramarao, S.; Cherevotan, A.; Jasil, M.; Vinod, C. P.; Singh, A. K.; Peter, S. C., Noble-Metal-Free Heterojunction Photocatalyst for Selective CO_2 Reduction to Methane upon Induced Strain Relaxation. *ACS Catal.* **2022,** *12*, 687-697.

26. Kim, W.; Frei, H., Directed Assembly of Cuprous Oxide Nanocatalyst for CO_2 Reduction Coupled to Heterobinuclear $ZrOCo^{II}$ Light Absorber in Mesoporous Silica. *ACS Catal.* **2015,** *5*, 5627-5635.

27. Ran, J.; Jaroniec, M.; Qiao, S. Z., Cocatalysts in Semiconductor-Based Photocatalytic CO_2 Reduction: Achievements, Challenges, and Opportunities. *Adv. Mater.* **2018,** *30*, 1704649.

28. Chen, X.; Li, Q.; Li, J.; Chen, J.; Jia, H., Modulating Charge Separation via In Situ Hydrothermal Assembly of Low Content Bi_2S_3 into UiO-66 for Efficient Photothermocatalytic CO_2 Reduction. *Appl. Catal., B* **2020,** *270*, 118915.

29. Jin, J.; He, T., Facile Synthesis of Bi_2S_3 Nanoribbons for Photocatalytic Reduction of CO_2 into CH_3OH. *Appl. Surf. Sci.* **2017,** *394*, 364-370.

30. Ma, Z.; Li, P.; Ye, L.; Zhou, Y.; Su, F.; Ding, C.; Xie, H.; Bai, Y.; Wong, P. K., Oxygen Vacancies Induced Exciton Dissociation of Flexible BiOCl Nanosheets for Effective Photocatalytic CO_2 Conversion. *J. Mater. Chem. A* **2017,** *5*, 24995-25004.

31. Tao, X.; Wang, Y.; Qu, J.; Zhao, Y.; Li, R.; Li, C., Achieving Selective Photocatalytic CO_2 Reduction to CO on Bismuth Tantalum Oxyhalogen Photocatalyst. *J. Mater. Chem. A* **2021**. *9*, 19631-19636.

32. Wu, Y.; Pan, H.; Zhou, X.; Li, M.; Zhou, B.; Yang, C.; Zhang, W.-H.; Jie, J.; Li, C., Shape and Composition Control of $Bi_{19}S_{27}(Br_{3−x},I_x)$ Alloyed Nanowires: The Role of Metal Ions. *Chem. Sci.* **2015,** *6*, 4615-4622.

33. Liu, D.; Chen, D.; Li, N.; Xu, Q.; Li, H.; He, J.; Lu, J., Surface Engineering of g-C_3N_4 by Stacked BiOBr Sheets Rich in Oxygen Vacancies for Boosting Photocatalytic Performance. *Angew. Chem.* **2020,** *132*, 4549-4554.

34. Chen, J.; Xin, F.; Niu, H.; Mao, C.-J.; Song, J.-M., Photocatalytic Reduction of CO_2 with Methanol over Bi_2S_3-$ZnIn_2S_4$ Nanocomposites. *Mater. Lett.* **2017,** *198*, 1-3.

35. Li, X.; Liu, H.; Luo, D.; Li, J.; Huang, Y.; Li, H.; Fang, Y.; Xu, Y.; Zhu, L., Adsorption of CO_2 on Heterostructure $CdS(Bi_2S_3)$/TiO_2 Nanotube Photocatalysts and Their Photocatalytic Activities in the Reduction of CO_2 to Methanol under Visible Light Irradiation. *Chem. Eng. J.* **2012,** *180*, 151-158.

36. Wu, Z.; Jiang, Y.; Xiong, X.; Ding, S.; Shi, Y.; Liu, X.; Liu, Y.; Huang, Z.; Hu, J., Synthesis and Characterization of Single-Crystalline $Bi_{19}Cl_3S_{27}$ Nanorods. *Catal. Sci. Technol.* **2017,** *7*, 3464-3468.

37. Kresse, G.; Hafner, J., Ab Initio Molecular Dynamics for Liquid Metals. *Phys. Rev. B* **1993,** *47*, 558-561.

38. Kresse, G.; Joubert, D., From Ultrasoft Pseudopotentials to the Projector Augmented-Wave Method. *Phys. Rev. B* **1999,** *59*, 1758-1775.

39. Perdew, J. P.; Burke, K.; Ernzerhof, M., Generalized Gradient Approximation Made Simple. *Phys. Rev. Lett.* **1996,** *77*, 3865-3868.

40. Giannozzi, P.; Baroni, S.; Bonini, N.; Calandra, M.; Car, R.; Cavazzoni, C.; Ceresoli, D.; Chiarotti, G. L.; Cococcioni, M.; Dabo, I.; Dal Corso, A.; de Gironcoli, S.; Fabris, S.; Fratesi, G.; Gebauer, R.; Gerstmann, U.; Gougoussis, C.; Kokalj, A.; Lazzeri, M.; Martin-Samos, L.; Marzari, N.; Mauri, F.; Mazzarello, R.; Paolini, S.; Pasquarello, A.; Paulatto, L.; Sbraccia, C.; Scandolo, S.; Sclauzero, G.; Seitsonen, A. P.; Smogunov, A.; Umari, P.; Wentzcovitch, R. M., Quantum Espresso: a Modular and Open-Source Software Project for Quantum Simulations of Materials. *J. Phys. Condens. Matter* **2009,** *21*, 395502.

41. Vanderbilt, D., Soft Self-Consistent Pseudopotentials in a Generalized Eigenvalue Formalism. *Phys. Rev. B* **1990,** *41*, 7892-7895.

42. Grimme, S.; Antony, J.; Ehrlich, S.; Krieg, H., A Consistent and Accurate Ab Initio parametrization of density functional dispersion correction (DFT-D) for the 94 elements H-Pu. *J. Chem. Phys.* **2010,** *132*, 154104.

43. Nørskov, J. K.; Rossmeisl, J.; Logadottir, A.; Lindqvist, L.; Kitchin, J. R.; Bligaard, T.; Jónsson, H., Origin of the Overpotential for Oxygen Reduction at a Fuel-Cell Cathode. *J. Phys. Chem. B* **2004,** *108*, 17886-17892.

44. Afeefy, H. J. N. C. W., Neutral Thermochemical Data. **2005**.

45. Zhu, L.; Xie, Y.; Zheng, X.; Yin, X.; Tian, X., Oxidative Catalytic Cracking of n-Butane to Lower Alkenes over Layered BiOCl Catalyst. *Inorg. Chem.* **2002,** *41*, 4560-4566.

46. Shi, X.; Yang, J.; Bai, S.; Yang, J.; Wang, H.; Chi, M.; Salvador, J. R.; Zhang, W.; Chen, L.; Wong-Ng, W., On the Design of High-Efficiency Thermoelectric Clathrates through a Systematic Cross-Substitution of Framework Elements. *Adv. Funct. Mater.* **2010,** *20*, 755-763.

47. Xu, H.; Wang, Y.; Dong, X.; Zheng, N.; Ma, H.; Zhang, X., Fabrication of In_2O_3/In_2S_3 Microsphere Heterostructures for Efficient and Stable Photocatalytic Nitrogen Fixation. *Appl. Catal., B* **2019,** *257*, 117932.

48. Das, R.; Chakraborty, S.; Peter, S. C., Systematic Assessment of Solvent Selection in Photocatalytic CO_2 Reduction. *ACS Energy Lett.* **2021**, 3270-3274.

49. Gao, W.; Li, S.; He, H.; Li, X.; Cheng, Z.; Yang, Y.; Wang, J.; Shen, Q.; Wang, X.; Xiong, Y., Vacancy-Defect Modulated Pathway of Photoreduction of CO_2 on Single Atomically Thin $AgInP_2S_6$ Sheets into Olefiant Gas. *Nat. Commun.* **2021,** *12*, 1-8.

50. Groom, R.; Jacobs, A.; Cepeda, M.; Drummey, R.; Latturner, S. E., $Bi_{13}S_{18}I_2$: (Re)discovery of a Subvalent Bismuth Compound Featuring $[Bi_2]^{4+}$ Dimers Grown in Sulfur/Iodine Flux Mixtures. *Chem. Mater.* **2017,** *29*, 3314-3323.

51. Xu, B.; Feng, T.; Agne, M. T.; Tan, Q.; Li, Z.; Imasato, K.; Zhou, L.; Bahk, J. H.; Ruan, X.; Snyder, G. J., Manipulating Band Structure through Reconstruction of Binary Metal Sulfide for High-Performance Thermoelectrics in Solution-Synthesized Nanostructured $Bi_{13}S_{18}I_2$. *Angew. Chem.* **2018,** *130*, 2437-2442.

52. Chen, F.; Huang, H.; Guo, L.; Zhang, Y.; Ma, T., The role of Polarization in Photocatalysis. *Angew. Chem., Int. Ed.* **2019,** *58*, 10061-10073.

53. Mondal, S.; Sarkar, S.; Bagchi, D.; Das, T.; Das, R.; Singh, A. K.; Prasanna, P. K.; Vinod, C. P.; Chakraborty, S.; Peter, S. C., Morphology Tuned Pt_3Ge Accelerates Water Dissociation to Industrial Standard Hydrogen Production over a wide pH Range. *Adv. Mater.* **2022,** *n/a* (n/a), 2202294.

54. Huang, H.; Raith, J.; Kershaw, S. V.; Kalytchuk, S.; Tomanec, O.; Jing, L.; Susha, A. S.; Zboril, R.; Rogach, A. L., Growth Mechanism of Strongly Emitting $CH_3NH_3PbBr_3$ Perovskite Nanocrystals with a Tunable Bandgap. *Nat. Commun.* **2017,** *8*, 1-8.

55. Li, X.; Sun, Y.; Xu, J.; Shao, Y.; Wu, J.; Xu, X.; Pan, Y.; Ju, H.; Zhu, J.; Xie, Y., Selective Visible-Light-Driven Photocatalytic CO_2 Reduction to CH_4 Mediated by Atomically Thin $CuIn_5S_8$ Layers. *Nat. Energy* **2019,** *4*, 690-699.

56. Sun, S.; Watanabe, M.; Wu, J.; An, Q.; Ishihara, T., Ultrathin $WO_3 \cdot 0.33H_2O$ Nanotubes for CO_2 Photoreduction to Acetate with High Selectivity. *J. Am. Chem. Soc.* **2018,** *140*, 6474-6482.

57. Dai, W.; Yu, J.; Deng, Y.; Hu, X.; Wang, T.; Luo, X., Facile Synthesis of MoS_2/Bi_2WO_6 Nanocomposites for Enhanced CO_2 Photoreduction Activity under Visible Light Irradiation. *Appl. Surf. Sci.* **2017,** *403*, 230-239.

58. Dai, W.; Yu, J.; Luo, S.; Hu, X.; Yang, L.; Zhang, S.; Li, B.; Luo, X.; Zou, J., WS$_2$ Quantum Dots Seeding in Bi$_2$S$_3$ Nanotubes: A Novel Vis-NIR Light Sensitive Photocatalyst with Low-Resistance Junction Interface for CO$_2$ Reduction. *Chem. Eng. J.* **2020,** *389*, 123430.

59. Dai, W.; Xiong, W.; Yu, J.; Zhang, S.; Li, B.; Yang, L.; Wang, T.; Luo, X.; Zou, J.; Luo, S., Bi$_2$MoO$_6$ Quantum Dots In Situ Grown on Reduced Graphene Oxide Layers: A Novel Electron-Rich Interface for Efficient CO$_2$ Reduction. *ACS Appl. Mater. Interfaces* **2020,** *12*, 25861-25874.

60. Sánchez-Rodríguez, D.; Jasso-Salcedo, A. B.; Hedin, N.; Church, T. L.; Aizpuru, A.; Escobar-Barrios, V. A., Semiconducting Nanocrystalline Bismuth Oxychloride (BiOCl) for Photocatalytic Reduction of CO$_2$. *Catalysts* **2020,** *10*, 998.

61. Dai, W.; Xu, H.; Yu, J.; Hu, X.; Luo, X.; Tu, X.; Yang, L., Photocatalytic Reduction of CO$_2$ into Methanol and Ethanol over Conducting Polymers Modified Bi$_2$WO$_6$ Microspheres under Visible Light. *Appl. Surf. Sci.* **2015,** *356*, 173-180.

62. Zhao, D.; Xuan, Y.; Zhang, K.; Liu, X., Highly Selective Production of Ethanol Over Hierarchical Bi@Bi$_2$MoO$_6$ Composite via Bicarbonate-Assisted Photocatalytic CO$_2$ Reduction. *ChemSusChem* **2021,** *14*, 3293-3302.

63. Maimaitizi, H.; Abulizi, A.; Kadeer, K.; Talifu, D.; Tursun, Y., In Situ Synthesis of Pt and N co-Doped Hollow Hierarchical BiOCl Microsphere as an Efficient Photocatalyst for Organic Pollutant Degradation and Photocatalytic CO$_2$ Reduction. *Appl. Surf. Sci.* **2020,** *502*, 144083.

64. Gao, S.; Gu, B.; Jiao, X.; Sun, Y.; Zu, X.; Yang, F.; Zhu, W.; Wang, C.; Feng, Z.; Ye, B., Highly Efficient and Exceptionally Durable CO$_2$ Photoreduction to Methanol over Freestanding Defective Single-Uunit-Cell Bismuth Vanadate Layers. *J. Am. Chem. Soc.* **2017,** *139*, 3438-3445.

65. Li, X.; Chen, J.; Li, H.; Li, J.; Xu, Y.; Liu, Y.; Zhou, J., Photoreduction of CO$_2$ to Methanol over Bi$_2$S$_3$/CdS Photocatalyst under Visible Light Irradiation. *J. Nat. Gas Chem.* **2011,** *20*, 413-417.

66. Tan, T. H.; Xie, B.; Ng, Y. H.; Abdullah, S. F. B.; Tang, H. Y. M.; Bedford, N.; Taylor, R. A.; Aguey-Zinsou, K.-F.; Amal, R.; Scott, J., Unlocking the Potential of the Formate Pathway in the Photo-Assisted Sabatier Reaction. *Nat. Catal.* **2020,** *3*, 1034-1043.

67. Kim, Y.; Park, S.; Shin, S.-J.; Choi, W.; Min, B. K.; Kim, H.; Kim, W.; Hwang, Y. J., Time-Resolved Observation of C-C Coupling Intermediates on Cu Electrodes For Selective Electrochemical CO_2 Reduction. *Energy Environ. Sci.* **2020,** *13*, 4301-4311.

68. Hammer, B.; Nørskov, J. K., Theoretical Surface Science and Catalysis-Calculations and Concepts. *Adv. Catal.* **2000,** *45*, 71-129.

69. Das, R.; Das, K.; Ray, B.; Prabhakaran, V.; Peter, S. C., Green Transformation of CO_2 to Ethanol using Water and Sunlight by Cooperative Endeavour of Naturally Abundant Red Phosphorus and Bi_2MoO_6. *Energy Environ. Sci.* **2022**.*15*, 1967-1976.

70. Li, H.; Gan, S.; Wang, H.; Han, D.; Niu, L., Intercorrelated Superhybrid of AgBr Supported on Graphitic-C_3N_4-Decorated Nitrogen-Doped Graphene: High Engineering Photocatalytic Activities for Water Purification and CO_2 Reduction. *Adv. Mater.* **2015,** *27*, 6906-6913.

71. Cheng, M.; Yang, S.; Chen, R.; Zhu, X.; Liao, Q.; Huang, Y., Copper-Decorated TiO_2 Nanorod Thin Films in Opto Fluidic Planar Reactors for Efficient Photocatalytic Reduction of CO_2. *Int. J. Hydrogen Energy* **2017,** *42*, 9722-9732.

72. Cai, B.; Wang, J.; Gan, S.; Han, D.; Wu, Z.; Niu, L., A distinctive red Ag/AgCl Photocatalyst with Efficient Photocatalytic Oxidative and Reductive Activities. *J. Mater. Chem. A* **2014,** *2*, 5280-5286.

73. He, Y.; Wang, Y.; Zhang, L.; Teng, B.; Fan, M., High-Efficiency Conversion of CO_2 to Fuel over ZnO/g-C_3N_4 Photocatalyst. *Appl. Catal., B* **2015,** *168*, 1-8.

74. Chen, X.; Zhuang, C.; Wang, X.; Liao, A.; Li, L.; Liu, Q.; Tang, Y.; Wu, C.; Shen, Q.; Yu, Z., Two-Step Synthesis of Laminar Vanadate via a Facile Hydrothermal Route and Enhancing the Photocatalytic Reduction of CO_2 into Solar Fuel through Tuning of the Oxygen Vacancies by in Situ Vacuum Illumination Treatment. *ACS Appl. Energy Mater.* **2018,** *1*, 6857-6864.

75. Yu, H.; Sun, C.; Xuan, Y.; Zhang, K.; Chang, K., Full Solar Spectrum Driven Plasmonic-Assisted Efficient Photocatalytic CO_2 Reduction to Ethanol. *Chem. Eng. J.* **2022,** *430*, 132940.

76. Li, S.; Wang, C.; Li, D.; Xing, Y.; Zhang, X.; Liu, Y., Bi_4TaO_8Cl/Bi Heterojunction Enables High-Selectivity Photothermal Catalytic Conversion of CO_2-H_2O Flow to Liquid Alcohol. *Chem. Eng. J.* **2022**, 135133.

77. Dai, W.; Yu, J.; Xu, H.; Hu, X.; Luo, X.; Yang, L.; Tu, X., Synthesis of Hierarchical Flower-Like Bi_2MoO_6 Microspheres as Efficient Photocatalyst for Photoreduction of CO_2 into Solar Fuels under Visible Light. *CrystEngComm* **2016,** *18*, 3472-3480.

78. Shown, I.; Samireddi, S.; Chang, Y.-C.; Putikam, R.; Chang, P.-H.; Sabbah, A.; Fu, F.-Y.; Chen, W.-F.; Wu, C.-I.; Yu, T.-Y., Carbon-Doped SnS_2 Nanostructure as a High-Efficiency Solar Fuel Catalyst under Visible Light. *Nat. Commun.* **2018,** *9*, 1-10.

79. Zhu, J.; Shao, W.; Li, X.; Jiao, X.; Zhu, J.; Sun, Y.; Xie, Y., Asymmetric Triple-Atom Sites Confined in Ternary Oxide Enabling Selective CO_2 Photothermal Reduction to Acetate. *J. Am. Chem. Soc.* **2021,** *143*, 18233-18241.

80. Yu, F.; Jing, X.; Wang, Y.; Sun, M.; Duan, C., Hierarchically Porous Metal–Organic Framework/MoS_2 Interface for Selective Photocatalytic Conversion of CO_2 with H_2O into CH_3COOH. *Angew. Chem.* **2021,** *133*, 25053-25057.

Chapter 6

Green Transformation of CO$_2$ to Ethanol Using Water and Sunlight by Cooperative Endeavour of Naturally Abundant Red Phosphorus and Bi$_2$MoO$_6$

Risov Das, Kousik Das, Bitan Ray, Chathakudath P Vinod, Sebastian C Peter*.

Green Transformation of CO₂ to Ethanol Using Water and Sunlight by Cooperative Endeavour of Naturally Abundant Red Phosphorus and Bi₂MoO₆
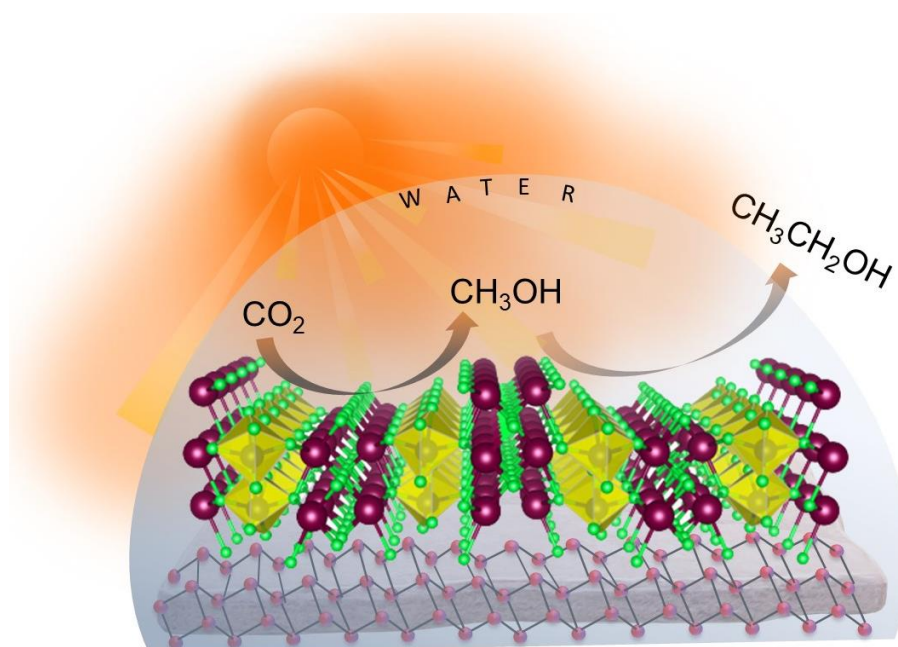
Chapter 6

Summary

Ethanol is an immediate alternative to crude oil. Therefore, up to 20% ethanol blending with petroleum has emerged in the oil industry. However, the existing ethanol synthesis process is not completely green. In this scenario, ethanol synthesis by abundant sunlight, water and CO_2 can provide the cheapest and greenest route. The existing literature based on photocatalytic CO_2 reduction is still stuck at C1 products due to multiple intermediate steps and the kinetically sluggish 12 proton coupled electron transfer route in the CO_2 to ethanol formation process. Direct photocatalytic conversion of CO_2 to ethanol remains a scientific challenge because of the sluggish kinetics of C-C coupling and complex multielectron transfer processes. To achieve a green transformation of CO_2 to C1+ products using naturally abundant sunlight and water requires smart design of an efficient catalyst by selecting the right combination of atoms either in elemental or in compound form. Herein, we report a composite photocatalyst composed of earth abundant red phosphorus (RP) in nano-sheet morphology decorated with Bi_2MoO_6 nano-particles. The composite synthesised by a facile ultrasonication method, produces 51.8 µmol $g^{-1}h^{-1}$ of ethanol from CO_2. The ability of RP for the conversion of CO_2 to C1 has been altered by the introduction of Bi_2MoO_6. The in-situ Diffuse Reflectance Infrared Fourier Transform Spectroscopy (DRIFTS) and Kinetic Isotopic Effect (KIE) analysis shed a light on the mechanistic pathway, which propose that the presence of Bi-Mo dual sites play a crucial role for the C-C coupling towards the formation of ethanol. The spectroscopic evidences and isotope labeling experiments of intermediate suggest OCH_3* is the key active species for ethanol formation via self-coupling followed by proton transfer.

Green Transformation of CO_2 to Ethanol using Water and Sunlight by Cooperative Endeavour of Naturally Abundant Red Phosphorus and Bi_2MoO_6

Risov Das, Kousik Das, Bitan Ray, Chathakudath P Vinod, Sebastian C Peter

6.1. Introduction

Ethanol was produced by single component catalyst in the last chapter. However, the rate of ethanol formation was not very promising. Therefore, more importance on increasing the ethanol yield was given in this work because ethanol is one of the most value added CO_2 reduction products. On top of that, an adequate amount of ethanol synthesis from solar energy is a dream project. There are several critical challenges that need to be addressed to achieve this dream concept, however, catalyst design is the key amongst them.[1] A wide range of materials such as metal oxides,[2-3] chalcogenides,[4] halide perovskites,[5] porous organic polymers (POP),[6] covalent organic frameworks (COF),[7] metal-organic frameworks (MOF)[8] and organometallic photocatalysts[9-10] have been explored for photocatalytic CO_2RR. However, poor efficiency and high cost limit the practical implementation of these potential catalytic systems. To elaborate further, enlisted below are the key targets to be achieved for the effective implementation of photocatalytic CO_2RR:

a. Enhancing CO_2RR efficiency by increasing the number of excited electrons with a potential equivalent to the desired product.

b. Avoiding charge recombination[11]

c. Enhancing the surface area of the catalysts to drive maximum CO_2 molecules adsorption at the active sites of a photocatalyst

d. Obtaining the desired selectivity towards C1+ products, while suppressing the competitive hydrogen evolution reaction (HER)

e. Reducing operational costs by discovering more durable low-cost catalyst for the formation of C1+ products[12]

Traditionally the photochemical CO_2 reduction route offers C1 (CO, CH_4, CH_3OH and HCOOH) products under mild conditions.[13] However, tuning the active sites and band structure can promote further coupling of these C1 products to form desired higher carbon products. Multi-electron and proton transfers are necessary to produce C1+ products, which must go through complex reaction pathways, resulting in low efficiency. Among the C1+ products, ethanol is of great value as it can be used as a potential energy storage fuel and for the production of several industrially important chemicals. Photocatalytic CO_2 to ethanol conversion has a very limited repository in terms of literature as compared to electrocatalytic processes due to low efficiency of the process. To the best of our knowledge, the highest

Green Transformation of CO₂ to Ethanol Using Water and Sunlight by Cooperative Endeavour of Naturally Abundant Red Phosphorus and Bi₂MoO₆

Chapter 6

conversion of CO_2 to ethanol was obtained with the formation rate of 50 µmol g^{-1} h^{-1} via AgBr–NG–g-C_3N_4 catalyst under visible- light.[14] However, photogenerated holes in this process had to be scavenged by organic pollutants rendering it a non-green process. On the other hand, all other CO_2 to ethanol reports, indicate formation rates lower than 20 µmol h^{-1} g^{-1} under visible light.[12, 15-17] These reports had other drawbacks including obscurity of the coupling mechanism involved, surface recombination and limited gas adsorption capacity over the catalysts.

In this work, we report the discovery of a novel photocatalyst composed of naturally abundant exfoliated red phosphorus (RP) and Bi_2MoO_6 (BMO) nanoparticles synthesized by a facile sonication process. RP is a non-toxic semiconducting element with relatively narrow band gap (about 1.72 eV) that has light-harvesting ability and a suitable conduction band edge for CO_2 photoreduction. The favourable band structure of RP can be exploited if it can be modified by the formation of a heterostructure with another strong light harvesting material. Various studies have suggested that Bi-based ternary metal oxides ($Bi_xM_yO_z$) have the potential to trigger C-C coupling.[18] Bi_2MoO_6 has already been known as a photocatalyst and it produces very small amount of methanol and ethanol.[19-20] In the light of these observations, we inferred that the interface of these two materials in a heterostructure composite should be a promising candidate to study the ability of dual-metal site to modulate C-C coupling in CO_2 photoreduction. The structural chemistry and chemical interactions of the catalysts are well characterized by several microscopic and spectroscopic techniques. A composite with optimized ratio of RP and BMO yields high CO_2-to-ethanol conversion efficiency (51.8 µmol $g^{-1}h^{-1}$) under visible light without any degradation for more than 5 consecutive runs. The role of dual metal site for ethanol formation was probed by kinetic isotopic effect (KIE) study, which was further supported by operando DRIFTS measurements. These experiments suggest that abundant RP wrapped dual-metal sites allow specific hydrogenation at Mo-OC* (Hydrogenation on C centre) and Bi-O* centres leading to the formation of high yield ethanol from CO_2.

6.2. Experimental section

Chemicals and reagents: The following chemicals were used: Red phosphorus (P, Sigma Aldrich), ethylene glycol [$(CH_2OH)_2$, Sigma Aldrich], bismuth nitrate pentahydrate [$Bi(NO_3)_3 \cdot 5H_2O$, Alfa Aesar], sodium molybdate dihydrate [$Na_2MoO_4 \cdot 2H_2O$, Alfa Aesar]. All the chemicals are commercially available certified reagents and used without further purification.

Synthesis

Synthesis of Bi_2MoO_6 by solvothermal method: Stochiometric amount of $Bi(NO_3)_3 \cdot 5H_2O$, $Na_2MoO_4 \cdot 2H_2O$ were immersed in 15 mL of ethylene glycol and 15 ml of hot water respectively, and then were mixed together. The resulting suspension was maintained at 160 °C for 24 h in a 45 mL Teflon-lined autoclave. Finally, the products were washed thoroughly with deionized water and dried in vacuum oven at 60° C for 10 hours.

Synthesis of exfoliated red phosphorus (RP): Commercially available RP was sonicated for 20 h in water to get exfoliated RP.

Synthesis of RP/Bi_2MoO_6 heterostructures by solvothermal method: Exfoliated RP and previously synthesised Bi_2MoO_6 were sonicated together for 12 hours. Finally, the composites were dried at 60 ºC for 6 h to get RP/Bi_2MoO_6 powders. The weight ratio of RP and Bi_2MoO_6 was varied from 1:1 to 3:1 to get different composites. The composite with 1:1, 2:1 and 3:1 weight ratio was named as **RP-BMO(11)**, **RP-BMO(21)**, and **RP-BMO(31)**. We have used the same nomenclature throughout this chapter.

Material characterization

X-Ray diffraction: The structural phase of pristine Bi_2MoO_6, RP and composites were confirmed by X–ray diffraction (XRD, Rigaku Advance X-ray diffractometer equipped with Cu *Kα* source for irradiation 1.54 Å).

Microscopy: To understand morphology of material high-resolution transmission electron microscopy (HRTEM) was taken. Sample preparation was done by drop casting small amount of sonicated powder in ethanol on a carbon coated copper grid. SEM images were taken by FEI NOVA NANOSEM 600 scanning electron microscope equipped with an energy-dispersive X-ray spectroscopy (EDAX) instrument (Bruker 129 eV EDAX instrument). Data was acquired by using an accelerating voltage of 20 kV and typical time taken for data accumulation is 100 s. The elemental analyses were performed using the P/B-ZAF standardless method (where, P/B = peak to background model, Z = atomic no. correction factor, A = absorption correction factor and F = fluorescence factor) for C, N, O, Co at multiple areas on the sample coated Si wafer.

Photoluminescence (PL): PL spectra of all the solid samples were recorded at room temperature on a steady state Luminescence spectrometer Perkin-Elmer (LS 55) at different excitation wavelength.

Green Transformation of CO₂ to Ethanol Using Water and Sunlight by Cooperative Endeavour of Naturally Abundant Red Phosphorus and Bi₂MoO₆

Chapter 6

The ultraviolet-visible diffuse reflectance spectrum (UV-vis DRS): UV-vis spectra were obtained in the range of 250 to 800 nm by using a Perkin-Elmer Lambda 900 UV/Vis/Near- IR spectrophotometer in reflectance mode for Bi_2MoO_6, RP and other composites with an integrating sphere attachment. $BaSO_4$ was used as a 100% reflectance standard. The absorption was calculated data using the Kubelka−Munk equation,[21] $\alpha/S = (1 − R)^2/2R$, where R is the reflectance and α and S are the absorption and scattering coefficients, respectively. Band gap was derived using Tauc plot.

X-ray photoelectron spectroscopy (XPS): XPS data were obtained using Omicron Nanotechnology spectrometer using an Al $K\alpha$. All the binding energies were referenced to the C 1s peak at 284.8 eV.

Surface area measurement: Specific surface area measurements were performed on BELSORP-MR6 by adsorption of nitrogen gas at – 77 K, applying the Brunauer-Emmett-Teller (BET) calculation.[22] Prior to adsorption analysis, the samples were degassed at 85 °C for 12h. Pore size distributions were derived from desorption isotherms using Barrett-Joyner-Halenda (BJH) method.

Photocatalytic measurements: A quartz photoreactor was used for CO_2 hydrogenation experiment under the illumination of 450 W xenon lamp (with UV cut-off filter (KG-2 filter and CGA-400) filter) solar simulator. About 5 mg of the sample was well dispersed in 20 mL of water by ultrasonication. Before illumination, the reaction setup was purged with N_2 to remove the air and then purged with high purity CO_2 for 45 minutes.

During irradiation, 3 mL of the gaseous product from the setup was sampled, and gas analysis study was done by GC (gas chromatography) (Agilent GC-7890 B) with TCD and FID detector and He carrier gas. Blank tests were conducted in the absence of CO_2 and light to confirm that these two factors are key for photocatalytic CO_2 reduction reaction. Rate of the evolved gases were calculated after at 10-hour reaction.

Liquid product analysis: The liquid products were analysed by and HPLC (Agilent 1220 Infinity II LC system) and GC-MS (Agilent). After each cycle, catalytic system was purged with N_2 for 40 minutes followed by fresh batch of CO_2 purging. Liquid products are also cross checked by proton NMR. 500 μl sample was added with 30 μl internal standard (10 mM DMSO and 50 mM phenol) for calculating the yield.

Control studies was done with UV grade ultra-pure methanol and CD_3OD using same photocatalytic setup for 10h. Control study with methane was done by maintaining similar procedure as CO_2 reduction. However, the purging was done by CH_4 instead of CO_2.

In-situ photocatalytic Fourier transform infrared spectroscopy: In-situ photochemical FT-IR spectroscopic studies were performed using a purged VERTEX FT-IR spectrometer equipped with the A530/P accessory and a mid-band Mercury Cadmium Telluride (MCT) detector. Spectra were recorded after 100 scans with a resolution of 4 cm^{-1}. A DRIFTS cell with a quartz window was used to perform catalytic experiment. Prior to catalytic testing, 5 mg of the sample was placed in the DRIFTS cell and treated in flowing N_2 for 30 min to remove impure gas mixtures. Then, CO_2 and water vapor were injected through rubber septa and light was illuminated through the quartz window for 100 minutes. Just before the light exposure on the DRIFTS cell the zero-minute data was collected and followed by data under light was collected every 10 minutes for 100 minutes.

Time resolved photoluminescence: Photoluminescence decay profiles were recorded using a Horiba Delta Flex time correlated single-photon-counting (TCSPC) instrument. A 520 nm laser diode with a pulse repetition rate of 1 MHz was used as the light source. The instrument response function (IRF) was collected using a scatterer (Ludox AS40 colloidal silica, Sigma-Aldrich).

Photoelectrochemical measurements: The transient photocurrent measurements under dark and light were done in a three-electrode system using a CHI 760 potentiostat under the illumination of a solar simulator (Newport) with an ultraviolet (UV) ($\lambda > 380$ nm) cut-off filter. Ag/AgCl was reference electrode, and platinum as the counter electrode was used. All samples were spin coated on fluorine-doped tin oxide (FTO) which were used as working electrode. 0.5 M Na_2SO_4 was taken as electrolyte.

The slurry was prepared by adding 10 mg of the sample, 200 μL of Nafion (5%), and 1 mL of isopropyl alcohol to fabricated photoelectrodes. The obtained paste was spin-coated on FTO with 1 cm^2 area and annealed at 100 °C for 1 h to get a homogenous film. Mott-Schottky (MS) plots were recorded at a scan rate of 10 mV/s in Na_2SO_4 neutral solution in the light at a frequency of 50 kHz. The obtained values (w.r.t Ag/AgCl) was converted w.r.t NHE by adding 0.20 V.

6.3. Calculations

Calculation of relative quantum yield (QY) rate ratio for ethanol production: AQY of **RP-BMO(21)** for photocatalytic CO_2 reduction reaction were calculated for simulated light source and sunlight. KG-2 filter CGA-400 filter were used to cut off UV and IR part of the simulated light (450 W xenon lamp from Newport). The light intensity was measured using a

power meter (Newport-843-R) the intensity of outputting light was measured. The intensity of Xe lamp ($P_{Xe\ lamp}$) is 116 mW/cm^2 and sunlight ($P_{direct\ sunlight}$) is 84 mW/cm^2.

$$QY(\%) = \frac{Number\ of\ reacted\ electrons\ for\ ethanol\ formation}{Number\ of\ incident\ photons} X\ 100\%$$

Number of reacted electrons were calculated from the yield of CO_2 reduced products. Because different number of electrons are required for the formation of different products, the total number of reacted electrons are

$$Number\ of\ reacted\ electrons\ for\ ethanol\ formation = [12n(CH_3CH_2OH)]\ X\ N_A$$

n(CH_3CH_2OH) is the rate of ethanol formation in moles/g/h, respectively. N_A is Avogadro's number.

Number of incident photons are calculated from the following equation:

$$Number\ of\ incident\ photons = \frac{PSt}{hc}$$

where, P is the power density of the incident light (W/m^2), S (m^2) is the irradiation area, t (s) is the duration of the incident light exposure.

Combining these two equations the ratio of QY(%) were calculated for ethanol formation rate under direct sunlight and simulated light (Xe lamp).

$$QY(\%)\ rate\ ratio$$

$$= \frac{Rate\ of\ Ethanol\ formation\ under\ direct\ sunlight\ X\ P_{Xe\ lamp}}{Rate\ of\ Ethanol\ formation\ under\ Xe\ lamp\ X\ P_{direct\ sunlight}} \times 100\%$$

$$= \frac{34.1}{51.8} \times \frac{116}{84} \times 100\%$$

$$= 90.91\%$$

6.4. Results and discussions

Material design: To investigate our proposal, several composites with different ratios of RP and BMO were synthesised. We deliberately exfoliated amorphous RP and impregnated previously synthesised BMO nanocrystals into it by prolonged sonication to develop an optimum interface between them for better CO_2 reduction efficiency. The powder X-ray

diffraction (PXRD) patterns showed the formation of amorphous RP and pure crystalline BMO (**Figure 6.1a**, and **6.1b**). RP, low angle peak at $2\theta = 16°$ is matching with reported literature. In the case of Bi2MoO6, the diffraction peaks observed at 28.25°, 32.59°, 33.07°, 46.72°, 47.07°, 55.46°, 55.53° and 56.16° can be perfectly indexed to the (131), (002), (060), (202), (260), (331), (133), and (191) planes of orthorhombic Bi_2MoO_6 ($Pca2_1$). For RP/Bi_2MoO_6 compositess all the peaks can be assigned to Bi_2MoO_6, along with a hump at around 16° corresponding to RP. The absence of extra peak (other than BMO XRD peak) in case of pure BMO and composites clearly indicates the phase purity of the catalyst. The broadness of BMO XRD patterns indiates the formation of BMO nanoparticles. The scanning electron microscopic (SEM) image of BMO (**Figure 6.2)**, and RP (**Figure 6.3)** showed nanoparticles and exfoliated thick sheet like morphology, respectively and the corresponding elemental mapping clearly indicates the uniform distribution of elements in BMO, and phosphorus only in RP. Absence of O atoms suggests that RP has not been oxidised to P_4O_{10} or $P_2O_5.$[23] SEM images and elemental mapping in **Figure 6.4a-6.4c** shows the dispersion of Bi_2MoO_6 nanoparticles on exfoliated RP in **RP-BMO(21)**. Transmission electron microscopy (TEM) images further confirmed the dispersion of BMO nanoparticles on exfoliated RP (**Figure 6.4d**). Small BMO nanoparticles were confirmed from HRTEM. As depicted in **Figure 6.4e**, and **6.4f**, BMO on the RP matrix exhibited d spacing of 0.32 nm corresponding to the (131) lattice plane which is the most prominent plane as observed from XRD too. The morphology and average particle size of BMO were also determined from TEM (**Figure 6.5a**, and **6.5b**).
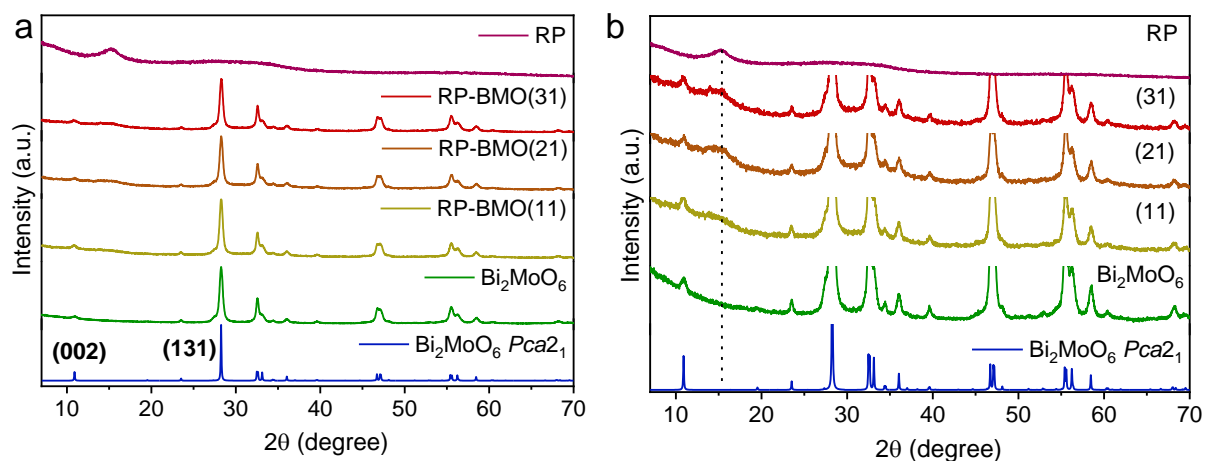

Figure 6.1. Powder X-ray diffraction (PXRD) patterns. **(a)** Phase purity characterization by PXRD of RP, **RP-BMO(31)**, **RP-BMO(21)**, **RP-BMO(11)** and Bi_2MoO_6. The line showed along (131) plane indicates, there is no shift of peak position upon composite formation. **(b)** zoomed version of **Figure 6.1a** for showing the presence of amorphous red phosphorus (RP).

Green Transformation of CO₂ to Ethanol Using Water and Sunlight by Cooperative Endeavour of Naturally Abundant Red Phosphorus and Bi₂MoO₆

Chapter 6
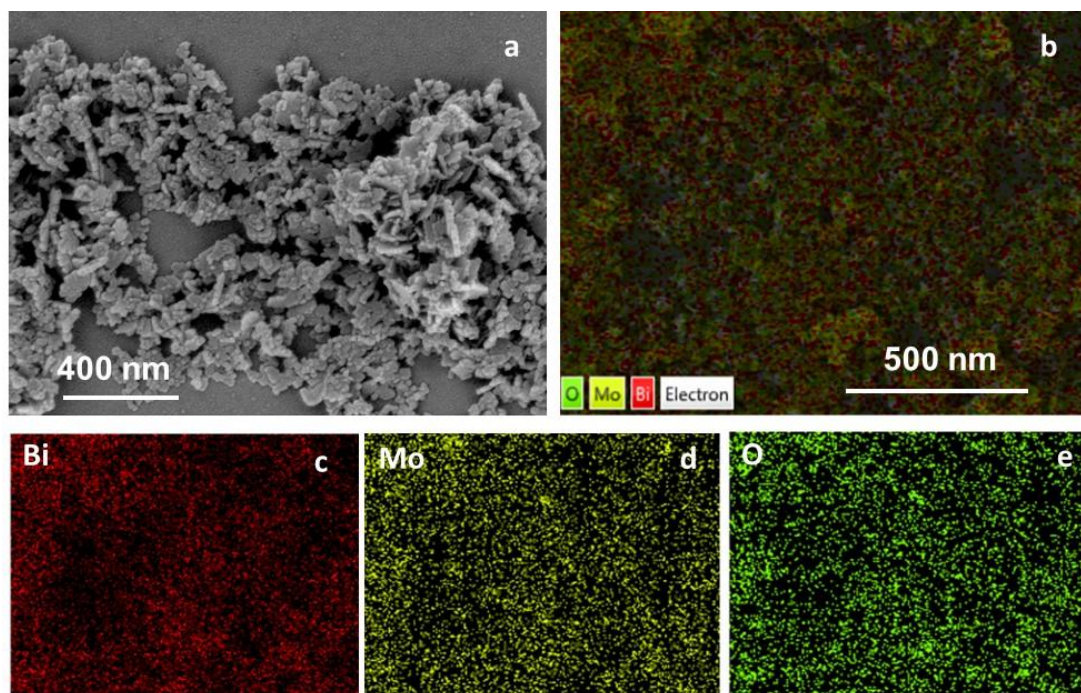
Figure 6.2. SEM images and color mapping of Bi_2MoO_6. **(a)** SEM images of pristine Bi_2MoO_6 nano particles. **(b)** SEM elemental mapping projecting a superimposition of the distribution of **(c)** bismuth, **(d)** molybdenum, and **(e)** oxygen.
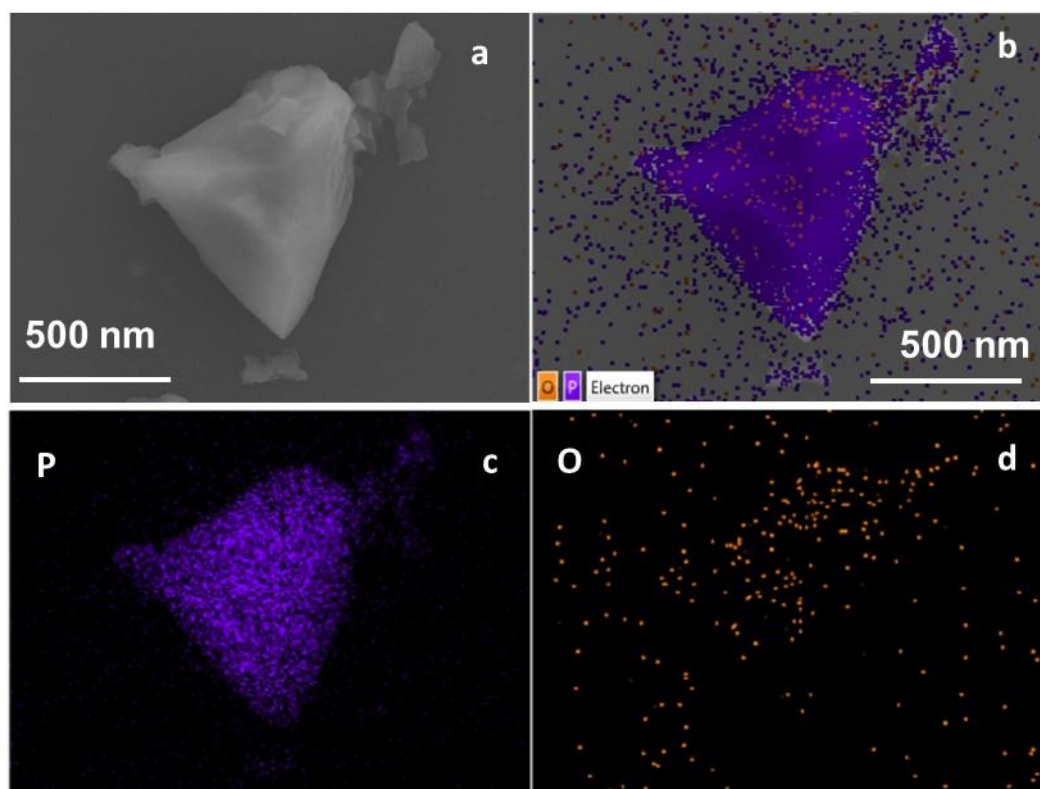

Figure 6.3. SEM images and color mapping of red phosphorus. **(a)** SEM images of pristine red phosphorus (RP). **(b-d)** SEM elemental mapping displaying a superimposition **(b)** of the distribution of phosphorus **(c)**, oxygen **(d).** Absence of oxygen eliminates the surface oxidation of phosphorus and the formation phosphorus oxide compounds.
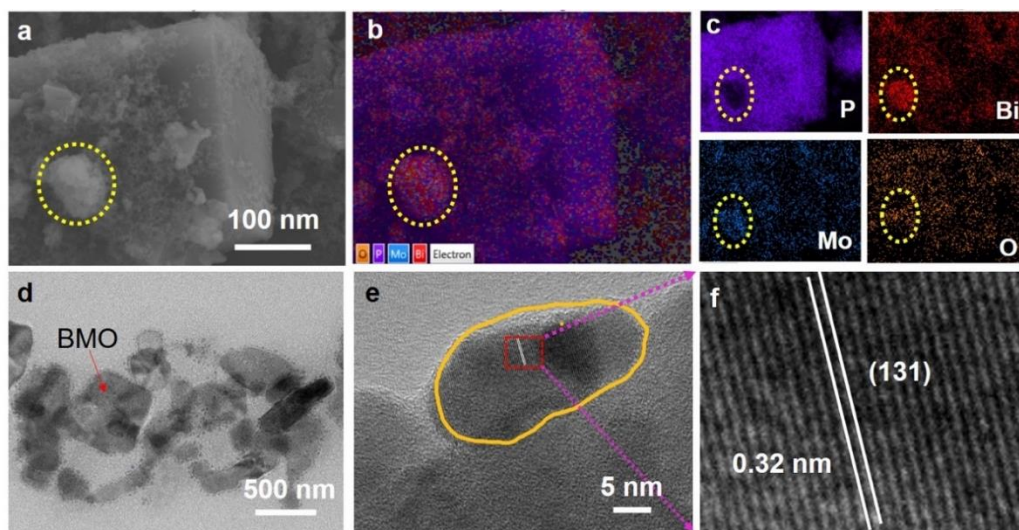
Figure 6.4. Characterization of composites and individual components. **(a)** SEM image showing that the Bi$_2$MoO$_6$ nanoparticles are lying on exfoliated RP. **(b)** SEM elemental mapping for the identification of 2 different material. **(c)** Elemental mapping of P, Bi, Mo and O. The less concentrate yellow colour hints that the composite formation does not trigger surface oxidation of red phosphorus. **(d)** TEM image of Bi$_2$MoO$_6$/RP composite. **(e)** HRTEM image of BMO nano particle on RP. The yellow border shows the BMO nano particle. **(f)** **Figure 6.4e** was zoomed to show the d-spacing. It shows the BMO (131) exposed plane.

In addition to that the exfoliated RP were characterized by TEM which shows a thin sheet like morphology of RP (**Figure 6.5c** and **6.5d**).
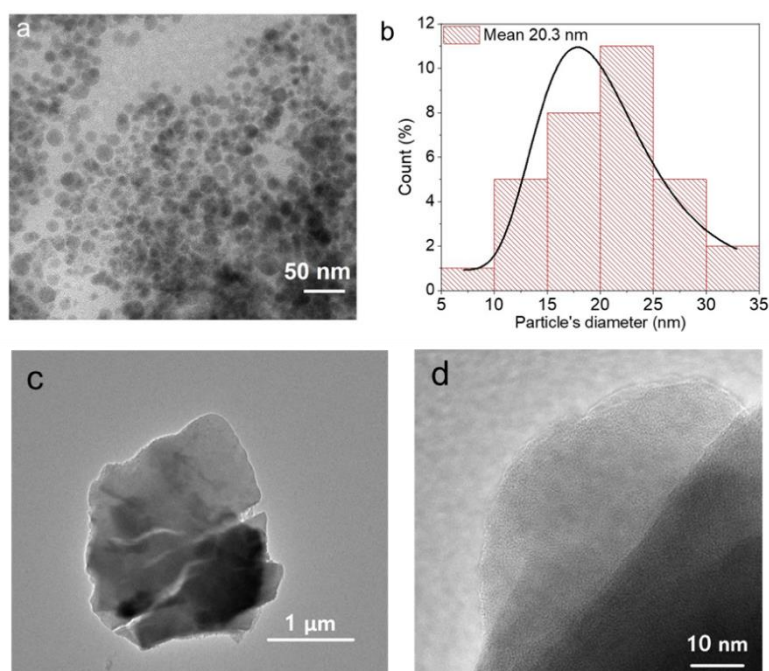
Figure 6.5. TEM images of pristine BMO. **(a)** TEM images showed uniform spherical BMO nanoparticle. **(b)** Particle size of BMO nanoparticle were calculated from **Figure 6.5a**. Microscopic images of exfoliated RP. **(c)** TEM and, **(d)** HRTEM image of exfoliated RP.

Further insight about the sonication induced time dependent exfoliation of RP was visualized by atomic force microscopy (AFM). **Figure 6.6a-d** clearly shows 2 layers of RP sheets where each layer has around 2 nm height after 10h sonication. On the other hand, 20h sonicated RP has single layer of around 2 nm height (**Figure 6.6e-h**). The single layer of RP can disperse BMO particle on it more compared to multiple layers which in turn helps in the formation of more heterojunctions and interfaces.
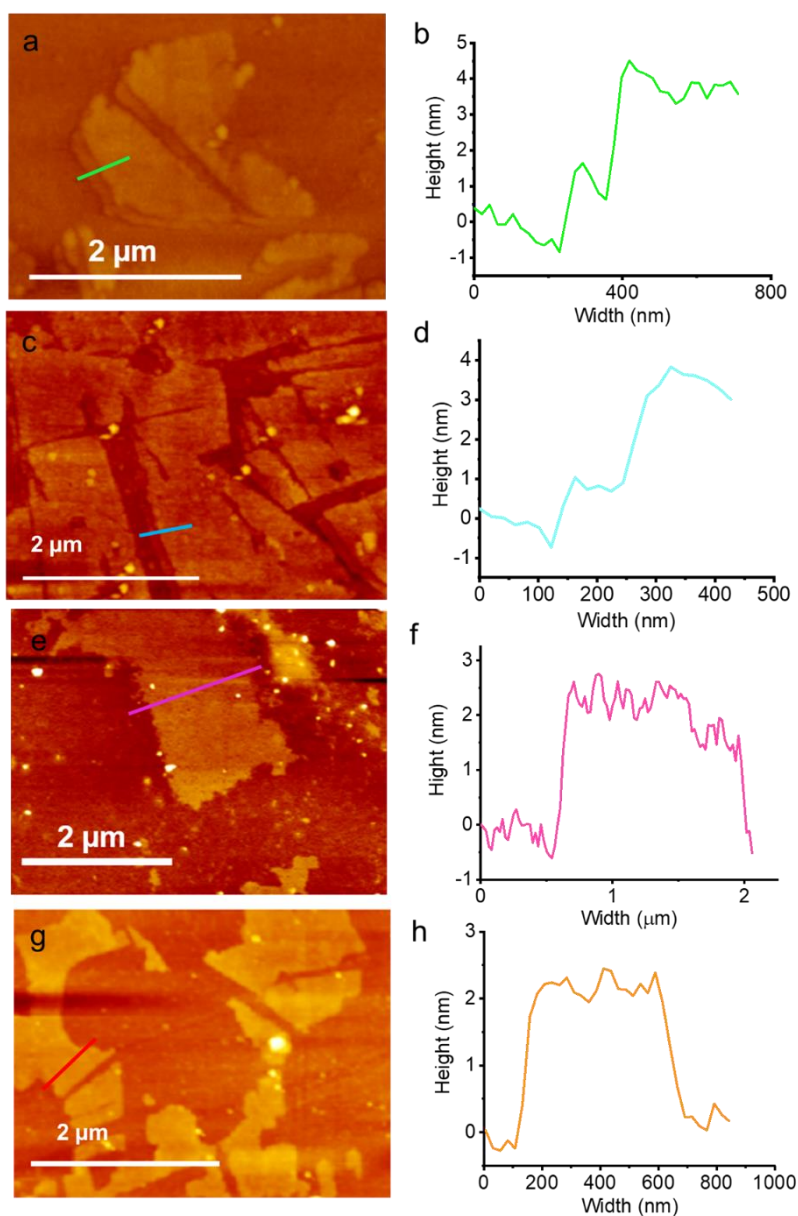
Figure 6.6. (**a**) AFM image of 10h sonicated RP which shows 2 layers of RP. (**b**) Presence of 2 layers was found by analyzing the height profile. Similar double layer (**c**) and height profile (**d**) was found in another region. AFM image of 20h sonicated RP (**e**) shows single layer of RP sheets. The corresponding height profile shows only one hump (**f**). Another AFM image of 20h sonicated RP sheet (**g**), and height profile (**h**). Height profile of 20h sonicated single layer RP shows the layer thickness of around 2 nm.

N$_2$ adsorption-desorption isotherm reveals better gas adsorption capacity of Bi$_2$MoO$_6$ compared to common oxide semiconductor materials (**Figure 6.7a**). However, RP has very poor gas-adsorption ability (**Figure 6.7b**). Therefore, a compromised surface area was obtained for RP-BMO composites (**Figure 6.7c-e**). **Figure 6.8a** shows the monotonic decrease of surface area upon increasing the impregnation of BMO on RP. Pure BMO consists of mesopores of 20 nm diameter (**Figure 6.7f**).
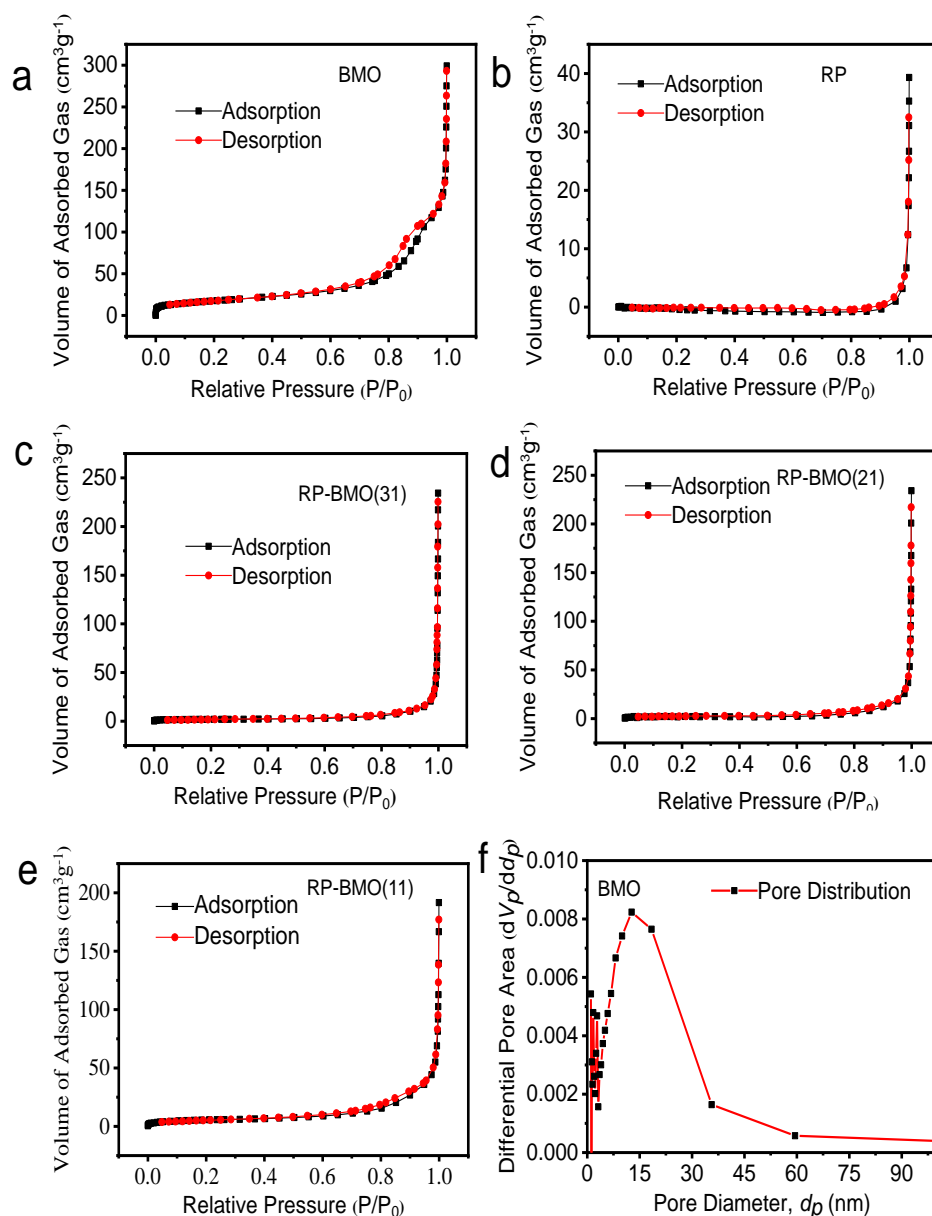
Figure 6.7. BET measurements of Bi$_2$MoO$_6$/RP composite and individual components. **a-e,** N$_2$ adsorption-desorption isotherms of **(a)** RP, **(b)** R**P-BMO(31)**, **(c) RP-BMO(21)**, **(d) RP-BMO(11)**, and **(e)** Bi$_2$MoO$_6$. **(f)** Mesopore size distribution of Bi$_2$MoO$_6$. This measurement shows that the RP less surface area compared to Bi$_2$MoO$_6$. This study shows that the BMO has suitable pores for accommodating adsorbate molecule. These pores can be classified as mesopores because the average pore size is in between 15nm-20 nm.

Green Transformation of CO₂ to Ethanol Using Water and Sunlight by Cooperative Endeavour of Naturally Abundant Red Phosphorus and Bi₂MoO₆

Chapter 6

Figure 6.8. (a) Surface area of composites, Bi_2MoO_6 and RP calculated from BET measurements for understanding the gas adsorption capacity. **(b)** UV-Vis DRS of composites and individual components. **(c)** Corresponding Tauc plots drawn by using Kubelka-Munk parameter $((\alpha h\nu)^2)$ as a function versus photon energy (eV).

This kind of mesopores is beneficial for the adsorption of CO_2 molecules and it helps in triggering the catalytic activity. The band structures of RP, BMO and composites were determined by ultraviolet-visible diffuse reflectance spectra (UV-DRS). RP and BMO exhibit the optical absorption edge at 689 nm and 459 nm, respectively, which is also observed in the case of the composite materials as well (**Figure 6.8b**). The prominent absorption edge of RP compared to BMO can be interpreted as better absorption ability of RP compared to BMO. Kub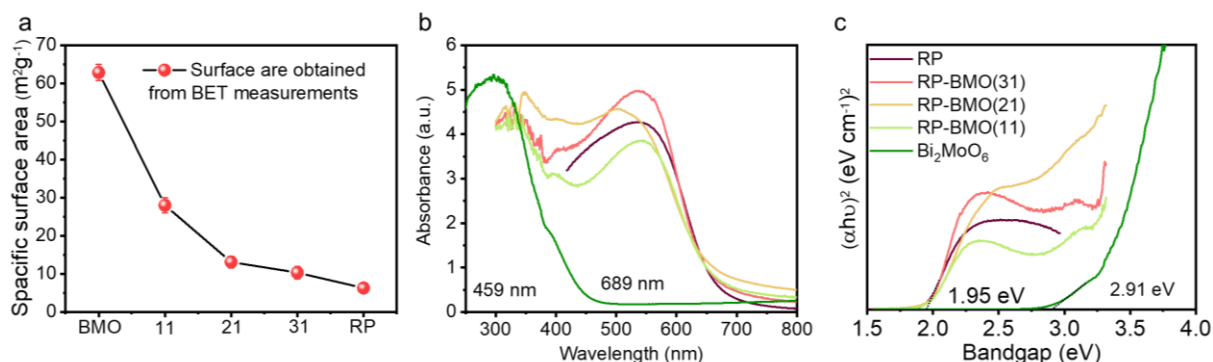elka–Munk function[24] was used to determine direct bandgaps of the RP, BMO and composites. The band gap of 1.95 eV and 2.91 eV observed for RP and BMO, respectively also were found in case of all composites (**Figure 6.8c**).

X-ray photoelectron spectroscopy was performed to verify the oxidation state of Bi in pristine BMO (**Figure 6.9a**) and RP-BMO composites (**Figure 6.9b**). RP-BMO composite show very small amounts of Bi^0 along with Bi^{3+} whereas pristine BMO comprised of only Bi^{3+}. Extensive sonication may lead to the formation of Bi^0 on the surface of the RP-BMO composite.[25] However, no Bi metal peak was observed in the powder XRD of RP-BMO composites because the amount of Bi^0 is very less. Presence of metallic Bi in the interface of RP and BMO may facilitate faster charge transfer between them.

The binding energy value of Bi^{3+} in the composite shifted towards a lower value (0.2 eV, this value is sufficient to show the interfacial charge transfer)[26] which suggested the charge transfer from red P to BMO (**Figure 6.10c**). The positive binding energy shift (+0.13 eV) of P-2p band in **RP-BMO(21)** compared to pristine RP (**Figure 6.10a**, and **6.10b**) further confirms the interfacial charge transfer and a substantial electrostatic interaction between the 2 individual components in the composite. Change of binding energy in RP and BMO upon composite formation due to drastic sonication is schematically represented in **Figure 6.10d.**
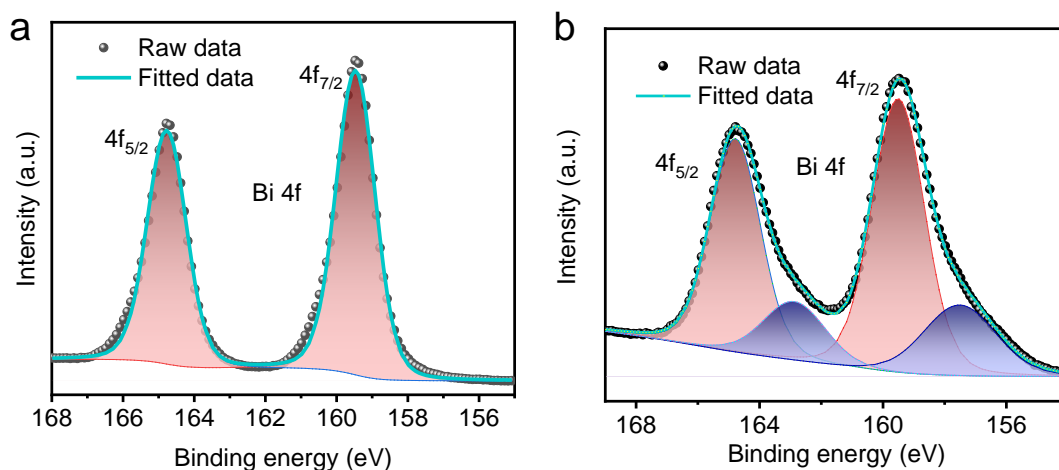
Figure 6.9. XPS measurements. **(a)** Bi 4f spectra corresponds to Bi^{3+} in pristine BMO. **(b)** Bi 4f spectra corresponds to Bi^{3+} (red) and Bi^0 (blue) in **RP-BMO(21)**. The presence of metallic Bi was indicated in **RP-BMO(21)**.
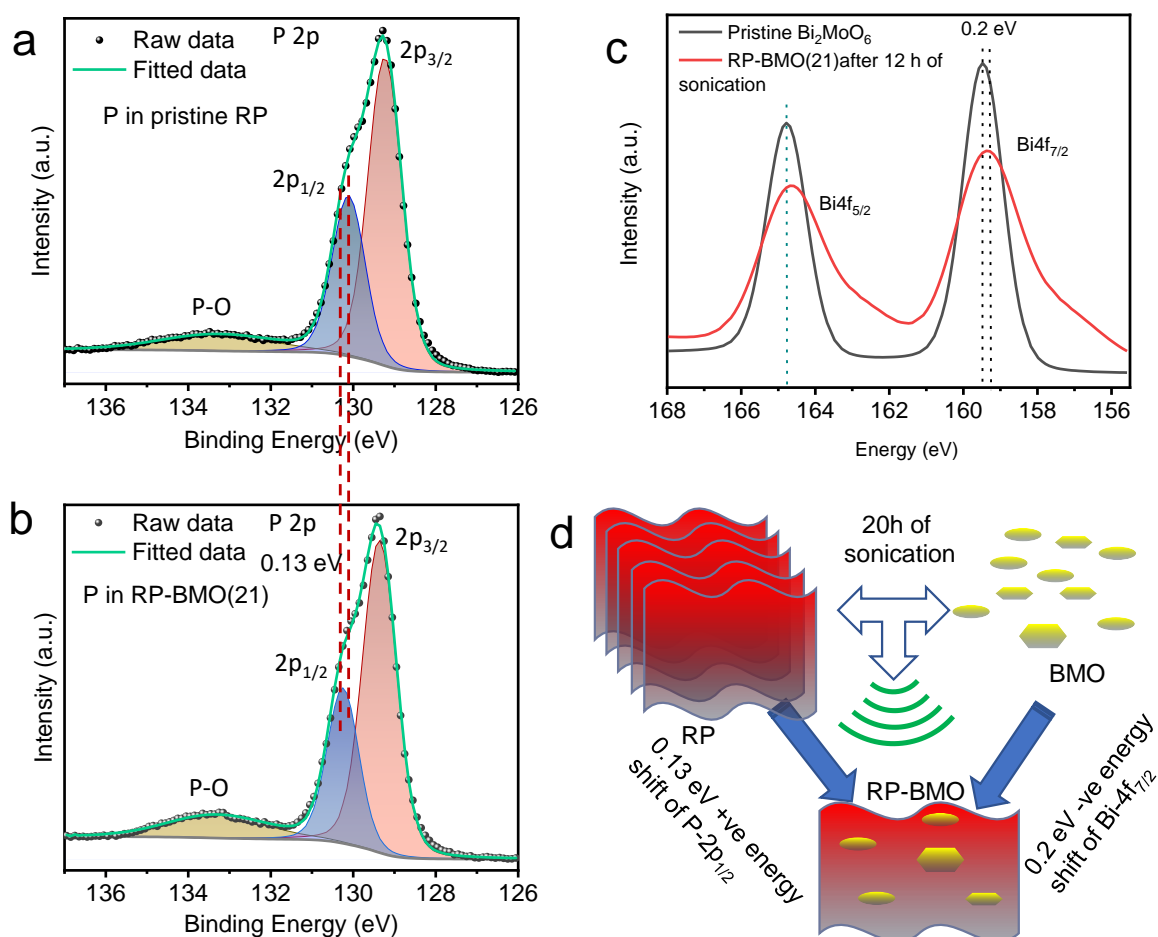
Figure 6.10. XPS analysis for understanding electronic interaction between BMO and RP. **(a-b)** Higher energy shift in P 2p XPS in **RP-BMO(21)** compared to pristine RP. **(c)** Lower energy shift of Bi 4f XPS in **RP-BMO(21)** compared to pristine BMO. **(d)** Schematic representation of RP-BMO composite formation due to sonication and its impact on XPS binding energy shift.

Green Transformation of CO₂ to Ethanol Using Water and Sunlight by Cooperative Endeavour of Naturally Abundant Red Phosphorus and Bi₂MoO₆

Chapter 6

CO₂ to methanol under visible light: CO₂ photoreduction was conducted under visible light illumination using CGA 400 nm UV-cutter filter. Detailed information of the photocatalytic CO₂ reduction measurements is given in experimental procedure.
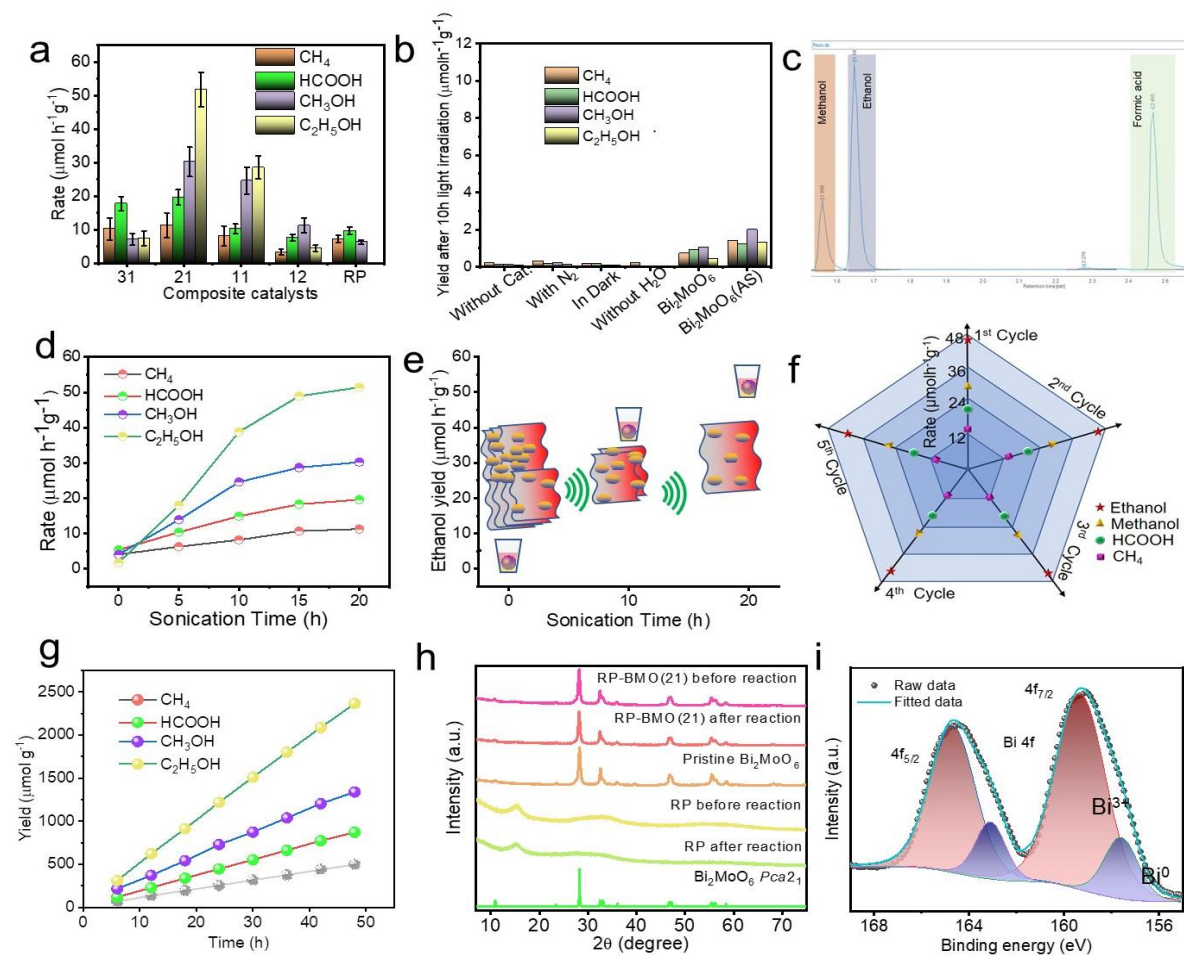
Figure 6.11. Quantitative and qualitative photocatalytic performance. **(a)** CO₂ photoreduction activity of BMO/RP composites with different composition under Xe lamp irradiation (>400 nm). All the experiments were done and average values are presented with error bars for standard deviation. **(b)** Photocatalytic control experiments. Experiments were done in absence of catalyst, CO₂, light and water. Pristine Bi₂MoO₆ showed very feeble photocatalytic performance. **(c)** Screenshot taken from GC. Liquid products were analyze by GC after the catalysis with **RP-BMO(21).** Effect of sonication on catalysis. **(d)** Photocatalytic CO₂ reduction activity of **RP-BMO(21)** upon different interval of sonication. **(e)** Schematic representation of effect of sonication in separating RP sheets and its correlation with ethanol formation efficiency. **(f)** The rate formation of each product at different cycle is presented. **(g)** 50 h stability tests with **RP-BMO(21)** catalyst where data collections were done after each 6h. Stability test of the catalysts after reaction. **(h)** XRD was taken before and after the photocatalytic tests (5 cycles). Phase purity and stability of pristine RP was also checked by recording XRD patterns before and after the photocatalytic reactions. **(i)** XPS of **RP-BMO(21)** sample taken after photocatalytic CO₂ RR studies.

As shown in **Figure 6.11a**, single phase RP favored the conversion of CO_2 to CH_4 and HCOOH with the formation rates of 5.2 µmol $g^{-1}h^{-1}$ and 9.6 µmol $g^{-1}h^{-1}$, respectively, after 10 h light irradiation. No considerable product was detected with pristine BMO catalyst (**Figure 6.11b**). The control experiment also showed that the presence of Bi^0 in BMO (BMO(AS)) due to extended sonication process did not change the CO_2 reduction efficiency considerably (**Figure 6.11b**). However, the composites (RP-BMO) made up of RP and BMO favored higher conversion of CO_2 with the large production of C_2H_5OH (51.8 µmol $g^{-1}h^{-1}$) (**Table 6.1, Figure 6.11c**). The obtained ethanol formation rate by visible light driven CO_2RR is the best compared to other literature reports (**Table 6.2**).

Table 6.1. Overall CO_2 reduction performance by different RP/Bi_2MoO_6 composite photocatalysts**.** Rate of product formation was given in µmol g^{-1} h^{-1} unit. ND: No product was detected (beyond detection limit). BMO(AS) means BMO after sonication.

Sample	Methane	Formic acid	Methanol	Ethanol
RP-BMO(31)	10.2	17.7	7.1	8.4
RP-BMO(21)	11.3	19.6	30.2	51.8
RP-BMO(11)	8.1	10.2	24.6	28.4
RP-BMO(12)	3.3	7.3	11.2	6.4
RP	7.2	9.6	6.2	ND
Bi_2MoO_6	0.71	0.89	1.03	0.42
Bi_2MoO_6(AS)	1.37	1.23	1.98	1.31

Table 6.2. CO_2 to ethanol formation by photocatalytic route. Comparison of ethanol formation rate by **RP-BMO(21)** with reported literature.

Entry	Catalyst	Product	Yield (µmolg^{-1}h^{-1})	Light source and mode of reaction	References
1	**RP-BMO(21)**	CH_3CH_2OH	51.8 (Xe-lamp) 34.1 (Sunlight)	Xe-lamp (450W), Solid-liquid	This work
2	AgBr–NG–g-C_3N_4	CH_3CH_2OH	51	Xe lamp (450W), Solid-liquid	[14]

Green Transformation of CO₂ to Ethanol Using Water and Sunlight by Cooperative Endeavour of Naturally Abundant Red Phosphorus and Bi₂MoO₆

Chapter 6

3	Cu^{2+} doped TiO_2	CH_3CH_2OH	47	365 nm LED lamp, Solid-vapour	[27]
4	$BiVO_4$	CH_3CH_2OH	22	Xe lamp (300 W) Solid-liquid (continuous gas flow).	[17]
5	Pt and N co-doped hollow hierarchical BiOCl	CH_3CH_2OH CH_3OH	14.2	Xe lamp (300 W) Solid-liquid (0.1M NaOH solution, continuous gas flow)	[28]
6	Conducting polymers modified Bi_2WO_6 microspheres	CH_3CH_2OH	5.13	Xe lamp (300 W) Solid -liquid	[16]
7	MoS_2/Bi_2WO_6 nanocomposites	CH_3CH_2OH	9.15	Xe lamp (300 W) Solid -liquid	[29]
8	Bi_2MoO_6 quantum dots in situ grown on reduced graphene oxide layers	CH_3CH_2OH	14.37	0.47 W/cm^2, Solid-liquid (continuous gas flow)	[30]
9	Red Ag/AgCl	CH_3CH_2OH	44.6	Xe lamp (500 W) Solid-liquid (0.1M $NaHCO_3$ solution, continuous gas flow)	[31]
10	$ZnO/g-C_3N_4$	CH_3CH_2OH	1.5	Xe lamp (500 W) Solid-liquid (continuous gas flow)	[32]
11	WS_2/Bi_2S_3	CH_3CH_2OH CH_3OH	6.95 9.55	Xe lamp (300 W) Solid -liquid	[33]
12	$LaVO_4$	CH_3CH_2OH CH_3OH	12.7 1.20	Xe lamp (300 W) Solid -liquid CO_2-saturated $NaHCO_3$ solution containing 0.2 M Na_2SO_3	[34]
13	STO/Cu@Ni/TiN	CH_3CH_2OH	21.3	Xe lamp (300 W) Solid -liquid	[35]
14	Bi_4TaO_8Cl/Bi	CH_3CH_2OH CH_3OH	5.11 2.34	Xe lamp (300 W) Solid -liquid Photothermal	[36]
15	Bi_2MoO_6/PVP	CH_3CH_2OH CH_3OH	4.7 6.2	Xe lamp (300 W) Solid -liquid	[20]

Additionally, this activity was obtained in water in absence of any external additives (sacrificial agents, carbonate solution). Bulk RP was exfoliated and separated upon extended sonication process. Therefore, the effect of sonication on catalytic activity was checked for **RP-BMO(21**) with different sonication time. Compared to the physical mixture sample (0h sonication), 10h sonicated sample showed very high activity. Especially ethanol formation has increased drastically. Upon further sonication up to 20h the activity has increased further (**Figure 6.11d**). Sonication process has separated RP sheets which in turn facilitated better dispersion of BMO and composite formation. This eased the interfacial charge transfer process which caused dramatic increment of activity (**Figure 6.11e).** High efficiency and stability are the two major quality of an industrially acceptable catalyst. Therefore, to check the reusability and stability, the best optimized catalyst, **RP-BMO(21)** was employed for 5 consecutive photocatalytic cycles (**Figure 6.11f)** and continuous 30h catalytic tests with fresh CO_2 and water (**Figure 6.11g**). No significant change in activity even after the 5th cycle and 30h catalysis was observed, confirming high recyclability and stability of the catalysts towards CO_2 photoreduction.

Apart from the performance stability, the structural stability of the catalyst was checked by probing powder X-ray diffraction (PXRD) and XPS after the photoreduction test (**Figure 6.11h,** and **6.11i**), which confirmed the original structure remains the same even after light irradiation. A set of controlled experiments confirmed that the combination CO_2, H_2O, light and catalyst are absolutely necessary for the photoreduction of CO_2 (**Figure 6.11b).** Inspired by the high activity of CO_2 to ethanol formation capabilities in the laboratory conditions, the CO_2 photoreduction of the best catalyst **RP-BMO(21)** was also tested under direct sunlight. Experiments were done in winter/summer and cloudy/sunny weatherusing water as the source of protons (**Figure 6.12a**). Similar yield of ethanol (34.1 μmol $g^{-1}h^{-1}$) was observed under direct sunlight compared to artificial arc lamp condition. The relative quantum yield (QY) of ethanol formation rate under sunlight is around 90.91% (**Figure 6.12b**) of ethanol formation rate under Xe lamp (51.8μmol $g^{-1}h^{-1}$ ethanol). These findings indicate the promising exploration and application of this catalyst for large-scale commercial use. CO_2 photoreduction experiments with $^{13}CO_2$ further confirm the source of produced ethanol is nothing but CO_2. **Figure 6.12c** shows the gas chromatography-mass spectrometry (GC-MS) fragmented peak of $^{12}CH_3{}^{12}CH_2OH$ and $^{13}CH_3{}^{13}CH_2OH$. GC-MS data for other products generated upon $^{13}CO_2$ experiment was given **Figure 6.13**.

Green Transformation of CO₂ to Ethanol Using Water and Sunlight by Cooperative Endeavour of Naturally Abundant Red Phosphorus and Bi₂MoO₆
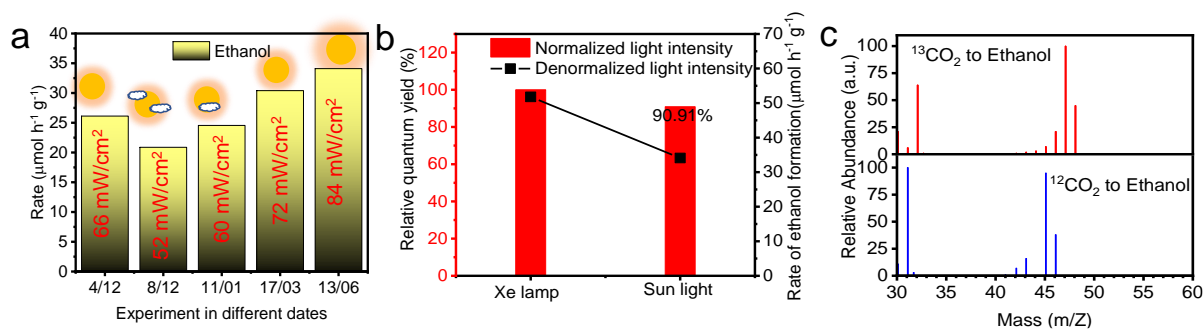
Chapter 6

Figure 6.12. Real time experiment. **(a)** Photocatalytic CO_2 to ethanol formation activity under sunlight with **RP-BMO(21).** The solar light intensity was given in mW/cm^2 in between bars. **(b)** Comparison of ethanol formation rate under sunlight and Xe lamp. **(c)** GC-MS of ethanol, generated from $^{13}CO_2$ photoreduction experiment.
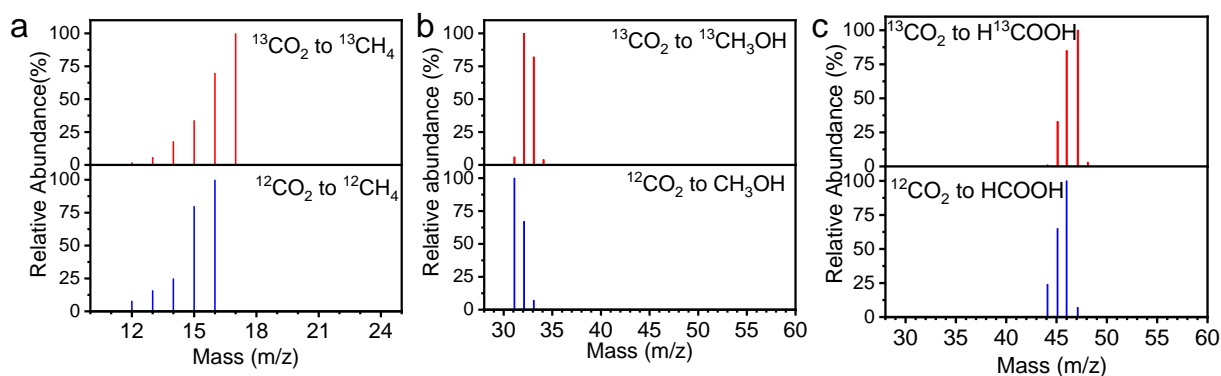

Figure 13. Product analysis by GC-MS after the reaction with **RP-BMO(21)** catalyst. MS of **(a)** $^{13}CH_4$, **(b)** $^{13}CH_3OH$, **(c)** $H^{13}COOH$ obtained upon the reactions with $^{13}CO_2$. The GC peak at a known retention time was chosen from previous calibration and the mass-spectrometry associated with that peak was analyzed for each product.

Hydrophilic catalytic surface provides more proton availability due to better water adsorption and in turn facilitates better CO_2 hydrogenation reaction.[37] As depicted by the contact angle measurements in **Figure 6.14**, RP and Bi₂MoO₆ have contact angles of 22.7° and 63.2° respectively. Consequently, **RP-BMO(21)** has contact angle of 29.1°. **RP-BMO(21)** provides optimum gas (**Figure 6.8a**) and water adsorption capabilities compared to the pristine components and other composites. These synergetic effects provided by the **RP-BMO(21)** composite indicate it is the most promising catalyst evaluated in this work and potentially in the existing literature on photocatalytic CO₂RR.

Role of C1 molecules in C-C coupling: C1 molecules (CO, CH₄, HCOOH, CH₃OH) transforming into liquid fuels or long-chain hydrocarbons are well studied.[38-41] However, harsh conditions like high temperature and pressure are required for such transformations and it is very rare in CO_2 photo-reduction especially for the formation of ethanol.[42]
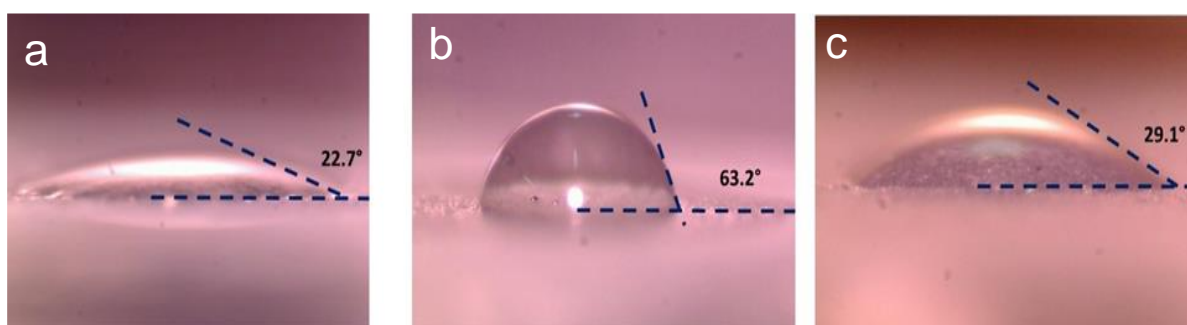
Figure 14. Surface wettability measurements. a-c, Static contact angles of water droplets on the surface of **(a)** RP, **(b)** Bi_2MoO_6, and **(c) RP-BMO(21)**. These contact angles indicate RP has best hydrophilic surface.

Since we have observed CH_4, MeOH and HCOOH in our CO_2 photo-reduction test, a set of controlled experiments were performed using the intermediate C1 molecule under light illumination with the best catalyst (**RP-BMO(21)**). No ethanol formation was observed when methane was used, but 996.3 µmol $h^{-1}g^{-1}$ ethanol was formed (**Figure 6.15a**) in when 300 mM methanol solution was used, confirming that methanol is the key intermediate for ethanol formation. Light-induced conversion of methanol to ethanol was further probed via kinetic isotopic effect (1° KIE) study using deuterated methanol (CD_3OD) to verify the involvement of OCH_3^*/OCD_3^* species in the rate-determining step. The deuterated ethanol species was identified from GC-Mass (**Figure 6.15b**). **Figure 6.15c** shows almost 3.6 times lesser activity for the formation of partially deuterated ethanol (**Figure 6.15b**) from CD_3OD compared to CH_3OH. Importantly, formation of formic acid was also affected by changing the reactant from CH_3OH to CD_3OD (**Figure 6.15c**).

However, methane formation rate remained similar upon switching the feed from CH_3OH to CD_3OD because C-H bond is not involved in OCH_3^* to CH_4 formation. This confirms direct involvement of C-D bond during C-C coupling for ethanol formation and methanol oxidation by C-D bond dissociation for the formic acid production. Generation of formic acid can be attributed to the photo-oxidation of methanol by photo-generated holes (**Figure 6.15d**). Furthermore, the synergistic effect of BMO and RP towards ethanol formation was verified by using methanol or methane as feed and pristine exfoliated RP, sonicated BMO (BMO(AS)) as a catalyst. When methane was used as reactant, both the catalysts have not shown activity. However, in 300 mM methanol RP has generated methane and formic acid, which indicates that RP has good C1 product formation capability but inability towards C-C coupling process (**Figure 6.15e**).
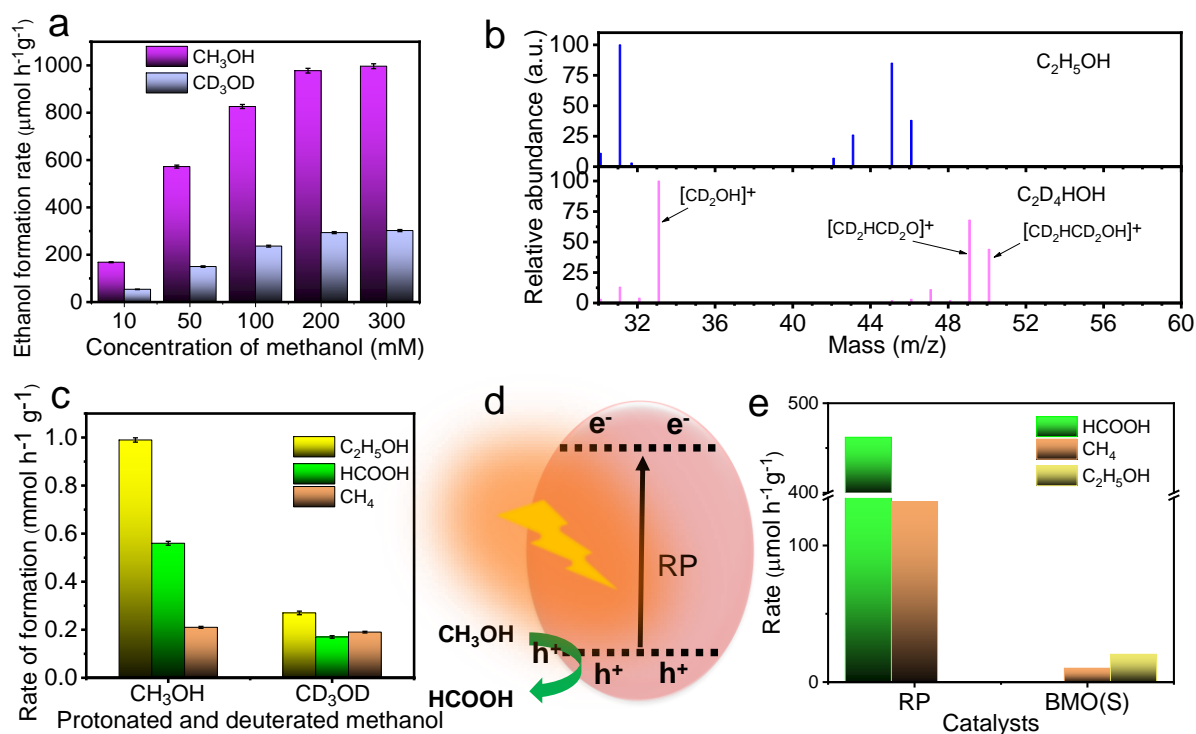
Green Transformation of CO₂ to Ethanol Using Water and Sunlight by Cooperative Endeavour of Naturally Abundant Red Phosphorus and Bi₂MoO₆

Chapter 6

Figure 6.15. Photocatalytic control experiment with methanol. **(a)** Ethanol formation rate from methanol feed under light illumination with different concentration methanol. CH₃OH and CD₃OD were exploited for studying the kinetics (Kinetic isotopic effect) of methanol to ethanol formation. **(b)** MS of ethanol obtained from CD₃OD after reaction with **RP-BMO(21).** Deuterated methanol converted to ethanol on **RP-BMO(21)** catalyst upon light illumination. **(c)** Overall methanol to other liquid product formation rate. **(d)** Methanol oxidation by the photogenerated holes (h⁺) of RP valence band counterpart. **(e)** Photocatalytic activity of exfoliated red phosphorus (RP) and 20h sonicated Bi₂MoO₆ (**BMO(AS)**), AS means after sonication) when 300 mM methanol was used as reactant. The reaction was carried out for 10h.

Interestingly, BMO(AS) has generated very less amount of ethanol along with methane from methanol (**Figure 6.15e**), meaning that it has C-C coupling power but it suffers from lack of adequate amount of photoexcited charges and blockage of active sites due to agglomeration. Therefore, the composite catalyst can stabilize photoexcited charges and supply methanol for C-C coupling. Exfoliated RP also provides proper dispersion of BMO(AS) where active sites get exposed for catalysis.

Mechanism via *in-situ* DRIFTS: Insight into the photocatalytic conversion of CO₂ to ethanol by **RP-BMO(21)** was obtained from the in-situ DRIFTS experiments, which were performed in the range of 400-4000 cm⁻¹ at room temperature (25° C). An absorption peak was observed at 1613 cm⁻¹ with a proportional increase of peak intensity upon irradiation time. This peak can be assigned to the COOH* group, which is considered as the common

intermediate for CH_4, $HCOOH$, CH_3OH and C2 product formation during CO_2 reduction (**Figure 6.16a**).[37, 43] Most importantly, **RP-BMO(21)** exhibited high activity for ethanol formation from CO_2 photoreduction at room temperature, flagged by the growth of OCH_3^* characteristic band at 1069 cm^{-1}.[26] Evolution of the characteristic CHO^* peak at 993 cm^{-1} was also observed upon irradiation time.[44] Both the CHO^* and OCH_3^* groups are the key intermediates for the production of CH_3OH, CH_4 and C_2H_5OH from CO_2. The peaks observed at 1290 cm^{-1} and 1,506 cm^{-1} (**Figure 6.16b)** could be assigned to asymmetric and symmetric stretching (ASS) of CO_3^*. FT-IR peaks corresponding to HCO_3^* ASS vibrations are observed at 1356 cm^{-1} and 1430 cm^{-1} respectively.[26, 45] Contextually, no CO absorption peak was found in the range of 2000-2200 cm^{-1} in the in-situ FTIR spectra,[46] indicating rapid conversion of CO intermediates to CHO^* instead of being desorbed to form CO molecules. DRIFTS experiments with pristine BMO indicated the formation of carbonate, bicarbonate and COOH species (**Figure 6.16c**). Presence of high amounts of carbonate and bicarbonate can be attributed due the presence of O-vacancies because these vacancies are capable of adsorbing CO_2 as carbonate species. The presence of O-vacancies was also confirmed from Electron spin resonance (ESR) spectroscopy.

Additionally, a very small peak observed at 1071 cm^{-1} can be assigned to OCH_3^* species confirming negligible CO_2 conversion activity of BMO (**Figure 6.11b**). Inappropriate CBM position with respect to HCOOH and CO formation potential[47] and excessive charge recombination in BMO hindered the CO_2 photoreduction process, hence no further intermediates like CHO^* or OCH_3^* peaks were observed in in-situ DRIFTS. On the other hand, DRIFTS studies on RP exhibited a strong band at 1067 cm^{-1} corresponding to OCH_3^*, which supports the formation of methane (**Figure 6.16d**). However, due to inefficient gas adsorption capabilities (**Figure 6.8a,** and **6.7b**), it shows very weak carbonate and bicarbonate peaks (**Figure 6.16d**). The moderate formation of methane from CO_2 on pristine RP has been supported by the increased in-situ FTIR peak intensities for CHO^* and OCH_3^* (key intermediates for CH_4 formation) upon irradiation time (**Figure 6.16d**). Hence, the co-operative efforts of RP and BMO in **RP-BMO(21)** offers optimum condition for optimum CO_2 and water adsorption and further hydrogenation as depicted from the presence of both high quantities of OCH_3^* intermediates and carbonate species (**Figure 6.16a**). Methanol has been identified as the active species which converted to ethanol via C-C coupling from controlled experiments (**Figure 6.15a,** and **6.15c**), which is further mapped by in-situ FTIR. As a control study, DRIFTS was done in presence of methane gas and methanol vapour.
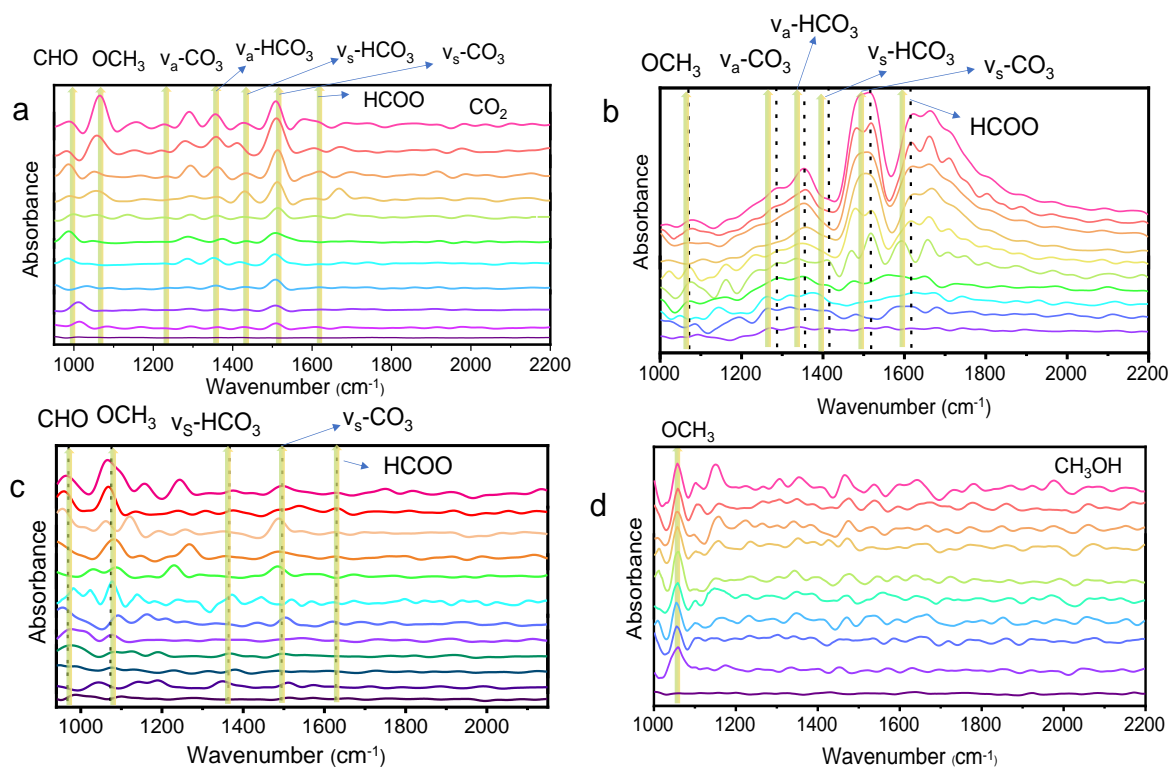
Green Transformation of CO₂ to Ethanol Using Water and Sunlight by Cooperative Endeavour of Naturally Abundant Red Phosphorus and Bi₂MoO₆

Chapter 6

Figure 6.16. *In-situ* FT-IR. **(a)** In-situ-DRIFTS recorded for **RP-BMO(21)** under light illumination after purging the in-situ cell with CO_2 and water vapour. *In-situ* FTIR spectra for **(b)** BMO, and **(c)** RP was performed for 100 minutes with 10 minute intervels. **(d)** *In-situ* FT-IR experiments were done with co-observed methanol and water vapour without CO_2.

A strong peak corresponding to OCH_3^* was observed at around 1062 cm^{-1} on **RP-BMO(21)** catalyst surface upon the in-situ DRIFTS experiments with methanol (**Figure 6.16b**). No significant spectral evolution was observed with long time light illumination due to presence of sufficient methanol vapour inside the DRIFT cell from the beginning of the experiment. No carbonate or bicarbonate stretching bands were observed because the cell was not purged with CO_2 during these control experiments. Most importantly on the other hand, completely silent FTIR spectra were found during methane and water vapour mediated experiment. These controlled experiments strongly support the transformation of methanol to ethanol through C-C coupling on RP-BMO catalyst.

C-C Coupling mechanism: There are two well known pathways for the transformation of CO_2 to ethanol: (1) formate pathway (**Figure 6.17; top**) and carbide pathway (**Figure 6.17; bottom**). The latter can be eliminated based on the in-situ DRIFTS, Kinetics Isotopic Effect (KIE) and controlled photochemical experiments as it is expected to form only methane, which clearly indicate the reaction mechanism occurred through C-adsorbed formate pathway (**Figure 6.17; top**). In general C2 product formation (**Figure 6.18; top**) requires stronger CO*

intermediate which couples with neighbouring CO*[48]. However, the absence of CO* peak in DRIFTS measurements suggest the transient life span of this species and rapid conversion into CHO* intermediate ruling out the coupling of the 2 CO* intermediate occurrence. It is reported that OCH_3* is the key intermediate for methanol and methane production. Proton (H^+) adsorption on the O center leads to the formation of methanol. On the other hand, H^+ adsorption on the C center produces methane.[37, 49] Since no OCH_3* peak was observed in our controlled DRIFTS measurements with methane and water vapour, we focused on the methanol to ethanol conversion step. Li and co-workers have reported that the insertion of methyl carbene (:CH_2) into the C-H bond of methanol drives the formation of ethanol on GaN nanowires under UV-vis-light irradiation at ambient temperature. However, this pathway will promote C3-alcohol formation upon further :CH_2 insertion on ethanol.[50] Since we didn't observe any C2+ alcohols, this pathway is not valid in this case. Insertion of CO into CH_2 (formed by carbide mechanism) can also lead to the formation of ethanol (**Figure 6.18; bottom**).[51] However, this process demands generation of CH_2* and CO (gaseous). In this study, the process is not following carbide mechanism and gaseous CO was not observed. Hence this pathway can also be ruled out. In this context, a novel mechanistic path can be proposed as the coupling of 2 OCH_3* groups on BMO surface, which is well complemented by the presence of strong OCH_3* peak in DRIFTS. As shown in **Figure 6.19,** one OCH_3* on Bi atom and another on Mo atom interact with a neighbouring OH* group on RP, facilitating the C-C coupling and C-H bond breaking in OCH_3. Subsequent formation of $C_2H_4O_2$* intermediate followed by the proton adsorption on center (attached with Bi) and C center (attached with Mo-O) will lead to the formation of ethanol.
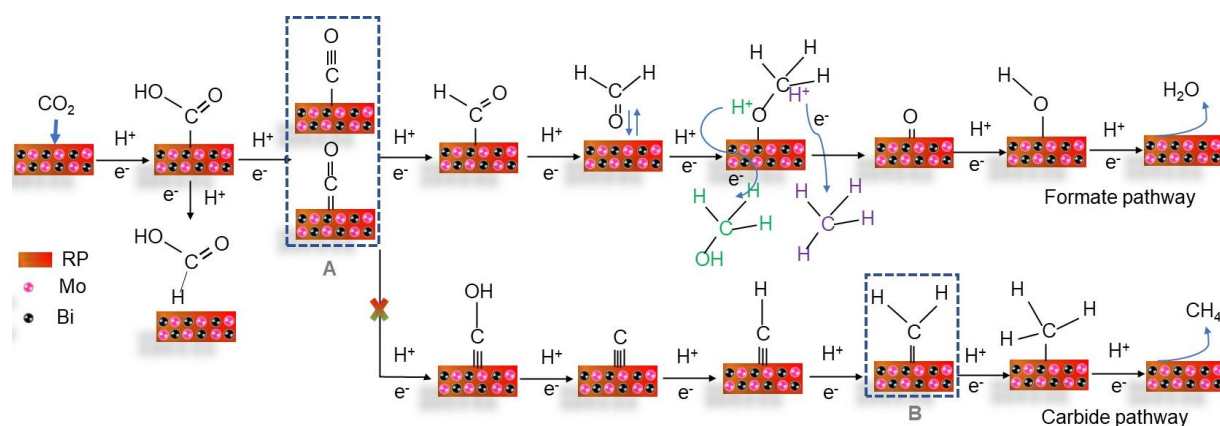

Figure 6.17. Plausible reaction pathways for CO_2 to C1 product formation. CO_2 to formic acid, methanol and methane formation mechanism by formate pathway (**top**) upon light irradiation. Selective methane formation by carbide mechanism (**bottom**) from CO_2 photoreduction.

Higher oxidation state and electropositivity of Mo atom compared to Bi in BMO leads to the formation of a stable $Mo=O$ bond, which drives the formation of water upon reacting with $2H^+$ and $2e^-$ (**Figure 6.20**). Rate of the reaction has reduced 3.6 times upon the use of CD_3OD instead of CH_3OH. Whereas, negligible changes in the methane formation rate implies O-D/H bond breaking is not involved in rate determining step. This observation asserts the direct involvement of C-D/H bond breaking in the process of ethanol formation.

Charge transfer: To understand the driving force for the enhanced CO_2 photoreduction, steady-state photoluminescence (PL) emission spectra were collected, which provide an insight on the charge recombination phenomenon. Almost complete PL quenching was observed in the case of **RP-BMO(21)** compared to the pristine BMO (**Figure 6.21a**) implying that the intrinsic radiative recombination of photogenerated charges in BMO has been drastically alleviated by the construction of the heterojunction. Heterojunction helped in stabilising photogenerated electrons and holes in CBM and VBM respectively. This confirms a strong interfacial charge transfer between well dispersed BMO nanoparticles and the exfoliated RP sheets. The band structures of the ultrathin **RP-BMO(21)** was determined by Tauc plot (**Figure 6.8c**) and Mott-Schottky measurements. As revealed from impedance spectroscopy (Mott-Schottky (MS) plot)[52] in **Figure 6.21b,** and **6.21c** the conduction band minima (CBM) position of RP and Bi_2MoO_6 lies at -0.66 V and -0.6 V (vs. RHE).
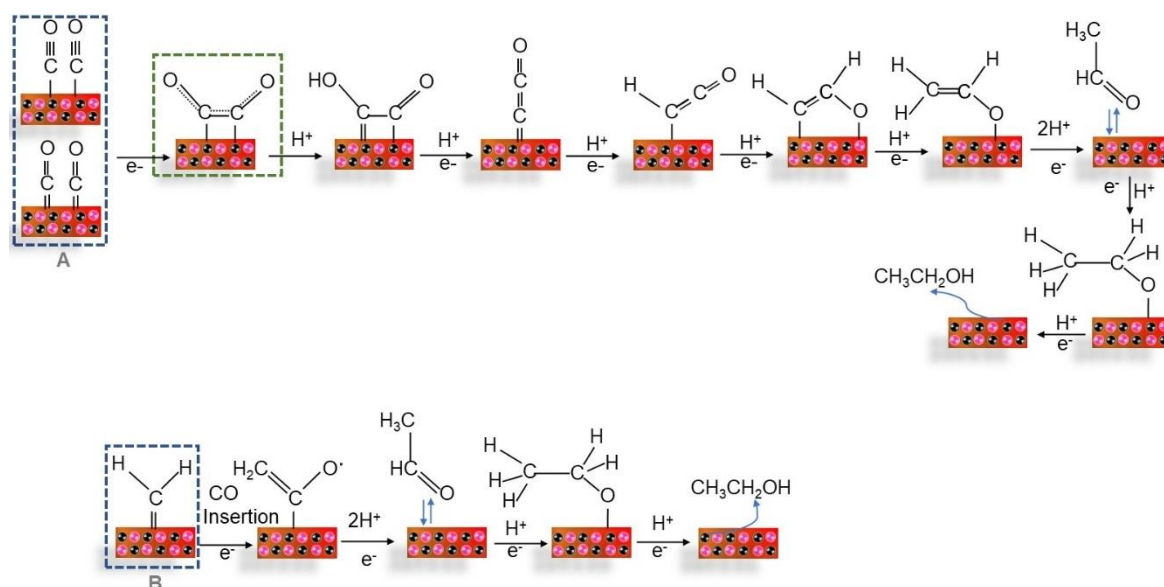
Figure 6.18. Plausible photocatalytic reaction pathways for CO_2 to ethanol formation. Coupling of 2 CO* (as shown by the dotted box (A) in **Figure 6.18**) leads to the formation of acetaldehyde followed by the conversion to ethanol by proton coupled electron transfer pathway (**top**). Ethanol formation by CO insertion into M-CH₂* (depicted by the dotted box(B) in **Figure 6.18**) which was obtained from carbide mechanism (**bottom**).
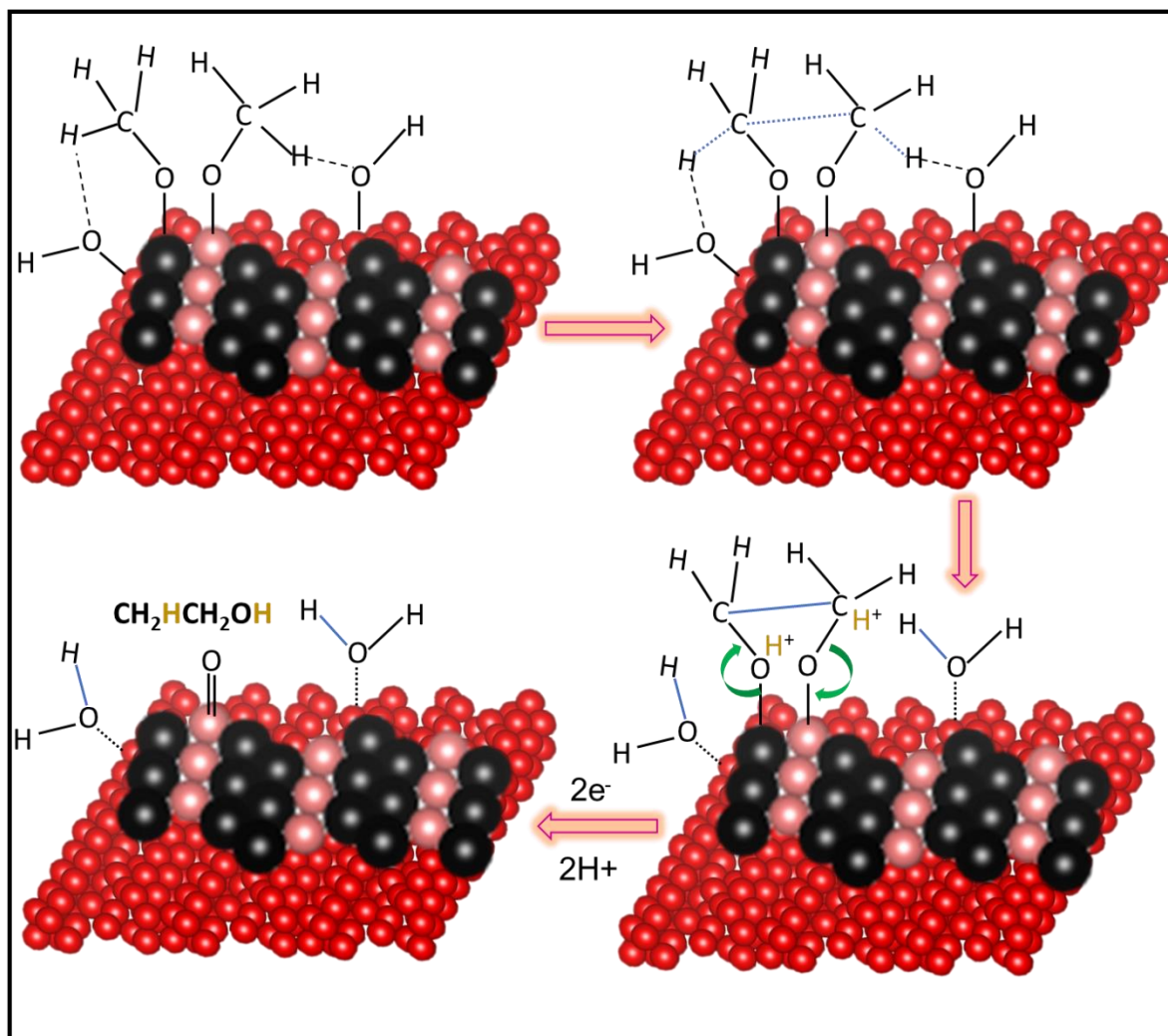
Figure 6.19. Photo induced CO_2 to ethanol formation and electron transfer mechanism in **RP-BMO(21)**. Methanol to ethanol formation via 2 OCH_3* coupling induced by co-operative efforts of Bi and Mo atom of BMO on RP.
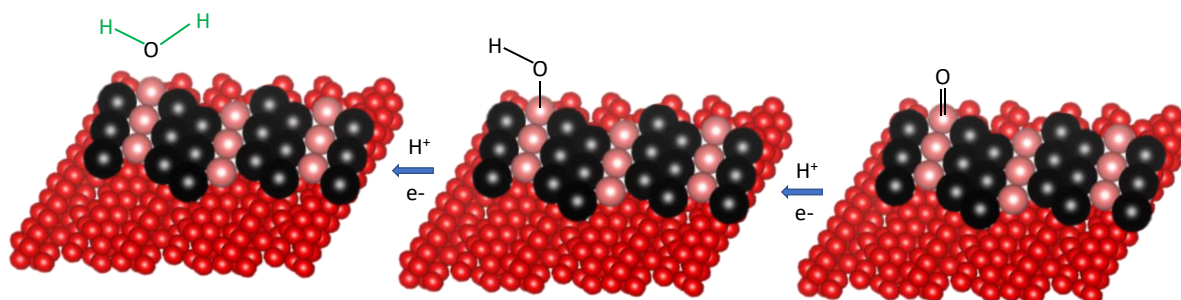
Figure 6.20. Regeneration of the catalyst after catalysis. 'Mo=O' bond further gets reduced to water via proton coupled electron transfer pathway and regenerate composite photocatalyst.

The valence band maxima (VBM) of RP and Bi_2MoO_6 lies at +1.29 V and +2.35 V, was calculated from the bandgap as well as flat band potential values (**Figure 6.8c, 6.21b**, and **6.21c**). As depicted in **Figure 6.21d**, upon irradiation, the photogenerated electrons at the CBM

Green Transformation of CO₂ to Ethanol Using Water and Sunlight by Cooperative Endeavour of Naturally Abundant Red Phosphorus and Bi₂MoO₆

Chapter 6

of the RP travel to the CBM of the BMO. Meanwhile, photogenerated holes transfer from the VBM of BMO to the CBM of RP through the intimate interfaces. Consequently, the CBM of BMO and VBM of RP in composites gain enough CO_2 reduction and O_2 production ability, respectively. Formation of HCOOH can only be explained by Z-scheme mechanism (**Figure 6.22a**) because CO_2 to HCOOH formation demands a potential of -0.58 V whereas BMO CB minima lies at -0.42 V. However, photoexcited electrons of RP can also convert CO_2 to formic acid. On the other hand, controlled study confirms methanol oxidation in the RP VBM counterpart is the main reason for formic acid production (**Figure 6.15d**)[53]. Here photogenerated holes have been consumed by the produced methanol. Therefore, in-situ generated methanol acts as a hole scavenger and increases the supply of electrons for CO_2 reduction on the CBM of BMO.

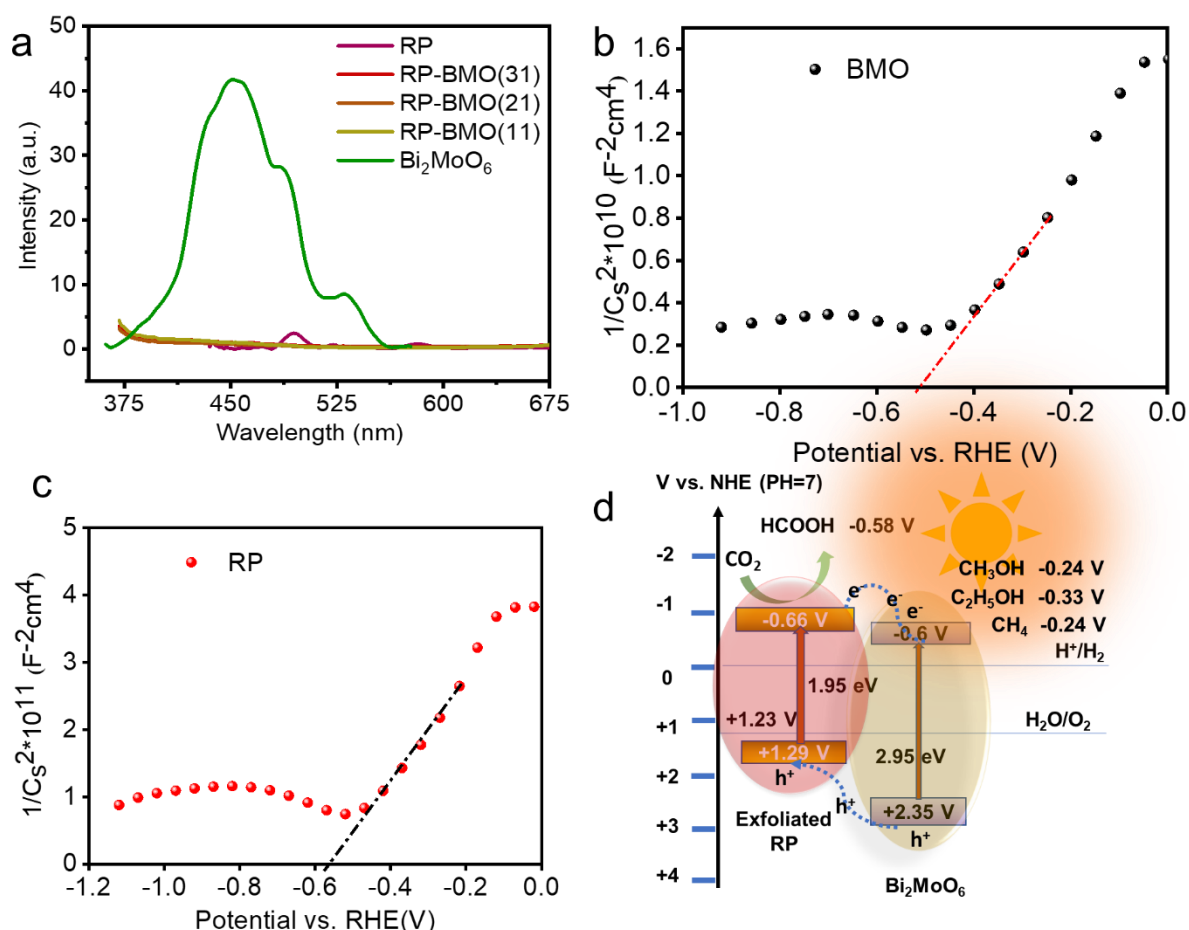**Figure 6.21. (a)** Static PL of **RP-BMO(21)** and other pristine individual components. Electrochemical band edge measurements by Mott-Schottky plot. Conduction band edge was checked by determining flat band potential of **(b)** Bi₂MoO₆, **(c)** RP. Negative slope of the materials confirms nature of the semiconductor is n-type. **(d)** Schematic illustration of photogenerated charge transfer by type-II mechanism.

Z-scheme mechanism (**Figure 22a**) in composites will lead to the accumulation of electrons on RP CBM and holes at BMO VBM.[54] However, RP alone has not shown any ethanol formation despite having a suitable bandgap, on the other hand control study with methanol by BMO has not shown formic acid production. Hence, reduction of CO_2 to ethanol by electrons and oxidation of methanol to HCOOH by holes over composite catalysts can only be done by the BMO (CBM) and RP (VBM) respectively.
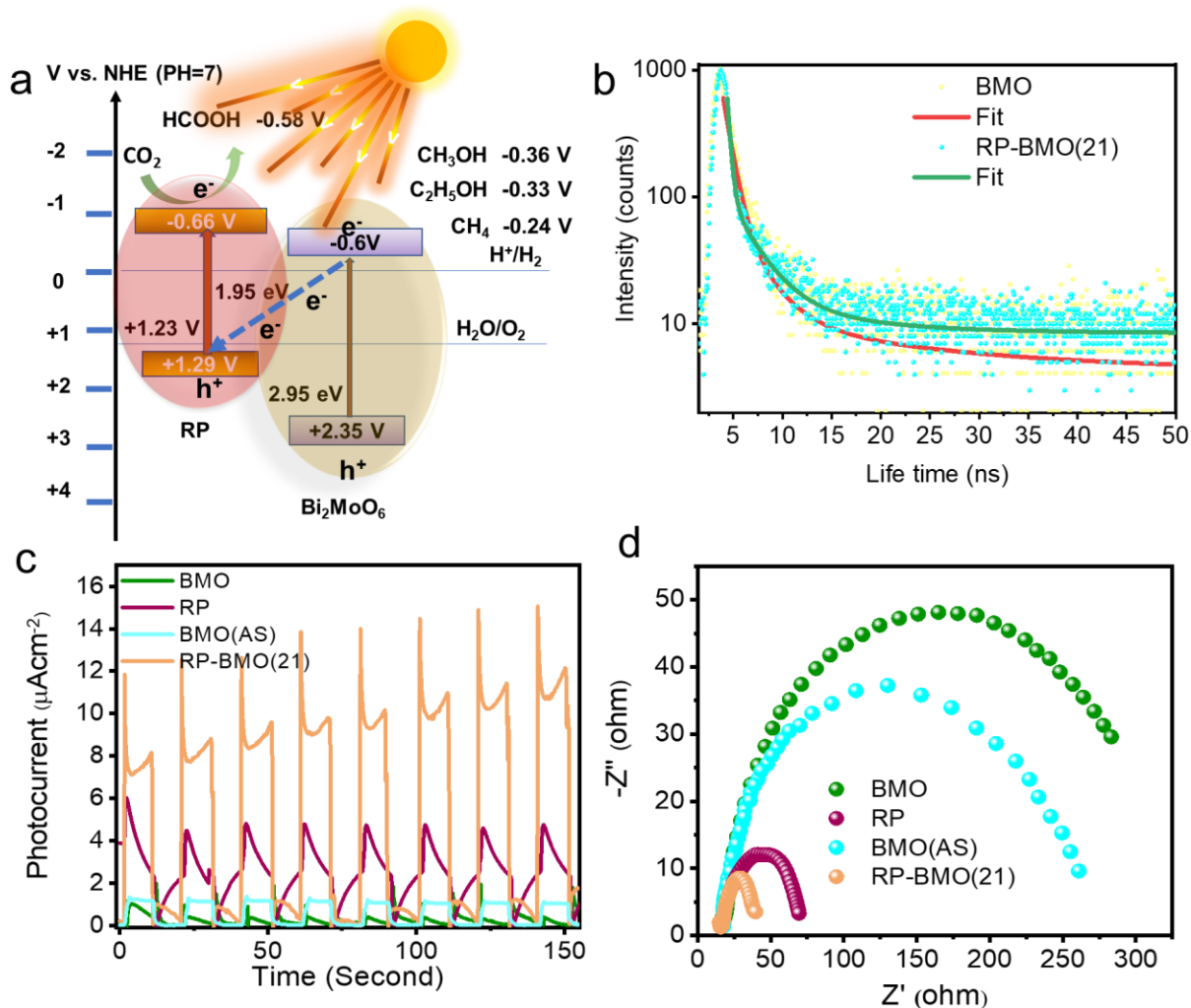
Figure 6.22. (a) Charge transfer by Z-scheme mechanism. Schematic illustration of Z-scheme mechanism. The photogenerated electrons at the CBM of Bi_2MoO_6 travel to the VBM of the RP and then consequently recombine with the photogenerated holes. Meanwhile, the photogenerated electrons and holes are left, respectively, at the CBM of RP and VBM of Bi_2MoO_6 perform reduction and oxidation respectively. **(b)** Time-resolved photoluminescence (TRPL) decay spectra of **RP-BMO(21)** and BMO. **(c)** Transient photocurrent density of BMO, RP and **RP-BMO(21)** at 0.1 V vs. Ag/AgCl. **(d)** Electrochemical impedance spectroscopy (EIS, Nyquist plot) to understand charge transfer resistance from the bulk to surface of the photocatalyst. BMO(AS) represents BMO after sonication.

Green Transformation of CO₂ to Ethanol Using Water and Sunlight by Cooperative Endeavour of Naturally Abundant Red Phosphorus and Bi₂MoO₆

Chapter 6

Therefore, flow of electrons from RP to BMO through Z-scheme route is not a favourable path for electron transfer, instead type-II charge transfer mechanism efficiently separates photo-generated charges and minimizes their recombination. This hypothesis was further supported by time-resolved photoluminescence (TRPL) emission decay spectra (**Figure 6.22b**), which shows longer average lifetime (τ_{avg}) of photogenerated charge carriers in RP-BMO(21) with respect to the pristine BMO (**Table 6.3**) suggesting substantial number of photogenerated electrons are available for longer time in the CBM of **RP-BMO(21)** for CO_2 reduction[56]. Furthermore, to obtain the qualitative insight of photogenerated charge transfer properties, transient photocurrent and electrochemical impedance spectroscopy (EIS) measurements were done for RP, BMO, and **RP-BMO(21)**. Transient photocurrent measurements exhibit a consistent increase of photocurrent for **RP-BMO(21)** compared to RP and BMO (**Figure 6.22c**). The smallest semicircle corresponding to **RP-BMO(21)** in EIS (**Figure 6.22d**) indicates lower charge transfer resistance of **RP-BMO(21)**, which implies better charge transfer efficiency of composites by the formation of type-II heterostructure. The role of sonication on pristine BMO was further understood from photo-current and electrochemical impedance spectroscopy. It showed very small increment (**Figure 6.22c**) of photocurrent and minor decrease of charge transfer resistance (**Figure 6.22d**), implying small amount of Bi^0 on BMO after sonication has very negligible impact in stabilizing excited photoelectrons. This observation also supports small increment of CO_2 reduction efficiency by BMO(AS) catalyst compared to BMO. However, Bi^0 in the interface of RP and BMO may play a crucial role in faster charge transfer. Based on these observations, the enhanced activity of CO_2 to ethanol on composite can be understood by considering type-II charge transfer pathway.

Table 6.3. Parameters of the TRPL decay. The data was fitted using the following equation. A+B1exp(-t/τ_1)+B2exp(-t/τ_2)+B3exp(-t/τ_3), where, B1, B2, and B3 are the pre-exponential factor (amplitude) corresponding to decay lifetimes τ_1, τ_2, and τ_3 respectively. Here $\tau_{avg.}$ is the average life time and χ is goodness of fit.[55]

Sample	τ_1 (ns)	B1	τ_2 (ns)	B2	τ_3 (ns)	B3	$\tau_{avg.}$ (ns)	χ^2
RP-BMO(21)	0.85	0.58	2.73	0.26	16.65	0.16	3.87	1.17
Bi_2MoO_6	0.32	0.38	2.7	0.47	10	0.15	2.8	1.10

The concept of using low-cost red phosphorus in photocatalysis after producing sheet like fragments from it upon ultra-sonication is absolutely unique in terms of material design. Record high amount of ethanol formation and its' formation analysis from isotopic study is very unique for this field.

6.5.   Conclusion

We have discovered a novel type-II composite heterostructure with earth-abundant, non-toxic, cost-effective exfoliated red phosphorus nano-sheet and Bi_2MoO_6 nanoparticles with manipulated band structure for selective conversion of CO_2 to ethanol. Formation of the photocatalyst was verified by a combination of several microscopic and spectroscopic techniques. A record high amount of ethanol was obtained under arc lamp as well as direct sunlight. Controlled experiments with the intermediate methanol and methane molecules revealed that the in-situ generated methanol is the actual active species that was consumed for the production of ethanol. With the help of kinetic study by deuterated methanol (CD_3OD) and in-situ DRIFTS, a new ethanol formation mechanistic pathway has been established for the first time. An efficient type-II charge transfer mechanism in the composite was proposed and supported by PL, TRPL, EIS, photocurrent density measurements. These findings prospects towards a relatively less explored photocatalyst that holds great promise for photocatalytic CO_2RR, and is selective towards value-added ethanol formation in higher yield through a new mechanistic pathway.

6.6.   References

1.   Zhou, Y.; Wang, Z.; Huang, L.; Zaman, S.; Lei, K.; Yue, T.; Li, Z. a.; You, B.; Xia, B. Y., Engineering 2D Photocatalysts toward Carbon Dioxide Reduction. *Adv. Energy Mater.* **2021,** *11*, 2003159.

2.   Ci, C.; Carbó, J. J.; Neumann, R.; Graaf, C. d.; Poblet, J. M., Photoreduction Mechanism of CO_2 to CO Catalyzed by a Rhenium(I)–Polyoxometalate Hybrid Compound. *ACS Catal.* **2016,** *6*, 6422-6428.

3.   Jia, J.; Qian, C.; Dong, Y.; Li, Y. F.; Wang, H.; Ghoussoub, M.; Butler, K. T.; Walsh, A.; Ozin, G. A., Heterogeneous catalytic hydrogenation of CO_2 by Metal Oxides: Defect Engineering – Perfecting Imperfection. *Chem. Soc. Rev.* **2017,** *46*, 4631-4644.

4.   Wang, J.; Lin, S.; Tian, N.; Ma, T.; Zhang, Y.; Huang, H., Nanostructured Metal Sulfides: Classification, Modification Strategy, and Solar-Driven CO_2 Reduction Application. *Adv. Funct. Mater.* **2021,** *31*, 2008008.

Green Transformation of CO₂ to Ethanol Using Water and Sunlight by Cooperative Endeavour of Naturally Abundant Red Phosphorus and Bi₂MoO₆

Chapter 6

5. Shyamal, S.; Pradhan, N., Halide Perovskite Nanocrystal Photocatalysts for CO_2 Reduction: Successes and Challenges. *J. Phys. Chem. Lett.* **2020,** *11*, 6921-6934.

6. Cheng, Y.-Z.; Ding, X.; Han, B.-H., Porous Organic Polymers for Photocatalytic Carbon Dioxide Reduction. *ChemPhotoChem* **2021,** *5*, 406-417.

7. Fu, Z.; Wang, X.; Gardner, A. M.; Wang, X.; Chong, S. Y.; Neri, G.; Cowan, A. J.; Liu, L.; Li, X.; Vogel, A.; Clowes, R.; Bilton, M.; Chen, L.; Sprick, R. S.; Cooper, A. I., A Stable Covalent Organic Framework for Photocatalytic Carbon Dioxide Reduction. *Chem. Sci.* **2020,** *11*, 543-550.

8. Diercks, C. S.; Liu, Y.; Cordova, K. E.; Yaghi, O. M., The Role of Reticular Chemistry in The Design of CO_2 Reduction Catalysts. *Nat. Mater.* **2018,** *17*, 301-307.

9. Boutin, E.; Merakeb, L.; Ma, B.; Boudy, B.; Wang, M.; Bonin, J.; Anxolabéhère-Mallart, E.; Robert, M., Molecular Catalysis of CO_2 Reduction: Recent Advances and Perspectives in Electrochemical and Light-Driven Processes with Selected Fe, Ni and Co Aza Macrocyclic and Polypyridine Complexes. *Chem. Soc. Rev.* **2020,** *49*, 5772-5809.

10. Guo, Z.; Chen, G.; Cometto, C.; Ma, B.; Zhao, H.; Groizard, T.; Chen, L.; Fan, H.; Man, W.-L.; Yiu, S.-M.; Lau, K.-C.; Lau, T.-C.; Robert, M., Selectivity Control of CO Versus $HCOO^-$ Production in the Visible-Light-Driven Catalytic Reduction of CO_2 with Two co-Operative Metal Sites. *Nat. Catal.* **2019,** *2*, 801-808.

11. Corby, S.; Rao, R. R.; Steier, L.; Durrant, J. R., The kinetics of Metal Oxide Photoanodes from Charge Generation to Catalysis. *Nat. Rev. Mater.* **2021**, *6*, 1136-1155.

12. Xie, S.; Ma, W.; Wu, X.; Zhang, H.; Zhang, Q.; Wang, Y.; Wang, Y., Photocatalytic and Electrocatalytic Transformations of C1 Molecules Involving C–C Coupling. *Energy Environ. Sci.* **2021**, *14*, 37-89.

13. Das, R.; Chakraborty, S.; Peter, S. C., Systematic Assessment of Solvent Selection in Photocatalytic CO_2 Reduction. *ACS Energy Lett.* **2021**, 3270-3274.

14. Li, H.; Gan, S.; Wang, H.; Han, D.; Niu, L., Intercorrelated Superhybrid of AgBr Supported on Graphitic-C₃N₄-Decorated Nitrogen-Doped Graphene: High Engineering Photocatalytic Activities for Water Purification and CO_2 Reduction. *Adv. Mater.* **2015,** *27*, 6906-6913.

15. Jeyalakshmi, V.; Mahalakshmy, R.; Krishnamurthy, K. R.; Viswanathan, B., Photocatalytic Reduction of Carbon Dioxide in Alkaline Medium on La Modified Sodium Tantalate with Different co-Catalysts under UV–Visible Radiation. *Catal. Today* **2016,** *266*, 160-167.

16. Dai, W.; Xu, H.; Yu, J.; Hu, X.; Luo, X.; Tu, X.; Yang, L., Photocatalytic reduction of CO_2 into Methanol and Ethanol over Conducting Polymers Modified Bi_2WO_6 Microspheres under Visible Light. *Appl. Surf. Sci.* **2015,** *356*, 173-180.

17. Liu, Y.; Huang, B.; Dai, Y.; Zhang, X.; Qin, X.; Jiang, M.; Whangbo, M.-H., Selective Ethanol Formation from Photocatalytic Reduction of Carbon Dioxide in Water with $BiVO_4$ Photocatalyst. *Catal. Commun.* **2009,** *11*, 210-213.

18. Liu, F.; Shi, R.; Wang, Z.; Weng, Y.; Che, C.-M.; Chen, Y., Direct Z-Scheme Hetero-phase Junction of Black/Red Phosphorus for Photocatalytic Water Splitting. *Angew. Chem. Int. Ed.* **2019,** *58*, 11791-11795.

19. Liu, X.; Gu, S.; Zhao, Y.; Zhou, G.; Li, W., $BiVO_4$, Bi_2WO_6 and Bi_2MoO_6 Photocatalysis: A Brief Review. *J Mater Sci Technol.* **2020,** *56*, 45-68.

20. Dai, W.; Yu, J.; Xu, H.; Hu, X.; Luo, X.; Yang, L.; Tu, X., Synthesis of Hierarchical Flower-Like Bi_2MoO_6 Microspheres as Efficient Photocatalyst for Photoreduction of CO_2 into Solar Fuels under Visible Light. *CrystEngComm* **2016,** *18*, 3472-3480.

21. Oshima, T.; Nishioka, S.; Kikuchi, Y.; Hirai, S.; Yanagisawa, K.-i.; Eguchi, M.; Miseki, Y.; Yokoi, T.; Yui, T.; Kimoto, K.; Sayama, K.; Ishitani, O.; Mallouk, T. E.; Maeda, K., An Artificial Z-Scheme Constructed from Dye-Sensitized Metal Oxide Nanosheets for Visible Light-Driven Overall Water Splitting. *J. Am. Chem. Soc.* **2020,** *142*, 8412-8420.

22. Cherevotan, A.; Raj, J.; Dheer, L.; Roy, S.; Sarkar, S.; Das, R.; Vinod, C. P.; Xu, S.; Wells, P.; Waghmare, U. V.; Peter, S. C., Operando Generated Ordered Heterogeneous Catalyst for the Selective Conversion of CO_2 to Methanol. *ACS Energy Lett.* **2021,** *6*, 509-516.

23. Comstock, M. J., Phosphorus Chemistry, Copyright, ACS Symposium Series, Forwarded. In *Phosphorus Chemistry*, Comstock, M. *J., Ed. Am. Chem. Soc:* **1981**, 171, 1-4.

24. Zhao, D.; Wang, Y.; Dong, C.-L.; Huang, Y.-C.; Chen, J.; Xue, F.; Shen, S.; Guo, L., Boron-Doped Nitrogen-Deficient Carbon Nitride-Based Z-Scheme Heterostructures for Photocatalytic Overall Water Splitting. *Nat. Energy* **2021,** *6*, 388-397.

25. Gomez, C.; Hallot, G.; Pastor, A.; Laurent, S.; Brun, E.; Sicard-Roselli, C.; Port, M., Metallic Bismuth Nanoparticles: Towards a Robust, Productive and Ultrasound Assisted Synthesis from Batch to Flow-Continuous Chemistry. *Ultrason. Sonochem.* **2019,** *56*, 167-173.

26. Tan, T. H.; Xie, B.; Ng, Y. H.; Abdullah, S. F. B.; Tang, H. Y. M.; Bedford, N.; Taylor, R. A.; Aguey-Zinsou, K.-F.; Amal, R.; Scott, J., Unlocking the Potential of the Formate Pathway in the Photo-Assisted Sabatier Reaction. *Nat. Catal.* **2020,** *3*, 1034-1043.

Green Transformation of CO₂ to Ethanol Using Water and Sunlight by Cooperative Endeavour of Naturally Abundant Red Phosphorus and Bi₂MoO₆

Chapter 6

27. Cheng, M.; Yang, S.; Chen, R.; Zhu, X.; Liao, Q.; Huang, Y., Copper-Decorated TiO_2 Nanorod Thin Films in Optofluidic Planar Reactors for Efficient Photocatalytic Reduction of CO_2. *Int. J. Hydrogen Energy* **2017,** *42*, 9722-9732.

28. Maimaitizi, H.; Abulizi, A.; Kadeer, K.; Talifu, D.; Tursun, Y., In Situ Synthesis of Pt and N co-Doped Hollow Hierarchical BiOCl Microsphere as an Efficient Photocatalyst for Organic Pollutant Degradation and Photocatalytic CO_2 Reduction. *Appl. Surf. Sci.* **2020,** *502*, 144083.

29. Dai, W.; Yu, J.; Deng, Y.; Hu, X.; Wang, T.; Luo, X., Facile Synthesis of MoS_2/Bi_2WO_6 Nanocomposites for Enhanced CO_2 Photoreduction Activity under Visible Light Irradiation. *Appl. Surf. Sci.* **2017,** *403*, 230-239.

30. Dai, W.; Xiong, W.; Yu, J.; Zhang, S.; Li, B.; Yang, L.; Wang, T.; Luo, X.; Zou, J.; Luo, S., Bi_2MoO_6 Quantum Dots In Situ Grown on Reduced Graphene Oxide Layers: A Novel Electron-Rich Interface for Efficient CO_2 Reduction. *ACS Appl. Mater. Interfaces* **2020,** *12*, 25861-25874.

31. Cai, B.; Wang, J.; Gan, S.; Han, D.; Wu, Z.; Niu, L., A Distinctive Red Ag/AgCl Photocatalyst with Efficient Photocatalytic Oxidative and Reductive Activities. *J. Mater. Chem. A* **2014,** *2*, 5280-5286.

32. He, Y.; Wang, Y.; Zhang, L.; Teng, B.; Fan, M., High-Efficiency Conversion of CO_2 to Fuel over ZnO/g-C_3N_4 Photocatalyst. *Appl. Catal., B* **2015,** *168-169*, 1-8.

33. Dai, W.; Yu, J.; Luo, S.; Hu, X.; Yang, L.; Zhang, S.; Li, B.; Luo, X.; Zou, J., WS_2 Quantum Dots Seeding in Bi_2S_3 Nanotubes: A Novel Vis-NIR Light Sensitive Photocatalyst with Low-Resistance Junction Interface for CO_2 Reduction. *Chem. Eng. J.* **2020,** *389*, 123430.

34. Chen, X.; Zhuang, C.; Wang, X.; Liao, A.; Li, L.; Liu, Q.; Tang, Y.; Wu, C.; Shen, Q.; Yu, Z., Two-Step Synthesis of Laminar Vanadate via a Facile Hydrothermal Route and Enhancing the Photocatalytic Reduction of CO_2 into Solar Fuel through Tuning of the Oxygen Vacancies by in Situ Vacuum Illumination Treatment. *ACS Applied Energy Materials* **2018,** *1*, 6857-6864.

35. Dai, W.; Yu, J.; Deng, Y.; Hu, X.; Wang, T.; Luo, X., Facile Synthesis of MoS_2/Bi_2WO_6 Nanocomposites for Enhanced CO_2 Photoreduction Activity Under Visible Light Irradiation. *Appl. Surf. Sci.* **2017,** *403*, 230-239.

36. Li, S.; Wang, C.; Li, D.; Xing, Y.; Zhang, X.; Liu, Y., Bi_4TaO_8Cl/Bi Heterojunction Enables High-Selectivity Photothermal Catalytic Conversion of CO_2-H_2O Flow to Liquid Alcohol. *Chem. Eng. J.* **2022**, 135133.

37. Li, X.; Sun, Y.; Xu, J.; Shao, Y.; Wu, J.; Xu, X.; Pan, Y.; Ju, H.; Zhu, J.; Xie, Y., Selective Visible-Light-Driven Photocatalytic CO_2 Reduction to CH_4 Mediated by Atomically Thin $CuIn_5S_8$ Layers. *Nat. Energy* **2019**, *4*, 690-699.

38. Yarulina, I.; Chowdhury, A. D.; Meirer, F.; Weckhuysen, B. M.; Gascon, J., Recent Trends and Fundamental Insights in the Methanol-to-Hydrocarbons Process. *Nat. Catal.* **2018**, *1*, 398-411.

39. Yang, M.; Fan, D.; Wei, Y.; Tian, P.; Liu, Z., Recent Progress in Methanol-to-Olefins (MTO) Catalysts. *Adv. Mater.* **2019**, *31*, 1902181.

40. Harmel, J.; Peres, L.; Estrader, M.; Berliet, A.; Maury, S.; Fécant, A.; Chaudret, B.; Serp, P.; Soulantica, K., hcp-Co Nanowires Grown on Metallic Foams as Catalysts for Fischer–Tropsch Synthesis. *Angew. Chem. Int. Ed.* **2018**, *57*, 10579-10583.

41. Xie, J.; Jin, R.; Li, A.; Bi, Y.; Ruan, Q.; Deng, Y.; Zhang, Y.; Yao, S.; Sankar, G.; Ma, D.; Tang, J., Highly Selective Oxidation of Methane to Methanol at Ambient Conditions by Titanium Dioxide-Supported Iron Species. *Nat. Catalysis* **2018**, *1*, 889-896.

42. Dorner, R. W.; Hardy, D. R.; Williams, F. W.; Willauer, H. D., Heterogeneous Catalytic CO_2 Conversion to Value-Added Hydrocarbons. *Energy Environ. Sci.* **2010**, *3*, 884-890.

43. Zhuo, T.-C.; Song, Y.; Zhuang, G.-L.; Chang, L.-P.; Yao, S.; Zhang, W.; Wang, Y.; Wang, P.; Lin, W.; Lu, T.-B.; Zhang, Z.-M., H-Bond-Mediated Selectivity Control of Formate versus CO during CO_2 Photoreduction with Two Cooperative Cu/X Sites. *J. Am. Chem. Soc.* **2021**, *143*, 6114-6122.

44. Yu, Y.; Chan, Y. M.; Bian, Z.; Song, F.; Wang, J.; Zhong, Q.; Kawi, S., Enhanced Performance and Selectivity of CO_2 Methanation over g-C_3N_4 Assisted Synthesis of $NiCeO_2$ Catalyst: Kinetics and DRIFTS Studies. *Int. J. Hydrogen Energy* **2018**, *43*, 15191-15204.

45. Wan, L.; Zhou, Q.; Wang, X.; Wood, T. E.; Wang, L.; Duchesne, P. N.; Guo, J.; Yan, X.; Xia, M.; Li, Y. F.; Jelle, A. A.; Ulmer, U.; Jia, J.; Li, T.; Sun, W.; Ozin, G. A., Cu_2O Nanocubes with Mixed Oxidation-State Facets for (Photo)catalytic Hydrogenation of Carbon Dioxide. *Nat. Catal.* **2019**, *2*, 889-898.

Green Transformation of CO₂ to Ethanol Using Water and Sunlight by Cooperative Endeavour of Naturally Abundant Red Phosphorus and Bi₂MoO₆

Chapter 6

46. Cherevotan, A.; Raj, J.; Dheer, L.; Roy, S.; Sarkar, S.; Das, R.; Vinod, C. P.; Xu, S.; Wells, P.; Waghmare, U. V.; Peter, S. C., Operando Generated Ordered Heterogeneous Catalyst for the Selective Conversion of CO₂ to Methanol. *ACS Energy Lett.* **2021,** *6*, 509-516.

47. Ran, J.; Jaroniec, M.; Qiao, S.-Z., Cocatalysts in Semiconductor-based Photocatalytic CO₂ Reduction: Achievements, Challenges, and Opportunities. *Adv. Mater.* **2018,** *30*, 1704649.

48. Wang, W.; Deng, C.; Xie, S.; Li, Y.; Zhang, W.; Sheng, H.; Chen, C.; Zhao, J., Photocatalytic C–C Coupling from Carbon Dioxide Reduction on Copper Oxide with Mixed-Valence Copper(I)/Copper(II). *J. Am. Chem. Soc.* **2021,** *143*, 2984-2993.

49. Wang, L.; Ghoussoub, M.; Wang, H.; Shao, Y.; Sun, W.; Tountas, A. A.; Wood, T. E.; Li, H.; Loh, J. Y. Y.; Dong, Y.; Xia, M.; Li, Y.; Wang, S.; Jia, J.; Qiu, C.; Qian, C.; Kherani, N. P.; He, L.; Zhang, X.; Ozin, G. A., Photocatalytic Hydrogenation of Carbon Dioxide with High Selectivity to Methanol at Atmospheric Pressure. *Joule* **2018,** *2*, 1369-1381.

50. Liu, M.; Wang, Y.; Kong, X.; Rashid, R. T.; Chu, S.; Li, C.-C.; Hearne, Z.; Guo, H.; Mi, Z.; Li, C.-J., Direct Catalytic Methanol-to-Ethanol Photo-conversion via Methyl Carbene. *Chem* **2019,** *5*, 858-867.

51. Sun, Z.; Ma, T.; Tao, H.; Fan, Q.; Han, B., Fundamentals and Challenges of Electrochemical CO₂ Reduction Using Two-Dimensional Materials. *Chem* **2017,** *3*, 560-587.

52. Li, J.; Pan, W.; Liu, Q.; Chen, Z.; Chen, Z.; Feng, X.; Chen, H., Interfacial Engineering of Bi₁₉Br₃S₂₇ Nanowires Promotes Metallic Photocatalytic CO₂ Reduction Activity under Near-Infrared Light Irradiation. *J. Am. Chem. Soc.* **2021,** *143*, 6551-6559.

53. Wang, F.; Ng, W. K. H.; Yu, J. C.; Zhu, H.; Li, C.; Zhang, L.; Liu, Z.; Li, Q., Red Phosphorus: An Elemental Photocatalyst for Hydrogen Formation from Water. *Appl. Catal. B-Environ.* **2012,** *111,* 409-414.

54. Das, R.; Sarkar, S.; Kumar, R.; D. Ramarao, S.; Cherevotan, A.; Jasil, M.; Vinod, C. P.; Singh, A. K.; Peter, S. C., Noble-Metal-Free Heterojunction Photocatalyst for Selective CO₂ Reduction to Methane upon Induced Strain Relaxation. *ACS Catal.* **2022,** *12*, 687-697.

55. Xu, Y.-F.; Yang, M.-Z.; Chen, B.-X.; Wang, X.-D.; Chen, H.-Y.; Kuang, D.-B.; Su, C.-Y., A CsPbBr₃ Perovskite Quantum Dot/Graphene Oxide Composite for Photocatalytic CO₂ Reduction. *J. Am. Chem. Soc.* **2017,** *139*, 5660-5663.

56. Zhang, H.; Wang, Y.; Zuo, S.; Zhou, W.; Zhang, J.; Lou, X. W. D., Isolated Cobalt Centers on $W_{18}O_{49}$ Nanowires Perform as a Reaction Switch for Efficient CO_2 Photoreduction. *J. Am. Chem. Soc.* **2021,** *143*, 2173-2177.

Chapter 7

Light-Induced Charge Accumulation on Polarized Indium in $In_{2.77}S_4$ from Porous Organic Polymer Tailoring C-C Coupling to Produce Ethylene from CO_2
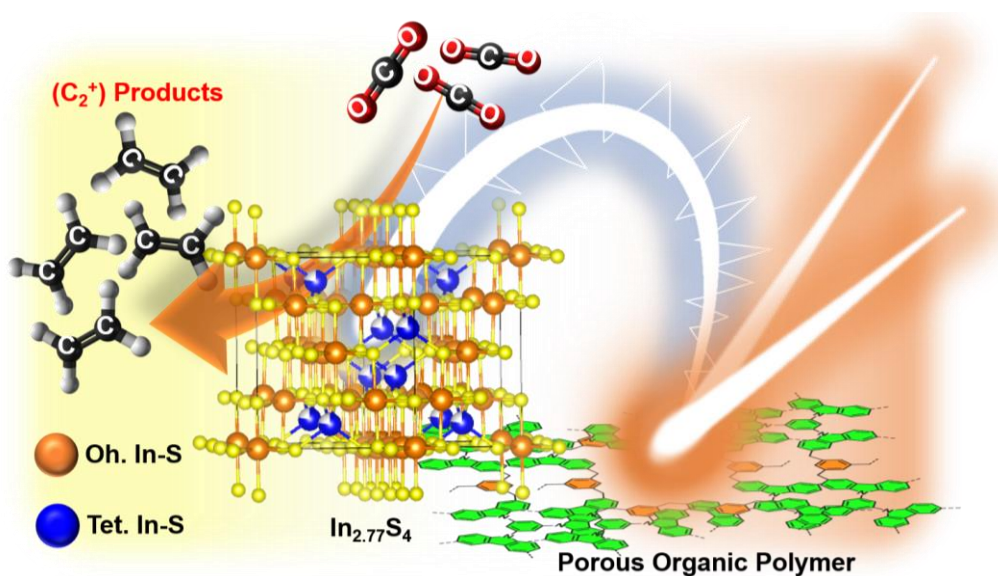
Risov Das, Ratul Paul, Arko Parui, Abhijit Shrotri, Cesare Atzori, Kirill A. Lomachenko, Abhishek Kumar Singh, John Mondal, Sebastian C. Peter. Under Revision

Summary

Development of an efficient photocatalyst for C2 product formation from CO_2 is of urgent importance towards deployment of solar-fuel production in recent time. Here, we report a template-free, cost-effective synthetic strategy to develop carbazole derived Porous Organic Polymer (POP) based composite catalyst with $In_{2.77}S_4$, which was held together by induced polarity driven electrostatic interaction. By using a co-operative endeavor of catalytically active In centers and light-harvesting POPs, the composite catalyst showed 98.9% C_2H_4 formation selectivity with 65.75 mmolg^{-1}h^{-1} rate. Two different oxidation states of $In_{2.77}S_4$ spinel were exploited for C-C coupling process and this phenomenon was investigated by X-ray Photoelectron Spectroscopy (XPS), X-ray Absorption Spectroscopy (XAS) and Density Functional Theory (DFT) calculations. The role of POP was unwrapped based on several photophysical and photoelectrochemical studies. The electron transfer was mapped by several correlated approaches and established the Z-scheme mechanism. Most importantly the mechanistic insight of C_2H_4 formation was enlightened based on DRIFTS and DFT calculation from multiple possible pathways.

Light-Induced Charge Accumulation on Polarized Indium in In$_{2.77}$S$_4$ from Porous Organic Polymer Tailoring C-C Coupling to Produce Ethylene from CO$_2$

Chapter 7

7.1. Introduction

The concept of charge polarization in the process of C-C coupling reaction was investigated in last 2 chapters and most of the chapters has exploited the heterostructure of two inorganic components. Therefore, organic-inorganic heterostructure was investigated here because the organic counterpart can boost CO$_2$ adsorption and light absorption. a large variety of sophisticated heterogeneous photo catalytic systems like metal oxides, metal sulphides, zeolites, porous organic polymers (POPs), metal-organic frameworks (MOFs) and covalent organic frameworks (COFs) have been already been explored to speed up the CO$_2$ conversion process producing CH$_4$, CO, CH$_3$OH and other hydrocarbon products.[1] However due to multi electron transfer and C-C coupling process, only a few works have been reported multi carbon (C$_{2+}$) products.[2] Although C$_2$H$_4$ is a thermodynamically achievable product, the low efficiency of CO$_2$ photoreduction to C$_2$H$_4$, which comprises multiple proton-coupled electron transfer (PCET) processes due to the involvement of various C1 intermediates on catalytic sites, remain a huge challenge.[3-4] Therefore, modulating the catalyst surface and manipulating the binding-energy between C1 intermediates and active sites to achieve efficient photochemical CO$_2$-to-C$_2$H$_4$ is of great significance.

To solve the aforementioned issue, scientists all around the world are working on developing new catalysts that can efficiently perform CO$_2$ to multi-carbon product (CMP) formation. A fluorine-modified copper catalytic system has been developed by Wang *et al.* exhibited CMP conversion, but unfortunately with very low yield of ethylene because of its narrow C$_2$+ selectivity.[5] *Chen et al.* reported Cu nanomaterial-based electrocatalytic system for CMP conversion with minimal ethylene selectivity.[6] Further improvement of selectivity was spotted from the work of *Sargent et al.* where N-aryl substituted tetrahydro-bipyridine was utilized for the CMP conversion.[7]

Moreover, the selectivity was improved recently by Xinyi and co-workers up to 87% by polyamine-incorporated Cu electrode.[8] Unfortunately, such stepwise development of C$_2$H$_4$ formation efficiency and selectivity is not started yet in the field of photocatalytic CO$_2$ reduction. Therefore, it is high time for showcasing this extraordinary outcome of our research where 99% C$_2$H$_4$ selectivity was obtained by Cu-free new class of porous organic polymer (POP) embedded **In$_{2.77}$S$_4$** photocatalyst. Most importantly the rate of C$_2$H$_4$ formation is highest in the field of photocatalysis compared to any other reported literature (**Figure 7.1**) Transition metal coordinated POPs has been explored for various
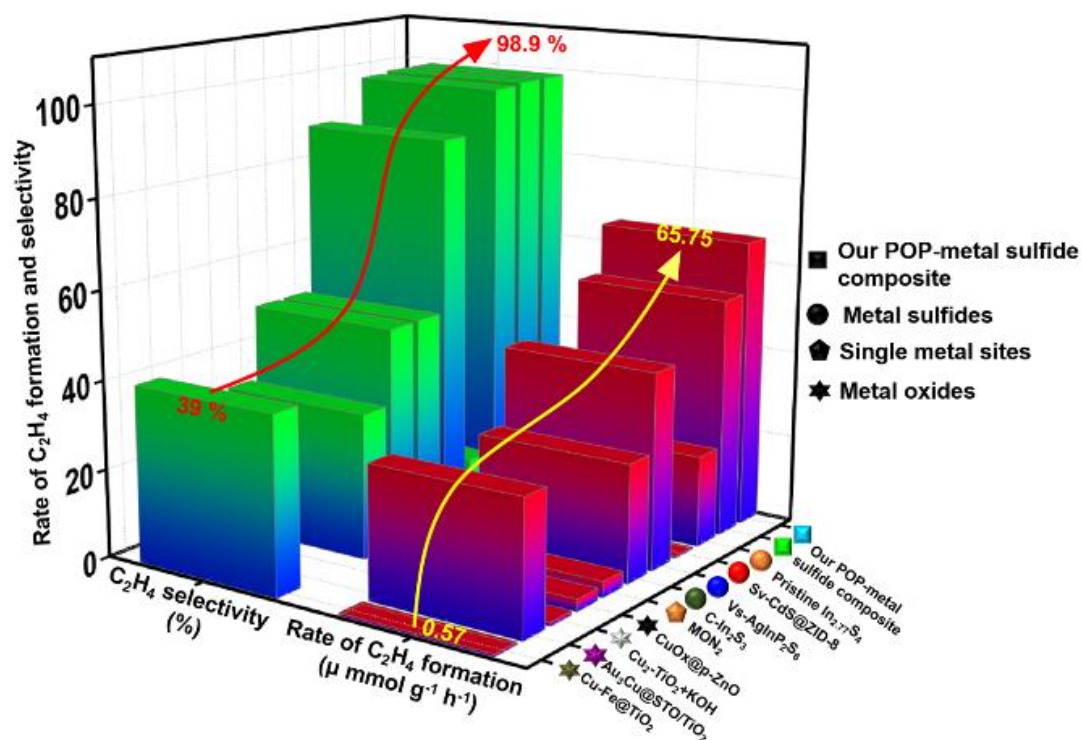
Figure 7.1. Comparison of this work with reported literature for C_2H_4 formation.

photocatalytic applications including CO_2 reduction but none of them has designed such organic-inorganic hybrid type-II semiconductor photocatalyst where POPs played versatile roles in terms of photosensitization, gas-adsorption and catalyst dispersion.[9] Moreover, it tampered the binding strength between In and C1 intermediates for facilitating C-C coupling process.

Herein, we report two novel carbazole functionalized porous organic polymer (**P4**, and **P6**) supported **In$_{2.77}$S$_4$** composite photocatalyst namely **In$_{2.77}$S$_4$(P4)** and **In$_{2.77}$S$_4$(P6)** for solar driven photochemical CO_2 conversion. It is already well established that carbazole can facilitate faster electron transfer.[10] In this work photo-active **In$_{2.77}$S$_4$** center of **In$_{2.77}$S$_4$(POP),** provides an upper hand over the pristine **In$_{2.77}$S$_4$** due the virtue of excited electron transfer from POP to **In$_{2.77}$S$_4$** via Z-scheme process.

The Z-scheme mechanism was investigated thoroughly by studying TRPL and AQY%. The charge transfer mechanism was also supported by studying in-situ EPR. The better light harvesting capacity of composites were understood from photoelectrochemical studies. Furthermore, mechanistic insight of photochemical CMP conversion over **In$_{2.77}$S$_4$(POP)** was unwrapped from *in-situ* DRIFTS spectroscopy and Density Functional Theory (DFT) analysis.

Light-Induced Charge Accumulation on Polarized Indium in In$_{2.77}$S$_4$ from Porous Organic Polymer Tailoring C-C Coupling to Produce Ethylene from CO$_2$

Chapter 7

Composite formation energy and the best possible pathway among 10 different possibilities of C$_2$H$_4$ formation are detailed for the first time.

7.2.   Experimental section

Chemicals and reagents: 4,4'-Bis(9H-carbazol-9-yl) biphenyl (BCB), 1,3,5-tri(9-carbazolyl)-benzene (TCB), 1,3,5-Tris(bromomethyl), anhydrous FeCl$_3$, InCl$_3$. 4H$_2$O and thioacetamide were purchased from Sigma Aldrich. 1,2-dichloroethane (DCE), ethylene glycol and MeOH were purchased from Finar Chemicals used as received without further purification.

Synthesis of porous organic polymer (POP): The carbazole based POPs were synthesized *via* FeCl$_3$ assisted template free Friedel-Crafts alkylation. In a typical synthesis procedure, 4,4'-Bis(9H-carbazol-9-yl) biphenyl (BCB; 0.375 mmol) and 1,3,5-Tris(bromomethyl)benzene (TBB; 0.5 mmol) in 1,2-dichloroethane (DCE; 30 ml) were added in a 100 ml round bottom flask and sonicated for 30 minutes to get a homogeneous mixture. After getting the homogeneous mixture the solution was stirred under N$_2$ atmosphere followed by the addition of anhydrous FeCl$_3$ (4 mmol). Further, the mixture was refluxed at 120 °C for 48 h (**Scheme 1**). After completion, the reaction mixture was cooled to room temperature and the slurry mixture was dipped into methanol under stirring conditions until precipitation. Finally, the precipitate was collected by centrifugation and washed with MeOH several times. To completely remove the excess iron from the as-synthesized porous organic polymer (**P4**) was subjected to soxhlet extraction with MeOH for 72 h followed by vacuum drying at 60 °C overnight yielded (90%) pale-yellow powder (**P4**). For the synthesis of **P6**, the exact above-mentioned procedure was followed where 1,3,5-tri(9-carbazolyl)-benzene (TCB; 0.25 mmol) was used instead of 4,4'-Bis(9H-carbazol-9-yl) biphenyl (BCB). After completion, **P6** was yielded (86 %) as pale-brown powder (**Scheme 2**).
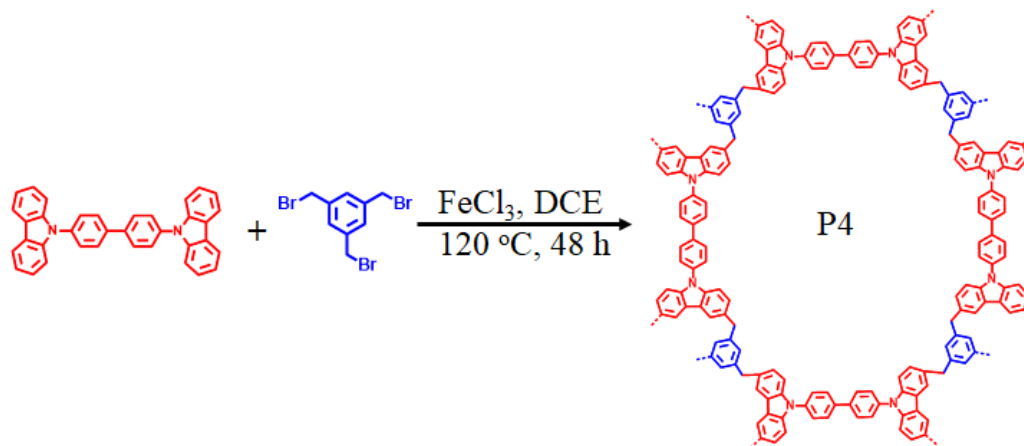
Scheme 7.1. Synthesis of **P4** *via* FeCl$_3$ assisted template free Friedel-Crafts alkylation.
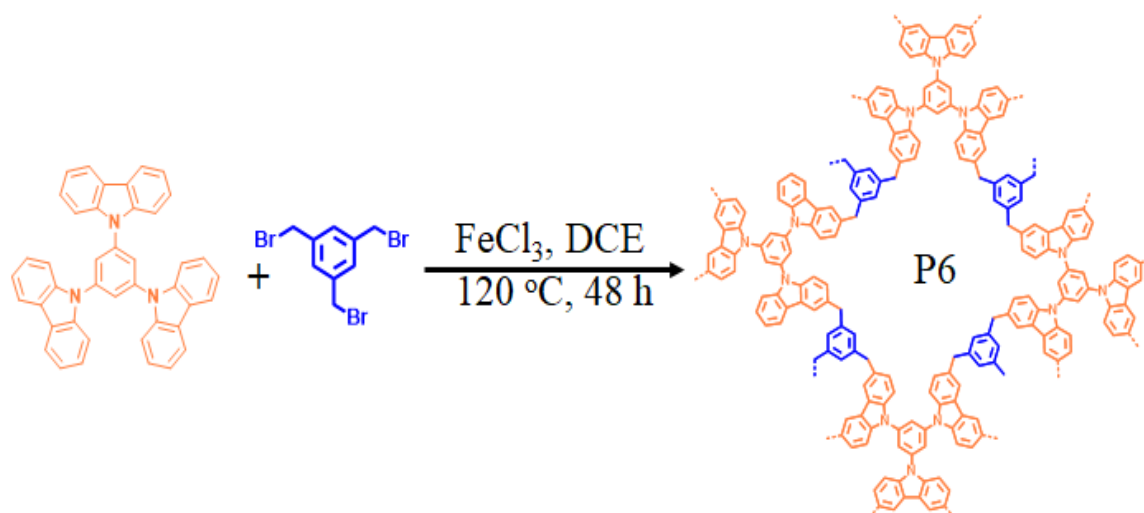
Scheme 7.2. Synthesis of **P6** *via* FeCl$_3$ assisted template free Friedel-Crafts alkylation.

Synthesis of pristine In$_{2.77}$S$_4$: According to the previous literature,[11] 1 mmol of InCl$_3$. 4H$_2$O and 5 mmol of thioacetamide were mixed uniformly in ethylene glycol (30 ml) and stirred for 3 h. Further, the reaction mixture was transferred in a teflon-lined stainless-steel auto clave and heated at 180 °C for 18 h. After being cooled at room temperature the bright orange precipitate was collected and washed several times with MeOH followed by overnight vacuum drying at 60 °C yielded pristine **In$_{2.77}$S$_4$**.

Synthesis of In$_{2.77}$S$_4$(POP) photo composite: Typically, a well-dispersed mixture of 200 mg **P4** in 10 ml ethylene glycol was added dropwise in a uniform mixture of 1 mmol of InCl$_3$. 4H$_2$O and 5 mmol of thioacetamide in 20 ml of ethylene glycol under staring conditions. The reaction mixture was sonicated for several minutes until we get a well-dispersed mixture. Then the reaction mixture was transferred to a Teflon-lined stainless-steel auto clave and heated at 180 °C for 18 h. After completion, the autoclave was cooled down to room temperature and the bright yellow precipitate **(In$_{2.77}$S$_4$(P4))** was collected, washed several times with methanol and dried under vacuum at 60 °C.

Similar synthesis procedure was followed for the synthesis of bright yellow colored **In$_{2.77}$S$_4$(P6)**, where 200 mg of **P6** was used in place of **P4**.

Materials characterization

X-Ray Diffraction: Powder X-ray diffraction (XRD) patterns of the catalysts were performed on a Rigaku Miniflex (Rigaku Corporation, Japan) X-ray diffractometer using Ni filtered Cu Kα radiation (λ = 1.5406 Å) with a scan speed of 2° min^{-1} and a scan range of 10-80° at 30 kV and 15 mA.

Light-Induced Charge Accumulation on Polarized Indium in In₂.₇₇S₄ from Porous Organic Polymer Tailoring C-C Coupling to Produce Ethylene from CO₂

Chapter 7

Microscopy: The morphology of the catalysts was obtained by scanning electron microscopy (SEM) technique. The SEM equipment was FEI Verios 460L field-emission SEM (FE-SEM) which is an ultra-high resolution Schott key emitter SEM equipped with an electron diffraction spectroscopy (EDS) detector. The elemental mapping EDS analysis were also performed in the same SEM instrument. Transmission electron microscopy (TEM) images of the catalysts were captured at 100 kV on a JEOL 1010 TEM.

N₂-adsorption/ desorption analysis: The surface area was determined through the Brunauer-Emmett-Teller (BET) method. The average pore volume and pore size were measured by Barrett-Joyner-Halenda (BJH) method. The BET surface area, pore volume and pore sizes were determined by using the N_2 adsorption-desorption method using BEL Sorb II Instruments, Japan at liquid nitrogen temperature. Before the measurement the samples were degassed at 200 °C for 2 h.

FT-IR analysis: FT-IR spectrums of catalysts were investigated on a DIGILAB (USA) IR spectrometer using the KBr disc method. Solid-state ^{13}C CP MAS NMR studies were performed by using a Bruker Avance III HD 400 MHz NMR spectrometer.

X-ray photoelectron spectroscopy (XPS): X-ray photoelectron spectroscopy (XPS) were investigated on a Thermo Scientific K-Alpha instrument (monochromatic Al Kα radiation, Ephoton = 1486.6 eV). The binding energy (B.E) in each case, that is, core levels and valence band maxima were corrected using an internal reference peak of C 1s peak centered at 284.8 eV.

Synchrotron based XAS analysis: In K-edge XAS (X-ray Absorption Spectroscopy) data were collected on the BM23 beamline of the European Synchrotron Radiation Facility (ESRF) based in Grenoble, France. The current stored in the ring during the experiment was about 65 mA. The white beam produced by a two-pole wiggler was monochromatized by the means of a double crystal Si(311) monochromator. The beam intensity was measured by the means of three ion chambers (30 cm, 1kV) placed before, (I0, filling 104 mbar Kr + 1896 mbar He), after (I1, filling 559 mbar Kr + 1441 mbar He) the sample and after the In foil reference sample (I2, 559 mbar Kr + 1441 mbar He filling). By comparing the spectra of the foil with the one of the samples we were able to reference the energy position of the edge and thus calibrate the energy for each spectrum. Samples were measured in the form of 5mm diameter self-supporting pellets, whose optimized weight were calculated with the XAFS mass code.[12] Data were reduced and analyzed by the means of the Demeter package.[13] Athena for raw data treatment

(energy calibration, normalization, extraction) and Artemis for the fitting of the EXAFS spectra. FEFF6[14] was used to calculate phase shifts and scattering amplitudes. Wavelet transforms (WT) were calculated using a Python code originally developed by Martini et al.[15]

Photocatalytic measurements: A quartz photoreactor was used for CO_2 hydrogenation experiment under the illumination of 450 W xenon lamp (Newport) through UV cut-off filter (CGA 400 filter and KG2 filter). Using a power meter (Newport-843-R) the intensity of outputting light was measured. The measured intensity during catalytic reaction is 110 mW/cm. (Note: The distance between light source and reactor is 10 cm). About 3 mg of the sample was well dispersed in 20 mL of water by ultrasonication. Before illumination, the reaction setup was purged with N_2 to remove the air and then purged with high purity CO_2 for 45 minutes. During irradiation, 5 mL of the gaseous product from the setup was sampled, and ensuing study was done by GC (gas chromatography) (Agilent GC-7890 B) with TCD and FID detector and He carrier gas. This can detect up to 0.25 ppm of methane and 16 ppm CO. To further verify the products gas chromatography Mass Spectrometry (Agilent GCMS) was used. Products were quantified by using RT® Molecular sieve 5A column (45 m, 0.32 mm ID, 30 μm df) with a mass detector. The calibration was done by a standard gas mixture of H_2, CO, CH_4, C_2H_4 and C_2H_6 of different concentrations in ppm-level. It has a detection limit up to 1 ppm. For liquid product analysis ^{1}H NMR (400 MHz, JEOL) and HPLC (Agilent 1220 Infinity II LC system) were employed. The following protocol was applied for the ^{1}H NMR analysis. Fifty μL of the solvent (after filtration) and 30 μL of an internal standard solution were transferred into a centrifuge tube. The internal standard solution consisted of 50 mM phenol (99.5%) and 10 mM dimethyl sulfoxide (99.9%) made in D_2O solvent. The mixture is transferred into an NMR tube. Solvent suppression was used to decrease the intensity of the water peak. Blank tests were conducted in the absence of CO_2 and light to confirm that these two factors are key for photocatalytic CO_2 reduction reaction. Used photocatalyst was amassed after each test and washed with water, and its performance was rechecked by the similar procedure. Rate of the C_2H_4 evolution was calculated by considering maximum rate at 10h for **In_{2.77}S_4(P6), In_{2.77}S_4(P4)** and individual components. [13]CO_2 was purged for 30 minutes and the reaction was continued for 10h. Then the products were checked by GC-MS to confirm the source of CO and C_2H_4 is CO_2. All the photocatalytic reactions were done in an air conditioning room (22°C). The local heat generated on the catalyst surface during light illumination was checked by infrared temperature gun (GM320) and it was not more than 38 °C. Heating was avoided by using KG-2 filter which cuts the UV and IR part of spectrum. Further the light comes through

Light-Induced Charge Accumulation on Polarized Indium in In$_{2.77}$S$_4$ from Porous Organic Polymer Tailoring C-C Coupling to Produce Ethylene from CO$_2$

Chapter 7

water filter which helps in eliminating heating probability. Maintaining all the reaction conditions similar, the catalysis was done at 38 °C in absence of light. However, no product was detected. This proves that the local heating due to light illumination does not affect the catalytic performance.

O$_2$ was evolved as H$_2$O to O$_2$ evolution reaction (OER) is the oxidation counterpart of CO$_2$ reduction. It was quantified by Micro-GC (Agilent). The OER process with respect to CO$_2$ reduction follows **equations 7.1-7.3**

$$2CO_2 + 2H_2O \rightarrow C_2H_4 + 3O_2 \tag{7.1}$$

$$CO_2 \rightarrow CO + \frac{1}{2}O_2 \tag{7.2}$$

$$H_2O \rightarrow H_2 + \frac{1}{2}O_2 \tag{7.3}$$

Electron spin resonance (ESR) measurements: DMPO (5,5-Dimethyl-1-pyrroline *N*-oxide) spin-trapping ESR spectra were recorded to directly study the •OH and •O$_2$ radicals generated during photocatalysis. Specifically, 3 mg of catalyst and 10 μL of DMPO were mixed in 1 mL deionized water to test the hydroxyl radicals (DMPO-•OH). On the other hand, 3 mg of as-prepared samples and 25 μL of DMPO were dispersed in 1 mL CH$_3$OH to detect superoxide radicals (DMPO-•O$_2$ $^{-}$).

Photoelectrochemical measurements: The transient photocurrent measurements under dark and light were done in a three-electrode system using a CHI 760 potentiostat under the illumination of a solar simulator (Newport) with an ultraviolet (UV) ($\lambda > 400$ nm) cut-off filter. Ag/AgCl was reference electrode, and platinum as the counter electrode was used. All samples were spin coated on fluorine-doped tin oxide (FTO) which were used as working electrode. 0.5 M Na$_2$SO$_4$ was taken as electrolyte. Photo-current was also measured in 0.1 M Na$_2$SO$_4$ solution. The slurry was prepared by adding 10 mg of the sample, 200 μL of Nafion (5%), and 1 mL of isopropyl alcohol to fabricated photoelectrodes. The obtained paste was spin-coated on FTO with 1 cm^2 area and annealed at 100 °C for 1 h to get a homogenous film. Mott-Schottky (MS) plots were recorded at a scan rate of 10 mV/s in Na$_2$SO$_4$ neutral solution in the light at a frequency of 50 kHz. The obtained values (w.r.t Ag/AgCl) was converted w.r.t NHE by adding 0.20 V.[16] Photocurrent was obtained by 10s light on and 10s off experiment with same spin coated FTO electrodes.

In-situ photocatalytic Fourier transform infrared spectroscopy (FT-IR): In-situ photochemical FT-IR spectroscopic studies were performed using a purged VERTEX FT-IR

spectrometer equipped with the A530/P accessory and a mid-band Mercury Cadmium Telluride (MCT) detector. Spectra was recorded after 100 scans with a resolution of 4 cm^{-1}. A DRIFTS cell with a quartz window was used to perform catalytic experiment. Prior to catalytic testing, 5 mg of the sample was placed in the DRIFTS cell and treated in flowing N_2 for 30 min to remove impure gas mixtures. Then, CO_2 and water vapor were injected through rubber septa and light was illuminated through the quartz window for 90 minutes. Just before the light exposure on the DRIFTS cell the zero-minute data was collected and after that, data was collected every 15 minutes for 75 minutes.

7.3. Computational details

DFT calculations for these systems were done with Vienna ab initio simulation (VASP) package.[17] The Electron-ion interactions were described using all-electron projector augmented wave pseudopotentials,[18] and Perdew-Bruke-Ernzehof (PBE) generalized gradient approximation (GGA)[19] were used to approximate the electronic exchange and correlations. The plane-wave kinetic energy cut off of 580 eV and 480 eV was used for optimization of bulk $In_{2.77}S_4$ and all other calculations, respectively. The Brillouin zone was sampled using $11\times11\times11$, $6\times6\times1$, $4\times4\times1$, $7\times7\times1$ and $3\times3\times1$ Monkhorst-Pack k-grid for bulk $In_{2.77}S_4$, unit cell of (400) surface of $In_{2.77}S_4$, $\sqrt{2} \times \sqrt{2} \times 1$ supercell of (400) surface of $In_{2.77}S_4$, POP and hetero up/hetero down structures, respectively. All the structures were relaxed using a conjugate gradient scheme until energies and each component of the forces converged to 10^{-7} eV and 0.0001 eV Å^{-1} for bulk $In_{2.77}S_4$ and 10^{-5} eV and 0.01 eV Å^{-1} for unit cell and $\sqrt{2} \times \sqrt{2} \times 1$ supercell of (400) surface of $In_{2.77}S_4$ and POP and 10^{-4} eV and 0.01 eV Å^{-1} for heterostructures, respectively. All calculations are spin polarized and a vacuum of 10 Å was added for the surfaces to ensure no interaction between two layers. For both the heterostructures, the POP was placed at a distance of 3 Å from the $In_{2.77}S_4$ surface. $In_{2.77}S_4$ surface with a net dipole moment, correction to the potential and forces was used. The dipole moment was calculated parallel to the third vector.

Initially, bulk structure of $In_{2.77}S_4$ with 32 S atoms and 24 In atoms was optimized with lattice parameters $a = b = c = 11.22$ Å. (400)-oriented surface of $In_{2.77}S_4$ was then considered as shows maximum intensity in the experimental diagram. Further, $\sqrt{2} \times \sqrt{2} \times 1$ supercell with lattice parameters $a = b = 15.87$ Å was optimized to form the heterostructure with POP ($a = 14.00$ Å and $b = 16.40$ Å) having ~8% lattice mismatch. Free energy was calculated using below equation

Light-Induced Charge Accumulation on Polarized Indium in In$_{2.77}$S$_4$ from Porous Organic Polymer Tailoring C-C Coupling to Produce Ethylene from CO$_2$

Chapter 7

$$\Delta G = \Delta E_{ads} + \Delta ZPE - T\Delta S + \Delta G_U + \Delta G_{pH}$$

Thermodynamic stability of intermediates and most probable mechanistic pathway for the CO$_2$ reduction reaction that forms C$_2$H$_4$ as a major product was realized by the free energy calculations following **equation 7.4**[20] after calculating the adsorption energies from **equation 7.5-7.21**).

$$\Delta G = \Delta E_{ads} + \Delta ZPE - T\Delta S + \Delta G_U + \Delta G_{pH} \qquad (7.4)$$

Here, ΔZPE and $T\Delta S$ are the differences in zero-point energies of the species and entropies due to contribution from the vibrational motions only, respectively. ΔG_U ($\Delta G_U = -eU$; e is the number of electrons transferred) and ΔG_{pH} ($\Delta G_{pH} = 2.303k_BT \times pH$) represents the free-energy corrections due to electrode potentials and pH, respectively. The value of T and pH were taken to be 298 K and 0, respectively, in this study.

Adsorption energy for intermediates was calculated as:

$$\Delta E_{ads}(CO_2) = E(*CO_2) - [E^* + E(CO_2)] \qquad (7.5)$$

$$\Delta E_{ads}(OCOH) = E(*OCOH) - [E^* + E(HCOOH) - 0.5E(H_2)] \qquad (7.6)$$

$$\Delta E_{ads}(CO) = E(*CO) - [E^* + E(CO)] \qquad (7.7)$$

$$\Delta E_{ads}(COH) = E(*COH) - [E^* + E(CH_3OH) - 1.5E(H_2)] \qquad (7.8)$$

$$\Delta E_{ads}(OCCOH) = E(*OCCOH) - [E^* + E(OHCCH_2OH\text{-}cis) - 1.5E(H_2)] \qquad (7.9)$$

$$\Delta E_{ads}(C_2O) = E(*C_2O) - [E^* + E(H_3CCO) - 1.5E(H_2)] \qquad (7.10)$$

$$\Delta E_{ads}(OCCOH) = E(*OCCH) - [E^* + E(OCCH_2) - 0.5E(H_2)] \qquad (7.11)$$

$$\Delta E_{ads}(OCCH_2) = E(*OCCH_2) - [E^* + E(OCCH_2)] \qquad (7.12)$$

$$\Delta E_{ads}(HOCCH_2) = E(*HOCCH_2) - [E^* + E(HOHCCH_2) - E(H_2)] \qquad (7.13)$$

$$\Delta E_{ads}(CCH_2) = E(*CCH_2) - [E^* + E(C_2H_4) - E(H_2)] \qquad (7.14)$$

$$\Delta E_{ads}(HOCCOH) = E(*HOCCOH) - [E^* + E(HOH_2CCH_3) - 2E(H_2)] \qquad (7.15)$$

$$\Delta E_{ads}(HOCC) = E(*HOCC) - [E^* + E(HOHCCH_3) - 2E(H_2)] \qquad (7.16)$$

$$\Delta E_{ads}(HOCCH) = E(*HOCCH) - [E^* + E(HOHCCH_3) - 1.5E(H_2)] \qquad (7.17)$$

$$\Delta E_{ads}(CCH) = E(*CCH) - [E^* + E(C_2H_2) - 0.5E(H_2)] \qquad (7.18)$$

$$\Delta E_{ads}(HCCH) = E(*HCCH) - [E^* + E(C_2H_4) - E(H_2)] \qquad (7.19)$$

$$\Delta E_{ads}(HCCH_2) = E(*HCCH_2) - [E* + E(C_2H_4)-0.5E(H_2)] \qquad \textbf{(7.20)}$$

$$\Delta E_{ads}(H_2CCH_2) = E(*H_2CCH_2) - [E* + E(C_2H_4)] \qquad \textbf{(7.21)}$$

7.4. Calculations

Apparent quantum yield (AQY%) calculation for CO_2 reduction to C_2H_4: The wavelength dependent AQY of CO_2 photo-reduction by **In$_{2.77}$S$_4$(P6)** were calculated using different monochromatic light source. Therefore, 6 (400 ± 10 nm, 425 ± 10 nm, 450 ± 10 nm, 475 ± 10 nm, 500 ± 10 nm, 550 ± 10 nm) different bandpass filters obtained from light source manufacturer (Newport) were used to obtain the monochromatic wavelengths and Newport-843-R power meter was used to measure the incident light intensity. After 6 hours of CO_2 reduction the AQY was estimated from the following equation:

$$AQY(\%) = \frac{Number\ of\ reacted\ electrons}{Number\ of\ incident\ photons} X\ 100\%$$

Number of reacted electrons were calculated from the yield of CO_2 reduced products (here selectively methane was obtained). Because different number of electrons are required for the formation of different products, the total number of reacted electrons are

$$Number\ of\ reacted\ electrons = [\ 12n(C2H_4)]\ X\ 2\ X\ N_A$$

$n(C_2H_4)$, is the yields of methane. N_A is Avogadro's number. Here 2 was multiplied because Z-scheme is the 2-step electron excitation process.[21-22]

Number of incident photons are calculated from the following equation:

$$Number\ of\ incident\ photons = \frac{PS\lambda t}{hc}$$

where, P is the power density of the incident monochromatic light (W/m^2), S (m^2) is the irradiation area, t (s) is the duration of the incident light exposure and λ (m) is the wavelength of the incident monochromatic light. h (Js) and c (m/s) correspond to planks constant and speed of light respectively.

Combining these two equations the AQY (%) for different monochromatic light was calculated. For example, the AQY (%) @400 nm is shown here-

$n(C_2H_4) = 29$ µmol/g, $n(CO) = 5.2$ µmol/g, $N_A = 6.023*10^{23}$ mol^{-1}, P= $51*10^{-3}$ W/cm^2, S= 4.52 cm^2, l= 400 nm, t=6h, h= $6.626*10^{-34}$ Joule second, c= $3*10^8$ m/s

AQY (%) @400 nm

Light-Induced Charge Accumulation on Polarized Indium in In$_{2.77}$S$_4$ from Porous Organic Polymer Tailoring C-C Coupling to Produce Ethylene from CO$_2$

Chapter 7

$$= \frac{[(29 \times 12)+(5.2 \times 2)]10^{-6} \times 2 \times 6.02 \times 10^{23}}{1} \times \frac{6.626 \times 10^{-34} \times 3 \times 10^8}{51 \times 10^{-3} \times 4.52 \times 400 \times 10^{-9} \times 3600 \times 6} \times 100\%$$

$$= 5.1\%$$

Similarly, AQY were calculated for 425 nm, 450 nm, 500 nm, 550 nm, 600 nm.

7.5. Result and discussion

Material synthesis and structural characterizations: In this study, we have picked a molecular template free cost-effective synthetic strategy using FeCl$_3$ as a catalyst to develop two carbazole based porous organic polymers (POP-4**: P4,** and POP-6**: P6**) by Friedel-Crafts alkylation carbazole moieties and 1,3,5-Tris(bromomethyl)benzene (TBB) as linker in dry DCE under inert (N$_2$) atmosphere (**Scheme 7.1** and **7.2**).[23] Further, **In$_{2.77}$S$_4$(P4)** and **In$_{2.77}$S$_4$(P6)** porous photo-composites were synthesized by solvothermal method in a Teflon-lined stainless-steel autoclave at 180 °C for 18 h using a well-dispersed mixture of **P4** or **P6**, InCl$_{3.}$4H$_2$O and thioacetamide (C$_2$H$_5$NS) in ethylene glycol (30 ml). The overall synthetic strategy of the as-synthesized POPs and **In$_{2.77}$S$_4$(P)** porous photo composites are depicted in **Figure 7.2a**. The ^{13}C CP MAS NMR analysis of **P4** and **P6** and their respective **In$_{2.77}$S$_4$(P)** composites have been conducted to understand the molecular connectivity and chemical environment of the polymeric framework (**Figure 7.2b** and **7.2c**). A significant peak situated at ~39 ppm corresponds to the methylene carbon atom of TBB linker, whereas the resonance peak at ~109.8 ppm is attributed to the unsubstituted carbon nuclei of the polymeric skeleton. The appearance of two intense resonance peaks at ~125.7 and 139.8 ppm attributed to the C-substituted and N-substituted carbon nuclei of BCB and/or TCB unit in the polymeric framework.

Almost similar kind of resonance signal with minimal shifting appears for the two as-synthesized porous photopolymers (**In$_{2.77}$S$_4$(P4)** and **In$_{2.77}$S$_4$(P6)**) indicating the intactness of structural integrity after the incorporation of **In$_{2.77}$S$_4$**. The formation of the polymeric network was also studied by FT-IR spectroscopy, where the peaks at around 1300 cm^{-1}, 1459 cm^{-1} and 1613 cm^{-1} contributed to the 'C-N' and 'C=C' aromatic ring vibration (**Figures 7.2d** and **7.2e**). The broad peak around 3500 cm^{-1} has raised due to moisture and surface adsorbed OH species' stretching band. The structural integrity of the POPs in **In$_{2.77}$S$_4$(P)** photo-catalyst was confirmed by the observed similar IR stretching frequencies even after the incorporation of **In$_{2.77}$S$_4$**. The C, H, N elemental analysis confirmed the presence of 50-55 wt% of carbon (C), 5-6 wt% of hydrogen (H), 6-9 wt% of nitrogen (N) and 40-50 wt% of sulfur (S) in the as-

synthesized $In_{2.77}S_4(P)$ photo catalysts. Further, the amount of In metal in $In_{2.77}S_4(P4)$ and $In_{2.77}S_4(P6)$ was 35% and 37%, respectively, calculated by inductively coupled plasma-atomic emission spectroscopy (ICP-AES) measurement. Porosity is one of the most important parameters in catalysis and here porous organic polymers are used to avail the luxury of higher surface area. Therefore, to have a better insight about the permanent porosity of the as-synthesized POPs and the corresponding $In_{2.77}S_4(P)$ photo-catalysts, N_2 adsorption-desorption isotherm analysis at 77K was carried out. As seen from the **Figure 7.3,** the N_2-sorption isotherm of all the materials could be assigned as a typical type-II isotherm by IUPAC classification without any significant hysteresis loop, indicating the existence of interparticle voids within the porous polymer-based materials. The calculated specific BET surface area of the **P4** and **P6** were found to be 909 m^2/g and 804 m^2/g, respectively. Whereas the $In_2S_3(P4)$ and $In_{2.77}S_4(P6)$ exhibited comparatively lower BET surface area 251 m^2/g and 373 m^2/g, respectively after the $In_{2.77}S_4$ incorporation which exactly matches with the earlier reports.

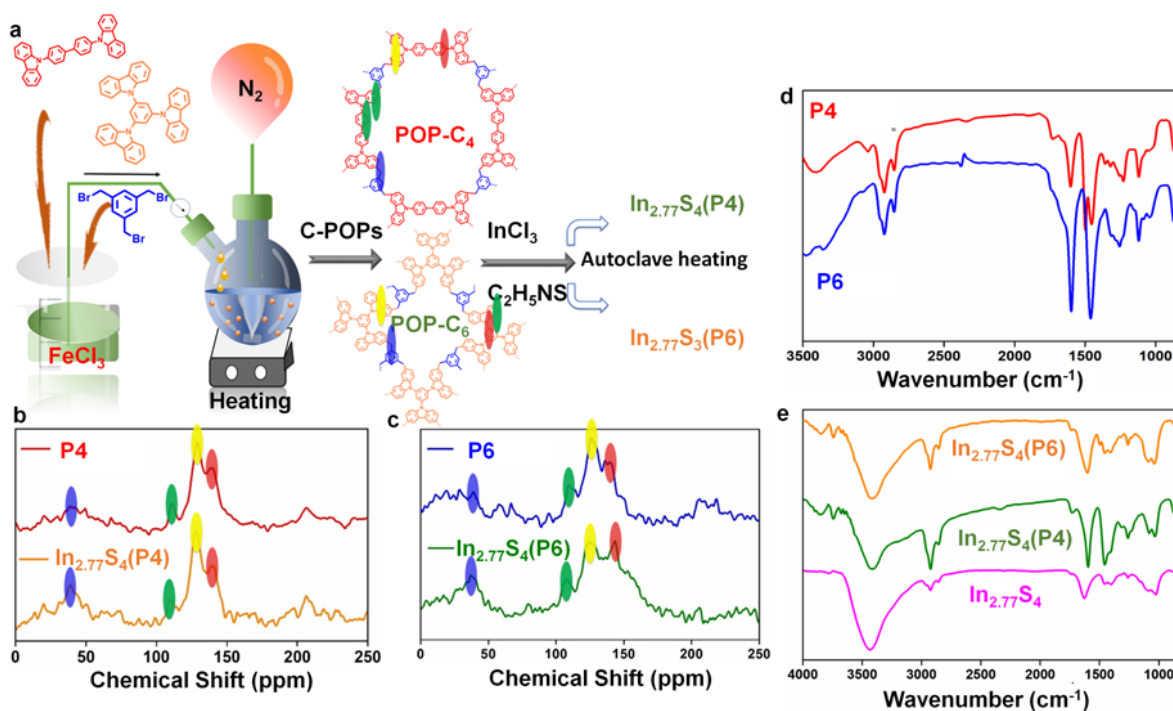**Figure 7.2.** Catalyst synthesis and microscopy. **(a)** Synthesis of carbazole based **P4**; **P6**; $In_{2.77}S_4(P4)$ and $In_{2.77}S_4(P6)$ following Friedel-Crafts alkylation and solvothermal method. The composites were made via solvothermal reaction in Teflon autoclave. The ^{13}C CP/MAS-NMR spectroscopic analysis of **(b)** P4, composite, and **(c)** P6, composite. The color code in **P4**, and **P6** are the functional group indicated by NMR. **(d)** FT-IR analysis of pristine POPs, and **(e)** $In_{2.77}S_4@POP$ composites along with the pristine $In_{2.77}S_4$, respectively.

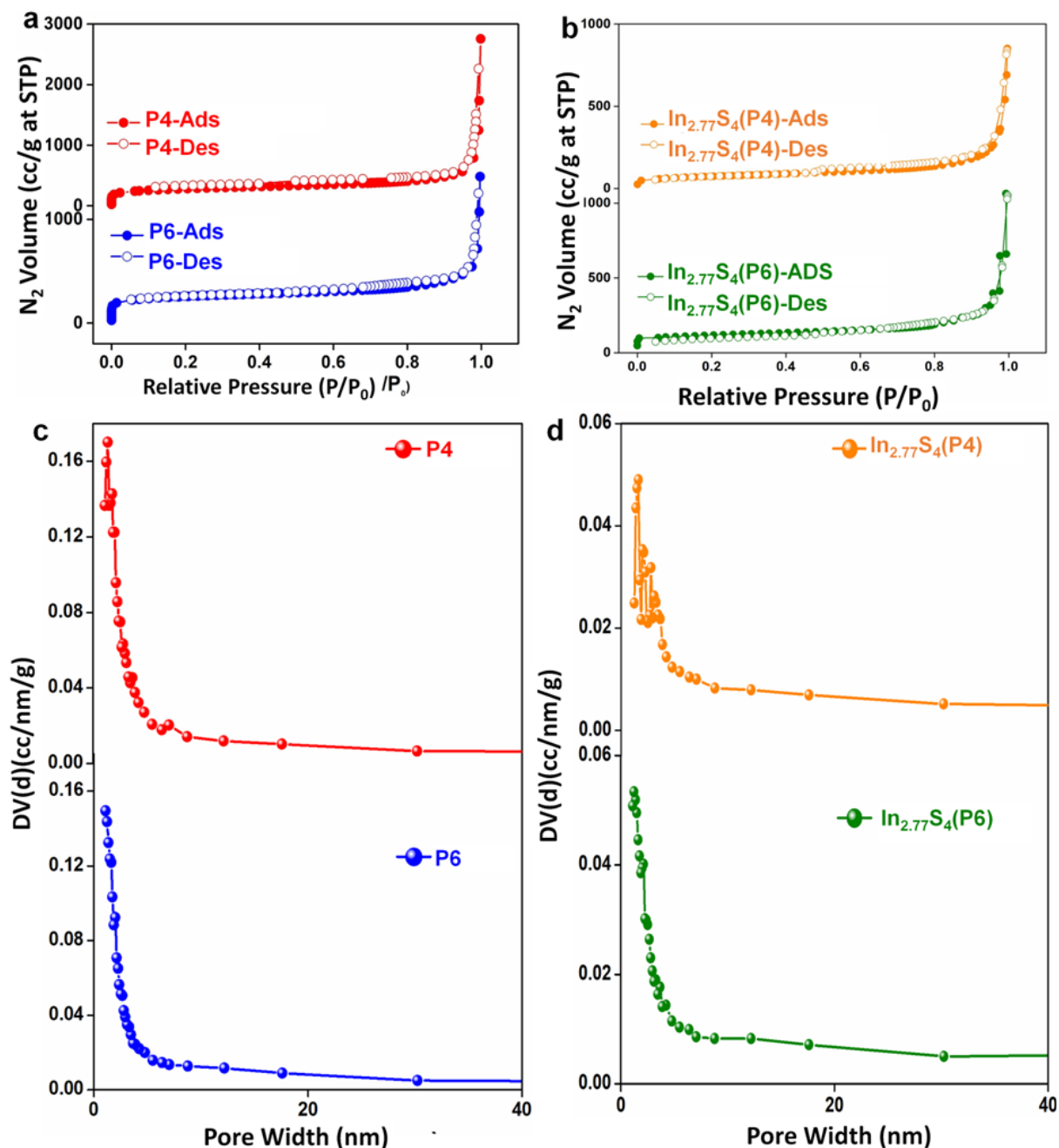**Light-Induced Charge Accumulation on Polarized Indium in In$_{2.77}$S$_4$ from Porous Organic Polymer Tailoring C-C Coupling to Produce Ethylene from CO$_2$**

Chapter 7

Figure 7.3. Nitrogen adsorption and desorption isotherms for **(a) P4**, **P6** and **(b) In$_{2.77}$S$_4$(P4)**, **In$_{2.77}$S$_4$(P6)** measured at 77.3 K. Pore size distribution (PSD) of **(c) P4**, **P6** and **(d) In$_{2.77}$S$_4$(P4)**, **In$_{2.77}$S$_4$(P6)**.

Also, the corresponding pore-size distributions (PSD) of **P4, P6, In$_2$S$_3$(P4)** and **In$_{2.77}$S$_4$(P6)** were calculated by BJH method and found to be 1.21 nm, 0.90 nm, 1.54 nm and 1.25 nm, respectively (**Figure 7.3c** and **7.3d**).

FE-SEM and HR-TEM analyses were conducted to understand the morphology of the as synthesized POPs and **In$_{2.77}$S$_4$(P).** FE-SEM and TEM images (**Figure 7.4**) of the parent POP reveal cloud-like surface morphology, resulting in a hyper-branched porous nature. On the

other hand, we obtained micro flower type nano nanostructures for the as-synthesized pristine **In$_{2.77}$S$_4$** (**Figure 7.5**). The comparison between the TEM images of pristine **In$_{2.77}$S$_4$** and **In$_{2.77}$S$_4$(P)** catalysts (**Figure 7.5a, 7.5c** and **7.5e**) also revealed similar type of hetero structure formation. As shown in a high-resolution TEM (HRTEM) image (**Figure 7.5b**) of pristine **In$_{2.77}$S$_4$,** the interplanar d-spacing between lattice fringes was 0.190 nm and 0.312 nm correspond to the (440) and (311) plane, respectively. Further, the selected area electron diffraction (SAED) pattern demonstrates the d-spacing corresponds to lattice fringes of pristine **In$_{2.77}$S$_4$** (**Figure 7.5a inset**). Similar results were obtained with **In$_{2.77}$S$_4$(P)** catalysts (**Figure 7.5d & 7.5f**) indicating the preservation of the **In$_{2.77}$S$_4$** in the hereto structure. Pure In$_{2.77}$S$_4$ has adopted beautiful flower like morphology (**Figure 7.5g**). Similar trunked flower like morphology was seen in case of pure **In$_{2.77}$S$_4$** in atomic force microscopy (AFM), where the height of petals is around 15 nm (**Figure 7.5h**). FE-SEM images of **In$_{2.77}$S$_4$(P)** revealed the **In$_{2.77}$S$_4$** micro flowers were wrapped by the micro-porous polymer, forming a heterojunction between **In$_{2.77}$S$_4$** and the POP through which the electron transfer was initiated.
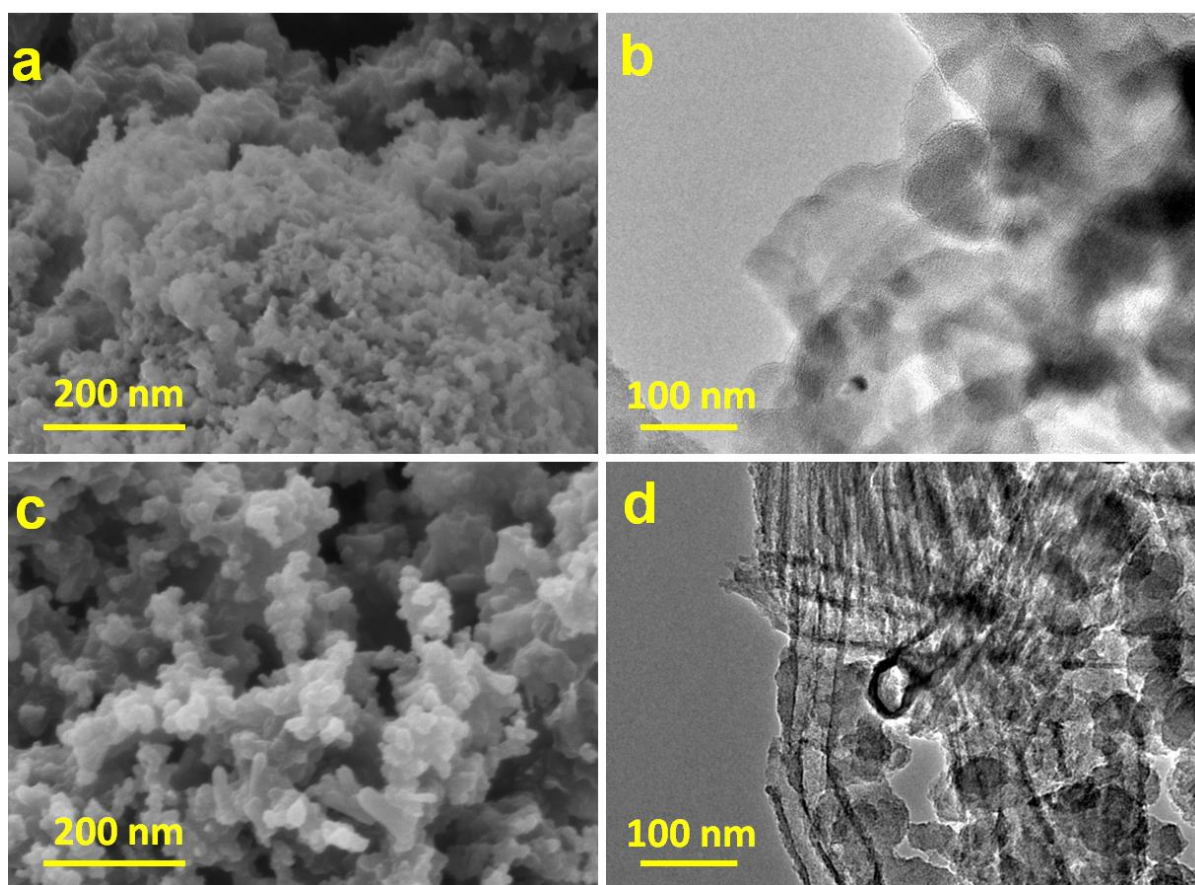

Figure 7.4. FE-SEM images of (**a**) **P4,** and (**c**) **P6**. TEM images (**b**) **P4**, and (**d**) **P6** of respectively. Both **P4**, and **P6** morphology resembles that they can adsorb higher amount of gas molecule as depicted from BET analysis.
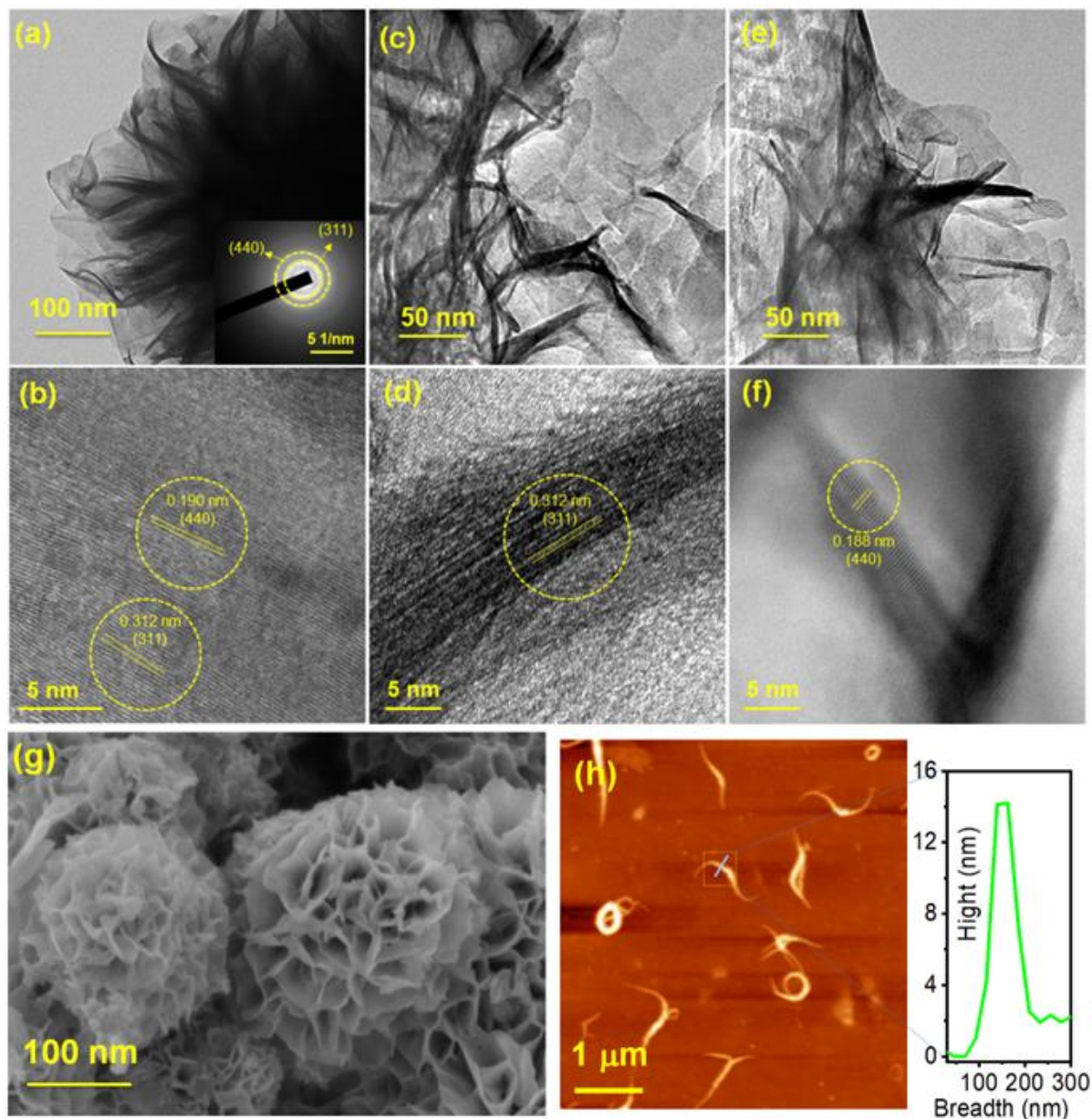
Light-Induced Charge Accumulation on Polarized Indium in In₂.₇₇S₄ from Porous Organic Polymer Tailoring C-C Coupling to Produce Ethylene from CO₂

Chapter 7

Figure 7.5. TEM & HR-TEM images of **(a, b) In$_{2.77}$S$_4$, (c, d) In$_{2.77}$S$_4$(P4),** and **(e, f) In$_{2.77}$S$_4$(P6)** respectively. **(g)** FESEM images of pristine **In$_{2.77}$S$_4$** shows nano flower like morphology. **(h)** AFM image of In$_{2.77}$S$_4$ nano -flowers. The nano flowers are destroyed upon drastic sonication, resulting fragmented part of nano flower in AFM.

Moreover, High angle annular dark-field scanning transmission electron microscopy (HAADF-STEM) images were used to determine the morphology of the as prepared **In$_{2.77}$S$_4$(P)** (**Figure 7.6**) catalysts. It revealed that the **In$_{2.77}$S$_4$** nano flowers are well dispersed over the microporous polymer matrix, indicating polymer incorporation does not alter the **In$_{2.77}$S$_4$** hereto structure. Calculated interplanar *d*-spacing between the well-defined lattice fringes were examined at 0.190 and 0.316 nm, which can be indexed to (440) and (311) planes of **In$_{2.77}$S$_4$** crystal structure. The HAADF elemental mapping of the **In$_{2.77}$S$_4$(P)** catalysts (**Figure 7.7**)

showed the presence of different elements like C (blue), N (yellow), S (red) and In (green) throughout the catalyst surface. Although the distribution of C (blue) and N (yellow) were observed throughout the catalyst surface, but the In (green) and S (red) are mainly located at some particular positions wrapped by the polymer.

CO$_2$ to ethene under light irradiation: The photocatalytic CO$_2$ reduction activity of In$_{2.77}$S$_4$ nanoflowers was evaluated in a batch reactor under simulated solar light irradiation (450 W Xe lamp with UV cut-off KG-2 filter). The CO$_2$ saturated water has been used as the only reaction medium without any organic additives makes the process more green, cost effective and suitable for real application.[24] Most interestingly, C$_2$H$_4$ was obtained as the major product along with small amount of CO. Here worth mentioning that CO$_2$ to C$_2$H$_4$ formation is kinetically slow, but commercially valuable product compared to any other C2 products.[25] As shown in **Figure 7.8a**, the C$_2$H$_4$ production rates revealed that **In$_{2.77}$S$_4$** is the key active species for CO$_2$ hydrogenation, exhibiting 20.7 µmol g^{-1} h^{-1} C$_2$H$_4$ production rate. On the other hand, **P6** and **P4** did not show notable performance towards CO$_2$ reduction (the result shown here falls in under the error limit). However, upon composite formation with POPs and **In$_{2.77}$S$_4$** an impressive increment of performance was observed.
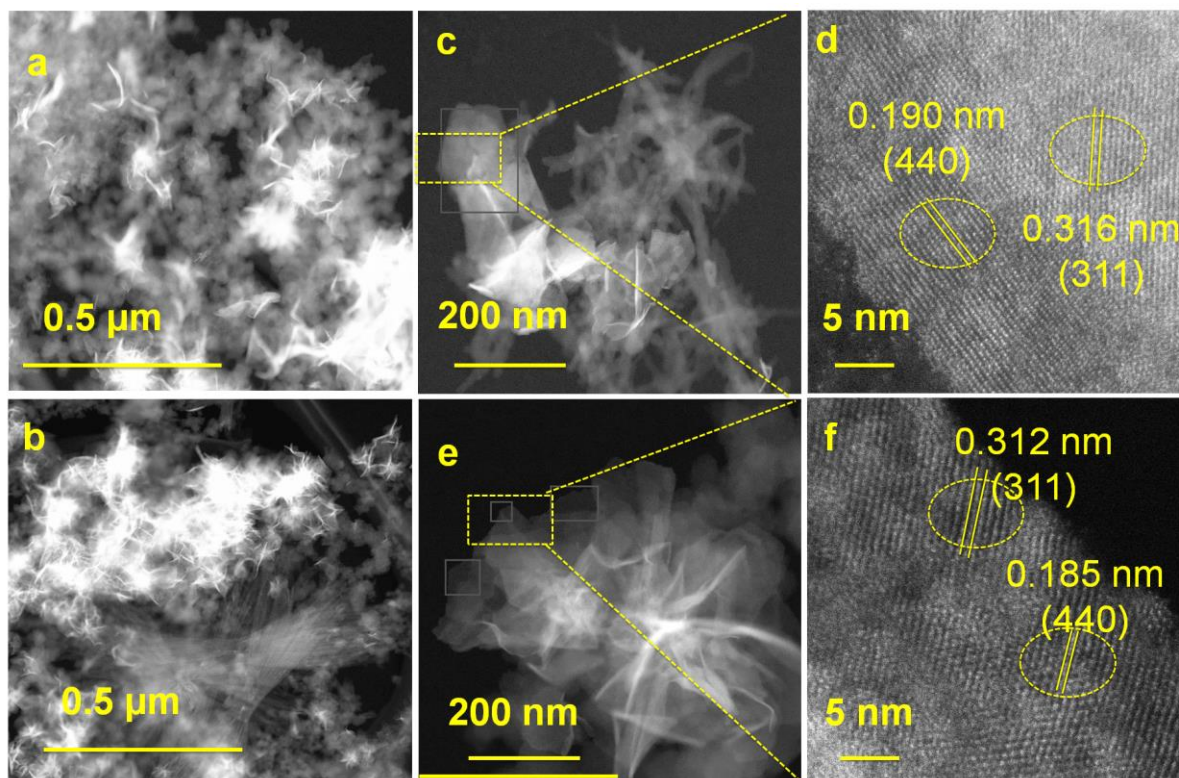

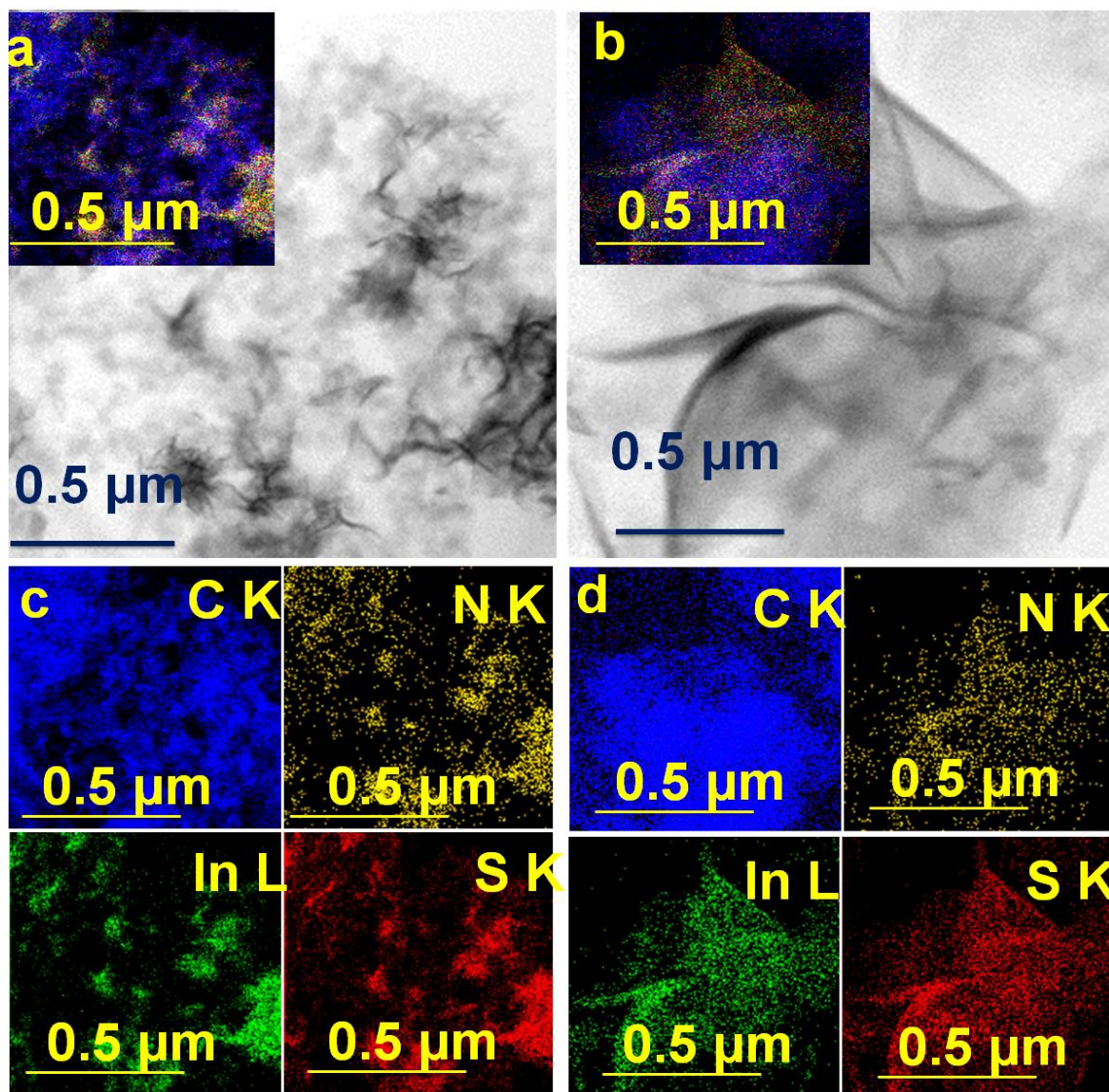**Figure 7.6.** HAADF-STEM images of **(a, c, d) In$_{2.77}$S$_4$(P4),** and **(b, e, f) In$_{2.77}$S$_4$(P6)** respectively.

Light-Induced Charge Accumulation on Polarized Indium in In₂.₇₇S₄ from Porous Organic Polymer Tailoring C-C Coupling to Produce Ethylene from CO₂

Chapter 7

Figure 7.7. (a, c) STEM-EDX elemental mapping of **In$_{2.77}$S$_4$(P4)**, and **(b, d) In$_{2.77}$S$_4$(P6)** exhibiting a uniform spatial distribution of C (blue), N (yellow), In (green) and S (red), respectively.

In$_{2.77}$S$_4$(P6) produced highest ethylene formation rate of **65.75** µmol g^{-1} h^{-1}, which is the highest among reported literatures (**Table 7.1**). **In$_{2.77}$S$_4$(P4)** also showed comparable ethylene formation rate of 54.9 µmol g^{-1} h^{-1}. Although lack of metal center in pristine POPs may restrict its CO$_2$ reduction ability, the extended Π-conjugation in POPs put remarkable assistance in suppling adequate charges thereby increasing 3-fold increment of ethylene formation rate. Ethylene production from CO$_2$ reduction is kinetically very difficult process because it involves consecutive 12 proton coupled electron transfer.[26] An impressive R$_{electron}$ value (involved electrons) was obtained in this process (**Figure 7.8b**). In one hand C$_2$H$_4$ formation process required 12 electron and in other hand CO formation needs only 2 electrons.

Therefore, to normalize these parameters the selectivity was calculated in terms of $R_{electron}$ and **98.9% C_2H_4** selectivity was found in case of **$In_{2.77}S_4$(P6)**.[27] Almost similar selectivity was obtained with **$In_{2.77}S_4$(P4)**. However, a dramatic fall of selectivity was observed in the case of pristine **$In_{2.77}S_4$**. Insufficient electron doner in pristine **$In_{2.77}S_4$** may hindered electron rich CO_2 to C_2H_4 formation process causing notable selectivity drop. Meanwhile isotope labelled $^{13}CO_2$ reduction under same reaction condition followed by product detection by GC-MS confirmed that the generated C_2H_4 (**Figure 7.8c**) and CO (**Figure 7.8d**) are unequivocal products from CO_2. Liquid product analysis by ^1H NMR confirmed no liquid product obtained after CO_2 reduction (**Figure 7.9a**). Further, few follow-up control experiments in absence of catalyst, CO_2, water and light implicitly specifies that the detected gas molecules are solely coming from CO_2 reduction and not from degradation of POP moiety as one may assume (**Figure 7.9b**).
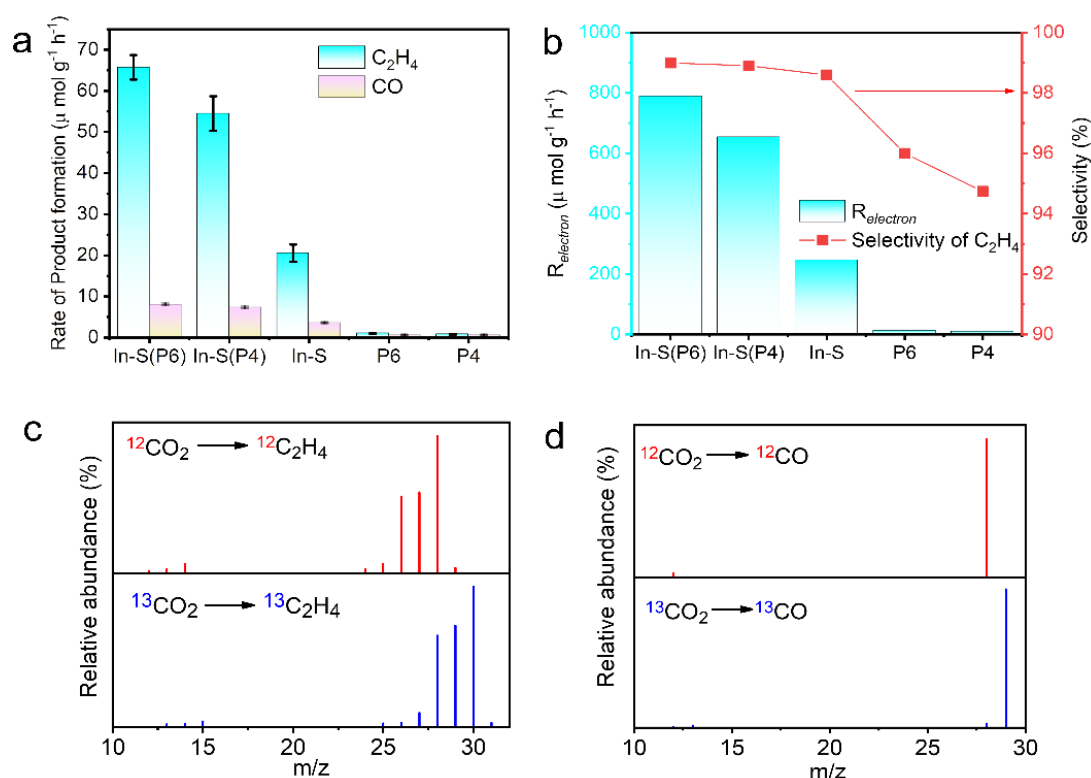

Figure 7.8. Photocatalytic performance in batch type reactor. **(a)** Overall photocatalytic CO_2 to product formation rate based on 10h reaction. **(b)** Based on the number of electrons involvement the activity (Rate) was normalized by a descriptor called $R_{electron}$ and finally the selectivity of C_2H_4 was calculated on the basis of $R_{electron}$. Here instead of **$In_{2.77}S_4$**, In-S was used due to lack of space in the figure. GC-MS of products obtained upon CO_2 and isotope labeled $^{13}CO_2$ photoreduction with **$In_{2.77}S_4$(P6)** catalyst for conforming the formation of **(c)** C_2H_4, and **(d)** CO. $R_{electron} = 12*nC_2H_4 + 2*nCO$ (nC_2H_4 and nCO means no. mole of C_2H_4 and CO produced per hour with per gram of catalyst respectively). Selectivity of C_2H_4 = $\frac{12*nC_2H_4}{2*nCO}*100\%$.

Photocatalytic activity was checked with spent catalyst for another 5 runs and the results remained unaltered, infaring the stability and cyclability of composite catalysts (**Figure 7.9c**). The powder XRD patterns, SEM and TEM analysis (**Figure 7.10a-e**) for the spent photocatalysts **In₂.₇₇S₄(P6)** and **In₂.₇₇S₄(P4)**) after 5 consecutive reactions demonstrate that oxidation states and morphology of nano flower photocatalyst were well maintained, validating their stability. Water oxidation to O_2 is the counter reaction of CO_2 reduction procedure which takes the hole away from the catalyst and suppress the recombination of photogenerated charges. In the course of this process a little amount of H_2 has also formed from water splitting. The observed O_2 amount is well corroborating according to the redox reaction (**equation 7.1-7.3**). Slightly less amount of O_2 was observed due to dissolution of evolved O_2 in water medium.
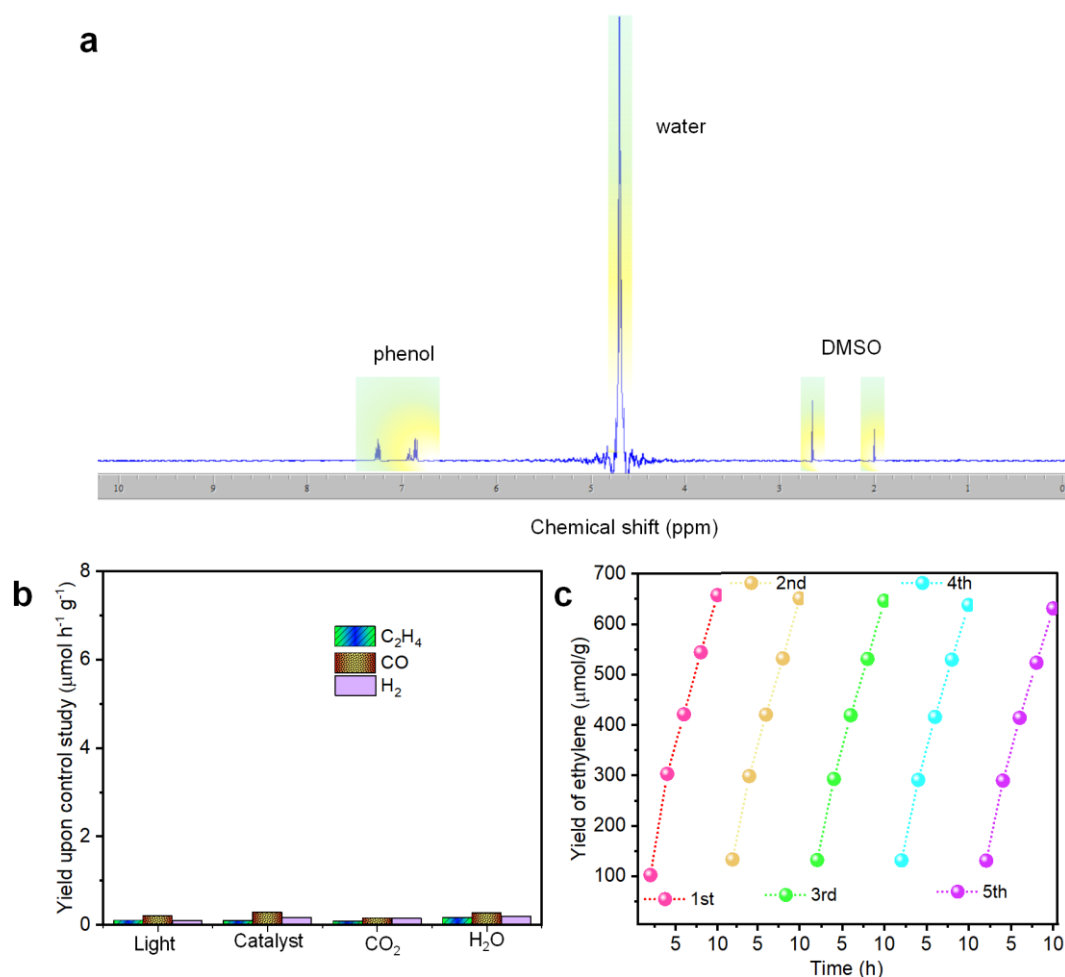
Figure 7.9. **(a)** Post reaction liquid product analysis. After 10h of reaction with **In₂.₇₇S₄(P6)** the solution (here water was used as reaction medium) was analyzed. **(b)** Control experiments in absence of light, catalyst, CO_2 and water. Each experiment was continued for 10h and no reportable production gas was detected. **(c)** Recyclability and stability of catalytic activity was checked with same catalyst (**In₂.₇₇S₄(P6)**) for 5 constitutive runs.

239

Figure 7.10. Post catalytic characterization. **(a)** Post catalytic PXRD patterns of **In₂.₇₇S₄(P4)** and **In₂.₇₇S₄(P6)**. SEM images taken after 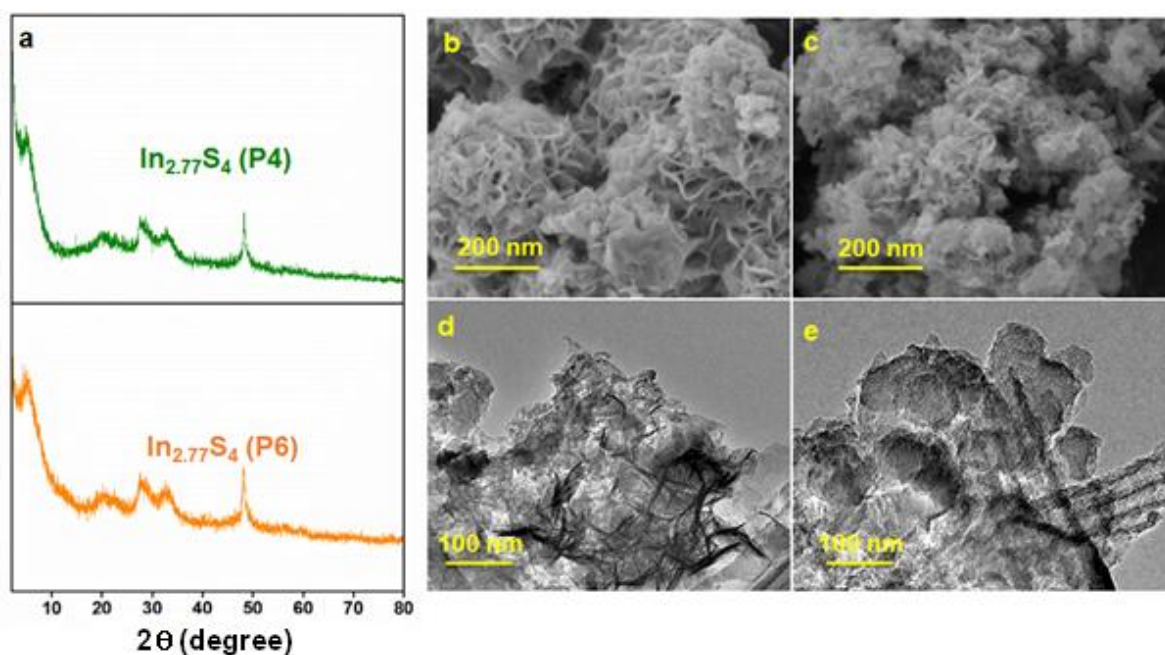catalysis for **(b) In₂.₇₇S₄(P4)**, and **(c) In₂.₇₇S₄(P6)**. TEM images collected for **(d) In₂.₇₇S₄(P4)**, and **(e) In₂.₇₇S₄(P6)** after photocatalysis, respectively.

Structure activity relationship: The as-synthesized porous organic polymers (**P4** and **P6)** and their composites (**In₂.₇₇S₄(P4)** and **In₂.₇₇S₄(P6))** are highly porous in nature with extended cross-linking along with higher thermal and photophysical stability. Wide-angle powder XRD (PXRD) was performed to check the crystallinity of the as-synthesized POPs, which clearly indicates the amorphous nature of the as-synthesized POPs, due to the π-π stacking of the aromatic units in the polymeric framework (**Figure 7.11a**).

On the other hand, the phase of indium sulphide was also confirmed from PXRD. As seen from **Figure 7.11b** the major PXRD peaks related to (311), (400), and (440) planes are exactly matching with In_3S_4 $Fd\overline{3}m$ space group. Additionally, the as synthesized catalyst depicted an interesting feature of specific peak missing. Specifically, (511) plane corresponding to 2θ degree of 43° is absent in the PXRD pattern of as synthesized catalyst. Spinal structure of In_3S_4 is composed of 2 In^{3+} and 1 In^{2+} ($In_2S_3 + InS = In_3S_4$). However, the tetrahedral pockets of In^{2+} have partial occupancy, leading to the formation of $In_{2.67}S_4$ structure with In^{2+} deficiency. Absence of (511) planes containing S atoms further increased the ratio of In and S from 2.67 to 2.77 and finally **In₂.₇₇S₄** was obtained. Similar structure formula was reported by Leqiang et al.[28] The structural similarities among $In_{2.77}S_4$, $In_{2.77}S_4(P4)$, and $In_{2.77}S_4(P6)$ were understood from **Figure 7.11c**.

Light-Induced Charge Accumulation on Polarized Indium in In$_{2.77}$S$_4$ from Porous Organic Polymer Tailoring C-C Coupling to Produce Ethylene from CO$_2$

Chapter 7
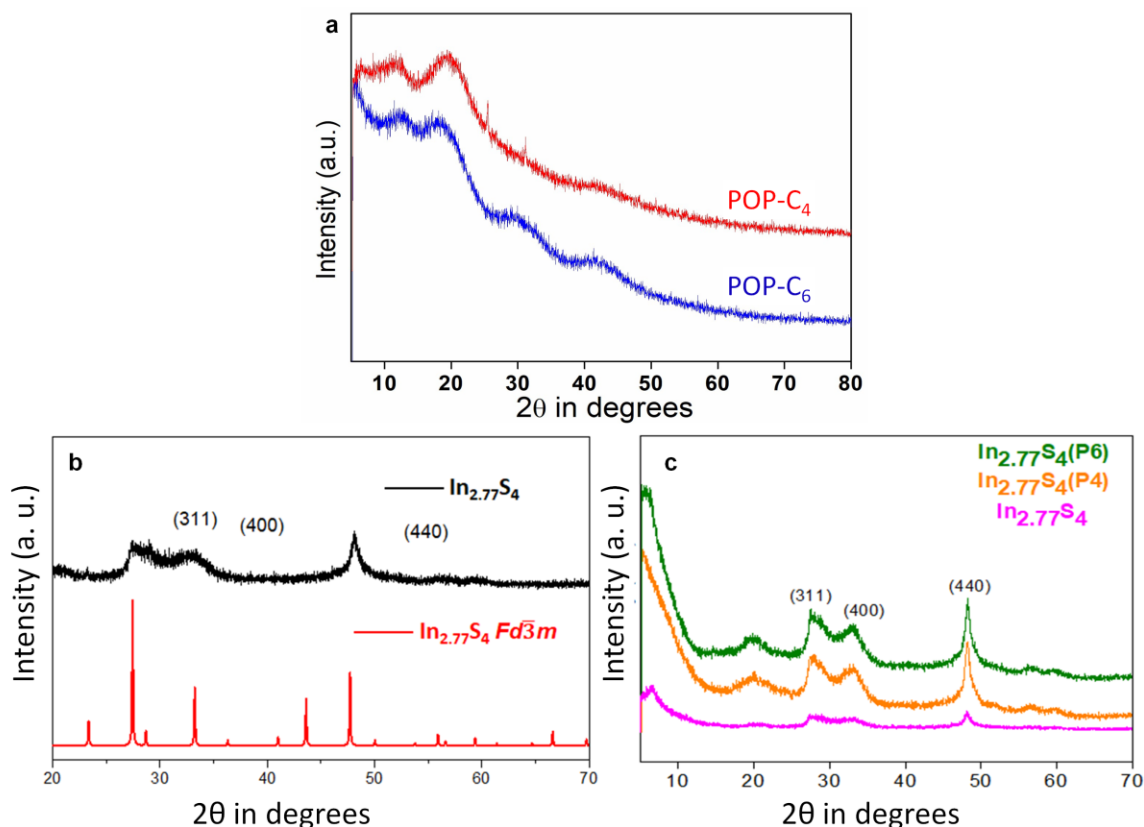
Figure 7.11. Powder X-ray diffraction (PXRD) patterns of **(a) P4** & **P6**, **(b) In$_{2.77}$S$_4$**, and **(c) In$_{2.77}$S$_4$(P4)**, **In$_{2.77}$S$_4$(P6)**, respectively.

The XPS survey spectra indicated the four characteristic binding energy peaks corresponds to the C 1s, N 1s, In 3d and S 2p. Further, the C 1s spectra (**Figure 7.12a**, and **7.12b**) can be deconvoluted into two different binding energies at ~286.9 and 286 eV corresponds to the C-N and aromatic C-C unit,[29] whereas N1s spectra (**Figure 7.12c,** and **7.12d**) deconvoluted in to a single binding energy peak at ~401.5 eV attributed to 'C-N' bond of carbazole.[30]

Slightly higher energy shift of In XPS peaks for **In$_{2.77}$S$_4$(P)** catalysts compare to the pristine **In$_{2.77}$S$_4$** and small negative energy shift in C1s and N1s binding energy in **In$_{2.77}$S$_4$(P)** composites implicitly indicated that there has been some electronic interaction between POP and **In$_{2.77}$S$_4$**. Therefore, the inbuilt heterojunction can promote facile charge transfer between In and porous polymer which in turn helps in availing the synergistic effect of **In$_{2.77}$S$_4$** and POPs for CO$_2$ photoreduction.[31] Slightly higher performance of **In$_{2.77}$S$_4$(P6)** compared to **In$_{2.77}$S$_4$(P4)** can be explained by better heterojunction formation between **P6** and **In$_{2.77}$S$_4$** as evident from higher C1s and N1s XPS peak shift (**Figure 7.12a-d**) because well-built heterojunction favors in facile movement of photo-excited charges. Furthermore, X-ray Photoelectron Spectroscopy (XPS) depicted the presence of In^{2+} (3d$_{5/2}$: 444.9 eV, 3d$_{3/2}$: 452.1

eV) and In^{3+} (3d$_{5/2}$: 446 eV, 3d$_{3/2}$: 454 eV) (**Figure 7.13a**).[32] The quantification of these 2-oxidation state from XPS revealed that it contains 87.5% In^{3+} and 12.5% In^{2+}, which led to the chemical formula of **In$_{2.77}$S$_4$**. Similar In ratio has been maintained upon composite formation with POPs with ~ 1-2% variation. Therefore, the indium sulphide phase is termed as **In$_{2.77}$S$_4$**, composites with **P6** and **P4** were termed as **In$_{2.77}$S$_4$(P6)** and **In$_{2.77}$S$_4$(P4)** respectively.
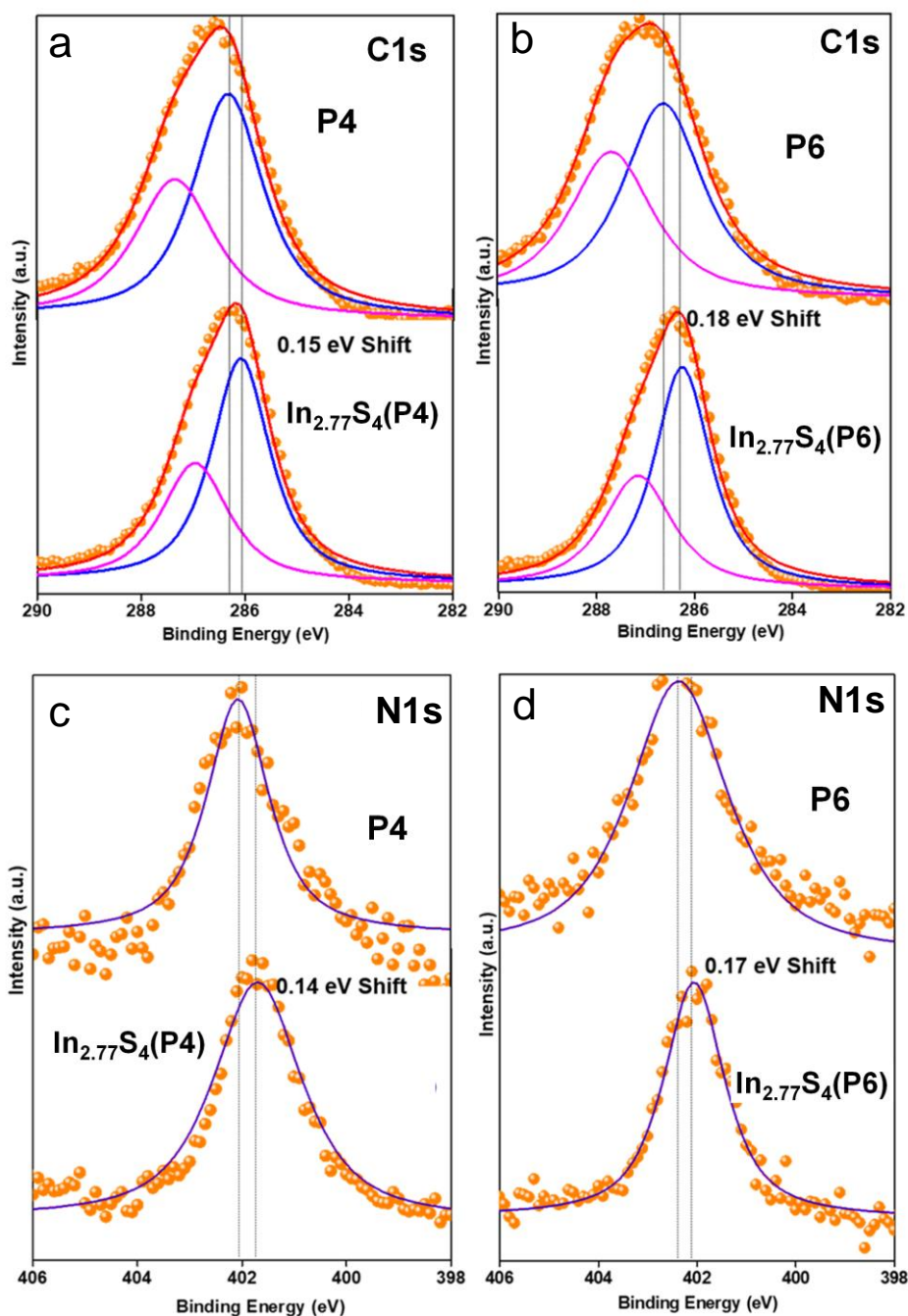
Figure 7.12. X-ray Photoelectron spectra (XPS) of **(a) P4**, **In$_{2.77}$S$_4$(P4)**, and **(b) P6**, **In$_{2.77}$S$_4$(P6)** in the core region of C 1s. XPS of **(c) P4**, **In$_{2.77}$S$_4$(P4)**, and **(d) P6**, **In$_{2.77}$S$_4$(P6)** in the core region of N 1s, respectively.

Light-Induced Charge Accumulation on Polarized Indium in In$_{2.77}$S$_4$ from Porous Organic Polymer Tailoring C-C Coupling to Produce Ethylene from CO$_2$
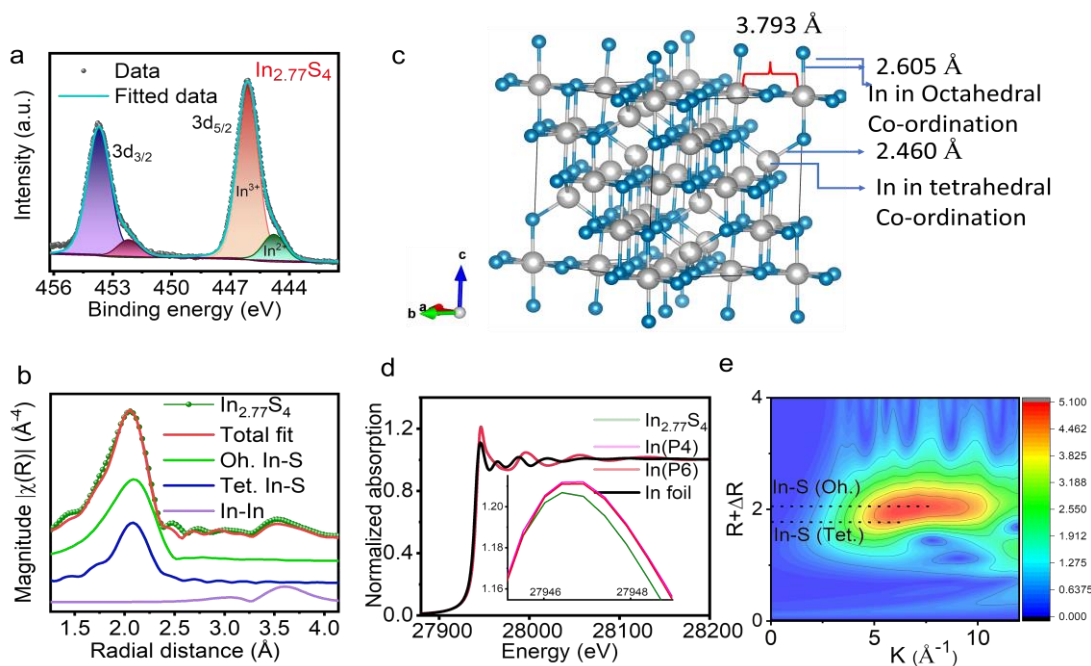
Chapter 7

Figure 7.13. Characterization of polarized charge center of In. **(a)** In 3d XPS of pure **In$_{2.77}$S$_4$**. **(b)** In K-edge Fourier-transform EXAFS spectra of In$_{2.77}$S$_4$ considering In1-S1, In2-S1 paths to obtains the local environment of In1 (In^{3+}) and In2 (In^{2+}). **(c)** Crystal structure of In$_{2.77}$S$_4$ showing octahedral (oh.) and tetrahedral (tet.) co-ordination environment of 'In' atoms. **(d)** X-ray absorption near-edge structure (**XANES**) of In K-edge in In$_{2.77}$S$_4$ and the POP composites, and **(e)**Wavelet transforms for k^2-weighted EXAFS data of **In$_{2.77}$S$_4$**.

Further, synchrotron radiation-based X-ray absorption spectroscopy (XAS) was employed to establish local structural environment of different In sites. The Fourier-transformed In K-edge extended X-ray absorption fine structure (EXAFS) spectra in **Figure 7.13b** are clearly represented a shoulder along with the main peak, representing 2 different In-S bond distances. The shoulder representing In^{2+}-S bond distance, and the main peak is corresponding to In^{3+}-S bond distance which is further supporting the presence of significantly high amount of In^{3+} compared to In^{2+}. The spectra were also fitted to understand the exact bond distance, co-ordination environment and key structural features of 2 distinct In (**Table 7.1**). A similar picture may be also inferred by having a look at the refined Debye-Waller factors (**Table 7.1**): the value of the octahedral In-S path, 0.01 Å, is relatively high if compared with a typical 0.003 Å at room temperature. Such fact may be reasoned considering that tetrahedral In may be replaced with a vacancy causing the neighboring octahedral In to be slightly distorted and thus letting the Debye-Waller factor to be refined at a higher value. Tetrahedral In-S paths are refined to a classical 0.003 Å as Debye-Waller factor and this can be due to the In^{2+} cations occupying only the tetrahedral sites, and not the octahedral ones because of the absence of distorted tetrahedral sites.

Table 7.1. Parameters obtained after fitting the XAS data of $In_{2.77}S_4$, $In_{2.77}S_4(P4)$ and $In_{2.77}S_4(P6)$.

Parameter	$In_{2.77}S_4$	$In_{2.77}S_4(P4)$	$In_{2.77}S_4(P6)$
R-factor	0.003	0.0027	0.0025
Fitting range in k (Å^{-1})	2.58-15.491	2.58-15.491	2.58-15.491
Fitting range in R (Å)	1.41-4	1.41-4	1.41-4
N_{ind}	21.08	21.08	21.08
N_{par}	8	8	8
S_0^2	0.88(4)	0.87(3)	0.88(3)
ΔE	4.9(3)	5.1(3)	5.0(3)
R_{In-S} octahedral (Å)	2.570(6)	2.569(6)	2.568(6)
σ^2_{In-S} octahedral (Å^2)	0.010(1)	0.010(1)	0.011(1)
R_{In-S} tetrahedral (Å)	2.495(10)	2.498(9)	2.498(9)
σ^2_{In-S} tetrahedral (Å^2)	0.0030(5)	0.0030(5)	0.0031(5)
R_{In-In} octahedral (Å)	3.80(1)	3.81(1)	3.80(1)
σ^2_{In-In} octahedral (Å^2)	0.017(2)	0.017(2)	0.017(1)

The In-In path, structurally bridging two octahedral In atoms, is refined with again a high Debye-Waller parameter as there is the chance that the absorber or the scatterer are close to a vacancy. Four coordinated In^{2+} with shorter bond distance (2.46 Å) compared to six coordinated In^{3+} with longer bond distance (2.6 Å) confirms that the In^{2+} holds tetrahedral void whereas In^{3+} occupies octahedral voids by creating normal spinel structure (**Figure 7.13c**). Wavelet transformation of these EXAFS data gives broad spot instead of concentrated single spot pattern (**Figure 7.13e**) meaning the presence 2 different kind of In-S bonds namely In-S(oh.) and, In-S(tet.).[33] The In K-edge X-ray absorption near-edge spectra (XANES) in **Figure 7.13d** shows similarities among pristine $In_{2.77}S_4$ and the composites with **P6** and **P4**. These resemblances are to be expected, given that In atoms in composites and pristine $In_{2.77}S_4$ maintained similar co-ordination structural properties. However, increase of white line intensities in $In_{2.77}S_4(P4)$ and $In_{2.77}S_4(P6)$ compared to pristine $In_{2.77}S_4$ indicates less electron density over In centres in composites, meaning a charge transfer from $In_{2.77}S_4$ to POPs and due to which the heterostructure stabilized.[25]

Furthermore, the charge transfer behavior was understood from DFT calculations. Two different types of heterostructures were made by considering the interaction of POP with two inequivalent surfaces of $In_{2.77}S_4$ (**Figure 7.14a,** and **7.14b**). These are designated as "hetero

Light-Induced Charge Accumulation on Polarized Indium in In$_{2.77}$S$_4$ from Porous Organic Polymer Tailoring C-C Coupling to Produce Ethylene from CO$_2$

Chapter 7

up" (HU) and "hetero down" (HD) where the POP interacts with the upper and below surface of In$_{2.77}$S$_4$, respectively (**Figure 7.14e** and **7**.**14f**). Bader charge calculations for these heterostructures showed that the charge separation is higher in HU as compared to HD where the **In$_{2.77}$S$_4$** surface donates electrons to POP for each case. This can be explained by the increased polarity of the In$_{2.77}$S$_4$ surface that interacts with the POP. **In$_{2.77}$S$_4$** has only one type of unsaturated In atoms (2-coordinated) on the upper surface, whereas two types of unsaturated In atoms (2 and 3-coordinated) on the below surface increased its polarity than upper surface. This increases the van der Walls' interaction of POP with the upper surface and correspondingly, the charge separation is higher in HD.
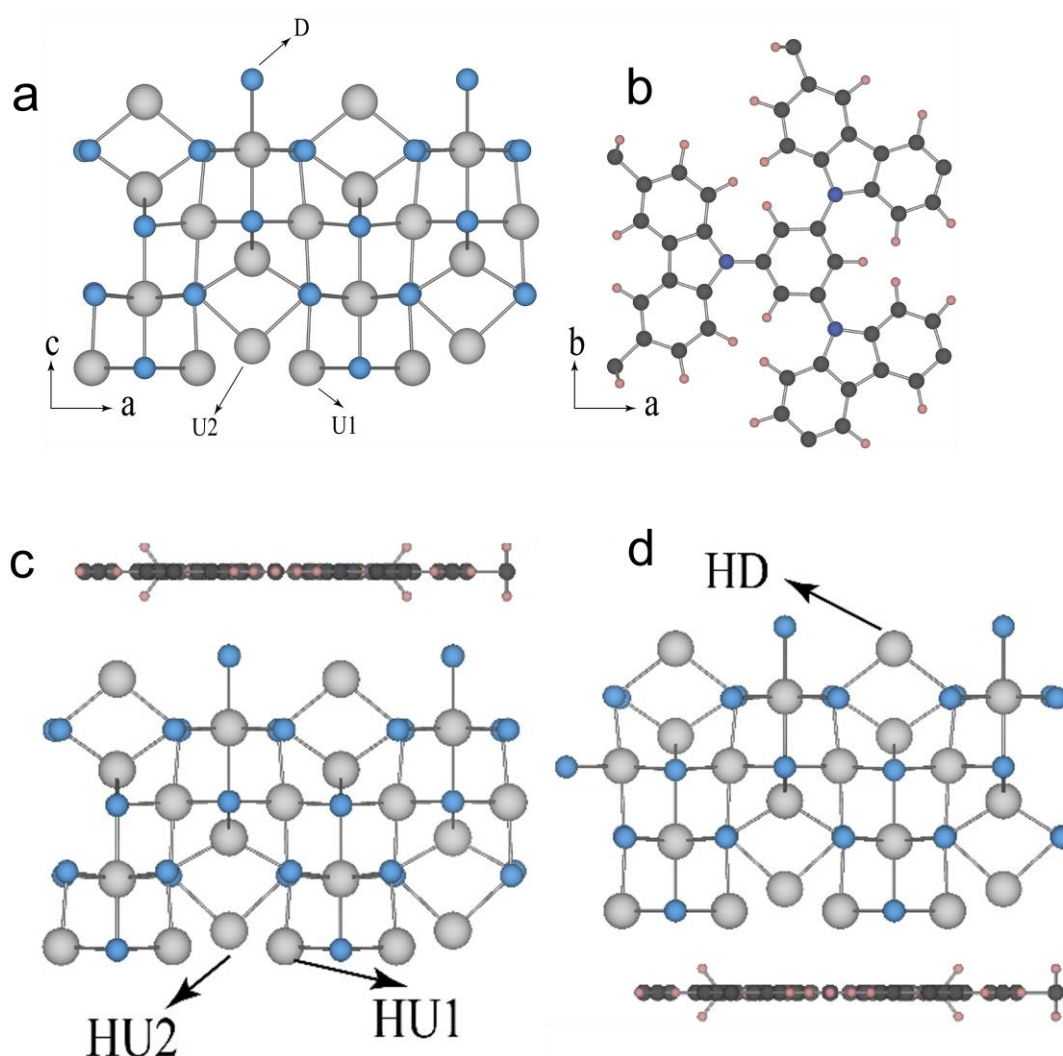
Figure 7.14. Side view of (400) surface of **(a) In$_{2.77}$S$_4$,** and **(b)** top view of **P6**. Grey colored balls are 'In' and sky-colored balls are 'S'. Theoretical model of **In$_{2.77}$S$_4$**/POP heterostructure considering the adsorption positions of POP on **(c)** upper side (Hetero up (HU)), and **(d)** down side (Hetero down (HD)) of In$_{2.77}$S$_4$ in the heterostructures where the grey, azure blue, black, pink, and blue balls represent the In, S, C, H, and N atoms respectively.

To evaluate the importance of charge separation in the considered heterostructures for CO_2 reduction reaction, probable active sites were identified through DFT calculations for POP, $In_{2.77}S_4$ surface and heterostructures to check the stability of CO_2 and CO molecules (**Figure 7.15a-f**). As the optimum binding energy of CO determines the probability of forming higher-carbon products. The optimized structure of CO_2 and Co adsorbed over N-atom of POP is not stable because, upon optimization, POP structure planarity breaks completely.

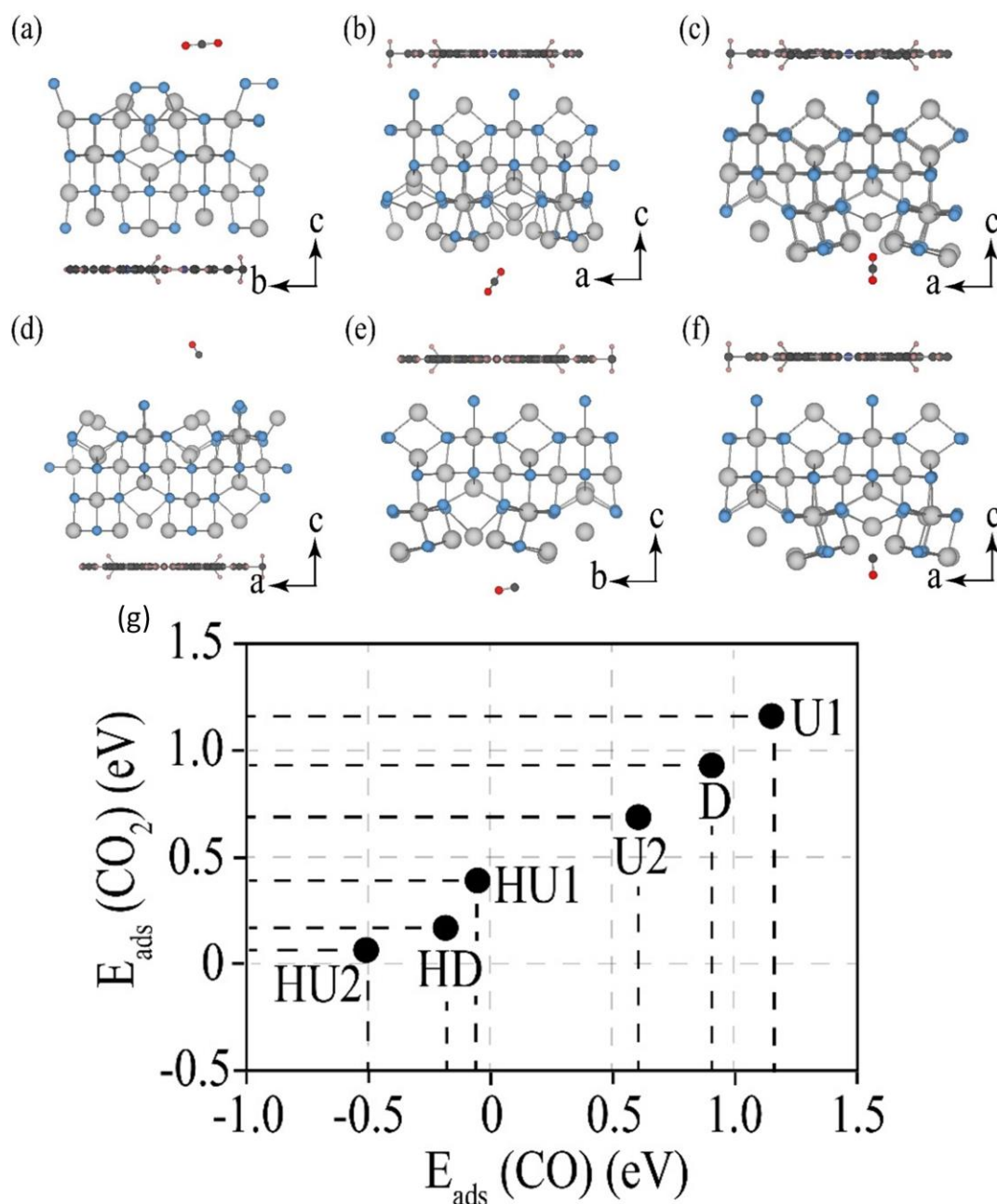**Figure 7.15.** Side view of adsorbed CO_2 over **(a)** HD, **(b)** HU1, and **(c)** HU2 and adsorbed CO over **(d)** HD, **(e)** HU1, and **(f)** HU2. **(g)** Comparison of adsorption energy of CO_2 and CO on different considered adsorption positions.

This is in line with the experimental evidences, which show the pristine POPs are inactive. Moreover, the stability of considered molecules increases on the surface $In_{2.77}S_4$ where the U2 position shows best adsorption ability, however still not satisfactory as the adsorption energies of CO_2 and CO are high positive (**Figure 7.15g**). Interestingly, all the considered adsorption positions on the heterostructure show better activity than pristine $In_{2.77}S_4$ surface and POP. This difference of activity between $In_{2.77}S_4$ surface and heterostructures can be attributed to the energy difference of their Fermi level with the lower unoccupied molecular orbital of gaseous CO and CO_2. The Fermi level of $In_{2.77}S_4$ and **$In_{2.77}S_4$(P6)** are situated at -4.62 eV and -3.89 eV, respectively (**Scheme 7.3**). Accordingly, the LUMO of CO and CO_2 at -2.13 eV and -0.97 eV, respectively, are farther from Fermi level of $In_{2.77}S_4$, which transfer less electrons to the adsorbates than the heterostructures (**Scheme 7. 3**). This is because, the POP increases the overall electron density of **$In_{2.77}S_4$/POP** heterostructures. Increased acceptance of electrons by CO_2 and CO also activates this adsorbed molecule for further proton-coupled electron transfer reaction on heterostructures as the LUMO of both CO_2 and CO are antibonding in nature. Therefore, further discussions are based on understanding the different active sites of heterostructures. HD, HU1, and HU2 have Bader charges of 0.64, 0.62, and 0.6, respectively (**Table 7.2**). This increased positive Bader charge on HD as compared to HU2 is expected though both of them are 2-coordinated as the charge separation is higher in HD heterostructure.
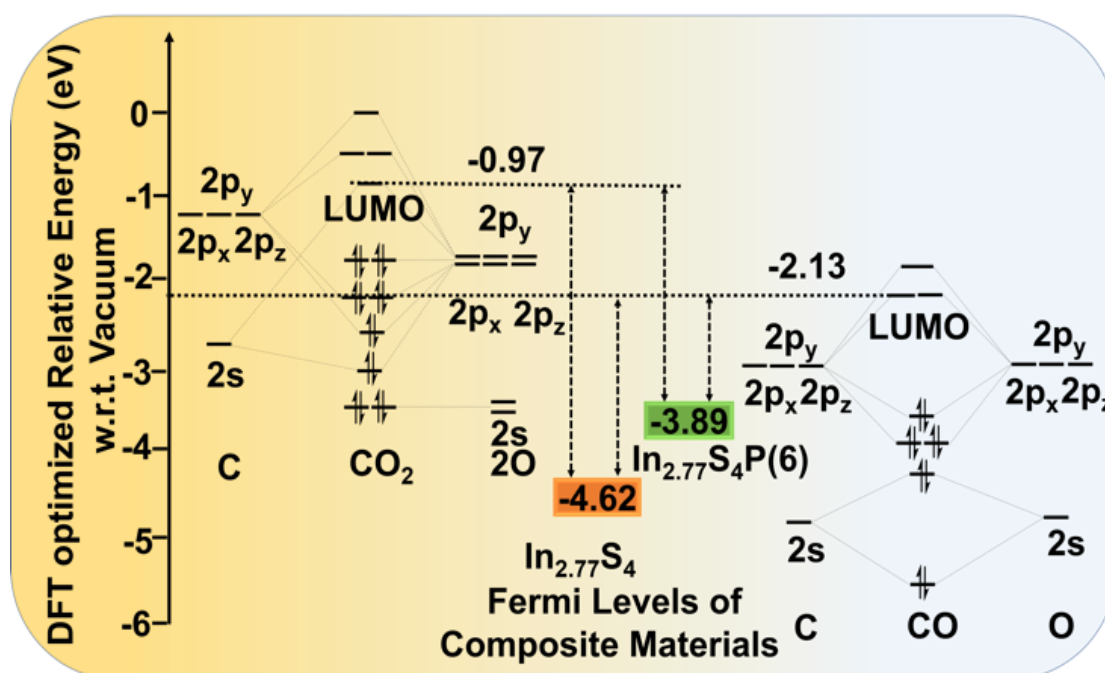
Scheme 7.3. Schematic representation of CO_2 and CO LUMO position with respect to the fermi level of **$In_{2.77}S_4$** and **$In_{2.7}7S_4$(P6)**, obtained from DFT calculation.

The stability of adsorbed CO_2 and CO over these active sites also showed a similar trend as with increasing positive Bader charge on the active sites, the electron acceptance by CO_2 and CO from the surface decreased and become less stable (**Table 7.2** and **Figure 7.15g**). However, the discrepancy of Bader charge-stability over HD and HU1 is due to the decreased coordination number of HD in comparison with HU1 that facile the stability of the considered important adsorbates over the HD. Bader charge of adsorbed CO_2 and CO over HU2 is -0.04, whereas the adsorption energies are 0.06 eV and -0.53 eV which indicates the slight activation of CO_2 and optimum activation of CO. Therefore, HU2 was considered for realizing the feasibility of the whole reaction. Further, it can be inferred that the low adsorption energy of CO on HD favors the formation of CO gas as final yield and supports the experimental observation.

Band structure and charge transfer properties: Suitable band alignment and band gap are basic criteria in CO_2 hydrogenation reaction by solar energy because it involves photon-absorption by visible light irradiation, electron-hole separation, and CO_2 activation by excited electrons. The first 2 step mainly governed by intrinsic nature of the photocatalyst however can be engineered by heterojunction formation, while the 3rd is highly dependent on the gas-solid interface. UV-DRS spectra in **Figure 7.16a** clearly demonstrated that the photocatalysts under this study have excellent visible light harvesting properties. A step-like optical absorption tail in composite compared to pristine POPs can be attributed to **$In_{2.77}S_4$** absorption-edge. Additionally, upon composite formation the absorption peak height has increased meaning better light harvesting ability of composites. A band gap 2.8 eV, 2.77 eV and 2 eV for **P6**, **P4** and **$In_{2.77}S_4$,** respectively, was calculated from Tauc plot.[30] Furthermore, the band diagram was established from the understanding of suitable flat band potential (V_{fb}) obtained from Mott-Schottky measurements (**Figure 7.16b-d**).[34] CBM position was determined by adding -0.1 with V_{fb} and VBM position was obtained by adding the band-gap value (obtained from UV-DRS) with CBM potential.

Table 7.2. Bader charges in different adsorption positions along with the bader charge transfer to the adsorbed CO_2 or CO over those adsorption positions.

Adsorption Position	Bader charge	Bader charge (*CO_2)	Bader charge (*CO)
HD	0.64	-0.01	-0.01
HU1	0.62	-0.03	-0.03
HU2	0.6	-0.04	-0.04

Light-Induced Charge Accumulation on Polarized Indium in In₂.₇₇S₄ from Porous Organic Polymer Tailoring C-C Coupling to Produce Ethylene from CO₂
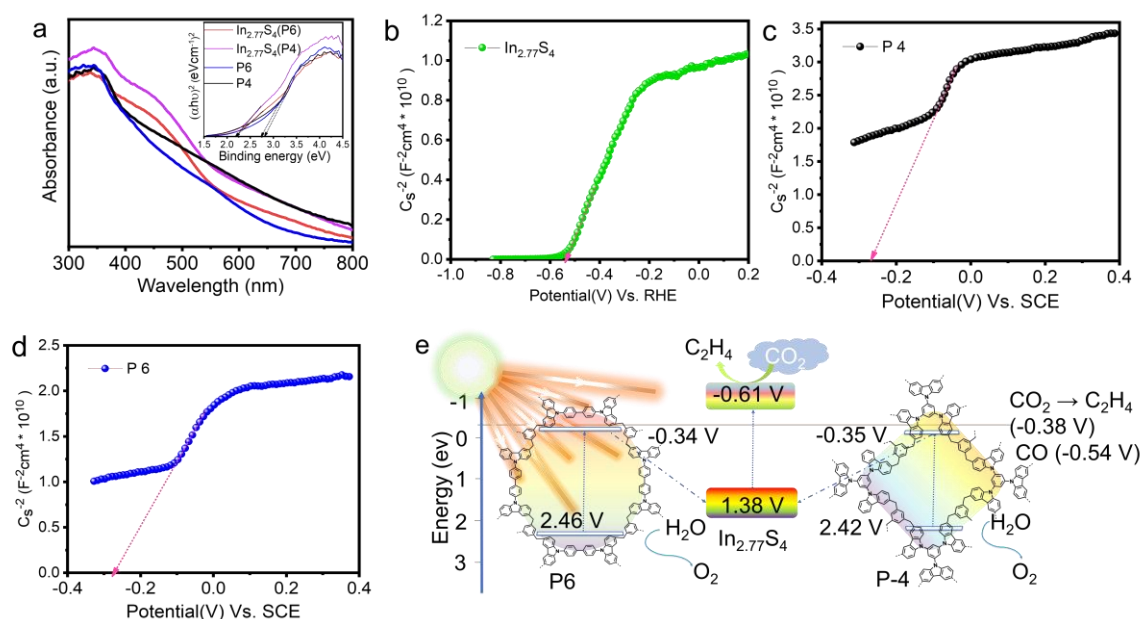
Chapter 7

Figure 7.16. Electronic structure and charge transfer properties. **(a)** UV-Vis DRS of composites and individual components. Inset: corresponding Tauc plots made by using Kubelka-Munk parameter $((\alpha h\nu)^2)$ as a function versus energy of photon (eV). Mott-Schottky plots of **(b) In₂.₇₇S₄, (c) P4**, and **(d) P6** for understanding flat band potential. -0.1V was added with flat bad potential to get the CBM positions of these n-type semiconductor. The intercept at the x-axis is regarded as flat band potential. The impedance study was done in 0.5M Na_2SO_3 electrolyte at an applied frequency of 50 kHz. **(e)** Schematic illustration of **In₂.₇₇S₄/POPs** band structure allingment along with CO_2 to ethylene formation thermodynamic potential. This scheme also illustrate the Z-scheme electron transfer process.

As shown in **Figure 7.16e**, both the POPs are having inappropriate CBM because minimum -0.38 V and -0.54 V potential required for CO_2 to C_2H_4 or CO formation, however, their CBM position lies at -0.34 V and -0.35 V. On the other hand, the CBM position of **In₂.₇₇S₄** situated at -0.61 V, which is enough negative for CO production and obviously C_2H_4 formation. In this scenario after comprehensive consideration of synergistic effect of POPs and **In₂.₇₇S₄** in enhancing the overall CO_2 photo-reduction performance and inappropriate band position of POPs, a direct Z-scheme pathway rather than type-II mechanism is proposed for the **In₂.₇₇S₄(P6)** and **In₂.₇₇S₄(P4)** heterostructures. The excited electron of POPs with weak reduction potential recombines with the photogenerated holes (weak oxidation potential) of **In₂.₇₇S₄.** By the virtue of Z-scheme process the photoexcited electrons with more reduction potential in the CBM of **In₂.₇₇S₄** and holes with better oxidation ability in the VBM of POPs are stabilizing in the **In₂.₇₇S₄/POP** heterostructure. Therefore, due to the increase of diffusion length, electrons and hole are getting separated and losing recombination tendency which in turn is beneficial for availing more excited electrons for CO_2 reduction in CBM of **In₂.₇₇S₄** and

water to O_2 formation by the holes in the VBM of POPs. Furthermore, strong evidence of Z-scheme was found from $\cdot O_2^-$ (**Figure 7.17a**) and $\cdot OH$ (**Figure 7.17b**) radical trapping experiment with 5,5-dimethyl-1-pyrroline N-oxide (DEMPO) via electron paramagnetic resonance (EPR) spectroscopy.[35] As depicted in **Figure 7.17a**, signals attributing to DMPO-$\cdot O_2^-$ adduct is high instance for **In$_{2.77}$S$_4$(P6)** and **In$_{2.77}$S$_4$(P4).** Contextually, this signal intensity is very poor for pristine POPs and intermediate for **In$_{2.77}$S$_4$** since the pristine POPs does not have enough negative overpotential to drive the $\cdot O_2^-$ formation reaction from O_2.
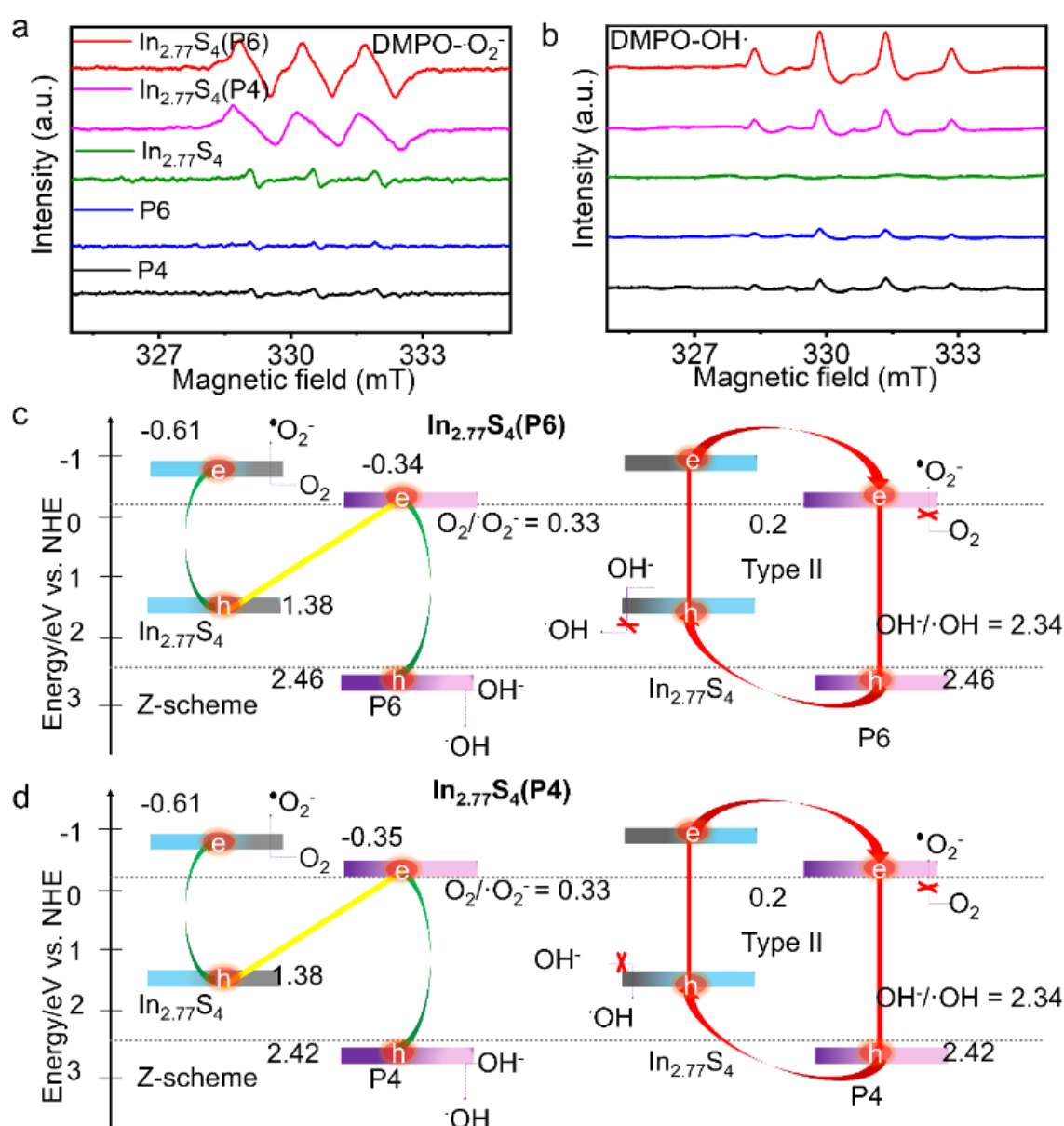
Figure 7.17. Establishment of Z-scheme electron transfer in **In$_{2.77}$S$_4$/POPs** *via* radical trapping. ESR spectra of **(a)** DMPO-$\cdot O_2$- in methanol, and **(b)** DMPO-$\cdot OH$ in water in the presence of **In$_{2.77}$S$_4$(P6), In$_{2.77}$S$_4$(P4), In$_{2.77}$S$_4$, P6 and P4**. Energy band diagram and reaction mechanism of type-II and Z-scheme system for **(c) In$_{2.77}$S$_4$(P6)**, and **(d) In$_{2.77}$S$_4$(P4)** heterojunctions.

Light-Induced Charge Accumulation on Polarized Indium in In$_{2.77}$S$_4$ from Porous Organic Polymer Tailoring C-C Coupling to Produce Ethylene from CO$_2$

Chapter 7

On the other hand, **In$_{2.77}$S$_4$** has enough negative overpotential but suffers from excessive charge recombination which was recovered by Z-scheme heterojunction formation with POPs where photogenerated holes of **In$_{2.77}$S$_4$** were annihilated by the photoexcited electrons of POPs (**Figure 7.17c,** and **7.17d**). Therefore, **In$_{2.77}$S$_4$(P6)** and **In$_{2.77}$S$_4$(P4)** again showed high instance DMPO-·OH signal compared to pristine POPs due to the stabilization of photo-excited holes in the valence band (VB) of POPs. Moreover, due to inappropriate VB position of **In$_{2.77}$S$_4$** for ·OH formation reaction, it has not given any signal related to DMPO-·OH adduct (**Figure 7.17b**). Hence, it is rational to propose that the photoexcited electrons of POPs moves to VB of **In$_{2.77}$S$_4$** and stabilizes the holes in POPs' VB and electrons in the CB of **In$_{2.77}$S$_4$** via Z-scheme process (**Figure 7.17c,** and **7.17d**). Additionally, the higher signal intensity of **In$_{2.77}$S$_4$(P6)** compared to **In$_{2.77}$S$_4$(P4)** indicates more electron accumulation on CBM of **In$_{2.77}$S$_4$** in **In$_{2.77}$S$_4$(P6)** compared to **In$_{2.77}$S$_4$(P4)**, which is one of the reasons for better CO$_2$ to C$_2$H$_4$ activity of **In$_{2.77}$S$_4$(P6)** hybrid. Further analysis of charge transfer dynamics depicted the contribution of Z-scheme process in separating photo-excited charges. **Figure 7.18a** displays the steady-state photoluminescence (PL) emission spectra of the pristine POPs and their composites with **In$_{2.77}$S$_4$**. A significant PL intensity drop occurs on the **In$_{2.77}$S$_4$/POP** heterostructures relative to pristine POPs, meaning that the radiative recombination of photoexcited electrons and holes in both the POPs has been suppressed by the formation of the Z-scheme system, due to the facile charge transfer through the intimate interfaces. Furthermore, the time-dependent transient PL decay spectra in **Figure 7.18b** shows that the composite catalysts are having distinctly longer average life time (τ_{avg}) of photogenerated charges than the pristine POPs, implying that there is significant charge separation due to facile interfacial charge transfer in the composites (**Table 7.3**). Relatively longer charge carrier life time of **In$_{2.77}$S$_4$(P6)** compared to **In$_{2.77}$S$_4$(P4)** can be due to better heterojunction formation with **P6**.[21] Apparent quantum yield (AQY%) was calculated for the best catalyst (**In$_{2.77}$S$_4$(P6)**) using different excitation wavelength and an excellent synergy between overall photocatalytic activity and Z-scheme mechanism was observed (**Figure 7.18c**).[21] Up to 500 nm excitation the AQY% was following absorption spectra where both POPs and **In$_{2.77}$S$_4$** has light absorption ability. After that the AQY% has fallen dramatically because POPs cannot harvest later part of solar spectra. Therefore, the photogenerated holes in **In$_{2.77}$S$_4$** are not getting annihilated by the photogenerated electrons of POPs resulting electron-hole pair recombination. Hence confirmed that photocatalytic activity greatly depends on Z-scheme mechanism.

Table 7.3. Parameters of the TRPL decay. The data was fitted using the following equation. $A+B1\exp(-t/\tau_1)+B2\exp(-t/\tau_2)+B3\exp(-t/\tau_3)$ where, B1, B2 and, B3 are the pre-exponential factor (amplitude) corresponding to decay lifetimes of τ_1, τ_2 and, τ_3 respectively. Here τ_{avg} is the average life time calculated by $\tau_{avg}= (B1\tau_1^2+B2\tau_2^2+B3\tau_3^2)/(B1\tau_1+B2\tau_2+B3\tau_3)$.[36]

Sample	τ_1(ns)	τ_2(ns)	τ_3(ns)	B1	B2	B3	τ_{avg}(ns)
P4	0.16	0.32	0.64	22.59	66.76	10.65	0.044
P6	0.17	0.35	0.71	18.02	74.81	7.17	0.040
In$_{2.77}$S$_4$(P6)	0.22	0.45	0.9	23.95	62.42	13.63	0.14
In$_{2.77}$S$_4$(P4)	0.28	0.56	1.13	27.41	18.96	53.63	0.11
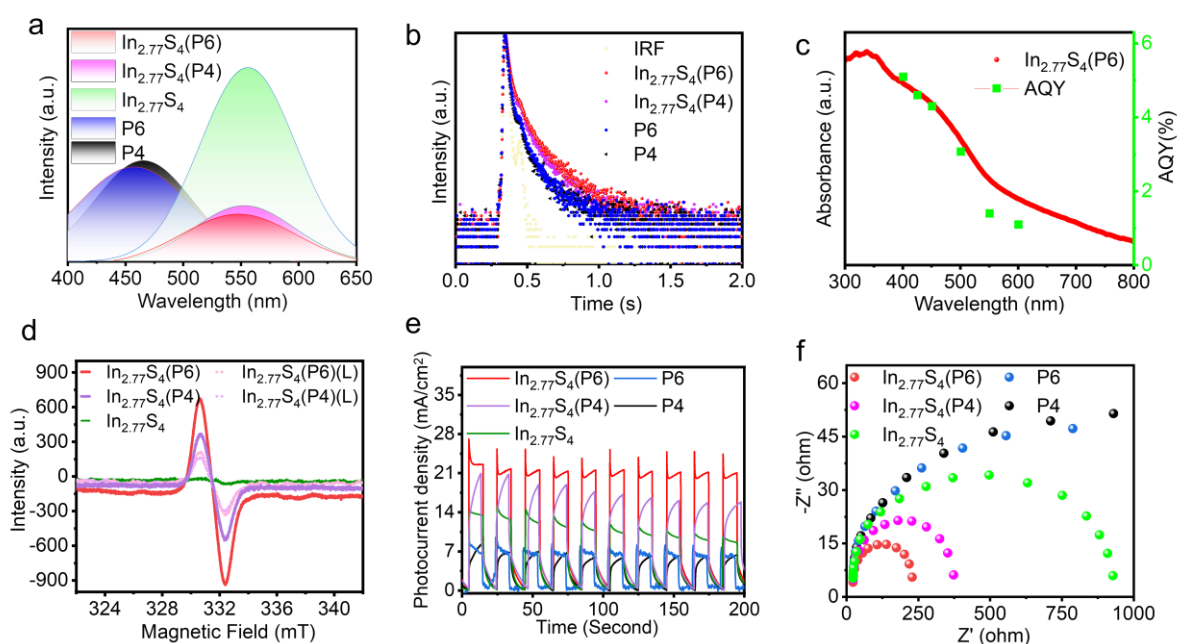
Figure 7.18. (a) Static PL of **In$_{2.77}$S$_4$/POPs** composites and other pristine individual catalysts. **(b)** Time-resolved photoluminescence (TRPL) decay spectra of **In$_{2.77}$S$_4$/POPs** composite and pristine catalysts. **(c)** AQY% calculation along with the absorption spectra of **In$_{2.77}$S$_4$(P6)** to understand the relationship between observed photocatalytic activity and Z-scheme charge transfer process. **(d)** Operando ESR spectroscopy with **In$_{2.77}$S$_4$/POPs** and pristine **In$_{2.77}$S$_4$** in presence and absence of light illumination. **(e)** Light on-off experiment to understand cathodic photocurrent density of **In$_{2.77}$S$_4$/POPs** and its individual components at 0.1 V vs. Ag/AgCl. **(f)** EIS (Nyquist plot) shows the charge transfer resistance in the composites and pristine photocatalyst from bulk to surface respectively.

Light-Induced Charge Accumulation on Polarized Indium in In2.77S4 from Porous Organic Polymer Tailoring C-C Coupling to Produce Ethylene from CO2

Chapter 7

Further evidence of charge carrier movements was understood from In-situ EPR experiment (**Figure 7.18d**). Encouragingly, the very sharp peak of **In2.77S4(P6)** and **In2.77S4(P4)** started diminishing upon light irradiation. Pure **In2.77S4** has very weak signal. Therefore, the strong signals are mainly due to the presence of unpaired electrons in POPs which are annihilated by the holes of **In2.77S4**, resulting the decrease of EPR signal intensity after light illumination in operando condition. Given the fact that composites are generating more photoexcited charges, the light on-off transient photocurrent density was measured by coating all the catalyst on conduction electrode (FTO) (**Figure 7.18e**). The **In2.77S4(P6)** and **In2.77S4(P4)** generated better photocurrent than that of individual components and pure **In2.77S4(P6)** has better photocurrent generation ability than that of pristine POPs.[37] Further evidence of charge transfer resistance was obtained upon electrochemical impedance spectroscopy (EIS, Nyquist plot) in **Figure 7.18f**. The **In2.77S4(P6)** and **In2.77S4(P4)** heterostructure catalysts exhibited much decreased charge transfer resistance (R_{ct}) compared to pure POPs and **In2.77S4**,[38] which is in accordance with the previous PL and TRPL study.[39] All these evidences firmly indicating the promoted charge transfer ability and positive contributions of POPs in composite systems enhance CO_2 reduction ability under light irradiation.

Mechanistic study: It is worth mentioning that up to now, the full mechanism for CO_2 to ethylene formation by photocatalytic route was not reported as only a few works reported for CO_2 to C_2H_4 formation via photocatalytic route. In our analysis we aimed to unwrap the complete mechanism for CO_2 to ethylene conversion consisting of $12e^- + 12H^+$ reduction process. Therefore, operando diffuse reflectance infrared Fourier transform spectroscopy (DRIFTS) was performed under light irradiation with **In2.77S4(P6)** catalyst (**Figure 7.19**).
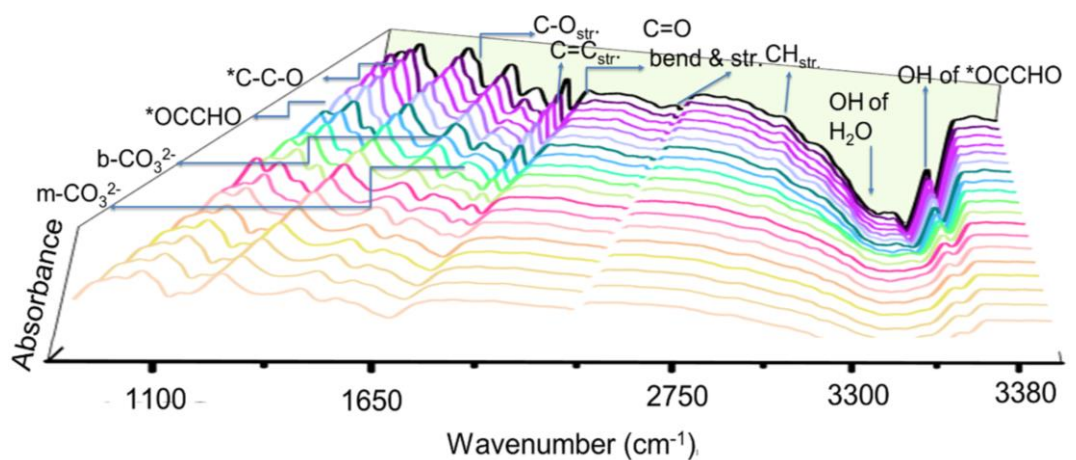

Figure 7.19. *In-situ* DRIFTS experiments of CO_2 adsorption and reduction. *In-situ* DRIFTS for the adsorption of CO_2 and H_2O vapor in presence of 450 W Xe light illumination.

The peak attributed to mono and bidentate carbonates are observed at 1523 cm^{-1} and 1402 cm^{-1}.[40] Evolution of IR peak at 1263 cm^{-1} corresponds to the C-O stretching vibration of *COOH which is regarded as the first and key intermediated of CO_2 reduction process.[41] Interestingly, very small *CO stretching and vibration peak increment was observed at 2160 cm^{-1} and 1747 cm^{-1} meaning the short life span of adsorbed *CO species.[32] More importantly, the asymmetric stretching vibration peaks of *OCCHO at 937 cm^{-1} and for *C-C-O at 1009 cm^{-1} were detected implying the coupling of 2 carbon species. The intermediate *OCCHO is regarded as the crucial one in producing multi carbon products, which was generated via selective protonation on *CO centre followed by C-C coupling.[42] C-H and C=C stretching vibration peaks at 2960 cm^{-1} and 1645 cm^{-1} has appeared after around 30 minutes light irradiation and monotonously increased with light irradiation time directly infaring the formation of *CHOCH intermediate.[43] This particular intermediate can further undergo proton coupled electron transfer process to produce C_2H_4.

The broad OH stretching peak of water has appeared as a deep instead of peak, indicating the consumption of water molecule with the progress of rection. As discussed before the water oxidation reaction is multi fold higher than the C_2H_4 formation reaction, similar observation was found in operando DRIFTS where water consumption signal is much prominent than the CO_2 reduction intermediate peaks. At around 3661 cm^{-1} one peak evolution was observed corresponding to OH group of adsorbed intermediates. Due to discrete position of these OH groups in intermediates, they don't participate in H-bonding, not showing broad spectra.[43] This information of intermediate can help in revealing the ethylene formation mechanism on **In$_{2.77}$S$_4$(P6).** In this context, DFT calculations were performed to identify other crucial intermediates in the course of ethylene formation reaction (**Figure 7.20a-o**) and can be divided into three major parts. prominent than the CO_2 reduction intermediate peaks. At around 3661 cm^{-1} one peak evolution was observed corresponding to OH group of adsorbed intermediates. Due to discrete position of these OH groups in intermediates, they don't participate in H-bonding, not showing broad spectra.[43] This information of intermediate can help in revealing the ethylene formation mechanism on **In$_{2.77}$S$_4$(P6).** Broadly, the formation of C-C coupled products *OCCO by 4e$^-$ + 4H$^+$ or *OCCOH by 5e$^-$ + 5H$^+$ processes (A) followed by the removal of oxygen (B) and formation of C_2H_4 from the C-C coupled intermediates (C). The reduction of CO_2 to *CO through *OCOH intermediate is the common initiation for both *OCCO or *OCCOH. Proton coupled electron transfer (PCET) to slightly activated adsorbed CO_2 over HU2 that yields *OCOH (2) is endothermic.

Light-Induced Charge Accumulation on Polarized Indium in In₂.₇₇S₄ from Porous Organic Polymer Tailoring C-C Coupling to Produce Ethylene from CO₂

Chapter 7
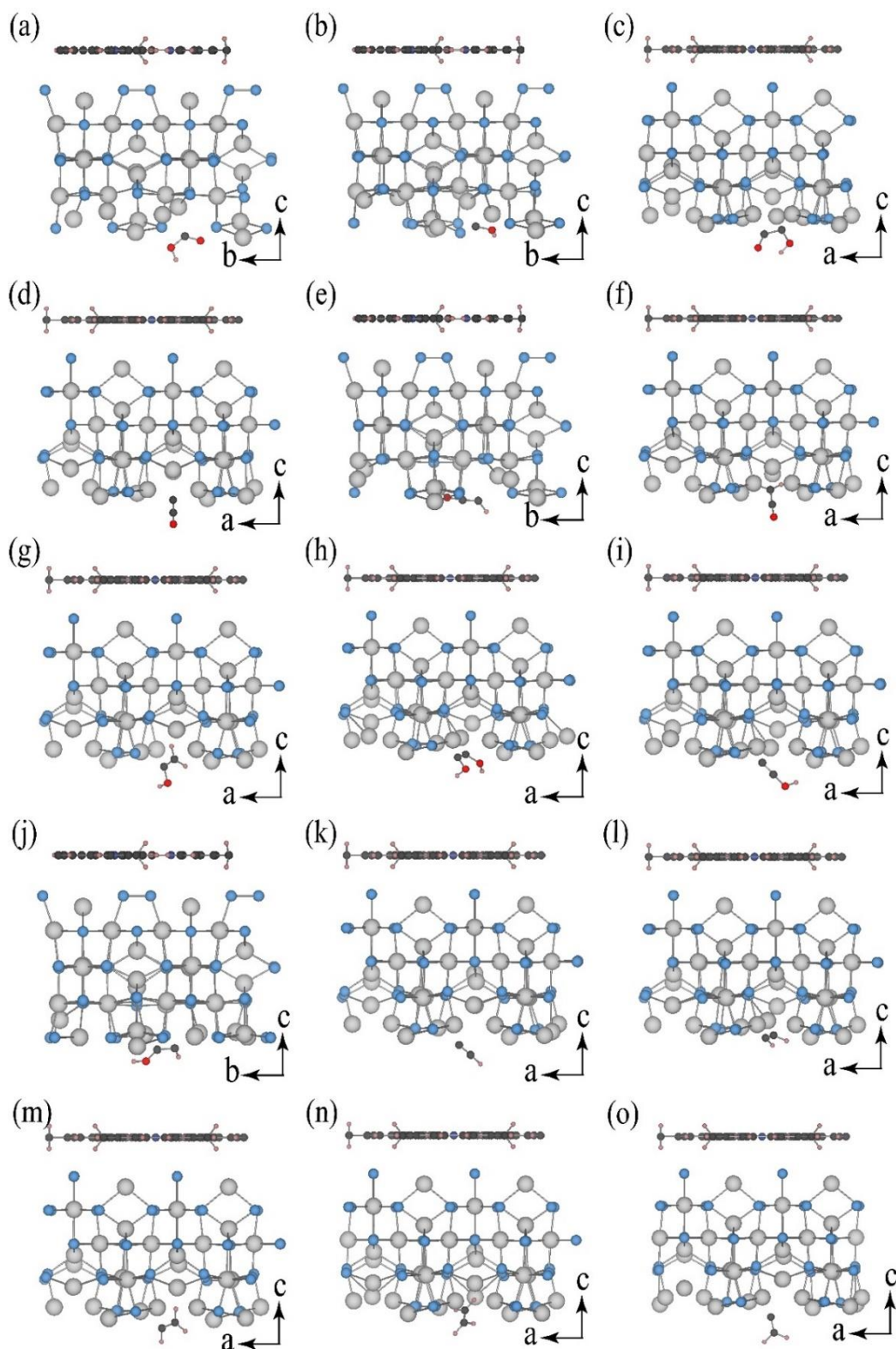
Figure 7.20. View of adsorbed intermediates **(a)** OCOH*, **(b)** COH* over HU2, and **(c)** OCCOH*, **(d)** C₂O*, **(e)** OCCH*, **(f)** OCCH₂*, **(g)** HOCCH₂*, **(h)** HOCCOH*, **(i)** HOCC*, **(j)** HOCCH*, **(k)** CCH*, **(l)** HCCH*, **(m)** HCCH₂*, **(n)** H₂CCH₂*, **(o)** CCH₂* respectively.

However, this endothermicity is compensated by high exothermic formation of CO (3) from *OCOH (2). Further, the less activated *CO (3) dimerized product *OCCO completely

breaks up to two *CO molecules upon optimization. Therefore, the slight endothermic formation (**Figure 7.21a)** of activated *COH (4) from *CO (3) was considered that favorably couple with the *CO, adsorbed over HU1 to form *OCCOH (5) which show its presence in experimental in-situ FTIR spectra. The intermediate *OCCOH (5) is stabilized by the intramolecular H-bonding in the cis form.
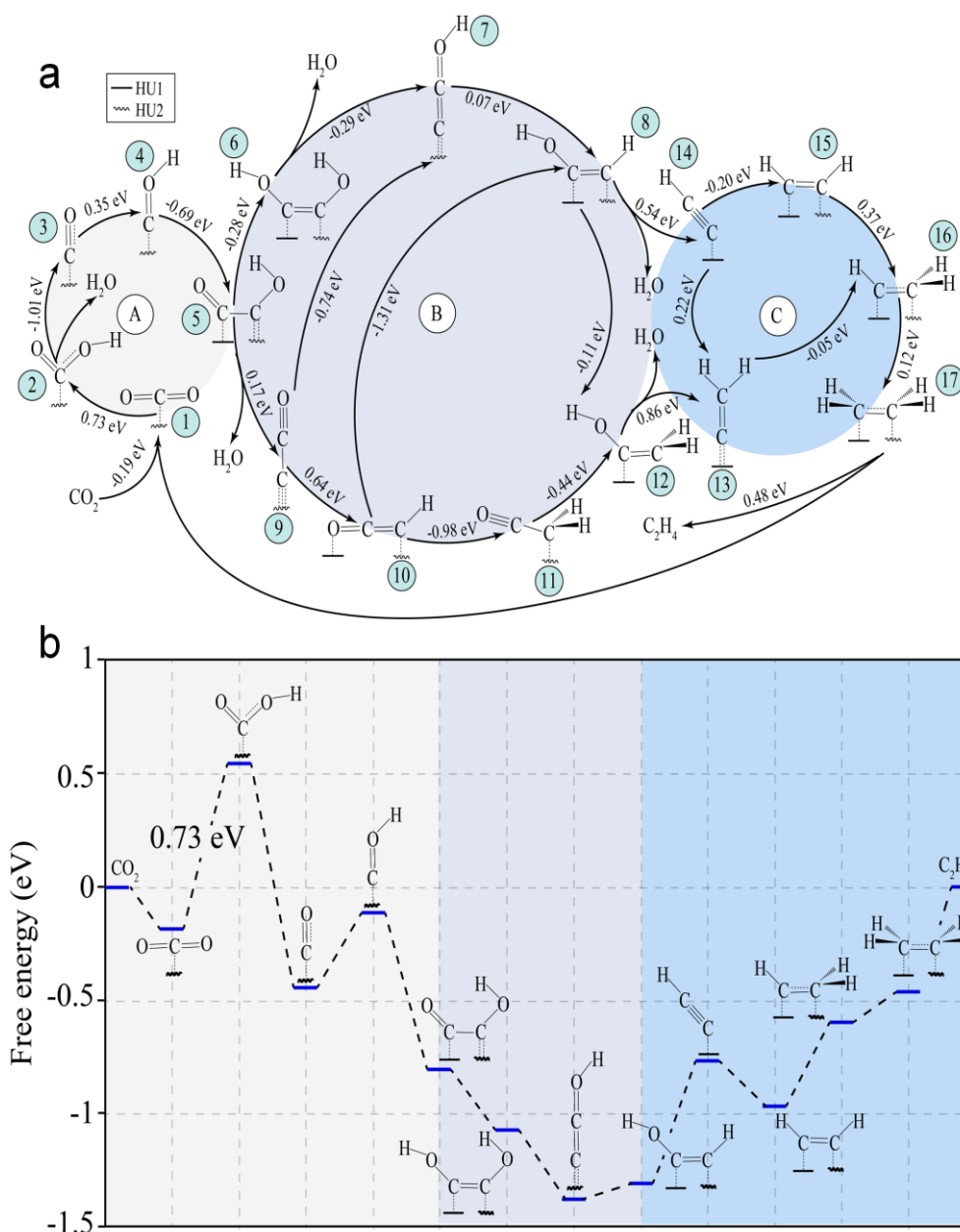
Figure 7.21. (**a**) All possible pathways for the formation of C_2H_4 along with the corresponding free energy changes in between intermediates. CO_2 to C_2H_4 formation was expressed in 3 segments, A, B and C which are formation of *OCCOH, removal of O' and formation of C_2H_4 from carbide intermediate respectively. Each intermediate was named by numbers (1→16). (**b**) Free energy diagram for the most suitable pathway among all different possibilities of C_2H_4 formation on **In$_{2.77}$S$_4$(P)** surface, respectively.

Light-Induced Charge Accumulation on Polarized Indium in In₂.₇₇S₄ from Porous Organic Polymer Tailoring C-C Coupling to Produce Ethylene from CO₂

Chapter 7

In the next part, removal of first oxygen from *OCCOH (5) can take place by either single protonation of -COH or subsequent protonation of -CO group followed by removal of H_2O that produces $*C_2O$ (9) or *HOCC (7), respectively. Both $*C_2O$ (9) and *HOCC (7) are stabilized by extended conjugation, however, the formation of *HOCC (7) is more favorable than $*C_2O$ (9). This is because, the first protonation on -CO of *OCCOH (5) forms *OHCCOH (6) that is stabilized by the intra-molecular hydrogen binding as well as +R effect of trans OH group, hence shows better stability than C_2O (9). For the second oxygen removal, further protonation of $*C_2O$ (9) or *HOCC (7) and subsequent oxygenate intermediates can occur on either C or O atom that finally form HOCCH (8) or $HOCCH_2$ (12). Both the final oxygenate products are stabilized by the +R effect of -OH group. Hence, one step C-protonation of HOCC (7) favorably form HOCCH (8). On the other hand, during the formation of $HOCCH_2$ (12) from C_2O (9), by double C-protonation followed by O-protonation, the first C-protonation to form OCCH (10) is unfavorable due to the loss of extended conjugation stability of C_2O (9). However, the subsequent C-protonation is favorable as the produced $OCCH_2$ (11) is stabilized by tautomerization. Further, removal of OH from $HOCCH_2$ (12) in the form H_2O is more endothermic than in the case of HOCCH (8). This favors the formation of CCH (14) which participate in alternating proton acceptance mechanism that finally forms C_2H_4 (17). Considering all possible pathways, CO_2 can yield C_2H_4 by 10 different mechanisms. Most favorable mechanism of these can be chosen on the basis of its least endothermic rate determining step (RDS). This is because the overpotential of a particular reaction mechanism depends on the potential of the RDS. The endothermicity is highest (0.86 eV) for the RDS of 1st, 5th, 7th, and 9th of possible pathways and can be discarded (**Figure 7.22, 7.25, 7.27, 7.29**). For other mechanisms, this endothermicity decreases to 0.73 eV and hence, further refining is carried by considering the highest endothermicity of the steps other than RDS. Accordingly, 4th and 8th mechanism show highest endothermicity of 0.64 eV and they are discarded further. (**Figure 7.24, 7.28**). In the remaining pathways endothermicity decrease to 0.57 eV (**Figure 7.21a, 7.23, 7.26, 7.30**) and therefore, have highest probability to be followed for the actual reaction. Finally, due to the extra stabilization of *OHCCOH compared to *C2O the 2nd pathway (**Figure 7.21b**) has been selected as the suitable reaction mechanism of C_2H_4 formation on charge polarized "In" centers. This mechanistic pathway rationalizes the synergistic endeavor of POPs and differentially charged coordinately unsaturated "In" centers for C-C coupling reaction. Moreover, the less selective CO formation by statistically less and isolated "In" centers are also validated by this unique approach.

Figure 7.22. Free energy diagram of 1st possible pathway.

Figure 7.23. Free energy diagram of 3rd possible pathway. 2nd possibility as depicted in **Figure 7.21b**.

Figure 7.24. Free energy diagram of 4th possible pathway.

Light-Induced Charge Accumulation on Polarized Indium in In$_{2.77}$S$_4$ from Porous Organic Polymer Tailoring C-C Coupling to Produce Ethylene from CO$_2$

Chapter 7

Figure 7.25. Free energy diagram of 5th possible pathway.

Figure 7.26. Free energy diagram of 6th possible pathway.

Figure 7.27. Free energy diagram of 7th possible pathway.
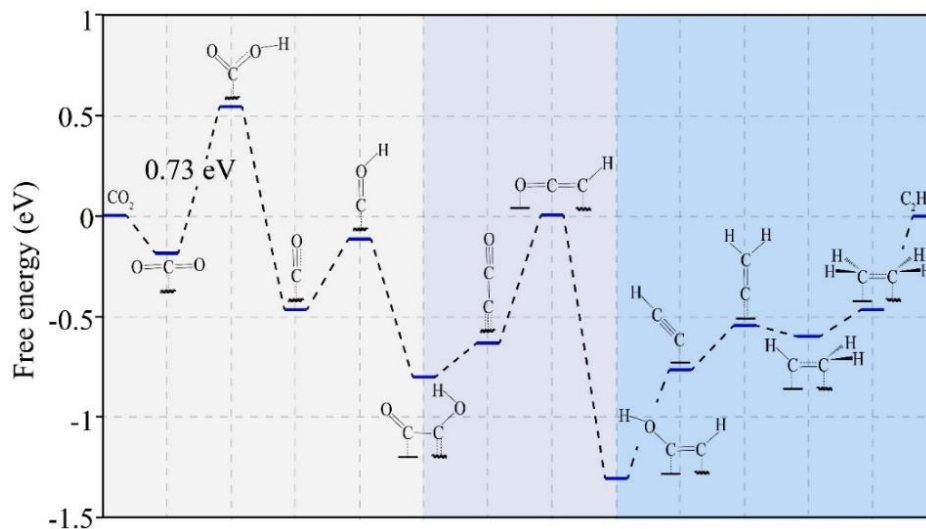
Figure 7.28. Free energy diagram of 8th possible pathway.
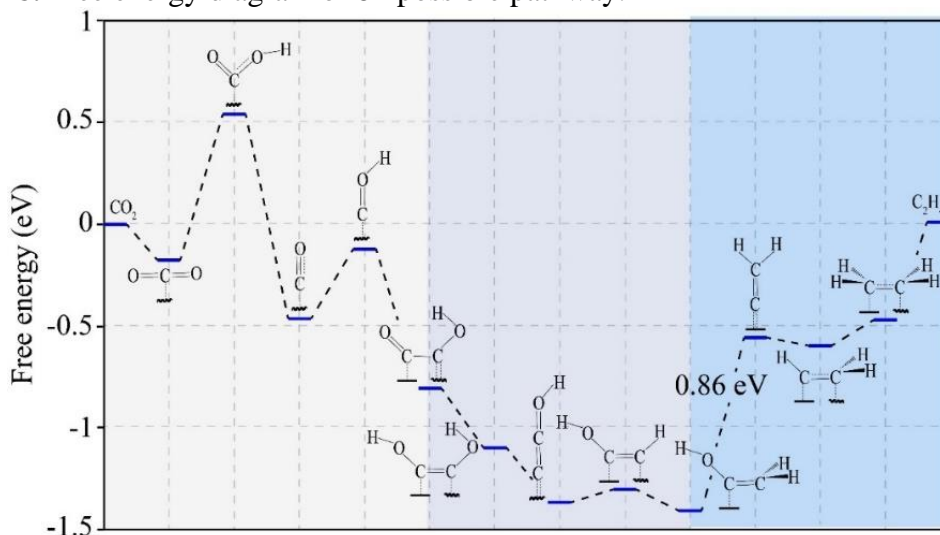
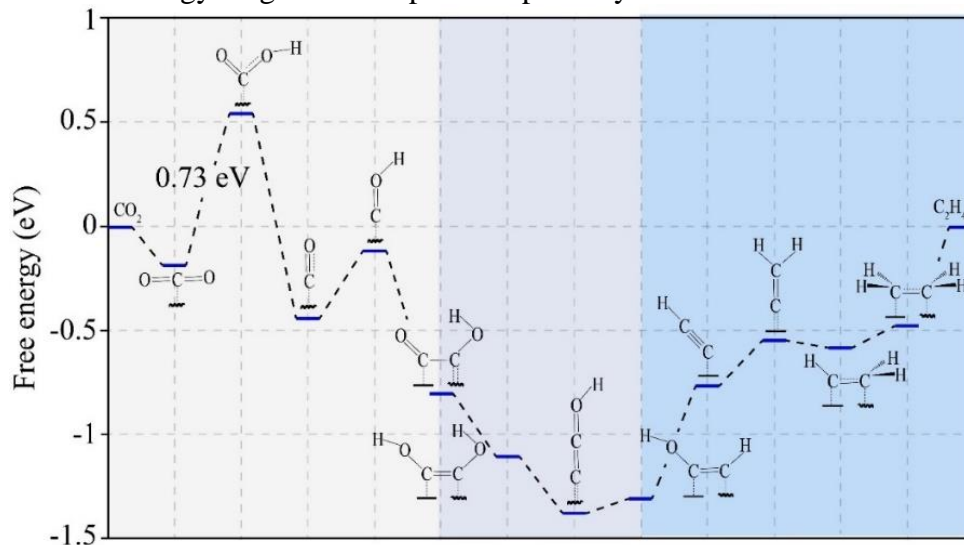**Figure 7.29.** Free energy diagram of 9th possible pathway.

Figure 7.30. Free energy diagram of 10th possible pathway.

Light-Induced Charge Accumulation on Polarized Indium in In$_{2.77}$S$_4$ from Porous Organic Polymer Tailoring C-C Coupling to Produce Ethylene from CO$_2$

Chapter 7

7.6. Conclusion

We have developed a photo-active **In$_{2.77}$S$_4$** flower and POP based porous photo-composite **In$_{2.77}$S$_4$(POP)**, which upon illumination converts CO$_2$ to ethylene (C$_2$H$_4$) selectively. To best of our knowledge in photocatalytic systems, this is the highest ever performance reported in the literature. XPS and XAS results showed the presence of In atoms with different charges in **In$_{2.77}$S$_4$**. The surface reaction sites of our newly developed porous photo-composite **In$_{2.77}$S$_4$(POP)** builds up with four coordinated In^{2+} and six coordinated In^{3+} sites which play a vital role in CO$_2$ to multi-carbon (C$_{2+}$) product formation. Moreover, the synergistic effect of POPs and **In$_{2.77}$S$_4$** enhanced the overall CO$_2$ photo-reduction performance *via* rarely observed Z-scheme pathway rather than type-II mechanism. Further, for the very first time we have identified key reaction intermediates, systematically investigated all the plausible mechanistic pathway, and established the structure activity relationship for light illuminated CO$_2$ to C$_2$H$_4$ formation with the help of *in-situ* DRIFTS and DFT analysis. Our detailed analysis sheds light on the most favorable mechanistic pathway, which can yield mainly CO$_2$ to C$_2$H$_4$. This work offers a new paradigm to accomplish CO$_2$ to multi carbon (C$_{2+}$) product formation under visible light illumination.

7.7. References

1. White, J. L.; Baruch, M. F.; Pander, J. E.; Hu, Y.; Fortmeyer, I. C.; Park, J. E.; Zhang, T.; Liao, K.; Gu, J.; Yan, Y.; Shaw, T. W.; Abelev, E.; Bocarsly, A. B., Light-Driven Heterogeneous Reduction of Carbon Dioxide: Photocatalysts and Photoelectrodes. *Chem. Rev.* **2015,** *115*, 12888-12935.

2. Albero, J.; Peng, Y.; García, H., Photocatalytic CO$_2$ Reduction to C2+ Products. *ACS Catal.* **2020,** *10* (10), 5734-5749.

3. Guo, Z.; Chen, G.; Cometto, C.; Ma, B.; Zhao, H.; Groizard, T.; Chen, L.; Fan, H.; Man, W.-L.; Yiu, S.-M.; Lau, K.-C.; Lau, T.-C.; Robert, M., Selectivity Control of CO Versus HCOO$^-$ Production in the Visible-Light-Driven Catalytic Reduction of CO$_2$ with Two Cooperative Metal Sites. *Nat. Catal.* **2019,** *2*, 801-808.

4. Wang, W.; Deng, C.; Xie, S.; Li, Y.; Zhang, W.; Sheng, H.; Chen, C.; Zhao, J., Photocatalytic C–C Coupling from Carbon Dioxide Reduction on Copper Oxide with Mixed-Valence Copper(I)/Copper(II). *J. Am. Chem. Soc.* **2021,** *143*, 2984-2993.

5. Ma, W.; Xie, S.; Liu, T.; Fan, Q.; Ye, J.; Sun, F.; Jiang, Z.; Zhang, Q.; Cheng, J.; Wang, Y., Electrocatalytic Reduction of CO_2 to Ethylene and Ethanol through Hydrogen-Assisted C–C Coupling over Fluorine-Modified Copper. *Nat. Catal.* **2020,** *3*, 478-487.

6. Chen, Y.; Fan, Z.; Wang, J.; Ling, C.; Niu, W.; Huang, Z.; Liu, G.; Chen, B.; Lai, Z.; Liu, X.; Li, B.; Zong, Y.; Gu, L.; Wang, J.; Wang, X.; Zhang, H., Ethylene Selectivity in Electrocatalytic CO_2 Reduction on Cu Nanomaterials: A Crystal Phase-Dependent Study. *J. Am. Chem. Soc.* **2020,** *142*, 12760-12766.

7. Li, F.; Thevenon, A.; Rosas-Hernández, A.; Wang, Z.; Li, Y.; Gabardo, C. M.; Ozden, A.; Dinh, C. T.; Li, J.; Wang, Y.; Edwards, J. P.; Xu, Y.; McCallum, C.; Tao, L.; Liang, Z.-Q.; Luo, M.; Wang, X.; Li, H.; O'Brien, C. P.; Tan, C.-S.; Nam, D.-H.; Quintero-Bermudez, R.; Zhuang, T.-T.; Li, Y. C.; Han, Z.; Britt, R. D.; Sinton, D.; Agapie, T.; Peters, J. C.; Sargent, E. H., Molecular Tuning of CO_2-to-Ethylene Conversion. *Nature* **2020,** *577*, 509-513.

8. Chen, X.; Chen, J.; Alghoraibi, N. M.; Henckel, D. A.; Zhang, R.; Nwabara, U. O.; Madsen, K. E.; Kenis, P. J. A.; Zimmerman, S. C.; Gewirth, A. A., Electrochemical CO_2-to-Ethylene Conversion on Polyamine-Incorporated Cu Electrodes. *Nat. Catal.* **2021,** *4*, 20-27.

9. Zhang, T.; Xing, G.; Chen, W.; Chen, L., Porous Organic Polymers: a Promising Platform for Efficient Photocatalysis. *Mater. Chem. Front.* **2020,** *4*, 332-353.

10. Rehmat, N.; Toffoletti, A.; Mahmood, Z.; Zhang, X.; Zhao, J.; Barbon, A., Carbazole-Perylenebisimide Electron Donor/Acceptor Dyads Showing Efficient Spin Orbit Charge Transfer Intersystem Crossing (SOCT-ISC) and Photo-Driven Intermolecular Electron Transfer. *J. Mater. Chem. C* **2020,** *8*, 4701-4712.

11. Li, S. Y.; Du, Z. N.; Zhang, Y. C., In Air Template-Free Synthesis of In_2S_3 Hierarchical Nanostructure from $InCl_3 \cdot 4H_2O$ and Thiourea. *Adv. Mater. Res.* **2011,** *152-153*, 63-66.

12. Klementiev, K.; Chernikov, R., XAFS Mass: a Program for Calculating the Optimal Mass of XAFS Samples. *J. Phys. Conf. Ser.* **2016,** *712*, 012008.

13. Ravel, B.; Newville, M., Athena, Artemis, Hephaestus: Data Analysis for X-Ray Absorption Spectroscopy using Ifeeffit. *J. Synchrotron Radiat.* **2005,** *12* (4), 537-541.

14. Teo, B. K., EXAFS*:* Basic Principles and Data Analysis. *Springer Sci. Busin. Media.* **2012,** *9.* 456-519.

15. Martini, A.; Signorile, M.; Negri, C.; Kvande, K.; Lomachenko, K. A.; Svelle, S.; Beato, P.; Berlier, G.; Borfecchia, E.; Bordiga, S., EXAFS Wavelet Transform Analysis of Cu-

Light-Induced Charge Accumulation on Polarized Indium in In$_{2.77}$S$_4$ from Porous Organic Polymer Tailoring C-C Coupling to Produce Ethylene from CO$_2$

Chapter 7

MOR Zeolites for the Direct Methane to Methanol Conversion. *Phys. Chem. Chem. Phys.* **2020,** *22*, 18950-18963.

16. Qin, J.-S.; Yuan, S.; Zhang, L.; Li, B.; Du, D.-Y.; Huang, N.; Guan, W.; Drake, H. F.; Pang, J.; Lan, Y.-Q.; Alsalme, A.; Zhou, H.-C., Creating Well-Defined Hexabenzocoronene in Zirconium Metal–Organic Framework by Postsynthetic Annulation. *J. Am. Chem. Soc.* **2019,** *141*, 2054-2060.

17. Kresse, G.; Hafner, J., Ab Initio Molecular Dynamics for Liquid Metals. *Phys. Rev. B* **1993,** *47*, 558-561.

18. Kresse, G.; Joubert, D., From Ultrasoft Pseudopotentials to the Projector Augmented-Wave Method. *Phys. Rev. B* **1999,** *59*, 1758-1775.

19. Perdew, J. P.; Burke, K.; Ernzerhof, M., Generalized Gradient Approximation Made Simple. *Phys. Rev. Lett.* **1996,** *77*, 3865-3868.

20. Sharma, L.; Katiyar, N. K.; Parui, A.; Das, R.; Kumar, R.; Tiwary, C. S.; Singh, A. K.; Halder, A.; Biswas, K., Low-Cost High Entropy Alloy (HEA) for High-Efficiency Oxygen Evolution Reaction (OER). *Nano Res.* **2021**.

21. Zhao, D.; Wang, Y.; Dong, C.-L.; Huang, Y.-C.; Chen, J.; Xue, F.; Shen, S.; Guo, L., Boron-Doped Nitrogen-Deficient Carbon Nitride-Based Z-Scheme Heterostructures for Photocatalytic Overall Water Splitting. *Nat. Energy* **2021,** *6*, 388-397.

22. Wang, Q.; Hisatomi, T.; Jia, Q.; Tokudome, H.; Zhong, M.; Wang, C.; Pan, Z.; Takata, T.; Nakabayashi, M.; Shibata, N.; Li, Y.; Sharp, I. D.; Kudo, A.; Yamada, T.; Domen, K., Scalable Water Splitting on Particulate Photocatalyst Sheets with a Solar-to-Hydrogen Energy Conversion Efficiency Exceeding 1%. *Nat. Mater.* **2016,** *15*, 611-615.

23. Xiong, S.; Tang, X.; Pan, C.; Li, L.; Tang, J.; Yu, G., Carbazole-Bearing Porous Organic Polymers with a Mulberry-Like Morphology for Efficient Iodine Capture. *ACS Appl. Mater. Interfaces* **2019,** *11*, 27335-27342.

24. Das, R.; Chakraborty, S.; Peter, S. C., Systematic Assessment of Solvent Selection in Photocatalytic CO$_2$ Reduction. *ACS Energy Lett.* **2021**, 3270-3274.

25. Xie, S.; Ma, W.; Wu, X.; Zhang, H.; Zhang, Q.; Wang, Y.; Wang, Y., Photocatalytic and Electrocatalytic Transformations of C1 Molecules Involving C–C Coupling. *Energy Environ. Sci.* **2021,** *14*, 37-89.

26. Zhang, W.; Hu, Y.; Ma, L.; Zhu, G.; Wang, Y.; Xue, X.; Chen, R.; Yang, S.; Jin, Z., Progress and Perspective of Electrocatalytic CO$_2$ Reduction for Renewable Carbonaceous Fuels and Chemicals. *Adv. Sci.* **2018,** *5*, 1700275.

27. Xu, Y.-F.; Yang, M.-Z.; Chen, B.-X.; Wang, X.-D.; Chen, H.-Y.; Kuang, D.-B.; Su, C.-Y., A CsPbBr$_3$ Perovskite Quantum Dot/Graphene Oxide Composite for Photocatalytic CO$_2$ Reduction. *J. Am. Chem. Soc.* **2017,** *139*, 5660-5663.

28. Shao, L.; Li, J.; Liang, X.; Xie, T.; Meng, S.; Jiang, D.; Chen, M., Novel β-In$_{2.77}$S$_4$ Nanosheet-Assembled Hierarchical Microspheres: Synthesis and High Performance for Photocatalytic Reduction of Cr(vi). *RSC Adv.* **2016,** *6*, 18227-18234.

29. Yuan, R.; Yan, Z.; Shaga, A.; He, H., Solvent-Free Mechanochemical Synthesis of a Carbazole-Based Porous Organic Polymer with High CO$_2$ Capture and Separation. *J. Solid State Chem.* **2020,** *287*, 121327.

30. Yu, W.; Gu, S.; Fu, Y.; Xiong, S.; Pan, C.; Liu, Y.; Yu, G., Carbazole-Decorated Covalent Triazine Frameworks: Novel Nonmetal Catalysts for Carbon Dioxide Fixation and Oxygen Reduction Reaction. *J. Catal.* **2018,** *362*, 1-9.

31. Das, R.; Sarkar, S.; Kumar, R.; D. Ramarao, S.; Cherevotan, A.; Jasil, M.; Vinod, C. P.; Singh, A. K.; Peter, S. C., Noble-Metal-Free Heterojunction Photocatalyst for Selective CO$_2$ Reduction to Methane upon Induced Strain Relaxation. *ACS Catal.* **2022,** *12*, 687-697.

32. Li, X.; Sun, Y.; Xu, J.; Shao, Y.; Wu, J.; Xu, X.; Pan, Y.; Ju, H.; Zhu, J.; Xie, Y., Selective Visible-Light-Driven Photocatalytic CO$_2$ Reduction to CH$_4$ Mediated by Atomically Thin CuIn$_5$S$_8$ Layers. *Nat. Energy* **2019,** *4*, 690-699.

33. Li, J.; Pan, W.; Liu, Q.; Chen, Z.; Chen, Z.; Feng, X.; Chen, H., Interfacial Engineering of Bi$_{19}$Br$_3$S$_{27}$ Nanowires Promotes Metallic Photocatalytic CO$_2$ Reduction Activity under Near-Infrared Light Irradiation. *J. Am. Chem. Soc.* **2021,** *143*, 6551-6559.

34. van de Krol, R.; Goossens, A.; Schoonman, J., Mott-Schottky Analysis of Nanometer-Scale Thin-Film Anatase TiO$_2$. *J. Electrochem. Soc.* **1997,** *144*, 1723-1727.

35. Jiang, Y.; Liao, J.-F.; Chen, H.-Y.; Zhang, H.-H.; Li, J.-Y.; Wang, X.-D.; Kuang, D.-B. J. C., All-Solid-State Z-Scheme α-Fe$_2$O$_3$/Amine-RGO/CsPbBr$_3$ Hybrids for Visible-Light-Driven Photocatalytic CO$_2$ Reduction. *Chem* **2020,** *6*, 766-780.

36. Sun, S.; Yuan, D.; Xu, Y.; Wang, A.; Deng, Z., Ligand-Mediated Synthesis of Shape-Controlled Cesium Lead Halide Perovskite Nanocrystals via Reprecipitation Process at Room Temperature. *ACS Nano* **2016,** *10*, 3648-3657.

37. Das, R.; Das, K.; Churipard, S. R.; Peter, S. C., Activating Oxygen Deficient TiO$_2$ in Visible Region by Bi$_2$MoO$_6$ for CO$_2$ Photoreduction to Methanol. *Chem. Commun.* **2022,** *58*, 6638-6641.

Light-Induced Charge Accumulation on Polarized Indium in In$_{2.77}$S$_4$ from Porous Organic Polymer Tailoring C-C Coupling to Produce Ethylene from CO$_2$

Chapter 7

38. Das, R.; Das, K.; Ray, B.; Vinod, C. P.; Peter, S. C., Green Transformation of CO$_2$ to Ethanol using Water and Sunlight by the Combined Effect of Naturally Abundant Red Phosphorus and Bi$_2$MoO$_6$. *Energy Environ. Sci.* **2022**, *5*,1967-1976.

39. Zheng, Y.; Zhou, T.; Zhang, C.; Mao, J.; Liu, H.; Guo, Z., Boosted Charge Transfer in SnS/SnO$_2$ Heterostructures: Toward High Rate Capability for Sodium-Ion Batteries. *Angew. Chem. Int. Ed.* **2016,** *55*, 3408-3413.

40. Tan, T. H.; Xie, B.; Ng, Y. H.; Abdullah, S. F. B.; Tang, H. Y. M.; Bedford, N.; Taylor, R. A.; Aguey-Zinsou, K.-F.; Amal, R.; Scott, J., Unlocking the Potential of the Formate Pathway in the Photo-Assisted Sabatier reaction. *Nat. Catal.* **2020,** *3*, 1034-1043.

41. Colomer, M. T., Straightforward Synthesis of Ti-Doped YSZ Gels by Chemical Modification of the Precursors Alkoxides. *J. Sol-Gel Sci. Technol.* **2013,** *67*, 135-144.

42. Liu, Q.; Cheng, H.; Chen, T.; Lo, T. W. B.; Xiang, Z.; Wang, F., Regulating the *OCCHO Intermediate Pathway Towards Highly Selective Photocatalytic CO$_2$ Reduction to CH$_3$CHO over Locally Crystallized Carbon Nitride. *Energy Environ. Sci.* **2022,** *15*, 225-233.

43. Zhang, R.; Wang, H.; Tang, S.; Liu, C.; Dong, F.; Yue, H.; Liang, B., Photocatalytic Oxidative Dehydrogenation of Ethane Using CO$_2$ as a Soft Oxidant over Pd/TiO$_2$ Catalysts to C$_2$H$_4$ and Syngas. *ACS Catal.* **2018,** *8*, 9280-9286.

Chapter 8

Summary and Future outlook

Photocatalytic CO_2 reduction is one of the emerging potential ways of cultivating renewable energy sources. It is considered as a green method as it uses abundant sunlight and water. Therefore, this particular area was chosen in this work for the production of high-energy dense fuels as alternatives to the existing energy sources. The initial chapters focused on the conversion of CO_2 to high market demanded C1 fuels such as methene and methanol. Although the production of these chemicals from CO_2 were highlighted in various platforms including publications and patents, this thesis introduces novel approaches to generate, rather discover novel catalysts to improve the efficiency and selectivity. While executing this research an important observation opens up an unwrap area of photocatalysis. The photolysis of organic additives under UV-visible light was seen. Unfortunately, these photolyze products are similar to CO_2 reduced products. Hence, this provides guidelines about the judicious selection of solvents for PCR, which is discussed in **Chapter 2**.

In the next chapter (**Chapter 3**), methane was synthesized from CO_2. The introduction of second semiconductor provides extra room to the first semiconductor for strain relaxation when they form heterostructure. To the best of our knowledge, strain relaxation concept in PCR reporting for the first time, which helps in obtaining very high yield and more than 99% methane selectivity. The restrictions of carbide mechanism on oxide semiconductor catalysts were also demonstrated for the first time. Methanol was the next target (**Chapter 4**), because of its niche market in global standard and can be generated by stopping the reduction process just one step ahead of methane formation. Here, oxygen vacancies were introduced deliberately to activate CO_2. On the other hand, Bi_2MoO_6 was added as electron donor. In the meantime, the concept of charge polarization has been efficiently exploited for C-C coupling reaction. $Bi_{19}S_{27}Cl_3$ was chosen for this purpose because it has 3 different Bi centers. Interestingly, ethanol was obtained as the major product. Here, COCOH* intermediate was identified as first C-C coupling step. For further understanding, the investigation was done on Bi_2S_3 as well having only one type of Bi center. However, only C1 products were found. Since the ethanol formation efficiency found less in this work, we extended our focus to boost the activity of ethanol formation as discussed in **Chapter 6**. Low-cost red phosphorus was used as a catalyst

along with Bi_2MoO_6. Record high amount of ethanol was produced even under direct sunlight and in various weather conditions. From primary kinetic isotopic analysis, two OCH_3 coupling process was proved. Thereafter in **Chapter 7**, a spinel compound having metal with two different oxidation states was employed for facilitating C-C coupling process. Spinel catalyst was wrapped by porous organic polymer for availing synergistic effect of better gas adsorption and light absorption. Very high amount of ethylene (highest as per the current literature survey) was generated by this strategy. Moreover, the ethylene formation mechanism was established for the first time from the DFT calculation in the field of PCR. This step wise progress of our work is given in **Scheme 8.1**. The motivation of these studies was obtained from previous pioneering studies which are discussed in brief in **Chapter 1**. We believe that our findings will provide some important scientific insight in the field of CO_2 reduction, photocatalysis, heterogeneous catalysis, green or environmental chemistry and renewable energy.

The improvisation of science and technology requires several additional optimizations by using various advanced techniques. Since the mechanism involved in the conversion of CO_2 to chemicals and fuels are complex in nature, more deep advanced analysis by different methods in combination with theoretical calculations required. Our discovery motivates to explore some excusive ideas on halide perovskites, plasmonic and covalent organic framework based photocatalytic systems. Supramolecular photocatalysts, Mxenes, bioinspired catalysts etc are emerging materials, where several chemical concepts can be modulated. Photo-electrocatalysis, photo-thermocatalysis, and plasmonic catalysis are the 3 major segments expected to have more avenues on testing PCR. In this thesis work I have explored in-situ IR and in-situ EPR study, which are absolute jewels in PCR. However, PCR is still limited compared to thermo and electrochemical methods because of the feasibility issue. In-situ Raman spectroscopy can be explored, which can monitor surface modification during catalysis and complementary to IR or even beyond when IR is inactive. This thesis motivates to investigate this particular phenomenon and its effect on overall catalysis by in-situ XPS, EXAFS and TEM. Artificial intelligence has predicted several outcomes of rigorous experiments. However, its use not yet explored in PCR due to thelack of adequate amount of data. Finally technoeconomic analysis and life cycle analysis can help to take the laboratory technology towards the commercialization.
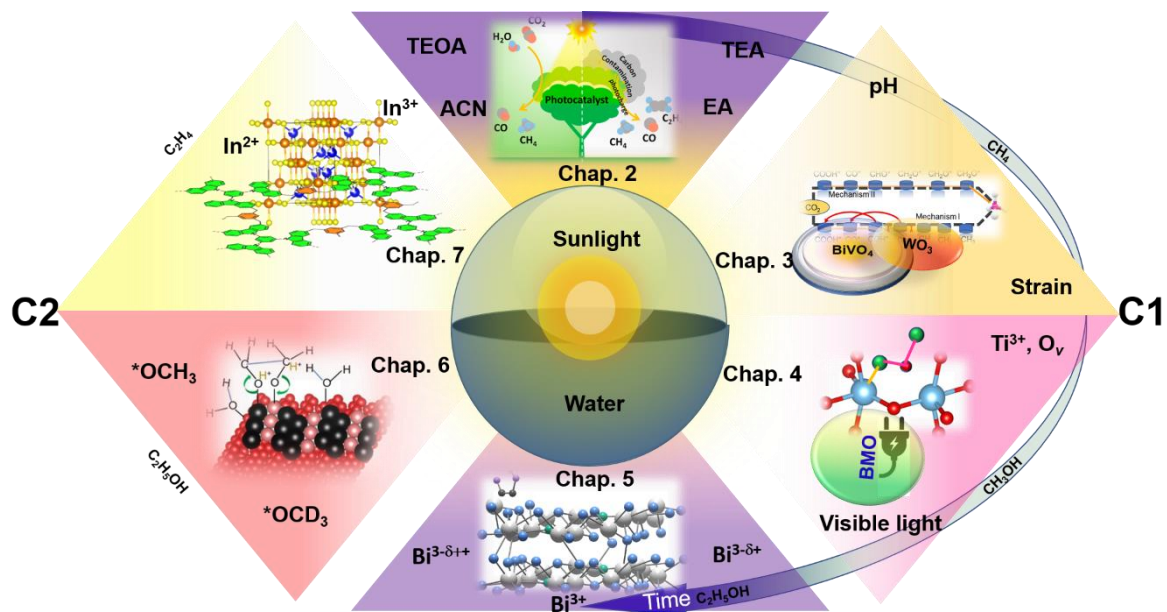
Scheme 1. Systematic development of photocatalysts for producing solar fuels from CO_2 reduction, starting from C1 to multi-carbon products.

LIST OF PUBLICATIONS

Peer-Reviewed Journals (Published 1st authored)

(1) **Das, R.,** Chakraborty, S. & Peter, S. C. Systematic Assessment of Solvent Selection in Photocatalytic CO_2 Reduction. *ACS Energy Lett.* **2021, 6,** 3270-3274.

(2) **Das, R.,** Sarkar, S., Ramarao, S. D., Jasil, P., Cherovotan A., Singh A., M.; Peter, S. C. Noble-Metal-Free Heterojunction Photocatalyst for Selective CO_2 Reduction to Methane upon Induced Strain Relaxation. *ACS Catal*. **2022,** *12*, 687-697.

(3) **Das, R.,** Das, K., Ray, B., Vinod, C. P., Peter, S. C. Green Transformation of CO_2 to Ethanol Using Water and Sunlight by the Combined Effect of Naturally Abundant Red Phosphorus and Bi_2MoO_6. *Energy Environ. Sci.* **2022**, *15*, 1967-1976.

(4) **Das, R**., Das, K., Churipard, S. R., Peter, S. C. Activating Oxygen deficient TiO_2 in visible region by Bi_2MoO_6 for CO_2 photoreduction to Methanol. *Chem. Commun.* **2022**, *58*, 6638-6641.

Manuscript under consideration

(5) **Das, R.,** Paul, R., Parui, A., Rotri, A., Atzori, C., Lomachenko, K., Singh, A., Mondal, J., Peter, S. C. Charge Accumulation from Porous Organic Polymer to Polarized In Sites in $In_{2.77}S_4$-POP Tailoring C-C Coupling Reaction to Produce Ethylene from CO_2 under Photo-irradiation (***ACS Nano).***

(6) **Das, R.,** Das, K., Parui, A., Singh, A., Vinod, C., Peter, S. C. Intrinsic Charge Polarization Promotes Selective C-C Coupling Reaction During Photoreduction of CO_2 to Ethanol (***J. Am. Chem. Soc.).***

Manuscript under preparation

(7) **Das, R**., Paul, R., Peter, S. C., Mondal, J. Tuning Photocatalytic CO_2 Reduction by Metal Precursor Manipulation in Salen-Based Porous Organic Polymer.

(8) **Das, R**., Das, K., Verma, P., Raja, R., Peter, S. C. Plasmonic Cu Single Atom on Zeolitic Alumino Phosphate Framework for CO_2 Photoreduction to C_2H_4.

(9) **Das, R.,** Das, K., Chakroborty, S., Peter, S. C. Using Quantum Confinement Effect of $MAPbBr_xI_{(3-x)}$ Embedded in Porous Silica for Tuning Photothermal CO_2 Reduction Products.

(10) **Das, R**., Paul, R., Mondal, J., Peter, S. C. Porous Organic Polymer Wrapped Cu_2O

Photocatalyst for Fast CO_2 Reduction under Visible Light.

(11) **Das, R.,** Das, K., Chakroborty, S., Peter, S. C. A Review in Catalyst Engineering and Mechanistic Investigation for C2 Product Formation from CO_2 Photoreduction (Invitation from *Nat. Rev. Mater.*).

Peer-Reviewed Journals (Published co-authored)

(1) Sarkar, S.; Ramarao, S. D., Das, T., **Das, R**., Vinod, C. P.; Chakraborty, S., Peter, S. C. Unveiling the Roles of Lattice Strain and Descriptor Species on Pt-like Oxygen Reduction Activity in Pd-Bi catalysts. *ACS Catal*. **2021**, *11*, 800-808.

(2) Cherevotan, A. Raj, J. Dheer, L. Roy, S.; Sarkar, S. **Das, R**. Vinod, C. P., Xu, S. Wells, P. Waghmare, U. W. Peter, S. C. Operando Generated Ordered Heterogeneous Catalyst for the Selective Conversion of CO_2 to Methanol. *ACS Energy Lett.* **2021**, *6*, 509-516.

(3) Bagchi, D., Phukan, N., Sarkar, S., **Das, R**., Ray, B., Bellare, P., Ravishankar, N., Peter, S. C. Ultralow Non-noble Metal Loaded MOF Derived Bi-functional Electrocatalysts for the Oxygen Evolution and Reduction Reactions. *J. Mater. Chem. A,* **2021***, 14*, 9319–9326.

(4) Mondal, S. Sarkar, S. Bagchi, D. Das, T. **Das, R**. Singh, AK. Prasanna, PK. Vinod, C.P., Chakraborty, S., Peter, S. C. Morphology Tuned Pt_3Ge Accelerates Water Dissociation to Industrial Standard Hydrogen Production over a wide pH Range. *Adv. Mater.*, **2022**, *34*, 2202294.

Manuscript under consideration

(5) Das, N., Paul, R., Biswas, S., **Das, R**., Chatterjee, R., Peter, S.C., Mondal, J. Photo-Responsive Signature in Porous Organic Polymer Enables Visible-Light-Driven Metal-Free CO_2 Fixation (*Acs. Sustain. Chem. Eng.*).

(6) Chakroborty, S., **Das, R.,** Das, K., Bagchi D., Singh, A., Vinod., C. P., Peter, S. C. In-Situ Surface Reconstruction Upon Aliovalent Substitution in ZnS to $CuGaS_2$ Selectively Converting CO_2 to Ethylene (*Angew. Chem. Int. Ed.*).

Manuscript under preparation

(7) Chakroborty, S., **Das, R.,** Peter, S. C. Coating BCN on $CsPbBr_3$ for Long-Term CO_2 Photoreduction in Vapor Phase.

(8) Das, K., **Das. R.,** Peter, S. C. Engineering Band Alignment for Selective Ethanol Formation from CO_2 Photoreduction via Cu and In Doping in $AgBiP_2S_6$.

BIOGRAPHY

I was born and raised in a beautiful village of West Bengal and studied Chemistry at Narendrapur Ramakrishna Mission Kolkata and IIT Madras. I developed an early interest in heterogeneous catalysis and solid-state chemistry and my PhD studies in the SCP group focused on 'Sunlight drove CO_2 hydrogenation to fuels by heterogeneous photocatalysts.' I subsequently worked on several classes of oxide, sulphide, halide perovskite, and carbon-based polymeric photocatalysts. I also try to unwrap the electron transfer and product formation mechanism by several *in-situ* and *ex-situ* spectroscopic techniques. I love to travel with my friends. My scientific journey at JNCASR is summarized as the PhD thesis entitled as "***Design and Development of Metal Oxide and Chalcogenides for Solar Fuel Synthesis from Carbon Dioxide***". I am currently working on many more exciting and challenging projects which will be helpful to resolve some real-time problems in the field of energy and environment.